IntechOpen

Optoelectronics

Advanced Device Structures

Edited by Sergei L. Pyshkin and John Ballato

OPTOELECTRONICS - ADVANCED DEVICE STRUCTURES

Edited by **Sergei L. Pyshkin** and **John Ballato**

Optoelectronics - Advanced Device Structures
http://dx.doi.org/10.5772/65136
Edited by Sergei L. Pyshkin and John Ballato

Contributors

A. Abdul Hamid, Norinsan Kamil Othman, Roslinda Shamsudin, Naif Al-Hardan, Francisco Javier De La Hidalga-Wade, Oleksandr Ivanovich Malik, Sanghyun Lee, Kaikai Xu, Chi-Wai Chow, Chien-Hung Yeh, Andrey Kosarev, Norbert Csaba Szekely, Madalina Sabina Sabau, Mircea Bojan, Petre Dorel Teodosescu, Ruby Srivastava, Hai-Zhi Song, Salah A. Ibrahim, Sergey Yurchuk, Sergey Didenko, Sergey Legotin, Oleg Rabinovich, Sergei L. Pyshkin, Yifei Yang, Xiaolu Zhu, Erinn Van Wynsberghe, Ayse Turak, Binhao Wang

Notice

First published in Croatia, 2017 by INTECH d.o.o.
eBook (PDF) Published by IN TECH d.o.o.
Place and year of publication of eBook (PDF): Rijeka, 2019. IntechOpen is the global imprint of IN TECH d.o.o.
Printed in Croatia

Legal deposit, Croatia: National and University Library in Zagreb

Additional hard and PDF copies can be obtained from orders@intechopen.com

Optoelectronics - Advanced Device Structures
Edited by Sergei L. Pyshkin and John Ballato
p. cm.
Print ISBN 978-953-51-3369-8
Online ISBN 978-953-51-3370-4
eBook (PDF) ISBN 978-953-51-4744-2

Meet the editor

John Ballato is a professor of materials science and engineering at Clemson University where he holds the Sirrine Endowed Chair in Optical Fiber. He earned his BS degree in Ceramic Science and Engineering (1993) and his PhD degree in Ceramic and Materials Engineering (1997) from Rutgers, The State University of New Jersey. He has published more than 350 technical papers and holds 34 US and foreign patents. Among numerous other honors, his collaborative work on Anderson-localizing optical fiber was chosen as one of Physics World's Top Ten Breakthroughs for 2014. He is a fellow of the Institute of Electrical and Electronics Engineers (IEEE), the Optical Society of America (OSA), the International Society of Optical Engineering (SPIE), and the American Ceramic Society (ACerS), as well as an elected member of the World Academy of Ceramics and the US National Academy of Inventors.

Contents

Preface XI

Chapter 1 **Properties of GaP Studied over 50 Years 1**
Sergei L. Pyshkin and John Ballato

Chapter 2 **Microcavities for Silica-Fiber-Based Quantum Information Processing 21**
Hai-Zhi Song

Chapter 3 **LED and Phototransistor Simulation 49**
Sergey Yurchuk, Oleg Rabinovich and Sergey Didenko

Chapter 4 **Hybrid Optoelectronic Router for Future Optical Packet-Switched Networks 69**
Salah Ibrahim and Ryo Takahashi

Chapter 5 **Research on the Characteristics of Silicon MOS-Like Light-Emitting Structure by Utilizing the Technology of Field-Induced Optical Radiation Mechanisms 91**
Kaikai Xu

Chapter 6 **Phosphor-LED-Based Wireless Visible Light Communication (VLC) and Its Applications 117**
Chien-Hung Yeh and Chi-Wai Chow

Chapter 7 **Microscopic Particle Manipulation via Optoelectronic Devices 139**
Xiaolu Zhu and Yifei Yang

Chapter 8 **Hybrid Silicon-Organic Heterojunction Structures for Photovoltaic Applications 161**
Andrey Kosarev, Ismael Cosme, Svetlana Mansurova, Antonio J. Olivares and Hiram E. Martinez

Chapter 9 **Modeling of Silicon Photonic Devices for Optical Interconnect Transceiver Circuit Design 187**
Binhao Wang

Chapter 10 **Candidate Materials as Gain Media in Organic, Triplet-Based, Room-Temperature masers Targeting the ISM Bands 211**
Erinn van Wynsberghe and Ayse Turak

Chapter 11 **Analysis of a Resonant AC-AC LED Driver 233**
Teodosescu Petre Dorel, Szekely Norbert Csaba, Sabau Madalina Sabina and Bojan Mircea

Chapter 12 **Ultraviolet Sensors Based on Two-Dimensional Zinc Oxide Structures 251**
Naif H. Al-Hardan, Muhammad Azmi Abdul Hamid, Roslinda Shamsudin and Norinsan Kamil Othman

Chapter 13 **The Optical Phenomena of Interplay between Nanobio Complexes: A Theoretical Insight into Their Biomedical Applications 269**
Ruby Srivastava

Chapter 14 **Sputtered Indium Tin Oxide Films for Optoelectronic Applications 297**
Oleksandr Malik and Francisco Javier de la Hidalga-Wade

Chapter 15 **Surface-Barrier Photodiodes with Transparent Electrodes for High-Performance Detection in the UV-NIR Spectrum 315**
Oleksandr Malik and Francisco Javier De la Hidalga-Wade

Chapter 16 **Spectral Responses in Quantum Efficiency of Emerging Kesterite Thin-Film Solar Cells 341**
Sanghyun Lee and Kent J. Price

Preface

Having emerged in the second half of the twentieth century at the interface between optics and electronics, optoelectronics has rapidly spread around the world as an enabler of novel science and everyday modern conveniences. As global society becomes even more connected through technology, further developments and improvements in new optoelectronic materials and structures are required to meet the requirements for next-generation optoelectronic devices.

With this in mind, together with InTech Publishing since 2011, we are pleased to release this fourth book in the Optoelectronics series. We happily note the growing number of countries, now from every populated continent, participating in this undertaking.

Specialists from more than 20 countries have published in this series their research into the properties of various materials suitable for use in optoelectronic devices, the development of new structures, and results of their practical application.

The future of optoelectronics is indeed bright!

Sergei L. Pyshkin, Editor
Professor, Principal Investigator
Institute of Applied Physics, Academy of Sciences of Moldova
Kishinev, Moldova
Adjunct Professor, Senior Fellow
Clemson University, SC, USA

John Ballato, Coeditor
FIEEE, FOSA, FSPIE, FACerS, NAI
Professor, Center for Optical Materials Science and Engineering Technologies (COMSET)
Department of Materials Science and Engineering
Clemson University, SC, USA

Chapter 1

Properties of GaP Studied over 50 Years

Sergei L. Pyshkin and John Ballato

Additional information is available at the end of the chapter

http://dx.doi.org/10.5772/67852

Abstract

A unique set of GaP semiconductor samples studied for over 50 years has exhibited significant improvement in their properties through the formation of the perfect host crystal lattice and the N-impurity crystal superlattice. This chapter reviews this evolution of properties and discusses their novel utility in advanced optoelectronic devices. More specifically, nitrogen-doped gallium phosphide (GaP:N) crystals that were originally prepared in the 1960s were theorized to form an excitonic crystal (1970s), and the best methods of their bulk, film, and nanoparticle crystal growth have subsequently been developed. The excitonic crystals yield novel and useful properties including enhanced stimulated emission and very bright and broadband luminescence at room temperature, which have been observed. These results provide a new approach to the selection and preparation of "perfect" materials for optoelectronics and offer a unique opportunity to realize a new form of solid-state host—the excitonic crystal—as a high-intensity light source with low thresholds for nonlinear optical effects.

Keywords: long-term evolution of crystal properties, excitonic crystal, close to ideal crystals

1. Introduction

Described herein are studies initiated by one of the authors (SLP) in 1961. Further studies on the same samples were conducted in the later 1960s through 1970s, then again in the 1980s, 1990s, and 2000s making these a very unique set of semi-centennial observations [1–34, 40–42].

One of the most important findings of this study was the observation, first recognized in the 1980s, of a significant improvement over time in the properties of GaP crystals under ambient temperature and pressure. In particular, it was found that ordering of host and impurity

atoms improved over time as did the GaP mechanical properties, luminescence with tunable spectral characteristics, and nonlinear optical effects, not observable in the freshly prepared (imperfect) crystals.

Over time, as confirmed by 50 years of experiments on the same samples, driving forces, such as diffusion along concentration gradients, strain relaxation associated with clustering, and minimization of the free energy associated with properly directed chemical bonds between host atoms, results in an ordered redistribution of impurities and host atoms in the crystal. In the particular case of GaP, as well as other compounds possessing highly volatile components, attempt to accelerate these processes through annealing at increased temperatures cannot be successful due to the potential for thermal decomposition (in GaP—due to P desorption). Accordingly, successful thermal processing of these compounds can only take place at temperatures below the sublimation temperatures of their volatile constituents, requiring a longer annealing time. For instance, as evaluated in the framework of the Ising model, the characteristic time of the substitution reaction during N diffusion along P sites in GaP:N crystals at room temperature constitutes 15–20 years [2]. Hence, the observations of highly excited luminescence and some other phenomena in the crystals made in the 1960–1970s and in the 1980–1990s were then compared with the results obtained in 2005–2014 under similar experimental conditions.

The long-term ordering of doped GaP and other semiconductors has been observed as an important accompanying process, which only can be studied using the same unique set of samples and decade time scales. More specifically, the optical and mechanical properties of single crystalline GaP and some other semiconductors, also grown in the 1960s, have been analyzed. Comparison of the properties of the same crystals was performed in the 1960s, 1970s, 1980s, and 1990s [1, 3–17] along with those of newly made GaP nanocrystals [18–20] and freshly prepared bulk single crystals [21–24]. Jointly with Refs. [25, 26, 31–34], this review provides a generalization of the results on these long-term observations of luminescence, absorption, Raman light scattering, and microhardness of the bulk single crystals in comparison with the same properties of the high-quality GaP nanocrystals. It is shown that the combination of these characterization techniques elucidates the evolution of these crystals over the course of many decades. It also clarifies the ordered state brought about by prolonged room-temperature thermal annealing, and the useful optical properties that accompany such ordering. It is demonstrated that long-term natural stimuli that improve the perfection of crystals prevail over other processes and can lead to novel heterogeneous device systems and new semiconductor devices with high temporal stability.

In this chapter, we summarize more than 50 years of results of the study of evolution of the properties of the GaP crystals stored under normal conditions and, on this basis, we propose a new approach to resource-saving production of optoelectronic materials and unique devices based on them.

2. Bulk perfect crystals

The method to grow gallium phosphide crystals from GaP solution melt was chosen due to the significant temperature reduction of the process and the presence of large amounts of

solvent which dramatically reduce impurities from the container. Note that lamellar crystals grown from this solution melt are the most convenient and economical material in the manufacture of many semiconductor devices.

The influence of the following factors on the quality of the grown single crystals has been investigated: (1) quantity and chemical nature of impurities; (2) geometric shape of the container and conditions of heat rejection; (3) accuracy of the temperature control; and (4) cooling rate and the law of heat-sink cooling.

The solution-melt method of GaP growth is described in detail in Refs. [1, 3, 7]. The focus here is only on the most essential details of the crystal growth.

Synthesis, alloying, and crystallization of Ga-P mixture were combined in a single cycle. Influence of impurities on the growth of GaP crystals was investigated using the highest-purity industrially produced materials at that time (1960) in the former USSR. The growth of the crystals was conducted in a sealed quartz container that was introduced into the programmable furnace with a vibrating mount to agitate the mixture of Ga, P, and any chosen dopant. This agitation was performed to facilitate chemical reaction between components and to avoid a possible explosion of the container in dangerous temperature points of the process of mass crystallization.

In order to study the form and quality of growing crystals, the crystallization process could be interrupted at any temperature below the point of liquidus. This interruption was achieved with the help of a specially designed growth container and its programmable heating furnace, which allow to stop the change of temperature of the solution melt, to identify and examine grown to this time crystals (see details in Refs. [1, 3]).

The solution, carefully heated to slightly over 400°C, was held at this temperature for about 2 h to transform the red phosphorus precursor into its white form. Then, the heating process may be smoothly prolonged until a temperature of about 1200°C is reached, which exceeds the liquidus point for 5% P solution in Ga (1123°C) and creates appropriate conditions for Ga-P reactions. After about 1–3 h, the samples are gradually cooled at a rate of 30°C/h to 600–700°C and then the furnace is turned off and naturally cooled to room temperature.

The following impurities were doped into the GaP individually: Cu, Zn, Cd, In, Si, Ge, Sn, S, Se, Te, Ni, Cr, Fe, Co, Sm, La, Gd, and Sm_2O_3. Typical features of the doped GaP crystals (size, color, polarity, lamellar structure, twinning, the dislocation structure, and others) were compared with similarly grown but undoped crystals.

It was found [1, 3] that the properties of the crystals depend on the chemical nature as well as on the quantity of the selected impurities. Their small admixtures did not significantly change the form of the crystals, while significant change of the crystallization environment composition created changes in forms of growth. It was also found that the following factors most significantly influenced the morphology of GaP crystals grown from the Ga-P solution: (a) the degree of supersaturation, which depends on the temperature of the solution and (b) its first derivative with time; the conditions of the heat crystallization removal and the accuracy of the temperature control in the solution.

Changing crystallization conditions, mainly the rate of cooling of the melt, significantly affects the morphology of crystals. Accordingly, the increase of the cooling rate thus reduced the size of the crystals, but the dislocation density was not changed and was primarily determined by the concentration and chemical nature of the impurities. The number of crystals having isometric forms increased with decreasing of cooling rate resulting in the simultaneous improvement of the quality of the crystal surface. Uneven removal of heat from the walls of the container led to the formation of up to 30-mm crystal needles elongated in the direction of the heat removal.

Significant impact on the crystal quality provides more accurate temperature control. The crystals obtained with the accuracy of temperature control ±0.5°C had the perfect planes (111), low dislocation density, and dimensions that were two to three times larger than the crystals obtained at the same conditions, but with the accuracy of ±5°C. Crystals reached 25 mm in length and had the dislocation density of $\sim 10^3$ cm^{-2}, which is significantly less than that of the crystals obtained with low accuracy of the temperature control [1, 3].

Based on the findings of this investigation, let us now present an overview of the growth of lamellar GaP crystals. The first crystals, having the form of dendritic needles with the length of the order of 5 mm and thickness of 0.15 mm, were grown at the temperature of 1107°C, which is approximately 16°C of undercooling. The crystals represent thin plates in the form of rhombs, triangles, or hexagons. The twinning on the transverse cross sections was observed at the study of microsections and cleaved facets. It turned out that the lamellar GaP crystals contain the plane of twinning, parallel to the planes (111) [1, 22].

The growth process of lamellar crystals can be formally divided into two components: the tangential growth in the plane (111) and layer-by-layer growth in the direction normal to the plane (111). Because the ratio of Ga and P atoms differed significantly from the stoichiometry, it is assumed that diffusion is the process that determines the rate of growth. Accepting the two-stage model of lamellar crystal growth, let us consider the ratio of the contributions of the tangential growth in the plane (111) and layer-by-layer growth in the direction normal to the plane (111). The growth in the tangential direction is limited by diffusion and by the size of the previous layer, that is, is determined by the initial conditions and the shape and size of the plates, formed during the cooling of the solution melt 10–20° below the point of liquidus. Since the formation of the initial crystals occurs in a very short time, the growth in the tangential direction is difficult to control, as it is in the case of the dendritic crystal growth. The growth in the direction normal to the plane (111) is sensitive to the fluctuations of the degree of supersaturation, resulting from the thermal motion of atoms and temperature fluctuations. In general, the better the homogeneity and perfection of the surface of the lamellar GaP crystals, the lesser the ratio of the time necessary for the formation of flat embryos on it, to the time for which the embryo is created on the next plane. The latter, obviously, in an extreme extent depends on fluctuations of the degree of supersaturation in different points of the growing plane and at different points in time. With the deterioration of precision temperature control, the number of fluctuations increases and low-quality crystals grow in the conditions of "entanglement" of the above-noted characteristic times. Small fluctuations of supersaturation also are probably the cause of twinning planes. Increase of the accuracy of temperature

regulation promotes some reduction in the number of twins, and this fact also confirms the notable influence of fluctuations on the twinning [1, 3, 34].

Thus, deteriorations of quality or shape of defects of GaP plates during their growth from Ga-P melt solution were observed in the following cases: (1) at a considerable increase of concentration of impurities in the GaP solution and dependently on the chemical nature of the chosen impurity and (2) at the change of the crystallization conditions, namely, at the sufficient deterioration of the cooling velocity control or in the case of nonuniform heat removal from the container for the crystal growth.

Processes for the formation of dendritic needles and their transformation to platelet crystals take place over a small temperature and time interval. As a result, they are hard to control, while crystal growth is easily controlled in the direction normal to the plate (111), due to the sensitive nature of velocity of the solution cooling and accuracy of the temperature control [1, 3].

The above-stated results imply that only high-quality and carefully controlled growth equipment will yield the highest-quality GaP crystals. However, despite these precautions, the subsequent text shows how to considerably increase the quality and utility of freshly prepared GaP crystals.

3. Elaboration of technologies for fabrication of GaP nanoparticles

GaP nanoparticles have been prepared using white P under mild aqueous low-temperature synthesis conditions using two colloidal methods from mixtures of $GaCl_3 \bullet nH_2O$ and dry $NaBH_4$ or Na_3P and $GaCl_3$ diluted in toluene. Details are provided in Refs. [17–20].

Uniform GaP nanoparticles formed following ultrasonic and other treatments were found to exhibit improved quality in their colloidal stability and brightness of luminescence at room temperature, which is found to be broadband with a maximum at 3 eV. Also discussed is their use in GaP/polymers nanocomposites for light-emissive device structures [28, 30, 31].

Photoluminescence, spontaneous Raman scattering, and X-ray diffraction, together with high-resolution electron microscopy of the nanoparticles prepared under different conditions, were compared with those from bulk single crystals.

For the first time to the best of our knowledge, it is shown that well-aged GaP bulk crystals as well as high-quality GaP nanoparticles have no essential difference in their luminescence behavior, brightness, or spectral position of emitted light.

While bulk and thin-film GaP has been successfully commercialized for many years, their application in nanocomposites as a new optical medium has only recently received attention. This section reviews recent efforts to advance the quality of GaP nanoparticles for light-emissive devices based on polymer/GaP nanocomposites.

This activity is the important milestone in the creation of the nanocomposites for advanced light-emissive device structures because GaP nanoparticles exhibit important luminescent and electroluminescent properties and are compatible with selected polymer matrices.

The quality of GaP nanoparticles was improved using mild aqueous synthesis and different colloidal reactions of Ga and P sources in toluene [26–37]. Ultrasonication and ultracentrifugation were applied during the synthesis and selection of nanoparticles to increase their quality and to control the size of the nanoparticles.

In 2005, the authors developed methods to fabricate GaP nanoparticles [18]. So, the technology and properties of the nanoparticles obtained in 2005–2006 and later [27–30] are a good reference point for comparison of the new data provided herein [31].

The first samples of GaP nanoparticles having a distinct luminescence at room temperature were obtained by hydrothermal method from aqueous solutions at a relatively low temperature (120–200°C). It was found that the composition of the nanoparticles corresponds to stoichiometric GaP. The colloidal method provides a good opportunity to control the conditions of the synthesis, to decrease power inputs, and to increase the quality of nanoparticles concerning their purity and uniformity of their dimensions. In actuality, the single parameter, which may be controlled in the other methods, is temperature, while using colloidal methods one can control nucleation of nanoparticles as well as velocity of their growth. The other important advantage of the colloidal method is the ability of the so-called "capping," that is, to isolate nanoparticles from each other, to prevent their agglomeration during storage, simultaneously inhibiting their further growth. Therefore, we have elaborated the methods of GaP nanocrystals colloidal synthesis using $NaBH_4$ and Na_3P compounds.

4. Development of methods of incorporation of the GaP nanoparticles into polymers

Polyglycidyl methacrylate (PGMA), polyglycidyl methacrylate-co-polyoligoethyleneglycol methacrylate (PGMA-co-POEGMA), and biphenyl vinyl ether (BPVE) polymers were used to synthesize GaP nanocomposites suitable for light-emissive luminescent device structures. Film nanocomposites of good quality with high brightness and broadband luminescence were realized. The thickness of the polymer composite film was within 250–300 nm defined from atomic force microscope (AFM) experiment. The following procedures have been used in the fabrication of the nanocomposites:

1. GaP powder was ultrasonicated in methylethylketone (MEK) using Branson 5210 ultrasonic bath. Then, PGMA was added to the MEK solution. GaP to polymer ratio was less than 1:10.
2. GaP powder was dispersed in water-ethanol mixture (1:1 volume ratio) and ultrasonicated using Branson 5210 bath for 120 min. Then, PGMA-co-POEGMA was added in the form of water-ethanol mixture (1:1 volume ratio) solution. GaP to polymer ratio was less than 1:3. Nanocomposite films were deposited on quartz slides via dip coating.
3. GaP powder was dispersed in the biphenyl vinyl ether/dichloromethane (BPVE/DCM) solution; the solution was stirred and filtered from the excess of the powder. A few milliliter drops of the settled solution were casted onto silicon wafer.

More details on the preparation and characterization of our GaP/polymers nanocomposites can be found in Refs. [31, 33–36].

Figure 1a shows transmission electron microscope (TEM) images of GaP nanoparticles obtained from aqueous synthesis. One can see GaP nanoparticles, having characteristic dimensions less than 10 nm. The washed, thoroughly ultrasonicated, and dried nanopowder contains mainly single nanoparticles, while the same powder obtained without ultrasonic treatment consists of the clusters with the dimensions of the order of 100 nm.

Figure 1b shows atomic force microscope (AFM) topographic images of the GaP/PGMA film nanocomposite deposited by dip coating from a suspension in water-ethanol mixture solution on the surface of a silica substrate. The AFM images demonstrated that no significant aggregation was caused by the polymerization. In general, individual particles were observed. The relevant luminescence spectra are presented in **Figures 2** and **3**.

Figure 2 shows the spectra for GaP/PGMA-co-POEGMA nanocomposites. Comparing the results for the nanocomposites prepared from GaP powder or suspension (**Figure 2**, spectra 1 and 2, respectively), it was established that the best quality has the nanocomposites obtained from the nanoparticles stored as a suspension in a suitable liquid (see spectrum 2).

According to our measurements, the matrix polymers PGMA-co-POEGMA or BPVE used in this work provide no contribution to the luminescence spectra of luminescence based on these matrixes GaP nanocomposites presented in **Figures 2** and **3**, so, the nanocomposite spectra coincide with those obtained from the relevant GaP powders or suspensions. It is noted that in the GaP/BPVE nanocomposite, the position of the luminescent maximum can be changed between 2.5 and 3.2 eV and the brightness is 20–30 more than in the PGMA and PGMA-co-POEGMA matrixes. We explain the broadening of the luminescence band and the shift of its maximum to low-photon energies in luminescence of the nanocomposite based on the GaP powder in **Figure 2**, spectrum 1, by the presence of the nanoparticles with the dimensions of 10–100 nm in the powder.

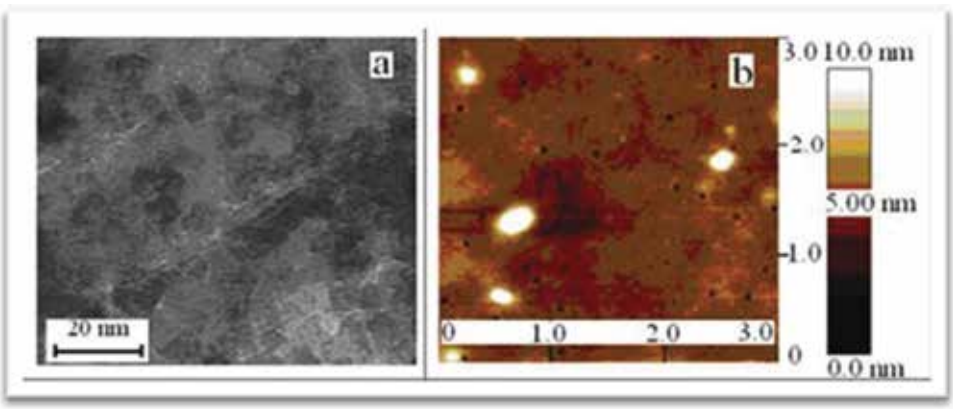

Figure 1. TEM image of GaP thoroughly ultrasonicated and dried nanoparticles obtained by mild aqueous synthesis (a) and AFM topography image of the GaP/PGMA nanocomposite (b) [17].

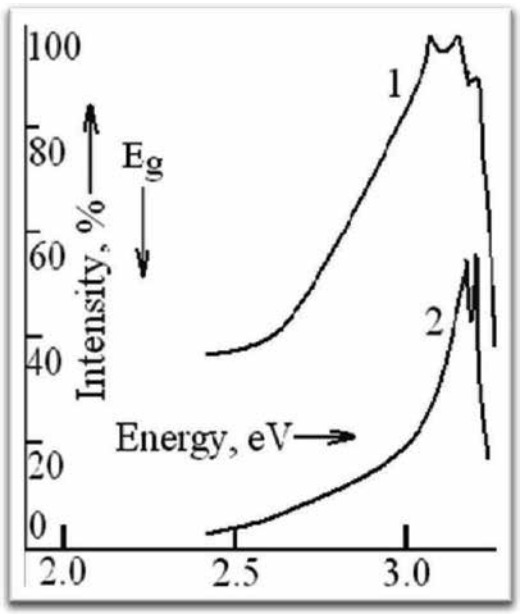

Figure 2. Spectra of luminescence from GaP/PGMA-co-POEGMA nanocomposites. Nanoparticles have been prepared using white P by mild aqueous synthesis and stored as the dry powder (spectrum 1) or suspension in a liquid (spectrum 2) [17].

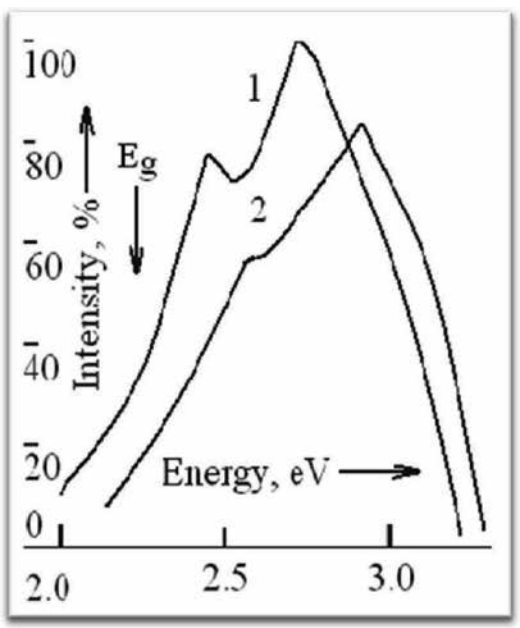

Figure 3. Luminescence spectra of 2 GaP/BPVE nanocomposites produced on the base of two parties of GaP nanoparticles prepared using different conditions [17].

Figures 2 and **3** present a clear image of the quantum confinement effect in the GaP nanoparticles. In accord with our data, the shift is about a few tenths of eV and, obviously, it is impossible to explain only through this effect the dramatic 1 eV enhancement to the region of luminescence at 300°K on the high-energy side of the spectrum.

In order to explain this interesting phenomenon, we postulate that the nanocrystals, much like the ideal long-term-ordered bulk GaP single crystals, exhibit this increase in blue-shifted luminescence due to (a) negligibly small influence of defects and non-radiative recombination of electron-hole pairs and very high efficiency of their radiative annihilation, (b) high perfection of nanocrystal lattice, and (c) high transparency of nanocrystals due to their small dimensions for the light emitted from high points of the GaP Brillouin zones, for instance, in the direct transitions Γ^1_c–Γ^{15}_v between the conductive and valence bands with the photon energy at 300°K equal to 2.8 eV [39] and (d) high efficiency of this so-called "hot" luminescence. On the basis of these improved technologies for the preparation of GaP nanoparticles and GaP/polymer nanocomposites, we can control within broad limits the main parameters of luminescence and expect therefrom to create a framework for novel light-emissive device structures using this dramatic 1-eV expansion of GaP luminescence to the UV region.

Thus, the film device structures, elaborated by us, demonstrate broadband luminescence in the region from UV until yellow-red with controlled width and position of maximum with the luminous intensity up to 1 cd compared with industrial light-emitting diodes.

5. Optical properties of perfect, long-term-ordered GaP:N in comparison with freshly prepared crystals

Investigating gallium phosphide (GaP) crystals grown by the author in the 1960s, clear improvement of their optical and mechanical properties was noted for the first time only after 10–12 years. It was unusual and interesting in the situation when all inorganic nature around us usually deteriorates in time. Therefore, the decision was taken to investigate, to understand, and to use this phenomenon in the future. In short, the investigation process can be described as follows.

Figure 4 provides a comparison of the evolution in luminescence spectra at low temperatures (80 K and below) from GaP:N over a period of 25 years. It is seen over this period zero-phonon line A of single N-impurity-bound excitons and their phonon replica are narrower in their line widths when compared to the freshly prepared single crystals. Further, as expected, zero-phonon line and replica in samples aged at room temperature for 25 years shift spectral position depending upon the concentration of N impurities (**Figure 4b**, spectra 1–3) according to Refs. [38, 39], while the same freshly prepared crystals exhibited broader luminescence line widths with increasing nitrogen content (**Figure 4b**, spectrum 4). These, along with other half-centennial findings, including modifications in luminescence kinetics, spontaneous Raman scattering, X-ray diffraction, absorption spectra, micro-hardness, and density of dislocations, that are reported elsewhere [1, 3–24], strongly suggest that close-to-ideal GaP:N crystals form over time due to the equally spaced disposition of N impurities instead of their chaotic distribution in the same freshly prepared crystals.

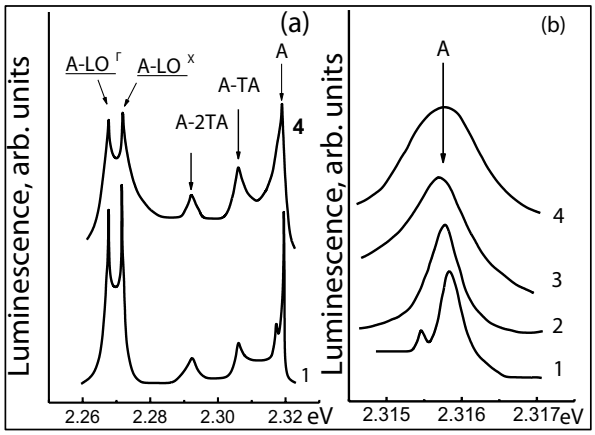

Figure 4. Evolution of the GaP:N luminescence with time and nitrogen concentration at the temperature of 15 K. (a) Zero-phonon line of the bound exciton A and its transversal acoustic (TA) and longitudinal optic (LO) phonon replica in as-prepared (4) and 25-year long-term-ordered (1) crystals. (b) Zero-phonon line A as a function of nitrogen (N) concentration. 1–3: 25-year-old crystals. 4: as-prepared. Curves 1 through 4 represent samples with nitrogen concentrations of 10^{17}, 10^{18}, 10^{19}, and 10^{18} cm^{-3}, respectively [34].

As first noted in Ref. [23], these results suggest a new type of crystal lattice in which the host atoms occupy their proper (equilibrium) positions in the crystal, while the N impurities are periodically substituted into the lattice portion into short chains of equal length. According to the data obtained from Raman light scattering [10, 14], host atoms of this new lattice develop harmonic vibrations, and high degree of lattice perfection leads to an abrupt decrease in the non-radiative recombination and an increase of efficiency and spectral range of luminescence.

Stimulated emission of light in these temporally ordered crystals (**Figure 5b**) also is observed. As was shown in Ref. [23], the GaP:N crystals aged for at least 40 years possess no discrete

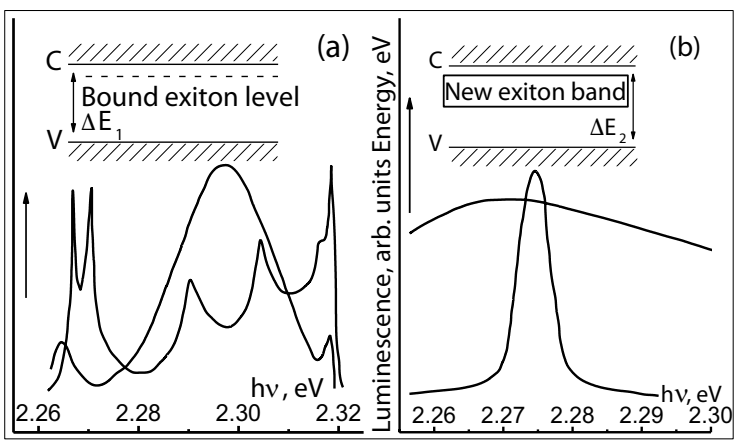

Figure 5. Luminescent spectra and schematic representation of the forbidden gaps (ΔE_1, ΔE_2) in the nitrogen-doped GaP aged for (a) 25 years and (b) 40 years [34].

impurity level for N-bound excitons in the forbidden gap. They also demonstrated a uniform luminescence from a broad excitonic band instead of the narrow zero-phonon line and its phonon replica as observed from the less-aged, 25-year-old crystals.

Thus, long-term-ordered GaP:N crystals demonstrate uniform bright luminescence from a broad excitonic band instead of the narrow zero-phonon line and its phonon replica in disordered and partly ordered (25-year-old) crystals. This is due to the fact that ordered crystals have no discrete impurity level in the forbidden gap. To the best of our knowledge, such transformation of a discrete level within the forbidden gap into an excitonic band (**Figure 5a, b**) is observed for the first time. In this case, the impurity atoms regularly occupy the host lattice sites and affect the band structure of the crystals, which are now a dilute solid solution of GaP-GaN with regular disposition of N atoms instead of freshly prepared GaP doped by occasionally located N atoms. Note that the increase of luminescence excitation in case of partly ordered GaP:N (**Figure 5a**, dotted line) leads to a broad luminescence band as a result of bound exciton interaction [9], while in the case of perfectly ordered crystals (**Figure 5b**), one can see an abrupt narrowing of the luminescence band due to stimulated emission in defect-free crystals. Earlier, in freshly prepared crystals, we observed a clear stimulated emission from a GaP:N resonator at 80 K [5], as well as the so-called superluminescence from GaP single crystals having natural faceting. Presently, our ordered crystals have a bright luminescence at room temperature that implies their perfection and very low light losses. In our studies [14, 23], we demonstrate that the stimulated emission in long-term-ordered GaP is also developed even at room temperature by electron-hole recombination of an electron at the bottom of the conduction band with a hole at the top of the valence band and the LO phonon absorption.

6. Comparison of optical properties of GaP:N nanocrystals and GaP perfect bulk single crystals

It is necessary to note that the very important for optoelectronics long-term ordering and considerable improvement of the semiconductor crystal lattice and accompanying phenomena have been discovered and observed over decade time scales only due to grown in 1960th [1, 3, 7] unique collection of samples and control of evolution of their properties for 50years. And up to now, this collection of long-term-ordered perfect GaP single crystals gives opportunities to find deep fundamental analogies in properties of the perfect single crystals and nanoparticles as well as to predict and to realize in nanoparticles and perfect bulk crystals new interesting properties and applications. Jointly with Refs. [3, 7, 9–17, 21–27, 31–34], this section is a generalization of the results on long-term observation of luminescence, absorption, and Raman light scattering in bulk semiconductors in comparison with some properties of the best to the moment GaP nanocrystals. Combination of these characterization techniques elucidates the evolution of these crystals over the course of many years, as well as the ordered state brought about by prolonged room-temperature thermal annealing, and the interesting optical properties that accompany such ordering. We demonstrate that long-term natural stimuli result in perfection of our crystals, which can lead to novel heterogeneous systems and new semiconductor devices with high temporal stability.

We further improved upon the preparation of GaP nanocrystals using the known methods of hydrothermal and colloidal synthesis [29–31].

The highest-quality GaP nanoparticles have been prepared using hydrothermal or colloidal synthesis from white phosphorus at a decreased temperature (125°C) and intense ultrasonication. It has been established that the maximum shift to ultraviolet and the best quality, in general, are from nanocomposites obtained from the nanoparticles stored as a suspension in a suitable liquid.

As noted earlier, different defects of high concentration in freshly prepared GaP single crystals completely suppress any luminescence at room temperature due to the negligible quantity of free path for non-equilibrium electron-hole pairs between the defects and their non-radiative recombination, while the quantum theory predicts their free movement in the field of an ideal crystal lattice. It was also shown the long-term-ordered and therefore close-to-ideal crystals demonstrate bright luminescence and stimulated emission repeating behavior of the best nanoparticles with pronounced quantum confinement effects.

Figure 6 compares the luminescence spectra of our long-term (up to 50 years)-ordered GaP single crystals (spectrum 1) to that from high-quality GaP nanoparticles and their GaP nanoparticles/polymers nanocomposites [15, 17]. Nanocrystals stored as dry powder demonstrate rather broad luminescent band with maximum at 2.8 eV (**Figure 6**, spectrum 2), while the nanocrystals of about 10-nm sizes, thoroughly separated and distributed in a suspension, which prevents their coagulation, mechanical, and optical interaction, exhibit bright narrow-band

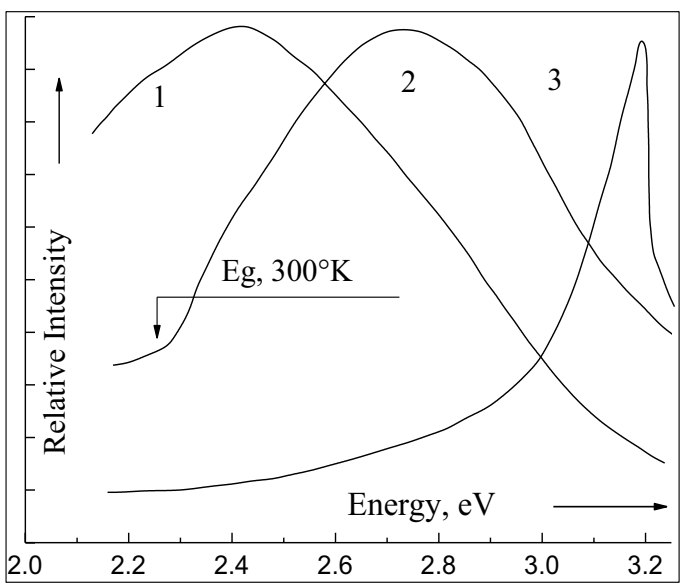

Figure 6. Luminescence of perfect bulk GaP single crystals (1) in comparison with the luminescence of GaP nanoparticles and GaP/polymers nano-composites (2, 3). Nanoparticles were prepared from white P by mild aqueous or colloidal synthesis at decreased temperature, stored as dry powder (spectrum 2) or suspension in a liquid (spectrum 3). Details can be found in Refs. [15, 17].

luminescence with maximum at 3.2 eV, approximately 1 eV above the position of the absorption edge in GaP at 300°K (**Figure 6**, spectrum 3).

The broadening of the luminescence band and the shift of its maximum to low-photon energies in the nanocomposite is explained based on the different dimensions (between 10 and 100 nm) of the GaP powder. Meanwhile, the nanocomposites on the basis of the suspensions containing only approximately 10-nm nanoparticles exhibit bright luminescence with maximum at 3.2 eV due to high transparency of 10-nm nanoparticles for these high-energy-emitted photons and pronounced quantum confinement effect.

Our first attempts to prepare GaP nanoparticles [18, 27] yielded room-temperature luminescence with maximum shifted only to 2.4 eV in comparison with the achieved now new maximum at 3.2 eV achieved today. It confirms significant progress in the technology of GaP nanoparticles and GaP/polymers nanocomposites. On the basis of these improved approaches to prepare GaP nanoparticles and GaP/polymer nanocomposites, we can change the main parameters of luminescence within the broad limits, and to create a framework for novel light-emissive device structures using dramatic 1-eV expansion of GaP luminescence to UV region.

7. Excitonic crystal and its importance in optoelectronics

The role and application of bound excitons in nanoscience and technology are discussed in this section. Bound excitons are well studied in semiconductors, especially in gallium phosphide doped by nitrogen (GaP:N). Doping of GaP with N leads to isoelectronic substitution of the host P atoms by N in its crystal lattice and to the creation of the electron trap with a large capture cross section. Therefore, any non-equilibrium electron in the vicinity of the trap will be captured by N atom, attracting a non-equilibrium hole by Coulomb interaction and creating the bound exciton—short-lived nanoparticle with the dimension of the order of 10 nm (it is the Bohr diameter of bound exciton in GaP:N). Note that none of the nanotechnology methods are used in the creation or selection of dimensions of these nanoparticles—only natural forces of electron-hole interaction and electron capture by the traps are necessary for the creation of these nanoparticles. As a result, we get something like neutral short-lived atom analog—a particle consisting of heavy negatively charged nucleus (N atom with captured electron) and a hole. The so-called "zero vibrations" do not destroy possible solid phase of bound excitons having these heavy nuclei that give an opportunity to reach their crystal state—short-lived excitonic crystal.

Taking into account the abovementioned results, a model for the crystal lattice and its behavior at a high level of optical excitation for well-ordered N-doped GaP (**Figure 7**) can be suggested. At the relevant concentrations of N, the anion sublattice can be represented as a row of anions where N substitutes P atoms with the period equal to the Bohr diameter of the bound exciton in GaP (approximately 10 nm) (**Figure 7a**). At some level of excitation, all the N sites will be filled by excitons, thereby creating an excitonic crystal (**Figure 7b**), which is a new phenomenon in solid-state physics and a very interesting medium for application in optoelectronics and nonlinear optics [4, 15, 17, 25, 26, 32–34].

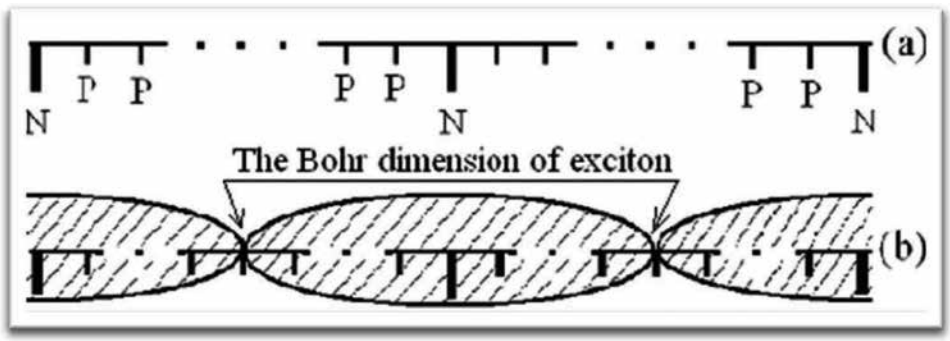

Figure 7. The models of the well-ordered GaP:N [34]. (a) The new type of crystal lattice with periodic substitution of N atoms for the host P atoms. (b) The excitonic crystal on the basis of this lattice. The substitution period is equal to the Bohr diameter of exciton (~100 Å), and optical excitation is enough for complete saturation of the N sublattice with non-equilibrium electron-hole pairs (please see details in Refs. [15, 17]).

Thus, using bound excitons as short-lived analogs of atoms and sticking to some specific rules, including the necessity to build the excitonic superlattice with the identity period equal to the bound exciton Bohr dimension in the GaP:N single crystal, we get a unique opportunity to create a new solid-state media—consisting of short-lived nanoparticles excitonic crystal, obviously, with very useful and interesting properties for application in optoelectronics, nanoscience, and technology.

8. Current approach to selection of materials for electronics and new prospects

The ability of matter to emit light of definite wavelengths and intensity depends on many factors; among them are the details of its band structure and crystal quality. Applied to light-emissive materials and device structures, the quality is characterized by the concentration of the defects damaging light emission due to non-radiative electron-hole recombination on these defects. The ways for minimization of expected losses of the light in non-radiative electron-hole recombination are (1) decrease of concentration of the defects in the material grown by an improved method; (2) considerable quality improvement of GaP crystal structure discovered by us during long-term (tens of years) ordering of the host and impurity atoms, and (3) application of nanocrystals with the dimensions less than the free paths of electrons and holes in the chosen light-emissive material.

Properties that can be used to achieve light emission at a definite spectral region include (1) selection of the material on the basis of its band structure peculiarities and the value of the forbidden gap, which as a rule sizes up the maximum value of the emitting photons; (2) doping of the selected material by impurities or, on the contrary, precise purification of the chosen material for the creation of new channels of light emission; and (3) selection of the temperature and/or excitation level that to change contribution of different channels into light emission due to their disappearance or saturation.

http://dx.doi.org/10.5772/67852

It is impossible or, at least, very difficult to realize all the above-noted possibilities in a single material. Therefore, the present technologies of light-emissive optoelectronics employ diverse range materials using very complicated and expensive technologies for their fabrication with the necessary application parameters. Down-selecting a set of various materials applied currently in optoelectronics at the maintenance or even improvement of their high parameters and quality is one of the most important goals for reduction in price and wide application in the practice of electronic devices. The most impressive demonstration of this approach would be the selection of a suitable material, the development of a peculiar technology of its preparation, its interesting properties and prospects for application in optoelectronics instead of a huge number of various materials and their technologies.

Sophisticated growth technique, knowledge of crystal growth mechanisms, of different processes, improving or deteriorating in time the prepared crystals, and the relevant comprehensive experience are necessary for the preparation of the perfect, free or almost free of contamination and doped GaP single crystals.

However, in the manufacture of artificial crystals, we are faced with the need to fabricate them for a very short time compared with the times for which naturally perfect crystals are grown. For example, a hundred years passes before the growing in the nature crystal acquires the dimensions necessary for its use as feedstock in jewelry making, while the commercial growth of moderately perfect semiconductors takes only a few hours. In such a short time, its own atom or dopant diffusing through the crystal usually cannot absolutely exactly occupy the places intended for them in ideal crystal lattice. This gives rise to lattice defects, which, in turn, hinder the achievement of perfect devices. Manufactured on the basis of such materials, greatly reduce their lifetime, as well as make it impossible manifestation of some very interesting and useful for the application of the effects observed in advanced materials. Significant levels of funds are spent on searching and implementing methods for creating materials, not existing in the nature, that can, even if in a narrow field of application and at short time service, replace the material with a perfect crystal lattice and the necessary concentration and location of dopants. Hence, there is an urgent need to develop methods for the creation of an ideal semiconductor material the required parameters for use in electronics. In this case, it will disappear or substantially decrease the need to develop a plurality of individual costly technology to produce a plurality of different materials with a limited resource and service applications, and as a very important result for any country involved in the production and use of electronic materials—a giant savings and the possibility of redeployment to other needs of funds spent on the production of low-quality materials and products.

Using the long-term-ordered perfect GaP or similar on behavior and properties material in electronic industry instead of current elaboration of very expensive and labor-consuming technologies for diverse materials with their limited application spectral region and other parameters, we get a big commercial, scientific, and technology advantage from their fabrication and application.

We hope that the methods based on the application of this long-term evolution of the important properties of our unique collection of semiconductor single crystals [31–34] as well as the combined methods of laser-assisted and molecular beam epitaxies [40–42] elaborated by us promise a novel approach to the development of a new generation of optoelectronic devices.

The epitaxial methods, elaborated by us [40–42], will be applied to the fabrication of device structures with artificial periodicity; together with classic methods of crystal growth, they can be employed to realize impurity ordering that would yield new types of nanostructures and enhanced optoelectronic device performance.

The long-term, tens of years ordered GaP, its artificial analogs, and nanoparticles have very interesting and properties for different application, which give an opportunity to apply them in optoelectronics with high economic effect instead of a lot of different compounds currently used in optoelectronics.

9. Conclusions

Thus, our half-of-a-century collection of results provides a new approach to the selection and preparation of perfect optoelectronics materials (please see references to this chapter) and a unique opportunity to realize a new form of solid-state host—the excitonic crystal [32–34]. These results confirm expedience of the efforts directed to the formation in GaP of the N-impurity superlattice having a lattice period equal to the bound exciton dimension. As noted in this chapter and the relevant references, high-quality material for industrial electronics can be prepared by storing freshly grown crystals for years in a special storage. Only old crystals with the attained necessary properties will then be annually retrieved for device fabrication, while new portions of fresh crystals will be placed for long-term ordering at room temperature, as is done with wines and fine liquors.

All of the results presented here and included in summary reviews [25, 26, 32–34] may sufficiently change the approach to the selection of materials necessary for electronics, and to make cheaper and simpler technology for the preparation of the selected materials and device structures on which they are based. This study of long-term convergence of bulk- and nanocrystal properties [15, 17] brings a novel perspective to improving the quality of semiconductor crystals. The author's unique collection of pure and doped crystals of semiconductors grown in the 1960s provides an opportunity to observe and understand the physics behind the long-term evolution of properties in these key electronic materials.

Acknowledgements

The authors are glad to note that the broad discussion and dissemination of their joint results stimulate further collaboration with reliable partners from the USA, Russia, Italy, Romania, France, and other countries.

Prof. Sergei L. Pyshkin expresses his cordial gratitude to his teachers, world-known scientists late Profs Nina A. Goryunova, Nobel Prize Laureate Alexander M. Prokhorov, and academicians Rem V. Khokhlov and Sergei I. Radautsan. He is also very grateful to the US Department of State, Institute of International Exchange, Washington, DC, the US Air Force Office for Scientific

Research, the US Office of Naval Research Global, Civilian R&D Foundation, Arlington, VA, the US Science & Technology Center in Ukraine, to his colleagues and coauthors from Clemson University, SC, University of Central Florida, FL, Istituto di elettronica dello stato solido, CNR, Rome, Italy, Universita degli studi, Cagliari, Italy, Lomonosov Moscow State University, Joffe Physico-Technical Institute and State Polytechnical University, St. Petersburg, Ac. Scie. Institute of General Physics, Moscow, Russia, Institute of Applied Physics and Academy of Sciences of Moldova for support and attention to this protracted (1961 to present time) research.

Author details

Sergei L. Pyshkin[1,2]* and John Ballato[2]

*Address all correspondence to: spyshkin@yahoo.com

1 Institute of Applied Physics, Academy of Sciences of Moldova, Kishinev, Moldova, Republic of Moldova

2 Clemson University, South Carolina, USA

References

[1] Goryunova NA, Pyshkin SL, Borshchevskii AS, et al. Influence of impurities and crystallization conditions on growth of platelet GaP crystals. In: Symposium on Crystal Growth at the 7th International Crystallography Congress (Moscow, July 1966). N.N. Sheftal, editor, Journal of Growth of Crystals 1969; 8: 68-72, New York.

[2] Pyshkin SL, Radautsan SI, Zenchenko VP. Processes of long-lasting ordering in crystals with a partly inverse spinel structure. Journal of Soviet Physics – Doklady 1990; 35(4): 301-4.

[3] Pyshkin SL. Preparation and Properties of Gallium Phosphide. Ph.D. thesis 1967, State University of Moldova, Kishinev.

[4] Pyshkin SL, Zifudin L. Excitons in highly optically excited gallium phosphide. Journal of Luminescence 1974; 9: 302-8.

[5] Pyshkin SL (presented by Nobel Prize Laureate A.M. Prokhorov). Stimulated emission in gallium phosphide. Journal of Soviet Physics – Doklady 1975; 19: 845-6.

[6] Pyshkin S. Luminescence of GaP:N:Sm crystals. Journal of Soviet Physics of Semiconductors 1975; 8: 912-3.

[7] Pyshkin SL. Photoconductivity and luminescence of highly optically excited semiconductors. Dr.Sc. thesis 1978, Lomonosov Moscow State University.

[8] Pyshkin S, Anedda A, Congiu F, Mura A. Luminescence of the GaP:N Ordered System. Journal of Pure and Applied Optics 1993; 2: 499-502.

[9] Pyshkin S., Alberto Anedda. Time-Dependent Behaviour of Antistructural Defects and Impurities in Cd-In-S and GaP. Institute of Physics Conference Series 1998, Ternary and Multinary Compounds; 152, Section E: 785-789

[10] Pyshkin S, Ballato J, Chumanov G. Raman light scattering from long-term ordered GaP single crystals. Journal of Optics A: Pure and Applied Optics 2007; 9: 33-6.

[11] Pyshkin SL, Ballato J, Bass M, Turri G. Luminescence of long-term ordered pure and doped gallium phosphide. TMS Annual Meeting, Invited Talk at the Symposium: Advances in Semiconductor, Electro Optic and Radio Frequency Materials, March 9-13, New Orleans, LA. J. Electronic Materials 2008; 37(4): 388-95.

[12] Pyshkin SL, Ballato J, Bass M, Chumanov G. Time-dependent evolution of crystal lattice, defects and impurities in $CdIn_2S_4$ and GaP. Journal of Physica Status Solidi 2009; C(6): 1112-5.

[13] Pyshkin SL, Ballato J, Bass M, Turri G. Evolution of luminescence from doped gallium phosphide over 40 Years. Journal of Electronic Materials 2009; 38(5): 640-6.

[14] Pyshkin S, Ballato J. Evolution of optical and mechanical properties of semiconductors over 40 Years. Journal of Electronic Materials 2010; 39(6): 635-41.

[15] Pyshkin S, Ballato J. Long-term convergence of bulk- and nano-crystal properties. In:Optoelectronics – Materials and Technics, InTech – Open Access Publisher, ISBN 978-953-307-276-0; Chapter 19: 2011; 459-476.

[16] Pyshkin S. Ballato J. Dramatic expansion of luminescence region in GaP/polymer nanocomposites. Supplemental Proceedings of the 2012 TMS Annual Meetings (Orlando, FL, USA, March 11-15); vol. 1: "Materials Processing and Interfaces": 2012; 353-359.

[17] Pyshkin S, John Ballato. Advanced light emissive device structures. In: Optoelectronics – Advanced Materials and Devices, S.L. Pyshkin and J. Ballato, editors, ISBN 978-953-51-0922-8, InTech – Open Access Publisher; Chapter 1: 2013; 1-24.

[18] Pyshkin S, Ballato J, Chumanov G, DiMaio J, Saha AK. Preparation and Characterization of Nanocrystalline GaP. Technical Proceedings of the 2006 NSTI Nanotech Conference; 3: 194-197.

[19] Pyshkin S, Ballato J, Chumanov G, Tsyntsaru N, Rusu E. Preparation and characterization of nanocrystalline GaP for advanced light emissive device structures. In: The 2010 NSTI-Nanotech Conference (Anaheim, CA) Proceedings: www.nsti.org, ISBN 978-1-4398-3401-5; vol. 1: 522-5.

[20] Pyshkin SL, Ballato J, Belevschii S, Rusu E, Racu A, Van DerVeer D. Synthesis and characterization of GaP nanoparticles for light emissive devices. In: The 2011 NSTI-Nanotech Conference, Boston, MA, June 13-16. Proceedings: www.nsti.org, ISBN 978-1 4398-7142-3; vol. 1, 327-30.

[21] Pyshkin SL, Ballato J, Bass M, Chumanov G, Turri G. Time-dependent evolution of crystal lattice, defects and impurities in $CdIn_2S_4$ and GaP. Physica Status Solidi 2009; C(6): 1112-5.

[22] Pyshkin S, Zhitaru R, Ballato J, Chumanov G, Bass M. Structural characterization of long-term ordered semiconductors. Proceedings of the 2009 MS&T Conference, International Symposium "Fundamentals & Characterization": 698-709.

[23] Pyshkin S, Ballato J, Bass M, Chumanov G, Turri G. Properties of the long-term ordered semiconductors. Suppl. Proceedings of the 2009 TMS Annual Meeting and Exhibition; 3: 477-84 (San Francisco, February 15-19, 2009).

[24] Pyshkin S, Ballato J, Chumanov G, Bass M, Turri G, Zhitaru R, et al. Optical and mechanical properties of long-term ordered semiconductors. Moldavian Journal of the Physical Sciences 2009; 8(3-4): 287-95. The 4th Int. Conference on Materials Science and Condensed Matter Physics, Kishinev, Sept 23-26, 2008.

[25] Pyshkin SL. Gallium Phosphide - New Prospect for Optoelectronics. J. Advances in Optoelectronic Materials (AOM), ISSN Online: 2327-7661, ISSN Print: 2327-767X); 2013; 1(4): 59-66.

[26] Pyshkin SL. Excitonic crystal and nanotechnology. Symbiosis Journal of Nanoscience & Technology: Open Access 2014; 1(2), 1-5. Available from http://symbiosisonlinepublishing. com/nanoscience-technology08.pdf

[27] Pyshkin S, John B. Advanced light emissive composite materials for integrated optics. Symposium: The Physics and Materials Challenges for Integrated Optics – A Step in the Future for Photonic Devices, Proc. of the 2005 MS&T Conference, Pittsburgh: 3-13.

[28] Pyshkin S, Ballato J, Luzinov I, Zdyrko B. Fabrication and characterization of the GaP/polymer nanocomposites for advanced light emissive device structures. The 2010 NSTI-Nanotech Conference; 1: 772-5. www.nsti.org, ISBN 978-1-4398-3401-5. Anaheim, CA, June 21-24, 2010.

[29] Pyshkin S, Ballato J, Chumanov G, Tsyntsaru N, Rusu E. Preparation and characterization of nanocrystalline GaP for advanced light emissive device structures. The 2010 NSTI-Nanotech Conference; 1: 522-5. www.nsti.org, ISBN 978-1-4398-3401-5.

[30] Pyshkin SL, Ballato J, Luzinov I, Zdyrko B. Fabrication and characterization of GaP/polymer nanocomposites for advanced light emissive device structures. Journal of Nanoparticle Research 2011; 13: 5565-70.

[31] Pyshkin SL. (Project Manager). Advanced Light Emissive Device Structures. STCU (www.stcu.int) Project 4610, 2009-2012.

[32] Sergei LP. Excitonic crystal, nanotechnology and new prospect for optoelectronics. The Open Optics Journal 2015; 9: 26-37.

[33] Pyshkin S. New prospect for optoelectronics. Nanoscience & Technology 2016; 3(1): 1-5.

[34] Pyshkin SL. Excitonic crystal and perfect semiconductors for optoelectronics. Chapter 1. In: Materials and Devices. SL Pyshkin and J Ballato, editors, Rijeka: InTech; 2015; 1-30.

[35] Shanmin G, Jun L, Nan C, Yan Z, Yi X. Aqueous synthesis of III-V semiconductor GaP and InP exhibiting pronounced quantum confinement. Chemical Communications 2002: 3064-5.

[36] Zhengang L, Yujun B, Deliang C, Qilong W. Preliminary insight into the formation process of InP and GaP nanocrystals. Solid State Sciences 2003; 5: 1037-40.

[37] Zhang Z-C, Wang B-P. Diamond and oxidized disordered graphite on the surface of gallium phosphide nanoparticles. Systems Characterization 2009; 26: 53-7.

[38] Paul W. Band structure of the intermetallic semiconductors from pressure experiments. Journal of Applied Physics 1961; 32: 2082-94.

[39] Zallen R, Paul W. Band structure of gallium phosphide from optical experiments at high pressure. Physical Review 1964; 134: A1628-41.

[40] Pyshkin SL, Fedoseev SA, Lagomarsino S, Giannini C. Preparation and structural properties of some III-V semiconductor films grown on (100) oriented Si substrates, Journal of Applied Surface Science, 1992; 56-58: 39-43.

[41] Budyanu VA, Chechuy SN, Pyshkin SL, et al. Investigation of III-V/Si heterojunction grown by laser deposition. Physica Status Solidi (a) 1985; 91: 737-44.

[42] Budyanu VA, Chechuy SN, Pyshkin SL, et al. Laser vacuum epitaxy of III-V semiconductors on silicon. Revue Roumaine de Physique 1987; 32(1-2): 216-19.

Chapter 2

Microcavities for Silica-Fiber-Based Quantum Information Processing

Hai-Zhi Song

Additional information is available at the end of the chapter

http://dx.doi.org/10.5772/67499

Abstract

High-quality optical microcavities are prospective in many optoelectronics fields like optical communication, nonlinear optics, and quantum information technology. For quantum telecommunication over 1.55 μm silica-fiber-based networks, micropillar cavities containing quantum dots (QDs) are strongly required to construct quantum devices such as single-photon sources (SPSs). The straight way could be using micropillars composed of traditional InGaAsP/InP distributed Bragg reflectors (DBRs), which can in principle serve as efficient 1.55 μm SPSs. To reduce the difficulty in fabricating such ~30 μm high pillars, structure hybridizing semiconductor with dielectric materials is designed. Consisting of Si/SiO_2 DBRs and an InP active layer, such a micropillar readily enhances the rate of single-photon emitting from an InAs/InP QD to be over GHz and serves as a photon-indistinguishable SPS. To strongly couple a 1.55 μm QD with an optical mode, the Si/SiO_2-InP hybrid micropillar cavity can be reformed by introducing tapered DBR structures. This new hybrid pillar cavity can be diminished to have a sub-micrometer diameter, giving small mode volume and ensuring single QD emission. With quality (Q) factor as high as 10^5–10^6, this cavity can behave as a coherently controllable quantum device. More effective might be the InGaAsP/InP-air-aperture micropillar cavity, which can be fabricated by a monolithic process without hybridizing.

Keywords: microcavity, optoelectronics, single-photon source, quantum dot, quantum information processing

1. Introduction

Optical microcavities are widely studied for their prospects in many optoelectronics-related fields of research and technology, such as optical communication, nonlinear optics, and quantum information technology [1–3]. For solid-state quantum information processing, microcavities

containing semiconductor quantum dots (QDs) have been demonstrated to be effective as indispensable devices such as efficient [4–6] and indistinguishable single-photon sources (SPSs) [7] and coherent quantum-control devices [8, 9].

For the purpose of quantum communication over silica-fiber-based networks, InAs/InP QDs are promising as SPSs, as evidenced by their use in quantum key distribution experiments [10, 11]. However, the spontaneous lifetime of InAs/InP QDs is so long (~1.2 ns) that the operation frequency is limited to several hundred MHz. Referred to the key generation rate of attenuated-laser-based QKD systems [12], it is demanding to improve the operation frequency of an InAs/InP quantum dot single-photon source (QD SPS) to the GHz range. For more sophisticated quantum information processing such as quantum repeaters [13], device-independent quantum key distribution [14], and all-optical quantum computing [15], a QD SPS needs to emit highly identical single-photon pulse trains. However, the photon indistinguishability of an InAs/InP QD is still bad due to the big gap between the excitonic coherence time (typically ~100 ps [16]) and the spontaneous lifetime. These two problems can be resolved by introducing InAs/InP QDs into optical microcavities possessing high Purcell factors F_P [6, 7]. Although the emission rate of 1.55 μm InAs/InP QDs was improved by a factor of 5 in a photonic crystal microcavity [17], micropillar cavities are more promising owing to easily isolating single QDs, light emission in the normal direction, and a single-lobed Gaussian-like pattern, which enable high coupling efficiency to fiber [18] and suitability for electrical driving [19]. Here, we are going to study and design micropillar cavities at 1.55 μm telecommunication band for silica-fiber-based quantum information processing.

2. Traditional micropillar cavity

Like the micropillar cavities for InAs/GaAs QDs [5], the straight way to construct an efficient cavity containing InAs/InP QDs might be using a pillar composed of InP-lattice-matched distributed Bragg reflectors (DBRs). On InP substrates, epitaxial growth can produce many types of lattice-matching DBRs including InGaAsP/InP and AlInGaAs/AlInAs. As a representative example, here we will study the former.

As shown in **Figure 1(a)**, the micropillar cavity is a cylinder standing on an InP substrate. It consists of periodic InGaAsP/InP pairs on the top and bottom side of an InGaAsP spacer layer. The InGaAsP/InP periodic structure is the DBRs taking the role of reflecting light toward the spacer. The bottom DBR has more pairs of InGaAsP/InP layers than the top DBRs so that there is less useless leakage to the bottom. Each layer in DBRs is set quarter-wavelength thick, and the spacer layer is one-wavelength thick. The InGaAsP layers are lattice matching to the InP substrate and have an energy gap larger than the photon energy of 1.3 μm wavelength, so that they are extremely transparent for ~1.55 μm light. A light source, representative of an InAs QD, is located in the spacer.

By using finite-difference-time-domain method, the optical properties of this conventional micropillar cavity are simulated. By launching a polarized impulse from the light source, the time evolution of the light intensity can be obtained at monitors set in the spacer layer.

http://dx.doi.org/10.5772/67499

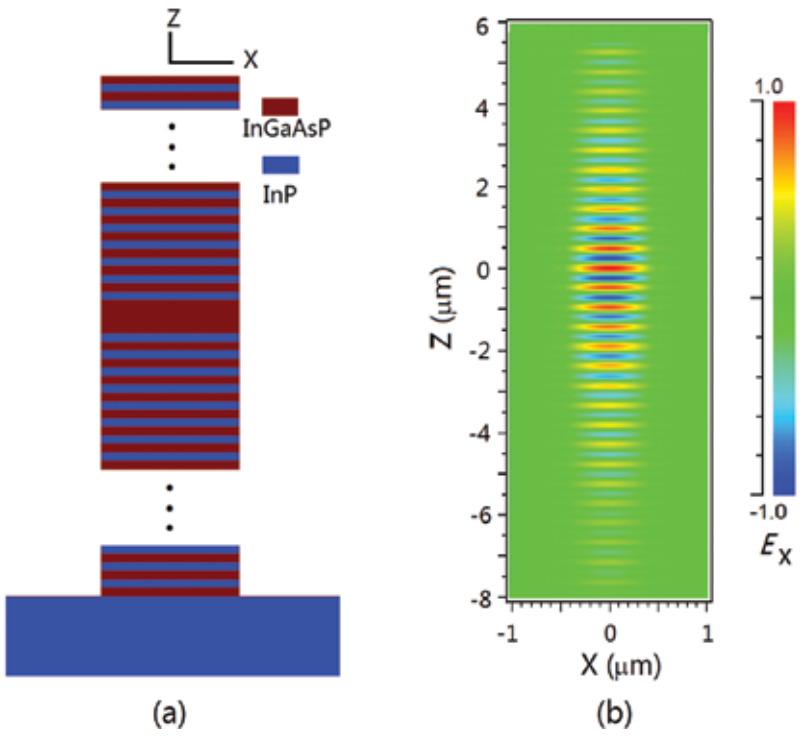

Figure 1. (a) Schematic cross section of the InGaAsP/InP micropillar cavity, (b) distribution profile of the x-polarized electric field E_x of the fundamental mode.

A Fourier transform gives a spectrum of the electric field intensity, showing some peaks representing the cavity modes. By setting the light source as a narrow-band emission around a mode wavelength λ, we obtain the intensity decay with time t and the steady state distribution, i.e., the mode profile. The quality factor Q can be obtained by fitting the exponential light intensity envelope to $\exp(-2\pi ct/Q\lambda)$, where c is the light velocity in vacuum.

The result of this conventional InGaAsP/InP micropillar cavity is as follows. As first, there does exist the fundamental mode peaked near 1.55 μm. The optical field, as shown in **Figure 1(b)**, is confined around the space layer so that the cavity can be of good quality. On a cavity with 30/50 pairs of top/bottom DBR layers, the Q factor is found to be about 2000; 40/70 pairs of DBR layers bring about Q factor close to 10^4. As shown in **Figure 2(a)**, the Q factor looks stable against the change of pillar diameter, which is different from some other micropillar cavities such as GaAs/AlGaAs [5]. It is more meaningful to examine the Purcell factor:

$$F_P = \frac{3Q\lambda^3}{4\pi^2 V n^3}, \tag{1}$$

where λ is the mode wavelength and n is the effective refractive index, and the mode volume:

$$V = \frac{\int \varepsilon(\mathbf{r})\mathbf{E}(\mathbf{r})^2 \mathrm{d}\mathbf{r}}{\varepsilon_M {E_M}^2}, \tag{2}$$

where ε is the relative dielectric constant, **E** the electric field of the light at the position **r**, and ε_M and E_M are the corresponding values at the point of the maximum light intensity. As shown in **Figure 2(b)**, the Purcell factor F_P changes with the cavity size. On a cavity with 30/50 pairs of DBR layers, there often occurs an F_P more than ten. More significantly, a cavity with 40/70 pairs of DBR layers exhibits F_P from 20 to more than 100. This happens with the pillar diameter being less than 1 μm. F_P is small at larger diameters because the mode volume is getting larger.

With the good quality, the above cavity can be considered to be used as a QD SPS. The best single-photon generation rate is inversely proportional to the spontaneous lifetime T_1 of the QD excitons. As such, our cavity with $F_P > 10$ could increase the operation frequency from several hundred MHz into GHz band. For photon indistinguishability, the required F_P is determined by the parameters of the QDs. The main principle is that there should be a coherence time T_2 comparable or longer than $2T_1$. On some InAs/GaAs QDs, remarkable indistinguishability was created by a microcavity with F_P of ~5 [7]. InAs/InP QDs are reported to have T_1 ~ 1.2 ns without a cavity [11] and have T_2 ~ 130 ps [16]. It turns out that a microcavity with $F_P > 2T_1/T_2$ ~ 20 would be required. Obviously, it could be expected that highly indistinguishable single photons could be produced from InAs/InP QDs, using the above traditional InGaAsP/InP DBR-micropillar cavities.

Like the GaAs/AlGaAs micropillar cavities, the InGaAsP/InP one can be in principle fabricated simply by epitaxial growth and dry etching. Noting that such a pillar would be 20–30 μm high, it is actually not easy to fabricate right now. The reason why it needs so many pairs of DBR layers is that InP-lattice-matched material systems such as InP/InGaAsP and AlInGaAs/AlInAs

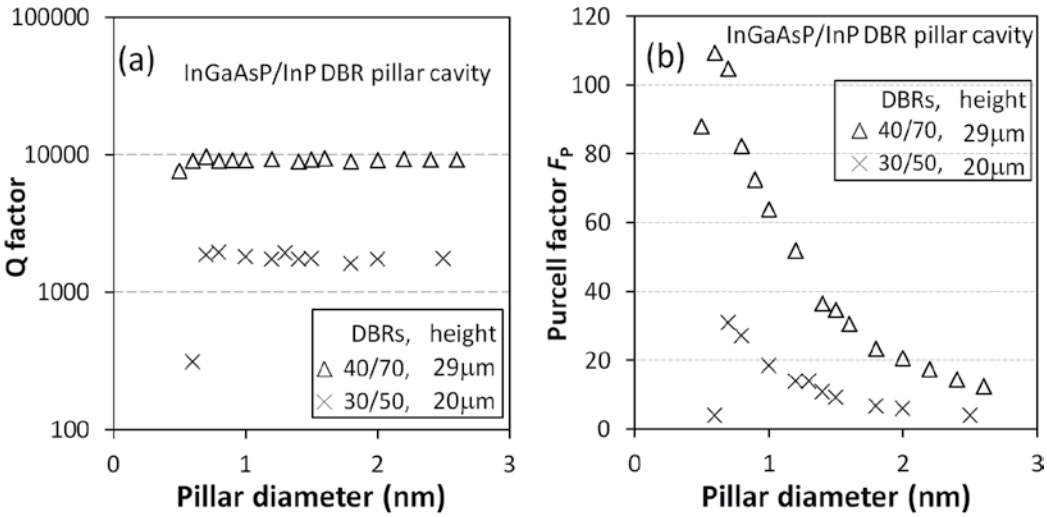

Figure 2. The *Q* factor (a) and Purcell factor (b) as functions of the diameters of InGaAsP/InP micropillar cavities.

http://dx.doi.org/10.5772/67499

have very small refractive index contrast (~0.2) [20]. Nevertheless, since dry-etching process has been available to fabricate pillars higher than 8 μm [21] and epitaxial growth has now enabled layer thickness more than 10 μm, useful InGaAsP/InP micropillar cavities might be producible in the near future.

3. Hybrid micropillar cavity

To resolve the problem with low refractive index contrast in InP-based materials, people may use a hybrid material system. A micropillar cavity consisting of Ta_2O_5/SiO_2 DBRs has been fabricated with an InP spacer containing 1.55 μm InAs/InP QDs [22]. However, this system has not exhibited any Purcell enhancement effect on 1.55 μm QD single-photon emission, because it is still difficult to construct sufficiently many DBR pairs required for enough F_P (noting that the index contrast of ~0.6 is not so large). Si/SiO_2 micropillar cavities have a refractive index contrast as large as ~2, meaning that fewer DBR pairs (than Ta_2O_5/SiO_2) would be sufficient for Purcell enhancement. On the other hand, recent technical advances reveal that wafer bonding [23] and film deposition techniques [24] are ready for hybridizing semiconductor thin layers with Si-based high refractive index contrast multilayers. It is thus relatively easy to fabricate Si/SiO_2 DBR-micropillar cavities with InP spacer layers. Therefore, a micropillar cavity consisting of Si/SiO_2 DBRs and a QD-containing InP central layer is proposed and studied as a Purcell-enhanced single-photon emitter at 1.55 μm [25].

Figure 3(a) shows the vertical xz-plane cross section of the proposed cavity structure. There is an InP layer, which is one-wavelength thick, in the cavity center as the spacer. There are Si/SiO_2 DBRs on the top and bottom sides of the spacer layer. Quarter-wavelength thick SiO_2 and Si layers are alternatively stacking in the DBRs. A light source is settled in the spacer as the InAs/InP QD. Set on a thick Si substrate, the whole micropillar is cylindrically shaped with lateral diameter D on the order of micrometer. With 4/6.5 pairs of the top/bottom DBRs, this micropillar has a pillar height of ~4.5 μm. By calculation using the transfer matrix method, the planar version of this cavity, i.e., with infinite D, is known to have reflectivity of 99.850 and 99.996% at the Bragg wavelength λ_B = 1.55 μm on the top and bottom DBRs, respectively.

The fundamental mode is found significant on this hybrid pillar cavity. At first, its optical field, as shown by the colored pattern in **Figure 3(a)**, is well confined inside the cavity and is highly symmetric. This ensures the usefulness of this cavity as an SPS coupled to fiber. Its mode wavelength λ exhibits a blueshift with respect to the designed Bragg wavelength λ_B = 1.55 μm, as shown in **Figure 3(b)**. As D decreases, the blueshift is getting faster. When $D > 2$ μm, the mode wavelength λ tends to saturate at Bragg wavelength λ_B. This behavior can be explained by waveguide dispersion, as is similar to other micropillar cavities with low index contrasts [26]. In physical sense, it results from more localized geometrical confinement of an optical mode, suggesting shorter mode wavelength, at smaller diameters.

The change of Q factor is somehow similar to the mode wavelength. With decreasing D, its envelope decreases slowly at first and then more rapidly, as shown in **Figure 3(b)**. Mostly larger than a few hundred, the Q factor is likely satisfying an efficient micropillar cavity as a

QD SPS [7]. At the large D extreme, Q factor tends to be close to the value of a planar cavity, ~8000. At the small D extreme, Q degrades to be less than 100. This is attributed to the increased effective incident angle of light on the DBRs [18]. In detail, however, there appear Q oscillations with respect to D, which give relatively high Q in some D areas (e.g., Q = 2000–3300 for D = 2.20–2.40 μm and Q = 3000–4700 for D = 3.20–3.50 μm).

The Purcell factor F_P also exhibits oscillations with respect to D. As shown in **Figure 3(c)**, the F_P oscillations are superimposed on a broad background. This background is mainly attributed to the competition between the opposite effects of Q factor and the mode volume V. It is easy to recognize that the mode volume usually increases with increasing cavity diameter. When D is larger than 1.30 μm, F_P is more than 10 so that the cavity can improve the spontaneous emission rate of a QD by more than one order of magnitude. Corresponding to the high Q areas, there appear also a series of F_P peaks such as F_P = 60–110 at D = 2.20–2.40 μm and F_P = 40–70 at D = 3.20–3.50 μm. By detailed examination, it is known that the maxima of the F_P oscillations are different from that of Q factor. For an example, maximum Q at D = 2.32 μm shifts slightly to D = 2.25 μm for the corresponding F_P maximum.

Further studies should be performed on the Q and F_P oscillations to understand why particular cavity sizes show higher cavity quality. There have reported similar oscillations on low index-contrast DBR-micropillar cavities [27]. These studies suggest that the fundamental HE_{11} cavity mode can be regarded as a combination of a guided HE_{11} mode in the spacer and a Bloch HE_{11} mode in the DBRs. Then, the coupling of these modes with higher-order propagating Bloch modes

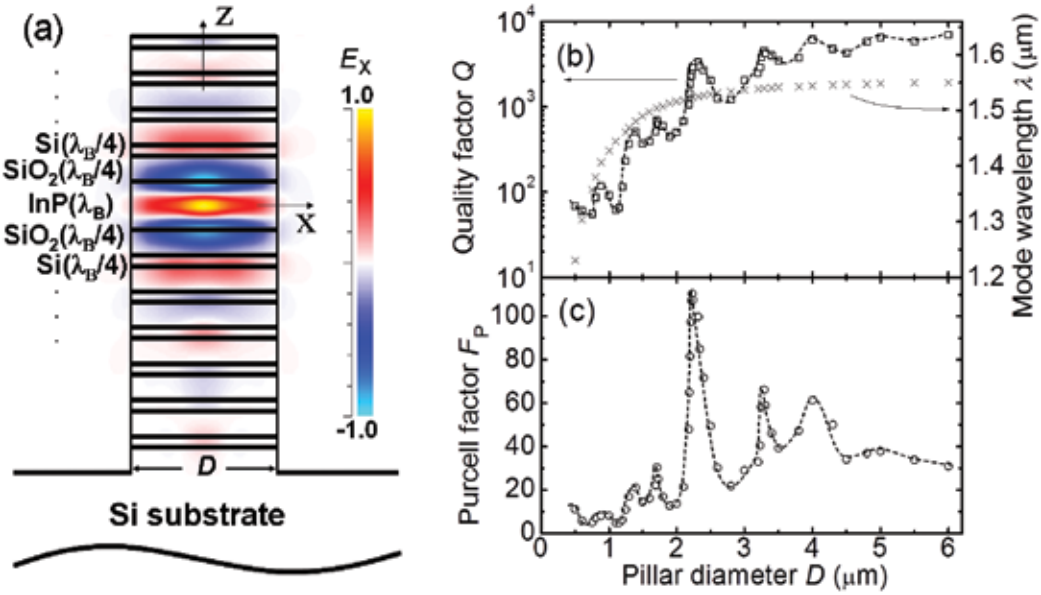

Figure 3. (a) Schematic cross section of the cavity model used for the simulation. The color-scaled pattern shows an example of the x-polarized electric field E_x of the fundamental mode. (b) Mode wavelength λ and quality factor Q and (c) Purcell factor F_P as a function of diameter D for cavities with 4/6.5 top/bottom DBR pairs. The dashed lines are guides for eyes.

http://dx.doi.org/10.5772/67499

gives rise to oscillatory behavior of the Q factor. Shown in **Figure 4(a)** are the x- and y-line profiles and xy-plane profiles of the electric field E_x of the fundamental modes, together with the ideal HE_{11} mode profiles. It is obvious that our cavity shows some fine structures, whereas the standard HE_{11} cavity mode is free of detailed structure. Close to the HE_{11} cavity mode, the profiles at $D = 2.30$ μm exhibit a single lobe at the cavity center and indicate relatively high axial symmetry. However, there remain small shoulders, suggesting a hybrid character of the cavity fundamental mode. Higher-order propagating modes with one or more radial nodes have been incorporated into the fundamental mode. It is worth mentioning that all the mode profiles within $D = 2.20$–2.40 μm are close to $D = 2.30$ μm. Stronger structure details appear in the mode profiles outside this range. It is ring-like at smaller D and has two lobes at larger D. This suggests that different higher-order propagating modes are coupling into the fundamental mode. Similar mode profile variation also happens around some other Q (F_P) peaks such as that at $D = 3.20$–3.50 μm. It is more meaningful to state that, as the result of Q oscillation or mode coupling, a radiation pattern with a single central lobe would be more beneficial for coupling into a fiber.

It is valuable to know how the Q oscillation or the change of mode profiles influences the cavity quality. For this purpose, we can investigate the cavity loss by observing the power flow through the simulation domain surfaces. The cavity loss includes transverse (through sidewalls) and longitudinal (through top and bottom DBRs). The fraction of the longitudinal loss corresponds to Q/Q_{DBR}, where Q_{DBR} is the partial quality factor defined by the loss through the

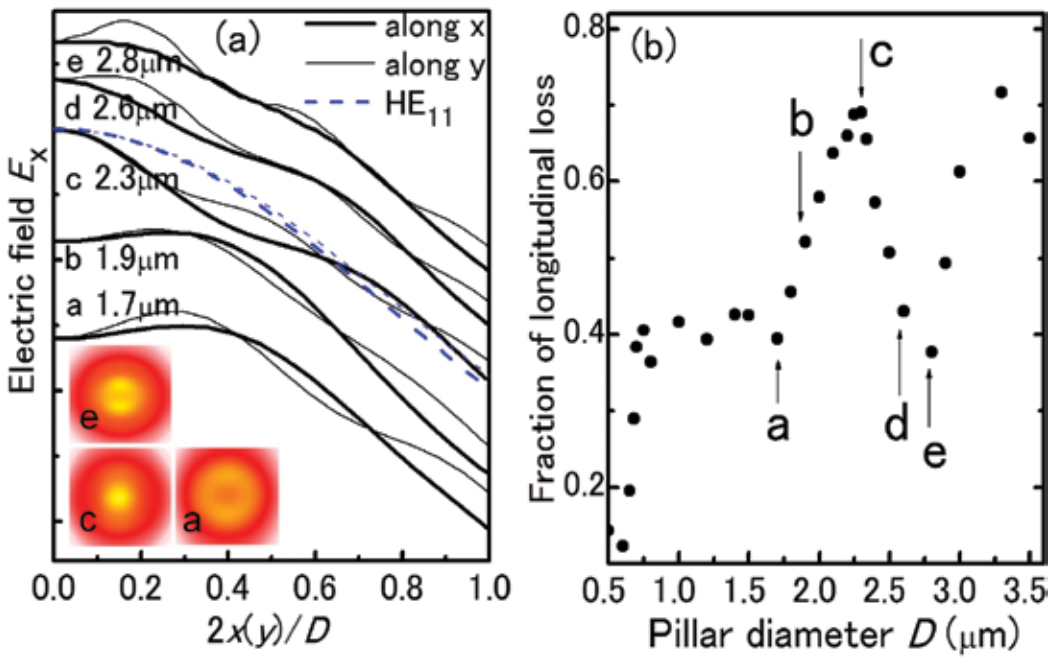

Figure 4. (a) The x- and y-line profiles and the xy-plane profiles (colored insets) of E_x of the fundamental modes in Si/SiO_2-InP hybrid micropillar cavities with different diameters. For clarity, the lines for different sizes are vertically moved away from each other. The blue dashed lines correspond to the ideal HE_{11} mode. (b) The fraction of longitudinal loss, ~Q/Q_{DBR}, as a function of the cavity diameter.

top and bottom DBRs. The fraction of the transverse loss corresponds to $1-Q/Q_{DBR}$. As can be seen in **Figure 4(b)**, Q/Q_{DBR} becomes highest (60–70%) when cavity diameter D is around 2.30 and 3.30 μm. As D deviates from these values, the longitudinal loss decreases. Comparing each mode profile in **Figure 4(a)** with the corresponding loss data in **Figure 4(b)**, one can easily see that a radiation pattern with a single central lobe correlates with the highest fraction of longitudinal loss, which is in practice quite meaningful. The most useful character is the ratio of light output collected in the normal direction. It corresponds to the loss through the top DBR, giving a partial quality factor Q_{top}. Owing to the reflectivity difference between the top and bottom DBR pairs, the loss through the top DBR occupies most, a fraction Q_{DBR}/Q_{top} of ~88%, of the longitudinal loss. The output efficiency can be calculated by $(Q/Q_{DBR})(Q_{DBR}/Q_{top})$ $F_P/(F_P+1)$ [28]. It will thus be ~60% on a cavity with diameter D in the range of 2.20–2.40 or 3.20–3.50 μm, as is an optimized character of the proposed cavity. Noting that the D ranges for high light output (e.g., D ~ 2.30 μm) coincides with those for maximum Q in **Figure 3(b)**, we may argue that a relatively low component of higher-order propagating modes are incorporated into the fundamental mode for single-lobed radiation.

Up to now, we have shown that a 4.5 μm high Si/SiO_2-InP hybrid micropillar cavity with 4/6.5 DBR pairs can present quality good enough for an efficient 1.55 μm band QD SPS. However, the mode wavelength seems not really targeting at 1.55 μm yet. To satisfy a mode wavelength near 1.55 μm, the simplest method may be tuning the Bragg wavelength λ_B to be more than the standard setting λ_{B0}. Setting $\lambda_B = 1.030\lambda_{B0}$, it is found that a cavity with D = 1.30–2.70 μm possesses $F_P > 10$ in the wavelength range of 1.510–1.580 μm. Concrete examples include the following: with D = 1.70 μm, F_P can be ~ 30 at λ =1.550 μm and with D = 2.30 μm, F_P comes up to ~ 100 at λ =1.570 μm. As a practical consideration, it is necessary to further optimize the cavity design for any desired QD emission wavelength. This is actually available if one modifies the design in the high Q (F_P) area, such as D = 2.20–2.40 μm. Viewing λ_B-dependent Purcell factors as a function of D/λ, as shown in **Figure 5(a)**, we learn that they roughly overlaps with that of the λ_{B0} case. It suggests that the best F_P can be obtained for any mode wavelength λ as long as the designs of D and λ_B are suitable. Taking 1.550 μm as the exact target of mode wavelength, we can figure out a cavity design with D = 2.24–2.44 μm and $\lambda_B = 1.017\lambda_{B0}$, resulting in Q = 2000–3300, F_P = 60–110, and λ= 1.550 ± 0.003 μm. For a target wavelength of ~1.580 μm (a practical wavelength for InAs/InP QD SPSs [12]), the best cavity design is determined to be D = 2.28–2.48 μm and $\lambda_B = 1.037\lambda_{B0}$, where Q = 2000–3300, F_P = 60–110, and λ= 1.580 ± 0.003 μm. **Figure 5(b)** displays the typical mode spectra for these two designs. Their line shapes are ideally Lorentzian and their mode widths are less than 1 nm. In addition, good radiation pattern and high output efficiency also remain in these modified designs. However, the spacer thickness was kept wavelength thick (λ_B/n) in all the above designs. The cavity quality could be further improved if the spacer thickness can be freely tuned [29].

It is obvious that our cavity with F_P 10–100 improves the spontaneous emission rate of an InAs/InP QD so that GHz operation of a 1.55 μm QD SPS becomes available. It could also be expected that highly indistinguishable single photons could be produced from InAs/InP QDs, using the above-designed cavities with a nominal F_P = 60–110. In comparison, a Ta_2O_5/SiO_2 cavity of the same quality would need 10/15 top/bottom DBR pairs and a pillar height of 11.5 μm. A practical Ta_2O_5/SiO_2 micropillar cavity, with 8/12 DBR pairs and an 8 μm high pillar

http://dx.doi.org/10.5772/67499

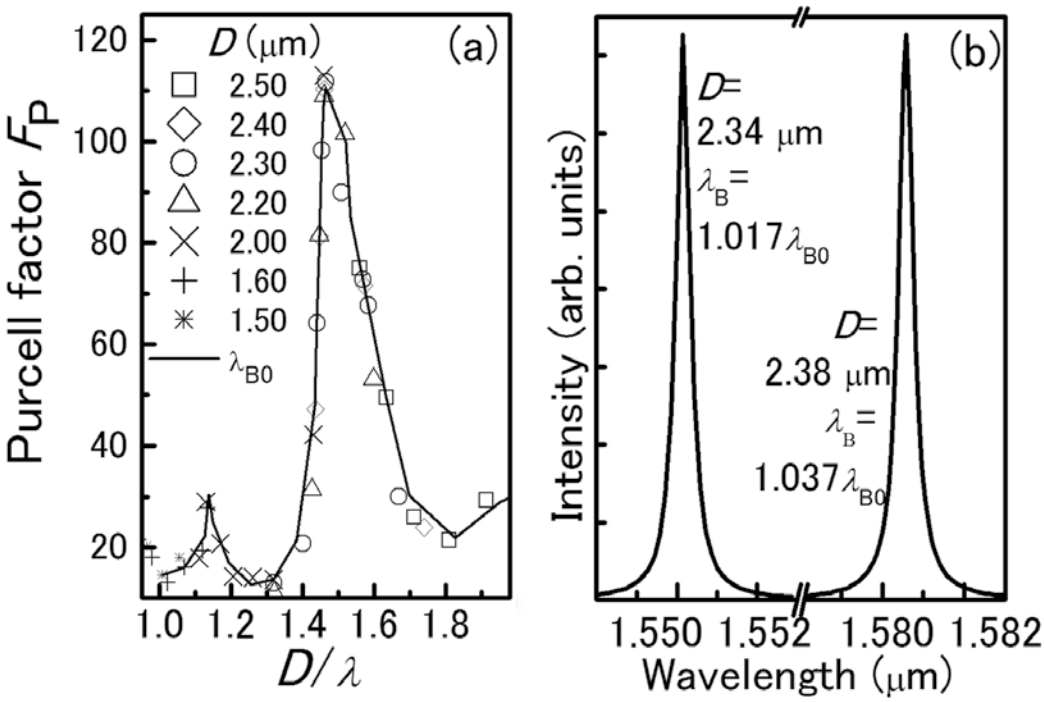

Figure 5. (a) F_P as a function of D/λ in the cases with (symbols) and without (line) tuning λ_B. (b) Two fundamental-mode spectra obtained with chosen diameters D and by suitably tuning λ_B.

[22], would be of lower quality and bulkier than our presently proposed cavities due to a lower refractive index contrast. It is thus reasonable to state that Si/SiO_2-InP hybrid DBR micropillar cavities are better candidates for 1.55 μm InAs/InP QD SPSs.

4. High-quality micropillar cavity

In the above, we proposed a promising micropillar cavity for the 1.55 μm band by combining Si/SiO_2 distributed Bragg reflectors (DBRs) with an InP spacer [25]. This type of microcavity with hybrid materials avoids the difficulty in monolithically fabricating conventional InP-based micropillar cavities. However, this cavity needs relatively large pillar diameter of ~2 μm which is not well satisfying a small mode volume V. This character limits the capability to separate a single QD resonant with the cavity mode and prevents the quantum devices from miniaturizing and integrating. Moreover, future large-scale quantum networks require 1.55 μm SPSs and other quantum devices allowing coherent transfer of quantum states between QDs and single photons via long-distance optical fibers [30], but a Q factor as high as enabling coherent operation seems still difficult in the last hybrid cavity. Very recently, novel structures of micropillar cavities with sub-micrometer diameter and high Q factor were proposed for GaAs/AlAs [31] and TiO_2/SiO_2 [32] systems in which the spacer layers were replaced by tapered DBRs. Although it was proved that such structures were very

effective to obtain improved Q and V, the mode wavelength was shorter than 1 μm. For practical applications, it is required to investigate whether and how the mode wavelength can be extended to 1.55 μm telecommunication band while exhibiting sufficiently high Q factor and small V. Therefore, we present the design of the hybrid micropillar cavity structure consisting of tapered Si/SiO_2 DBRs and InP-based materials containing single InAs QDs [33].

The structure of the proposed micropillar cavity is schematically shown in **Figure 6(a)**. The top and bottom parts of the pillar are conventional DBRs composed of alternating Si and SiO_2 layers. Each layer in these DBRs is set quarter-wavelength thick, i.e., the layer thickness $t_1 = \lambda_B/(4n_{e1})$ for Si, $t_2 = \lambda_B/(4n_{e2})$ for SiO_2, where λ_B is the Bragg wavelength here firstly set to be 1.55 μm and $n_{e1(2)}$ is the effective refractive index of Si(SiO_2), which is calculated and known to be dependent on D by using the standard waveguide theory [34]. In between the conventional DBRs, we incorporate more Si/SiO_2 segments as tapered DBRs on both the top and bottom sides. Here "taper" means adiabatically deducing the layer thicknesses as the DBR extends toward the cavity center (spacer) [31, 32]. In detail, the tapered DBRs have linearly decreasing layer thicknesses $t_{1i} = t_1(1-\rho(2i-1))$ for Si and $t_{2i} = t_2(1-2\rho i)$ for SiO_2, where i is the taper segment number and ρ the tapering slope of the layer thickness, i.e., the decreased fraction per tapered layer. In between the tapered Si/SiO_2 DBRs, an InP layer containing InAs QD as the light source is inserted as the spacer layer with thickness:

$$t_0 = \lambda_B\left(1 - 2\rho N\right)/(4n_{e0}), \tag{3}$$

where n_{e0} is the effective refractive index of the spacer material and N the total taper segment number. The whole micropillar is standing on a semi-infinite Si substrate.

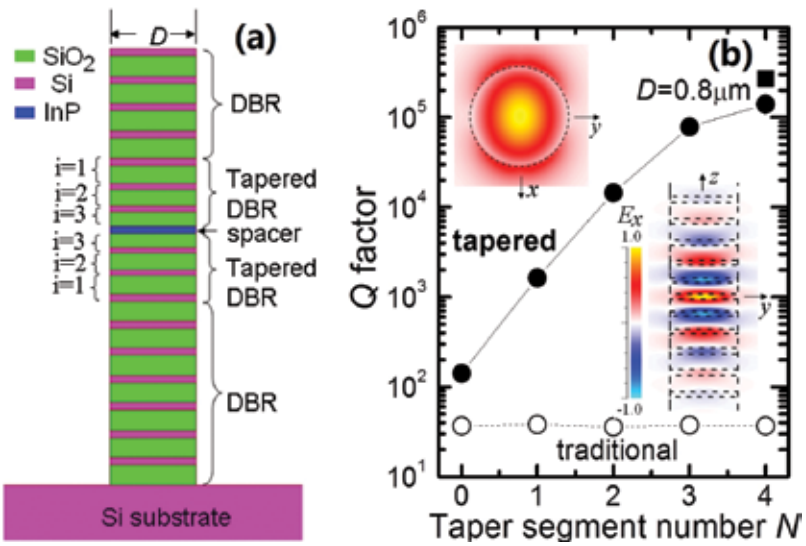

Figure 6. (a) The schematic cross section of the high-quality tapered hybrid micropillar cavity. (b) The Q factors as a function of the total taper segment number for optimized cavities with 0.8 μm of pillar diameter. Those of traditional micropillar cavities are shown as a contrast. Colored insets at the left-up and right-down corners are the profile patterns of E_x of the mainly x-polarized fundamental mode. As a size reference, the cavity outlines are drawn on the mode patterns by dashed lines.

The study was started from all-Si/SiO_2 tapered micropillar cavities, which are similar to the reported tapered cavities absent of a third material [31, 32], by setting the spacer in **Figure 6(a)** to be Si. On such cavities, quality factor Q for the fundamental mode is optimized by simply tuning the tapering slope ρ. Not surprising, a different structure has different ρ for optimizing the Q factor. As an example, a cavity with diameter D = 0.8 μm, DBR of 4/6.5 pairs, and taper segment number N = 3 exhibits an optimized Q factor of 1.1 × 10^5 if ρ = 0.045. Based on the optimized conditions obtained from these all-Si/SiO_2-tapered cavities, one might intuitively expect a good hybrid cavity simply by changing the spacer to InP with the appropriate thickness t_0 determined by Eq. (3), but this does not really give a high Q factor. It is found that it is better to tune the InP spacer thickness as

$$t_0 = \sigma\lambda_B\left(1 - 2\rho N\right)/(4n_{e0}), \tag{4}$$

with the tuning parameter $\sigma > 1$ while using the optimized ρ of the all-Si/SiO_2 case. Naturally, different N corresponds to different σ for the optimized Q factor. Shown in **Figure 6(b)** is the result of an example structure, the cavity with D = 0.8 μm and 4/6.5 pairs of conventional DBRs. It is seen that the Q factor increases monotonically with the total taper segment number N, by in average one order for every additional taper segment.

Compared to traditional counterparts, which have (4+N)/(6.5+N) pairs of quarter-wavelength-thick Si/SiO_2 DBRs and a wavelength-thick InP spacer and show Q factor of below 100, tapered DBRs increase the Q factor for 1–3 orders of magnitude. Typically, the Q factor is increased to be ~ 8 × 10^4 by three segments of tapered Si/SiO_2 DBRs. With 4 taper segments, there seems a saturation effect so that the Q factor reaches 1.4 × 10^5, only about twice that of 3 taper segments. This is because that there are no longer enough conventional DBR pairs to take the role of vertical optical confinement for the would-be higher Q factor. As a matter of fact, when increasing the conventional DBR pairs to 6/9.5, the Q factor can be further increased to be 2.7 × 10^5, as shown by a solid square symbol in **Figure 6(b)**. We may note that the above Q factors are a bit lower than those of all-Si/SiO_2 tapered micropillar cavities. This is the result of replacing Si with InP as the spacer. The mismatch in the refractive indices between Si and InP (~8.5%) determines that the mode-profile matching between the spacer and the DBRs, which is considered to be associated with the Q improvement in tapered cavities [32], is not as perfect as that in all-Si/SiO_2 tapered cavities. Fortunately, the index mismatch is not so large that we can still obtain high Q factors in the Si/SiO_2-InP hybrid tapered micropillar cavities. It can be confirmed by replacing InP with InGaAsP which has an index mismatch of 3.5% with respect to Si. In this case, optimized Q factor of three-segment tapered cavity is ~9.5 × 10^4, much closer to that of all-Si/SiO_2 tapered cavities.

In such a hybrid micropillar cavity, taper design is not necessarily restricted to Si/SiO_2, but we learned that InP/InGaAsP tapered DBRs are far less effective than Si/SiO_2 in improving the cavity quality, because of the difficulty in mode-profile matching between InP/InGaAsP and Si/SiO_2.

The above high Q factors suggest thus the nice property of the presently proposed micropillar cavities. Their good character also lies at the mode profiles, as shown by the insets of **Figure 6(b)**. The mode profile of the fundamental mode is single lobed and highly symmetrical (by the

in-plane xy profile), which makes it beneficial to couple the QD emission from the cavity into a fiber. The mode profile is well confined in the tapered region (by the vertical yz profile), which could probably be one of the reasons for high Q factors in such tapered micropillar cavities.

In optimizing the Q factor by only tuning the parameter σ as in the above, the mode wavelength may not exactly match a specific target wavelength. We can resolve it by tuning the cavity structure together in parameter σ, tapering slope ρ, and Bragg wavelength λ_B, all of which describe the vertical structure of the cavities. For the last parameter λ_B, we label the previous setting as λ_{B0} = 1.55 μm from now on. Using these procedures on three-segment tapered cavities with D = 0.8 μm and 4/6.5 conventional DBR pairs, we find that the best Q factor of 8×10^4 for an exact mode wavelength λ = 1.550 μm can be obtained by setting σ = 1.18, ρ = 0.05, and $\lambda_B = 1.02\lambda_{B0}$.

An optimized design needs detailed knowledge of the dependence on various parameters, which is a little complicated. For simplification, we here characterize the effects of the three tuning parameters σ, ρ, and λ_B in terms of the variation in spacer thickness $\Delta t_0 = t_0 - t_{0m}$, since they all give rise to changes in the spacer thickness t_0. **Figure 7(a)** shows the mode wavelength and the Q factor depending on $\Delta t_0/t_{0m}$, the relative change in the spacer thickness, in the three cases of cavity structure tuning. As σ only is tuned, meaning that only the InP spacer thickness is changing, the mode wavelength changes weakly, but the Q factor degrades fast. Viewed in a wider range, the variation of Q factor is actually something like a degrading sinusoidal function of the spacer thickness (not shown). As the spacer thickness increases, it is deduced to a minimum of ~100 at $\Delta t_0/t_{0m}$ ~ 1.1, then comes up again to another maximum of ~ 500 at $\Delta t_0/t_{0m}$ ~ 2.5, and goes down once more. As the tapering slope ρ only is tuned, meaning that the tapered DBRs and the spacer are changing together, the mode wavelength changes faster, but the Q factor decreases more slowly. As the Bragg wavelength λ_B only is tuned, meaning that the thicknesses of all layers are changing, the mode wavelength changes even faster, but the Q factor almost remains high. As a whole, Q factor can be preserved over 10^4, while the mode wavelength λ is limited within the range of 1.50–1.60 μm, if the layer thickness fluctuation is within ±5%, as is indicated by a shaded area in **Figure 7(a)**.

The above Q variations versus vertical structure suggest that a local change destroys, while an overall harmonic change keeps the quality of a cavity. To further understand it, we may try viewing the mode-profile matching, which was considered responsible for high Q factors in tapered cavities [32]. **Figure 7(b)** shows the line profiles of the fundamental mode along the in-plane y direction for a few cavity structures O, A, B, and C, as marked in **Figure 7(a)**. The two lines in each set are taken from the central planes of the spacer layer and of the Si layer closest to the spacer. It is clear that the optimized cavity structure O shows good mode matching. The structure A, whose Q factor is just a bit lower than structure O, has mode matching a little bit worse than structure O. The structure B, whose Q factor is greatly degraded, has remarkably mismatching mode profiles. However, the structure C has mode matching not as bad as structure B but as good as structure A although its Q factor is even worse than structure B. It suggests that mode-profile mismatching only cannot perfectly explain the Q factors of our tapered micropillar cavities. Probably, phase mismatching [35] may take a role in determining the Q factor, which is open for future investigation.

http://dx.doi.org/10.5772/67499

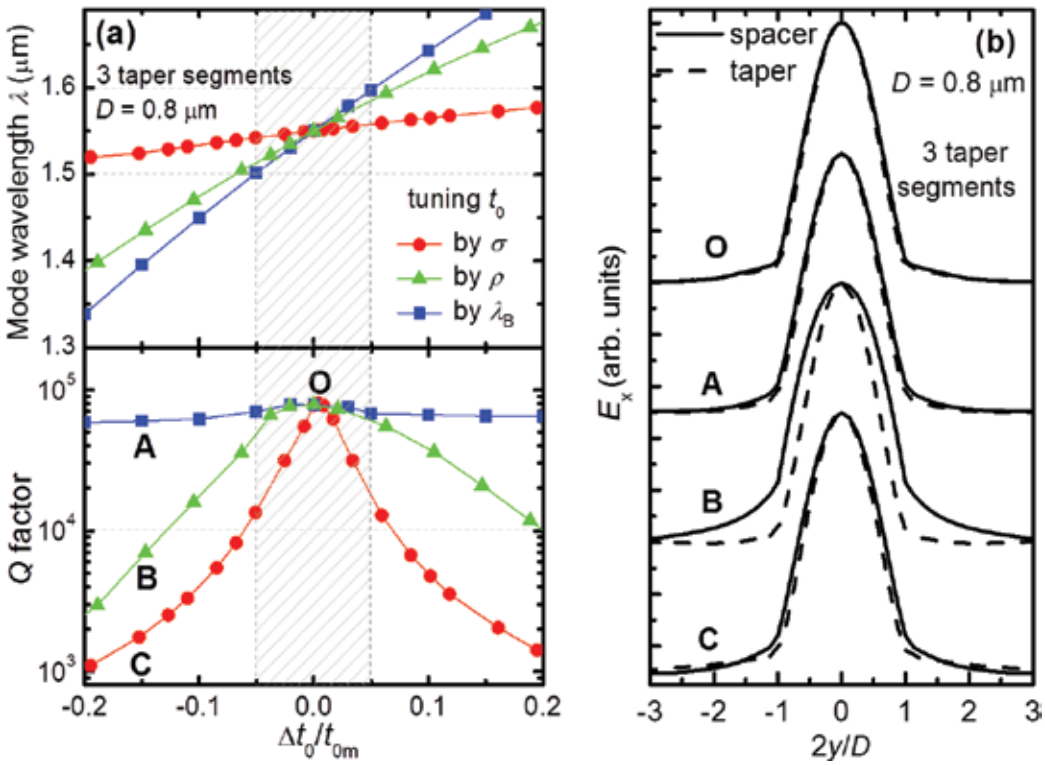

Figure 7. (a) Mode wavelength λ and Q factor as functions of the relative variation in the spacer thickness in different parameter-tuning cases for typical tapered hybrid micropillar cavities. (b) Line profiles of the electric field E_x of the fundamental modes in the central plane of the spacer (solid) and of the Si layer closest to the spacer (dashed) for four different cavity structures as marked in (a). For clarity, the lines for different cavity structures are vertically shifted away from each other.

After describing the dependence on the vertical structure as above, we examine here how the cavity property varies with the lateral size, the pillar diameter D. As examples, we show the results of three structures as depicted in **Figure 8**.

The red square symbols in **Figure 8(a)** and **(b)** show that, with 2/3.5 pairs of conventional DBRs and two tapered segments, an optimized Q factor of more than 3000 for 1.55 μm emission happens with pillar diameter of 0.85 μm, and changing the pillar diameter in 0.60–0.95 μm gives Q factors of over 1000 for wavelength 1.35–1.60 μm. Compared to the last hybrid cavity, the Q factor is the same, and the Purcell factor F_P, shown in **Figure 8(c)**, is somehow higher because the pillar diameter is greatly decreased to below 1 μm. Besides, the pillar height remains the same as the last one, 4.5 μm, suggesting the superiority of this cavity beyond the previous structure in generating indistinguishable single photons and enabling ultrahigh-speed SPSs operating in several GHz clock.

The more typical is the structure with 4/6.5 pairs of conventional DBRs and three taper segments, whose vertical structure is fixed to that optimized with D = 0.8 μm. The blue circles in **Figure 8** show that the Q factor of this structure is 1–8 × 10^4 in the range of D = 0.45–1.10 μm, 1–2 orders

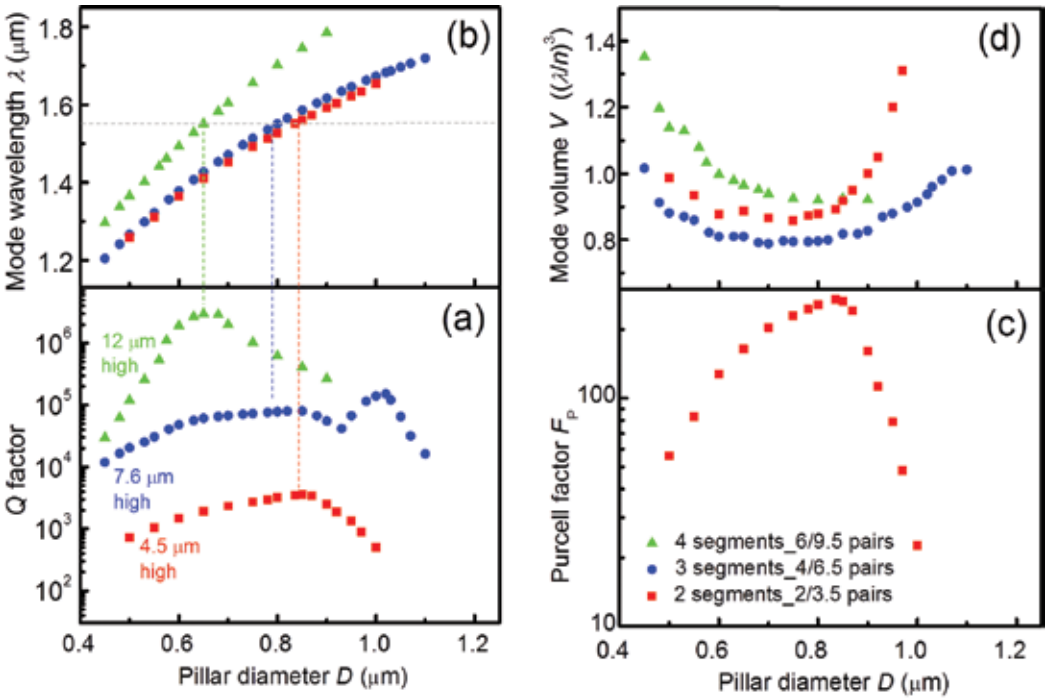

Figure 8. The (a) Q factor, (b) mode wavelength λ, (c) Purcell factor F_P, and (d) mode volume V as functions of the pillar diameter D for the tapered Si/SiO_2-InP micropillar cavities with vertical structures fixed at optimized conditions.

of magnitude higher than that of the previous cavities, from below 100 for $D < 1$ μm to a few thousands for $D > 2$ μm. Especially, it remains over 6×10^4 in a D range of 0.65–0.90 μm, exhibiting the robustness against diameter variation. There is a peak around $D = 1.0$ μm, appearing somehow abnormal. It is probably a result of oscillation behavior also observed in GaAs/AlAs tapered cavity [31] and is probably related to the coupling with higher-order modes, which often occurs in the previous micropillar cavities [36]. This good quality is in debt to a ~7.6 μm high micropillar, higher than that of the last hybrid cavity, because not only of tapered layers incorporated but also of smaller effective refractive indices, increasing the thickness of each DBR layer.

Similarly, we examined cavities with 6/9.5 conventional DBR pairs and four taper segments. We fix the vertical structure to an optimized cavity with $D = 0.65$ μm, which gives a Q factor as high as 3×10^6 at mode wavelength of 1.55 μm. Fixing the vertical structure to this condition, we get the cavity properties as functions of the pillar diameter D, as shown in **Figure 8** by green triangle symbols. At the expense of a pillar height 12 μm, a Q factor of over 1×10^5 can be obtained in a cavity with diameter ranging from 0.5 to 0.9 μm. Especially, $Q > 2 \times 10^6$ are available for mode wavelength $\lambda = 1.55 \pm 0.05$ μm with $D = 0.60$–0.70 μm in this cavity. Since the traditional cavities with 6/9.5 DBR pairs have typically just ~20% higher Q factors (not shown) than 4/6.5 DBR pairs, the four-segment tapered cavity here improves the Q factor for 2–3 orders of magnitude.

Just due to thicker DBR layers, all these three structures show mode wavelength varying with the diameter D faster than that of the previous cavities, as seen in **Figure 8(b)**. **Figure 8(c)** does not show F_P for three and four taper segments because most of their nominal values are too high to be physically meaningful due to the property beyond weak coupling regime. As another important parameter, the mode volume V of these cavities is shown in **Figure 8(d)** in the unit of $(\lambda/n)^3$, where n is the refractive index of the spacer material. It is found mostly less than 1, which is not so different but definitely smaller than that of the previous cavity in the small D area, although recent study suggests significant reduction of the mode volume as low as ~0.1 with the benefit of the tapered DBRs [32]. Anyway, the structure with three taper segments can typically have V as small as ~0.8, which is reduced to be half of that of our last hybrid cavities, ~1.6 at D ~ 2.2 μm.

In the above, the allowed pillar diameter for mode wavelength around 1.55 μm is restricted to a small range spanning within 0.1 μm, due to fixed vertical structures. This, however, does not mean that an effective cavity for ~1.55 μm band can only be obtained in such a narrow size range. By employing vertical structure tuning at various diameters, we can see that a high Q factor for mode wavelength of ~1.55 μm is available in a wider diameter range. Q factors over 6×10^4 can be obtained with pillar diameter of 0.70–0.95 μm. The degradation of Q factor at diameter less than 0.6 μm is partly because that lateral confinement of the optical mode is more difficult. There is a peak at $D = 0.9$ μm, appearing somehow unusual though good for application. Similar to the case of fixed vertical structure, this is probably a result of oscillation behavior likely related to the coupling with higher-order modes. Generally, based on vertical cavity structures of high Q factors, tapered Si/SiO_2-InP micropillar cavities with sub-micrometer diameters can have Q factors of near 10^5 to a few 10^6, improved for up to three orders of magnitude compared to the previous ones, with mode wavelength of 1.55 ± 0.05 μm.

With the good properties described above, we shall now discuss our tapered Si/SiO_2-InP micropillar cavities on their effectiveness for applications.

At first, for SPS-based quantum devices, it is important to isolate a single QD effectively emitting from the cavity. Supposing a high QD density of the order of 10^{10} cm^{-2} and an inhomogeneous width of ~50 meV, there could be less than 1 QD resonant to a cavity mode with Q factor more than 3000 in a cavity with diameter of 1 μm. It guarantees the single-photon nature of an InAs/InP QD SPS using this sub-micrometer micropillar cavity. Since the saturated effective emission rate is proportional to the square of the coupling strength $g^2 \propto 1/V$ [37], the small mode volume helps increasing the limit in the quantum key rate of an SPS by a factor of 2 with respect to the previous case. This is quite beneficial to enable ultrahigh-speed SPSs operating in several GHz clock.

Coherent operation of SPS requires strong coupling between the QD and the cavity mode, which can be satisfied if [37]

$$g/|\kappa - \gamma - \gamma * | > 1/4 \tag{5}$$

where g is the coupling strength, $\kappa = 2\pi c/Q\lambda$ the loss rate of the cavity mode, γ the spontaneous emission rate, and γ^* the pure dephasing rate of the QD. When Q is not higher than a few 10^4, κ is much larger than $\gamma = 1/T_1$ (T_1 ~ 1.2 ns [12]) and $\gamma^* = 1/T_2^* = 1/T_2 - 1/2T_1$ (T_2 ~ 0.13 ns

[17]) [38], so the condition in Eq. (5) can be simplified as $g > \kappa/4$. Using $g = \sqrt{e^2 f/(4\varepsilon_0 n^2 m_0 V)}$ [31], where ε_0 is the vacuum permittivity, e the elementary charge, m_0 the free-electron mass, and $f = \varepsilon_0 m_0 c\lambda^2/(2\pi n e^2 T_1)$ [39] the oscillator strength of the QD; the simplified condition reads $Q/\sqrt{V} > \sqrt{\pi\lambda/r_e n f}/2 = 2200$, where $r_e = e^2/(4\pi\varepsilon_0 m_0 c^2)$ is the classical radius of electron and V is the mode volume normalized to $(\lambda/n)^3$. As Q goes higher than that of the satisfied simplified condition, Eq. (5) is always available since $|\kappa - \gamma - \gamma^*|$ is decreasing to zero and then approaching $\gamma + \gamma^*$ (~30 μeV), which is much less than $4g$ (~365 μeV). Obviously, this condition can be easily satisfied by our tapered micropillar cavity since its $Q/\sqrt{V}$ can be ~10^5–10^6 and ~2–3 orders of magnitude higher than that of the previous cavity, maximally ~ 2000. It is indicative of the feasibility of constructing a coherent SPS or other quantum devices for 1.55 μm band quantum information processing.

As the actual fabrication process is concerned, our cavity design has an advantage in lowering the pillar height as compared with those of GaAs/AlAs and SiO_2/TiO_2 tapered micropillar cavities. The GaAs/AlAs case gives a pillar height of 9.6 μm for mode wavelength λ ~ 0.9 μm [31]; then it would be ~16 μm high for λ ~1.55 μm. The TiO_2/SiO_2 tapered cavity gives a pillar height of 6.2 μm for λ ~ 0.64 μm [32]; thus it would be ~15 μm high for λ ~ 1.55 μm. Our present cavities thus serve as better candidates for λ ~ 1.55 μm.

Finally we may argue that the tapered Si/SiO_2-InP hybrid micropillar cavities here proposed are not only promising as 1.55 μm quantum information processing devices based on InAs/InP QDs; their high Q and small V also support the applications in other fields such as ultrasmall lasers, slow-light engineering, and optical switching.

5. High-quality and monolithic microcavity

Although being of high quality at 1.55 μm telecommunication band, the hybrid tapered Si/SiO_2-InP hybrid micropillar cavity is not yet ideal due to the complicated fabrication process, defecting near the light source caused by thin active layer and mismatching thermal expansion in different materials. As a matter of fact, up to now a practically good pillar cavity has not been available yet as a SPS applied in 1.55 μm quantum information processing. More efforts must thus be devoted to finding methods of overcoming the left problems. We are herewith considering some techniques beyond material hybrid. In the case of planar DBR cavity, an effective way to increase refractive index contrast of InP-based materials is to introduce air gaps by sacrificing some layers [20, 40]. We note that a pillar DBR cavity might be reformed by incorporating partial air-gap layers. In this section, therefore, we propose a micropillar cavity consisting of InGaAsP/InP layers with partial air gaps, which can be monolithically fabricated. It is presented that this microcavity has high quality (Q) factors and small mode volumes, satisfying the requirements of SPS at 1.55 μm telecommunication band.

The proposed cavity structure is schematically demonstrated in **Figure 9(a)**. It shows that disk-shaped (in the XY plane) and coaxially set (in the Z direction) InGaAsP and InP layers with different diameters D and d, respectively, are alternatively stacked on an InP substrate. Effectively, the small-sized InP layers are compassed by surrounding air gaps, or, namely, with air

http://dx.doi.org/10.5772/67499

apertures. The InGaAsP layers are lattice matching to the InP substrate and have an energy gap larger than the photon energy of 1.3 μm wavelength, so that they are extremely transparent for ~1.55 μm light.

In more detail, the top and bottom parts of the cavity are conventional DBRs composed of periodical InGaAsP and InP layers. Each InP layer in the DBRs is set as thick as $t_1 = \lambda_B/4$, where λ_B is the Bragg wavelength, set to be around 1.55 μm. This thickness is actually a quarter-wavelength of air because the optical media of this layer in the pillar is mainly air rather than InP. In the case of planar air-gap DBR cavities [20, 40], semiconductor layers are usually set to be three-quarter-wavelength thick, but our simulation implies that this design in our case hardly has good cavity quality. Thus the InGaAsP layers in the DBRs are set quarter-wavelength thick, i.e., $t_2 = \lambda_B/(4n_2)$, where n_2 is the refractive index of InGaAsP. Inserted between the conventional DBRs are more InGaAsP/InP-air-aperture segments (pairs) as tapered DBRs on both the top and bottom sides. In detail, the tapered DBRs have linearly decreasing layer thicknesses $t_{1i} = t_1(1-\rho(2i-1))$ for InP and $t_{2i} = t_2(1-2\rho i)$ for InGaAsP, where i stands for the taper segment number and ρ is the tapering slope of layer thickness, i.e., the decreased fraction per tapered layer. In between the tapered DBRs, an InP layer is inserted as the spacer layer with thickness $t_0 = t_1(1-2\rho N)$, where N is the total taper segment number in one tapered DBR. An InAs QD is set in this layer as the light source.

It is found that the InGaAsP/InP-air-aperture microcavity is of high quality when it has 4/6.5 pairs of InGaAsP and InP layers in the top/bottom DBRs and $N = 3$ segments in the tapered DBRs. The pillar of this cavity structure appears some 7–8 μm high, which is the same as the

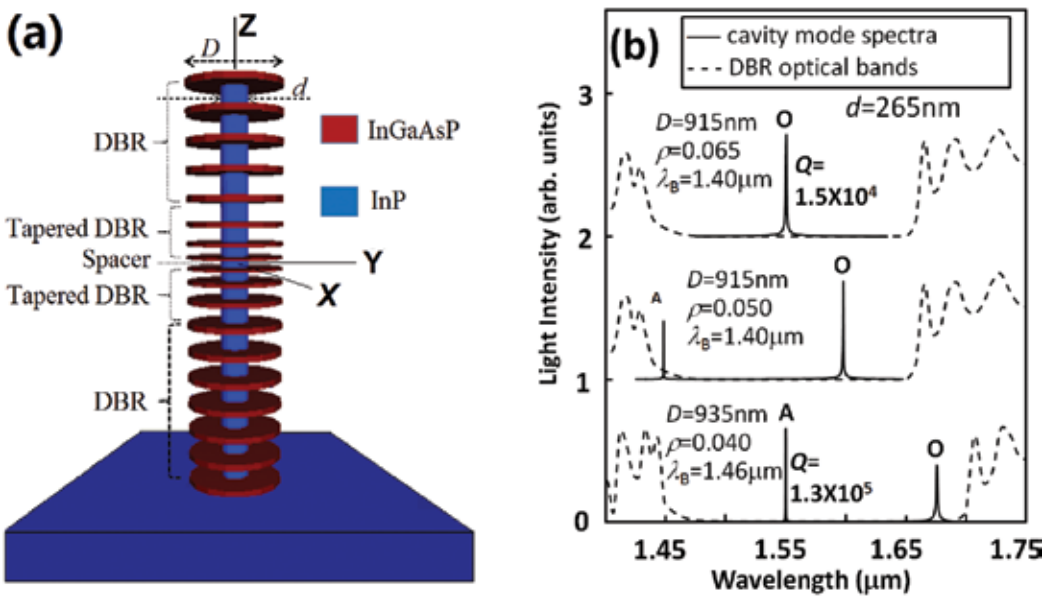

Figure 9. (a) Three-dimensional schematic demonstration of the InGaAsP/InP-air-aperture microcavity. (b) Examples of the calculated optical mode spectra with corresponding DBR optical bands. In (b), the lines for different design conditions are vertically shifted for clarity.

high-quality Si/SiO_2-InP hybrid pillar cavity [33] and the high-quality GaAs/AlGaAs monolithic pillar cavity [31]. By massively trying out different cavity geometrical parameters D, d, λ_B, and ρ, the optical properties were systematically studied. When d = 265 nm, D = 915 nm, λ_B = 1.40 μm, and ρ = 0.065, it is observed that the optical mode with the longest wavelength, i.e., the fundamental cavity mode, peaks at 1.550 μm with Q factor of 1.5×10^4, as shown by the topmost spectrum in **Figure 9(b)**. This is surprising because a similarly high InGaAsP/InP DBR pillar cavity exhibits Q factor of only a hundred or so. It indicates that the air apertures resolve the problem of low refractive index contrast in InP-based pillar cavities. We label this fundamental mode as mode O hereafter. It is roughly at the center of the DBR stopband, corresponding to an optimized condition. As shown by the middle spectrum in **Figure 9(b)**, when ρ is tuned to be 0.05, mode O shifts to a longer wavelength with Q factor decreasing to 6000. Meanwhile, there arises a new mode near the shorter stopband edge. Further changing ρ to be lower, the new mode, termed mode A hereafter, shifts toward the middle of stopband and its Q factor increases, while mode O is shifting toward the longer stopband edge with smaller and smaller Q factor. The lower spectrum in **Figure 9(b)** shows that, by changing all the three parameters D = 935 nm, ρ = 0.04, and λ_B = 1.46 μm, we obtain an optimized mode A, peaking at 1.550 μm and with Q factor of 1.3×10^5. This Q factor is one order of magnitude higher than the optimized mode O and even higher than that of a typical Si/SiO_2-InP hybrid pillar cavity with a similar pillar size [33]. At the same time, mode O becomes a peak near the longer stopband edge with Q factor below 3000.

It is worth stressing that the proposed cavity is a nanometer-scaled pillar structure since the cavity lateral size, especially the air-aperture diameter, is less than 1 μm. The direct result of this nanoscale is the small mode volume V, which is 1.08 and $0.94(\lambda/n)^3$ for optimized modes O and A, respectively, where λ is the mode wavelength and n is the refractive index at the point of maximal light intensity. The light intensity distribution, which determines the mode volume through integrating over the cavity [1], is shown in **Figure 10**. We note that both modes are twofold degenerate with orthogonal main polarizations, but for simplicity, we arbitrarily select X as the main polarization direction to describe their properties. The colored patterns tell us that the light fields of both modes O and A are laterally well confined within the semiconductor cavity media, i.e., quite weak in the air, and vertically confined mainly within the tapered DBRs and the spacer region. This is resulted by the air apertures, which tend to compact the light fields laterally into an area with diameter d and vertically into a few DBR layers by increasing the reflective rate of DBRs.

The vertical distribution patterns in **Figure 10** also show the effect of adiabatic design in the tapered DBRs. That the light intensity extends over a few segments implies gentle confinement of light fields, which provides a reasonable explanation for the high Q factors [41] in both modes O and A. What is more important, there really exists a large difference in the two modes. Mode O has strong light fields both in the small-diameter InP spacer and the large-diameter InGaAsP layers, while mode A leaves its optical field mainly in the InGaAsP layers. With sub-wavelength lateral size $d < \lambda_B/n$, the InP spacer with air aperture is more subjective of leaking through the side wall. This is likely the reason why the optimized mode A has higher Q than mode O. In terms of the Z-dependent line profile of the main electric field along the X direction, E_X, mode O is symmetric, whereas mode A is antisymmetric to the cavity

http://dx.doi.org/10.5772/67499

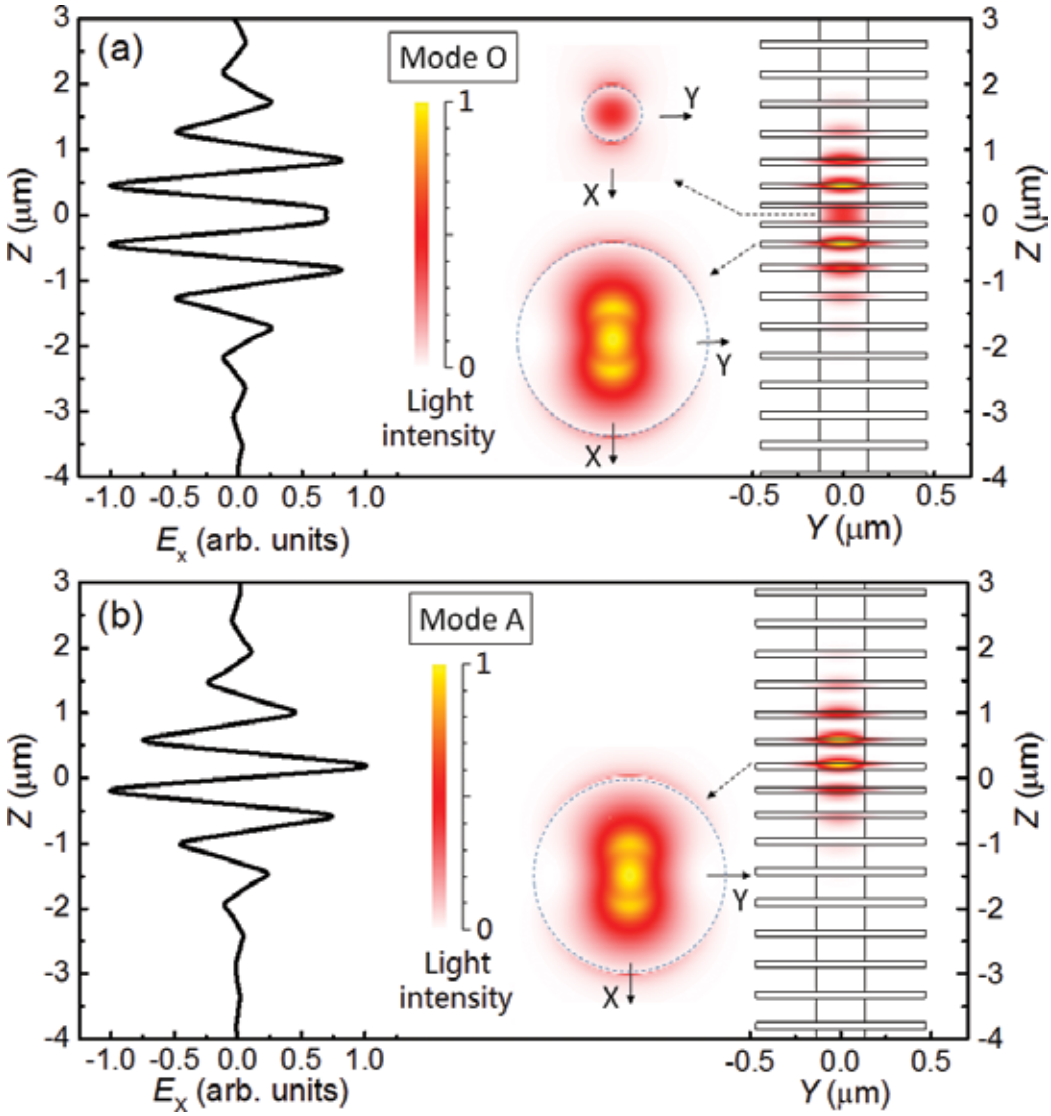

Figure 10. Line mode profiles along vertical Z direction and patterned mode profiles on the YZ and XY planes of the optimized optical (a) mode O and (b) mode A. Note that the line profiles are indicated by the x-polarized electric field, while the plane profiles are displayed by light intensity. The thin lines on the light intensity patterns show the outlines of the optimized cavities.

central plane $Z = 0$. This might be understood by a mode coupling between two fundamental modes corresponding to two differently sized nanopillars, as could bring in some new modes like bonding (symmetric) and antibonding (antisymmetric) states, since a present cavity looks like a mixture of two pillars with different sizes.

To use a cavity with optimized mode A, there seems a problem that the light source in the InP spacer has a weak interaction with the mode field due to minimum field intensity in the spacer.

As a matter of fact, 1.55 μm InAs QD can also be settled in the InGaAsP layer [42]. In addition, we find that exchanging InGaAsP and InP layers can give similarly good cavity properties.

Although we have obtained high Q factors on cavities with some special designs, it is necessary to further investigate the dependence on cavity design parameters, because the practical fabrication process may not be that exact. First let us look at the dependence on vertical size. For simplicity, we here characterize the effects of the tuning parameters λ_B and ρ in terms of the variation in spacer thickness $\Delta t_0 = t_0 - t_{0m}$, where t_{0m} is the optimized spacer thickness, since both of them give rise to changes in the spacer thickness t_0. As shown in **Figure 11(a)**, the mode wavelength λ varies linearly with the relative change in layer thickness at different rates. The tapering slope ρ has less effect on λ because it causes a more local geometric change in the cavity. Conservatively speaking, λ remains within 1.55 ± 0.05 μm range as the layer thickness changes within ±5%. To this degree of thickness deviation, the Q factors of modes O and A do not degrade a lot but remain over 1.3×10^4 and 10^5, respectively, although they would decay almost by factors of 3 and 10 with thickness deviation of ±15%. In more detail, λ_B degrades Q factor more weakly than ρ does because an entire geometric change by λ_B remains, to a high degree, the mode profile, while a local geometric change by ρ breaks the mode profile. By the way, mode O is more robust than mode A, since its Q factor remains over 10^4 with thickness change of ±10%. Given that t_0 is typically over 100 nm, ±5–10% precision means a layer thickness control error within ±5–10 nm, which is rather easy in modern epitaxial techniques enabling controllability at atomic layer level.

Now let us examine the dependence on lateral size. **Figure 11(b)** shows the variations in the cavity properties versus the relative change in cavity diameter $\Delta D/D_m = (D - D_m)/D_m$ and in air-aperture diameter $\Delta d/d_m = (d - d_m)/d_m$, where D_m and d_m are the optimized D and d values,

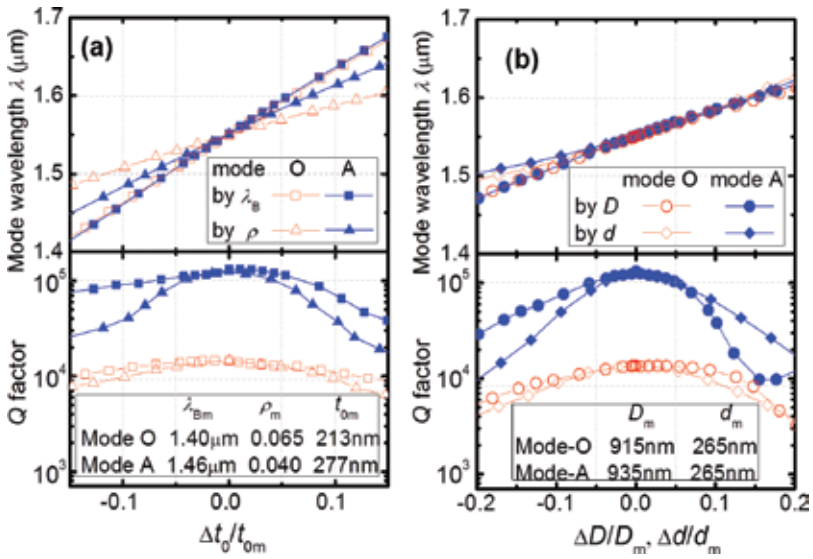

Figure 11. Varying mode wavelength λ and Q factor as the (a) vertical and (b) lateral sizes deviate from the optimized conditions for both modes O and A. Note that the vertical sizes, i.e., the layer thicknesses are tuned by λ_B or ρ but displayed in terms of the spacer thickness t_0. The lateral sizes are tuned by cavity diameter D or air-aperture diameter d.

http://dx.doi.org/10.5772/67499

respectively. It is normal that smaller lateral scale results in a shorter mode wavelength λ due to more localized geometrical confinement. A slight difference lies in the dependences of mode wavelength λ on D and d. The weakly sublinear change with D resembles conventional pillar cavities and can be explained by waveguide dispersion [26]. The super-linear dependence on d might be related to the existence of air apertures. Anyway, D and d have influences on λ to the similar extent in both modes O and A. It stays within 1.55 ± 0.05 μm as the lateral sizes deviate by up to ±10%. As to the Q factor, its degradation with D and d deviations, caused by deviated effective incident angle of light on the DBRs [18], is as much as that with thickness deviations. In a more quantitative view, ±5% change in D or d keeps mode O almost of no degradation and mode A over 10^5 in Q factor. Again, Mode O seems a little more robust than mode A, since ±8% deviation in lateral dimensions can keep its Q factor over 10^4. For a typical diameter of ~200 nm, the lateral size precision of ±5–10% means an error within ±10–20 nm. This degree of controllability has been already available in the state-of-the-art nanotechnology [43]. The robustness against the uncertainty of the fabrication process implies the high technical feasibility to fabricate high-quality microcavity at 1.55 μm telecommunication band.

Remember that in some cases, mode O and mode A coexist. Within the above tuning ranges, however, the main mode always stands with much higher Q factor than the other. There thus will be no serious interference from the useless mode when the main mode is working. By the way, Q versus D in mode A appears a little abnormal, i.e., Q rising back as D becomes large enough. It may result from coupling with higher-order optical modes as is mentioned in previous pillar cavities [25, 27].

With the simulated high quality, the proposed InGaAsP/InP-air-aperture micropillar cavity is hopefully a candidate for a 1.55 μm QD SPS. Let us analyze now how the application aspects of the proposed microcavity would be.

Above all, the likeliness of single-photon emission is enhanced by the nanoscale of the cavity. A single InAs/InP QD is a good single-photon emitter under usual excitation conditions [10, 11] since the excitation pulse duration can easily be in the order of picosecond or less, much shorter than the exciton lifetime of nanosecond order. Isolating a single QD is thus sufficient for single-photon emission. Supposing a high QD density of 6×10^{10} cm^{-2} and a good inhomogeneous width of ~50 meV, it is easy to get that there will be less than 1 QD resonant to a 1.55 μm cavity mode with Q factor of 10^4 (i.e., mode width less than 0.08 meV) in a pillar cavity with a diameter of 1 μm. This property highly guarantees the single-photon nature of an InAs/InP QD SPS composed of this micropillar cavity. In addition, the sub-micrometer-scaled structure is also beneficial to incorporating SPSs into a photonic integration chip, which is necessary in the future quantum information processing network. With Q/V over 3000, the Purcell factor F_p of a weak coupling cavity, simply speaking the enhancement degree of spontaneous emission of the light source, is estimated to be more than 100. This degree can reduce the spontaneous emission lifetime of InAs/InP QDs (a few ns [11]) to be shorter than the coherence time (~100 ps [16]). It suggests that a present cavity with optimized mode O ($Q \sim 10^4$ and $V \sim 1(\lambda/n)^3$) could be used as a photon-indistinguishable SPS [7] and GHz operating SPS at 1.55 μm band. In the case of strong coupling, which enables coherent transfer of quantum states between a light emitter and a cavity mode, theoretical criteria [37] suggest that $Q/V^{1/2} > 10^4$ is more than enough for a 1.55 μm InAs/InP QD

emitter. A present cavity with optimized mode A (Q ~ 10^5, $V < 1(\lambda/n)^3$) is thus able to realize coherently controllable single-photon devices at 1.55 μm band.

As compared to other pillar cavities, the microcavity proposed here takes some advantages. The widely used GaAs/AlGaAs DBR pillar cavity can also be of high-quality $Q > 10^5$ and sub-micrometer size [31]. If it is applied for 1.55 μm band, however, the pillar would be ~16 μm high, much more difficult to fabricate than the present ~7 μm high pillar. Furthermore, it is hard to contain 1.55 μm QDs in GaAs-based DBR structures. Therefore, a GaAs/AlGaAs pillar cavity is less usable as a 1.55 μm SPS than the present one. As to the InP-based materials, the calculations in Section 2 suggest that a conventional InGaAsP/InP DBR pillar cavity with a sub-micrometer diameter can work with Q factor of ~10^4 and Purcell factor of ~100 at 1.55 μm, able to weakly couple a single InAs/InP QD with a cavity mode. However, there should be ~40/70 periods of DBRs, meaning a pillar too high (~30 μm) to be currently producible. It is thus clear that, even only for weak coupling, InP-based DBR pillar cavity is much less suitable than the present one. The hybrid pillar cavities, such as Ta_2O_5/SiO_2–InP [22] or Si/SiO_2-InP [25, 33], are subject to interface defects and different thermal expansion coefficients. The present cavity consists of only InP-based epitaxial materials so that it is free of interface defects and thermal expansion difference. More significantly, it can be fabricated by a monolithic process, e.g., epitaxial growth for the multilayer structure, dry etching to form a pillar, and selective wet etching to develop air apertures. The fabrication process is obviously simpler and of lower cost than the techniques for fabricating hybrid pillar cavities [22].

There may arise a problem that the good cavity quality we have obtained may have a distance from that of a real cavity, because the above fabrication process could be not well determined to make an ideal cavity structure. One aspect may be that, with size less than 1 μm, process-induced surface roughness might degrade the cavity quality by, e.g., edge scattering [44]. At present, however, InP-based nanocavities, e.g., 100–400 nm-sized photonic crystal cavities, have readily exhibited practical Q factors above 10^4 [45] although surface roughness does exist. On the other hand, the present advanced techniques allow controlling sidewall surface roughness of InP-based nanostructures to be less than 1 nm while remaining of good optical quality [46, 47]. Primitive calculations on our nanocavities suggest that a sidewall roughness of 1 nm degrades the Q factor by 5–10%. There may be another aspect that the chemical etching influences the optical quality by introducing surface states [48]. Nevertheless, recent researches demonstrate that, when some suitable etchant and/or surface passivation are used, a wet-etched InP-based nanopillar presents nice optical properties [49]. A sophisticated wet-etching process would have only a minor effect on the quality of a nanocavity [50]. Furthermore, it is worth noting that InP/InGaAsP materials have a relatively low surface recombination velocity than GaAs/AlGaAs materials [51]. Consequently, a real cavity as here proposed could be expected to have optical quality very close to what is designed here.

We see that the InGaAsP/InP-air-aperture micropillar cavity proposed here is of high quality for weak and strong coupling, able to give single photons from InAs/InP QDs, producible by a monolithic process, robust against process uncertainty, and thus better than conventional GaAs/AlGaAs, InP/InGaAsP, and hybrid pillar cavities. It is therefore prospective as a candidate for 1.55 μm QD SPSs applied in silica-fiber-based quantum information system.

http://dx.doi.org/10.5772/67499

6. Summary

For quantum information processing over 1.55 μm silica-fiber-based networks, micropillar cavities containing QDs are designed to construct quantum devices such as SPSs. The straight way could be using micropillars composed of traditional InGaAsP/InP distributed Bragg reflectors (DBRs), which can in principle enable weak coupling between a single InAs/InP QD and an optical mode for an efficient 1.55 μm SPS. To reduce the difficulty in fabricating such ~30 μm high pillars, a pillar structure hybridizing semiconductor with dielectric materials is designed. Consisting of Si/SiO_2 DBRs and an InP active layer, such a micropillar cavity can greatly enhance the rate of single-photon emitting from an InAs/InP QD to be over GHz and thus serve as a photon-indistinguishable SPS. To further realize strong coupling between a 1.55 μm QD and an optical pillar mode, the Si/SiO_2-InP hybrid micropillar cavity is reformed by introducing tapered DBR structures into the central spacer. This new hybrid micropillar cavity can be diminished to have a sub-micrometer diameter, giving small mode volume and strongly ensuring single-photon emission. With Q factor as high as 10^5–10^6, this high-quality hybrid micropillar cavity can behave as a coherently controllable quantum device at 1.55 μm telecommunication band. To overcome the problems of complicated fabrication process and interface defects in the hybrid cavities, a novel structure, InGaAsP/InP-air-aperture micropillar, is finally proposed. This cavity can be fabricated by using a simple monolithic process. Owing to the air apertures and tapered distributed Bragg reflectors, such a microcavity with sub-micrometer diameter is capable of both weakly and strongly coupling a single quantum dot with an optical mode. It could thus be the promising candidate for a QD SPS at 1.55 μm telecommunication band applicable in silica-fiber-based quantum information processing.

Acknowledgements

This work was partially supported by the Project for Developing Innovation Systems of the Ministry of Education, Culture, Sports, Science and Technology (MEXT), Japan; by the Recruitment Program of Global Experts, China; and by the 1000 Talents Plan of Sichuan Province, China. We thank Dr. K. Takemoto, Dr. T. Miyazawa, Dr. M. Takatsu, and Prof. T. Yamamoto of Fujitsu Lab. Ltd., Japan, for their help in simulations and thank Prof. Zh. M. Wang of the University of Electronic Science and Technology of China for constructive discussions.

Author details

Hai-Zhi Song

Address all correspondence to: hzsong1296@163.com

1 Southwest Institute of Technical Physics, Chengdu, China

2 Institute of Fundamental and Frontier Sciences, University of Electronic Science and Technology, Chengdu, China

References

[1] Vahala KJ: Optical microcavities. Nature. 2003;424:839–846. DOI: 10.1038/nature01939

[2] Park SG, Kim SH, Kwon SH, Ju YG, Yang JK, Baek JH, Kim SB, Lee YH: Electrically driven single-cell photonic crystal laser. Science. 2004;305:1444–1447. DOI: 10.1126/science.1100968

[3] Shomroni I, Rosenblum S, Lovsky Y, Bechler O, Guendelman G, Dayan B: All-optical routing of single photons by a one-atom switch controlled by a single photon. Science. 2014;345:903–906. DOI: 10.1126/science.1254699

[4] Michler P, Kiraz A, Becher C, Schoenfeld WV, Petroff PM, Zhang L, Hu E, Imamoğlu A: A quantum dot single-photon turnstile device. Science. 2000;290:2282–2285. DOI: 10.1126/science.290.5500.2282

[5] Moreau E, Robert I, Gérard JM, Abram I, Manin L, Thierry-Mieg V: Single-mode solid-state single photon source based on isolated quantum dots in pillar microcavities. Appl. Phys. Lett. 2001;79:2865–2867. DOI: 10.1063/ 1.1415346

[6] Pelton M, Santori C, Vučković J, Zhang B, Solomon GS, Plant J, Yamamoto Y: Efficient source of single photons: a single quantum dot in a micropost microcavity. Phys. Rev. Lett.. 2002;89:233602. DOI: 10.1103/PhysRevLett. 89.233602

[7] Santori C, Fattal D, Vučković J, Solomon GS, Yamamoto Y: Indistinguishable photons from a single-photon device. Nature. 2002;419:594–597. DOI: 10.1038/nature01086

[8] Reithmaier JP, Sęk G, Löffler A, Hofmann C, Kuhn S, Reitzenstein S, Keldysh LV, Kulakovskii VD, Reinecke TL, Forchel A: Strong coupling in a single quantum dot–semiconductor microcavity system. Nature. 2004;432:197–200. DOI: 10.1038/nature02969

[9] Nomura M, Kumagai N, Iwamoto S, Ota Y, Arakawa Y: Laser oscillation in a strongly coupled single-quantum-dot–nanocavity system. Nat. Phys. 2010;6:279–283. DOI: 10.1038/NPHYS1518

[10] Takemoto K, Nambu Y, Miyazawa T, Sakuma Y, Yamamoto T, Yorozu S, Arakawa Y: Quantum key distribution over 120 km using ultrahigh purity single-photon source and superconducting single-photon detectors. Sci. Rep. 2015;5:14383. DOI: 10.1038/srep14383

[11] Takemoto K, Nambu Y, Miyazawa T, Wakui K, Hirose S, Usuki T, Takatsu M, Yokoyama N, Yoshino K, Tomita A, Yorozu S, Sakuma Y, Arakawa Y.: Transmission experiment of quantum keys over 50 km using high-performance quantum-dot single-photon source at 1.5 μm wavelength. Appl. Phys. Express. 2010;3:092802. DOI: 10.1143/APEX.3.092802

[12] Dixon AR, Yuan ZL, Dynes JF, Sharpe AW, Shields AJ: Continuous operation of high bit rate quantum key distribution. Appl. Phys. Lett. 2010;96:161102. DOI: 10.1063/1.3385293

[13] Sangouard N, Simon C, Minář J, Zbinden H, de Riedmatten H, Ginsin N: Long-distance entanglement distribution with single-photon sources. Phys. Rev. A. 2007;76:050301. DOI: 10.1103/PhysRevA.76.050301

[14] Gisin N, Pironio S, Sangouard N: Proposal for implementing device-independent quantum key distribution based on a heralded qubit amplifier. Phys. Rev. Lett. 2010;105:070501. DOI: 10.1103/PhysRevLett.105.070501

[15] O'Brien JL: Optical quantum computing. Science. 2007;318:1567–1570. DOI: 10.1126/science.1142892

[16] Kuroda T, Sakuma Y, Sakoda K, Takemoto K, Usuki T: Decoherence of single photons from an InAs/InP quantum dot emitting at a 1.3 μm wavelength. Phys. Stat. Sol. (c). 2009;6:944–947. DOI: 10.1002/pssc. 200880661

[17] Birowosuto MD, Sumikura H, Matsuo S, Taniyama H, van Veldhoven PJ, Nötzel R, Notomi M: Fast Purcell-enhanced single photon source in 1,550-nm telecom band from a resonant quantum dot-cavity coupling. Sci. Rep. 2012;2:321. DOI: 10.1038/srep00321

[18] Pelton M, Vučković J, Solomon GS, Scherer A, Yamamoto Y: Three-dimensionally confined modes in micropost microcavities: quality factors and Purcell factors. IEEE J. Quant. Electron. 2002;38:170–177. DOI: 10.1109/3.980269

[19] Faraon A, Fushman I, Englund D, Stoltz N, Petroff PM, Vučković J: Coherent generation of non-classical light on a chip via photon-induced tunnelling and blockade. Nature Phys. 2008;4:859–863. DOI: 10.1038/nphys1078

[20] Lin C-K, Bour DP, Zhu J, Perez WH, Leary MH, Tandon A, Corzine SW, Tan MRT: High temperature continuous-wave operation of 1.3- and 1.55-μm VCSELs with InP/air-gap DBRs. IEEE J. Sel. Topics Quantum Electron. 2003;9:1415–1421. DOI: 10.1109/JSTQE.2003.820924

[21] Gazzano O, Michaelis de Vasconcellos S, Arnold C, Nowak A, Galopin E, Sagnes I, Lanco L, Lemaître A, Senellart P: Bright solid-state sources of indistinguishable single photons. Nature Commun. 2013;4:1425. DOI: 10.1038/ncomms2434

[22] Dalacu D, Poitras D, Lefebvre J, Poole PJ, Aers GC, Willianms RL: InAs/InP quantum-dot pillar microcavities using SiO_2/Ta_2O_5 Bragg reflectors with emission around 1.55 μm. Appl. Phys. Lett. 2004;84:3235–3237. DOI: 10.1063/1.1728318

[23] Niklaus F, Stemme G, Lu JQ, Gutmann RJ: Adhesive wafer bonding. J. Appl. Phys. 2006;99:031101. DOI: 10.1063/1.2168512

[24] Jang SJ, Song YM, Yeo CI, Park CY, Lee YT: Highly tolerant a-Si distributed Bragg reflector fabricated by oblique angle deposition. Opt. Mater. Express. 2011;1:451–457. DOI: 10.1364/OME.1.000451

[25] Song HZ, Takemoto K, Miyazawa T, Takatsu M, Iwamoto S, Yamamoto T, Arakawa Y: Design of Si/SiO_2 micropillar cavities for Purcell-enhanced single photon emission at 1.55 μm from InAs/InP quantum dots. Opt. Lett. 2013;38:3241–3244. DOI: 10.1364/OL.38.003241

[26] Rivera T, Debray JP, Gérard JM, Legrand B, Manin-Ferlazzo L, Oudar JL: Appl. Phys. Lett. 1999;74:911–913. DOI: 10.1063/1.123407

[27] Gregersen N, Reitzenstein S, Kistner C, Strauss M, Schneider C, Höfling S, Worschech L, Forchel A, Nielsen TR, Mørk J, Gérard JM: Numerical and experimental study of the Q factor of high-Q micropillar cavities. IEEE J. Quantum Electron. 2010;46:1470–1483. DOI: 10.1109/JQE.2010.2052095

[28] Barnes WL, Björk G, Gérard JM, Jonsson P, Wasey JAE, Worthing PT, Zwiller V: Solid-state single photon sources: light collection strategies. Eur. Phys. J. D. 2002;18:197–210. DOI: 10.1140/epjd/e20020024

[29] Vučković J, Petlton M, Scherer A, Yamamoto Y: Optimization of three-dimensional micropost microcavities for cavity quantum electrodynamics. Phys. Rev. A. 2002;66:023808. DOI: 10.1103/PhysRevA.66.023808

[30] Kimble HJ: The quantum internet. Nature. 2008;453:1023–1039. DOI: 10.1038/nature07127

[31] Lermer M, Gregersen N, Dunzer F, Reitzenstein S, Höfling S, Mørk J, Worschech L, Kamp M, Forchel A: Bloch-wave engineering of quantum dot micropillars for cavity quantum electrodynamics experiments. Phys. Rev. Lett. 2012;108:057402. DOI: 10.1103/PhysRevLett.108.057402

[32] Zhang Y, Lončar M: Submicrometer diameter micropillar cavities with high quality factor and ultrasmall mode volume. Opt. Lett. 2009;34:902–904. DOI: 10.1364/OL.34.000902

[33] Song HZ, Takemoto K, Miyazawa T, Takatsu M, Iwamoto S, Ekawa M, Yamamoto T, Arakawa Y: High quality-factor Si/SiO_2-InP hybrid micropillar cavities with submicrometer diameter for 1.55-μm telecommunication band. Opt. Express. 2015;23:16264–16272. DOI: 10.1364/OE.23.016264

[34] Yariv A Optical Electronics. San Francisco: Saunders College; 1991.

[35] Lalanne P, Mias S, Hugonin J: Two physical mechanisms for boosting the quality factor to cavity volume ratio of photonic crystal microcavities. Opt. Express. 2004;12:458–467. DOI: 10.1364/OPEX. 12.000458

[36] Lalanne Ph, Hugonin JP, Gerard JM: Electromagnetic study of the quality factor of pillar microcavities in the small diameter limit. Appl. Phys. Lett.. 2004;84:4726–4728. DOI: 10.1063/1.1759375

[37] Auffèves A, Gerace D, Gérard JM, França Santos M, Andreani LC, Poizat JP: Controlling the dynamics of a coupled atom-cavity system by pure dephasing. Phy. Rev. B. 2010;81:245419. DOI: 10.1103/ PhysRevB.81.245419

[38] Bennett AJ, Patel RB, Shields AJ, Cooper K, Atkinson P, Nicoll CA, Ritchie DA: Indistinguishable photons from a diode. Appl. Phys. Lett. 2008;92:193503. DOI: 10.1063/1.2918841

[39] Kojima O, Nakatani H, Kita T, Wada O, Akahane K, Tsuchiya M: Photoluminescence characteristics of quantum dots with electronic states interconnected along growth direction. J. Appl. Phys. 2008;103: 113504. DOI: 10.1063/1.2936320

[40] Hillmer H, Daleiden J, Prott C, Römer F, Irmer S, Rangelov V, Tarraf A, Schüler S, Strassner M: Potential for micromachined actuation of ultra-wide continuously tunable optoelectronic devices. Appl. Phys. B. 2002;75:3–13. DOI: 10.1007/s00340-002-0957-x

[41] Zhou PY, Dou XM, Wu XF, Ding K, Luo S, Yang T, Zhu HJ, Jiang DS, Sun BQ: Photoluminescence studies on self-assembled 1.55-μm InAs/InGaAs/InP quantum dots under hydrostatic pressure. J. Appl. Phys. 2014;116:023510. DOI: 10.1063/1.4890013

[42] Akahane Y, Asano T, Song BS, Noda S: High-Q photonic nanocavity in a two-dimensional photonic crystal. Nature. 2003;425:944–947. DOI: 10.1038/nature02063

[43] Seo K, Wober M, Steinvurzel P, Schonbrun E, Dan Y, Ellenbogen T, Crozier KB: Multicolored vertical silicon nanowires. Nano Lett. 2011;11:1851–1856. DOI: 10.1021/nl200201b

[44] Shields AJ: Semiconductor quantum light sources. Nat. Photonics. 2007;1:215–223. DOI: 10.1038/ nphoton.2007.46

[45] Canet-Ferrer J, Prieto I, Muñoz-Matutano G, Martínez LJ, Muñoz-Camuniez LE, Llorens JM, Fuster D, Alén B, González Y, González L, Postigo PA, Martínez-Pastor JP: Excitation power dependence of the Purcell effect in photonic crystal microcavity lasers with quantum wires. Appl. Phys. Lett. 2013;102:201105. DOI: 10.1063/1.4807439

[46] Jiao Y, de Vries T, Unger R-S, Shen L, Ambrosius H, Radu C, Arens M, Smit M, van der Tol J: Vertical and smooth single-step reactive ion etching process for InP membrane waveguides. J. Electrochem. Soc. 2015;162:E90–E95. DOI: 10.1149/2.0371508jes

[47] Naureen S, Shahid N, Dev A, Anand S: Generation of substrate-free III–V nanodisks from user-defined multilayer nanopillar arrays for integration on Si. Nanotechnology. 2013;24:225301. DOI: 10.1088/0957-4484/24/22/225301

[48] Chang RR, Iyer R, Lile DL: Surface characterization of InP using photoluminescence. J. Appl. Phys. 1987;61:1995–2004. DOI: 10.1063/1.337995

[49] Oh DY, Kim S-H, Huang J, Scofield A, Huffaker D, Scherer A: Self-aligned active quantum nanostructures in photonic crystals via selective wet-chemical etching. Nanotechnology. 2013;24: 265201. DOI: 10.1088/0957-4484/24/26/265201

[50] Gehl M, Gibson R, Hendrickson J, Homyk A, Säynätjoki A, Alasaarela T, Karvonen L, Tervonen A, Honkanen S, Zandbergen S, Richards BC, Olitzky JD, Scherer A, Khitrova G, Gibbs HM, Kim JY, Lee YH: Effect of atomic layer deposition on the quality factor of silicon nanobeam cavities. J. Opt. Soc. Am. B. 2012;29:A55–A59. DOI: 10.1364/JOSAB.29.000A55

[51] Baba T: Photonic crystals and microdisk cavities based on GaInAsP–InP system. IEEE J. Sel. Top. Quantum Electron. 1997;3:808–830. DOI: 10.1109/2944.640635

Chapter 3

LED and Phototransistor Simulation

Sergey Yurchuk, Oleg Rabinovich and
Sergey Didenko

Additional information is available at the end of the chapter

http://dx.doi.org/10.5772/intechopen.69629

Abstract

Optoelectronics (e.g., light-emitting diodes, photodetectors) is one of the most widely used fields nowadays. But it is still necessary to improve their characteristics for using in general lighting. In this chapter, the heterostructure conductivity type, impurity and indium atoms influence on the LEDs and phototransistor characteristics are investigated by computer simulation. It was found that current-voltage characteristic and quantum efficiency depend on impurity and indium atoms change a lot. By varying impurity and indium atom concentration, controlling their distribution in InGaN and AlGaP heterostructure LEDs and photodetector characteristics can be improved.

Keywords: light-emitting diode, InGaN, simulation, photodetector, phototransistor, AlGaP

1. Introduction

The ancients said: "Per crucem ad lucem" ("Through the cross to the light"). Another field of modern science and technology could be hardly remembered, which has influenced economics and science so greatly as semiconductor devices, especially optoelectronics. Such devices have a very fascinating history. The optoelectronics started at the beginning of the twentieth century, and its progress was so dynamic that it can be compared with the modern scientific and technological revolution.

Below, valuable steps of optoelectronics development should be briefly pointed out. In 1907, a captain Henry Joseph Round (**Figures 1** and **2**), personal assistant to Guglielmo Marconi, took a piece of carborundum and saw the yellow light by applying voltage to this material, but he in the paper described only experiment without any physical explanation of this phenomenon [1–4].

Figure 1. Henry Joseph Round.

A Note on Carborundum.

To the Editors of Electrical World:

SIRS:—During an investigation of the unsymmetrical passage of current through a contact of carborundum and other substances a curious phenomenon was noted. On applying a potential of 10 volts between two points on a crystal of carborundum, the crystal gave out a yellowish light. Only one or two specimens could be found which gave a bright glow on such a low voltage, but with 110 volts a large number could be found to glow. In some crystals only edges gave the light and others gave instead of a yellow light green, orange or blue. In all cases tested the glow appears to come from the negative pole, a bright blue-green spark appearing at the positive pole. In a single crystal, if contact is made near the center with the negative pole, and the positive pole is put in contact at any other place, only one section of the crystal will glow and that the same section wherever the positive pole is placed.

There seems to be some connection between the above effect and the e.m.f. produced by a junction of carborundum and another conductor when heated by a direct or alternating current; but the connection may be only secondary as an obvious explanation of the e.m.f. effect is the thermoelectric one. The writer would be glad of references to any published account of an investigation of this or any allied phenomena.

NEW YORK, N. Y. H. J. ROUND.

Figure 2. H.J. Round's paper.

http://dx.doi.org/10.5772/intechopen.69629

Oleg Vladimirovich Losev's first papers were at the beginning of the twentieth century.

O.V. Losev investigated and carried out physical explanation for injectional and prebreakdown luminescence effects in details [2–6]. Even more, O.V. Losev received first patent for presample of light-emitting diode (LED) in 1927 (**Figures 3** and **4**).

As it was written by Egon E. Loebner upto 50th year, such effects were called "Losev light" [3]. First contemporary explanation of p-n junction lighting effect was proposed by Kurt Lehovec et al. from Signal Corps Engineering Laboratories (New Jersey) in 1951. In the 1960s, the first GaAs-based near-infrared semiconductor lasers and red-orange light-emitting diodes were introduced by Nick Holonyak and Mary George Craford. In parallel to that development, photodetectors based on III–V semiconductors were developed [4, 7]. In 1963, Zhores Ivanovich Alferov proposed the idea of using nanoheterojunctions (NH) in emitters (**Figure 5**).

Under Alferov leadership, GaAs-AlGaAs heterojunction investigations were carried out [5, 8, 9]. In 1966, for the first time, effective radiative recombination at p-n junction of four-component solid solution $As_xP_{1-x-y}GaIn_y$ was discovered. In 1970, Zh. I. Alferov et al. proposed to use four-component structure for achieving heterojunctions. In 1966, N. Holonyak presented epitaxial growth process [8, 10]. In 1969, Herbert Paul Maruska and James J. Tietjen grew the first GaN

Figure 3. Oleg Vladimirovich Losev.

Класс 21 а, 27 № 12191

ПАТЕНТ НА ИЗОБРЕТЕНИЕ

ОПИСАНИЕ

светового реле.

К патенту О. В. Лосева, заявленному 28 февраля 1927 года (заяв. свид. № 14672).

О выдаче патента опубликовано 31 декабря 1929 года. Действие патента распространяется на 15 лет от 31 декабря 1929 года.

Предлагаемое изобретение использует общеизвестное явление свечения в карборундовом детекторе и состоит в том, что в световом реле для быстропишущего телеграфного или телефонного приема, передачи изображений на расстояние и других целей, в качестве модулируемого электрическим током источника света, применяется свечение в точке контакта карборундового детектора, включенного непосредственно в цепь модулирующего тока.

На чертеже фиг. 1 изображает схему предлагаемого светового реле и фиг. 2—схему устройства для фотографической записи сигналов с применением светового реле.

К зажимам *A* источника тока сигналов, подлежащих записи, через потенциометр P включается светящийся карборундовый детектор *D*, в цепь которого включена батарея *B*, дающая дополнительное постоянное напряжение для наложения его на напряжение тока сигналов и усиления действия реле; путем регулировки этой батареи создаются наивыгоднейшие условия работы детектора *D*. Оптическая система *L* предназначена направлять световой поток, излучаемый карборундовым детектором, на движущуюся фотографическую пластинку *F*, на которой производится запись изменений этого потока. Детектор *D*, оптическая система *L* и пластина *F* заключены в светонепроницаемую камеру. Примерное включение светового реле показано на чертеже 2, где *E*—приемник-усилитель высокой частоты, *T*—автотрансформатор высокой частоты, а остальная часть схемы вполне аналогична только-что описанной.

Предмет патента

1. Световое реле для быстропишущего телеграфного или телефонного приема, передачи изображений на расстояние и для других целей, характеризующееся применением, в качестве модулируемого электрическим током источника света, свечения в точке контакта карборундового детектора общеизвестного устройства, каковой детектор включен непосредственно в цепь модулирующего тока.

2. Видоизменение охарактеризованного в п. 1 светового реле, отличающееся тем, что последовательно с указанным детектором *D* включен источник дополнительного напряжения постоянного тока *B* (фиг. 1 и 2) с целью усиления действия реле.

Figure 4. O.V. Losev's patent for preLED.

single crystal on a Al_2O_3 by hydride vapor phase epitaxy. The first bluish-green LED having a metal-insulator-semiconductor (MTS) structure was developed by Jacques I. Pankove et al. in 1971. In 1985, Isamu Akasaki and Hiroshi Amano et al. succeeded in growing extremely high-quality GaN with a surface on a sapphire substrate by pioneering a low-temperature-deposited (LT) buffer layer technology using organometallic vapor phase epitaxy (OMVPE). In 1989, they achieved fixing Mg concentration in the GaN growth by OMVPE using Cp_2Mg. Then, first, they discovered distinctly p-type GaN with low resistance by low-energy electron-beam irradiation (LEEBI) on high-quality Mg-doped GaN grown with the LT-buffer layer, which lately led to the creation of high-efficiency LEDs. They and Shuji Nakamura demonstrated the first p-n junction UV (edge emission) and violet LED and also achieved p-type AlGaN in 1991 and p-type GalnN in 1994, accordingly [2, 10–13].

Figure 5. Zhores Ivanovich Alferov.

Quantum-sized semiconductors used in photonics and optoelectronics (e.g., light-emitting diodes, lasers, photodetectors, etc.) are AIIIBV and AIIBVI N. Their solutions are very interesting due to their unique properties—the wide band gap, strong bonds, and high thermal conductivity. The main outstanding properties of nitride heterostructures are forbidden gap energy that depends on the indium concentration and could change in the range 1.95–6.3 eV. AlGaInN has very bright future in various applications fields—short-wavelength electroluminescence and high-power/temperature/frequency electronic devices. Now, problem of limited color range and lack of high-power white LEDs that previously prevented LED usage for general lighting have been solved. Unfortunately, there are still several problems need to be solved, e.g., LED degradation, efficiency droop nature understanding, quantum efficiency (QE) increase, obtaining optimal quantum size area structure, photodetectors efficiency increase, and developing the method for quick NH and device investigation.

For complex materials and optoelectronic devices, the basic factors that determine their quality, such as current-voltage characteristics (I-V) and the efficiency, can be investigated by computer simulations and include taking into account major structural and physical NH and device parameters [15–24].

2. Simulation basis

For complex materials and optoelectronic devices, the basic factors that determine their quality, such as I-V characteristics and the efficiency, can be investigated by computer simulations

that include taking into account major structural and physical NH and device parameters [14–23]. The last decade proved an increased usage of the software for simulation semiconductor devices. Device simulations play an important role in their research. The formulas for devices are complicated. The growth process was simulated, and light propagation and extraction, and the possibility of the external efficiency increase of AlGaInN LED were studied by simulation; explanation of the electroluminescence efficiency degradation at increasing current was suggested.

Freeware computer program SimWindows was used in our investigation [14]. The specific features of this program are: (1) the electrical, optical, and thermal device properties for simulation based on system of exact physical equations, (2) the simulation possibilities with different approximations for two-lead devices and (3) the quantum-sized device simulation. The software extends a lot of traditional electrical models by adding effects such as quantum confinement, tunneling current, and complete Fermi-Dirac statistics. The optical model includes computing electromagnetic field reflections at interfaces. The software is very flexible for semiconductor device simulation. Exact solutions of electrical, optical, and heat transport phenomena in 1D situation are included. For example, drift-diffusion currents, thermoionic and tunneling currents for electrons and holes are taken into account, and in recombination of charge carriers, radiating and nonradiating are included. For band diagram calculations of devices, Fermi-Dirac or Boltzmann statistics and full version of Poisson differential equation have been used. During our investigation, special files for NH, photodetectors, and LED simulations were created. Of course, piezoelectric and spontaneous effects were additionally taken into consideration by including piezo and elastic matrix coefficients. The main parameters for NH, photodetector, and LED type were included into the individual, relating each device and material, special files for simulation. In those files, parameters such as geometric sizes for emitters, QW, and barriers; the QW and barriers quantity; the solid solution content; the conductivity type; and doping concentrations were included. In the materials file for heterostructures, more than 25 parameters such as the band gap, refractive index, optical absorption, thermal conductivity, mobility, and lifetime of charge carriers, and the coefficients of radiative and nonradiative recombination were included. Initial data-preparing files were based on Refs. [24–30].

3. Light-emitting diode improvements

One of the most important parameters that describe LED is the QE (η_{QE}). By definition, QE is equal to the sum of the radiative and nonradiative recombination rates. If the NH active area is a QW set with the equal length, the QE expression (Eq. (1)) is:

$$\eta_{QE} = \frac{\sum U^k_{B-B}}{\sum U^k_{Total}}, \tag{1}$$

where k is the QW number from 1 to m.

Understanding the QE dependence according to different influence is very useful for predicting the NH and LED reliability.

Blue InGaN NH contained, n-GaN-emitter ($N_D = 10^{19}$ cm^{-3}), in active area were QW and GaN-$In_{0.2}Ga_{0.8}N$ barriers. The QW quantity varied from 1 to 5. In the first group of simulated NH, the QW width was 2 nm and the GaN-barrier was 3 nm, whereas 3.5 and 4.5 nm in the second group. For each QW set, three types of devices with different doping QW and barriers were simulated: i-type, n-type (the ionized concentration was $N_D = 10^{18}$ cm^{-3}), and p-type ($N_A = 10^{18}$ cm^{-3}); for the p-GaN-emitter, the (Mg) acceptor concentration was $N_A = 10^{18}$ cm^{-3}; green InGaN LEDs were identical in parameters to blue ones except for the QW structure—$In_{0.35}Ga_{0.65}N$. Red AlGaInP NH had the following structure: n-$Al_{0.4}Ga_{0.1}In_{0.5}P$-emitter, the donor concentration was $N_D = 10^{18}$ cm^{-3}; the active area consisted of QW and $Ga_{0.5}In_{0.5}P/Al_{0.1}Ga_{0.4}In_{0.5}P$ barrier set. The QW quantity varied from 1 to 10. In the first group of NH, the QW width was 2 nm and the barrier width was 3 nm, while 3.5 nm and 4.5 nm in the second group, 10 nm and 10 nm in the third group and 50 nm and 50 nm in the fourth group. NH simulation was carried out with doping QWs and barriers with an acceptor impurity (Zn) $N_A = 5 \times 10^{17}$ cm^{-3}, while for the p-$Al_{0.4}Ga_{0.1}In_{0.5}P$-emitter, the acceptors (Zn) were $N_A = 5 \times 10^{17}$ cm^{-3}. In the case of the yellow AlGaInP, the NH was identical to the red one $Al_{0.17}Ga_{0.33}In_{0.5}P$, and the barriers were $Al_{0.4}Ga_{0.1}In_{0.5}P$. LED simulation was performed at 100 A/cm^2 and at a temperature of 300 K.

In **Figure 6**, it could be seen as main characteristics that could be done during simulation, e.g., InGaN heterostructure. The dependence for main parameters vs. voltage is shown below.

With applying no voltage, electrons and holes are mainly concentrated in n- and p-type areas, respectively, and after applying voltage, they are redistributed into the middle QWs (**Figure 6**). Basic dependence trend of simulation results blue/green LED (**Figure 7**). Based on the results, it can be seen that the most economically sound and effective (based upon internal quantum efficiency) production is LEDs with 4 QWs (3.5 nm width). It is due to LED with 4 QWs, the internal quantum efficiency is maximum, and at the same time, resistance is not at its maximum value.

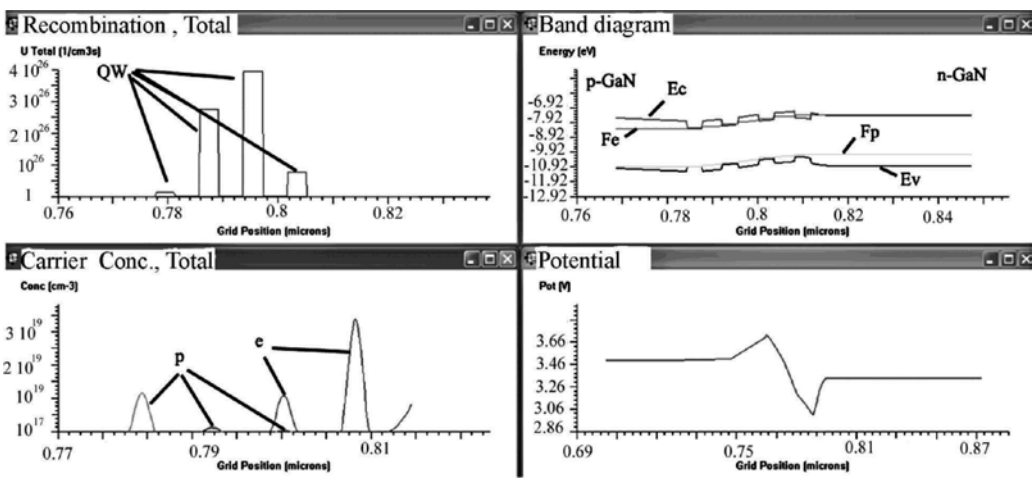

Figure 6. Basic characteristics.

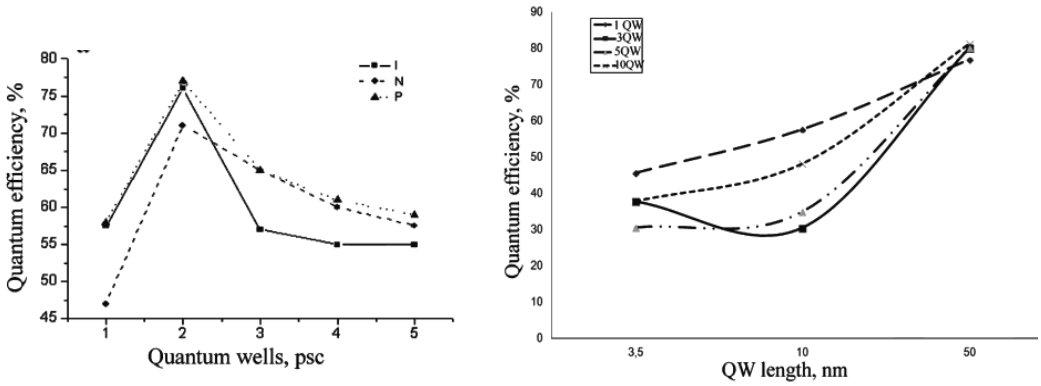

Figure 7. Internal quantum efficiency for nitride (left) and phosphide (right) LED per QW quantity (QW 3.5 nm) at 100 A/cm^2.

The maximum QE was in the central QWs. It is detected that the active region should contain 4 QWs (central ones are according to recombination and edge concentrate carrier currents for a higher recombination). In red and yellow NH (**Figure 7**, right), the QE increase at different QW width is observed. Maximum QE occurs at QW width—50 nm. For yellow NH, the QE was three times less than in the red one. The difference is because of reducing the radiative recombination efficiency and small energy gap between the G- and X-minimum in the conduction band.

Now, let us discuss on the investigation including green and blue InGaN LEDs simulation with different indium atom concentration for blue $X = 0.15 – 0.25$ and green $X = 0.25 – 0.35$. In published experimental works, it was detected that in $In_XGa_{1-X}N$ quantum, well-active region of blue and green LED spatial indium content fluctuations are responsible for many peculiarities of electrical and optical characteristics of devices. In Refs. [31, 32], the idea was given that QW area in blue and green LEDs should be described as a combination of spatially distributed regions which have their own fixed indium atom concentration. In such description, each small area can be as a local NanoLED, which has its own p-n junction area. In general, the LED = NanoLEDs sum with the electrical parallel connection. In our theoretical calculations, it was proposed to use Gauss distribution function for calculations of "NanoLED" p-n junction areas. In this case, the area $S(x)$ for each indium content x is described by expression (Eq. (2)):

$$S(x) = 10^{-2} S_{LED} 1/[\sigma * (2\pi)^{0.5}] * \exp - \left\{ \left(x - x_0 \right)^2 / 2\,\sigma^2 \right\}, \quad (2)$$

where NanoLED—LED p-n junction area, x_0—indium content value.

It was supposed that, for blue LED, indium concentration varies $X = 0.15 – 0.25$ and $X_0 = 0.20$. In this situation, $\sigma = 0.017$ to have fulfillment of the "3 σ" rule, providing 0.999 reliability of calculations. The Gauss distribution of $S(x)/S_{LED}$ values on X and NanoLED connection are presented in **Figures 8** and **9**, respectively.

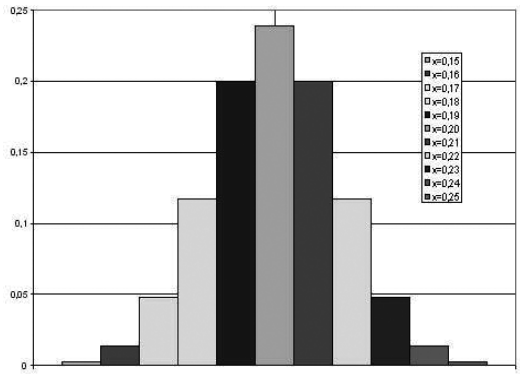

Figure 8. The Gauss distribution of $S(x)/S_{LED}$ values on x.

The current density-voltage dependences on p-n junctions having different indium content X are shown in **Figure 10**.

Spectrum is with asymmetric shape. Simulation proves the "blue shift" vs. current increase even at quantum Stark-Keldysh effect neglecting is proved by the simulation (**Figure 11**).

It was detected that by In concentration changes I-V or spectrum curves could be shifted. Doping into the p-emitter of NH (e.g., $Al_{0.2}Ga_{0.8}N$) was suggested to eliminate electron injection from the active region, which is especially important in device simulation with a low content of In (X) atoms (**Figure 12**).

Next, on the basis of the optimized structure of the NH, the effect of the impurity and In atoms doped into the barriers between QWs in the NH active region was studied; this effect is shown by the nonideality coefficient dependence, as shown in **Figure 13**.

With no QWs in the active area ($X = 0$), the I-V has standard dependence. At low current densities, $\eta > 1$, an interesting dependence of electron and hole recombination in the space-charge

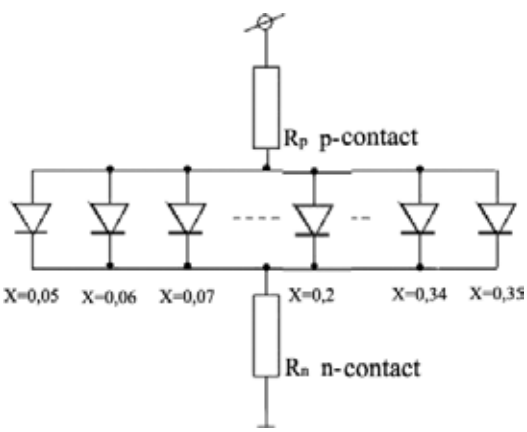

Figure 9. Parallel connection of nanodimensional elements (NanoLEDs).

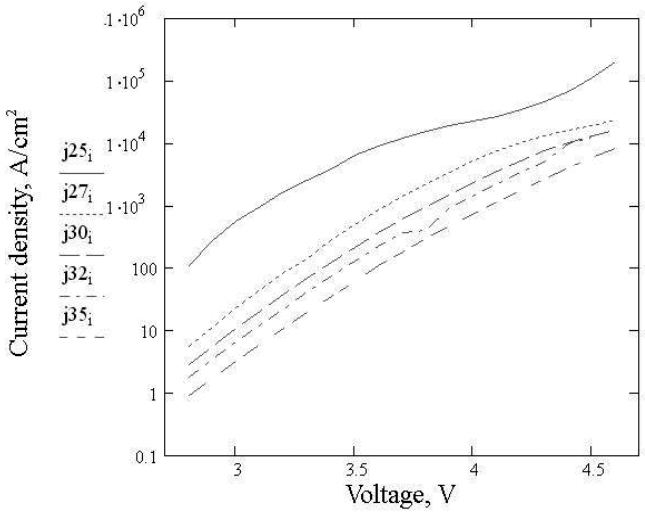

Figure 10. Current densities per voltage (at different In concentration X = 0.25, 0.27, 0.3, 0.32, and 0.35).

region (SCR) vs. current is observed. The above barrier-current carrier injection increasingly begins to predominate at $\eta \rightarrow 1$ at a low injection level (J = 1–20 A/cm^2) and $\eta \rightarrow 2$ with increasing injection level (J = 20–500 A/cm^2). For $X > 0.1$, the η increases over the range of J = 0.1–500 A/cm^2, reaching $\eta > 2$ and even higher for $X > 0.15$. The nonideality coefficient decreases with increasing donor impurity concentration in the barrier for the same values of X and J.

Then, the impurity influence on the I-V was studied. The optimum impurity concentration in barriers between QWs was detected at about $N_d = 10^{18}$ cm^{-3}, and the indium atoms concentration at 7 %. This doping shifts the I-V to the lower voltage region and increases the QE (**Figure 14**).

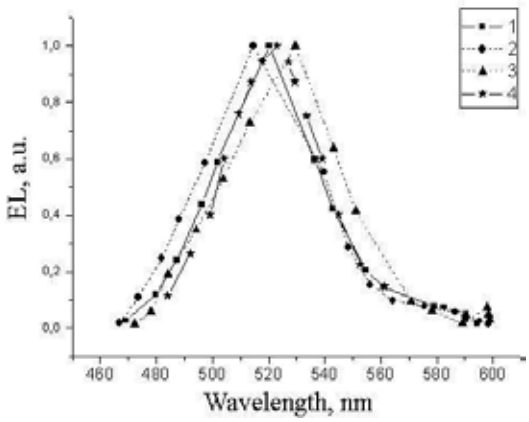

Figure 11. Electroluminescence spectral characteristics: 1—X = 0.15, 2—X = 0.20, 3—X = 0.25, and 4—X = 0.30.

http://dx.doi.org/10.5772/intechopen.69629

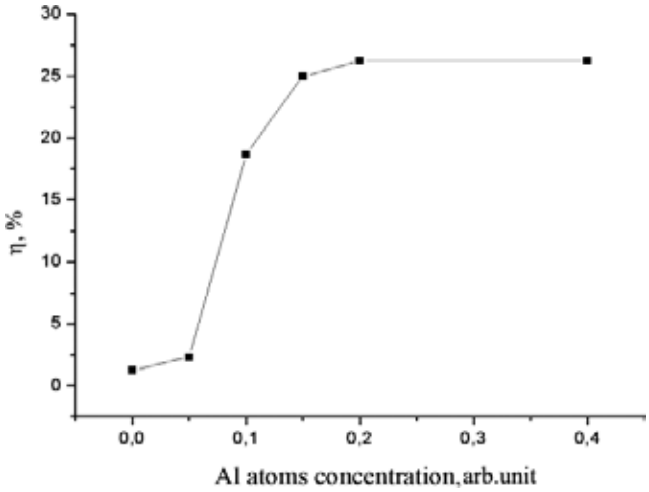

Figure 12. The influence of the Al atom content in p-emitter on QE.

This effect is due to potential barrier decrease between QWs and barriers among them, so J increases at a constant voltage. By varying the indium atom concentration and doping concentration in the active region, we could rise QE at the same voltage. Blue LED electrical and optical parameters and characteristics vs. current density trend and temperature are proved by direct computer simulation based on the new model of a LED QW active region, having spatial indium content fluctuations: I-V characteristics. At current densities less than 1 A/cm^2, I-V dependences are very close. They are close to exponent dependencies $J \sim \exp(eU/nkT)$ at all X and temperatures in the range of −40°C to +125°C, where n is so-called nonideality factor. At higher current densities and at voltage increase, n-values are gradually increasing.

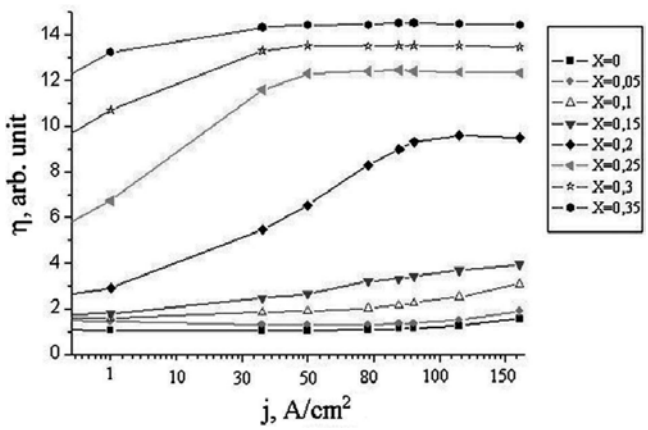

Figure 13. Nonideality coefficient η vs. j dependence.

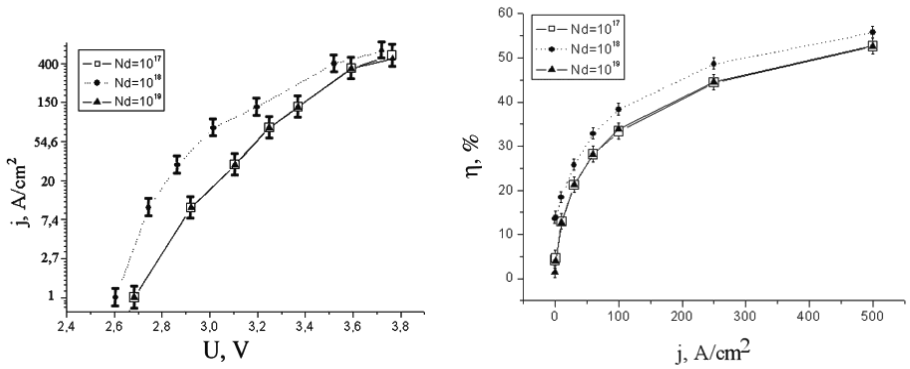

Figure 14. I-V, η vs. j according to barriers doping between QWs.

In **Figure 15**, satisfactory agreement between the simulation and experimental results is evident, despite the fact that the simulation results are obtained without any additional (other than those of the base physical models) approximations.

During simulation, efficiency droop was investigated too. It was detected that the injected electrons and holes are irregularly distributed in the QW. Carrier recombination is concentrated in the QW. In the active region, the local electrostatic potential change is due to the spatial of electrons and holes in active region distribution. Simulation was carried out initially at the assumption that there is little difference between the carriers' lifetime $\tau_{n0} \approx \tau_{p0} = 10^{-9}$ s, without detecting efficiency droop (**Figure 16**, curve 1).

It was suggested that there is a big difference between $\tau_{n0} = 10^{-11}$ s and $\tau_{p0} = 10^{-8}$ s, which was in correlation with the experimental results. It was detected that the capture coefficient in radiative recombination was $B = 10^{-10}$ cm^3/s. This significant asymmetry of carrier lifetimes is according to deep donor/acceptor levels from defects or autodoping process. Generally, this is due to indium atom redistribution in active area. AlGaInN NH were grown by MOCVD on

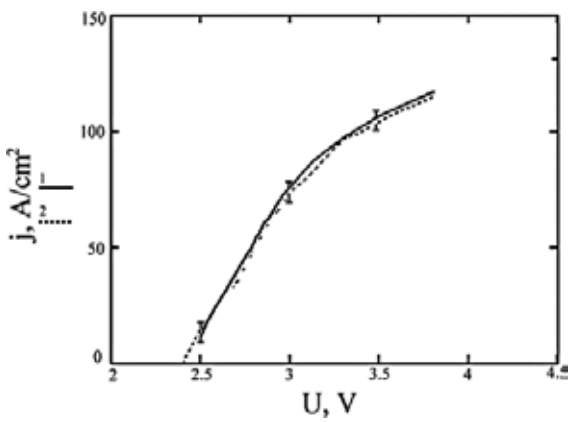

Figure 15. I-V LED: simulation (1) and experiment (2).

http://dx.doi.org/10.5772/intechopen.69629

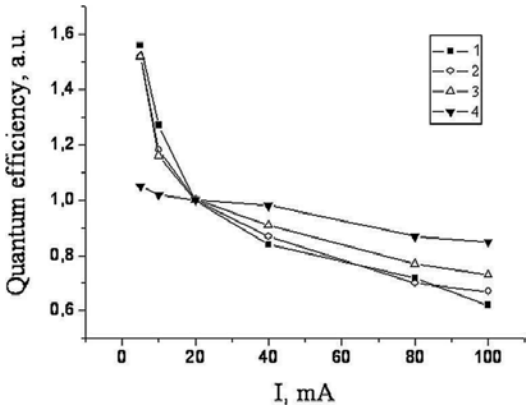

Figure 16. Quantum efficiency vs. current.

SiC and Al_2O_3 substrates after simulation suggestions. Based on growth results (e.g., photoluminescence spectral curve and Peak lambda), it was detected that the characteristics have similar trend. The spectral mapping for NH is shown in **Figure 17**.

In **Figure 17**, indium atom concentration distribution over wafer is shown. Impurity-defect cluster creates deep energy levels near the middle of the band gap, and the electron capture will be faster than the holes by the centers, due to the fact that its efficiency droop will be based on injected carrier redistribution between the QWs. For reducing droop, it needs to improve NH growth quality by usage Si (111) or better GaN substrates [33].

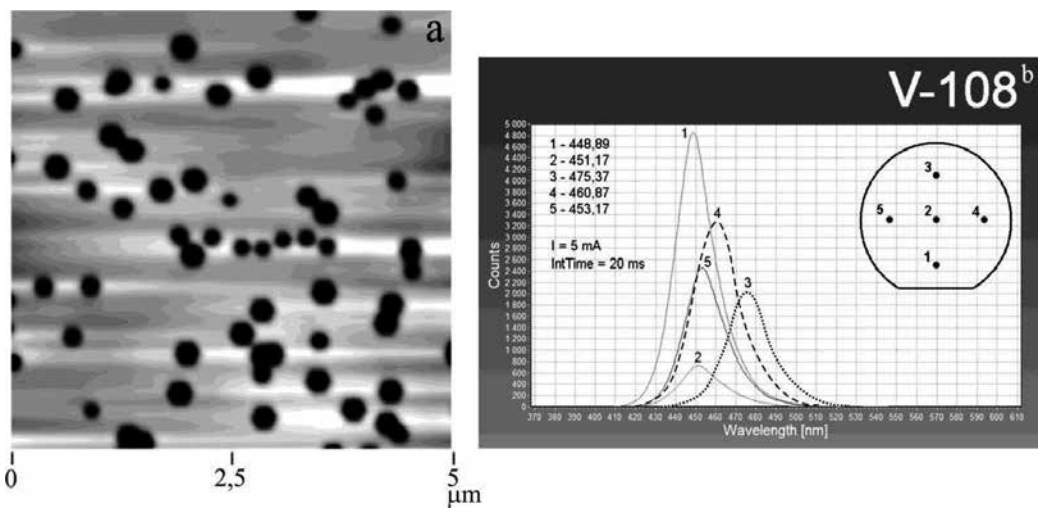

Figure 17. (a) AFM scan of the InGaN/GaN heterostructure with different indium concentration across active region [32]; (b) photoluminescence spectral curve and peak lambda of the InGaN/GaN heterostructure with different indium concentration across wafer.

4. Photodetector (phototransistor) improvements

Photodetector efficiency increase for the ultraviolet spectral range is discussed. Such devices can be widely used in various fields of technology, including devices that analyze the composition of gases and liquids, and in the open optical communication lines with increased noise immunity in high solar radiation.

One of the most promising ways to create UV photodiodes is $Al_XGa_{1-X}N$ NH usage, and the base technology of their growth is metal organic chemical vapor deposition compounds (MOCVD), which allows producing NH with high performance. Theoretically, this NH allows creating photodiodes in the wavelength range of 220–350 nm. Now, it has been developed and manufactured a photodiode AG38S-SMD with sensitivity 0.12–0.16 A/cm^2 for the radiation wavelength range of 250–350 nm [34].

Our investigations based on computer simulation showed that, based on such NH, not only photodiodes but also phototransistors (PT) with a sensitivity of more than 100 A/cm^2 can be produced, in this wavelengths area [35–43]. Ultraviolet phototransistor (UV PT) structure has been proposed, based on the capabilities of this technology with GaN and AlGaN collector. Here, the first step of the PT development is investigated, defining the multilayer NH constructor by computer simulation: the structure type (n-p-n or p-n-p), the aluminum content, dopant thickness, and concentration in the layer structure and other parameters.

For $Al_XGa_{1-X}N$ photodetector (photodiodes and phototransistors) simulation, special materials and device files were created in the same style as were previously for NH and LEDs. **Figure 18** shows the energy band diagram of a symmetric structure n-AlGaN/p-GaN/n-AlGaN.

Photodetectors are characterized by high values of gain for both shift polarities. Effective injection capacity is provided by the fact that the p-GaN base layer has a narrower band gap than the emitter and collector layers. During NH simulation for high efficiency and high sensitive phototransistor, the structure consisted of the p-$Al_{0.3}Ga_{0.7}N$ collector, n-$Al_{0.3}Ga_{0.7}N$ emitter with an aluminum content of 30% and a p-GaN base. The emitter and collector thickness was 0.875 μm, and the base thickness was 0.3 μm. Acceptor concentration in p-$Al_{0.3}Ga_{0.7}N$ collector was 10^{17} cm^{-3}, donors in n-$Al_{0.3}Ga_{0.7}N$ emitter were 10^{17} cm^{-3} and the acceptor concentration in the p-GaN base was 10^{17} cm^{-3} or 10^{18} cm^{-3}. The lifetime values of the nonequilibrium electrons and holes in all areas of PTs were equal to 50 ns. The device files have been created for both the concentration of acceptors in the base.

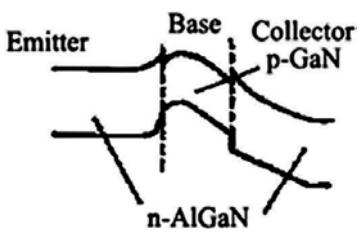

Figure 18. The current-voltage characteristic of a phototransistor double heterojunction.

Method for PT characteristics simulation at two acceptor concentrations in PTs base (Na = 10^{17} cm^{-3} or Na = 10^{18} cm^{-3}) includes steps as it is shown below: (1) for the dark current density value J_{Ph}, A/cm^2 determination at different voltage U between the PT emitter and collector (plus on p-$Al_{0.3}Ga_{0.7}N$ collector), the voltage range was U = (1–9) V; (2) for the photocurrent density value J_f determination at various lighting power density values P was P = (10^{-6} to 10^{-1}) W/cm^2 and voltage between the PT emitter and the collector (plus on p-$Al_{0.3}Ga_{0.7}N$ collector) was U = (1–9) V. The energy of quanta during lighting was E = 3.5 eV. The Al mole fraction in the collector and emitter was varied from X = 0.2 to X = 0.3.

Dark current density J_{Ph} dependence at the voltage on PT is shown in **Figure 19**.

It is clearly seen that in the PTs at an acceptor concentration in the base N_a = 10^{17} cm^{-3}, dark current begins to rise sharply at a voltage greater than 8 V, which obviously corresponds with start of the clamping of the emitter and collector (Early's effect). When the acceptor concentration in the base N_a = 10^{18} cm^{-3}, this effect occurs at higher voltages. At voltages less than 8 V, dark current density does not exceed 10^{-8} A/cm^2. This value limits the minimum magnitude of photocurrent density and, consequently, the minimum value of the recorded radiation power. Photocurrent density J_f dependence at the light power density P at a constant voltage U between the PTs emitter and the collector is shown in **Figures 20** and **21**. Lighting power range was P = (10^{-6} to 10^{-1}) W/cm^2; the voltage range was U = (1–9) V. Due to huge data, it is presented by three subrange voltages (1–3), (4–6), and (7–9) V.

Figure 22 clearly shows that at the acceptor concentration in the base N_a = 10^{18} cm^{-3}, the PTs sensitivity has a large value in a wide range of lighting, especially in the region of small power values P.

At the same time, at the acceptor concentration in the base N_a = 10^{17} cm^{-3}, the PT sensitivity is maximum at relatively larger values of the power P, which makes them very promising in a variety of applications. **Figure 23** shows the PT sensitivity dependence at voltage in the range from 1 to 9 V at a power density of light 1 mW/cm^2, which is typical in many applications of UV photodetectors.

Conclusion of this dependence is quite obvious—to obtain a high sensitivity at voltage, applied to the PT, it must be in the range of 6–9 V. At the end of the discussion of UV phototransistor characteristics simulating, data of the PTs sensitivity spectral dependence are presented (**Figure 24**).

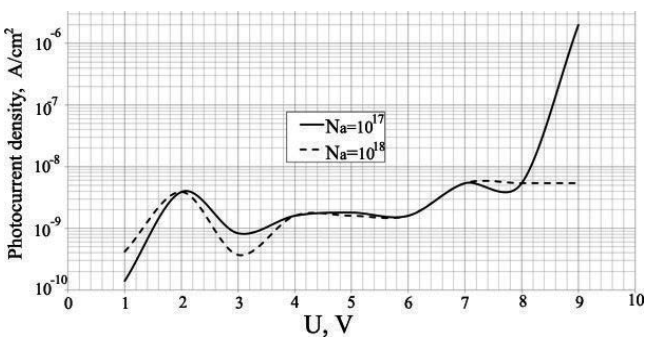

Figure 19. Dark current density J_{Ph} vs. the PT voltage.

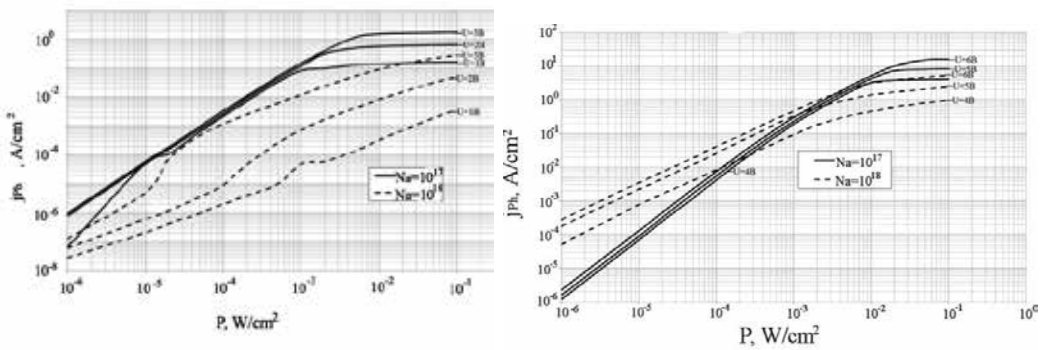

Figure 20. Photocurrent density J_{Ph} vs. irradiation power P at U = 1–6 V.

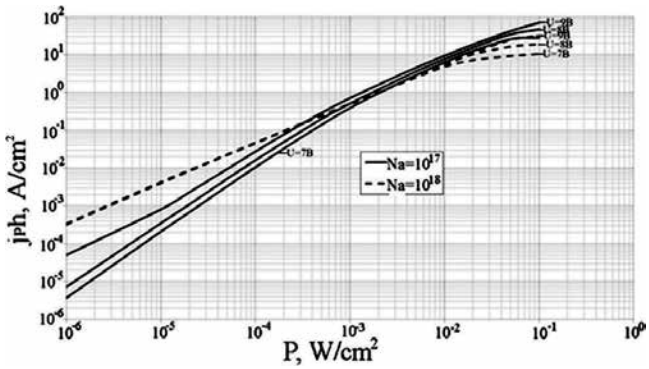

Figure 21. Photocurrent density J_{Ph} vs. irradiation power P at U = 7–9 V.

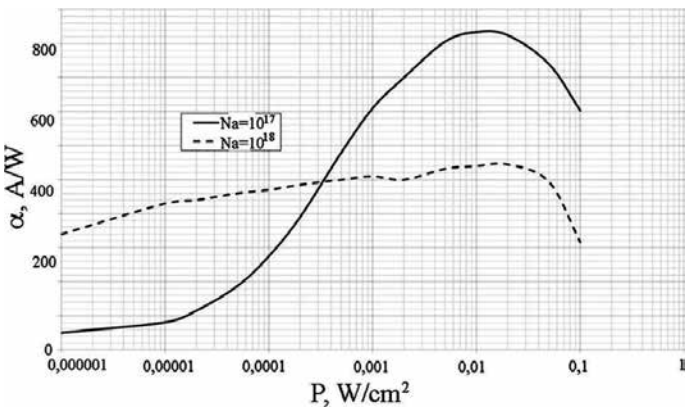

Figure 22. Phototransistor sensitivity vs. light power at U = 9 V.

http://dx.doi.org/10.5772/intechopen.69629

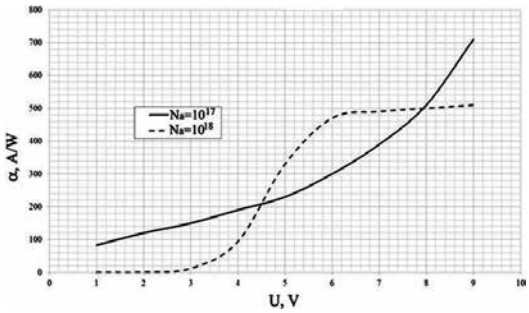

Figure 23. Phototransistor sensitivity vs. voltage at the power illumination density of 1 mW/cm^2.

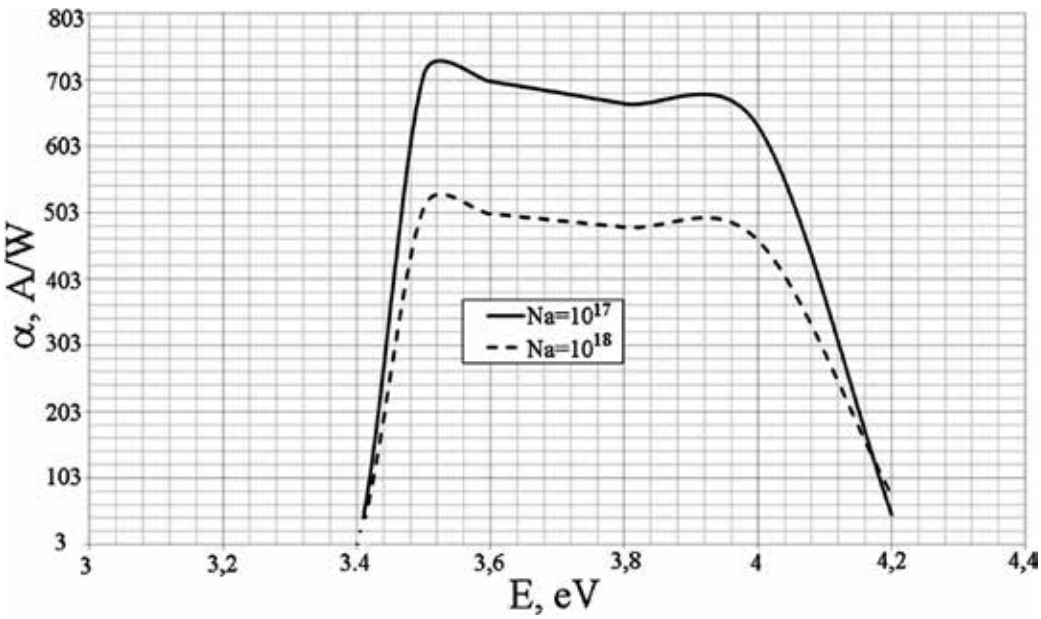

Figure 24. Phototransistor sensitivity vs. quanta energy E at $P = 10^{-3}$ W/cm^2 and $U = 9$ V.

It is clearly seen that the PTs sensitivity is very high in the range of photon energies from 3.5 to 4 eV (wavelength range from 354 to 309 nm), which allows to use them as selective photodetectors. PTs selectivity can be increased by reducing the aluminum concentration in the p-$Al_{0.3}Ga_{0.7}N$ collector up to 20%. Sensitivity also can be increased by improving MOCVD technology for more high-quality AlGaN multilayer structures (with minimum defect concentration). If the sapphire substrate could be replaced by a gallium nitride substrate grown on sapphire, the lifetimes of nonradiative recombination in the PTs base will be increased significantly.

Author details

Sergey Yurchuk, Oleg Rabinovich* and Sergey Didenko

*Address all correspondence to: rawork2008@mail.ru

The National University of Science and Technology "MISiS", Moscow, Russian Federation

References

[1] Round HJ. A Note on Carborundum Electrical World. 1907;**49**:309

[2] Schubert EF. Light-Emitting Diodes. Cambridge: Cambridge University Press; 2006. p. 422. DOI: 0-521-01784-X

[3] Loebner EE. Subhistories of the light emitting diode. IEEE Transactions on Electron Devices. 1976;**23**:675-699. DOI: 10.1109/T-ED.1976.18472

[4] Craford MG. Visible light emitting diodes: Past, present and very bright future. MRS Bulletin. 2000:27-31. DOI: 10.1557/mrs2000.252

[5] Novikov MA. Oleg Vladimirovich Losev: Pioneer of semiconductor electronics. Soviet Physics: Semiconductors. 2004;**1**:5-9 [in Russian]

[6] Losev OV. Optical Relay. Patent No. 12 191, February 2, 1927

[7] Hangleiter A. III–V nitrides: A new age for optoelectronics. MRS Bulletin. 2003:350-353. DOI: 10.1557/mrs2003.99

[8] Holonyak N Jr. Light emitting diode birth. MRS Bulletin. 2005:509-517. DOI: 10.1557/mrs2005.5

[9] Osinski BI, et al. Optoelectronic structures based on many component semiconductors. Nauka i technika, Minsk. 1981:288 [in Russian]

[10] Akasaki I. Nitride semiconductors—Impact on the future world. Journal of Crystal Growth. 2002;**237-239**:905-911. DOI: 10.1016/S0022-0248(01)02077-2

[11] Available from: http://en.nagoya-u.ac.jp/news/nobel2014.html

[12] Nakamura S, Pearton S, Fasol G. The Blue Laser Diode. The Complete Story. New York: Springer; 2000. p. 368. DOI: 10.1007/978-3-662-04156-7

[13] Morkoc H. Handbook of Nitride Semiconductors and Devices. New Jersey: Wiley-VCH Verlag GmbH&Co; 2008. pp. 323-760. DOI: 978-3-527-62846-9

[14] Winston DW. Physical simulation of optoelectronic semiconductor devices. Colorado: University of Colorado; 1999. p. 135. Available from: http://www.simwindows.com

[15] Karpov SY, Prokofyev VG, Yakovlev EV, et al. ROLE OF GASEOUS SPECIES IN GROUP-III NITRIDE GROWTH MRS Internet Journal of Nitride Semiconductor Research. 1999;**4**:126

[16] Mymrin VF, Bulashevich KA, Podolskaya NI. Modelling study of MQW LED operation. Physica Status Solidi (c). 2005;**2**:2928-2931. DOI: 10.1002/pssc.200461289

[17] Bertolotti M, Bloemer MJ, Bowden CM, et al. Blue and green light emission: New directions and perspectives of applications of one-dimensional photonic band gap structures. Physics and Simulation of Optoelectronic Devices VIII. 2000;**3944**:680-687. DOI: 10.1117/12.391475

[18] Rozhansky IV, Zakheim DA. Analysis of the causes of the decrease in the electroluminescence efficiency of AlGaInN light-emitting-diode heterostructures at high pumping density. Semiconductors. 2006;**40**(7):861-867. DOI: 10.1134/S1063782606070190

[19] Burylova IV. Mathematical simulation of distribution of minority charge carriers, generated in multi-layer semiconducting structure by a wide electron beam. Semiconductors. 2007;**41**(4):458-461. DOI: 10.1134/S1063782607040161

[20] Zapol P, Pandey R, Gale JD. An interatomic potential study of the properties of gallium nitride. Journal of Physics: Condensed Matter. 1997;**9**:9517-9525. DOI: S0953-8984 (97)82806-8

[21] Aichoune N, Potin V, Ruteranaet P, et al. An empirical potential for the calculation of the atomic structure of extended defects in wurtzite GaN. Computational Materials Science. 2000;**17**:380-383. DOI: 10.1016/S0927-0256(00)00056-2

[22] Bere A, Serra A. Atomic structure of dislocation cores in GaN. Physical Review B. 2002;**65**:205323. DOI: 10.1103/PhysRevB.65.205323

[23] Zabelin VA, Gurevich CA. LEDS optimization. LEDs and Lasers. 2003;**1-2**:15

[24] Ambacher O, Foutz B, Smart J, et al. Two dimensional electron gases induced by spontaneous and piezoelectric polarization in undoped and doped AlGaN/GaN heterostructures. Journal of Applied Physics. 2000;**87**:334. DOI: 10.1063/1.371866

[25] Vurgaftman J, Meyer JR. Band parameters for nitrogen-containing semiconductors. Journal of Applied Physics. 2003;**94**:3675. DOI: 0.1063/1.1600519

[26] Takeuchi T, Amano H, Akasaki I. Theoretical study of orientation dependence of piezoelectric effects in wurtzite strained GaInN/GaN heterostructures and quantum wells. Japanese Journal of Applied Physics. 2000;**39**:413-416. DOI: 10.1143/JJAP.39.413

[27] Monemar B, Pozina G. Group III-nitride based hetero and quantum structures. Progress in Quantum Electronics. 2000;**24**:239-290. DOI: 10.1016/S0079-6727(00)00009-4

[28] Wetzel C, Takeuchi T, Amano H, Akasaki I. III-Nitride Semiconductors: Optical Properties. New York: Taylor & Francis; 2002. p. 291

[29] Ambacher O, Majewski J, Miskys C. Pyroelectric properties of Al(In)GaN/GaN hetero- and quantum well structures. Journal of Physics: Condensed Matter. 2002;**14**:3399-3434. DOI: 10.1088/0953-8984/14/13/302

[30] Huang X, Du C, Zhou Y, et al. Piezo-phototronic effect in a quantum well structure. ACS Nano. 2016;**10**(5):5145-5152. DOI: 10.1021/acsnano.6b00417

[31] Abramov VS, Nikiforov SG, Sushkov VP. GaN LEDs simulation. LED & Lasers. 2002;**1-2**:30-33

[32] Chichibu S, Uedono A, Onuma T, et al. Origin of defect-insensitive emission probability in In-containing (Al,In,Ga)N alloy semiconductors. Nature Materials. 2006;**5**:810. DOI: 10.1038/nmat1726

[33] Adyr FG, Simpsion TE. Nitride LED measurements. Applied Physics Letters. 2008;**93**: 023109. DOI: 10.1063/1.2992582

[34] Sg Lux GmbH Company. SiC UV Photodiodes. 2009 Available from: http://sglux.de/en/product-category/sic-uvphotodiodes/

[35] Rabinovich OI. InGaN and InGaP heterostructure simulation. Journal of Alloys and Compounds. 2014;**586**:S258. DOI: 10.1016/j.jallcom.2013.03.214

[36] Rabinovich OI, Sushkov VP. The study of specific features of working characteristics of multicomponent heterostructures and AlInGaN-based light-emitting diodes. Semiconductors. 2009;**43**(4):524. DOI: 10.1134/S1063782609040228

[37] Rabinovich O, Legotin S, Didenko S, et al. Heterostructure optimization for increasing LED efficiency. Japanese Journal of Applied Physics. 2016;**55**:05FJ131. DOI: 10.7567/JJAP.55.05FJ13

[38] Yang W, et al. Phototransistor. Patent No. US006137123A, October 24, 2000

[39] Sushkov VP, Vigdorovich EN. Abstracts IV. Russian-Japanese Workshop; 4-16 July 2006; **2**:659

[40] Rabinovich OI. Quantum yield of LEDs based on InGaN/GaN structures at silicon substrates. Light & Engineering. 2013;**21**(2):78-82

[41] Rabinovich OI. Compound semiconductor materials and devices. III-nitride optical devices. SPIE, Bellinghain. Vol. 1635. In: Materials Research Society Fall Meeting 2013, Symposium T; 2-4 December 2013; Boston, MA, USA. pp. 15-22. DOI: 10.1557/opl.2014.336

[42] Rabinovich OI, Legotin SA, Didenko SI. Impurity influence on nitride LEDs. Journal of Nano and Electronic Physics. 2014; **6**(3):030021-030022

[43] Rabinovich OI, Didenko S, Legotin S. Nitride heterostructure influence on efficiency droop. SPIE, Bellinghain In: Proceedings of SPIE, Vol. 9383. Light-Emitting Diodes: Research, Manufacturingand Application for Solid State Lighting XIX; 2-10 February 2015; San Francisco,California, USA. pp. 938310-1-938310-6. DOI: 10.1117/12.2078317

Chapter 4

Hybrid Optoelectronic Router for Future Optical Packet-Switched Networks

Salah Ibrahim and Ryo Takahashi

Additional information is available at the end of the chapter

http://dx.doi.org/10.5772/67623

Abstract

With the growing demand for bandwidth and the need to support new services, several challenges are awaiting future photonic networks. In particular, the performance of current network nodes dominated by electrical routers/switches is seen as a bottleneck that is accentuated by the pressing demand for reducing the network power consumption. With the concept of performing more node functions with optics/optoelectronics, optical packet switching (OPS) provides a promising solution. We have developed a hybrid optoelectronic router (HOPR) prototype that exhibits low power consumption and low latency together with high functionality. The router is enabled by key optical/optoelectronic devices and subsystem technologies that are combined with CMOS electronics in a novel architecture to leverage the strengths of both optics/optoelectronics and electronics. In this chapter, we review our recent HOPR prototype developed for realizing a new photonic intra data center (DC) network. After briefly explaining about the HOPR-based DC network, we highlight the underlying technologies of the new prototype that enables label processing, switching, and buffering of asynchronous arbitrary-length 100-Gbps (25-Gbps × 4λs) burst-mode optical packets with enhanced power efficiency and reduced latency.

Keywords: optical packet switching, optical signal processing, optoelectronic devices

1. Introduction

Optical networks have been playing a pivotal role in achieving the current unprecedented capability of communications that has transformed human experience. In addition to their conventional role in the infrastructure core, metro, and access networks, optical networks are also indispensable in enabling other vital applications such as large-scale data centers (DCs) and supercomputers. With such diversity of application domains, the traffic handled by the

network varies between stable and bursty traffic. The network should thus utilize the optical transmission scheme that matches its traffic nature.

Among different schemes of optical transmission, optical circuit switching (OCS) and optical packet switching (OPS) are two basic schemes that possess complementary features. The OCS scheme allows uninterrupted data transmission where a link is established between two network nodes before starting to transmit data in between. The optical link is realized in a way similar to reserving a closed circuit and thus the scheme is entitled circuit switching. The OCS scheme is suitable for transmission of stable traffic and hence it is widely utilized in core networks. Differently, no link establishment is required with the OPS scheme as data is transmitted as individual packets in a connectionless manner. Each packet is equipped with a given label and based on that label, the packet is forwarded along network nodes until arriving at its destination. More importantly, the packets are forwarded without going through optical-electrical-optical (OEO) conversion in a real photonic network. This feature together with the elimination of the link establishment time makes the OPS scheme very suitable for handling bursty traffic.

On the other hand, the capacity of optical links has been significantly boosted [1] by using higher data rates and complex data formats, which increases the burden on current network nodes that are mostly relying on electrical packet switching (EPS). The resulting extensive dependence on electronic processing is the reason for several shortcomings that are difficult to overlook such as the high power consumption and end-to-end latency. The EPS approach can be also identified as a limiting factor for the network scalability which is the problem faced by current large-scale DC networks. This condition can be overcome by realizing a photonic network instead, and in this regard, we have proposed a new photonic intra DC network based on the hybrid optoelectronic router (HOPR).

In this chapter, we review our recent HOPR prototype developed for realizing the DC network. We briefly explain about the HOPR-based photonic DC network, and highlight the underlying technologies of the new prototype that enable label processing, switching, and buffering of asynchronous arbitrary-length 100-Gbps (25-Gbps × 4λs) burst-mode optical packets with enhanced power efficiency and reduced latency.

2. New photonic data center network

DCs have considerably evolved to become main players in the big-data era, providing a diversity of services with unprecedented volumes of data traffic [2–4]. However, as mentioned earlier, current intra DC networks that are mainly based on EPS have been facing increasing difficulties to cope with the growing demand. The advancement of the EPS-based DC networks has continuously relied on the progress of the CMOS and transceiver technologies. But these technologies have already reached an advanced level after which it becomes difficult to achieve further improvement at the quick pace required for fulfilling the ongoing demands [5]. Realizing a photonic DC network is a radical solution that can let DCs surpass their current difficulties. To serve this end, we have proposed the photonic intra DC network

http://dx.doi.org/10.5772/67623

[6] illustrated in **Figure 1**. The network has a torus topology and it depends on the deployment of HOPRs and a centralized network controller. More about the key network aspects can be found as follows.

- **Basic operation:** A HOPR unit is located at each node of the torus DC network and connected to neighboring HOPRs via optical links. High-speed burst-mode optical packets are transmitted over these links. Each HOPR unit is also connected to a group of Top-of-Rack (ToR) switches that handle Ethernet packets from the servers connected to them. An Ethernet packet is transformed into a burst-mode optical packet at the corresponding HOPR unit and from there on it is transmitted in the optical domain throughout the torus network until it reaches the HOPR unit attached to the destination server. Thus, each HOPR unit has a twofold role as an optical-packet switch that forwards the optical packets of the torus network and an aggregation switch that handles the servers' packets.
- **Topology:** A highly dimensional torus topology is considered for realizing the network. This topology has been widely adopted in supercomputers such as the CRAY (3D), Blue Gene (3–5D), and K Computer (6D). It enables a highly scalable network that can strongly support fault tolerance with redundancy of links. The torus topology also exhibits several features that are advantageous for the OPS scheme; as (1) it is a direct topology in which a low-radix switch is sufficient for deployment at each network node, (2) the uniform arrangement of the network nodes allows the utilization of a simple deterministic algorithm for forwarding incoming packets, and (3) the presence of multiple equidistant routes between the source and destination nodes with the same latency can efficiently help in resolving packet contention when it occurs.
- **Transmission schemes:** Three data transmission schemes are supported by the photonic DC network; namely the OPS, OCS, and virtual V-OCS schemes. Unlike current DC networks, the OPS scheme is used to allow latency-sensitive applications over a wide network scale without being limited to nodes in close proximity.

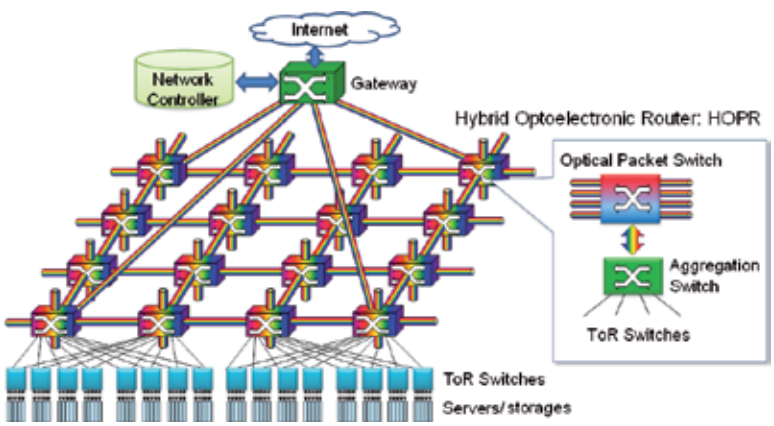

Figure 1. Illustration for the torus DC network based on HOPR and NW controller.

However, an OPS packet can reach its destination via different routes and might encounter collision with other packets and thus the probability of packet loss cannot be completely avoided. For the OCS case, an optical path is reserved before transmission is started to avoid packet loss and the sent packets arrive with the same order and same latency. However, as the number of OCS paths increases, the normal OPS packets are strongly counteracted due to the increasing difficulty of finding a vacant route to reach their destination. Hence, the virtual OCS scheme has been devised [7, 8] to enable the coexistence of the OPS and OCS packets almost without counter effects. To realize such DC network, we have developed a new HOPR prototype that can meet the demand of handling burst-mode optical packets without OEO conversion unless necessary.

3. Hybrid optoelectronic router

In this section, we highlight HOPR's operation, architecture, and implementing approach. **Figure 2a** shows HOPR unit for a 3-D torus network, and **Figure 2b** shows a 6-D network where a 16 × 16 optical switch is used and the shared buffer interface is upgraded to 200 Gbps allowing the aggregation of more servers' traffic. Using the WDM configuration as shown in **Figure 2c**, the link capacity can be increased as the product of the number of wavelength layers and data rate of generated packets to allow achieving 0.4–1 Tbps.

When an optical packet arrives at HOPR, the destination address is recognized by the label processor (LP) while keeping the packet in the optical domain. The optical switch is then configured to forward the packet via the desired output switch-port. If the port is occupied, a contention resolution plan is followed to resolve the condition. At the torus DC network, the packet can be forwarded to another output switch-port and still goes through one of the shortest routes toward its destination, that is, deflection routing. HOPR is also equipped with optical and optoelectronic buffers to help with resolving contention, where (1) the packet can have a fixed time delay by going through a fiber delay line (FDL) without OEO conversion, or (2) it can be electronically stored in the optoelectronic buffer for an arbitrary storage time.

Unlike most conventional electrical routers that adopt the store-and-forward mechanism for packet forwarding, HOPR relies on the cut-through mechanism where the optical switch is configured once the packet label is recognized without demanding the whole packet to be received first. This matches well with forwarding the packets without OEO conversion. The packet path via HOPR only includes the LP and optical switch, whereas the shared buffer is located in parallel without obstructing the normally forwarded packets. The role of these three basic functional units is summarized in the following.

- **Label processor:** The LP's role is divided into: (1) extraction and recognition of the incoming packet label, (2) deciding the output switch-port accordingly, (3) performing arbitration for colliding packets, and then (4) configuring the switch with the corresponding control signals. On the other hand, the LP should be realized with (1) low power consumption to enable a widely scalable network, (2) low latency as the packet remains in the optical domain and the label processing time is compensated for just by delaying it, (3) a sufficiently high dynamic range to exhibit tolerance for power variation among the incoming packets.

http://dx.doi.org/10.5772/67623

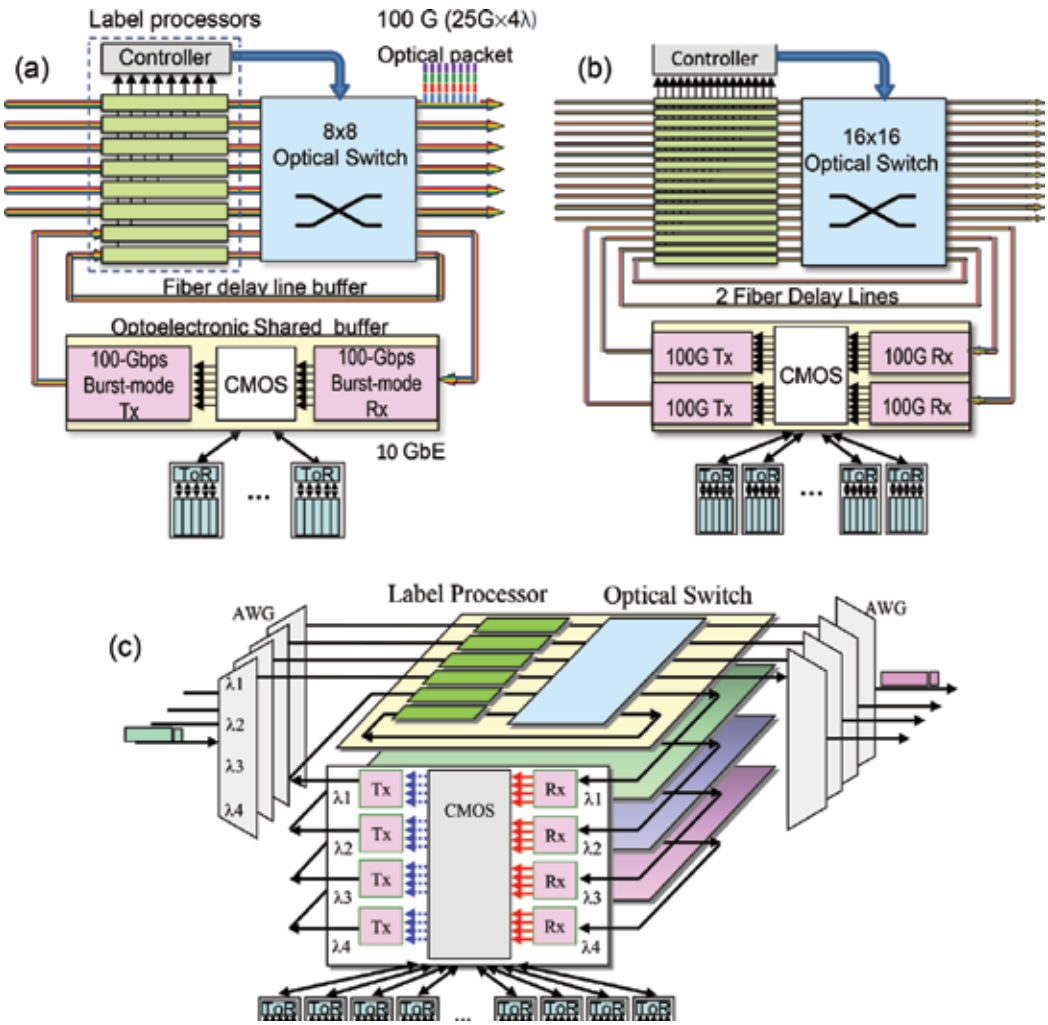

Figure 2. HOPR's architecture and basic subsystems in different configurations.

- **Optical switch**: There is a general trade-off between the switch speed and its maximum port count. For example, mechanical switches such as MEMS-based switches [9] can exhibit large port-counts, that is, over 1000 ports, but their reconfiguration time lies in the millisecond order. Differently, the OPS switch should operate in the nanosecond order; and with current technologies, only low port-count switches, for example, 16 × 16 ports, are available. A fast switch with low port-count can still enable realizing a highly scalable network with good performance if a suitable network topology is selected. It is beneficial to realize a switch with independent characteristics in terms of bit-rate, packet format, wavelength, and polarization. The switch is also demanded to possess low power consumption, high extinction ratio, low crosstalk, and ease of controllability. To meet these demands, several switch types have been considered by researchers [10–12]. Examples include the matrix switch that consists of cascaded smaller switches,

phased-array switch, wavelength routing switch, and broadcast-and-select (B&S) switch. Among them, the B&S switch is selected as it meets most of the requirements to a good extent. We have also considered wavelength-routing switches to achieve a switch with higher port-counts.

- **Optoelectronic shared buffer:** Realizing an optical memory has attracted a lot of research interest [13, 14] but a reliable solution is still missing. Available solutions are either passive all-optical buffering via an FDL [15] for a fixed duration or electrical buffering where the optical packets are interfaced to an electronic memory. The role of shared buffer exceeds the demand for packet storage as it is essential for resolving contention and for enabling higher network functionalities such as packet regeneration, Quality of Service (QoS) control, and format conversion. Another important role for the optoelectronic buffer is interfacing the photonic network to other transmission domains with different data formats and data rates, where for the DC network case, it should act as an aggregation switch for the servers Ethernet packets.

Unlike conventional electrical routers handling continuous data streams to prevent clock loss at the receiver side, HOPR should operate in a burst-mode fashion where a packet suddenly arrives after a period of no received signal. Knowing the bit timing of the incoming packet is essential, but there is no prior synchronization between the incoming packets and HOPR. To enable clock recovery, burst-mode routers rely on preamble bits [16] that precede the packet, where a conventional way for clock recovery is used such as the phase locked loop (PLL) method that demands a long locking time [17], or the phase picking method [18] that is widely selected for handling lower data rates (~10 Gbps). The over-sampling method [19] is another alternative, where a clock recovery time of 31 ns has been recently reported [20] by combining this method and an approximation algorithm. However, the continuous increase of data rates reduces the packet duration, and keeping the dependence on preamble bits will degrade the efficiency of utilizing the optical link. Thus to allow HOPR to handle preamble-free optical packets, special burst-mode optoelectronic devices are developed to interface optical packets to electronic circuits with a novel optical clocking (triggering) method.

HOPR prototype (**Figure 2a**) is developed with (1) total throughput of 1.28 Tbps, where six input/output ports handle 100-Gbps optical packets and four input/output ports handle the 10-GbE connections, (2) total power consumption of 110 W, with ~40 W for the optical packet switch part that includes 8 LPs and an 8 × 8 optical switch, and ~70 W for the aggregation switch (optoelectronic shared buffer), including the contribution of the control plane, cooling, GUI, 10-GbE transceiver modules, and so on, and (3) latency of 140 ns, with ~60 ns for the transmission delay via the optical switch and EDFA, and ~80 ns for the LP dominated by the arbitration time for resolving contention. Electrical switches have also been significantly enhanced, but still they require a Network Interface Card (NIC) and optical transceiver module at each port. The CFP 100-GbE optical transceiver, for example, demands 6–20 W for different transmission ranges. HOPR's optical packet switch part consumes 5 W/100-G-port which is lower than a single CFP module. The future increase in packets data-rates, the power of optical packet switch would remain almost unchanged. The power consumed by the

http://dx.doi.org/10.5772/67623

shared buffer can also be further reduced if instead of combining a Field Programmable Gate Array (FPGA) and discrete electronic components, the state-of-the-art Application Specific Integrated Circuit (ASIC) technologies are used in a way similar to the electrical switches.

As the name implies, the hybrid optoelectronic router is based on a hybrid implementation approach, where both electrical and optical technologies are used, each where it fits most. This approach has been vital for fulfilling the basic demand of reducing HOPR's power consumption and latency without sacrificing its performance. The hybrid approach can be seen at HOPR's underlying device level, where, for example, the operation principal of some essential devices is based on using optical timing pulses, that is, clock pulses, for triggering electronic circuits to enable handling the packets' ultrafast bits in an efficient way. Moreover, the hybrid approach can also be seen at the subsystem level as for instance in the presence of different packet buffering options, represented by the all-optical FDL-based buffer and the optoelectronic buffer. These alternatives provide the flexibility demanded to efficiently cope with diversified conditions of operation.

4. Optical label processing technologies

In this section, we explain about our latest LP [21] that handles 25-Gbps burst-mode optical labels without preamble bits. **Figure 3** shows the structure of the LP that consists of a set of label extractors (LE) connected to a shared controller.

At each input port of HOPR, a split from the incoming packet is directed to the attached LE, whereas the main part goes toward the optical switch but first passes through an FDL to compensate for the label processing time. Unlike traditional Serializer/Deserializer (SerDes)

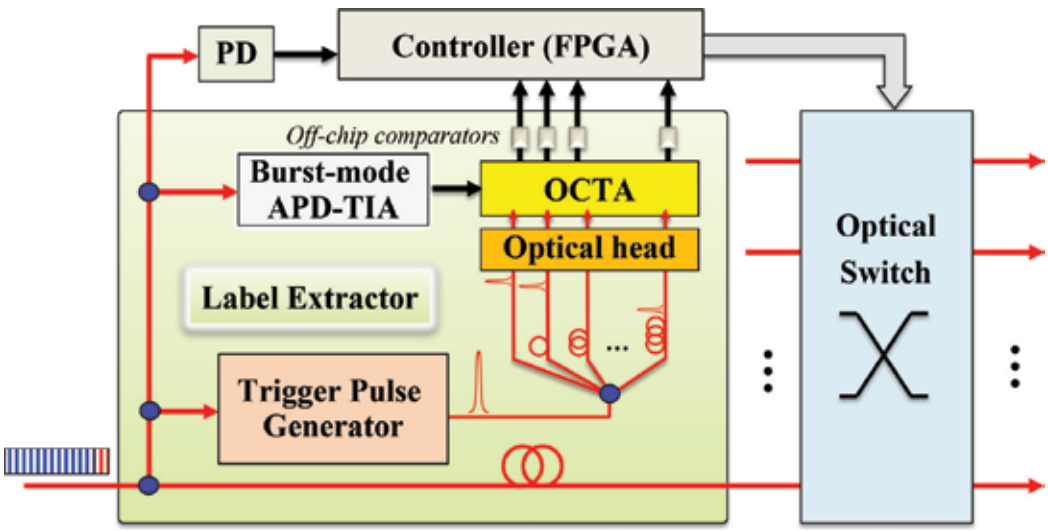

Figure 3. The overall structure of the burst-mode label processor.

that converts the bits of the whole packet, the LE handles only the packet label. The label's ultrafast bits are separated in parallel and their speed is sufficiently slowed down by undergoing serial-to-parallel conversion to allow their direct latching into the CMOS based LP's shared controller. At the LP controller, the forwarding table is looked up with the extracted label and when a match is found and the corresponding output port of the switch comes out as the result. The occupancy of the resulting output port is examined; and if the port is free, the control signals necessary for configuring the optical switch are generated and applied, whereas if the port is occupied, the second priority output is selected and so on until finding an available port. To enable label processing of preamble-free packets, the LE adopts an operating mechanism that relies on two basic elements: (1) a burst-mode serial-to-parallel converter (SPC) that operates once supplied by optical triggers and it is referred to as the optically clocked transistor array (OCTA), and (2) a burst-mode optical trigger pulse generator (TPG) that selectively utilizes the first bit of incoming packet to produce a synchronized optical trigger pulse for OCTA.

4.1. Optical trigger pulse generator

The TPG produces an optical trigger pulse by selectively amplifying the first bit of incoming packet with a semiconductor optical amplifier (SOA). Being originally a part of the incoming cket, the resulting optical pulse is a synchronized trigger that allows jitter-free serial-to-parallel conversion when applied to OCTA. **Figure 4a** shows the SOA's driver integrated circuit developed to drive a narrow current pulse (~1 ns) of high peak current (>600 mA).

A split from the incoming packet as shown in **Figure 4b** is applied to the metal-semiconductor-metal (MSM)-PD at the driver's discharge-based (DB) circuit and produces a single electrical pulse that undergoes reshaping before turning on a set of integrated high electron mobility transistors (HEMTs) shortly to enable the flow of high electric current through the SOA. The red curve in **Figure 4c** shows the normalized amplified spontaneous emission (ASE) of the

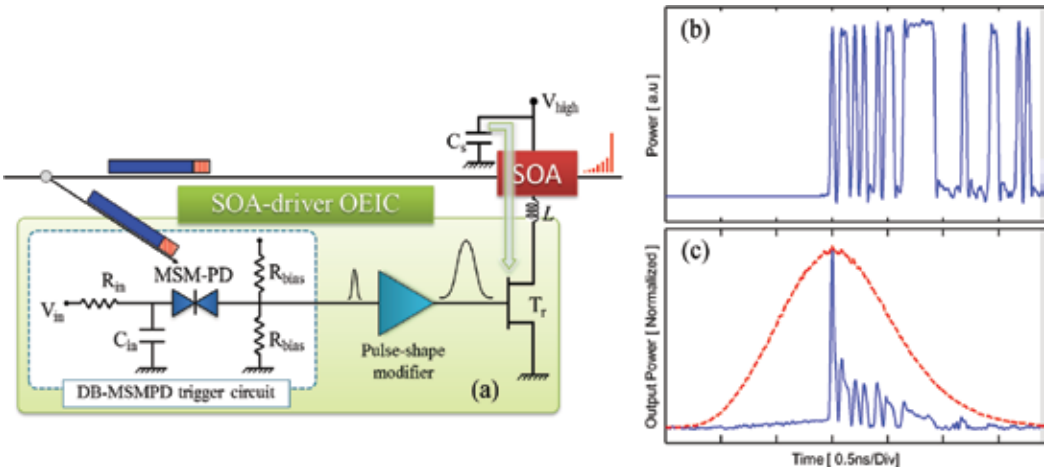

Figure 4. (a) The TPG circuit, (b) incoming packet, and (c) SOA output.

http://dx.doi.org/10.5772/67623

SOA that corresponds to its gain profile when the current pulse of the driver is applied to the SOA without having it supplied with any optical input. The packet arrival at the SOA is roughly adjusted to be around the gain peak. The packet's first optical pulse experiences strong amplification and quenches the accumulated carriers at the SOA, and the following pulses fade out due to lack of gain as shown in **Figure 4c**. As the SOA's power dissipation is limited only to a short instant after packet arrival, the power consumption of the TPG has been significantly reduced to 120 mW compared to an older TPG [21] that consumed 3 W.

The DB circuit [22] is a fundamental element in our burst-mode devices, used for converting an optical trigger signal into a narrow electrical pulse that can control the gate of a HEMT transistor. It utilizes an MSM-PD that has a fabrication advantage due to its surface structure. Unlike PIN photodetectors whose response is limited by an RC time constant, the MSM-PD has a very quick rise-up time only limited by the electron transit time due to its ultralow capacitance. However, the MSM-PD response suffers from a long tail due to the low mobility of holes. The discharge-based configuration is thus employed to allow the MSM-PD to generate a sufficiently narrow electrical pulse. The input capacitor C_{in} of the DB circuit is initially charged maintaining a high bias voltage. When an optical pulse is then applied to the MSM-PD, it causes the flow of photocurrent. A corresponding electric current cannot be injected by V_{in} due to the high resistance R_{in}, and thus C_{in} is discharged resulting in the reduction of the bias voltage. One important feature of the MSM-PD is that in the absence of bias voltage, the current cannot flow even when the carriers are still present. The first pulse of incoming packet almost depletes the carriers of C_{in} leaving the following packet bits ineffective. Thus even with the MSM-PD direct irradiation with the whole packet, the DB circuit can produce a single short electrical pulse.

4.2. Optically clocked transistor array

Figure 5 illustrates the structure of OCTA which is a monolithically integrated circuit that consists of 16 serial-to-parallel conversion channels attached to a common transmission line (TL) each via a separate HEMT (T_m).

An avalanche photodetector and trans-impedance amplifier (APD-TIA) burst-mode module is used to convert the packet split at the LE unit (**Figure 3**) into an electrical signal that is then coupled to OCTA and propagated along its TL. The channels are used in turn, each for converting a different label bit. The timing of a separate optical trigger pulse is adjusted to match the presence of a given bit at the TL, and the bit is converted by applying that trigger pulse to the respective channel. OCTA's correct operation demands T_m to be turned on shortly to convert only a single bit, and hence the DB-MSMPD trigger circuit is used to produce a single narrow electrical pulse to control T_m. OCTA-based serial-to-parallel conversion was initially done by the sample-and-hold (S&H) scheme as shown in **Figure 5a**, where an electric charge corresponding to the considered bit level is sampled into the capacitor C_{hold} through T_m. The voltage-change induced at C_{hold} is then amplified to produce the channel's final output. This SPC scheme suffers the limited difference between the sampled charge that corresponds to the "1" and "0" bits, respectively. The reason is that charging C_{hold}, that is, in case of a "1" bit, increases the voltage at T_m source terminal and hence forces it to get turned-off. Moreover,

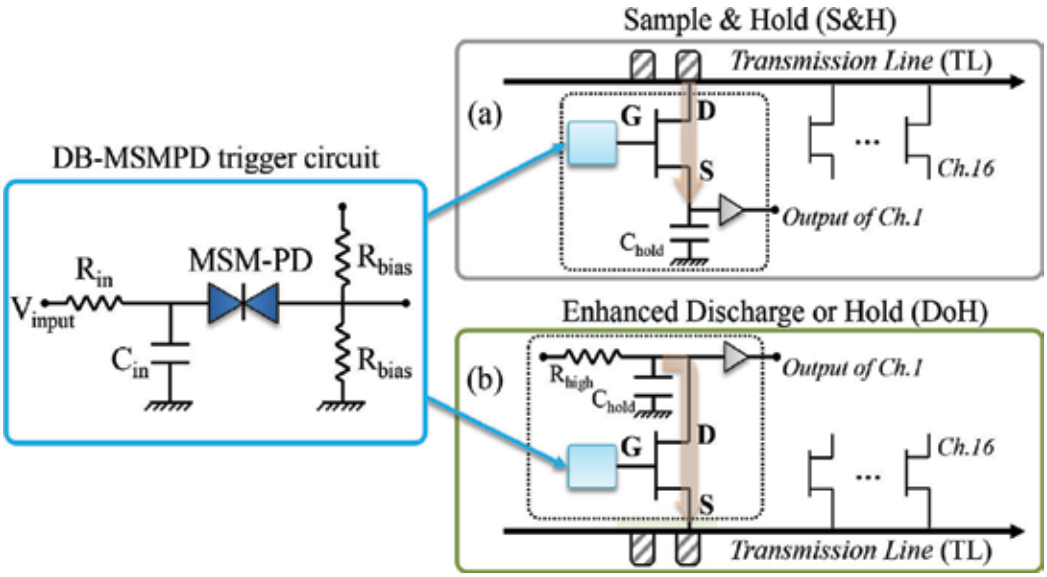

Figure 5. The structure of OCTA and illustration of its operation schemes (a), and (b).

charging C_{hold} cannot be done efficiently as a part of the bit voltage is unavoidably dissipated in the TL's characteristic impedance that is present in parallel to the turned-on conversion channel. The S&H scheme was then replaced by the discharge-or-hold (DoH) scheme [21] illustrated in **Figure 5b**, where the charge initially present at C_{hold} is either discharged into the TL or kept unchanged. Discharging C_{hold} is done more efficiently than charging it, and a much higher difference of charge is produced at C_{hold}. The benefit of the DoH scheme has been further elevated by using a label signal with negative voltage span, that is, negative voltage for a "1" bit and zero voltage for a "0" bit.

Figure 6 shows a comparison for using the DoH scheme with the TL signal having either a positive or a negative polarity. The gate voltage signal generated by the optical trigger pulse is shown in solid line. When the transistor T_m is turned on as V_{GS} exceeds the threshold voltage V_{th}, the bias voltage between its drain and source terminals, that is, ΔV_{DS}, is obviously higher in case of negative polarity. This allows a more efficient discharge for C_{hold} with the higher electrical current enabled by the higher ΔV_{DS}. Then if the energy of optical trigger pulse is reduced, a corresponding reduction in the gate pulse amplitude takes place as highlighted by the dotted line. Even with this reduction in ΔV_{GS}, the initially higher value of ΔV_{DS} enables conversion as efficient as in the case of a positive polarity signal with unreduced optical trigger energy.

4.3. Enhanced packaging

Optoelectronic integrated circuits (OEICs) are attractive for their high-speed operation and low power consumption. To make the best use of these key features, the optical trigger pulses

http://dx.doi.org/10.5772/67623

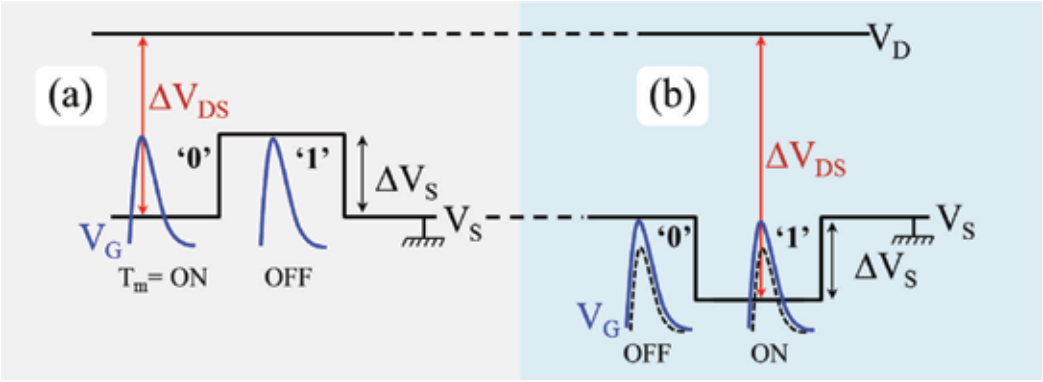

Figure 6. The DoH scheme with TL signals of (a) positive and (b) negative polarities.

necessary for OEIC operation should be provided with suitable device packaging. The older way of device packaging was complicated and costly, and thus it had to be revised.

Figure 7a shows a photo for the old packaged OCTA, where a set of lens array is used to focus the optical triggers on the MSM-PDs located at the front side of the chip. The old packaging method was wasting the trigger energy due to the shadowing effect that occurs for front-illuminated light by the MSM-PD's interdigitated metal electrodes [23]. This method also had other shortcomings such as the need for active alignment and an expensive lens array. To overcome these issues, a new method was developed as shown in **Figure 7b**. The optical head employed is a commercially available fiber-array block, where SMF fibers are placed in grooves with the same pitch as the chip's MSM-PDs. The chip is directly attached to the optical head after reducing its thickness to ~130 μm. The high refractive index of the chip's InP substrate limits the divergence of the optical beams launched from the SMF fibers. The $1/e^2$

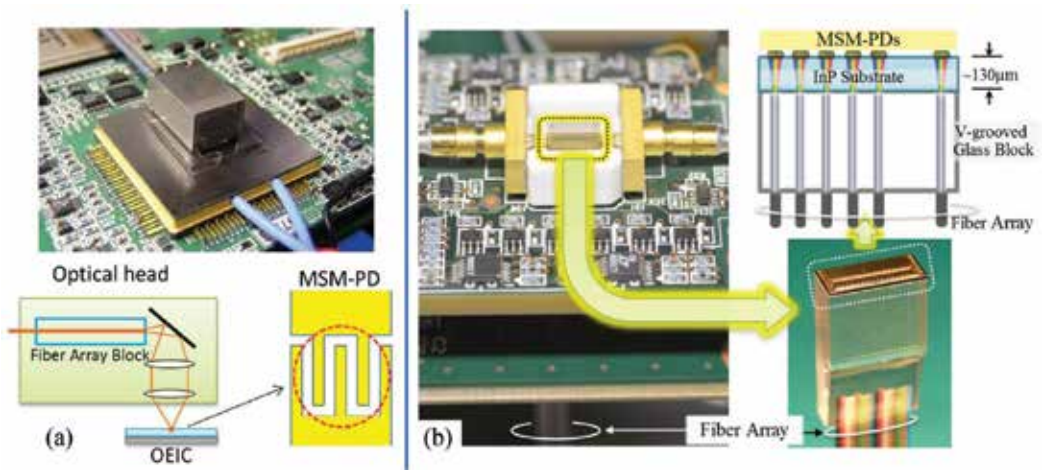

Figure 7. (a) Old packaging of OCTA versus (b) new packaging.

diameter of the optical spot resulting at the MSM-PD is ~13 μm, which is narrow enough to fit into the 20-μm active area of the MSM-PD without using lenses and while still exhibiting a large misalignment tolerance. Another key feature of this method is that optical triggers are supplied via the backside of the chip. With back illumination, the responsivity of the MSM-PDs is almost doubled and the trigger pulse energy necessary for performing serial-to-parallel conversion for 25-Gbps label bits has been reduced to 0.35 pJ/bit.

When an optical signal is applied to the MSM-PD via its backside, a part of the signal goes though the MSM-PD and can still be seen from the chip's front side. A simple alignment process has been developed by making use of this feature, where the optical beams coming out of the MSM-PDs of all the conversion channels are simultaneously observed by using an infrared camera. The best alignment position is achieved simply when a full set of clear optical spots is visually observed.

5. Optical switching technologies

In this section, we present two types of fast optical switches that we have been considering, namely the wavelength-routing switch and the broadcast-and-select switch.

5.1. Wavelength routing switch

Figure 8a illustrates the basic architecture of an N × N optical switch that operates with the wavelength routing mechanism. The switch consists of a cyclic arrayed waveguide grating (AWG) equipped with a tunable wavelength converter (TWC) at each input port and a fixed wavelength converter (FWC) at each output port. By changing the wavelength of the optical signal input to the AWG with the TWC, the signal can be directed to a different output port, whereas the FWC is used to return the signal back into its original wavelength. Based on the well-established AWG technology, it is feasible to realize such switch with a medium port-count, for example, 64 × 64 ports, provided that the used TWC can cover the whole C-band. The full exploitation of this switching method demands a TWC with independent characteristics in terms of modulation format and data-rate, but it is still hard to realize such TWC.

Currently, the most reliable TWCs are based on signal regeneration with OEO conversion where the wavelength of a TL is changed to match the desired output port, and the data of incoming packet is converted into an electrical signal that is then used to modulate the new wavelength. The OEO-based TWC does not allow the switch usage for handling WDM packets or coherent packets.

The components required for realizing the OEO-based TWC are (1) a fast tunable laser for generating an optical carrier with desired wavelength, (2) a burst-mode photodetector and an electrical amplifier for converting the incoming optical packet into electrical signal with sufficient amplitude, and (3) a modulator for modulating the desired wavelength with the electrical packet signal. We have developed a parallel-ring resonator-based tunable laser (PRR-TL) that is integrated with an electro-absorption modulator (EAM) on the same InP chip. The

http://dx.doi.org/10.5772/67623

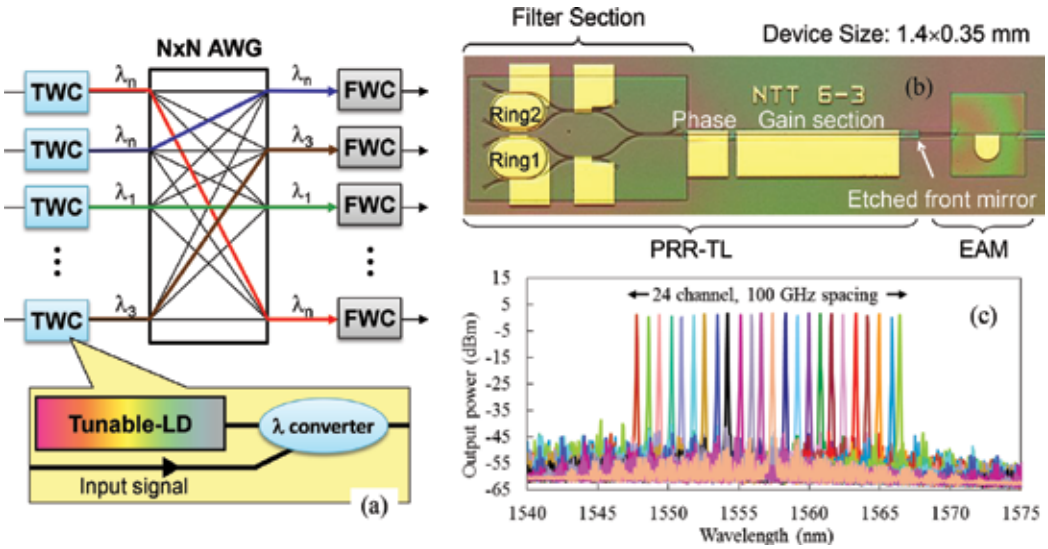

Figure 8. (a) Illustration for wavelength-routing switch, (b) photo of tunable transmitter chip, and (c) superposed spectrum of the PRR-TL.

PRR-TL relies on the Vernier effect for providing a wide tuning range [24]. The chip's photo is shown in **Figure 8b** where the TL consists of a phase section, gain section, and parallel-ring resonator (PRR). The TL has a partially reflective output port, whereas the PRR section is the other end of its laser cavity that selectively reflects the optical signal with desired wavelength. The wavelength is tuned with low current injection, that is, mA order. This enables the PRR-TL to exhibit a very low wavelength drift of less than 5 GHz. The low current injection and parallel ring design results in a laser cavity with low optical loss. This allows the PRR-TL to exhibit an output power variation of less than 1 dB over a wide tuning range of 35 nm as shown in **Figure 6c**. Moreover, it also allows the TL to generate a high output power while exhibiting a high-speed wavelength tuning of less than 6 ns.

5.2. Broadcast-and-select switch

As the wavelength-routing switch is not suitable for handling WDM packets (25-Gbps × 4λs), we have considered the B&S switch instead. **Figure 9a** illustrates the basic structure of the B&S switch, where an optical 1 × N passive splitter is located at each input port, with an optical gating unit placed at each of the splitter outputs. On the other hand, an optical N × 1 coupler is placed at each output port, with each coupler input connected to one output of the splitter that serves for a different input switch port. The packet undergoes switching by turning on the optical gate that can lead it to the desired output port.

- **Optical gate:** SOAs are widely selected as optical gating units in the B&S switches as they can provide optical gain to compensate for the optical loss while unavoidably adding some ASE noise. SOAs exhibit pattern-dependent effects for high bit-rate packets and inter-channel crosstalk for DWDM-based packets due to four-wave mixing and cross-gain modulation,

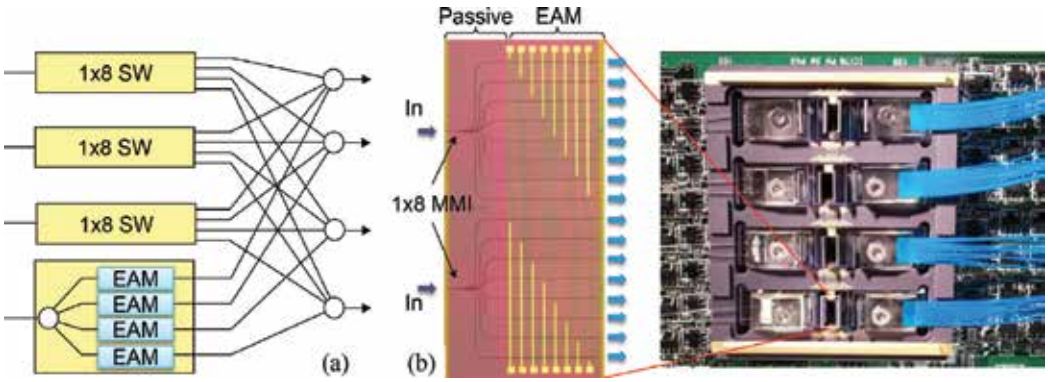

Figure 9. (a) Illustration for the B&S switch and (b) realized switch with inset of fabricated chip.

and they also require high-speed drivers with large current modulation which leads to high power consumption. Instead of SOAs, we have considered EAMs as optical gates, and the full switch system requires an EDFA for loss compensation at each output port. But yet still the total power consumption is lower than that of the SOA-based switch as the power consumption of an EDFA can be reduced (~1 W) by optimizing it for a given gain range (~25 dB). In addition, the power consumption of the reverse-biased EAM and its electrical driver is very low compared to the SOA.

- **Device and module**: **Figure 9b** shows the device photo for two monolithically integrated 1 × 8 EAM gate switches. The EAM section has a shallow-ridge waveguide structure and the passive waveguide section including the 1 × 8 multimode interference splitter is formed as a deep-ridge to reduce the required bending radius. The bulk InGaAsP (λ_{gap} = 1.4 μm) used for the absorption layer of the EAM section operates based on the Franz-Keldysh (FK) effect. To simplify the fabrication process, the EAM and passive sections share the same core/cladding layers, in which EAMs are not electrically isolated from each other. Thus when voltage is applied to a given EAM, an undesirable change is caused in the output power of other switch ports due to the electro absorption by FK effect induced in the passive waveguide section. One way to eliminate such electrical crosstalk is to replace the p-InP cladding layer by a high-impedance material such as Fe-doped InP. However, this would demand an additional step of regrowth process. To avoid that, a surface-ground electrode is used to cover the MMIs of the passive waveguide section. The simple addition of the surface ground electrode has been successful in suppressing the electrical crosstalk [25].

A set of micro-lenses is used for the optical coupling between an optical fiber array and the switch waveguide array. High coupling loss and loss variation among different waveguides were observed due to the large and asymmetric numerical aperture of ridge waveguide (NA ~ 0.8). To improve coupling loss and alignment tolerance, spot size converters (SSCs) were then added at both switch sides to decrease the waveguide's NA by expanding its optical mode field. The core size is set to 0.4 μm × 0.4 μm to achieve a symmetric NA of 0.5. The fabricated module exhibits low WDL and PDL of typically ±0.5 dB in the wavelength range of

http://dx.doi.org/10.5772/67623

1540–1560 nm. The module is attached to an electrical control board including an FPGA and EAM drivers that enable a switching rise/fall time of less than 10 ns. With a reverse bias of ~7 V, all the output ports exhibited extremely high extinction ratios of more than 50 dB, which is sufficient to avoid any signal degradation caused by inter-symbol interference.

6. Optical buffering technologies

HOPR comprises an FDL-based all-optical and optoelectronic shared buffer. This section is devoted to the optoelectronic shared buffer where packet processing is performed to enable higher network functions such as packet regeneration, QoS control, and format conversion.

6.1. Operation

Figure 10 illustrates the optoelectronic buffer used to handle 100-Gbps WDM optical packets composed of four wavelengths each modulated at 25 Gbps. A CMOS processor is located at the buffer core, and it can independently handle the servers' Ethernet packets delivered through the ToR switches, and the network OPS packets. The OPS packets are fed into and out of the processor by using a set of burst-mode serial-to-parallel converters (SPCs) and parallel-to-serial converters (PSCs), respectively. The incoming packet four wavelengths are de-multiplexed with an AWG at the buffer input. Each packet part belonging to a different wavelength is converted into fast electrical signal by using an APD-TIA module. Each two

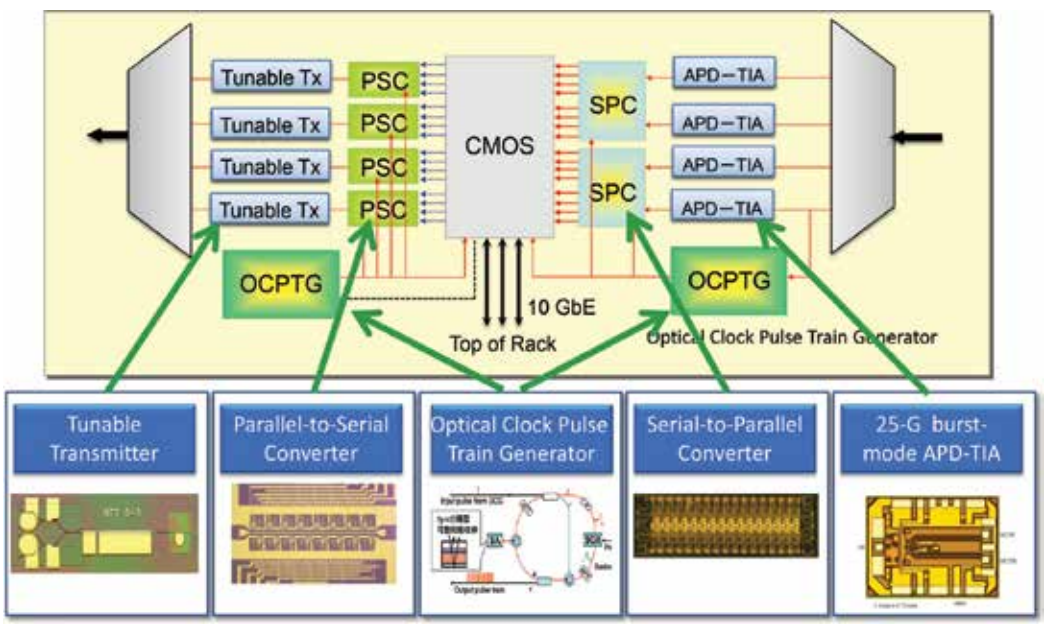

Figure 10. The optoelectronic shared buffer that can handle burst-mode WDM packets.

packet parts are then simultaneously fed into the same SPC device, where the speed of their ultrafast bits is reduced by the ratio of 1:16.

The two SPC devices are supplied with optical clock pulses to keep them operating until the serial-to-parallel conversion is done for the whole packet. The optical clock pulse train generator (OCPTG) module present at the buffer input side provides the optical clock pulses necessary for operating the SPCs and also the optical clock pulses required to latch the SPCs output to the CMOS processor.

To generate a 100-Gbps optical packet, four different PSCs separately receive the electrical data for each wavelength from the processor, and operated in parallel to reduce the speed of the data bits by the ratio of 16:1. Each PSC output is used at a separate tunable transmitter that generates an optical carrier adjusted to a desired wavelength. After modulation, the four wavelengths are multiplexed by an AWG to form the output 100-Gbps optical packet. The OCPTG module at the buffer output side provides the optical clock pulses required for reading out data from the processor and for operating the PSCs.

6.2. Enabling devices

The devices necessary for realizing the shared optoelectronic buffer are briefly highlighted here, and more details can be found in the corresponding references.

- **OCPTG:Figure 11** illustrates the OCPTG structure that has an optical clock generator (OCG) at the input followed by the pulse train generator (PTG)'s optical loop that includes an SOA and spin-polarized saturable absorber (SA) with high-extinction ratio. The OCG generates a single optical pulse in response to the first bit of incoming packet. This pulse is then fed into the PTG module to produce a train of optical pulses with fixed separating intervals between pulses throughput the whole length of the packet. The OCPTG [26] can thus handle preamble-free asynchronous optical packets with variable lengths.

The optical pulse train is generated by tapping out a portion of the circulating seed pulse initially provided by the OCG. The loop is made to have a round-trip gain function with

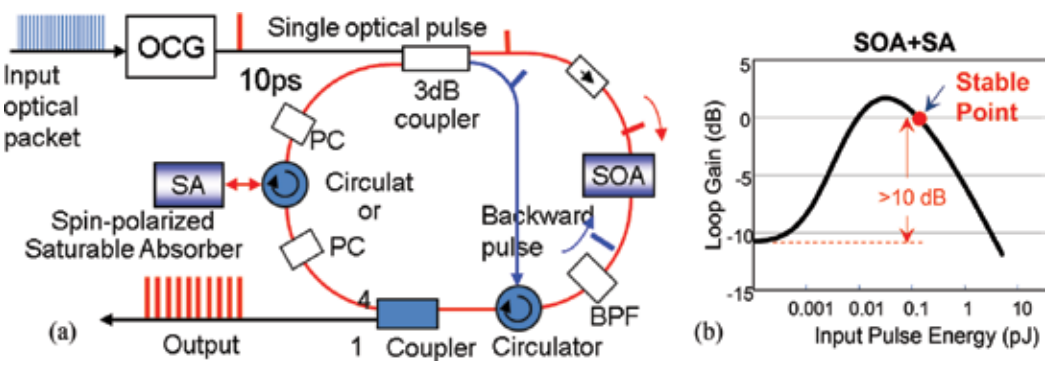

Figure 11. (a) The structure of OCPTG and (b) loop transfer function of PTG.

http://dx.doi.org/10.5772/67623

negative slope based on the SOA gain saturation (**Figure 11b**). This allows the circulating pulse energy to converge even if some fluctuation occurs, where the gain and absorption of the SOA and SA, respectively, finally balance out. The ASE of the SOA is suppressed by the SA. The SA is characterized by fast absorption recovery due to spin relaxation, but still after the pulse comes out of the SA, a backward optical pulse is launched into the SOA to prevent the increase of the ASE inside the loop with the recovery of SOA gain. Without any external control for the loop gain, a stable optical pulse train with low jitter is generated from a single 10-ps seed optical pulse even with a 10-dB variation in the seed pulse intensity.

- **APD-TIA module:** The high-speed avalanche photodetector (APD) and burst-mode transimpedance amplifier (TIA) module have been newly developed [27]. The APD has a new p-down inverted structure [28] to prevent undesirable edge breakdown and to suppress surface leakage current. A back-illuminated InAlAs/InGaAs APD based on this structure exhibited a 3-dB bandwidth of 27 GHz. On the other hand, the TIA was designed and fabricated by using 0.13-μm SiGe BiCMOS technology with a cut-off frequency (f_t) and maximum frequency (f_{max}) of 200 and 270 GHz, respectively. Both chips are DC coupled to enable burst-mode operation with a record of high sensitivity.

- **SPC:** The basic structure of the SPC used at the optoelectronic buffer resembles that of the SPC used at the LP, and operates based on the same discharge-or-hold scheme. But unlike the LP's SPC that is used in a single shot fashion every several 10's of nanoseconds when a new label comes in, each conversion channel of the buffer SPC is operated repeatedly every 640 ps, that is, 16 bits at 25 Gbps, until the whole packet is converted, and thus the implementation circuits are different. More details about the buffer's SPC can be found in [29].

- **PSC:** The parallel-to-serial converter (PSC) is an optoelectronic integrated circuit (OEIC) that resembles the SPC in consisting of several conversion channels attached to a common TL. The input to each channel of the PSC is a low speed electrical signal provided by the CMOS processor, whereas the TL carries the final device output which is the high-speed electrical pulses that form a packet part used in a following step to modulate a given wavelength. Each channel comprises a customized MSM-PD discharge-based circuit operated with an optical trigger pulse to produce a positive electrical pulse and a negative electrical output from the opposite sides of the MSM-PD. Both pulses are used to generate a non-return-to-zero (NRZ)-like output electrical pulse. More details about the buffer's PSC can be found in [30].

- **Tunable transmitter**: A fast tunable transmitter is realized by monolithically integrating an EAM section composed of InGaAlAs MQWs [31] and a PRR-based tunable laser (**Figure 8b**). The InGaAlAs MQWs allow for a steep extinction curve and large E/O frequency bandwidth [32], and hence can support operation at 25-Gbit/s with a sufficient extinction ratio and over a wide wavelength range. **Figure 12a** shows the NRZ eye diagram for a 25-Gbps pseudorandom bit stream (PRBS) of 2^{31}-1. A dynamic ER larger than 10 dB was achieved for wavelengths up to 1570 nm with DC bias levels ranging from -0.8 to -1.5 V, and with a constant voltage swing of 2.0 V maintained at all wavelengths (**Figure 12b**).

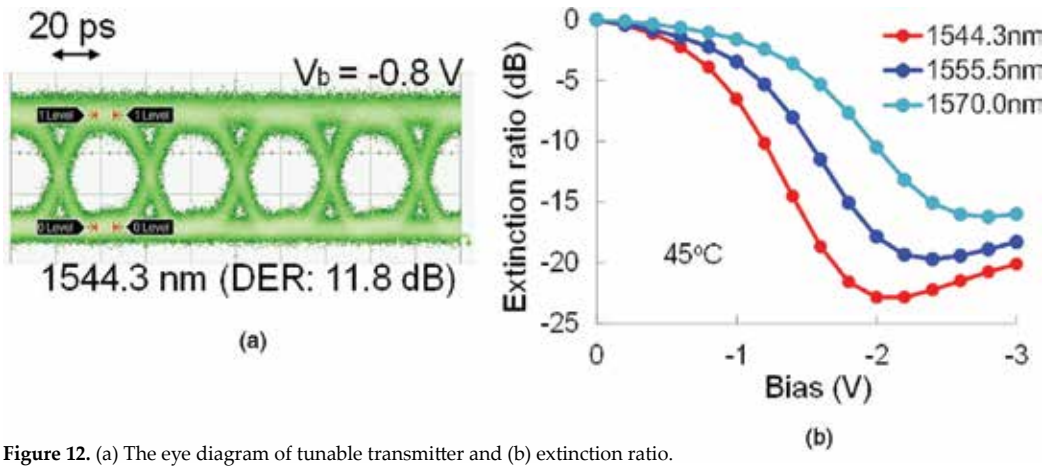

Figure 12. (a) The eye diagram of tunable transmitter and (b) extinction ratio.

7. Conclusion and outlook

In this chapter, we have reviewed our recent HOPR prototype developed to realize a new photonic intra DC network. The basic aspects of the network have been briefly introduced, followed by highlighting the enabling technologies of the new prototype. HOPR's role at the DC network has two folds as an optical-packet switch for forwarding high-speed burst-mode optical packets in a torus-topology network, and as an aggregation switch for handling the traffic of the DC servers. HOPR's operation relies on three functional units namely the label processor, optical switch, and shared buffer. HOPR is realized based on a hybrid implementation approach with an attempt to make optimal use of optics and electronic for enabling low power consumption and latency without sacrificing performance. The use of both all-optical and optoelectronic shared buffers shows the hybrid approach adopted at the subsystem level. The hybrid approach can also be seen at the device level where, for example, special optoelectronic devices are developed to efficiently interface preamble-free optical packets to electronic circuits with a novel optical clocking mechanism.

To meet the pressing demand for power reduction, HOPR is developed to have the power dissipation limited to incoming packet duration. The dissipation time has been even further reduced as, for example, in the label processor case where it occurs only during the short label duration. HOPR's latency is dominated by performing arbitration for resolving packet contention where a fast arbitration algorithm is demanded. On the other hand, to maintain a high-quality signal after multi-hop transmission, EDFAs and not SOAs are used for packet amplification, whereas other than amplification, the SOA attractive features of high-speed operation and compactness are employed for signal processing. New device packaging has been also considered as for instance in the label processor to enhance the responsivity of used photodetectors and to enable an easy lens-free and low-cost alignment.

OPS-based photonic DC networks provide a radical solution that can take data centers into new frontiers, and let them surpass their current difficulties caused by excessive electronic processing. Performing more node functions by combining optics/electronics is thus pivotal, and to enable that the demand for new innovative concepts and implementation strongly exists. HOPR's new prototype is a step toward fulfilling this objective which together with other community achievements reveals the high potential of this networking approach.

Acknowledgements

This work has been funded by the National Institute of Information and Communications Technology (NICT) R&D program Basic Technologies for High-Performance Hybrid Optoelectronic Router (2011–2016).

Author details

Salah Ibrahim* and Ryo Takahashi

*Address all correspondence to: ibrahim.salah@lab.ntt.co.jp

NTT Device Technology Laboratories, NTT Corporation, Kanagawa, Japan

References

[1] D.J. Richardson, J.M. Fini, and L.E. Nelson. Space division multiplexing in optical fibers. Nature Photonics 7: 353-362, 2013.

[2] Cisco visual networking index: forecast and methodology, 2013-2018. White paper c11-481360.pdf, 10 June 2014.

[3] M. AI-Fares, A. Loukissas, and A. Vahdat. A scalable, commodity data center network architecture. In Proceedings of the ACM SIGCOMM, USA, pp. 1-12, 2008.

[4] C. Kachris, K. Kanonakis, and T. Tomkos. Optical interconnection networks in data centers: recent trends and future challenges. IEEE Communications Magazine 51(9), pp. 39-45, 2013.

[5] K. Bernstein, R.K. Cavin, W. Porod, A. Seabaugh, and J. Welser. Device and architecture outlook for beyond CMOS switches. Proceedings of the IEEE 98(12), pp. 2169-2184, 2010.

[6] R. Takahashi, T. Segawa, S. Ibrahim, T. Nakahara, H. Ishikawa, A. Hiramatsu, Y-C. Huang, and K-I. Kitayama. Torus data center network with smart flow control enabled by hybrid optoelectronic routers. Journal of Optical Communications and Networking 7: B141–B152, 2015.

[7] Y-C. Huang, Y. Yoshida, S. Ibrahim, R. Takahashi, A. Hiramatsu, and K-I. Kitayama. Novel virtual OCS in OPS data center networks. Photonic Network Communications 31(3): 448-456, 2016.

[8] Y-C. Huang, Y. Yoshida, S. Ibrahim, R. Takahashi, A. Hiramatsu, and K-I. Kitayama. Bypassing route strategy for optical circuits in OPS-based data center networks. IEEE Photonics Journal 8(2): 1-10, 2016.

[9] W. Mellette, G. Schuster, G. Porter, G. Papen, and J. Ford, "A scalable, partially configurable optical switch for data center networks," J. Lightwave Tech., 35(2), pp. 136-144, Jan.15, 2017.

[10] S. J. Ben Yoo. Optical packet and burst switching technologies for the future photonic internet. Journal of Lightwave Technology 24, pp. 4468-4492, 2006.

[11] G. I. Papadimitriou, C. Papazoglou, and A. S. Pomportsis. Optical switching. Hoboken, NJ: Wiley-Interscience, 2006.

[12] M.-J. Kwack, T. Tanemura, A. Higo, and Y. Nakano. Monolithic InP strictly non-blocking 8×8 switch for high-speed WDM optical interconnection. Paper presented at the European Conference and Exhibition on Optical Communication, Amsterdam, The Netherlands, 2012, Paper Th.3.B.3.

[13] R. S. Tucker, P.-C. Ku, and C. J. Chang-Hasnian. "Slow-light optical buffers: capabilities and fundamental limitations," J. Lightwave Tech., 23(12), 2005.

[14] K. Nosaki, A. Shinya, S. Matsuo, Y. Suzaki, T. Segawa, T. Sato, Y. Kawaguchi, R. Takahashi, and M. Notomi. Ultralow power all-optical RAM based on nanocavities. Nature Photonics 6: 248-252, 2012.

[15] T. Zhang, K. Lu, and J. R. Jue. Shared fiber delay line buffers in asynchronous optical packet switches. IEEE Journal on Selected Areas in Communications 24(4): 118-127, 2006.

[16] S. Porto, C. Antony, A. Jain, D. Kelly, D. Carey, G. Talli, P. Ossieur, and P. D. Townsend, "Demonstration of 10 Gbit/s burst-mode transmission using a linear burst-mode receiver and burst-mode electronic equalization," J. Opt. Comm. and Net. 7(1), A118–A125 (2015).

[17] Roland E. Best. Phase locked loop: design, simulation and applications, 4th ed. New York: McGraw-Hill, 1999.

[18] R. Yu, R. Proietti, S. Yin, J. Kurumida, and S. J. Ben Yoo. "IO-Gb/s BM-CDR circuit with synchronous data output for optical networks," IEEE Photon. Technol. Lett., 25, pp. 508-511, 2013.

[19] N. Suzuki, K. Nakura, T. Suehiro, M. Nogami, S. Kosaki, and J. Nakagawa. Over-sampling based burst-mode CDR technology for high-speed TDM-PON systems. In Optical Fiber Communication Conference and Exposition (OFCINFOEC), 2011 and the National Fiber Optic Engineers Conference, Los Angeles, CA, 2011, pp. 1-3.

[20] A. Rylyakov, J. Proesel, S. Rylov, B. G. Lee, J. Bulzacchelli, A. Ardey, C. Schow, and M. Meghelli. A 25 Gb/s burst-mode receiver for low latency photonic switch network. IEEE Journal of Solid-State Circuits 50(12), pp. 3120-3132, 2015.

[21] S. Ibrahim, T. Nakahara, H. Ishikawa, and R. Takahashi. Burst-mode optical label processor with ultralow power consumption. Optics Express 24: 6985-6995, 2016.

[22] K. Takahata, R. Takahashi, T. Nakahara, H. Takenouchi, and H. Suzuki. 3.3 ps electrical pulse generation from discharge-based metal-semiconductor-metal photodetector. Electronics Letters 41(1): 38-40, 2005.

[23] H. Kim Jae, H. T. Griem, R. A. Friedman, E. Y. Chan, and S. Ray. High-performance back-illuminated InGaAs/InAlAs MSM photodetector with a record responsivity of 0.96 A/W. IEEE Photonics Technology Letters 4(11): 1241-1244, 1992.

[24] T. Segawa, S. Matsuo, T. Kakitsuka, T. Sato, Y. Kondo, and R. Takahashi. Semiconductor double-ring-resonator-coupled tunable laser for wavelength routing. IEEE Journal of Quantum Electronics 45(7): 892-899, 2009.

[25] Y. Muranaka, T. Segawa, Y. Ogiso, T. Fujii, and R. Takahashi. Performance improvement of an EAM-based broadcast-and-select optical switch module. In The Proceedings of the International Conference on Photonics in Switching (PS), Florence, 2015.

[26] T. Nakahara, and R. Takahashi. Self-stabilizing optical clock pulse-train generator using SOA and saturable absorber for asynchronous optical packet processing. Optics Express 21, pp. 10712-10719, 2013.

[27] M. Nada, M. Nakamura, and H. Matsuzaki. 25-Gbit/s burst-mode optical receiver using high-speed avalanche photodiode for 100-Gbit/s optical packet switching. Optics Express 22, pp. 443-449, 2014.

[28] M. Nada, Y. Muramoto, H. Yokoyama, N. Shigekawa, T. Ishibashi, and S. Kodama. Inverted InAlAs/InGaAs avalanche photodiode with low–high–low electric field profile. Japanese Journal of Applied Physics 51, p. 02BG03-1, 2012.

[29] S. Ibrahim, H. Ishikawa, T. Nakahara, and R. Takahashi. A novel optoelectronic serial-to-parallel converter for 25-Gbps burst-mode optical packets. Optics Express 22, pp. 157-165, 2014.

[30] H. Ishikawa, T. Nakahara, H. Sugiyama, and R. Takahashi. A parallel-to-serial converter based on a differentially-operated optically clocked transistor array. IEICE Electronics Express 10(20); pp. 20130709, 2013.

[31] T. Segawa, W. Kobayashi, T. Sato, S. Matsuo, R. Iga, and R. Takahashi. A flat-output widely tunable laser based on parallel-ring resonator integrated with electroabsorption modulator. Optics Express 20: B485-B492, 2012.

[32] W. Kobayashi, M. Arai, N. Fujiwara, T. Fujisawa, T. Tadokoro, K. Tsuzuki, Y. Kondo, and F. Kano. Design and fabrication of 10-/40-Gb/s, uncooled electroabsorption modulator integrated DFB laser with butt-joint structure. Journal of Lightwave Technology 28(1): 164-171, 2010.

Chapter 5

Research on the Characteristics of Silicon MOS-Like Light-Emitting Structure by Utilizing the Technology of Field-Induced Optical Radiation Mechanisms

Kaikai Xu

Additional information is available at the end of the chapter

http://dx.doi.org/10.5772/intechopen.68273

Abstract

As a well-known core material, silicon is becoming one of the most promising materials of photonic integration field. The chapter provides the research of integrated silicon MOS-like light-emitting structure utilizing the technology of field-induced optical radiation mechanisms. The silicon light-emitting device (Si-LED) plays an important role in realizing the on-chip optical interconnects, but Si-LED integrating on bulk silicon is facing many challenges due to the hybrid integration. In addition to be fully compatible with the standard complementary-metal-oxide-semiconductor (CMOS) process technology, the Si-LED also avoids the challenges that are mentioned above through integrating with bulk silicon substrate monolithically.

Keywords: light emitting device, optical radiation mechanism

1. Introduction

Silicon is the material par excellence. It is the most widely studied material in the history of civilization. In fact, the present-day information age has dawned with an electronics revolution brought about by the maturity of silicon-based microelectronics. The growth of the silicon industry follows the no-famous Moore's law, which states that the number of transistors in an integrated circuit chip doubles every 18 months. However, during the last decade there has been an indication of the decline of Moore's law. There are doubts whether in future silicon-based integrated circuits (ICs) will deliver the same advantages and increased functionalities over time as in the past.

The p-n junction is the vital component of most semiconductor devices. In this chapter, the concept of a light-emitting p-n junction is developed and characterized. Many studies in the past have correlated breakdown occurring in silicon p-n junctions with impact ionization and with material and structure parameters, especially some radiative recombination occurs while electron-hole pairs are produced during avalanche breakdown. Both the electrons and the holes can be heated by the electric field. The radiative transition between hot carriers emits photons larger than the energy gap. Hence, the luminescence during avalanche breakdown is characterized by a broad emission spectrum that extends to the energy of ∼3.36 eV (i.e., with the shortest wavelength of ∼369.05 nm), which represents the energy separating the hottest electron from the hottest hole. It is noted that ∼3.36 eV is equal to $3E_g$ and the energy for impact ionization by a hot carrier is about $1.5E_g$. Substantial progress has been made in the field of silicon p-n junctions emitting visible light when operating in reverse-avalanche mode. The silicon-based light-emitting device (Si-LED), which is actually a simple p-n junction that is fully compatible with standard complementary-metal-oxide-semiconductor (CMOS) technology, is a potential light source that can monolithically be integrated with the silicon dioxide waveguide, photo-detector, and receiver circuit on a single silicon chip. The widespread use of SOI for PMIC and RF applications has added to the potential applications of Si-LEDs.

The weakest point of silicon is that proper light emitters and modulators cannot be realized due to its indirect bandgap. On the other hand, there is a steady advance in the field of photonics. Although discrete devices using the compound semiconductor materials and their alloys show very good performance, the levels of integration and performance are far below what has already been achieved in electronic integration on the same substrate. It is natural to expect that OEIC will provide the same advantages, that is, low cost due to batch fabrication, high functionality, scaling for denser integration, and so on, as provided by silicon ICs. Instead, if OEIC could grow on silicon and integrate with electronic ICs by using the same production facilities, the benefits to be accrued need no further elaboration. Si-based systems will then be used in all fields of electronics, computers, and communication. Therefore, Si-based photonics remains an active area of research and over the last 10–15 years some significant milestones have been achieved [1].

Another important area of application of silicon photonics is in very large-scale integrated (VLSI) circuits. The complexity of present-day ICs has reached a high level on different levels shown in **Figure 1**. The metallic interconnects, mainly Cu, produce delay due to resistor-capacitor (RC) time constants, which far exceed the transit time delay associated with the individual transistors. If the increase in speed is to be maintained at the same rate for the next-generation ICs, the interconnect bottleneck must be properly addressed. Optics is believed to be the right solution for the problem [2].

In the present chapter, the authors give an overview of the recent developments and the present status in silicon optoelectronics. A short history of the development of silicon-based light sources is given in Section 2. Next, Section 3 is devoted to point out why the Bremsstrahlung model is definitely not adequate to describe the radiative relaxation of hot carriers in reverse-biased silicon p-n junctions; other radiative processes, such as spontaneous radiative relaxation of electrons between states in two conduction bands, is suggested to be most likely

http://dx.doi.org/10.5772/intechopen.68273

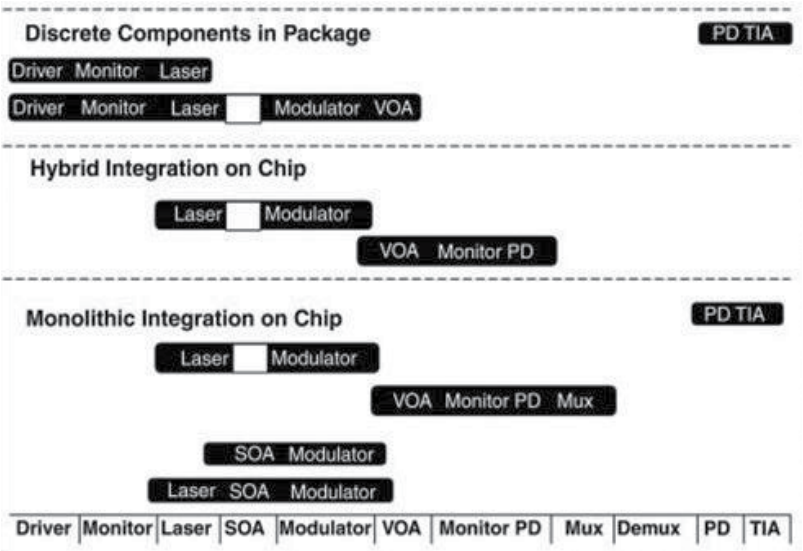

Figure 1. Level of device integration in commercially available product (After Ref. [3]).

responsible for the hot-carrier-induced luminescence. For the purpose of high-speed performance in electro-optic modulation, the high-frequency modulator optical response and data transmission are reviewed in Section 4. Finally, Section 5 concludes that the silicon light-emitting device with high-speed data transmission capability will be one of the key building blocks for the integrated silicon photonic chip for next-generation communication networks as well as future high-performance computing applications for optical interconnections.

2. Two- and multi-terminal CMOS/BiCMOS silicon LEDs

Silicon photonics has become one of the most promising photonics integration platforms in the last decade. This is mainly due to the combination of a very high index contrast and the availability of silicon CMOS fabrication technology, which allows the use of electronics fabrication facilities to make photonic circuitry. Unfortunately, the indirect bandgap of silicon leads to low efficiency. The rate of electron-hole recombination in silicon material is too low to produce emitted photons in forward-biased silicon p-n junctions, but light emission observed from reverse-biased silicon p-n junctions under avalanche breakdown was reported in 1955 by Newman [4]. The photograph of a silicon p-n junction being biased in the reverse direction at breakdown emits a yellowish light in the junction region as shown in **Figure 2**.

Next, Kramer et al. demonstrates that light-emitting devices can be integrated using industrial CMOS technology and operated at CMOS voltage level [5]. The reverse-biased p-n junction is capable of broad-band visible-light emission between 450 and 800 nm in the avalanche breakdown region under reverse bias with efficiency of the order of 10^{-8}. The spectral output of a $p^{+}n^{-}$ junction operated in avalanche breakdown is given in **Figure 3**.

Figure 2. A photograph of the light emitted from a worked silicon p-n junction unit operating in the breakdown region. The junction is the horizontal bow-shaped curve. Current flows vertically across it (After Ref. [4]).

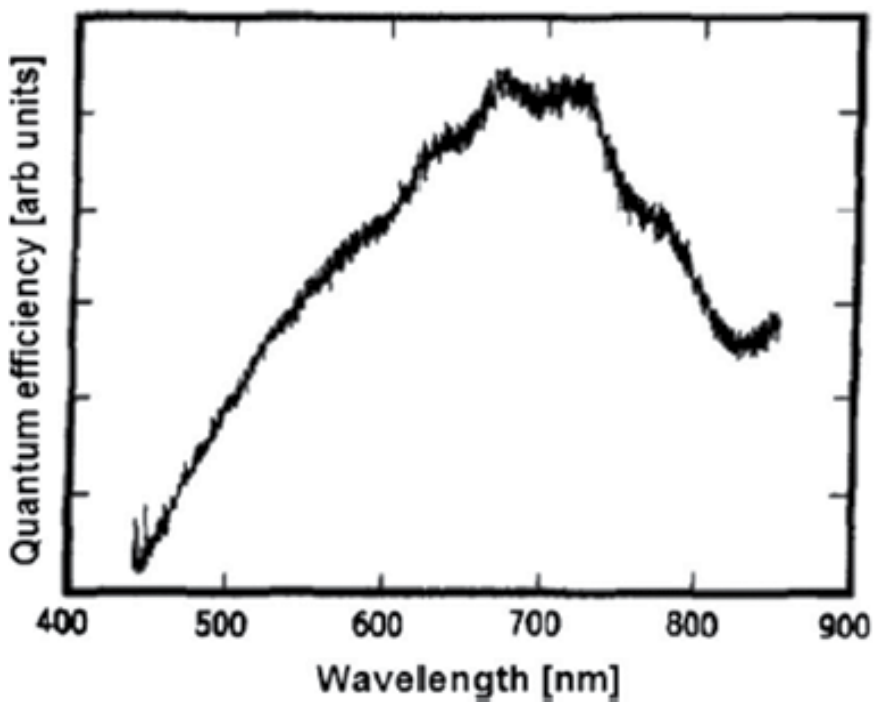

Figure 3. Emission spectrum of the silicon p^+n^- junction in the avalanche breakdown regime; typical reverse voltage is 33.2 V at reverse current of 25 mA, peak wavelength occurs at 700 nm, electric-to-optical power conversion efficiency is 1.1×10^{-9}, and quantum efficiency is 2.0×10^{-8} (After Ref. [5]).

Reference [6] shows a planar n^+p shallow-junction structure that is fabricated using a standard 1.2-μm CMOS process with no adaptations of the process at all. Excellent uniformity has been

obtained for large area devices. Furthermore, it is demonstrated that the light levels and intensity levels generated from the devices are indeed useful for on-chip electro-optical coupling and for chip-to-environment electro-optical coupling.

In addition to the study of silicon diode LED in which the light emission is due to the avalanche breakdown of the silicon p-n junction, a novel gate-controlled diode MOS-like multi-terminal device is described where both the light intensity and spatial light pattern of the device are controlled by an insulated MOS gate voltage.

Indeed, a metal-oxide-semiconductor field-effect transistor (MOSFET) consists of two identical gate-controlled diodes (i.e., "p^+ Source/Drain to n-Substrate," in a PMOSFET device) [7]. Since source and drain are grounded (i.e., $V_d = V_s = 0$ V), the reverse bias of the two p-n junctions is defined by the substrate voltage V_{sub} which is a fixed value. By changing the gate voltage V_g, the channel layer in the PMOSFET device can be categorized by the following three types:

a. *Inversion layer*

The gate voltage V_g varies while the substrate voltage V_{sub} is fixed. As shown in **Figure 4(a)**, the channel layer is a p-type inversion layer if $V_g < V_{sub}$. In addition, the concentration of the surface channel layer decreases with the increase in V_g.

b. *Depletion layer*

If the gate voltage V_g is high enough to be approximately equal to the substrate voltage V_{sub}, the p-type inversion layer will disappear in the channel and be replaced by the n-type substrate. As shown in **Figure 4(b)**, the depletion width of channel surface should be comparable to the depletion width of the "p^+ Source/Drain to n-Substrate" junction diode.

c. *Accumulation layer*

If $V_g > V_{sub} > 0$, electrons will move toward the channel surface. The greater V_{gsub} (i.e., $V_g - V_{sub}$) is, the stronger an n^+ accumulation layer will be generated near the surface channel. It is well known that the concentration of the layer is exponentially monotonic with a maximum at the channel's surface and a minimum that is equal to the substrate concentration at the bottom of the channel layer. The depletion width has the minimum at point B in **Figure 4(c)** and the maximal depletion width equals the depletion width of the "p^+ Source/Drain to n-Substrate" junction, which is point A in **Figure 4(c)**. **Figure 4(d)** provides more characterizations referring to point B, which actually is the transition between the p^+ Source/Drain region and the channel layer underneath the gate. If $V_g = V_{sub}$, depletion width is unchanged as to be Xd (i.e., the depletion width of "p^+ Source/Drain to n-Substrate" junction in thermal equilibrium). If $V_g > V_{sub}$, the depletion width at the transition will decrease from Xd to $x2$ because of the accumulation layer (n-type) with a thickness 2. If $V_g >> V_{sub}$, the depletion width at the joint will continue to decrease from $x2$ to $x1$ and the thickness of accumulation layer will increase to thickness 1. Furthermore, $x1 < x2$ means that gate voltage V_g is proportional to the concentration of the surface channel.

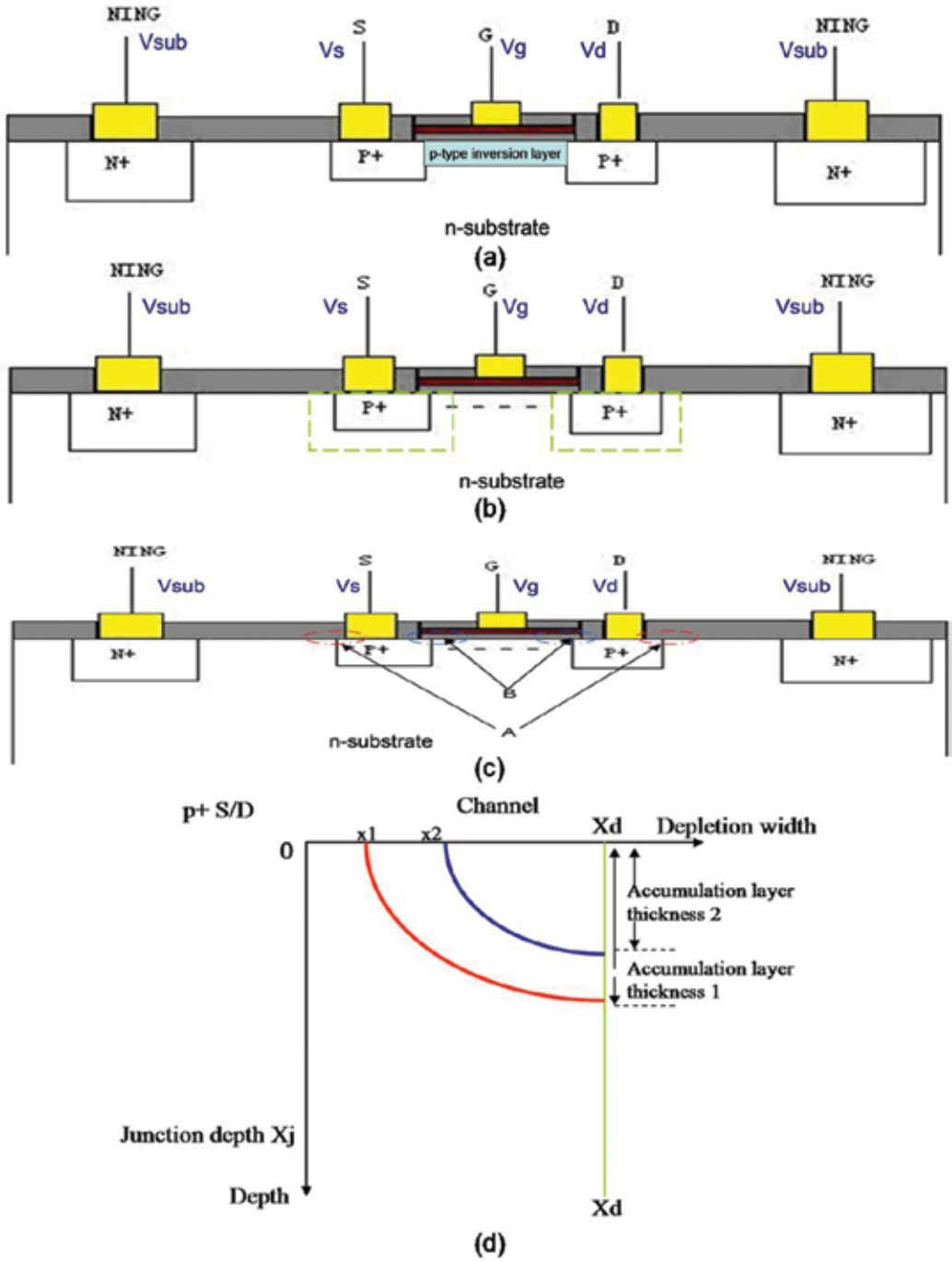

Figure 4. The characterization of the channel layer: (a) inversion, (b) depletion, (c) accumulation, and (d) depletion region width near the channel surface.

Indeed, in the accumulation layer, the thickness is just a few tens of nanometers. For the MOS structure in the accumulation mode, the relationship between the gate voltage and the accumulation layer's concentration and thickness is analyzed in the subsequent text. A derivation of the accumulation layer thickness as a function of substrate-doping concentration will show that the layer is very small and hence can be considered as a surface charge. The distribution of the charge as a function of depth, x, can be found using Poisson's equation [8]

$$\frac{d^2\Phi(x)}{dx^2} = -\frac{\rho}{\varepsilon_{si}} = -\frac{q}{\varepsilon_{si}}(p - n + N_d - N_a) \tag{1}$$

with

$$p(x) = p_{p0}\exp\left(-\frac{q\Phi(x)}{kT}\right) = N_a\exp\left(-\frac{q\Phi(x)}{kT}\right) \tag{2}$$

and

$$n(x) = n_{p0}\exp\left(\frac{q\Phi(x)}{kT}\right) = \frac{n_i^2}{N_a}\exp\left(\frac{q\Phi(x)}{kT}\right) \tag{3}$$

where p_{p0} is the equilibrium hole concentration in the p-type material, n_{p0} is the equilibrium electron concentration in the same material, and $\Phi(x)$ is the potential in the silicon as a function of depth. Far from the surface of the silicon, the potential is equal to zero: $\Phi(x \to \infty) = 0$, which will be used as a boundary condition for Eq. (1).

In the hole accumulation layer formed in p-type substrate shown in **Figure 4(c)**, one can assume that $n \ll p$ and $N_d \ll N_a$, thus Eq. (1) can be rewritten as

$$\frac{d^2\Phi(x)}{dx^2} = -\frac{\rho}{\varepsilon_{si}} = -\frac{q}{\varepsilon_{si}}N_a\left[\exp\left(-\frac{q\Phi(x)}{kT}\right) - 1\right] \tag{4}$$

where ε_{si} is the permittivity of silicon. From a numerical calculation, it is finally found that the thickness of the accumulation layer, x_{acc}, can be found using the condition that $\Phi(x = x_{acc}) = 0$:

$$x_{acc} = \sqrt{2}L_D\cos^{-1}\left(\exp\left(\frac{q\Phi_s}{2kT}\right)\right) \tag{5}$$

The thickness of the accumulation layer, x_{acc}, can thus vary between 0 and $\frac{\sqrt{2}}{2}\pi L_D$, depending on the accumulation charge.

The result is also drawn in **Figure 5**. Since the carrier (*hole*) concentration is an exponential function of the potential, the charge density increases very rapidly close to the surface and most of the accumulation charge is concentrated within a depth much smaller than x_{acc} as shown in **Figure 6**. Hence, the charge in the accumulation layer can be considered as a surface charge.

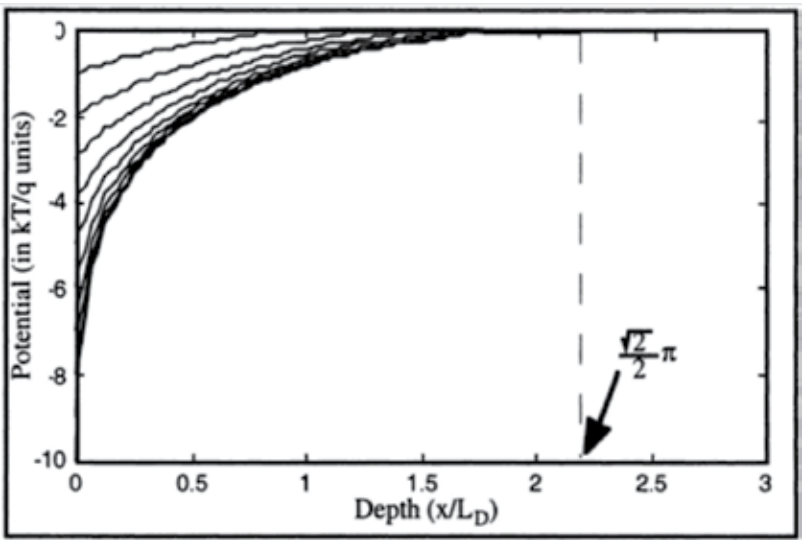

Figure 5. Potential (normalized to kT/q) in an accumulation layer (holes in p-type silicon) as a function of depth (normalized to L_D) for different values of surface potential (After Ref. [8]).

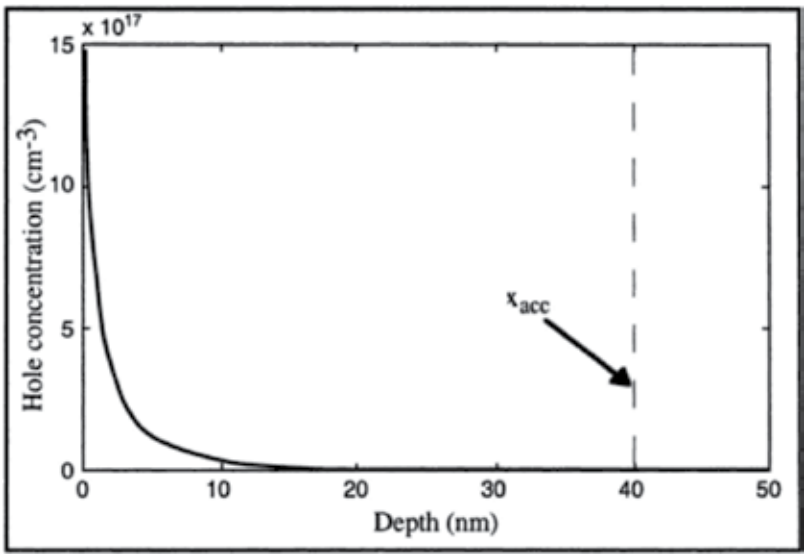

Figure 6. Hole concentration profile in an accumulation layer. The substrate-doping concentration, N_a, is equal to 10^{16} cm^{-3} and the surface potential, Φ_s, is equal to $-5kT/q$ (After Ref. [8]).

Due to the increase in the concentration of accumulation layer and the decrease in the depletion width near the surface channel, the breakdown voltage BV of the "p^+ Source/Drain to n-Substrate" junction decreases with the increase in gate voltage V_g. Moreover, if the accumulation layer is approximately treated to consist of numerous n-type thin layers that are individually with their own concentrations, the PMOSFET being in the operating condition mentioned above is a combination of Zener breakdown p-n junctions and avalanche breakdown p-n junctions.

As shown in **Figure 7**, it is shown that the breakdown voltage BV of a p^+n junction (i.e., the "p^+ Source/Drain to n-Substrate" junction in a PMOSFET device) decreases with the increasing gate voltage V_g.

On the other hand, the mixture of Zener breakdown and avalanche breakdown (i.e., a transition from avalanche to tunneling) could be the major reason for the reduction in BV of the two parallel-connected p-n junctions (i.e., the "p^+ Source/Drain to n-Substrate" junction shown in **Figure 4**) because it is known that the Zener breakdown voltage is usually much lower than the avalanche breakdown voltage. More specifically, at large positive gate voltages, a strong accumulation layer occurs and the surface electron concentration shields the electric field within the peripheral junction depletion region from the gate, reducing the effect of the gate voltage on avalanche breakdown in the "p^+ Source/Drain to n-Substrate" junction of the PMOSFET device [10].

As discussed previously, a higher gate voltage V_g can induce the lower breakdown voltage BV of the two p-n junctions (i.e., the "p^+ Source/Drain to n-Substrate" junction in the PMOSFET device). Next, the reverse current I_{sub} flowing through the p-n junctions with breakdown mechanisms will increase with gate voltage V_g while the substrate voltage V_{sub} (i.e., the reverse bias of the two p-n junctions) is a fixed value [11]. Since the optical emission power is linear with the reverse current I_{sub} [12], increasing the gate voltage V_g is a significant method to realize electro-optic modulation in the three-terminal gate-controlled diode Si-PMOSFET device [13–15].

It is noted that the Si-diode LED (i.e., the p-n junction is reverse-biased to avalanche breakdown) is a two-terminal device and the Si gate-controlled-diode LED (i.e., the reverse-biased p-n junction with varying the gate voltage) is a three-terminal device. In particular, a silicon light-emitting device with the structure of a Si-PMOSFET device that is fully compatible with the standard Si-CMOS process technology experimentally demonstrates that the reverse current I_{sub}

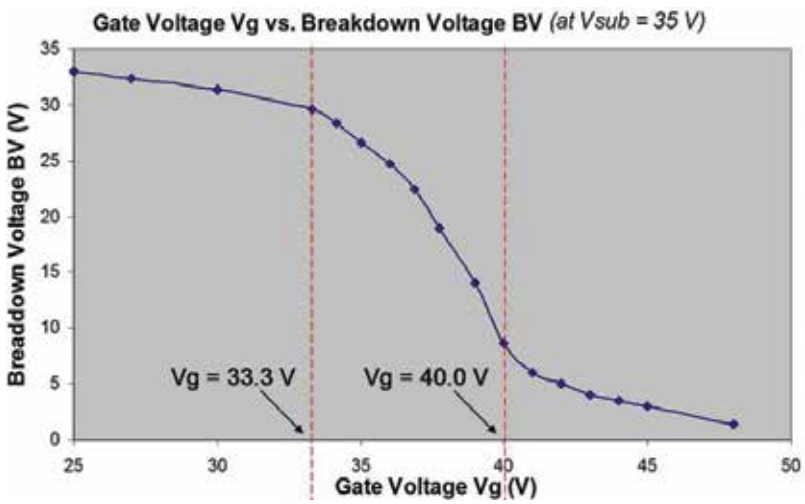

Figure 7. The high-voltage extreme for BV saturation occurs if V_g is being lower than ~33.3 V (i.e., the turn-on voltage), the low-voltage extreme for BV saturation occurs if V_g is being higher than ~40 V, V_g is almost linear (with a symbol of -) with BV in the intermediate range 33.3 V < V_g < 40 V, and BV tends toward 38 V if V_g is approaching 0 V (After Ref. [9]).

is always linearly proportional to optical emission power whether the Si-PMOSFET device acts as a two-terminal device (i.e., p-n junction diode, the "p^+ Source/Drain to n-Substrate" junction with floating the gate, Si-diode LED) or acts as a three-terminal device (i.e., gate-controlled diode, the "p^+ Source/Drain to n-Substrate" junction in the course of varying the gate voltage, Si gate-controlled diode LED). The optical power measured from the device is divided by the photon energy to obtain the number of collected photons, and then the external quantum efficiency is defined as the ratio of the number of collected photons to the number of injected electrons. Such linearity implies that the control of the increasing current is a significant way to enhance the quantum efficiency of this light source device no matter what the physical structure (i.e., two or three terminals) of the device is.

For the first time, it has been discovered that, at the same reverse current, the optical output power in the gated diode structure is higher than the optical output power in diode structure. In other words, for this PMOSFET-like device, the three-terminal operating mode (i.e., Si gate-controlled-diode LED) is more efficient than the two-terminal operating mode [12].

Furthermore, the Si gate-controlled-diode LED can be treated as an efficient low-voltage optical source. It is observed that both the quantum efficiency and electrical-optical power conversion efficiency increase obviously though the reverse current I_{sub} is much lower because of the reduction in reverse-bias voltage V_{sub}. Such a phenomenon may be explained by the absorption coefficient of silicon at different wavelengths and is suggested to be a practical approach to realizing emission efficiency enhancement in near future [11].

3. Characterization of the optical properties

Assuming that the classic Bremsstrahlung model is approximately applicable, the origin of optical radiation observed in the reverse-biased silicon p-n junction could be explained by the Coulomb interaction between impact ionized carriers and charged centers in the depletion region. The charged center, also known as quantum dot, is an artificial atom in fact even if it has a mass that is approximately equal to one atom. Besides the properties of atoms such as having discrete energy levels and shell structure, the artificial atom, quantum dot, including tenability and comparability of level spacing, Coulomb scattering, and thermal energy are more advanced than the natural atom by allowing transport measurement [16].

Since the number of carriers is proportional to the number of emitted photons, the number of light spots increases with the reverse current rather than individual spots growing brighter. It is concluded that the avalanching current is carried through the junction by these localized emitting spots (i.e., quantum dots). Despite a great deal of theoretical and experimental work to clarify the mechanism of the strong visible luminescence from reverse-biased silicon p-n junctions, it still remains unclear because of this complication. Overall, the major mechanism is drawn in **Figure 8** and can be interpreted by the three different transitional processes below:

http://dx.doi.org/10.5772/intechopen.68273

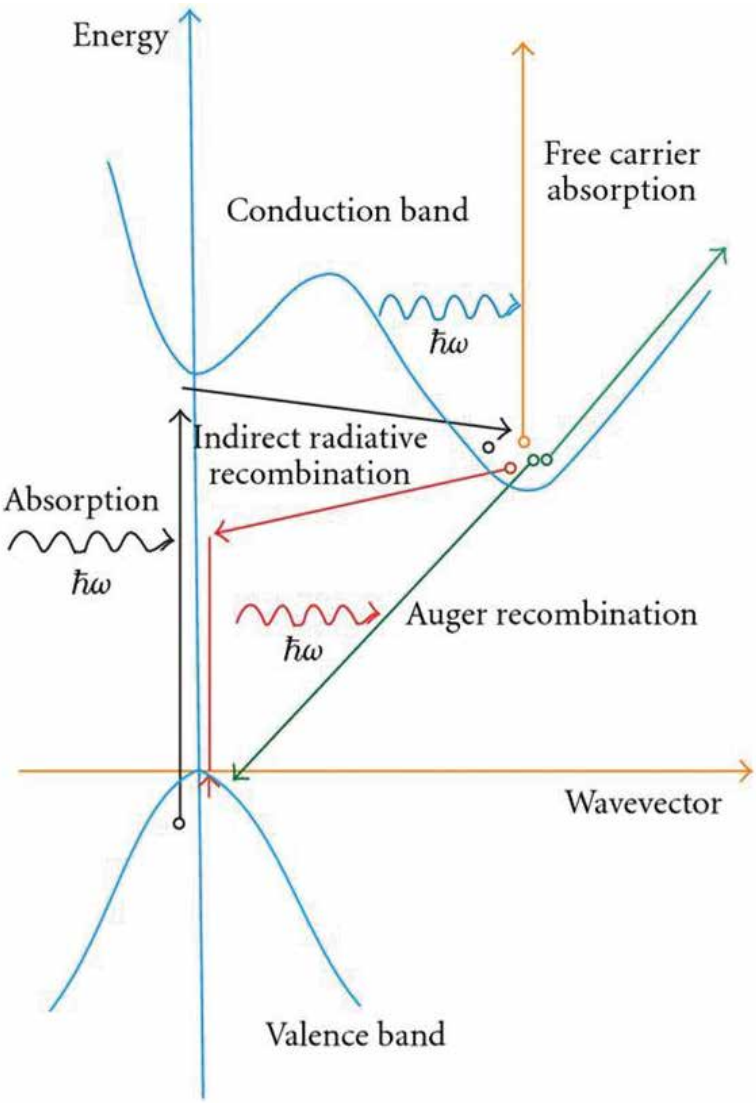

Figure 8. Band structure of bulk Si with the various possible transitions for an electron-hole pair: radiative recombination, Auger recombination, and free-carrier absorption (After Ref. [17]).

a. *Intra-band direct transition*

Most hot carriers do not find suitable transition partners with the same vector in *k*-space for photon radiation transition. As a substitute, phonon radiation is the most possible result for getting back to a low-energy state. The output light power per unit optical frequency is expressed as

$$I(v)_{Intraband} = C_1(h\nu)^{3.5\frac{1-3/\alpha}{2+3/\alpha}} \exp\left[-b(1.41h\nu - E_0)\right] \tag{6}$$

where C_1 is a constant, b is the function of mean-free path, E_0 is the threshold energy for ionization, and α is a positive value that is related to the electric field and mean-free paths of ionized electrons and emitted photons [18].

b. *Intra-band indirect transition*

This transition only occurs by the intervention of phonon assistance, in which phonons are radiated mostly by intra-band direct transition. Since the transition is the well-known Bremsstrahlung radiation (i.e., the scattering of an electron by an external field, accompanied by the emission of a photon), the output light power per unit optical frequency can be written as

$$I(\nu)_{Bremsstrahlung} = C_2 \exp\left(\frac{h\nu}{kT_e}\right) \tag{7}$$

where C_2 is a constant, k is the Boltzmann's constant, and T_e is the effective temperature [19]. The optical radiation is induced by the inelastic collision (i.e., inelastic X-ray scattering) between carriers (e.g., electron and hole) and charged centers (e.g., artificial atom). The probability of finding a carrier in state E_B is

$$P(E_B) = \frac{\exp(-\beta E_n)}{\sum_n \exp(-\beta E_n)} \tag{8}$$

which is known as canonical or Maxwell-Boltzmann distribution. Assuming the electric and magnetic fields each represents one degree of freedom, the average energy β will be equal to kT_e.

c. *Inter-band transition*

Under most situations, inter-band composition is the most effective process of photon emission. It must satisfy many conditions, such as same vector in k-space and direct transition of hot carriers. Commonly, the transverse momentum of a wave vector is written as

$$k(\varsigma) = \sqrt{\frac{2m_e}{\hbar}(PE - E_e)} \tag{9}$$

where ς is the distance from the electron energy to the center of the band, m_e is the effective mass of electron, PE is the potential energy of the Si-SiO_2 barrier, and E_e is the energy of incoming electron. Further, the detailed form of $PE - E_e$ is given by

$$PE - E_e = \frac{(0.5E_g)^2 - (qE_y\varsigma)^2}{E_g} \tag{10}$$

where E_g is the bandgap energy of silicon and E_y is a vertical field induced by the gate-to-source/drain voltage drop.

http://dx.doi.org/10.5772/intechopen.68273

It should be mentioned that silicon is a material with indirect bandgap. For indirect gap materials, the wave vector dependence is essential in order to get a sharp peak in the emission spectrum of exciton molecules [20]. Accordingly, the output light power per unit optical frequency can be written as [21]

$$I(v)_{Interband} = I(v)_{Emission} - I(v)_{Absorption} \tag{11}$$

Correspondingly, the electroluminescence spectra captured from the Si-PMOSFET device operating as Si gate-controlled-diode LED by the optical spectrometer is given in **Figure 9**. There is a distinct emission peak at 625 nm in the emitting wavelength range of 400–900 nm, and the light intensity increases with the gate voltage V_g. No obvious phenomenon of spectral shifting is observed with different operating voltages and currents.

Figielsky and Torun [22] proposed the intra-band transition, specifically Bremsstrahlung of hot tcarriers at charge centers. Chynoweth and McKay [23] explains emission with wavelength longer than 539 nm using intra-band transitions. Wolff [24] proposed intra-band hole transition near $k = 0$ to explain low-energy spectra, but cannot fit the emitting wavelength longer than 620 nm. It is concluded tha

- Photons with emitting wavelength longer than 620 nm are attributed to indirect inter-band process in high-field carrier populations.
- Bremsstrahlung radiation appears to dominate at intermediate range of 539–620 nm.
- The mechanism can be treated as near-direct inter-band transition for emitting wavelength shorter than 539 nm.

The phenomenon of and the physical mechanisms for the generation of minority carriers in the Si-MOSFET are also studied, since carrier transport in submicron silicon CMOS MOSFET

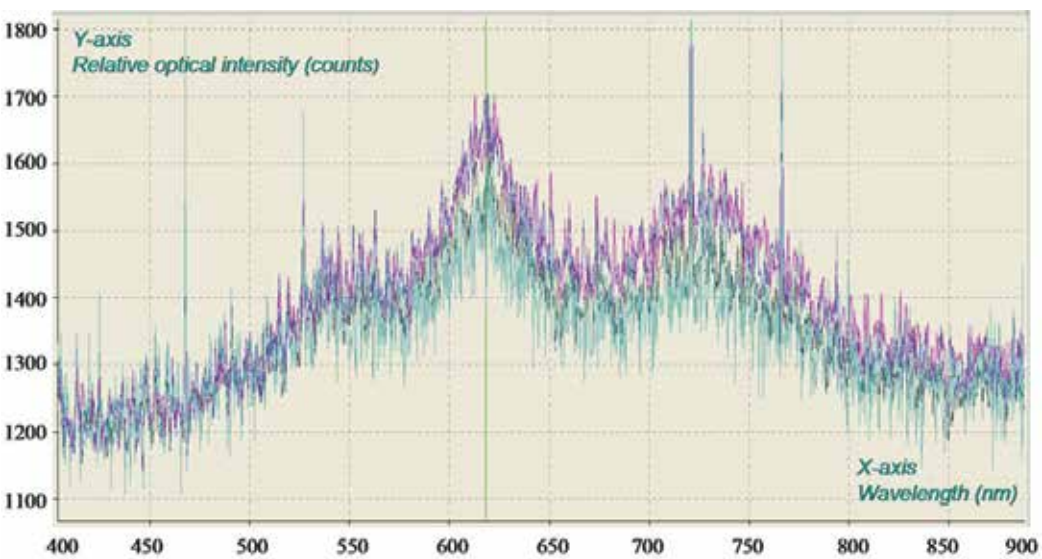

Figure 9. Output electroluminescence spectra.

demonstrates strong hot-carrier effects. A reverse-biased p-n junction is shown at a fixed separation for a MOSFET biased in the saturation region; because this p-n junction is reverse-biased, it acts as a collector of minority carriers in the substrate [25]. In Ref. [26], the spectral characteristics of the emitted photons from n-channel MOSFETs biased into saturation were investigated directly using photon emission spectroscopy; the correlation between the substrate current of the bias voltages, channel current, and channel length were presented; theoretical calculation of the photon emission intensity based on the Bremsstrahlung radiation mechanism does not agree well with the experimental measurements when the variation of the channel electric field with bias was accounted for; this suggests that Bremsstrahlung radiation of hot electrons in the Coulomb-scattering field of the dopant atoms is unlikely to be the dominant mechanism of photon emission in n-channel MOSFETs; other mechanisms such as direct and phonon-assisted conduction-to-conduction band transitions have to be considered to explain the hot-carrier-induced photon emission mechanism.

4. Analysis of modulation speed in the reverse-biased silicon p-n junction-based LED

As a centrosymmetric material, silicon has no electro-optic effect. The only way to achieve a modulator is to use the free-carrier effect where the free-carrier concentration is controlled in a p-n junction by injection, accumulation, or depletion. Demonstrations of high-speed modulation in free-carrier-depleted silicon-based modulators have been made theoretically [27] and experimentally [28, 29]. A four-terminal p^+pnn^+ vertical modulator integrated into a SOI rib waveguide, based on carrier depletion in a *p-n* junction formed in one arm of a Mach-Zehnder interferometer, was proposed in 2005. Based on a similar design, Intel in 2007 developed a high-speed and high-scalable optical modulator based on depletion of carrier in a vertical p-n junction diode showing data transmission up to 30 Gbit/s at 1550 nm [28]. Pinguet et al. [30] realized a lateral modulator either with *pn* or with *pipin* structure both achieving about 10-GHz roll-off frequency and insertion losses of 3 and 5 dB, respectively. Due to the low refractive effects, these modulators have to be mm-long. In order to reduce the device dimensions of optical resonators, a compact device using a ring resonator with a diameter of 10 μm was reported in Ref. [31].

The modulation speed of the silicon p-n junction can be categorized by the following two types: (a) the forward-biased operation of p-n junctions for light emission is a slow, inefficient, and unreliable process because of the indirect band structure of silicon; (b) the reverse-biased operation of p-n junctions for light emission is a fast process in which the limiting speed of light modulation is determined by the transit time of the minority carriers across the junction during the filament of breakdown currents.

In particular, light modulation at 20 GHz is reported for the first time for a reverse-biased p-n junction operating in avalanche breakdown mode [32]. The light modulation at such a high speed rules out any possibility of phonon-assisted indirect transitions, but implies the existence of intra-band transitions of hot carriers. Furthermore, gigahertz range modulation can be

explained through intra-band transition of avalanche-generated hot carriers, which have broad energy distribution explaining the broadband light emission of 430–800 nm [33].

In contrast to reverse-biased p-n junction-based Si-diode LED in which the modulation speed is limited by the minority carrier's lifetime, the modulation speed of Si gate-controlled-diode LED is limited by the discharge time of the metal-oxide-semiconductor (MOS) capacitor instead of the natural carrier lifetime. Carrier confinement occurs in the band-bending region near the silicon surface, and the MOS capacitor discharge time can presumably be controlled via the RC time constant or other effects in the circuit. The Si gate-controlled-diode LED operates on the principle of the MOS capacitor and not on the abovementioned standard p-n junction diode [34].

It is important to note that a Si-PMOSFET device is able to work as two identical gate-controlled diodes (i.e., the "p^+ Source/Drain to n-Substrate" junctions with varying gate voltage V_g) [15] or as two p-n junction diodes (i.e., the "p^+ Source/Drain to n-Substrate" junctions with floating gate terminal) [35]. Accordingly, the electro-optic modulation schematics for both the two-terminal Si-diode LED and the three-terminal Si gate-controlled-diode LED are presented in Ref. [36].

Snyman et al. [37] further discusses the speed of Si-diode LED. With the dynamic on-resistance of the p-n junction in avalanche in the tens of kilo-ohms range and the reverse-biased junction capacitance in the range of fF, the RC time constant will be in the range of tens of psec. This will be sufficient to produce modulation in excess of 10 GHz. For the speed of Si gate-controlled-diode LED, the intrinsic modulation speed could be as high as a few hundred GHz [36, 37]. Furthermore, it shows the expected Si gate-controlled-diode LED modulation frequency range as a result of parasitic capacitances in the MOSFET device for a given biasing condition; these derivations verify that the modulation speed is about a few hundred GHz, and a new model is proposed to further predict the modulation speed at a chosen DC-biasing condition [38].

Gardes et al. [39] proposed a ring-resonator modulator which is based on the carrier depletion in a reverse-biased p-n junction and is formed on a 300 nm wide, 150 nm etch depth, and 200 nm high-rib waveguide. A linearly polarized light beam emitted from a tunable laser with emitting wavelength range of 1520–1620 nm was coupled into the waveguide using a polarization-maintaining lensed fiber, and then the output light was collected by an objective and focused on an IR detector. Regarding the transient analysis, the frequency response of the MOS-structure-based electro-optical modulator was measured using an AC signal generated by an opto-RF vector network analyzer. As presented in **Figure 10**, the RF signal was coupled to the ring resonator using ground-signal-ground electrodes, and the modulated optical signal was then coupled back to the opto-RF vector network analyzer. As a candidate for highly compact, wide bandwidth modulator, the device could exhibit an electrical small signal bandwidth of 19 GHz shown in **Figure 11**.

In addition, a comparison between the Si-diode LED and Si gate-controlled-diode LED in the field of phase modulation can be obtained from the modulation curves shown in **Figures 12** and **13**. For the case of two-terminal Si-diode LED, the depletion width of the reverse-biased p-n junction depends on the bias voltage and doping concentration: the charge density change

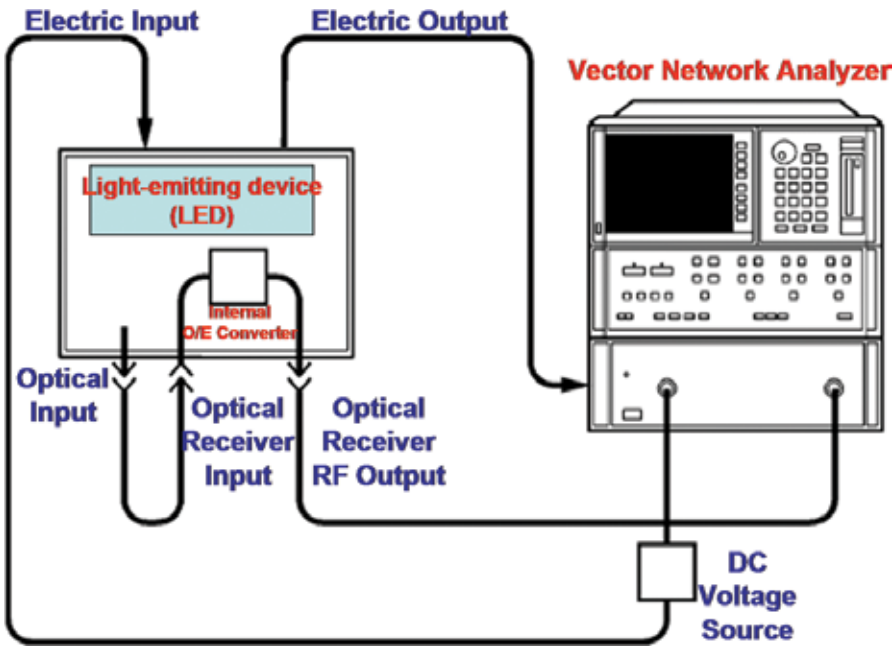

Figure 10. Schematics for the transient measurement.

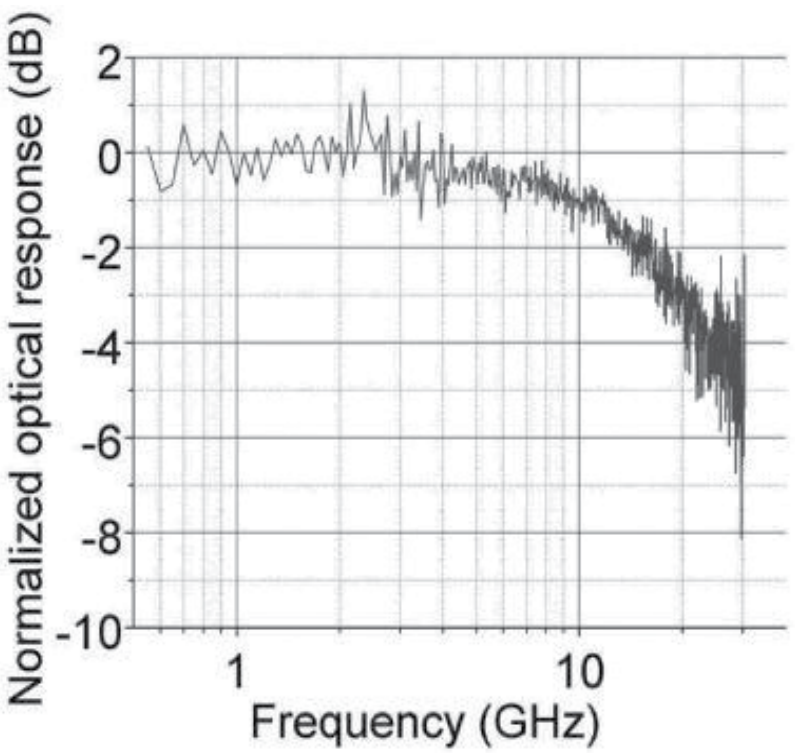

Figure 11. Normalized optical response as a function of frequency (After Ref. [40]).

http://dx.doi.org/10.5772/intechopen.68273

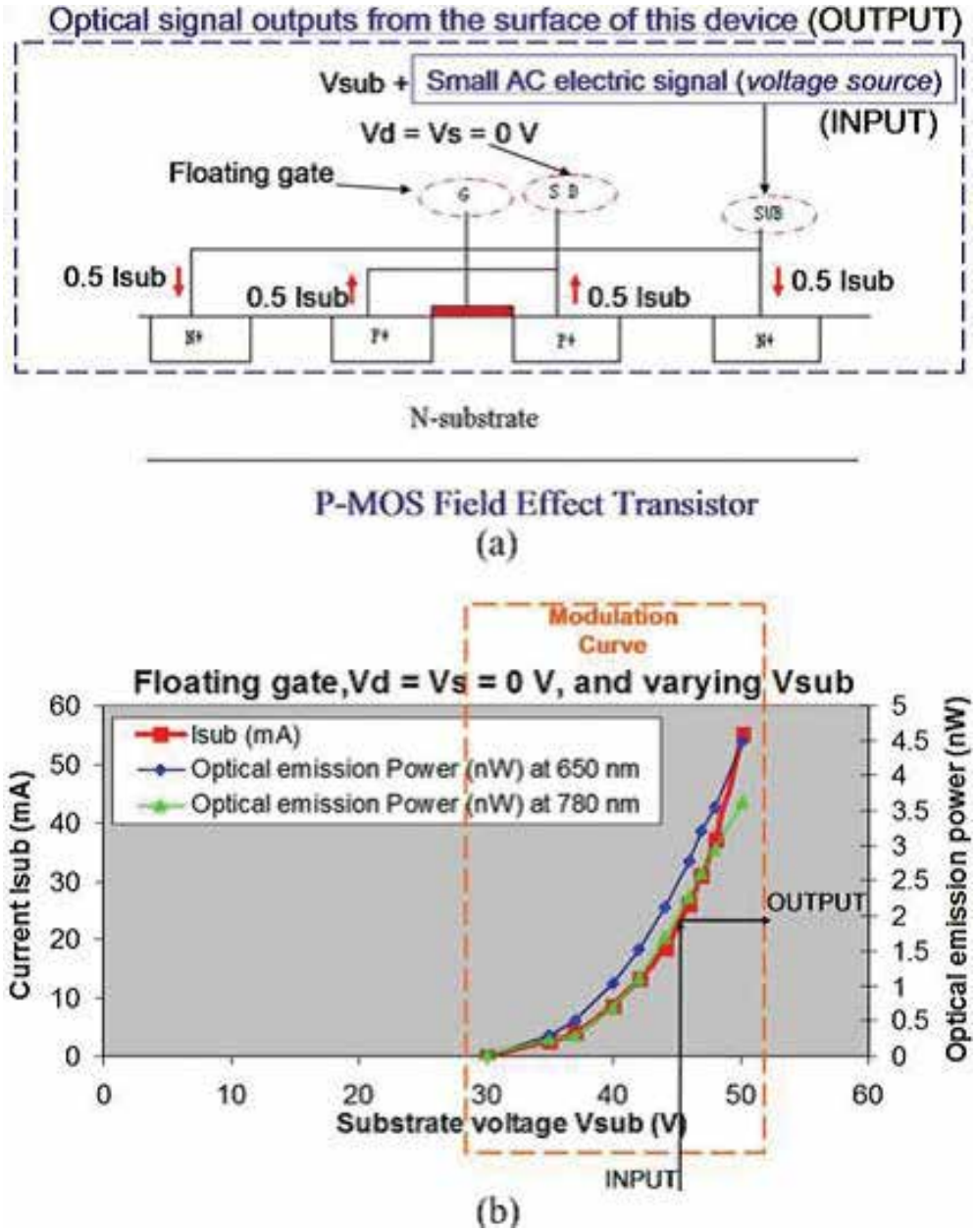

Figure 12. (a) V_{sub}, a DC source, is the reverse bias across the "p^+ S/D to n-sub" junction. (b) V_{sub} is varied to realize optical modulation in the two-terminal device. The transfer function between the electric input and the optical output is determined by the slope of the modulation curve.

associated with the depletion width change due to the bias voltage V_{sub}. Because the depletion width is not linearly dependent on the drive voltage V_{sub}, it is similarly expected that the phase shift is not to be linearly dependent on the voltage. Accordingly, the modulation curve shown in **Figure 12** is nonlinear. This is quite different from the MOS-capacitor modulator, which

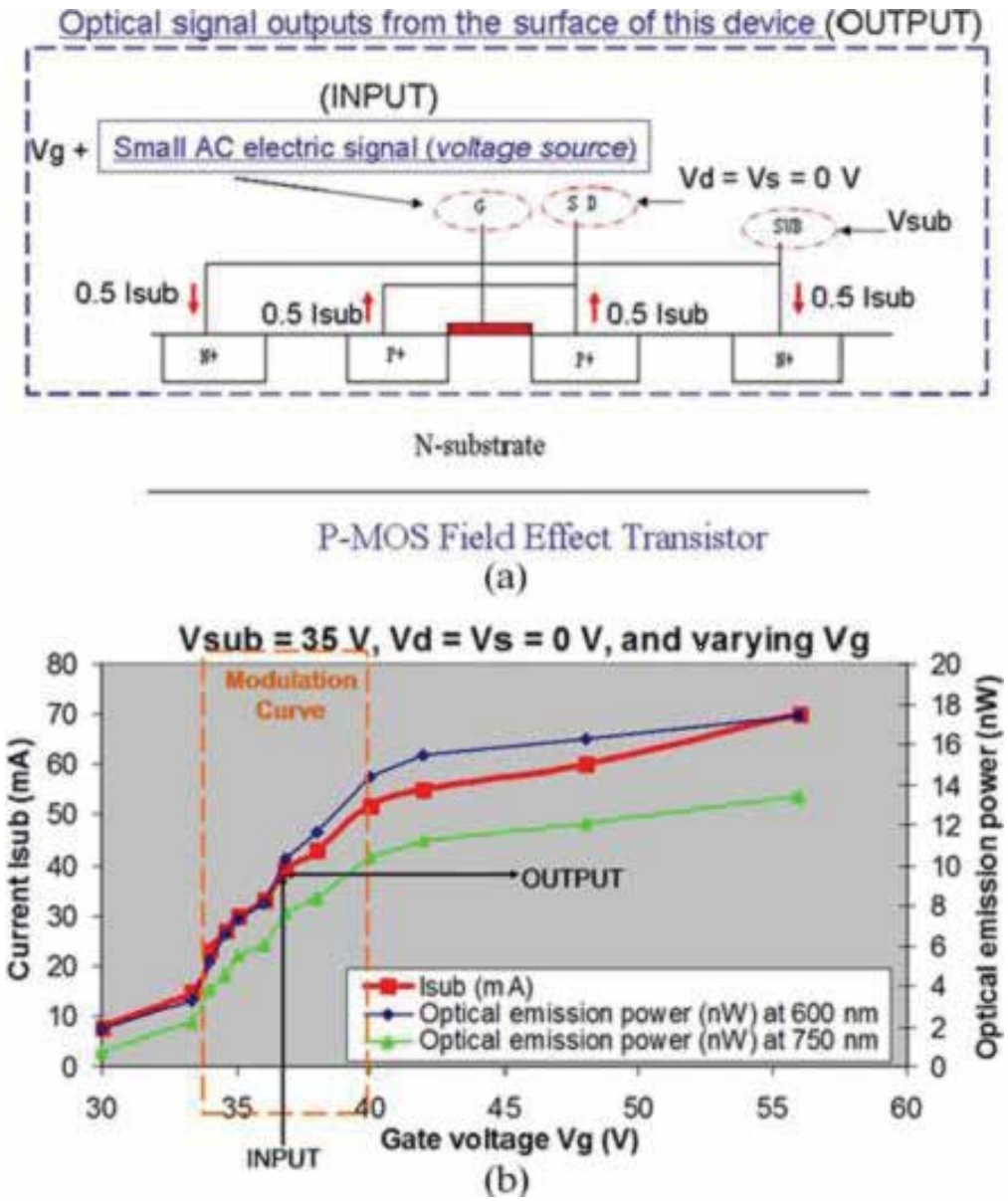

Figure 13. (a) V_g, a DC source, is the gate voltage. V_{sub}, a DC source, is the reverse bias across the "p^+ S/D to n-sub" junction. (b) V_g is varied to realize optical modulation in the three-terminal device. The transfer function between the electric input and the optical output is determined by the slope of the modulation curve (After Ref. [36]).

shows linear dependence of the phase shift versus the drive voltage V_g. Accordingly, the modulation curve shown in **Figure 13** is almost linear.

The potential application of the Si-LED is for monolithic integration in silicon CMOS-integrated circuits (Si CMOS ICs). The importance of the realization of chip-scale optical interconnection by

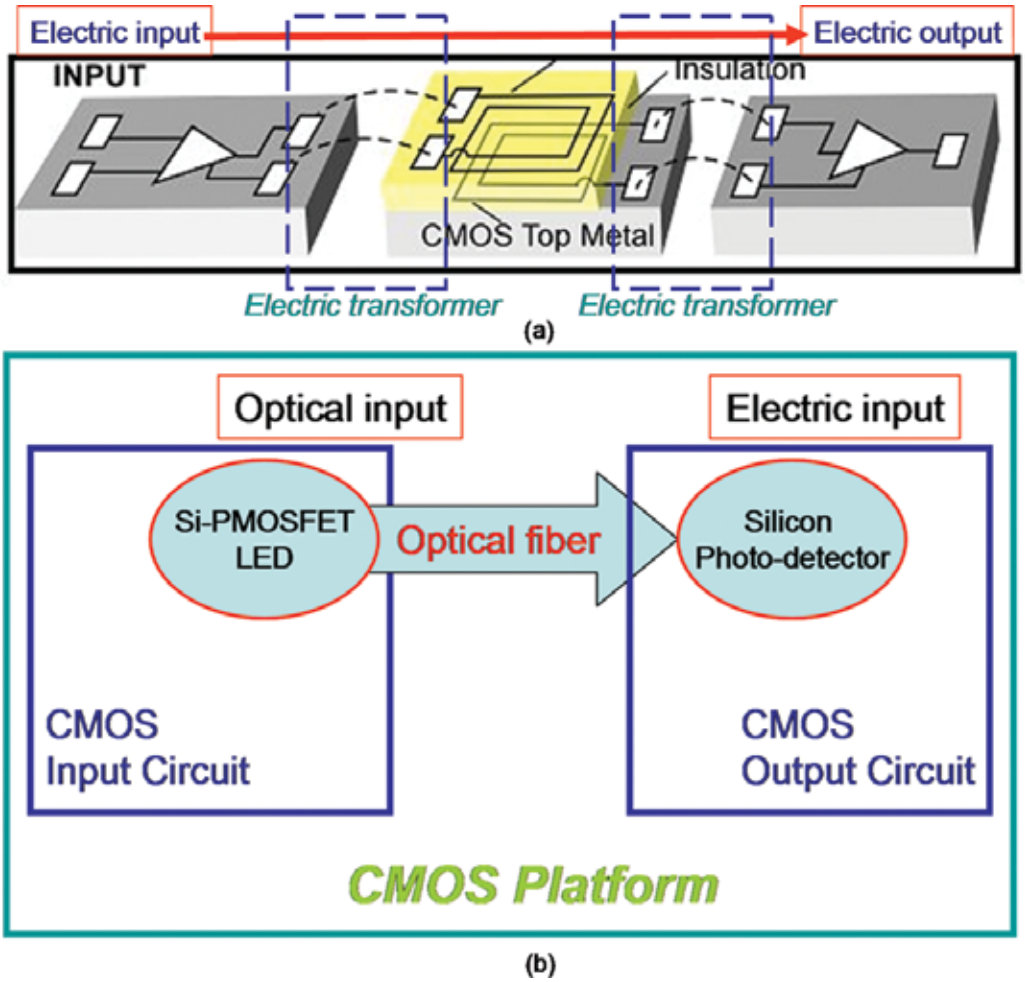

Figure 14. Interconnect: (a) electric interconnection and (b) optical interconnection.

silicon light source should be mentioned. Conventional electric interconnection in today's computers has a bottleneck for high-speed and large-capacity data transmission.

As shown in **Figure 14(a)**, *i*Couple uses the electric transformer as the isolator and the metal as the interconnect [40]. To break through the bottleneck, a replacement of electric interconnection by optical interconnection is the only possible way with great potential. More specifically, the concept of on-chip optical interconnect with silicon light emitter, waveguide, input, and output circuits integrated on the standard CMOS fabricating platform is simply illustrated in **Figure 14(b)**. The silicon light source with a PMOSFET device structure, Si-PMOSFET LED, has been analyzed in detail in Refs. [11–15], and the PMOSFET device is fully compatible with the Si-CMOS process technology that is schematically shown in **Figure 15**.

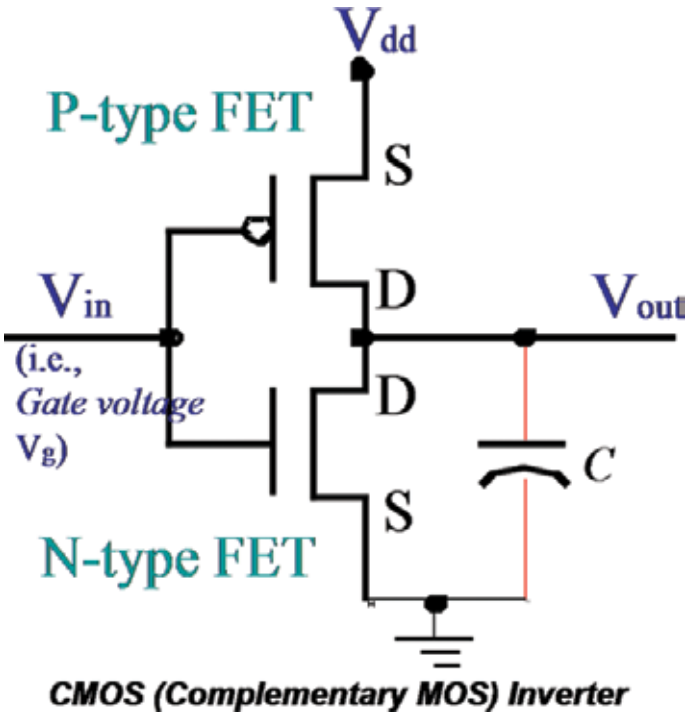

Figure 15. Schematic diagram of CMOS (complementary MOS) inverter: modern MOSFET technology has advanced continually since its beginning in the 1950s. The complementary nature of p-type FETs and n-type FETs makes it possible to design low-power circuits called CMOS or complementary MOS circuits. Because of the advantages of low-power dissipation, short propagation delay, controlled rise and fall times, and noise immunity equal to 50% of the logic swing, the CMOS process is defined as the standard fabricating technology for semiconductor devices and electronic circuits in industry [41].

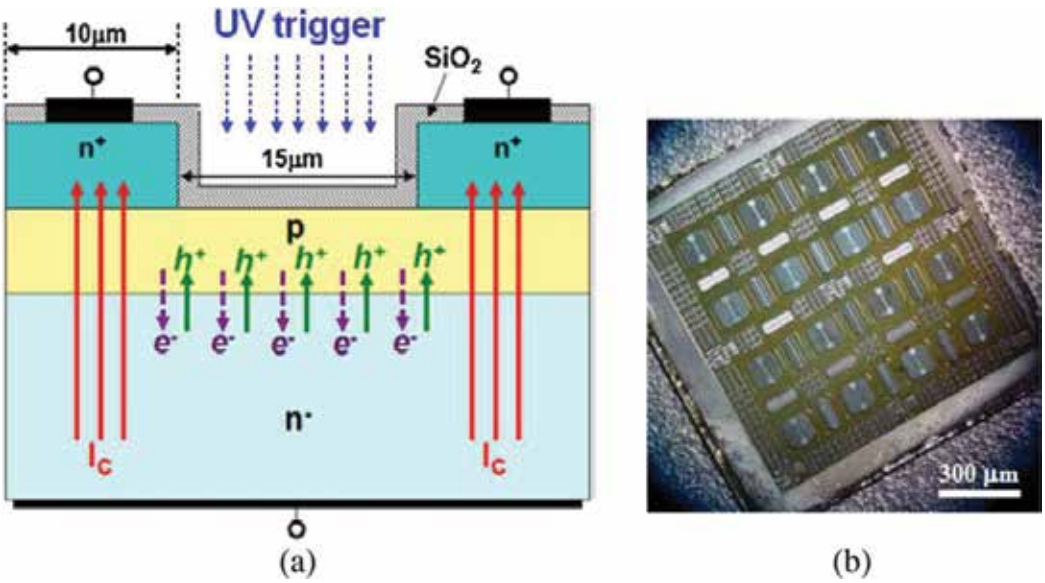

Figure 16. (a) Schematic and (b) micro for optically activated power transistors on an n-type SiC substrate (After Ref. [42]).

http://dx.doi.org/10.5772/intechopen.68273

Moreover, the Si-LED is also a satisfactory substitution for the ultra-violet (*UV*) light source given in **Figures 16** and **17** to optically activate the SiC power photo-transistor. Although the optical power emitted from Si-LED is very low, the bipolar-transistor-structured photo-transistor with internal current gain can amplify the photo-induced current. The power devices such as the lateral insulator gate bipolar transistor (L-IGBT) and the lateral extended drain MOS (LEDMOS) can be seen. **Figure 18** shows the schematic cross-sectional view of the investigated n-type L-IGBT, n-type LEDMOS, and p-type LEDMOS devices in the plasma display panel (PDP) scan driver ICs.

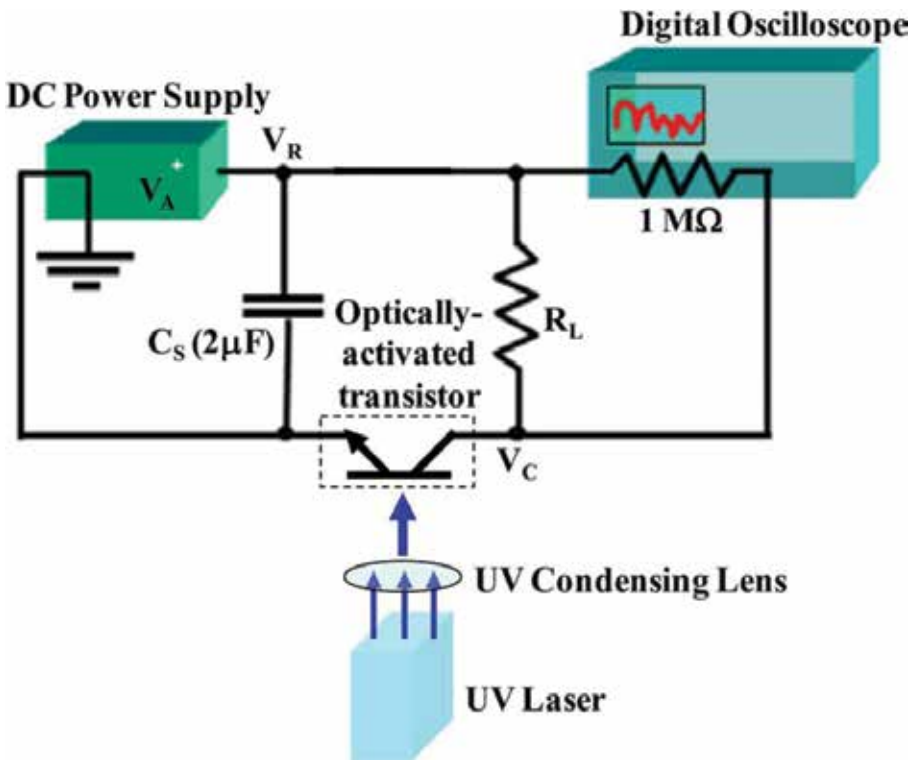

Figure 17. Test circuit for optical switching evaluation (After Ref. [42]).

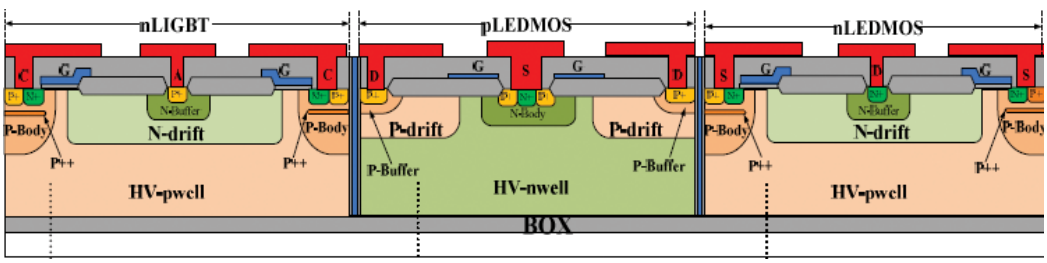

Figure 18. The schematic cross sections of the nLIGBT, nLEDMOS, and pLEDMOS devices (After Ref. [43]).

5. Optocoupler applications

Optical coupling is increasingly used in systems where complex communications must occur across a galvanic isolated boundary. Specially, in factory automation there exists a need for various pieces of equipment to communicate with each other and with a central computer via a bus. Because many of these pieces of equipment involve power devices, disruptive transient electrical signals are generated. To prevent these signals from corrupting the communication bus, optical isolation is used.

Industrial control applications also require optocoupler. An example is the motor controller which includes sophisticated DSP-based functions. Optical isolation is used by the motor controller to control the electrical power to the motor and to monitor the motor's response both electrically and mechanically. In addition, the so-called Internet of Thing (IoT) requires the control of many actuators using Internet communication. There are cases were the internet controller will need to be isolated from the actuator because of severe noise generated in the actuator such as inductive spikes.

Typically, today's optocoupler manufactures place only a single GaAs LED chip on the sending side of the optocoupler. It is left up to the user to provide an interface to the electrical requirements of the LED. This typically entails using discrete components to convert logic level signals or other types of signals to a signal suitable for driving the LED. With a silicon-based LED, however, interface circuits can be built on the same chip as the LED, thus eliminating the need for external, discrete components. Thus, the ability to place circuits on the LED side reduces component count.

Integration of the light-emitting function with silicon allows two distinct advantages over existing technology. One is the integration of a complex circuit function on the LED side of an optocoupler. GaAs LED technology does not support circuit functions. The other is the potential to make multiple bi-directional transmit and receive channels using only two pieces of silicon in a single package. Using SOI offers the potential to integrate both the receive and the transmit functions onto a single chip. The resulting higher level of integration not only lowers cost but simplifies manufacturing for both optocoupler manufacturer and the customer. An added caveat is that many optocouplers do not require high bandwidths with 1 MHz being adequate.

6. Conclusion

The article reviews a Si-LED with the structure being similar to the PMOSFET device. The electroluminescence of reverse-biased silicon p-n junctions could be explained by the direct inter-band, Bremsstrahlung, and indirect band with phonon assistance. Even if the optical emission efficiency of the reverse-biased silicon p-n junctions is very low [6, 44], extremely fast modulation speed can still make them a good choice for light emitters for many applications requiring low-intensity light, such as inter-chip optical interconnects [45–47].

Worley [48] described the methods of laying out avalanche light-emitting diodes in which a heavily doped region of one type of polarity, a second, lighter-doped region of like polarity,

and a heavy-doped region of opposite type polarity are disposed in a silicon substrate. Electrodes are laid out such that light emitted by the avalanching p-n junction is not blocked. Such a structure provides shallow implants to improve efficiency by avoiding the silicon-oxide interface for stability and by avoiding concentrating injections around junction corners to avoid concentrating injections. Combining with the structures like vertical and side-emitting junctions and side-emitting system-on-insulator (SOI) junctions, the reverse-biased silicon p-n junction diode LED is useful in SOI-based optocouplers for the IGBTs [49].

Acknowledgements

Encouragement from Mr. Eugene Worley is greatly appreciated. This work is supported by the Natural Science Foundation of China under Contract 61674001, the Department of Science and Technology of Sichuan Province under Contract 2016JY0217, and the Open Foundation of State Key Laboratory of Electronic Thin Films and Integrated Devices under Contract KFJJ201508.

Author details

Kaikai Xu

Address all correspondence to: kaikaix@uestc.edu.cn

State Key Laboratory of Electronic Thin Films and Integrated Devices, University of Electronic Science and Technology of China, Chengdu, China

References

[1] Deen M, Basu P. Silicon Photonics: Fundamentals and Devices. 1st ed. John Wiley & Sons, Ltd., West Sussex, UK; 2012

[2] Young I, Bergman K, Krishnamoorthy A, Stojanovic V. Introduction to the issue on optical interconnects for data centers. IEEE Journal of Selected Topics in Quantum Electronics. 2014;**19**(2):00200302

[3] Pavesi L, Lockwood D. Silicon Photonics: Topics in Applied Physics. Vol. 94. Berlin: Springer; 2004

[4] Newman R. Visible light from a silicon p-n junction. Physical Review. 1955;**100**(2):700-704

[5] Kramer J, Seitz P, Steigmeier E, Auderset H, Delley B. Light-emitting devices in industrial CMOS technology. Sensors and Actuators A: Physical. 1993;**37/38**:527-533

[6] Snyman L, Aharoni H, duPlessis M, Biber A, Marais J, Niekerk D. Planar light-emitting electro-optical interfaces in standard silicon complementary metal oxide semiconductor integrated circuitry. Optical Engineering. 2002;**41**(12):3230-3240

[7] Xu K, Ning N, Ogudo K, Polleux J, Yu Q, Snyman L, Polleux J. Light emission in silicon: from device physics to applications. Proceedings of SPIE. 2015;**9667**:966702

[8] Colinge J, Colinge C. Physics of Semiconductor Devices. Norwell, MA: Kluwer Academic Publishers; 2002. pp. 171-174

[9] Xu K, Li G. Silicon electro-optic modulator based on the theory of gate-controlled diode. In: International Photonics and Optoelectronics Meetings (POEM), OSA Technical Digest; 2013

[10] El-Kareh B, Bombard R. Introduction to VLSI Silicon Devices: Physics, Technology and Characterization. Chap. 5. Boston, MA: Kluwer Academic Publisher; 1986. pp. 396-401

[11] Xu K. Current-voltage characteristics and increase in the quantum efficiency of three-terminal gate and avalanche-based silicon LEDs. Applied Optics. 2013;**52**(27):6669-6675

[12] Xu K, Li G. A novel way to improve the quantum efficiency of silicon light emitting diode in a standard silicon complementary metal-oxide-semiconductor technology. Journal of Applied Physics. 2013;**113**(10):103106

[13] du Plessis M, Aharoni H, Snyman L. A silicon transconductance light emitting device (TRANSLED). Sensors and Actuators A: Physical. 2000;**80**(3):242-248

[14] du Plessis M, Aharoni H, Snyman L. Two- and multi-terminal silicon light emitting devices in standard CMOS/BiCMOS IC technology. Physica Status Solidi A. 2004;**201** (10):2225-2233

[15] Xu K, Li G. A three terminal silicon-PMOSFET like light emitting device (LED) for optical intensity modulation. IEEE Photonics Journal. 2012;**4**(6):2159-2168

[16] Kastner M. Artificial atoms. Physics Today. 1993;**46**(1):24-31

[17] Pavesi L. Silicon-based light source for silicon integrated circuits. Advances in Optical Technologies. 2008;**2008**:1-12

[18] Akil N, Kerns S, Kerns D, Jr, Hoffmann A, Charles J. Photon generation by silicon diodes in avalanche breakdown. Applied Physics Letters. 1998;**73**(7):2-3

[19] Lacaita A, Zappa F, Bigliasrdi S, Manfredi M. On the Bremsstrahlung origin of hot-carrier-induced photons in silicon devices. IEEE Transactions on Electron Devices. 1993;**40**(2):577-582

[20] Cho K. Emission line shapes of exciton molecules in direct and indirect gap materials. Optics Communication. 1973;**8**(4):412-416

[21] Gautam D, Khokle W. Effect of absorption on photon emission from reverse-biased silicon p-n junctions. Solid State Electron. 1988;**31**(6):1119-1121

[22] Figielsky T, Torun A. On the origin of light emitted from reverse biased p-n junctions. In: Proceedings of the International Conference on Semiconductors Physics (Exeter, UK); 1962. p. 853

[23] Chynoweth A, McKay K. Photon emission from avalanche breakdown in silicon. Physical Review. 1956;**102**(2):369-376

[24] Wolff P. Theory of optical radiation from breakdown avalanches in germanium. Journal of Physics and Chemistry of Solids. 1960;**16**:184-190

[25] Xu K, Li G. Hot-carrier induced photon-emission in silicon metal-oxide-semiconductor field-effect-transistor. Journal of Physics: Conference Series. 2014;**488**:132036

[26] Tao J, Chan D, Chim W. Spectroscopic observations of photon emissions in n-MOSFETs in the saturation region. Journal of Physics D: Applied Physics. 1996;**29**(5):1380-1385

[27] Marris D, Cassan E, Vivien L. Response time analysis of SiGe/Si modulation-doped multiple-quantum-well structures for optical modulation. Journal of Applied Physics. 2004;**96**(11):6109-6111

[28] Liu A, Liao L, Rubin D, Nguyen H, Ciftcioglu B, Chetrit Y, Izhaky N, Paniccia M. High-speed optical modulation based on carrier depletion in a silicon waveguide. Optics Express. 2007;**15**(2):660-668

[29] Gunn C. CMOS photonics for high-speed interconnects. IEEE Micro. 2006;**26**(2):58-66

[30] Pinguet T, Armijo G, Balardeta J et al. Advanced silicon photonic transceivers. Proceedings of Group IV Photonics. 2015:21-22

[31] Xu Q, Scmidt B, Pradhan S, Lipson M. Micrometre-scale silicon electro-optic modulator. Nature. 2005;**435**:325-327

[32] Chatterjee A, Bhuva B, Schrimpf R. High-speed light modulation in avalanche breakdown mode for Si diodes. IEEE Electron Device Letters. 2004;**25**(9):628-630

[33] Chatterjee A, Bhuva B. Reversible light coalescence phenomena of Si photo-emitter under stressing at low breakdown currents. Solid State Electron. 2003;**47**(4):665-670

[34] Kuai S, Meldrum A. Rapid color-switching micro-LEDs from silicon MIS diodes. Physica E. 2009;**41**(6):916-919

[35] Xu K, Li G. Light-emitting device with monolithic integration on bulk silicon in standard complementary metal oxide semiconductor technology. Journal of Nanophotonics. 2013;**7**(1):073082

[36] Xu K. On the design and optimization of three-terminal light-emitting device in silicon CMOS technology. IEEE Journal of Selected Topics in Quantum Electronics. 2014;**20**(4):8201208

[37] Snyman L, du Plessis M, Bellotti E. Photonic transitions (1.4 eV–2.8 eV) in silicon p^+np^+ injection-avalanche CMOS LEDs as function of depletion layers profiling and defect engineering. IEEE Journal of Quantum Electronics. 2010;**46**(6):906-919

[38] Xu K. Electro-optical modulation processes in Si-PMOSFET LEDs operating in the avalanche light emission mode. IEEE Transactions on Electron Devices. 2014;**61**(6):2085-2092

[39] Gardes F, Brimont A, Sanchis P, Rasigade G, Morini D, O'Faolain L, Dong F, Fedeli J, Dumon P, Vivien L, Krauss T, Reed G, Martí J. High-speed modulation of a compact silicon ring resonator based on a reverse-biased pn diode. Optics Express. 2009;**17** (24):21986-21991

[40] Wayne S. *i*Coupler® Digital Isolator Protect RS-232, RS-485, and CAN Buses in Industrial Instrumentation, and Computer Applications. Analog Dialogue, **39-10**. Analog Devices Inc., Norwood, MA, USA; October 2005

[41] CMOS, the Ideal Logic Family, Fairchild Semiconductor Application Note 77; January 1983

[42] Zhao F, Islam M. Optically activated SiC power transistors for pulsed-power application. IEEE Electron Device Letters. 2010;**31**(10):1146-1149

[43] Liu S, Sun W, Huang T, Zhang C. Novel 200V power devices with large current capability and high reliability by inverted HV-well SOI technology. In: Proceedings of the 25th International Symposium on Power Semiconductor Devices & ICs. 2013. pp. 115-118.

[44] Lee B, Biberman A, Chan J, Bergman K. High-performance modulator and switches for silicon photonic networks-on-chip. IEEE Journal of Selected Topics in Quantum Electronics. 2010;**16**(1):6-22

[45] Ogudo K, Schmieder D, Schmieder D, Foty D, Snyman L. Optical propagation and refraction in silicon complementary metal-oxide-semiconductor structures at 750 nm: Toward on chip optical links and micro-photonic systems. Journal of Micro/ Nanolithography, Microfabrication, and Microsystems. 2013;**12**(1):013015

[46] Xu K, Sun W, Ogudo K, Snyman L, Polleux J, Yu Q, Li G. Silicon avalanche based light emitting diodes and their potential integration into CMOS and RF integrated circuit technology. In: Advances in Optical Communication. Chapter 5. Intech, Rijeka, Croatia; 2014. pp. 115-142

[47] Ogudo K, Snyman L, Polleux J, Viana C, Tegegne Z. Realization of 10 GHz minus 30dB on-chip micro-optical links with Si-Ge RF bi-polar technology. Proceedings of SPIE. 2014;**9257**:925701

[48] Worley E. Method on constructing an avalanche light emitting diode. Patent No.: US 6365951 B1; April 2, 2002

[49] Xu K, Liu S, Zhao J, Sun W, Li G. A new silicon LED concept for future opto-coupler system applications in short distance. Optik—International Journal for Light and Electron Optics. 2016;**127**(5):2895-2897

Chapter 6

Phosphor-LED-Based Wireless Visible Light Communication (VLC) and Its Applications

Chien-Hung Yeh and Chi-Wai Chow

Additional information is available at the end of the chapter

http://dx.doi.org/10.5772/67426

Abstract

In this chapter, we review our recent works on the phosphor white-light light-emitting diode (LED)-based wireless visible light communication (VLC) and its applications. This chapter is divided into two sections for introduction. In the first section, in order to enhance the transmission rate in phosphor-LED VLC system, we propose and demonstrate a novel multiband orthogonal-frequency-division-multiplexed (OFDM) modulation format for capacity enhancement. Based on the proposed scheme, various bands of OFDM signals are employed to different LED chips of the LED luminary; it can prevent the power fading and nonlinearity effects of transmission signal. Therefore, the maximum enhanced percentage of VLC data rate is 41.1%. In the second section, we also demonstrate a 71.3–148.4 Mbps phosphor-LED wireless VLC system at the free space transmission distance between 1.4 and 2.1 m. Finally, to understand and demonstrate the real-time LED VLC transmission, a commercial OFDM-based digital signal processor (DSP) is used in the LED transmitting side and client side, respectively. Therefore, the proposed real-time half-duplex VLC system can complete around 70 Mbps downstream and upstream traffic throughputs, in a free space transmission distance of 2 m long for practical in-home illumination and smart city applications.

Keywords: phosphor LED, visible light communication (VLC), Li-Fi, OFDM modulation, Internet of thing (IoT), smart city

1. Introduction

Recently, because of the benefits of low power consumption, high-efficiency, and long lifetime for light-emitting diodes (LEDs), the traditional incandescent and fluorescent lamps are inherited by the LEDs [1–5]. Furthermore, the LEDs have a broad modulation bandwidth comparing to these conventional lighting components [6–8]. Hence, utilizing

the LED devices to combine illumination and wireless visible light communication (VLC) system has interested many advertences for the future lighting and network access markets [9–12]. Due to the LED-based VLC system without electromagnetic interference (EMI) effect, it also can be employed in wireless communication inhibited areas, such as hospital or aircraft [13–14]. Besides, compared with the red-green-blue (RGB) white-light LED, the white-light phosphor-LED is naturally used for the wireless VLC transmission [15, 16]. However, the long relaxation time of yellow phosphor nature will narrow the modulation bandwidth of white-light LED in a few MHz and reduce the VLC capacity for end-user [1, 17].

In order to increase and extend the modulation bandwidth of phosphor-LED, utilizing a blue optical filter in client side to remove the slow response produced by phosphor [18], employing spectral-efficient advanced discrete multitone (DMT) or orthogonal-frequency-division-multiplexed quadrature-amplitude-modulation (OFDM-QAM) modulations [19, 20], applying multi-input multi-output (MIMO) algorithm in VLC [21], and exploiting analogy equalization and filtering circuits in transmitter (Tx) and receiver (Rx) sides [22] have been proposed and demonstrated, respectively. In addition, utilizing advanced OFDM modulation signal for high data rate VLC transmission has also been demonstrated by Prof. Haas's group. They proposed using asymmetrically clipped optical (ACO) OFDM and DC-biased optical (DCO) OFDM for the indoor LED VLC network system to reducing LED clipping distortions [23, 24]. While the RBG-based white-light LED was employed in the VLC transmission, 110 Mbps OFDM traffic rate was also reached [25].

If the key function of the LED luminary is applied for lighting, it will confront the communication characteristics of optical wireless VLC [26]. Hence, how to use the commercially available white-light LED luminary to optimize both the illumination and communication is important and desirable issue for practical in-home illumination application [6, 13].

In this chapter, we will introduce our recent works on the white-light phosphor-LED-based wireless VLC system and its applications. This chapter will be divided into two sections for introduction. In the first section, to enhance the data rate in phosphor-LED VLC system, we propose and demonstrate an advanced multiband OFDM modulation design for VLC capacity enhancement. According to the proposed VLC scheme, various bands of OFDM signals are applied on different LED chips of the LED luminary; the special modulation design can prevent the power fading and nonlinearity effects of transmission signal by utilizing the same OFDM signal to the entire LED chips. As a result, the maximum enhanced percentage of VLC data rate is 41.1%, when we use the proposed novel new multiband OFDM modulation.

In the second section, we will demonstrate a 71.3–148.4 Mbps phosphor-LED wireless VLC system at the free space transmission distances between 1.4 and 2.1 m. Moreover, a commercial phosphor LED luminary with five phosphor-LED chips in series is applied for illumination and communication simultaneously. In the measurement, optical OFDM modulation signal with bit-loading algorithm is applied for proposed VLC transmission. We also investigate an optimal bias-tee circuit with equalization and filtering method to extend the modulation bandwidth from 1 to 27 MHz. Finally, to understand and demonstrate the real-time LED VLC

http://dx.doi.org/10.5772/67426

transmission, a commercial OFDM-based digital signal processor (DSP) is used in the LED Tx side and client Rx side, respectively. Therefore, the proposed real-time half-duplex VLC system can complete the around 70 Mbps downstream and upstream traffic throughputs, in a free space transmission distance of 2 m long. We believe that it can be a cost-effective and promising candidate for practical in-home illumination and smart city applications.

2. Multiband OFDM in phosphor-LED VLC system

In the first section, we will present demonstrating a multiband OFDM modulation format in phosphor-LED VLC system for data rate enhancement [27]. First of all, **Figure 1(a)** and **(b)** presents the proposed optical setup of phosphor-LED VLC transmission by utilizing single-band and triple-band OFDM modulation formats. In this experiment, we use a phosphor-LED luminary with six LED light chips for serving as the VLC transmitter (Tx). Besides, the lenses can be applied in front of the phosphor-LED-based Tx and the receiver (Rx) of client side to focus and enhance the VLC light performance simultaneously. Here, the modulated OFDM signal can be directly applied on the LED luminary via a bias-tee (BT) without analogy equalization for VLC transmission. Furthermore, the proposed BT circuit without pre-equalization function has also been demonstrated in Ref. [10]. Conventionally, the entire OFDM signal would be applied on the six LED chip in Tx-side for VLC transmission, as seen in **Figure 1(a)**. However, due to the power fading and nonlinear effect of LED, the relative electrical power spectrum drops quickly in the higher frequency range. These influences will limit the traffic rate of VLC. To overcome this issue, we propose a multiband OFDM modulation format to increase the total VLC rate. As shown in **Figure 1(b)**, the real architecture of three-band OFDM VLC transmission is investigated. Hence, the total OFDM data rate in VLC system can be divided in three data ranges ($Data_1$, $Data_2$, and $Data_3$) within a total frequency bandwidth. Each modulation bandwidth ($Data_1$, $Data_2$, and $Data_3$) has the same range for data transmission. In the measurement, the phosphor-LED luminary has six lighting chips. The triple-band OFDM signals are employed on the LED luminary directly and divided into three groups of phosphor-LED chip via three BTs for direct OFDM modulation. Hence, each group has two phosphor-LED chips. And each LED chip is driven at 3 V.

Due to the power fading and nonlinear effects, the relative electrical power spectrum drops quickly in the higher frequency range, as shown in **Figure 2(a)**, when single-band OFDM modulation is used. It would also produce poor signal-to-noise ratio (SNR) of each OFDM subcarrier for VLC transmission. Hence, the VLC rate could also be restricted under the available frequency bandwidth. To solve the issues, using triple-band OFDM would be choice for phosphor-LED VLC system. The relative electrical power spectra of triple-band OFDM signals ($Band_1$, $Band_2$, and $Band_3$) are depicted conceptually in **Figure 2(b)**. If the OFDM signal has a high peak-to-average power ratio (PAPR) by separating the OFDM into triple-band OFDM, various OFDM bands are utilized to various groups of LED chips. Therefore, much higher driving power can be employed to each LED group for enhancement. The obtained SNR of each OFDM subcarrier would enhance in each OFDM-band obviously. As a result, the total VLC rate could be improved by using proposed triple-band OFDM modulation scheme.

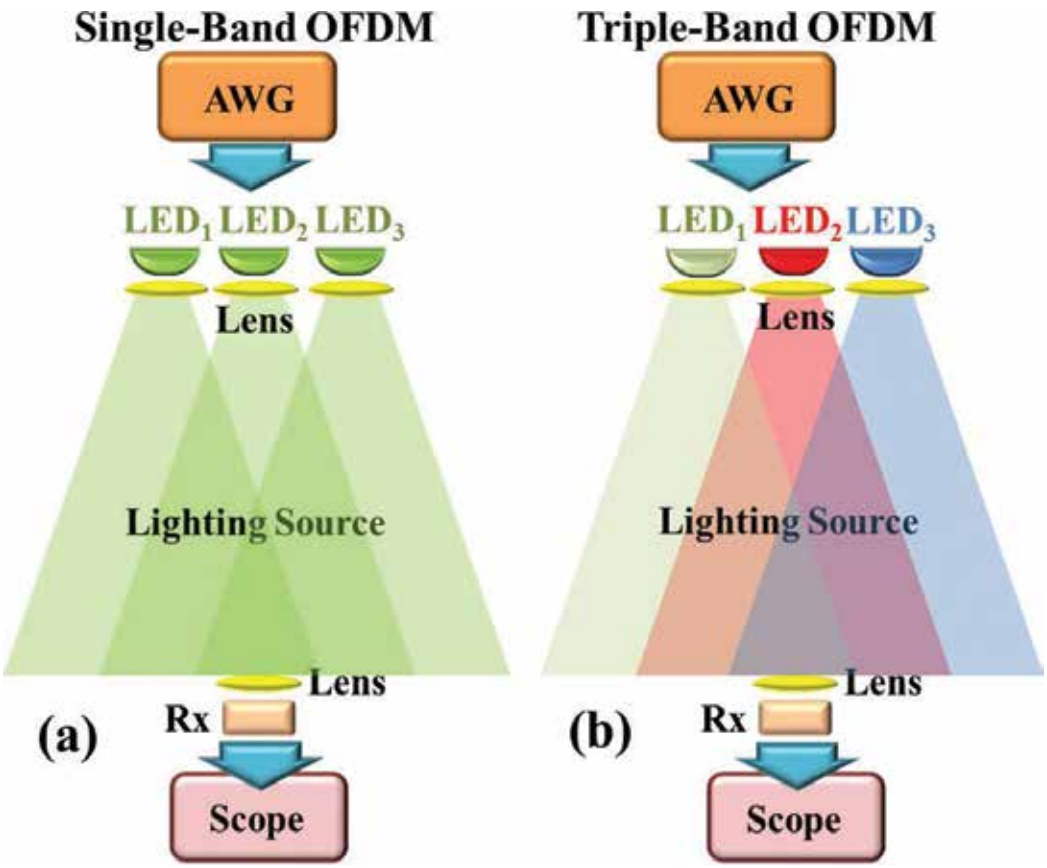

Figure 1. Proposed phosphor-LED VLC architectures using (a) single-band and (b) triple-band OFDM modulations.

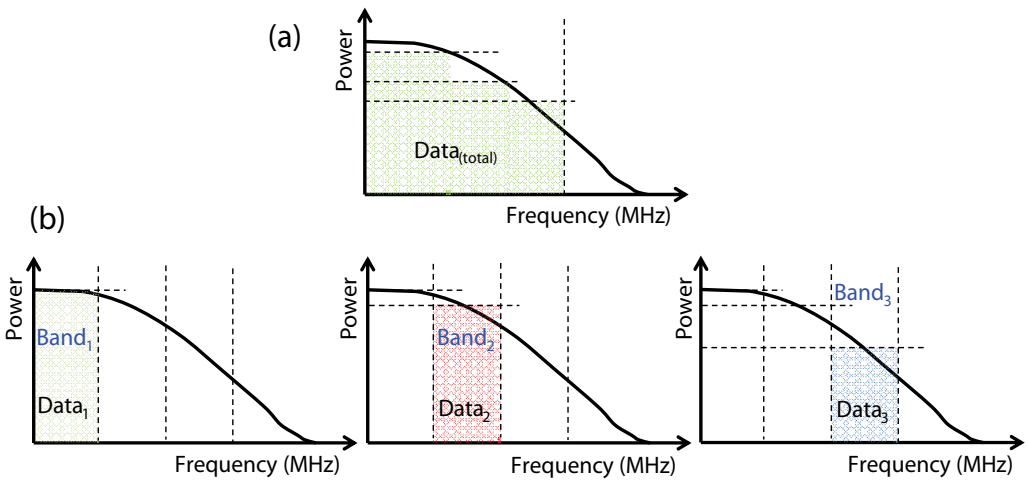

Figure 2. The relative electrical spectra under (a) single-band and (b) triple-band OFDM modulation format.

http://dx.doi.org/10.5772/67426

We utilize six white-light phosphor-LED chips with series connection in the experiment. Thus, the used LED luminary is driven around ~18 V. We utilize an arbitrary waveform generator (AWG) to produce OFDM-QAM signal applying on LED luminary for VLC transmission. As shown in **Figure 1(a)**, the white-light VLC emits from the LED luminary and is detected by a silicon-based PIN Rx. Here, the detection wavelength ranges and active area of detected PIN Rx are between 350 and 1100 nm with responsivity of 0.63 A/W 150 mm^2, respectively. Besides, the operated bandwidth and the root mean square (rms) noise of Rx are 50 MHz of 530 μV, respectively. Then, the VLC wireless signal will be directly detected by a PIN Rx. Next, the detected VLC signal is amplified by a broadband electrical amplifier, and is linked by a real-time oscilloscope for signal demodulation. Finally, the corresponding bit error rate (BER) will be calculated and obtained based on the observed SNR of each OFDM subcarrier. In addition, in order to prevent the power fading and nonlinearity problems of the LED, the multi-band OFDM modulation method is first proposed in VLC system to improve the traffic rate, as seen in **Figure 2(a)**.

Normally, the phosphor-LED only reaches a few MHz modulation bandwidth without any related improvements [1, 12]. To extend the frequency bandwidth of LED, the proposed BT circuit only needs to adjust the resistance (R), inductance (L), and capacitance (C) suitably for matching the impedance of LED. Hence, we measure the modulation bandwidth of proposed VLC system, while the BT circuit is utilized. **Figure 3** displays the frequency response of phosphor-LED, while the detected illumination at Rx side is at 1000 lx. The available modulation bandwidth of 25 MHz can be reached as shown in **Figure 3**. According to the proposed BT in LED Tx side, the frequency bandwidth can be widened from a few MHz to 25 MHz. As a result, the modulation capacity of VLC system should be increased via proposed multiband OFDM signal.

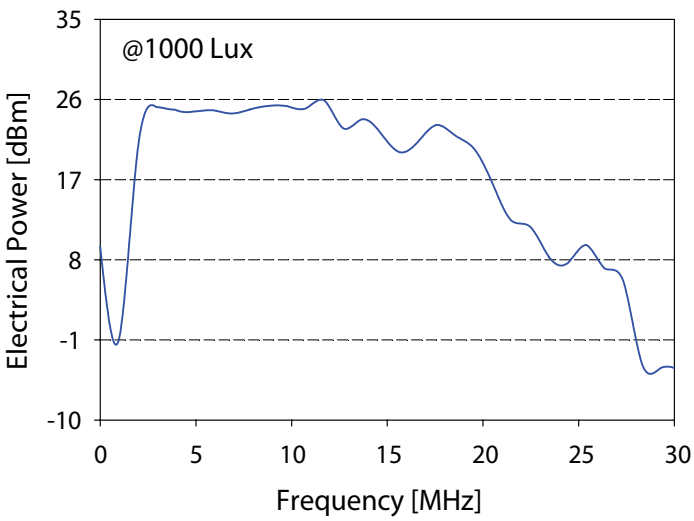

Figure 3. Measured frequency response spectrum of phosphor-LED, as the received illumination of Rx-side is 1000 lx.

Then, to understand the connection of VLC illumination and SNR, we utilize the 16-QAM OFDM modulation signal with 30 subcarriers in a frequency bandwidth of 1.95–30.27 MHz for VLC transmission. Based on the observed results of **Figure 3**, using bit-loading 16-QAM OFDM signal to apply on LED luminary for wireless VLC transmission is around the 30 MHz modulation bandwidth. In the measurement, **Figure 4(a)–(c)** presents the measured SNR of each OFDM subcarrier by using single-, dual-, and triple-band OFDM modulations, since the unlike illuminations of 200, 500, and 1000 lx are detected at the client Rx side, respectively. Here, ~20, 26, and 30 MHz available bandwidths can be employed by using multiband OFDM signal, respectively, while the SNR can be greater than 10 dB, under the different illuminations of 200, 500, and 1000 lx, as seen in **Figure 4(a)–(c)**. Compared with the single- and dual-band OFDM formats, the observed SNR characteristics of triple-band OFDM signal is superior in proposed VLC system. If the measured VLC illumination rises increasingly in the client Rx, the observed SNR would also increase under each OFDM modulation format. Moreover, when proposed triple-OFDM band modulation is applied on LED luminary, the measured SNR can improve by 4–21 dB comparing with the single-OFDM band, as depicted in **Figure 4(a)–(c)**. Therefore, when the proposed triple-band OFDM modulation in phosphor-LED VLC system, the all of received SNR also can be increased. In the experiment, the proposed multiband OFDM modulation can be actually enhanced the VLC traffic rate based on the measured results of **Figure 4**. In addition, the related VLC transmission lengths of 2.1, 2.0, and 1.4 m are also executed and measured, as the detected illuminations of 200, 500, and 1000 lx are observed in the Rx, respectively.

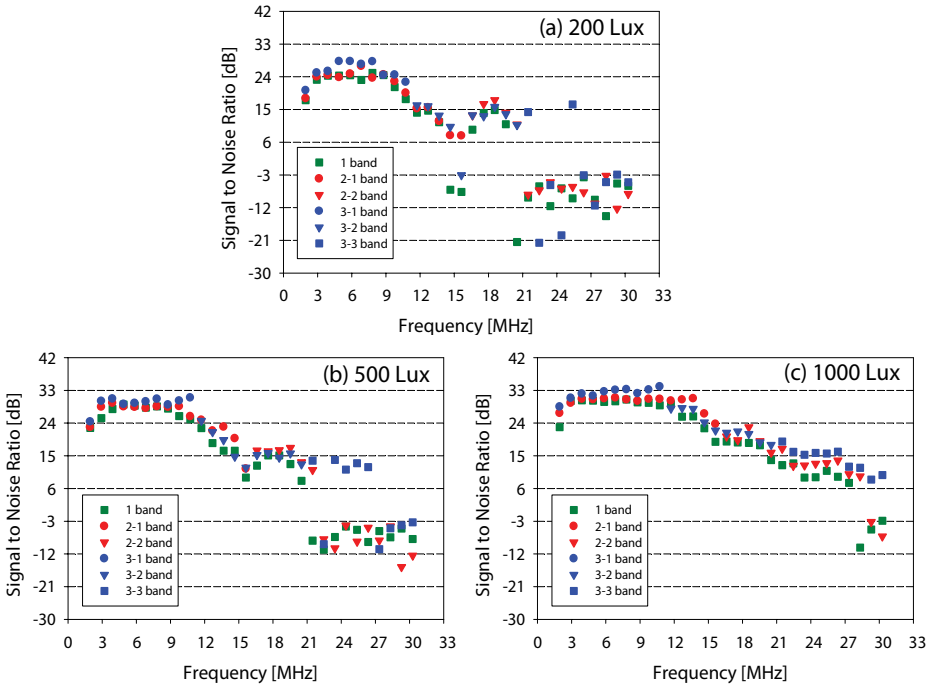

Figure 4. Experimental setup of the proposed fiber laser scheme in linear cavity scheme.

http://dx.doi.org/10.5772/67426

Next, we perform the evaluation of BER experimentally under different observed illuminations. **Figure 5(a)–(c)** shows the measured VLC traffic rate and homologous BER at the observed illuminations of 200, 500, and 1000 lx in the Rx, respectively. Here, the single-, dual- and triple-band OFDM signals are used at the available bandwidth of 1.95–30.27 MHz. As shown in **Figure 5**, if we use the single-band OFDM modulation, the obtained VLC data rates and NERs are 71.3, 109.4, and 148.8 Mbps, and 3.13×10^{-4}, 1.89×10^{-3} and 1.76×10^{-3}, respectively, under the various illuminations of 200, 500, and 1000 lx. Besides, **Figure 5(a)–(c)** also displays the measured VLC data rate and BER of each sub-band, while the proposed multiband OFDM formats are employed. When we use the dual-band OFDM signal, the VLC rates are 79.1 and 15.6 Mbps (total = 94.7 Mbps), 101.6 and 20.5 Mbps (total = 122.1 Mbps), and 113.3 and 46.9 Mbps (total = 160.2 Mbps), respectively, can be achieved under the different illuminations. The measured BER of each sub-band would be less than that of forward error correction (FEC) threshold (BER = 3.8×10^{-3}), and the average BERs are nearly 2.60×10^{-3}, 1.30×10^{-3} and 5.11×10^{-4}, respectively. Finally, while we utilize the proposed triple-band OFDM signal in VLC transmission, the VLC data rates of each band and the average BERs are 69.4, 27.3, and 3.9 Mbps, 76.2, 43.0, and 9.7 Mbps, and 77.1, 63.5, and 34.2 Mbps and 1.71×10^{-3}, 1.20×10^{-3}, and 1.50×10^{-3}, respectively, as shown in **Figure 5**.

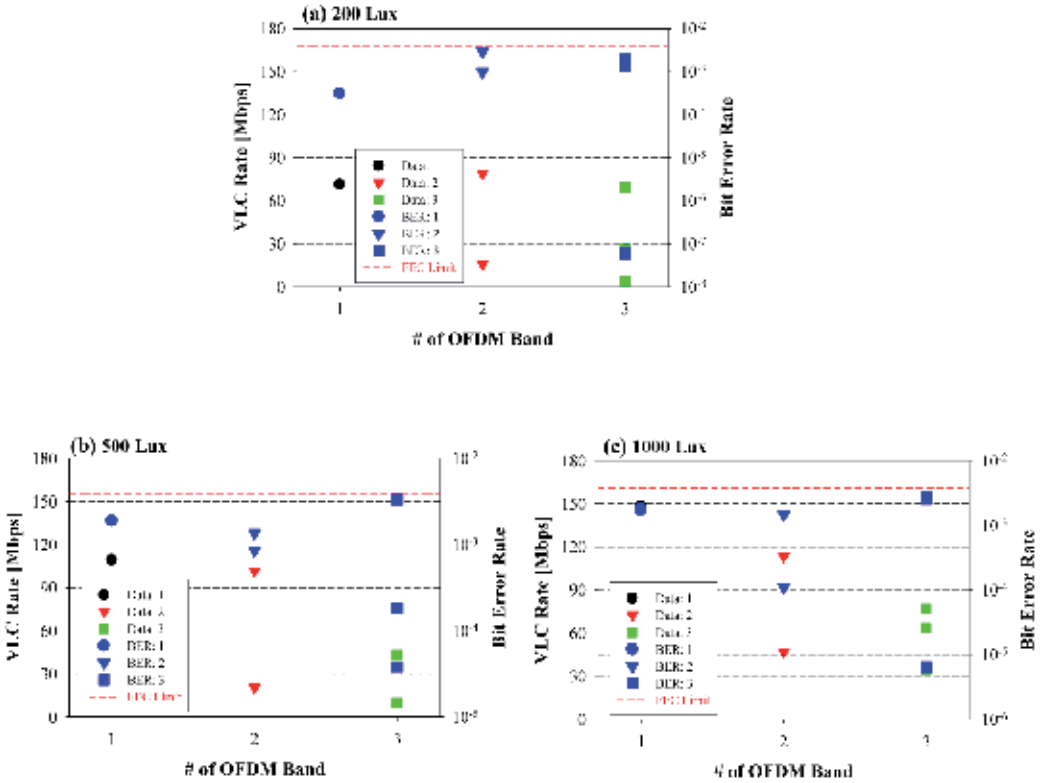

Figure 5. Measured VLC rate and corresponding BER at the detected illumination of (a) 200, (b) 500, and (c) 1000 lx in the Rx, respectively, while the single-, dual-, and triple-band OFDM modulations are applied.

Finally, we will analyze and discuss the VLC performance of obtained triple-band OFDM signal. **Figure 6** shows the detected total VLC rates and increase percentage of rate at the single-, dual-, and triple-band OFDM modulations, respectively, under the detected illuminations of 200, 500, and 1000 lx. In the experiment, when the proposed dual-band and triple-band OFDM signals are used, the VLC traffic data can reach 94.7, 122.1, and 160.2, and 100.6, 128.9, and 174.8 Mbps, respectively, as seen in **Figure 6**. Hence, the greatest increase percentages of VLC rates of 32.9%, 11.6%, and 7.9%, and 41.1%, 17.8%, and 17.8% are observed, while the various illuminations are 200, 500, and 1000 lx, respectively, and the designed dual-band and triple-band OFDM formats are applied on the VLC transmission. Furthermore, based on the results of **Figure 6**, as the number of OFDM-band increases slowly, the retrieved total VLC traffic rate will also enhance. However, if more sub-band OFDM signal is used in the proposed VLC system, the corresponding cost will be higher. Therefore, the proposed multiband OFDM method can improve and enhance the total VLC rate in phosphor-LED VLC wireless transmission.

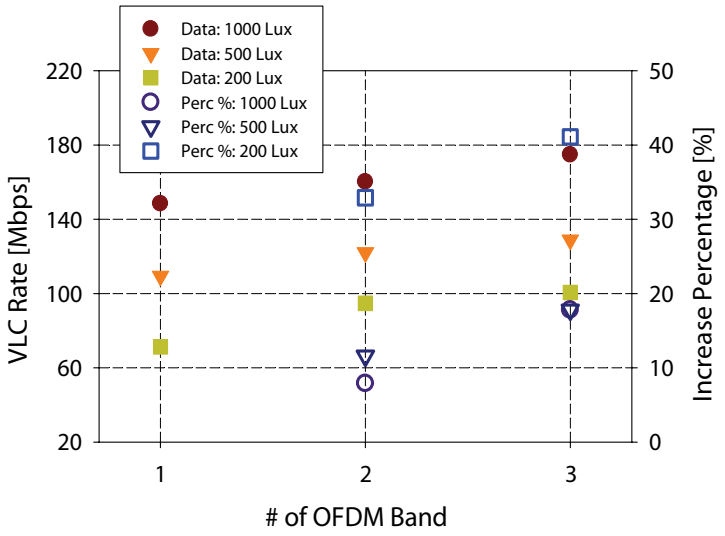

Figure 6. Observed total VLC rate and data increase percentage under the single-, dual-, and triple-band OFDM modulation at the observed illuminations.

In summary, the triple-band OFDM format in phosphor-LED VLC system to improve the VLC data rate have been proposed and demonstrated. In this proposed VLC architecture, various signal bands of OFDM formats are applied on unalike LED chips in the same LED luminary. The proposed VLC technology could avoid the power fading and nonlinearity issue by using the same OFDM signal to all the LED chips. In this measurement, we did not use a blue optical filter to enhance the VLC data rate of phosphor-LED. Furthermore, as we use single-OFDM-band modulation in the LED luminary, which has six white-light phosphor-LED chips, the VLC system could reach 148.4 and 71.3 Mbps traffic rates, respectively, when the detected illuminations were 1000 and 200 lx in the client end-user. If we used the proposed triple-band OFDM method at the same detected illuminations, the total VLC rates could be considerably improved to 174.8 and 100.6 Mbps, respectively. Therefore, employing proposed multiband

http://dx.doi.org/10.5772/67426

OFDM modulation could enhance the 41.1% and 17.8% VLC rates in VLC wireless transmission, while the observed illuminations were 200 and 1000 lx, respectively. In addition, the analysis and verification by experiments have been also executed in this section.

3. Rate improvement of VLC and real-time half-duplex VLC

In this section, we introduce and investigate the high-speed phosphor-LED VLC system together with real-time half-duplex transmission [13]. **Figure 7(a)** presents the optical setup of proposed phosphor-LED VLC architecture. In the measurement, a LED luminary with five phosphor-LED chips for acting as the Tx for VLC wireless transmission. **Figure 7(b)** indicates the related illuminations of LED, which is measured by using a light meter (LUTRON lx-1102) at the different transmission lengths in the field of view (FOV) in proposed VLC transmission system. As the measured illuminances are 200, 500, and 1000 lx, respectively, the corresponding free space transmission lengths of 210, 200, and 100 cm, are also obtained as shown in **Figure 7(b)**.

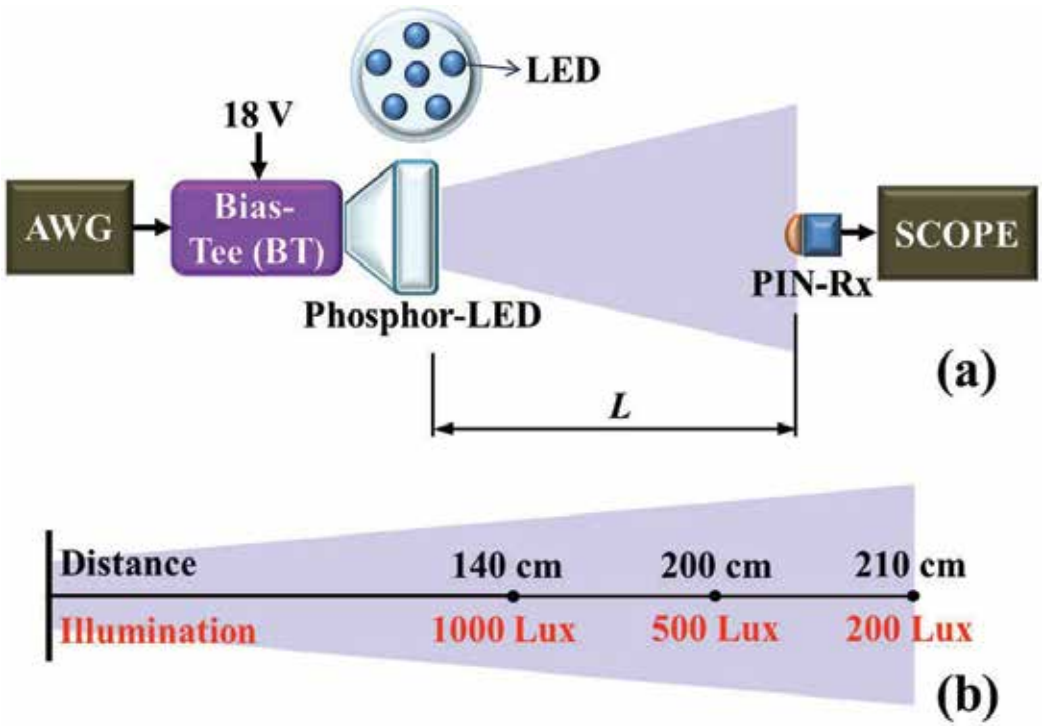

Figure 7. (a) Proposed phosphor-LED VLC wireless system. (b) Corresponding illuminations under different transmission lengths in the field of view of the proposed VLC.

In the VLC-Tx side, the LED luminary has five phosphor-LED chips for lighting and communication. Here, each LED chip is covered by a lens with divergent angle of 45°. Besides, an imaging lens in front of the client Rx is used for focusing and enhancing the detected VLC power. To

reach a higher VLC data capacity in phosphor-LED VLC system, we can utilize OFDM-QAM modulation format with bit-loading, which is directly applied on the LED luminary by using proposed BT circuit, as shown in **Figure 8**. The resistance (R) of BT circuit is nearly 3 Ω . The proposed BT circuit without complicate pre-equalization design has been also demonstrated in Ref. [28]. Hence, we adapt the resistance (R), inductance (L), and capacitance (C) suitably for matching the impedance of five LED chips in the LED-Tx side. The AC modulated signal can be generated by the AWG and is connected to the "SMA" port at the lower left corner of **Figure 8**, whereas the LED is linked to the "LED_P" port at the upper right corner of **Figure 8**.

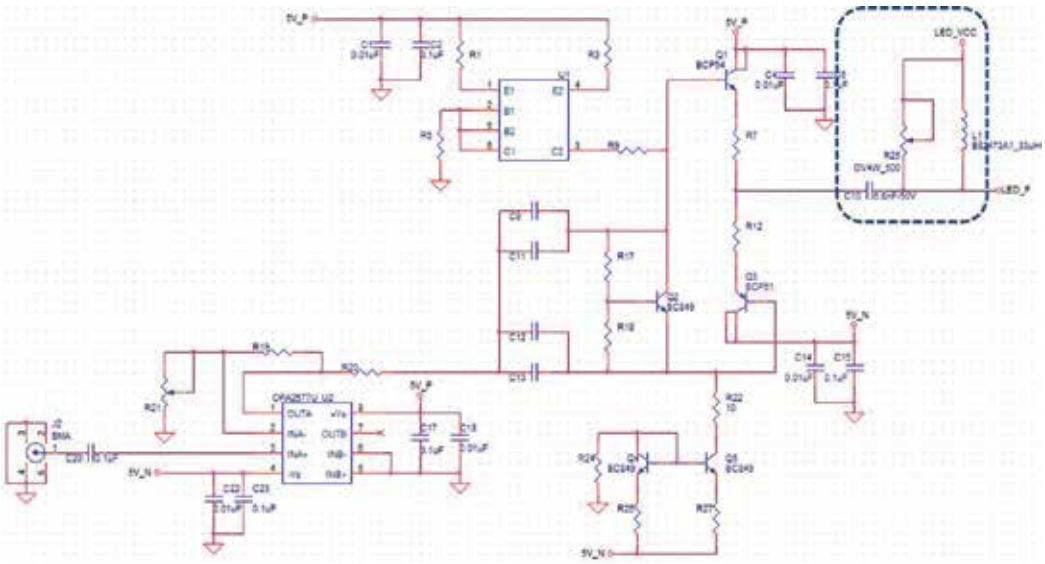

Figure 8. The proposed BT circuit topology.

In the experiment, we employ the five white-light phosphor-LED chips with series connection scheme for indoor illumination. Therefore, the OFDM-QAM signal can be applied on the LED luminary for direct modulation by employing an arbitrary waveform generator (AWG) for VLC wireless communication. In **Figure 7(a)**, the white-light VLC signal emits from the LED-Tx and detected by using the silicon-based PIN Rx. Then, the detected VLC signal will be amplified through a wideband RF amplifier (Picosecond 5867), and connected to a real-time oscilloscope for VLC signal demodulation.

In the measurement, the OFDM-QAM, which uses bit-loading algorithm, and the OFDM symbol can be encoded offline using the MATLAB program. The flow diagram for proposed OFDM-QAM algorithm is shown in **Figure 9**. The serial binary stream can be converted into several parallel streams, and each parallel binary flow is plotted into 16-QAM symbols. The inverse fast Fourier transform (IFFT) process with 256 IFFT size is executed on the QAM symbols to create the digital OFDM symbols. Cyclic prefix (CP) of 1/32 will be added in each OFDM symbol to reduce the dispersion-induced characteristic deprivation. The encoded digital OFDM

http://dx.doi.org/10.5772/67426

symbol can be delivered into an AWG and altered into analogue electrical signal via the digital-to-analogue converter (DAC). Here, we use the 250 Msample/s sampling rate and 8-bit DAC resolution from the AWG for measurement. Then, in the Rx-side, the VLC wireless signal can be directly detected via a PIN-PD, which is linked by a real-time oscilloscope with sampling rate of 250 Msample/s for VLC signal decode. Finally, the VLC OFDM signal can be demodulated offline by retreat process of the encoder.

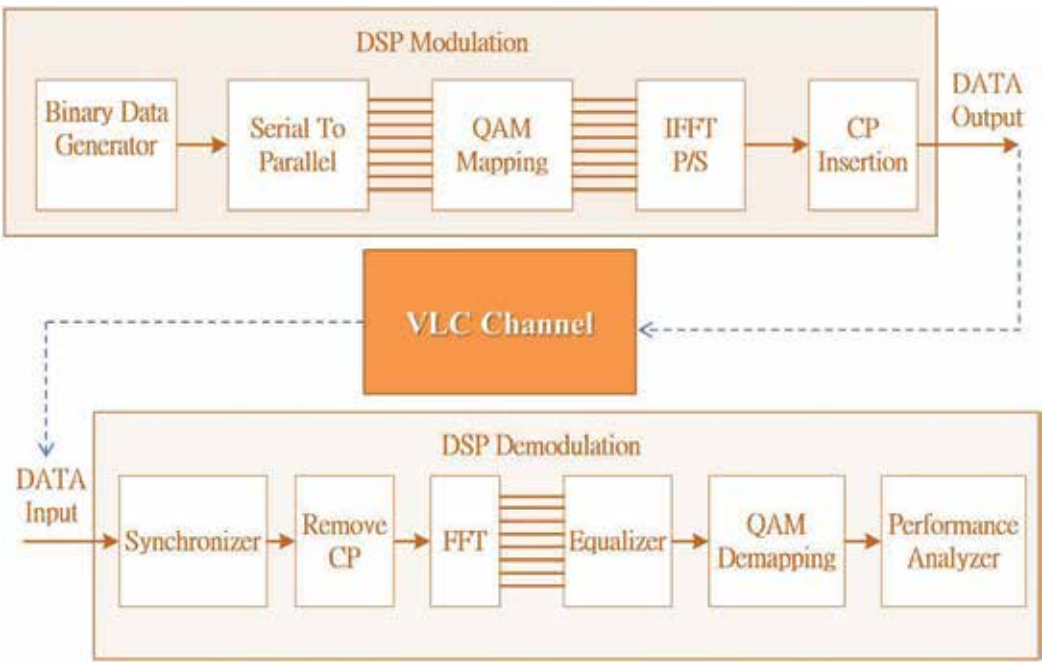

Figure 9. The flow chart of OFDM-QAM algorithm.

Figure 10 presents the observed electrical power spectra of phosphor-LED at the various detected illuminances of 200, 300, 400, 500, and 1000 lx, respectively. And the measured response frequency regions are around 20, 21, 21, 21, and 27 MHz, respectively, as depicted in **Figure 10**. When we decrease the illuminance of client side gradually, the relative powers will also reduce, as shown in **Figure 10**. Furthermore, the available electrical power range will fall rapidly in a higher frequency region, as seen in **Figure 10**. As we know, the smaller electrical power would lead to the poor SNR of each OFDM subcarrier. Thus, the corresponding VLC traffic rate would be restrained in the frequency bandwidth. In the measurement, the SNR is observed from the measured constellation of Rx-side. Moreover, in digital modulation applications, the SNR can be stated usually by measuring the modulation-error ratio from constellation information.

Then, **Figure 11(a)** displays the measured SNR of each OFDM subcarriers using 16-QAM modulation format in the different illuminances of 200, 300, 400, 500, and 1000 lx, respectively. Moreover, we utilize 30 OFDM subcarriers in the modulation range from 1.95 to 30.27

MHz for creating VLC OFDM signal. To completely employ the unflatten SNR, the modulated signal of each OFDM subcarrier can be adapted with bit-loading algorithm based on the obtained SNR value. While we use the bit-loading with QAM order from 4 to 256, the measured SNR spectra can be obtained, as shown in **Figure 11(b)**. Hence, each OFDM subcarriers with their corresponding SNRs are among 9.4 and 25.1, 15.6 and 25.7, 8.3 and 29.1, 8.1 and 29.1, and 7.5 and 30.5 dB in the frequency regions of 1.95–19.53, 1.95–20.50, 1.95–20.50, 1.95– 20.50, and 1.95–26.36 MHz, when the obtained illuminances are 200, 300, 300, 400, 500, and 1000 lx, respectively. Here, the measured corresponding constellations of 4, 16, and 256 QAM under the results of **Figure 11(b)** at 500 lx state are illustrated in **Figure 12**. Therefore, the available modulation range can achieve nearly 27 MHz by using the proposed LED-Tx unit. In addition, the frequency bandwidth can be defined as the available bandwidth. The obtained SNR can satisfy the FEC (i.e., BER = 3.8×10^{-3}) requirement when the bit-loading OFDM is utilized. The useful bit range of the algorithm is adjusted between 4- and 128-QAM adaptively, thus the available frequency range can support at least 4-QAM data traffic (i.e., SNR = ~8 dB).

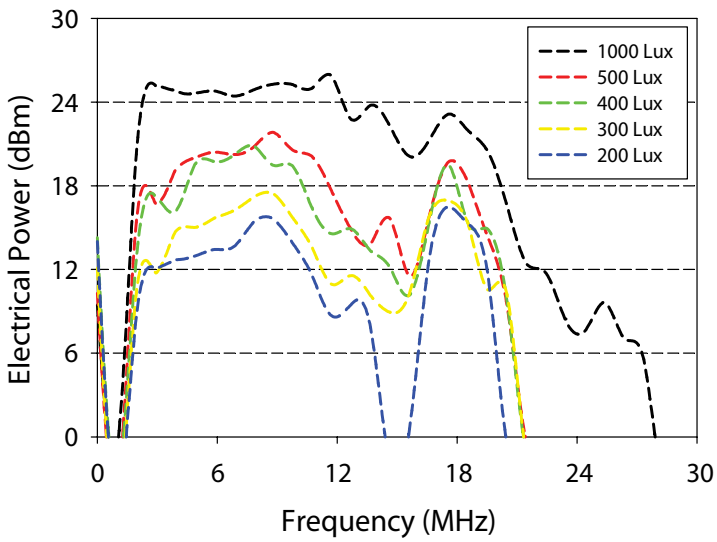

Figure 10. Observed electrical power spectra at the various detected illuminances of 200, 300, 400, 500, and 1000 lx, respectively.

Furthermore, the measured VLC data rates are 71.3, 89.8, 102.5, 109.4, and 148.4 Mbps, respectively, under the different illuminances of 200, 300, 400, 500, and 1000 lx, as also shown in **Figure 13**. In this measurement, all of the measured corresponding BERs are below the FEC threshold under the various detected illuminances, as illustrated in **Figure 13**. In addition, the FEC threshold was also determined as Ref. [29]. EFC would indicate 7% overhead which is used for the coding to measure error-free in the proposed VLC wireless system.

http://dx.doi.org/10.5772/67426

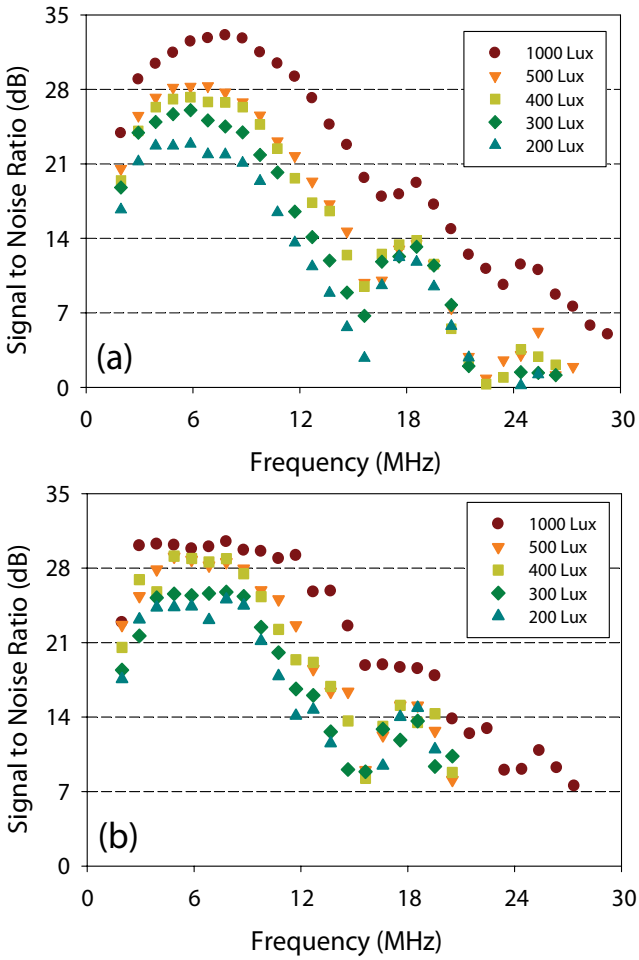

Figure 11. Measured SNR spectra of each OFDM subcarrier (a) without and (b) with bit-loading at the detected illuminances of 200, 300, 400, 500, and 1000 lx, respectively.

Then, a real-time bidirectional phosphor-LED VLC transmission is also proposed and demonstrated. Here, the commercial OFDM-based DSP chip is applied in the Tx and Rx simultaneously sides to replace the AWG and oscilloscope for encoding and decoding VLC channel. However, the commercial DSP chip only has half-duplex transmission function for VLC. In the real-time DSP VLC transmission, we use a commercial DSP chip and Ethernet port for VLC signal processing and connecting, respectively. The modulation bandwidth of DSP chip is from 2 to 100 MHz with adaptively OFDM-QAM formats from QPSK to 16-QAM. The maximum data rate could reach 250 Mbps via the OFDM DSP chip. In the measurement, five phosphor-LED chips in the LED-Tx side carry the same modulated data for VLC transmission. The VLC channel was analyzed and discussed fully in Ref. [2], while the modulation rate of the demonstration was low, the crosstalk influence could be ignored. If some LEDs are utilized in the DC mode or AC mode for VLC transmission, they could generate the background noises affecting

the VLC performance within the frequency of 2 MHz, as investigated in Ref. [30]. Hence, the OFDM DSP chip can be used in VLC system to avoid the low-frequency noise interference.

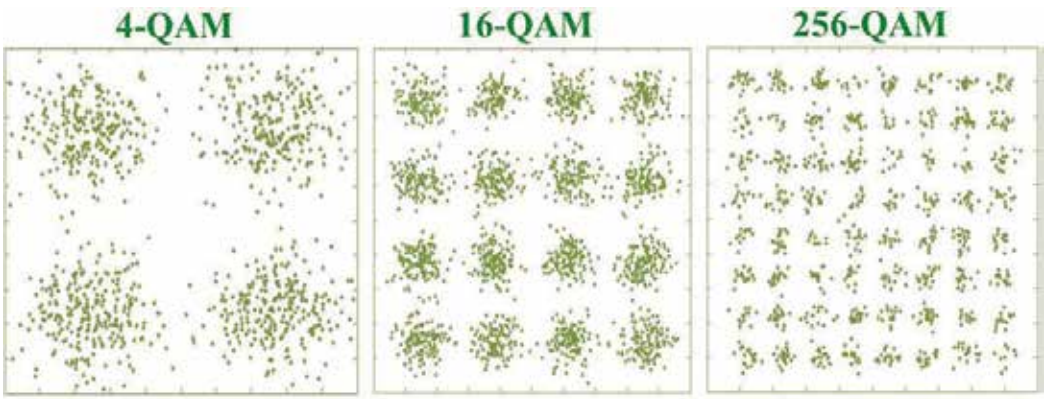

Figure 12. The obtained corresponding constellations at 500 lx of the result in **Figure 11(b)**.

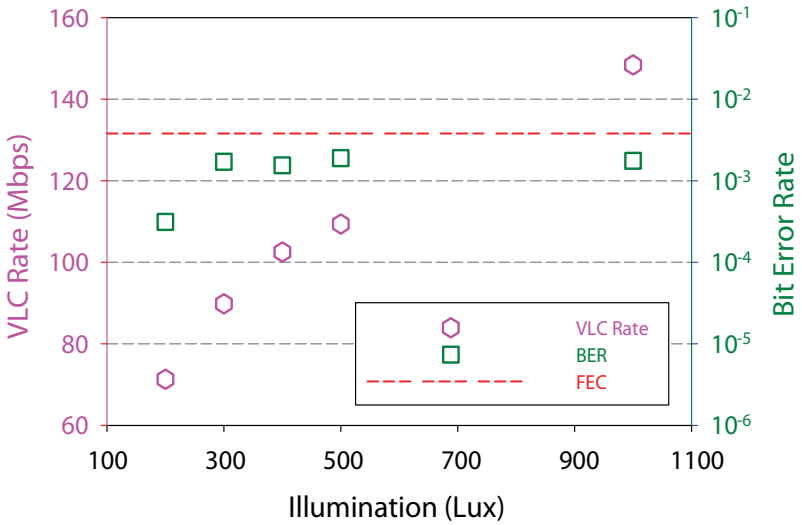

Figure 13. Measured VLC traffic rates and related BERs under different detected illuminances.

Figure 14 presents the new proposed setup of real-time bidirectional phosphor-LED VLC transmission system. In the LED luminary, five phosphor-LED chips with series connection are driven at 15 V for illumination and VLC transmission. In the experiment, the LED Tx-side and client side both contains the analog front-end (AFE) and DSP parts for signal encoding and decoding, as shown in **Figure 14**. Here, we add an infrared (IR) PIN-Rx in the LED luminary, as

http://dx.doi.org/10.5772/67426

shown in **Figure 14**, to detect the upstream IR wireless signal emitted from the client end-user. An 850 nm IR-LED with 40 MHz modulation bandwidth is used in client side to act as the upstream emitter for upstream traffic signal. The emission angle of IR-LED is set at 30°. Besides, a PIN-Rx, having 50 MHz bandwidth in the client side, is used to receive the downstream VLC traffic. Here, we also add the lenses in front of each Tx and Rx for maximizing the performance of VLC signal, as also shown in **Figure 14**. In this work, an 850 nm IR-LED is employed serving as an upstream channel for real-time bidirectional VLC transmission.

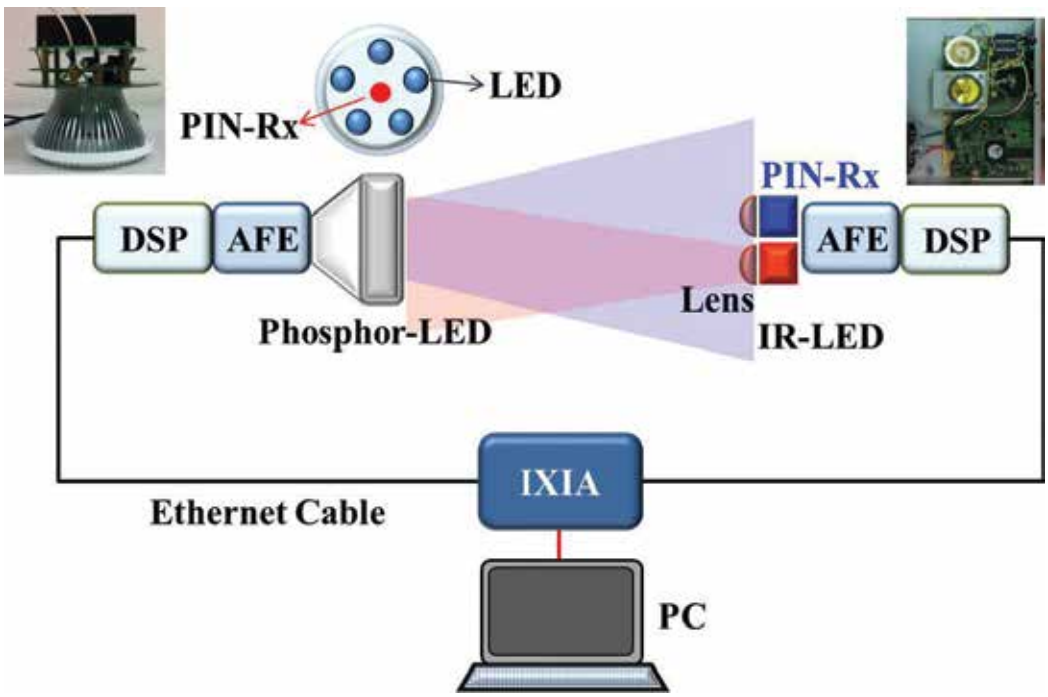

Figure 14. New proposed real-time bidirectional phosphor-LED VLC transmission system.

Furthermore, to understand the connection of the lighting illuminance and the horizontal location of the client side, the VLC vertical transmission distance is set at 200 cm in the central position, as shown in **Figure 15**. And the proposed user client module can be changed at various horizontal positions for detecting VLC signal, as shown in **Figure 15**. In the proposed VLC system, if the horizontal positions are 0, 25, 40, and 60 cm, as depicted in **Figure 15**, respectively, the corresponding illuminances are measured at 500, 400, 300, and 200 lx. In addition, to execute and evaluate the performance of proposed real-time VLC transmission, a network analyzer (IXIA 1600T) is used to test the IP-based throughput for real-time data traffic. Here, a 70 Mbps testing rate of network analyzer can be utilized in the half-duplex VLC transmission for performing VLC performance.

The downstream throughput performance can be performed in relation to the VLC setup of **Figure 15**. Here, the illuminance is 500 lx, when the vertical transmission length is 200 cm.

Figure 16 displays the downstream throughputs under the different data frame sizes of 64, 128, 256, 512, 1024, and 1518, respectively, while the client module is placed to 60 cm away from center location. Hence, we can understand the corresponding illuminance for receiving and decoding the VLC signal under different location. Thus, the illuminances of 500, 400, 300, and 200 lx are measured, when the related horizontal locations are 0, 25, 40, and 60 cm, respectively. Moreover, while the data frame size rises increasingly, the measured traffic throughputs also enhance, as shown in **Figure 15**. The measured throughputs are 15.7, 54.2, 60.2, and 70.0 Mbps under the illuminances of 200, 300, 400, and 500 lx at the 1518 frame size. If the frame size is set at 64, the measured throughputs will be 14.4, 49.5, 55.6, and 63.2 Mbps, respectively.

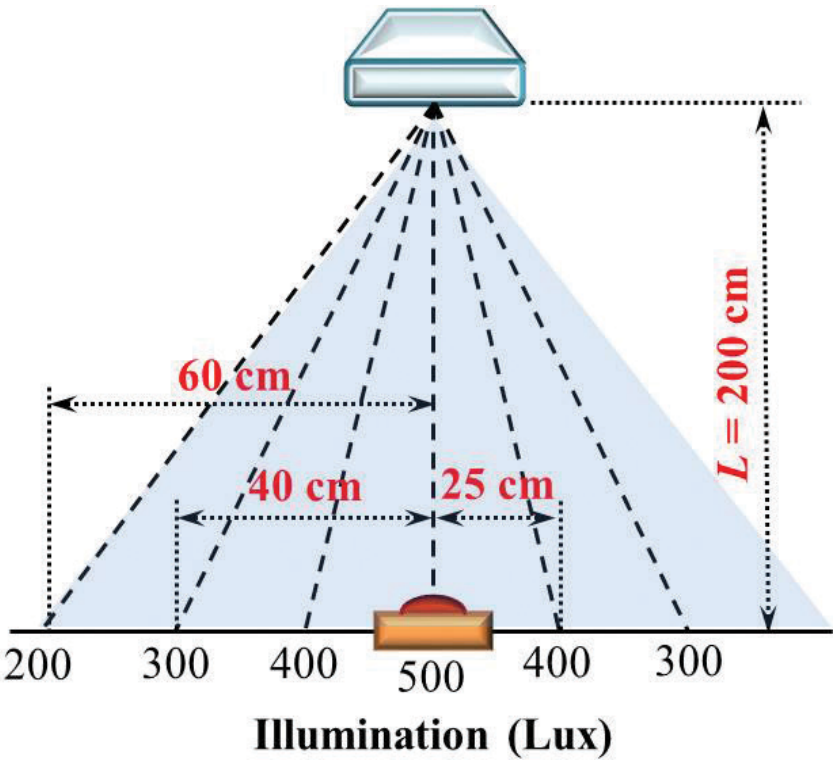

Figure 15. Observed illuminances in the client side at various horizontal positions under a 200 cm vertical transmission distance.

Moreover, to comprehend the practical VLC performance, one to four client modules are used in the same setup of **Figure 15**. Here, the illuminance is set at 500 lx. **Figure 17** present the downstream throughputs under different data frames of 64, 128, 256, 512, 1024, and 1518, respectively, while one to four client modules are employed at the tested LED luminary for measuring VLC traffic. As seen in **Figure 17**, while the frame data size is raised gradually, the retrieved data throughputs also improve. When one client module is utilized in the VLC system, the observed VLC efficiency is the same as **Figure 16**. As the client number increases,

http://dx.doi.org/10.5772/67426

the relative throughput would be decreased, as shown in **Figure 16**. While the frame size is 1518, the observed throughput is 70.0, 31.5, 21.7, and 14.8 Mbps, respectively, if one to four client modules are also employed.

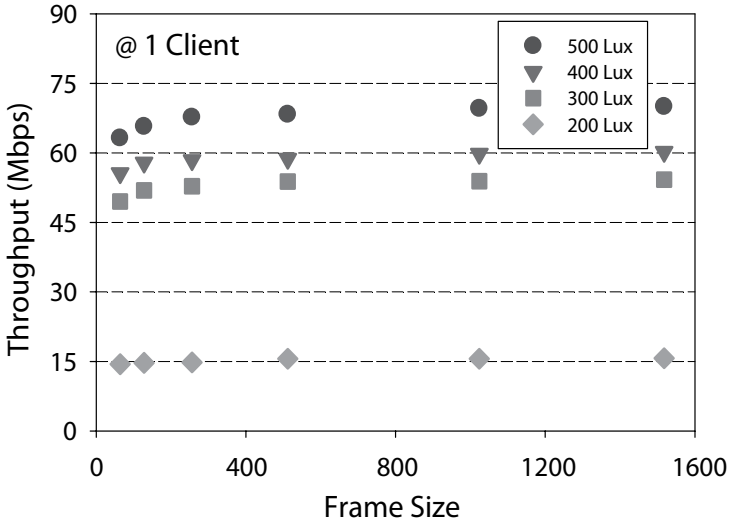

Figure 16. Measured downstream throughputs under the various data frame sizes, when a client module is move outward from central point to 60 cm (200 lx).

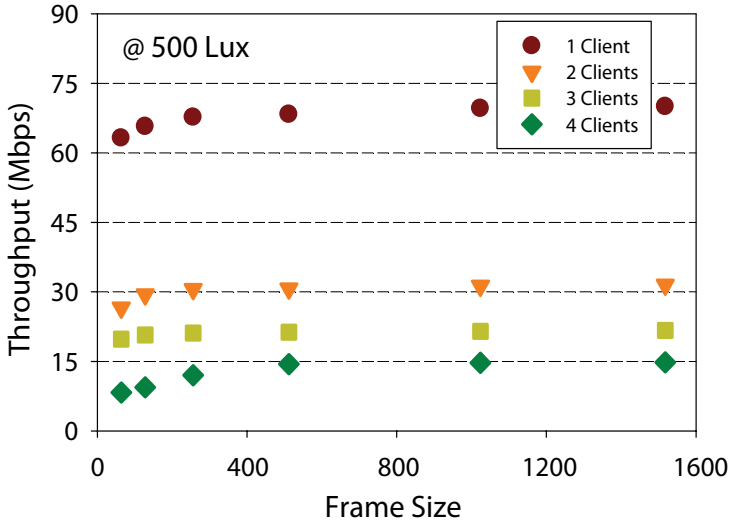

Figure 17. Measured downstream throughput spectra under various data frame sizes of 64, 128, 256, 512, 1024, and 1518, respectively, when one, two, three, and four client modules are used.

Finally, we also execute the 850 nm IR-LED upstream traffic in a 200 cm vertical transmission distance. In this experiment, the real setup is the same as in **Figure 15**. The client module is moved away from the center position to 25, 40, and 60 cm, respectively, for upstream throughput measurement. **Figure 18** shows the maximum upstream throughput with random frame size from 1.7 to 70 Mbps under different illuminances of 200–1000 lx. Therefore, when the commercial half-duplex DSP chip is applied in LED VLC system, the VLC traffic can reach 70 Mbps for real-time bidirectional transmission.

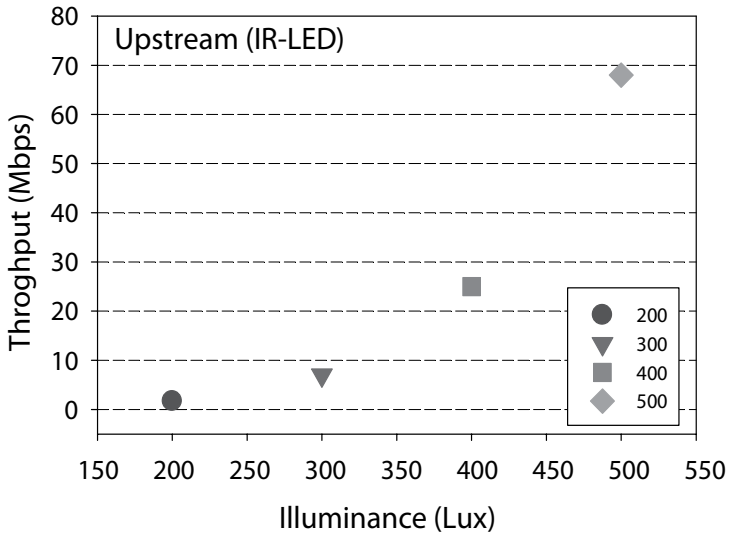

Figure 18. Observed upstream data rate under different detected illuminances in the proposed real-time VLC system.

In summary, we proposed and investigated a 71.3–148.4 Mbps white phosphor-LED VLC system in the free space transmission distance of 140–210 cm in the different illuminances of 200–1000 lx, respectively. Here, a white-light LED luminary, having five cascaded LED chips, was utilized for indoor illumination and wireless access simultaneously. Here, we used the bit-loading OFDM-QAM modulation signal and a novel bias-tee circuit in AFE to improve the modulation bandwidth from 1 to 27 MHz. In addition, we did not utilize a blue optical filter in the client side for improvement. To understand and demonstrate the real-time wireless VLC performance in the proposed phosphor-LED VLC system, a commercial OFDM-based DSP chip was used in the LED lighting side and client sides, simultaneously. Here, the OFDM-DSP chip would result in half-duplex operation. In this investigation, we used a network analyzer to measure the throughput of practical VLC data in the proposed VLC system at different illuminances. As a result, the proposed real-time bidirectional VLC system could accomplish the 70 Mbps data throughputs in a practical transmission distance of 200 cm at the luminance of 500 lx.

http://dx.doi.org/10.5772/67426

4. Conclusion

In conclusion, we reviewed our recent works on the phosphor white-light LED-based wireless VLC and its practical applications. This chapter was divided into two sections. In the first section, to enhance the transmission rate in phosphor-LED VLC system, we proposed and demonstrated a novel multi-band OFDM modulation format for capacity enhancement. According to the proposed architecture, different bands of OFDM signals were used to different LED chips of the LED luminary; it can avoid the power fading and nonlinearity effects of transmission signal by using the same OFDM signal to the whole LED chips. Hence, the maximum enhanced percentage of VLC data rate was 41.1% when the proposed new multi-band OFDM modulation was used.

In the second section, we also demonstrated a 71.3–148.4 Mbps phosphor-LED wireless VLC system at the free space transmission distance between 140 and 210 cm. Moreover, a commercial white-light phosphor-LED luminary with five phosphor-LED chips in series was used for illumination and communication, simultaneously. Here, optical OFDM signal with bit-loading algorithm was applied for VLC transmission. We also investigate an optimal bias-tee circuit with equalization to improve the modulation bandwidth from 1 to 27 MHz. Finally, to understand and demonstrate the real-time LED VLC transmission, a commercial OFDM-based DSP chip was used in the LED transmitting side and client side, simultaneously. Therefore, the proposed real-time half-duplex VLC system could complete around 70 Mbps downstream and upstream traffic throughputs, in a free space transmission distance of 200 cm long for practical in-home illumination and smart city applications.

Acknowledgements

This work was supported by Ministry of Science and Technology, Taiwan, under grants MOST-103-2218-E-035-011-MY3, MOST-104-2628-E-009-011-MY3, and MOST-103-2221-E-009-030-MY3.

Author details

Chien-Hung Yeh[1]* and Chi-Wai Chow[2]

*Address all correspondence to: yehch@fcu.edu.tw

1 Department of Photonics, Feng Cha University, Taichung, Taiwan

2 Department of Photonics, National Chiao Tung University, Hsinchu, Taiwan

References

[1] C. W. Chow, C. H. Yeh, Y. F. Liu, and Y. Liu, "Improved modulation speed of the LED visible light communication system integrated to the main electricity network," Electron. Lett., vol. 47, pp. 867-868, 2011.

[2] T. Komine and M. Nakagawa, "Fundamental analysis for visible-light communication system using LED lights," IEEE Trans. Consum. Electron., vol. 50, pp. 100-107, 2004.

[3] S. Cha, D. Park, Y. Lee, C. Lee, J. Choi, J. Lee, and H. Lee, "AC/DC converter free LED driver for lightings," in Proc. ICCE, pp. 706-708, 2012.

[4] H. H. Tsai, H. C. Chen, C. H. Wang, K. J. Chen, C. W. Hung, C. C. Yeh, C. C. Lin, H. C. Kuo, and T. C. Lu, "Improving the lumen efficiency by air-gap embedded package in white light-emitting diodes," in Proc. CLEO-PR, pp. 138-140, 2011.

[5] N. T. Tran, J. P. You, and F. G. Shi, "Effect of phosphor particle size on luminous efficacy of phosphor-converted white LED," J. Lightwave Technol., vol. 27, pp. 5145-5150, 2009.

[6] Z. Wang, C. Yu, W.-D. Zhong, J. Chen, and W. Chen, "Performance of a novel LED lamp arrangement to reduce SNR fluctuation for multi-user visible light communication systems," Opt. Express, vol. 20, pp. 4564-4573, 2012.

[7] C. W. Chow, Y. Liu, C. H. Yeh, J. Y. Sung, and Y. L. Liu, "A practical in-home illumination consideration to reduce data rate fluctuation in visible light communication", IEEE Wirel. Commun., vol. 22, pp. 17-23, 2015.

[8] W. O. Popoola, "Impact of VLC on light emission quality of white LEDs," J. Lightwave Technol., vol. 34, pp. 2526-2532, 2016.

[9] J. Vucic, C. Kottke, S. Nerreter, K. Habel, A. Buttner, K. D. Langer, and J. W. Walewski, "230 Mbit/s via a wireless visible-light link based on OOK modulation of phosphorescent white LEDs," in Proc. OFC, pp. 1-3, 2010.

[10] C.-H. Yeh, Y.-L. Liu, and C.-W. Chow, "Real-time white-light phosphor-LED visible light communication (VLC) with compact size", Opt. Express, vol. 21, pp. 26192-26197, 2013.

[11] C.-W. Hsu, J.-T. Wu, H.-Y. Wang, C.-W Chow, C.-H. Lee, M.-T. Chu, and C.-H. Yeh, "Visible light positioning and lighting based on identity positioning and RF carrier allocation technique using a solar cell receiver", IEEE Photon. J., vol. 8, #7905507, 2016.

[12] C. H. Yeh, Y. F. Liu, C. W. Chow, Y. Liu, P. Y. Huang, and H. K. Tsang, "Investigation of 4-ASK modulation with digital filtering to increase 20 times of direct modulation speed of white-light LED visible light communication system," Opt. Express, vol. 20, pp. 16218-16223, 2012.

[13] C.-H. Yeh, C.-W. Chow, H.-Y. Chen, Y.-L. Liu, and D.-Z. Hsu, "Investigation of phosphor-LED lamp for real-time half-duplex wireless VLC system", J. Opt., vol. 18, p. 065701, 2016.

[14] Y. F. Liu, C. H. Yeh, C. W. Chow, Y. Liu, Y. L. Liu, and H. K. Tsang, "Demonstration of bi-directional LED visible light communication using TDD traffic with mitigation of reflection interference," Opt. Express, vol. 20, pp. 23019-23024, 2012.

[15] G. Cossu, A. M. Khalid, P. Choudhury, R. Corsini, and E. Ciaramella, "3.4 Gbit/s visible optical wireless transmission based on RGB LED," Opt. Express, vol. 20, pp. B501–B506, 2012.

[16] H. Le-Minh, D. C. O'Brien, G. Faulkner, L. Zeng, K. Lee, D. Jung, and Y. Oh, "High-speed visible light communications using multiple-resonant equalization," IEEE Photon. Technol. Lett., vol. 20, pp. 1243-1245, 2008.

[17] C.-H. Yeh, C.-W. Chow, Y.-L. Liu, H.-Y. Chen, Y. Liu, and J.-C. Hsu, "Investigation of no analogue-equalization and blue filter for 185 Mbps phosphor-LED wireless communication", Opt. Quantum Electron., vol. 47, pp. 1991-1997, 2015.

[18] J.-Y. Sung, C.-W. Chow, and C.-H. Yeh, "Is blue optical filter necessary in high speed phosphor-based white light LED visible light communications?", Opt. Express, vol. 22, pp. 20646-20651, 2014.

[19] E. Costa and S. Pupolin, "M-QAM-OFDM system performance in the presence of a nonlinear amplifier and phase noise," IEEE Trans. Commun., vol. 50, pp. 462-472, 2002.

[20] J.-Y. Sung, C.-W. Chow, and C.-H. Yeh, "Dimming-discrete-multi-tone (DMT) for simultaneous color control and high speed visible light communication," Opt. Express, vol. 22, pp. 7538-7543, 2014.

[21] H.-H. Lu, Y.-P. Lin, P.-Y. Wu, C.-Y. Chen, M.-C. Chen, and T.-W. Jhang, "A multiple-input-multiple-output visible light communication system based on VCSELs and spatial light modulators," Opt. Express, vol. 22, pp. 3468-3474, 2014.

[22] H. Le Minh, D. O'Brien, G. Faulkner, L. Zeng, K. Lee, D. Jung, Y. Oh, and E. T. Won, "100-Mb/s NRZ visible light communications using a postequalized white LED," IEEE Photon. Technol. Lett., vol. 21, pp. 1063-1065, 2009.

[23] H. Elgala, R. Mesleh, H. Haas, and B. Pricope, "OFDM visible light wireless communication based on white LEDs," in Proc. IEEE VCT, pp. 2185-2189, 2007.

[24] R. Mesleh, H. Elgala, and H. Haas, "Performance analysis of indoor OFDM optical wireless communication systems," in Proc. IEEE WCNC, pp. 1005-1010, 2012.

[25] H. Chun, S. Rajbhandari, G. Faulkner, D. Tsonev, H. Haas, and D. O'Brien, "Demonstration of a di-directional visible light communication with an overall sum-rate of 110 Mb/s using LEDs as emitter and detector," in Proc. IEEE IPC, pp. 132-133, 2014.

[26] A. Tsiatmas, C. P. M. J. Baggen, F. M. J. Willems, J. –P. M. G. Linnartz, and J. W. M. Bergmans, "An illumination perspective on visible light communications," IEEE Comm. Mag., vol. 52, no. 7, pp. 64-71, 2014.

[27] C.-H. Yeh, H.-Y. Chen, C.-W. Chow, and Y.-L. Liu, "Utilization of multi-band OFDM modulation to increase traffic rate of phosphor-LED wireless VLC", Opt. Express, vol. 23, pp. 1133-1138, 2015.

[28] C.-H. Yeh, C.-W. Chow, H.-Y. Chen, J. Chen, and Y.-L. Liu, "Adaptive 84.44-190 Mbit/s phosphor-LED wireless communication utilizing no blue filter at practical transmission distance", Opt. Express, vol. 22, pp. 9783-9788, 2014.

[29] Y. Wang, X. Huang, J. Zhang, Y. Wang, and N. Chi, "Enhanced performance of visible light communication employing 512-QAM N-SC-FDE and DD-LMS," Opt. Express, vol. 22, pp. 15328-15334, 2014.

[30] C. W. Chow, C. H. Yeh, Y. F. Liu, and P. Y. Huang, "Background optical noises circumvention in LED optical wireless systems using OFDM," IEEE Photon. J., vol. 5, no. 2, #7900709, 2013.

Chapter 7

Microscopic Particle Manipulation via Optoelectronic Devices

Xiaolu Zhu and Yifei Yang

Additional information is available at the end of the chapter

http://dx.doi.org/10.5772/67928

Abstract

The optoelectronic tweezers (or optically induced dielectrophoresis (DEP)) have showed the ability to parallelly position a large number of colloidal microparticles without any template. The microparticles can be trapped and driven by the dielectrophoretic forces induced by the optical micropatterns in OET devices. In this chapter, the design and fabrication of flat optoelectronic devices (FOD) and hybrid optoelectronic device (HOD) are described. In the typical FOD, the manipulation modes including filtering, transporting, concentrating and focusing controlling regimes are experimentally demonstrated and analyzed. The controllable rotation of self-assembled microparticle chains in FOD has also been investigated, and a method incorporating the optically induced electrorotation (OER) and AC electroosmotic (ACEO) effects is numerically and experimentally implemented for manipulating microparticle chains. Based on the above research of FOD, a hybrid DEP microdevice HOD is conceptually and experimentally proposed. The HOD integrates with metallic microelectrode layer and the underneath photoconductive layer with projected optical virtual electrodes. FOD and HOD hybrid device enables the active driving, large-scale patterning and local position adjustment of microparticles. These techniques make up the shortcoming of low flexibility of traditional metallic microelectrodes and integrate the merits of both the metal electrode-induced and microimage-induced DEP techniques.

Keywords: optoelectronic device, dielectrophoresis, optically induced electrorotation, AC electroosmosis

1. Introduction

The manipulation technique based on dielectrophoresis (DEP) [1–3] is easy-to-use and requires no moving parts, thus can achieve massively paralleled and non-contact manipulation for

particles or cells [4, 5]. It is becoming an important enabling technology in filtering [6–8], concentrating [9–11], transporting [12–14] and flow focusing [15, 16] for microparticles. However, these DEP technologies require design and fabrication of sophisticated electrode structures, which lack flexibility and could not provide real-time alterable electrode-patterns for diverse manipulations. Therefore, how to improve the electrodes' flexibility and reconfigurability has become the key concern in the extended application of DEP. The proposal of optically induced DEP (ODEP) [17, 18] based on photoconductive effect in an optoelectronic device offered a potential option for the design of highly flexible and real-time reconfigurable optical microelectrodes. ODEP-based optoelectronic device offers more opportunity to develop miscellaneous particle manipulating techniques in biomedical microsystems, although ODEP device could not fully supersede the traditional physical electrode array.

Usually, the sample pretreatment process in microfluidic analysis system should include functional units capable of filtering, concentrating, transporting and focusing microparticles to be applicable to different sample handing requirements [9, 19, 20]. Filtration is essentially a separation technology, such as the insulative DEP approach for particle separation [21] and the DEP method for characterizing and distinguish stem cells [6]. Once the target particles are isolated after the filtration or separation, the concentration of the target particle population is sometimes low and requires the concentrating steps for the following detection. By now various DEP concentrations of viruses, bacteria have been reported in the literature [22–24]. The function of transporting microparticles nearly runs through the whole process in the microanalysis system, and biological/chemical applications [14, 25–27]. Besides, as an important approach for the continuous single-particle detection and counting, focusing particles into a straight line are also applied in microfluidic devices. The hydrodynamic forces [28, 29] and electrokinetic force [30, 31] are usually employed to realize flow focusing. However, the above sample handling approaches require fabricating complex multi-functional electrode array or structures to achieve versatile manipulation of the micro/nano bio-particles, and the previous work also has difficulties in providing real-time alterable electrode patterns to accommodate different manipulation requirements. So, the promotion of DEP technology in the application of the micro/nano manipulation faces some restrictions. In recent years, Chiou et al. [18, 32] reported parallel manipulation of single particles using a variant of DEP mechanism—ODEP mechanism which offers the ability to trap single particles parallelly and massively. ODEP has also been used to discriminate normal oocytes at a certain frequency [33]. However, the manipulation regimes still need more systematic study. Therefore, this chapter will experimentally verify and analyze the optical pattern and controlling regimes for filtering, transporting, concentrating and focusing based on ODEP.

In addition to the above manipulation modes for microparticle or cells, the ODEP-based optoelectronic device could serve as a more powerful tool to spatially manipulate and regulate the posture, orientation and position of microparticle chains or other microstructures. The previous methods for manipulating micro-objects usually need templates, physical or chemical reaction process involving more extra techniques [34]. Many of the created particle chains or closely linked chains are immobilized, and their relative positions cannot be stably controlled. The ODEP (also called optoelectronic tweezers, OETs) has showed the ability to parallelly

position colloidal particles without any template [18, 35]. The microparticles can be trapped and driven by the DEP forces induced by the optical micropatterns in optoelectronic devices [36, 37]. However, the rotation of assembled microparticle chains by OETs has rarely been investigated, and the degree of freedom for varying the postures, positions or orientations of the microparticle chains still has limitations. To demonstrate the promoted ability of optoelectronic devices, this chapter will experimentally demonstrate the method incorporating optically induced electrorotation (OER) and alternating current electroosmotic (ACEO) effects, for the formation and motion control of microparticle chains.

By comprehensively analyzing the traditional physical electrode array and ODEP-based optoelectronic device, we further developed a hybrid optoelectronic device (HOD) that could integrate the merits of both the traditional physical electrode array and ODEP-based optoelectronic device. The ODEP-based optoelectronic device offers a flexible and real-time dynamic manipulating scheme but needs more external optic devices; the traditional physical electrode array offers a more stable working status and higher integration but lack the ability of real-time particle manipulation. In Section 5 of this chapter, HOD is conceptually proposed, and its prototype is designed and fabricated. This type of hybrid device enables the active driving, large-scale patterning and locally position adjustment of microparticles.

2. Design and fabrication of optoelectronic devices

2.1. The design and fabrication of flat optoelectronic devices

The flat optoelectronic devices (FOD) consisted of several layers, including indium tin oxide (ITO) and photoconductive layers. To fabricate photoconductive layer of FOD chip (as shown in **Figure 1(a)**), 50-nm doped hydrogenated amorphous silicon (n + *a*-Si:H), 1.5-μm intrinsic *a*-Si:H and 25-nm silicon carbide (SiC*x*) passivation layer were consecutively deposited by plasma-enhanced chemical vapor deposition (PECVD) method on the bottom ITO-coated glass at 200°C. The n+ *a*-Si:H was deposited from a gas ratio of 1% PH_3 in SiH_4, and then, the intrinsic *a*-Si:H was deposited from a gas mixture containing SiH_4 and H_2. Afterwards, the

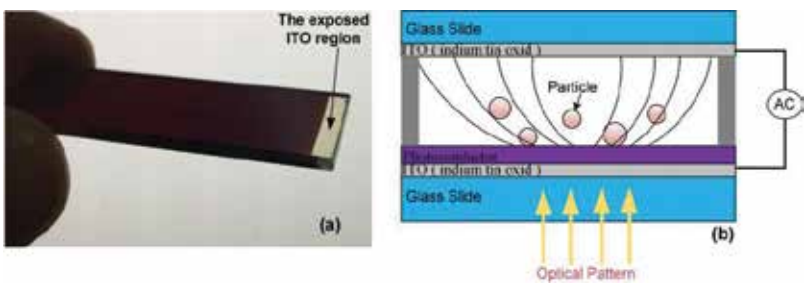

Figure 1. Schematic diagram of the FOD chip based on ODEP mechanism. (a) Photograph of the photoconductive substrate; (b) structure diagram of the ODEP microdevice.

SiC*x* layer was deposited by a SiH_4, CH_3 and N_2 mixture. After that, the ITO layer for bias connections was exposed via reactive ion etch (RIE), as shown in **Figure 1a**. The photoconductive layer of the microdevice consisted of n +*a*-Si:H layer, intrinsic *a*-Si:H layer and SiC*x* layer (as shown in **Figure 1b**). The n + *a*-Si:H layer was used as both a transitionary and adhesive layer from the intrinsic *a*-Si:H layer to the bottom ITO-coated glass. During chip packaging, firstly, a double-faced adhesive tape with a thickness of ~ 100μm was pasted on the four edges of the photoconductive surface to form a microchamber with a scale of ~15 mm × 8 mm. Then a droplet containing microsphere particles was dripped into the microchamber using a pipette. Lastly, the top ITO-glass slide was placed onto the roof of the microchamber to make the microchamber sealed as shown in **Figure 1b**. In the whole ODEP device, a 100-μm insulating spacer was used to maintain the gap between the upper ITO film and lower photoconductive layer (see **Figure 1b**). The alternating current (AC) voltage was supplied between the top and bottom ITO layers.

For the fabricated FOD chip as shown in **Figure 1**, the photoconductor has a high electric impedance (about 1×10^{-6} S/m, for example) prior to illumination, so at this time the majority of the applied voltage drops across the photoconductive layer, which causes a weak, uniform electric field inside the liquid layer. At this state, no ODEP force generates. When a projected light source hits the amorphous silicon layer (photoconductive layer), electron-hole pairs are excited, thus decreasing the impedance of the photoconductive layer by thousands of times (~5000 times, for example), and the electrical conductivity of the photoconductor increases to ~5×10^{-3} S/m. At this state, the virtual electrodes are formed in the photoconductor, and the voltage drop across the liquid layer in the illuminated area is much higher than that in the dark area. Consequently, the bright-dark pattern induces a non-uniform electric field inside this device. The dense electric filed lines appear at the illuminated areas, and the sparse field lines appear at the dark areas as shown in **Figure 1b**. Thus, a DEP force acting on microparticles can be induced in the liquid chamber(or called fluidic chamber), and the time-averaged DEP force acting on the spherical microparticle suspended inside liquid chamber can be mathematically described as follows [38]

$$\langle \mathbf{F}_{\mathrm{DEP}} \rangle = \pi R^3 \varepsilon_{\mathrm{m}} \mathrm{Re}\left[\frac{\tilde{\varepsilon}_{\mathrm{p}} - \tilde{\varepsilon}_{\mathrm{m}}}{\tilde{\varepsilon}_{\mathrm{p}} + 2\tilde{\varepsilon}_{\mathrm{m}}}\right] \nabla E^2 \tag{1}$$

where R is the particle radius, E is the amplitude of electric field, $\tilde{\varepsilon}_{\mathrm{p}}$ and $\tilde{\varepsilon}_{\mathrm{m}}$ are the complex permittivities of the microparticle and suspending medium, respectively, $\tilde{\varepsilon}_{\mathrm{p}} = \varepsilon_{\mathrm{p}} - j\sigma_{\mathrm{p}}/\omega$, and $\tilde{\varepsilon}_{\mathrm{m}} = \varepsilon_{\mathrm{m}} - j\sigma_{\mathrm{m}}/\omega$. Here, σ_{p} and σ_{m} are ohmic electrical conductivities of the microparticle and liquid medium, respectively; ε_{p} and ε_{m} are the permittivities of the microparticle and liquid medium; ω is angular frequency of the electric field or the applied AC voltage. In Eq. (1), the expression in brackets (i.e., $(\tilde{\varepsilon}_{\mathrm{p}} - \tilde{\varepsilon}_{\mathrm{m}})/(\tilde{\varepsilon}_{\mathrm{p}} + 2\tilde{\varepsilon}_{\mathrm{m}})$) is referred to as the Clausius-Mossotti (CM) factor that is denoted as f_{CM}. When $\mathrm{Re}[f_{CM}] > 0$, positive DEP occurs and particles move toward high field regions; when $\mathrm{Re}[f_{CM}] < 0$, negative DEP occurs and particles move toward weak field regions. The particles in solution also undergo the opposing Stokes' drag [39], as follows

$$\boldsymbol{F}_{\mathrm{drag}} = -6\pi\eta RV \tag{2}$$

where V is the particle velocity, and η is the dynamic viscosity of the liquid.

http://dx.doi.org/10.5772/67928

2.2. The design and fabrication of hybrid optoelectronic device (HOD)

The hybrid optoelectronic device (HOD) has a more compact structure, integrating another layer of physical electrode array above the photoconductive layer. In another word, the HOD (several cm^2) integrates with photoconductive layer and metal microelectrodes including the quadrupole electrodes and spiral electrodes as shown in **Figures 2** and **3**. **Figure 2** is the schematic design diagram of this microdevice. This HOD has a hamburger-like structure. The upper plate was transparent ITO conductive glass. The lower plate included the photoconductive layer (or called photoconductor) and the bottom glass slide. The photoconductive *a*-Si:H layer was on the bottom ITO film, and the insulating silicon nitride (or silicon carbide)

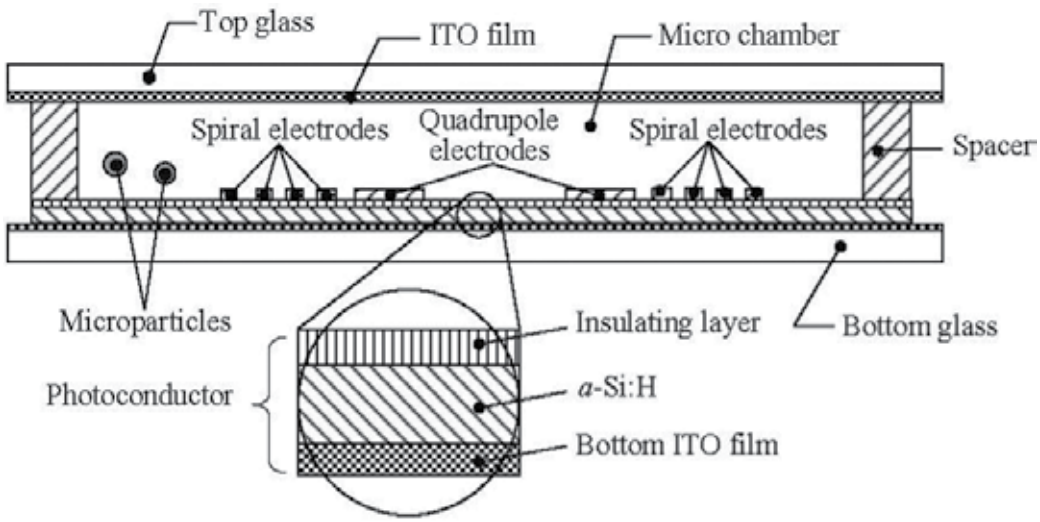

Figure 2. Schematic representation of HOD cross section along the line of AA' in **Figure 3**. The photoconductor consists of insulating layer, *a*-Si:H layer and the bottom ITO film. Only a few representative electrodes are drawn for simplicity.

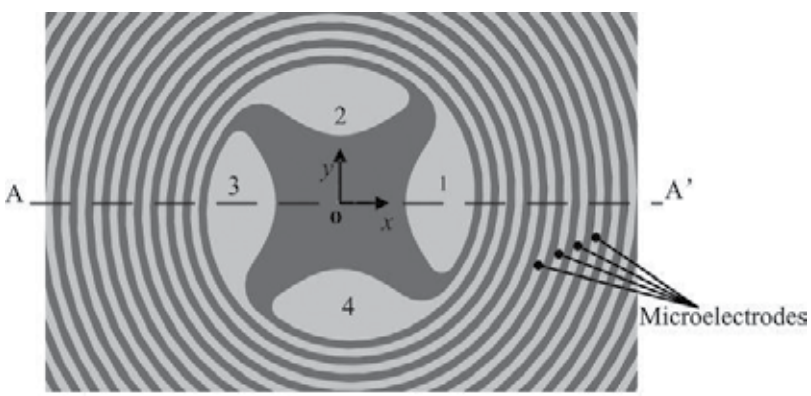

Figure 3. The enlarged drawing of quadrupole electrodes and spiral electrode bars with a width of 25 μm above the photoconductor. The coordinate system is shown, and the direction of z axis complies with right-handed screw rule [40].

layer and metal microelectrode layer were consecutively fabricated above the *a*-Si:H layer. The microfluidic chamber was designed and fabricated for suspending and manipulating particles. The photoconductor layer consisted of a 25–nm-thick insulating silicon nitride layer—to keep the insulation between the metal electrode layer and *a*-Si:H layer, a 1–2-μm-thick *a*-Si:H layer (include intrinsic *a*-Si:H layer and n + *a*-Si:H layer), and a bottom ITO conductive film (50 nm thick) in sequence. The potential of each successive signal could be set as phase shifted by a further multiple of 90° to produce quadrature signals or phases of 0°, 180°, 0°, 180° to produce traditional non-uniform field. It integrated metallic microelectrodes and the underneath photoconductive layer with LED-illuminating microspot.

The microelectrode layer contains of four parallel spiral electrodes as presented in **Figure 2**. When the four spiral electrode elements are energized with sinusoidal voltages with relative phase differences, a travelling electric field is generated and travels along the radial direction of the spiral array. A rotating electric field is also generated in the central free-space region denoted as central region. The spiral electrodes have the advantages of equivalent driving force to the particles at an arbitrary peripheral position. The quadrupole electrodes are located in the central area of spiral electrode array. The central region is surrounded by the quadrupole electrodes as shown in **Figure 3**. The geometrical shape of central region somewhat influences the distribution of the electric field around, and thus the sharp geometry should be avoided.

The experimental platform was established by assembling commercial optics, projector and an upright microscope. A digital micromirror device (DMD)-based projector (SHARP XG) was used as both the light source (via its dc lamp) and the interface between DMD driver circuit and the computer. The DMD forms a light image (or called optical pattern) according to the output signal of the PC's external monitor port. The optical image at the output of the projector lens was collimated, collected and reflected through the reflector at 45 degree to the horizontal and upward directed into a 10X driven lens from the lower location. The optical image was focused by the object lens and finally projected onto the photoconductive layer of ODEP device.

3. Manipulation modes and controlling regimes in FOD

3.1. Filtering

Usually, the impurities or non-target stuff (such as some types of microparticles) in the raw sample should be filtered firstly in the pre-treatment for the sample. The filtering experiment was implemented via an optical line scanning as shown in **Figure 4**. In the filtering experiment, with an applied 20 V_{pp} at 600 kHz, the normal pollen grains with diameters of 17–21 μm and most of the 30-μm diameter polystyrene particles were driven by the optical line with a width of ~70 μm from the upper area (**Figure 4a-b**) toward the bottom area of the view (**Figure 4c-d**). In contrast, the degenerative pollen grains and few polystyrene particles were left behind and stayed in their original positions. Therefore, the filtering function was able to be realized. This separation phenomenon is probably because the particles left behind were difficult to be polarized relative to the normal ones, which resulting in a much smaller DEP force for the abnormal ones. As long as the optical line velocity did not exceed the maximum synchronous velocity

http://dx.doi.org/10.5772/67928

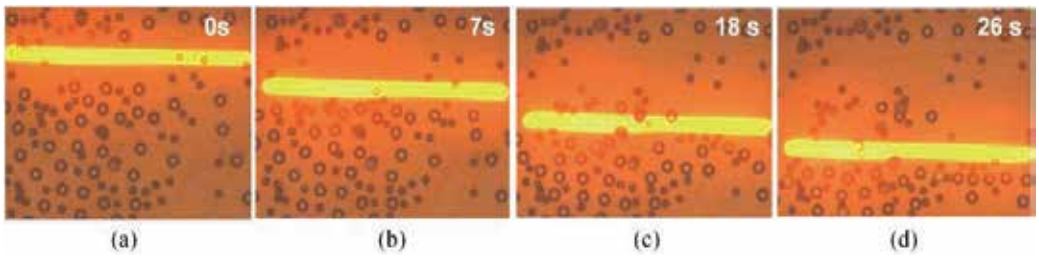

Figure 4. Snapshots of the filtering process in which a scanning light line moved from the top (a) to the bottom (d) of the viewing frame. Degenerative pollen grains and few polystyrene particles were left behind the optical line (b-d), while the normal particles were kinetically actuated by the scanning optical line.

(MS-velocity) of the normal particles [41] (i.e., maximum filtering velocity), the filtering function could be achieved. If the optical line velocity exceeded the MS-velocity, all particles would be left behind the scanning optical line, which made the filtering unavailable. This filtering experiment demonstrated the feasibility of the ODEP filtering.

3.2. Transporting

DEP can trap single particles and then transport the particles to desired positions, and the moving paths can be programed and controlled. As shown in, under the AC voltage of 20 V_{pp} and 1 MHz, two 30-μm diameter particles (**Figure 5a**) were trapped individually and moved along the programmed motion paths (two particles were marked by numbers 1 and 2 shown in **Figure 5**). These two particles were able to move simultaneously according to their own routings. The optical patterns can be controlled by the ODEP controlling software developed by our group. The polystyrene particles were always trapped by two optical rings those have an external diameter of ~150 μm and an interior diameter of ~40 μm during the transporting. Particle 1 and particle 2 kept moving and following the kinetic motion of the optical rings from the initial positions at the upper area (**Figure 5a**) to the lower area (**Figure 5h**) of the snapshot. The two particles moved simultaneously and always kept away from each other during the transporting, as shown in **Figures 5b–g** until they exchanged their positions and arrived at the terminative destinations.

3.3. Concentrating

In many biochemical applications, the reaction is very weak between a single bioparticle and other reagent, but a concentrated population of particles can react with other reagent intensively with much more obvious phenomena. Thus, when the raw sample was filtered and transported to the target locations, the selected particles would need concentration for the following detecting operations. The experiment presented in **Figure 6** serves as a typical example for presenting the concentrating regime of ODEP.

With an applied voltage of 20 V_{pp} at 800 kHz, at an arbitrary area (**Figure 6a**), the microlight pattern with a ring-shape can be used to collect a population of particles and can move the trapped particle population to an arbitrary location. The microparticles stayed inside the optical ring with a uniformly patterned array during the concentrating process (**Figure 6a-f**), and

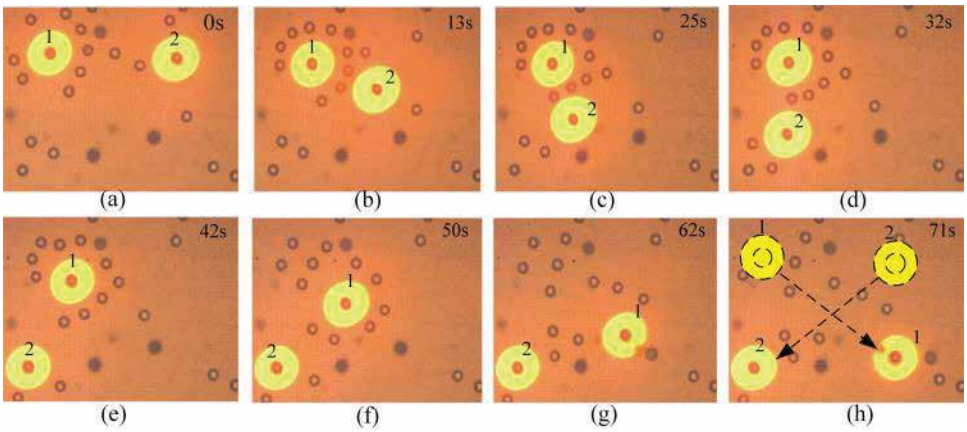

Figure 5. Snapshots of the transporting of two individual polystyrene particles parallelly. Particle 1 and particle 2 were driven from the upper area (a) toward the lower region (h) of the view field and the two particles switched their positions during the downward transporting process over time (c-g). The optical rings drawn by dashed lines in (h) indicate the original positions of the two particles [39].

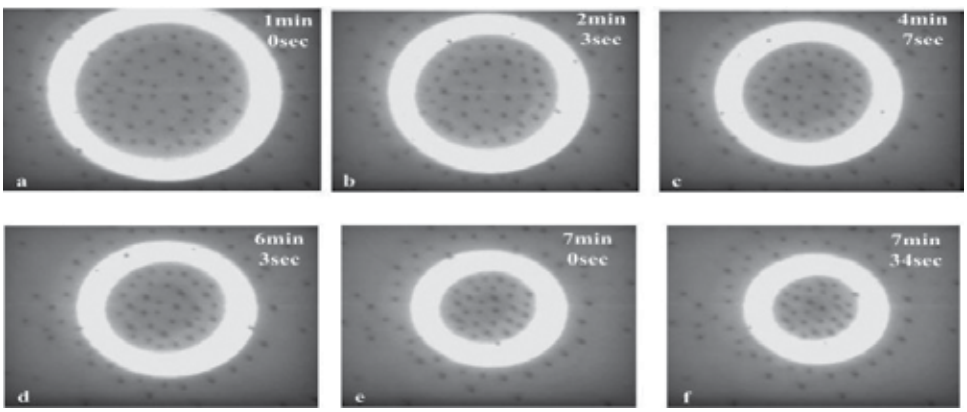

Figure 6. Concentration procedure for the microparticles with a diameter of 4 μm (20 Vpp, 800 kHz). (a) The initial distribution of microparticles. (b-e) The concentrating process of particles over time. (f) The final distribution of concentrated particles.

the distances between adjacent particles always kept the same. At this voltage magnitude, due to the dipole-to-dipole interaction between adjacent particles, the distance between adjacent particles is difficult to eliminate. The distances between particles were obviously larger than the particle diameter (**Figure 6**). If the voltage increased, the ODEP force would increase, which seems to drive the particles more concentrated. However, it is not that case when the voltage was larger than 20 V_{pp} in this experiment, because the increased voltage also enforced the interactional repelling force between particles.

http://dx.doi.org/10.5772/67928

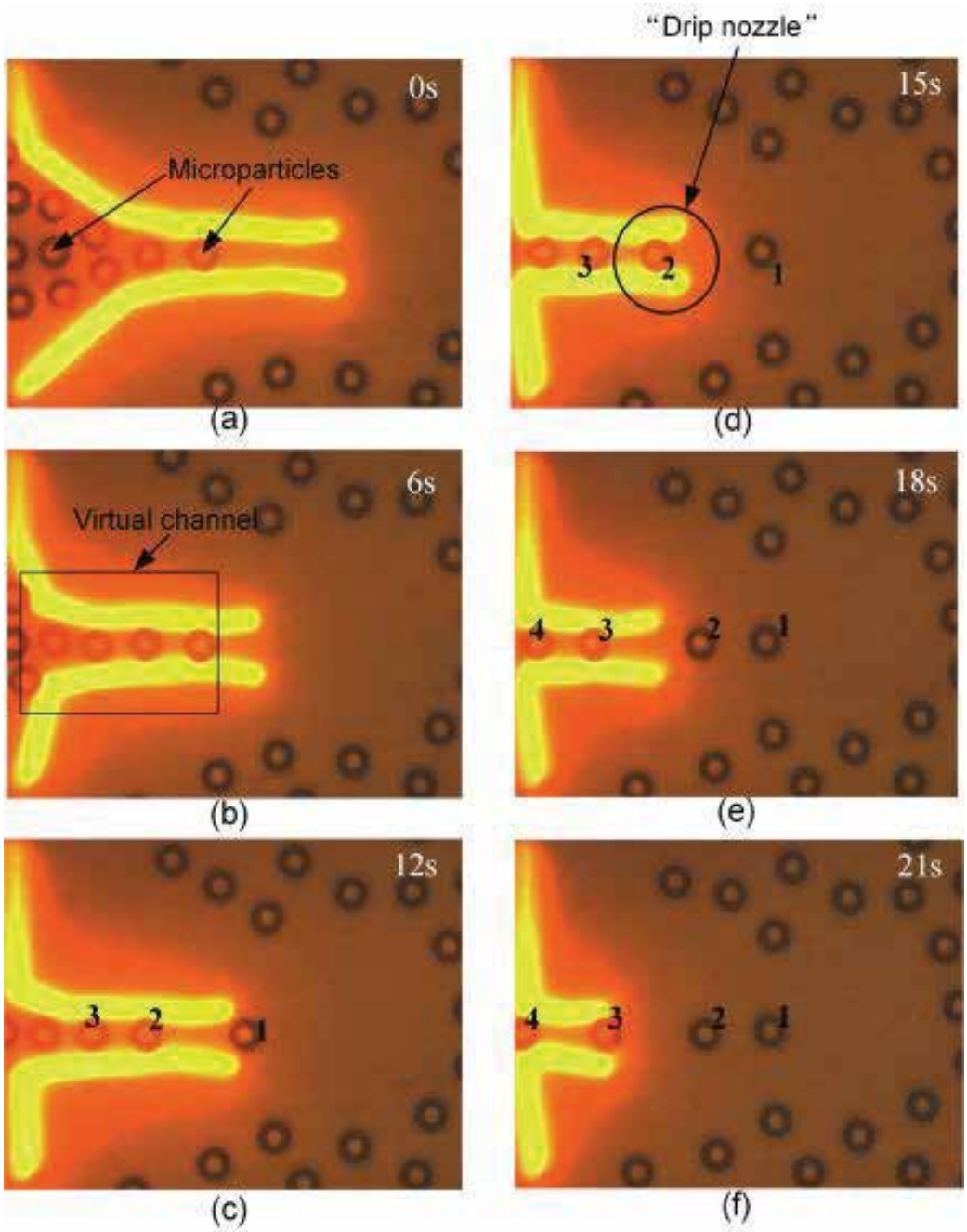

Figure 7. Microparticles are focused into a narrow particle line and ejected one-by-one by optical virtual channel and "drip nozzle." The micropattern projected onto the photoconductive layer to generate a negative ODEP force. Original state (a) is the initial spatial distribution of microparticles. While the optical virtual channel and "drip nozzle" deformed continuously, the random-located particles were gradually forming a straight particle line as shown in (b–d). Finally, the particles formed a linear array, and there were obvious spacing distances between particles as shown in (e–f).

3.4. Focusing

In many biochemical analyses, focusing is another important postprocessing mode apart from the procedures of concentrating particles. Focusing is mainly utilized to continuously and automatically count and detect individual particles. The ability to focus and eject particles based on ODEP is demonstrated in **Figure 7**.

In this study, a "drip nozzle" formed by the optical micropattern projected on the photoconductive layer was used to focus the microparticles in a straight sample flow and eject particles one by one. The optical lines forming the "drip nozzle" were set with a width of around the diameter of microparticles (**Figure 7**). The geometrical shape of optical pattern was real-time controlled so that the "drip nozzle" could continuously deform according to the current distribution of microparticles. The particles with 30-μm diameter moved out from the "drip nozzle" under the repelling ODEP force. This relative motion could also be regarded as the linear flow of particles relative to optical patterns. With an applied 24 V_{pp} at 600 kHz, the microparticles underwent negative ODEP force which always drove particles away from the virtual electrodes (optical micropattern) and thus kept particles horizontally swam in the virtual channel and then swam out of the "drip nozzle" accompany by the deformation of the optical virtual channel and "drip nozzle." Finally, the microparticles were focused into a straight particle line and had obvious spacing distances between particles 1 and 4 (**Figures 7e–f**). In this operation mode, there was no substantial fluidic flow to assist the focusing of the microparticles. The focusing efficiency grew when the optical line width increased but less than twice the particle diameter.

4. Manipulation of self-assembled microparticle chains by electroosmotic flow-assisted electrorotation in FOD

4.1. Background for microparticle chain manipulation

The microscopic particle chain is a common form of assembled particles, which involves in the colloidal, biological, electronic, photonic, magnetic fields. It plays an important role in these fields, as it serves as a link between the nanoscale world and meso- or macroscale objects. Currently, the methods for manipulating microparticle chains have become crucial for developing techniques on patterning magnetic nanoparticle arrays [42], forming regular superstructures by nanoparticles [43], constructing strings of particles [44], and creating multicellular assemblies [45] and live colloidosome structures [46]. In order to flexibly manipulate particle chains, various methods were developed, including the physical methods based on electric field, geometric constraint, dipole-dipole interactions or surface roughness direction [47] and the chemical methods based on linker molecules, oriented aggregation or non-uniform stabilizer distributions [34]. In this study, the formation and rotational manipulation of microparticle chains in real time are experimentally demonstrated by using optically induced electrorotation (OER) and ACEO flow in FOD.

http://dx.doi.org/10.5772/67928

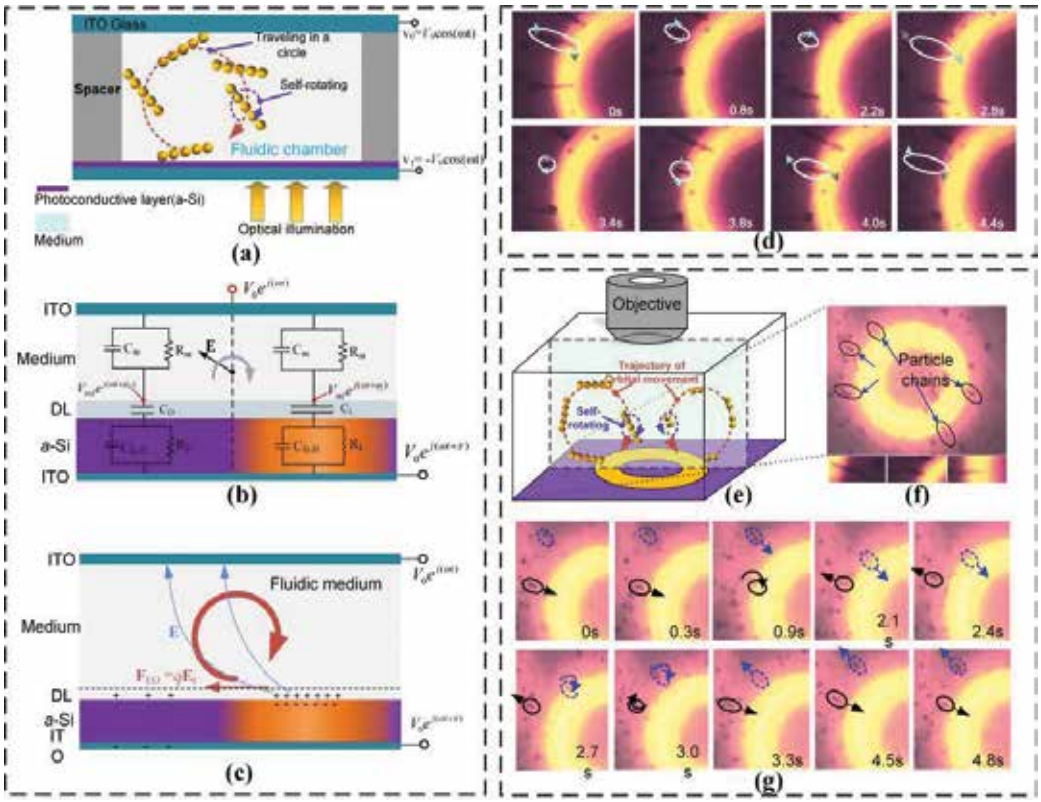

Figure 8. Schematically illustration of the OET device configuration and the principle for generating rotating electric field and ACEO flows. (a) Conceptual illustration of the self-rotation and circular travelling of an entire particle chains. The motion trajectories of the particle chain around the edge of illuminated area are indicated by dashed curve lines. (b) Device structure and mechanism for generating the rotating electric field around the border between dark and light regions. ω is the angular frequency, t is time, and V_0 is amplitude of AC voltage. (c) Electroosmotic fluid roll formed around the border between light and dark regions. (d–g) Experimental results of self-rotation and orbital travelling of an entire particle chains [48].

4.2. Experiment setup and working principle

The structure of the OET device and the scheme for rotating particle chains are conceptually illustrated in **Figure 8**. The equivalent circuit of the OET device is shown in **Figure 8b**. The device is composed by the upper and lower indium tin oxide (ITO) slides, photoconductive layer (hydrogenated amorphous silicon, *a*-Si:H) with a thickness of t_a and a relative permittivity ε_{ar}, and a fluidic chamber with a height of t_m and the applied AC voltages. The electrical conductivity of the photoconductor layer at unilluminated and illuminated areas is denoted as σ_{al} and σ_{ad}, respectively. The microfluidic chamber contains fluidic medium with a relative permittivity ε_{mr} and an electrical conductivity of σ_m. The micro-particles are suspended uniformly in the fluidic chamber at the initial time. The potentials applied at the upper and lower ITO layers.

The principle of the light-dark binary image induced rotating electric field (e-field) is indicated in **Figure 8a–b**. The a-Si:H layer has different impedances on light and dark sides, which leads to the amplitude and phase difference in the electric potentials at upper surface ($V_0 e^{j\omega t}$), photoconductive layer/medium interface in light area ($V_{ml} e^{j(\omega t+\phi_l)}$) and dark area ($V_{md} e^{j(\omega t+\phi_d)}$). In a particular frequency range, these three AC potentials can create a rotating e-field in fluidic medium around the border between light and dark regions, which will lead to self-rotating of the one-dimensional particle chains due to the interaction between the dipole moment of particle chain and rotating e-field.

According to equivalent circuit of the OET device shown in **Figure 8b**, and assuming that the impedance of conjunction between the light and dark regions in the a-Si:H layers is very large indicating no current flows across the border, the potential phasor at the bottom surface of fluidic chamber denoted as Φ_i is given by

$$\Phi_i = V_0 e^{j\omega t}\left(\frac{Z_a + Z_{DL} - Z_m}{Z_a + Z_{DL} + Z_m}\right) = V_{mi} e^{j(\omega t+\varphi_i)} \tag{3}$$

In (3), the subscript i in voltage amplitude V_{mi} and initial phase φ_i and can be replaced by "l" or "d" indicating the light or dark condition for the optical projection onto photoconductor, respectively. The impedance of photoconductor per unit area at light and dark regions is, respectively, expressed as follows

$$Z_{a\_l} = \frac{R_{a\_l}}{1 + j\omega C_a R_{a\_l}} \tag{4}$$

$$Z_{a\_d} = \frac{R_{a\_d}}{1 + j\omega C_a R_{a\_d}} \tag{5}$$

Here, the $C_a\left(=\varepsilon_{ar}\varepsilon_0/t_a\right)$ is the capacitance of *a*-Si:H layer per unit area, $R_{a\_l} = t_a/\sigma_{al}$ and $R_{a\_d} = t_a/\sigma_{ad}$ are the resistances of illuminated and unilluminated *a*-Si:H layer per unit area, respectively. Here, the double layer (DL) forms at medium/a-Si:H interface due to the interfacial polarization as shown in **Figure 8b**. The characteristic thickness of DL (t_{DL}) can be estimated by Debye length [38]. The detailed information could be found in Ref. [49]. The microparticle chain can be self-assembled under an e-field **E**, and then, a polarization could be induced in the particle chain. The effective dipole of the entire particle chain (denoted as **P**c) forms after the establishment of the field **E** with a time delay, because it takes finite time for the dipole moment to completely form. When the e-field **E** rotates, **P**c will follow it and rotates with a phase lag. The particle chain experiences a rotational torque as follows [50, 51],

$$\Gamma = \frac{1}{2}\mathrm{Re}[\,\mathbf{P}_c \times \mathbf{E}^*\,] \tag{6}$$

where $\mathbf{P}_C$ is the complex phasor of the effective dipole moment of a particle chain, and E^* is conjugated complex phasor of the e-field acting on particle chains. More information on effective dipole moment of a particle chain could be found in Refs. [49, 52].

ACEO flow is also induced at appropriate frequencies in the OET or ODEP device. ACEO flow is the motion of fluid due to an interaction between an e-field and the DL induced at medium/a-Si:H interface as shown in **Figure 8c**. The tangential e-field mainly arises around the edges of optical micropatterns. Therefore, the ACEO flow mainly occurs around the optical micropatterns projected on the photoconductive layer. ACEO flow lets the particle chains traveling in a nearly circular trajectory as shown in **Figure 8c**. After applying the voltage,

http://dx.doi.org/10.5772/67928

counterions accumulate in the DL mainly within the illuminated region. Due to the distortion of electrical field induced by the optical pattern, a tangential component of e-field arises round the medium/a-Si:H interface. As a result, the ions in DL are subjected to the tangential electrostatic force along the a-Si:H surface. This force is then transmitted to the fluid and drive the boundary liquid to flow with a slip time-averaged velocity that can be calculated by using the Helmholtz–Smoluchowski equation as in Refs. [53, 54]

$$\langle u_{EO} \rangle = -\frac{1}{2}\frac{\varepsilon_{mr}\varepsilon_0}{\eta_b}\mathrm{Re}\left[(\boldsymbol{\varphi}-\boldsymbol{\varphi}_s)(-\tilde{\mathbf{E}}_t^{\,*})\right], \tag{7}$$

where $\boldsymbol{\phi}$ is the potential phasor just outside the DL, $\boldsymbol{\phi}_s$ is the potential at the non-slip plane close to the solid surface of the DL. $\tilde{E}_t^*$ is the conjugated complex phasor of the tangential e-field just outside the DL. η_b is dynamic viscosity of the bulk solvent. $\eta_b = 1 \times 10^{-3}$ Pa·is for aqueous medium. The electrorotation of particle chains can be solely operated at relative higher frequencies because the ACEO flow decreases significantly at higher frequencies. Appropriately tuning down the frequency can make the ACEO flow available and then assist the self-rotating particle chains to travel along circled trajectory.

In experiment, the polystyrene (PS) microparticles did not form particle chains with a low voltage, but would start to form particle chains when the voltage increases to a threshold value. The PS particles with a diameter of 4 μm self-assembled into chains within the fluidic medium when the applied voltage was increased to 15 V_{pp}. The kinetic motion of particle chains could be enhanced with the increased voltage until 28 V_{pp}. The self-rotation of particle chain around its geometric center was obtained inside fluidic medium at 700 kHz because the ACEO flow can approximately be dismissed at these relatively higher frequencies. As shown in **Figure 8d**, the two ends of particle chains exchanged their positions after 2.8 s and had accomplished the first half-cycle of the rotation. Then, the particle chains continued to self-rotate through the other half-cycle, and it took only 1.6 s. The rotation rate of particle chain varied with time within a single period.

At lower frequencies, the particle chains circularly travelled around the center of fluid roll generated by the optically induced ACEO effect. As indicated in **Figure 8e**, the ACEO flow assisted particle chain rotation can be decomposed into two component motions: the self-rotation and orbital movement of the entire particle chain. **Figure 8f** shows the optically projected ring-shaped micropattern and the formed microparticle chains around the optical ring. The ACEO flow assisted microparticle chain rotation at 480 kHz is shown in **Figure 8g**. The particle chains were moving closer to the edge of optical pattern and turned around through the vertical planes after a short time (less than one second or a few seconds). Then, the particle chains were moving away from the optical ring along the circular path. They continued to turn around at the other corner of the circular path and then moved closer to optical ring again. The orbital moving of particle chains was not uniform motion and the vertical plane in which the circularly orbital movement occurred was approximate parallel to the diametrical dimension of optical ring. The complex movement of particle chains exhibited a three-dimensional (3D) movement of distributed particle chains that had more degrees of freedom than the 2D motion. These results offer more opportunities for spatially controlling the position, posture and orientation of particle chains for the applications regarding electrics, mechanics, optics and biodevices.

5. Manipulation of microparticles in a prototypical HOD

5.1. Integrated design and fabrication of metal electrode array and photoconductive layer

The virtual electrode is actually the microlight image in which we project in vertical direction on the photoconductive layer. It can precisely locate single microparticles and dynamically drive them. On the silicon nitride layer, we fabricated the planar microelectrode structure by photolithography. The microlight pattern could be designed according to specific experimental or application requirement, and it may be, for example, a linear or a spiral microelectrode array. In practical operations, we usually imposed low voltage to prevent insulating layer from breaking down by strong electric field. The spacer to mechanically support the fluidic chamber can be fabricated by polydimethylsiloxane (PDMS) or just double-sided tapes. The electric pads of microelectrodes were led out and connected to external PCB by gold wires. Then, the connectors on PCB were further connected to the external signal generator. The HODs were finally fabricated as shown in **Figure 9**.

The microelectrode array was fabricated by the depositing about 2000nm-thick layer of aluminum or gold on top of the insulating layer through electron beam evaporation. Then, the spiral pattern (**Figure 9**) was produced by standard or "lift-off" lithography process. In the standard lithography process, the corrosion rate needs to be strictly controlled in order to prevent possible damage to the insulating layer as well as the photoconductive layer. In our study, we had also sputtered gold over the silicon carbide layer (insulating layer) and then fabricated microelectrodes. Sputtering process and standard lithography process had a certain impact on the layer-to-layer electrical connections. In general, after the deposition by electron beam evaporations, the insulating property between the aluminum layer and the substrate is better. This usually could meet the insulating requirement of layers in this device. On the other hand, depositing gold by sputtering method onto the photoconductive film usually involved a relatively higher sputtering power or higher temperature in vacuum chamber (typically the sputtering involved a much higher temperature than the electron beam evaporation). These process features may result in that the *a*-Si:H layer was locally damaged within very tiny scale, which may enhance the partial defects in the thin film. More importantly,

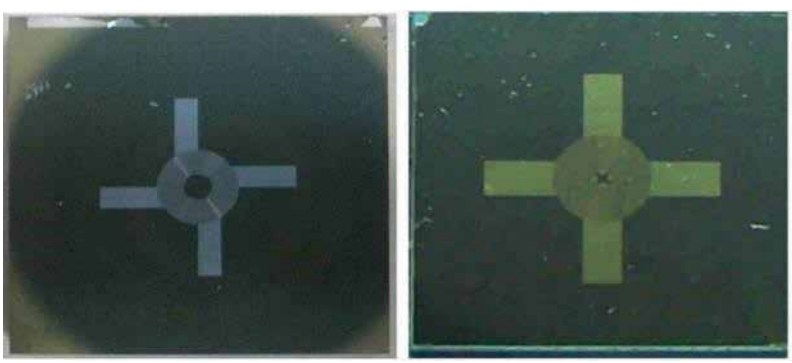

Figure 9. The prototypical photos of the substrates with metal microelectrodes and photoconductive layers for HOD.

http://dx.doi.org/10.5772/67928

the sputtering process also could form the Schottky contact between the metal layer and the below semiconductor layers. Consequently, the time-averaged magnitude of local AC impedance between the metal layer and bottom ITO layer was smaller. The measurement results showed a low resistance of a few hundred ohms to thousands of ohms between the metal layer and the bottom ITO layer.

5.2. Experiment result of the distribution of particles when light pattern is off

In this experiment, a 10 V peak-to-peak (V_{pp}) AC bias with a frequency of 1 MHz is applied between the top and bottom ITO electrodes, and the light pattern is not projected onto the HOD. The metal electrodes might be connected to the bottom ITO layer by a very low resistance through the Schottky contact between the metal and photoconductive layer and/or through the local defects of *a*-Si:H layer, when the AC voltage was applied. Therefore, most of the applied voltage drops across the liquid layer (for the resistance between the metal electrodes, and bottom ITO electrode is very small). However, in the gap region between the metal electrodes, most of the voltage drops across the photoconductive layer, only minority of the voltage drops across the liquid layer. Therefore, most of the particles moved to the gap region between metal electrodes by the negative DEP, as the white dotted circles indicated in **Figure 10A** and **B**. In addition, a few particles remained on the metal electrodes, as shown in **Figure 10A**. The single particle on metal electrode was initially near the center region of the metal electrodes where the DEP is very small, and it was already under the balanced state from the very beginning. That is why it remained on the electrodes instead of being driven to the gap region. The Schottky contact formed at the interface of the gold layer and photoconductive layer, the electrons flew from the photoconductive layer to the metallic layer. It enhanced the short connection effect between the bottom ITO film and the metal electrodes.

5.3. Experiment result of the particle's assembly under the assistance of light pattern

Before the microlight pattern was projected onto the HOD, the particles had distributed along the trend of spiral electrodes (**Figure 10**). The particles could be actuated by moving the microlight pattern when the light pattern (the diameter was nearly 120μm in this experiment)

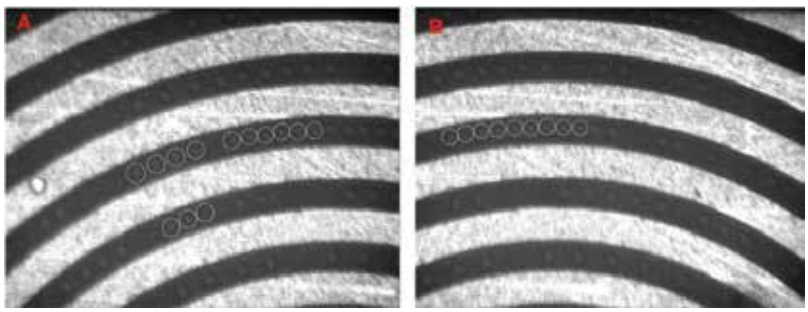

Figure 10. Generation and distribution of particle array or chains when ac voltage (10 Vpp, 1 MHz) was applied between the top and bottom ITO layers. (A) The arrayed microparticles in the gap of electrodes and a few ones on the metal electrodes. (B) The arrayed microparticles all in the gap of electrodes. The metallic electrode array was not energized by external voltages. Particles diameter is 10 μm. The widths of the electrodes and gap are both 20 μm.

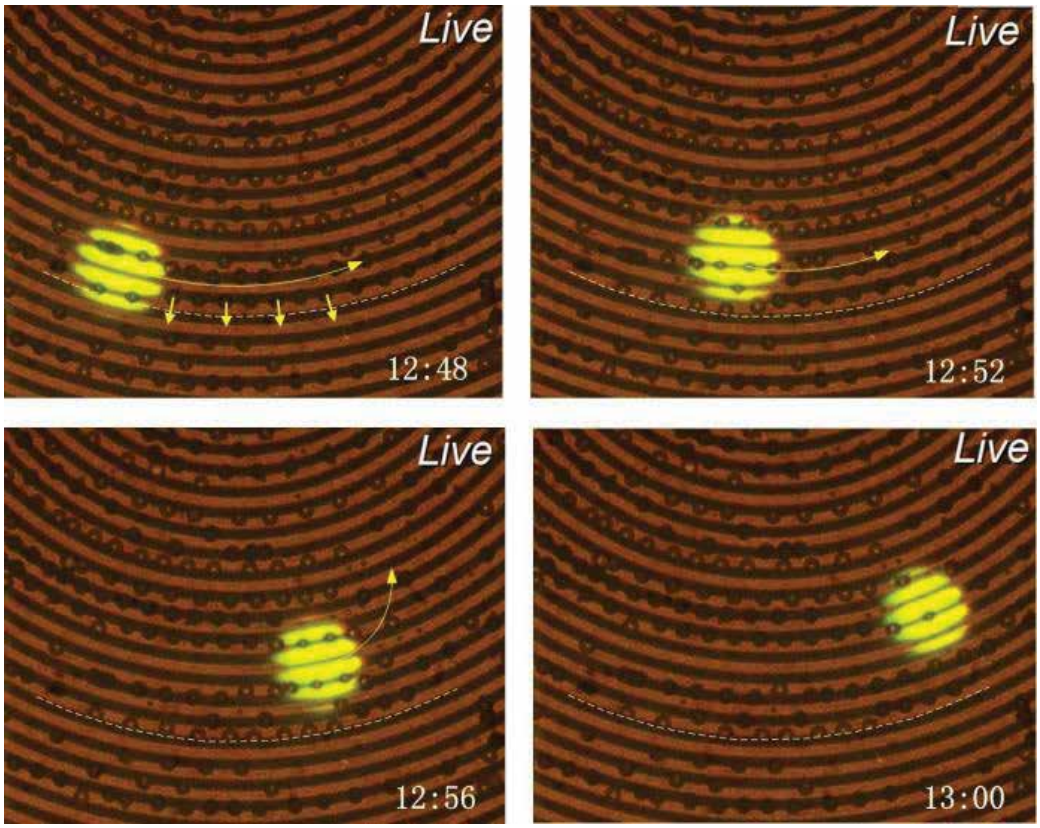

Figure 11. Particle manipulation in typical HOD. The curve arrow indicated the moving track of the light spot. Particles along spiral electrode and away from the white dotted arc were gradually moving closer to the position marked by the dotted arc due to the repulsive force from the light spot. The AC voltage between the top and bottom ITO layers is 5 V_{pp} and 1 M Hz. The particle diameter was 30 μm, and the widths of the electrode and gap were both 20 μm.

was projected as shown in **Figure 11**. The light pattern produced by LED can meet the needs of the power for operation. The spatial interval between the particles can be manipulated by adjusting the magnitude of the voltage applied between the upper and lower ITO layers, and the increase in voltage leads to larger separation between the particles. The metallic electrode array was not electrically energized. As shown in **Figure 11**, the DEP forces acting on microparticles were generated due to the participation of both the planar metal electrodes and microlight pattern in the electric field generated by the voltage applied between the upper and lower ITO layers. The curve arrow indicated the moving track of the light spot. Particles along spiral electrode and away from the white dotted arc were gradually moving closer to the position marked by the dotted arc due to the repulsive force from the light spot. This HOD can meet the need of the large-scale particles manipulation requiring the particles to form specific geometrical array. In this device, incorporation of metal microelectrode array was more suitable for the situation that the required separation between particles was small, and the tracks of particle distribution are more elaborate than the virtual electrode produced by light projection system. That is because microlight pattern needs to be produced by using

http://dx.doi.org/10.5772/67928

even more complex and higher cost optical device, and the Gaussian distribution of light pattern border, the diffraction and the scattering may also limit the light pattern to have the smaller, finer and sharper geometry. This combination of metal microelectrode and light-induced virtual electrode in HOD is appropriate for the situation that the area for arranging particles is compact, and the particular geometric form (like curve shape distribution) is expected. This technique may also have the potential for manipulating large number of cells and be incorporated into the self-organization scheme for constructing multicellular structure [55, 56], in order to develop biomaterials applied in regenerative medicine.

6. Summary

In this chapter, *firstly*, the design and fabrication of flat optoelectronic devices (FOD) and hybrid optoelectronic device (HOD) were elucidated. *Secondly*, the scanning filtering, multiparticle parallel transportation, particle concentration and the focusing for single particle queue were experimentally demonstrated and analyzed. *Thirdly*, the self-electrorotation and circularly orbital movement of the microparticle chains in real time are experimentally demonstrated by FOD. The rotating electrical field for implementing the optically induced electrorotation (OER) of particle chains can be generated by utilizing the different impedances of photoconductor layer at light and dark areas. The optically induced ACEO flow was simultaneously produced accompanying the OER effect. This non-contact manipulation method for rotating particle chains has the potential for spatially regulating the posture, orientation and position of microparticle chains or microstructures. *Fourthly*, The hybrid device HOD enables rapid large-scale patterning and locally position adjustment of single microparticles. This technique makes up the shortcoming of lacking flexibility possessed by metallic microelectrodes and takes advantages of both electrode-based DEP and microimage-based DEP technologies.

Acknowledgements

This work was supported by grants from the National Natural Science Foundation of China (51505127), the Natural Science Foundation of Jiangsu Province (BK20161197), the Changzhou Sci&Tech Program (CE20165029), and the Fundamental Research Funds for the Central Universities of China (2015B04414). Parts of this chapter are reproduced from authors' recent conference publication [40, 48].

Author details

Xiaolu Zhu* and Yifei Yang

*Address all correspondence to: zhuxiaolu@hhu.edu.cn

College of Mechanical and Electrical Engineering, Hohai University, China

References

[1] Medoro G, Nastruzzi C, Guerrieri R, Gambari R, and Manaresi N. Lab on a chip for live-cell manipulation. IEEE Design & Test of Computers. 2007; 24(1): 26-36.

[2] Vahey MD and Voldman J. An equilibrium method for continuous-flow cell sorting using dielectrophoresis. Analytical Chemistry. 2008; 80(9): 3135-3143.

[3] Wang X-B, Huang Y, Gascoyne PRC, and Becker FF. Dielectrophoretic manipulation of particles. IEEE Transactions on Industry Applications. 1997; 33(3): 660-669.

[4] Gascoyne PRC and Vykoukal JV. Dielectrophoresis-based sample handling in general-purpose programmable diagnostic instruments. Proceedings of the IEEE. 2004; 92(1): 22-42.

[5] Small WR, Stoyanov SD, and Paunov VN. Scaffold free fabrication of linear multicellular assemblies by dielectrophoretic hydrogel trapping technique. Biomaterials Science. 2013; 1(9): 996-1002.

[6] Flanagan LA, Lu J, Wang L, Marchenko SA, Jeon NL, Lee AP, and Monuki ES. Unique dielectric properties distinguish stem cells and their differentiated progeny. Stem Cells. 2008; 26(3): 656-65.

[7] Iliescu C, Tresset G, and Xu G. Dielectrophoretic field-flow method for separating particle populations in a chip with asymmetric electrodes. Biomicrofluidics. 2009; 3(4): 044104-10.

[8] Eguchi M, Imasato H, Yamakawa T, and Ieee, Separation of blood cells by employing dielectrophoresis and traveling-wave electric fields. 2012 World Automation Congress; 2012.

[9] Schonfeld F, Griebel A, Konrad R, Rink S, and Karlsen F. Development of a [mu]-concentrator using dielectrophoretic forces. Journal of the Association for Laboratory Automation. 2002; 7(6): 130-134.

[10] Yokokawa R, Manta Y, Namura M, Takizawa Y, Le NCH, and Sugiyama S. Individual evaluation of DEP, EP and AC-EOF effects on lambda DNA molecules in a DNA concentrator. Sensors and Actuators B-Chemical. 2010; 143(2): 769-775.

[11] Cheng IF, Chang HC, Chen TY, Hu CM, and Yang FL. Rapid (<5 min) identification of pathogen in human blood by electrokinetic concentration and surface-enhanced raman spectroscopy. Scientific Reports. 2013; 3: 2365. DOI: 10.1038/srep02365

[12] Crews N, Darabi J, Voglewede P, Guo F, and Bayoumi A. An analysis of interdigitated electrode geometry for dielectrophoretic particle transport in micro-fluidics. Sensors and Actuators B: Chemical. 2007; 125(2): 672-679.

[13] Dos Santos MVP, Lima LPB, Mayer RA, Beron F, Pirota KR, and Diniz JA. Dielectrophoretic manipulation of individual nickel nanowires for electrical transport measurements. Journal of Vacuum Science & Technology B. 2015; 33(3): 031804.

[14] Hossan MR, Dutta P, Dillon R, and ASME. Numerical investigation of DC dielectrophoretic particle transport. ASME Fluids Engineering Division Summer Meeting—2014, Vol 2: Fora; 2014.

[15] Fu LM, Yang RJ, Lin CH, Pan YJ, and Lee GB. Electrokinetically driven micro flow cytometers with integrated fiber optics for on-line cell/particle detection. Analytica Chimica Acta. 2004; 507(1): 163-169.

[16] Yao B, Luo GA, Feng X, Wang W, Chen LX, and Wang YM. A microfluidic device based on gravity and electric force driving for flow cytometry and fluorescence activated cell sorting. Lab on a Chip. 2004; 4(6): 603-607.

[17] Jamshidi A, Pauzauskie PJ, Schuck PJ, Ohta AT, Chiou PY, Chou J, Yang PD, and Wu MC. Dynamic manipulation and separation of individual semiconducting and metallic nanowires. Nature Photonics. 2008; 2(2): 85-89.

[18] Chiou PY, Ohta AT, and Wu MC. Massively parallel manipulation of single cells and microparticles using optical images. Nature. 2005; 436(7049): 370-372.

[19] Tsutsui H and Ho CM. Cell separation by non-inertial force fields in microfluidic systems. Mechanics Research Communications. 2009; 36(1): 92-103.

[20] Cheng IF, Chang HC, Hou D, and Chang HC. An integrated dielectrophoretic chip for continuous bioparticle filtering, focusing, sorting, trapping, and detecting. Biomicrofluidics. 2007; 1(2): 021503.

[21] Hawkins BG, Smith AE, Syed YA, and Kirby BJ. Continuous-flow particle separation by 3D insulative dielectrophoresis using coherently shaped, dc-biased, ac electric fields. Analytical Chemistry. 2007; 79(19): 7291-7300.

[22] Yeo WH, Lee HB, Kim JH, Lee KH, and Chung JH. Nanotip analysis for dielectrophoretic concentration of nanosized viral particles. Nanotechnology. 2013; 24(18):185502. DOI: 10.1088/0957-4484/24/18/185502

[23] Maruyama H, Kotani K, Masuda T, Honda A, Takahata T, and Arai F. Nanomanipulation of single influenza virus using dielectrophoretic concentration and optical tweezers for single virus infection to a specific cell on a microfluidic chip. Microfluidics and Nanofluidics. 2011; 10(5): 1109-1117.

[24] Cho YK, Kim TH, and Lee JG. On-chip concentration of bacteria using a 3D dielectrophoretic chip and subsequent laser-based DNA extraction in the same chip. Journal of Micromechanics and Microengineering. 2010; 20(6): 1023-1035.

[25] Sen AK and Sajeesh P. Electrokinetic transport and separation of droplets in a microchannel. Microfluidics and Nanofluidics. 2014; 17(1): 97-106.

[26] Wang CH, Wang XZ, and Jiang ZD. Dielectrophoretic driving of blood cells in a microchannel. Biotechnology & Biotechnological Equipment. 2011; 25(2): 2405-2411.

[27] Khoshmanesh K, Nahavandi S, Baratchi S, Mitchell A, and Kalantar-Zadeh K. Dielectrophoretic platforms for bio-microfluidic systems. Biosensors & Bioelectronics. 2011; 26(5): 1800-1814.

[28] Zhang JM, Aguirre-Pablo AA, Li EQ, Buttner U, and Thoroddsen ST. Droplet generation in cross-flow for cost-effective 3D-printed "plug-and-play" microfluidic devices. RSC Advances. 2016; 6(84): 81120-81129.

[29] Pittermannova A, Ruberova Z, Zadrazil A, Bremond N, Bibette J, and Stepanek F. Microfluidic fabrication of composite hydrogel microparticles in the size range of blood cells. RSC Advances. 2016; 6(105): 103532-103540.

[30] Song YX, Wang CF, Li MQ, Pan XX, and Li DQ. Focusing particles by induced charge electrokinetic flow in a microchannel. Electrophoresis. 2016; 37(4): 666-675.

[31] Li D, Lu XY, Song YX, Wang JS, Li DQ, and Xuan XC. Sheathless electrokinetic particle separation in a bifurcating microchannel. Biomicrofluidics. 2016; 10(5): 1-13.

[32] Park S, Pan C, Wu T-H, Kloss C, Kalim S, Callahan CE, Teitell M, and Chiou EPY. Floating electrode optoelectronic tweezers: light-driven dielectrophoretic droplet manipulation in electrically insulating oil medium. Applied Physics Letters. 2008; 92(15): 151101.

[33] Hwang H, Lee D-H, Choi W, and Park J-K. Enhanced discrimination of normal oocytes using optically induced pulling-up dielectrophoretic force. Biomicrofluidics. 2009; 3(1): 14103.

[34] Kitching H, Shiers MJ, Kenyon AJ, and Parkin IP. Self-assembly of metallic nanoparticles into one dimensional arrays. Journal of Materials Chemistry A. 2013; 1(24): 6985-6999.

[35] Hwang H and Park JK. Optoelectrofluidic platforms for chemistry and biology. Lab Chip. 2011; 11(1): 33-47.

[36] Zhu XL, Yin ZF, and Ni ZH. Dynamics simulation of positioning and assembling multi-microparticles utilizing optoelectronic tweezers. Microfluidics and Nanofluidics. 2012; 12(1-4): 529-544.

[37] Yang YJ, Mao YF, Shin KS, Chui CO, and Chiou PY. Self-locking optoelectronic tweezers for single-cell and microparticle manipulation across a large area in high conductivity media. Scientific Reports. 2016; 6: 22630. DOI: 10.1038/srep22630

[38] Morgan H and Green NG. AC electrokinetics: colloids and nanoparticles. Micro-technologies and Microsystems Series, 2. 2003, Philadelphia, PA: Research Studies Press.

[39] Zhu XL, Yin ZF, Gao ZQ, and Ni ZH. Experimental study on filtering, transporting, concentrating and focusing of microparticles based on optically induced dielectrophoresis. Science China-Technological Sciences. 2010; 53(9): 2388-2396.

[40] Zhu XL, Yi H, Ni ZH, and IEEE. Novel design of multiphase optoelectronic microfluidic device for dielectric characterization of single biological or colloidal particles. 2009 ICME International Conference on Complex Medical Engineering. 2009. 542-547.

[41] Zhu XL, Yi H, and Ni ZH. Frequency-dependent behaviors of individual microscopic particles in an optically induced dielectrophoresis device. Biomicrofluidics. 2010; 4(1) :013202. DOI:10.1063/1.3279788

[42] Schelhas LT, Farrell RA, Halim U, and Tolbert SH. Directed self-assembly as a route to ferromagnetic and superparamagnetic nanoparticle arrays. Advanced Functional Materials. 2014; 24(44): 6956-6962.

[43] Zhou F, Xie MX, and Chen DY. Structure and ultrasonic sensitivity of the superparticles formed by self-assembly of single chain janus nanoparticles. Macromolecules. 2014; 47(1): 365-372.

[44] Termonia Y. Entropy-driven self-assembly of nanoparticles into strings. Colloids and Surfaces A: Physicochemical and Engineering Aspects. 2014; 447: 23-27.

[45] Brandy M-L, Cayre OJ, Fakhrullin RF, Velev OD, and Paunov VN. Directed assembly of yeast cells into living yeastosomes by microbubble templating. Soft Matter. 2010; 6(15): 3494-3498.

[46] Fakhrullin RF, Brandy M-L, Cayre OJ, Velev OD, and Paunov VN. Live celloidosome structures based on the assembly of individual cells by colloid interactions. Physical Chemistry Chemical Physics. 2010; 12(38): 11912-11922.

[47] Kraft DJ, Ni R, Smallenburg F, Hermes M, Yoon K, Weitz DA, van Blaaderen A, Groenewold J, Dijkstra M, and Kegel WK. Surface roughness directed self-assembly of patchy particles into colloidal micelles. Proceedings of the National Academy of Sciences of the United States of America. 2012; 109(27): 10787-10792.

[48] Zhu X. Electroosmotic flow assisted rotation of self-assembled microparticle chains using optoelectronic tweezers. in IEEE International Conference on Nano/micro Engineered and Molecular Systems. 2015.

[49] Zhu X. Manipulation of self-assembled microparticle chains by electroosmotic flow assisted electrorotation in an optoelectronic device. Micromachines. 2015; 6(9): 1387-1405.

[50] Jones TB. Electromechanics of Particles. 1995, New York: Cambridge University Press.

[51] Jones TB. Basic theory of dielectrophoresis and electrorotation. IEEE Engineering in Medicine and Biology Magazine. 2003; 22(6): 33-42.

[52] Jiang ZH, He XD, Han JC, Zhang BM, and Du SY. Fractal characterization of the dipole moments of dielectric particle chains. Journal of Electrostatics. 1998; 44(1-2): 47-51.

[53] Ramos A, Morgan H, Green NG, Gonzalez A, and Castellanos A. Pumping of liquids with traveling-wave electroosmosis. Journal of Applied Physics. 2005; 97(8): 084906.

[54] Lyklema J. Fundamentals of Interface and Colloid Science, Volume II: Solid–Liquid Interfaces. Vol. 2. New York: Academic Press; 1995.

[55] Zhu X, Gojgini S, Chen T-H, Teng F, Fei P, Dong S, Segura T, and Ho C-M. Three dimensional tubular structure self-assembled by vascular mesenchymal cells at stiffness interfaces of hydrogels. Biomedicine & Pharmacotherapy. 2016; 83: 1203-1211.

[56] Zhu X and Yang H. In-silico constructing three-dimensional hollow structure via self-organization of vascular mesenchymal cells. in *The 16th International Conference on Nanotechnology (IEEE NANO 2016)*. 2016. Sendai, Japan: IEEE.

Chapter 8

Hybrid Silicon-Organic Heterojunction Structures for Photovoltaic Applications

Andrey Kosarev, Ismael Cosme,
Svetlana Mansurova, Antonio J. Olivares and
Hiram E. Martinez

Additional information is available at the end of the chapter

http://dx.doi.org/10.5772/67565

Abstract

The concept for inorganic-organic device is an attractive technology to develop devices with better characteristics and functionality due to the complementary advantages of inorganic and organic materials. This chapter provides an overview of the principal requirements for organic and inorganic semiconductor properties and their fabrication processes and focus on the compatibility between low temperature plasma enhanced chemical vapor deposition (PECVD) and polymer organic materials deposition. The concept for inorganic-organic device was validated with the fabrication of three hybrid thin film photovoltaic structures, based on hydrogenated silicon (Si:H), organic poly(3-hexythiophene): methano-fullerenephenyl-C61-butyric-acid-methyl-ester (P3HT:PCBM), and poly(3,4 ethylenedioxythiophene): poly(4-styrenesulfonate) (PEDOT:PSS) films. Optoelectronic characteristics, performance characteristics, and interfaces of the different configurations aspects are discussed. Hybrid ITO/PEDOT:PSS/(i)Si:H/(n)Si:H structure results in a remarkably high short circuit current density as large as 17.74 mA/cm^2, which is higher than the values in organic or inorganic reference samples. Although some hybrid structures demonstrated substantial improvement of performance, other hybrid structures showed poor performance, further R&D efforts seem to be promising, and should be focused on deeper study of organic materials and related interface properties.

Keywords: organic semiconductors, plasma deposited materials, thin film devices, hybrid devices, solar cells

1. Introduction

Polymer-based organic semiconductors have attracted considerable attention due to their excellent light absorption properties and compatibility with the solution processing technologies enabling new approaches to fabricate cost-effective, organic thin-film solar cells by printable process. On the other hand, hydrogenated silicon (Si:H) prepared by plasma enhanced chemical vapor deposition (PECVD) is a widely known inorganic semiconductor with rather mature deposition technology, which has been successfully implemented in several commercial optoelectronic devices, including photovoltaics. Important advantages of Si:H and related semiconductors are their high photocarrier generation, good transport properties of photocarriers, possibility to vary optical gap in the range of 1.2–3 eV, and acceptable stability under sun irradiation. Organic solar cells based on conjugated polymers as electron-donor materials blended with small molecule sensitizer as an electron acceptor have achieved 7–9% conversion efficiency in small area single bulk heterojunction devices. The efficiency of single-junction Si:H solar cells is around 10% even with optimal optical design. A few attempts have been undertaken to merge the beneficial properties of both materials in the so-called hybrid silicon-organic heterojunction solar cells. The main idea behind this concept is based on the possibilities to enhance photovoltaic performance characteristics by engineering suitable material and improving interface properties and design. Rather developed deposition and doping process of amorphous silicon and related thin films (intrinsic and p-n-doped) allow to tune the important structural and electronic parameters (such as degree of order, optical gap, mobility, Fermi level position, etc.) of the material which determines the device performance characteristics. Thus, the combination of organic and inorganic materials would be a promising approach for developing new types of large area, lightweight, thin film efficient solar cells.

We present a concept for silicon-organic heterojunction structures for photovoltaic devices, based on mainly PECVD noncrystalline silicon (can be also extended and involve crystalline semiconductors) describe fabrication of both plasma deposited films and organic materials and their relevant electronic properties, fabrication of hybrid device structures, and their characteristics comparing with those reported in literature.

2. Fabrication and electronic properties of plasma deposited and organic materials

2.1. Inorganic materials based on silicon deposited by PECVD

Technology based on amorphous silicon semiconductors has become an important part in the multibillion business in electronics in the last decades. There was a time, when the theory of the physical properties of solids seems to be impossible without considering a stable and periodic structure, Ziman [1]. However, nowadays, the theory of amorphous materials has not only been developed but also technology based on these materials has become omnipresent in wide range of electronic applications. The breakthrough of amorphous silicon materials was directly related to the development of a new method called GD that allowed for the first time

http://dx.doi.org/10.5772/67565

to deposit intrinsic hydrogenated amorphous silicon (a-Si:H) films [2, 3] with high photoconductivity and low concentration of ESR centers, p-type and n-type doped amorphous silicon films, Spear and Le Comber [4], with sufficient quality (low DOS) to be used in functional p-n junctions [5].

The modern approach of the GD system used for first time is now well-known (PECVD). The actual PECVD technique has reached the versatility to deposit not only amorphous silicon but also silicon materials in their entire range of structure: nanostructured [6], microcrystalline [7, 8], epitaxial crystalline silicon [9], and alloys such as SiGe:H, SiC:H, SiO:H, SiN:H, etc. The optoelectronic properties of these materials depend on the deposition parameters such as pressure, flow rate, substrate temperature, power, and excitation frequency. Good electronic properties for interesting high Ge-content nanostructured Si_xGe_y:H films deposited at 300°C, high H-dilution ratio, and low frequency have been systematically reported in Ref. [10]. On the other hand, one of the main characteristics of the PECVD technique to take advantage for actual applications is the relative low temperature process in the range of 100–300°C. Low temperature process is a requirement for new applications such as large area, lightweight, flexible devices on low-cost plastic substrates, and, more recently, hybrid organic-inorganic devices based on polymers. It was general to think that reduction of temperature below 200°C leads to the increase of dangling bonds (defects) and results in films with electronic properties that are generally poor [11]. However, it has been found that deterioration of electronic properties in materials deposited at temperature lower than $T < 300$°C can be corrected by other fabrication parameters. Low-temperature (LT) a-Si:H and LT nanocrystalline (nc) Si:H have been optimized at $T = 120$ and 75°C as reported in Ref. [12].

A-Si:H films deposited at reference temperature ($T = 300$°C) show a dark conductivity in the range of 10^{-10} Ω^{-1} cm^{-1} in comparison to LT a-Si:H films that show values of 4×10^{-11} Ω^{-1} cm^{-1} for 120°C and 9×10^{-11} Ω^{-1} cm^{-1} for 75°C, and optical gap parameters were 1.75, 1.92, and 1.90 eV for 300, 120, and 75°C, respectively [12]. The higher optical gap of LT films could be explained for changes in the way that hydrogen is incorporated to the films at low temperatures: 10% for 300°C, 10.9% for 120°C, and 9.5% for 75°C, this effect should be considered for optimization at low temperatures. Intrinsic LT (75°C) nc-Si:H films show a dark conductivity 3×10^{-7} Ω^{-1} cm^{-1}, a crystallinity of 75% and a grain size of ~20 nm, and a doped n^+-doped nc-Si:H film shows a dark conductivity of 0.3 Ω^{-1} cm^{-1}, a crystallinity of 72%, and a grain size of ~15 nm. As reference, a nc-Si:H deposited at 300°C shows a dark conductivity of 10^{-6} Ω^{-1} cm^{-1}, crystallinity of 82%, and a grain size of ~30 nm [12]. For solar cell development, the use of μc-Si:H and a-SiGe:H layers is critical to improve IR long wavelength sensitivity [13]. However, only few systematic studies of the role of temperature on the film growth process and its effect on the film optoelectronic properties have been reported. Modeling of properties for microcrystalline silicon films deposited by PECVD at low temperature (175°C) on flexible low-cost substrate is reported in Ref. [14]. Films under microcrystalline growth conditions with different deposition temperatures for solar cell devices were studied [15]. In Ref. [16], amorphous and microcrystalline silicon films were deposited by RF PECVD at deposition temperatures of 25 and 100°C. Values of properties for μc-Si:H films deposited by RF PECVD were at 25°C: deposition rate $V_d = 0.09$ A°/s, optical gap $E_{opt} = 2.10$ eV, dark conductivity $\sigma_d = 8.6 \times 10^{-9}$ Ω^{-1} cm^{-1}, photoconductivity $\sigma_{ph} = 5.9 \times 10^{-8}$ Ω^{-1} cm^{-1}, and activation energy

E_a = 0.63 eV, and at 100°C: V_d = 0.12 A°/s, E_{opt} = 2.14 eV, $\sigma_d = 3 \times 10^{-5}$ Ω^{-1} cm^{-1}, $\sigma_{ph} = 1.7 \times 10^{-5}$ Ω^{-1} cm^{-1}, and E_a = 0.31 eV. On the other hand, a-SiGe films could be an option for application on flexible hybrid solar cells. Deposition of silicon-germanium alloys at low temperatures has been studied since the 1970s [17–20]. The Ge atom is slightly larger and remarkably heavier compared to Si atom, thus changing growth, structure, and consequently electronic properties of Si-Ge:H and Ge:H films. To compensate this, several approaches have been made, such as ion bombardment [21], thickness optimization [22], and hydrogen dilution [23]. Nanostructured high Ge-content GeSi:H films have been studied in [10] (**Figure 1**). These films demonstrated good electronic properties such as low defect and tail state-related absorption (**Figure 2**). Nanostructured $Ge_{0.96}Si_{0.4}$:H films deposited by LF PECVD at deposition temperature T_d = 300°C and high H-dilution ratio R_H = 75 showed a E_{opt} = 0.94 eV, $\sigma_d = 2.5 \times 10^{-4}$ Ω^{-1} cm^{-1}, and E_a = 0.28 eV. A comparison of the nanostructured $Ge_{0.96}Si_{0.4}$:H film deposited at 300°C and a LT GeSi:H film deposited at 160°C is presented in Ref. [24]. The LT GeSi:H shows a $\sigma_d \sim 10^{-4}$ Ω^{-1} cm^{-1} and E_a = 0.32 eV, the absorption coefficient spectra also showed good electronic properties as low defect. **Table 1** shows a summary of electronic properties of silicon-based films deposited by PECVD at high and low temperature. Thus, these results show that high quality silicon materials can be deposited at low temperatures compatible with organic polymer semiconductors deposited on plastic substrates.

2.2. Polymer organic materials

Organic materials based on polymer semiconductors have been in focus during the last decade. The most studied materials such as the bulk heterojunction P3HT:PCBM and the conductive semiconductor PEDOT:PSS have been widely implemented in new organic thin-film solar cells [26]. One important advantage of these materials is their solution type processing techniques for fabrication that allows printable deposition of the films at room temperature and at atmospheric pressure in comparison to inorganic material deposition that usually

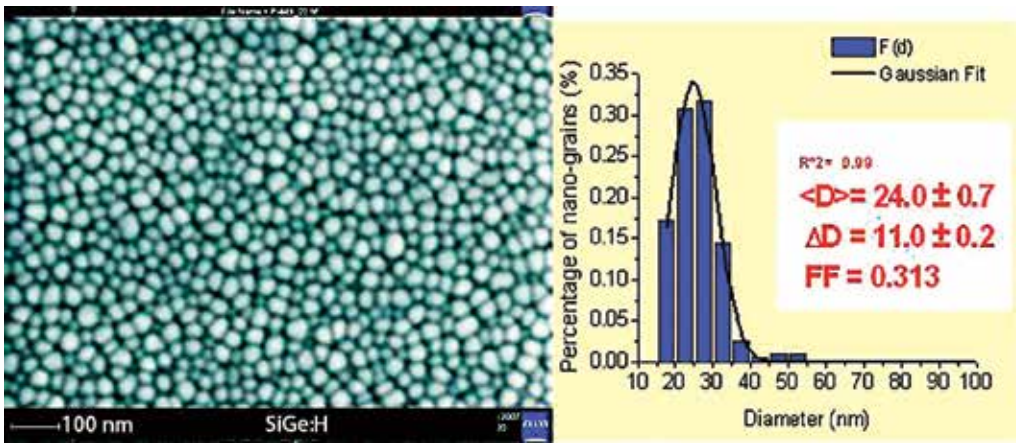

Figure 1. SEM images (left) of nanostructured $Ge_{0.96}Si_{0.4}$:H films deposited by LF PECVD at high H-dilution ratio R_H = 75. Diameter distribution function of grains (right).

http://dx.doi.org/10.5772/67565

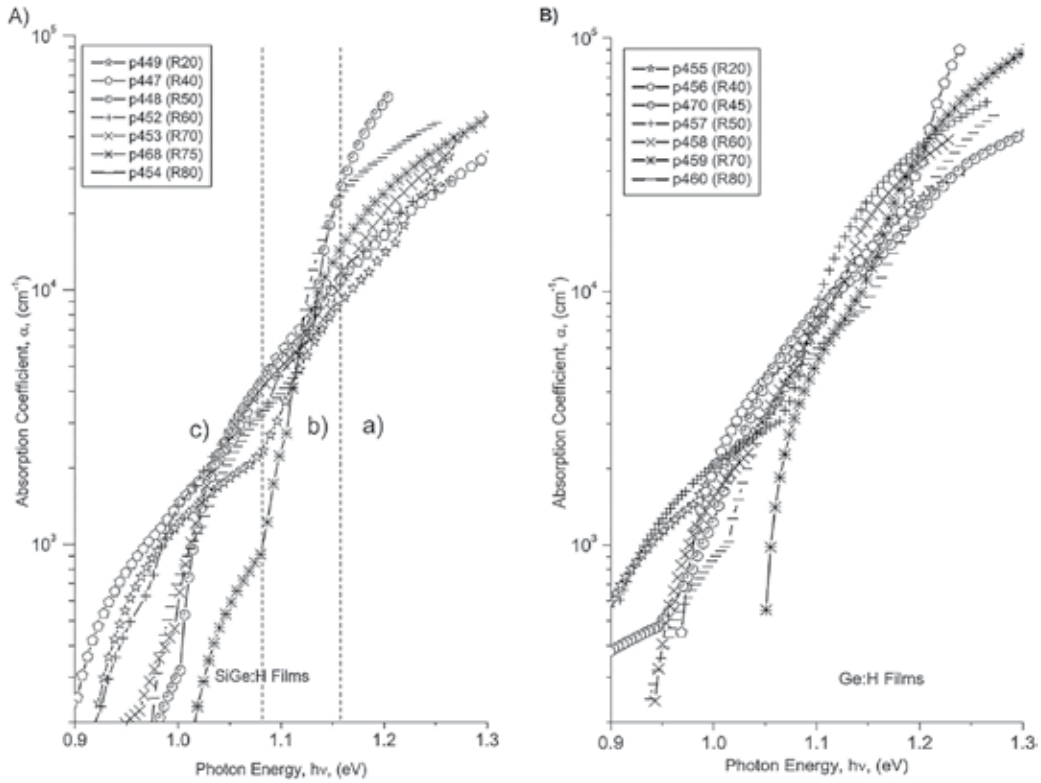

Figure 2. Spectral dependence of optical absorption coefficient $\alpha(hv)$for different hydrogen dilution, *R*, (a) SiGe:H and (b) Ge:H films.

Film	Temperature (°C)	V_d (A°/s)	E_{opt} (eV)	σ_d (Ω^{-1} cm^{-1})	σ_{ph} (Ω^{-1} cm^{-1})	E_a (eV)	Other	Ref.
a-Si:H	300	–	1.8	8×10^{-10}	–	0.60	–	[24]
		–	1.75	~10^{-10}	–	–	–	[12]
	220	0.93	1.72	1.1×10^{-9}	1.8×10^{-4}	0.93	RF	[16]
	120	–	1.92	4×10^{-11}	–	–	–	[12]
	75	–	1.90	9×10^{-11}	–	–	–	[12]
nc-Si:H	300	–	–	~10^{-6}	–	–	–	[12]
	75	–	–	3×10^{-7}	–	–	–	[12]
μc-Si:H	100	0.12	2.14	3×10^{-5}	1.7×10^{-5}	0.31	RF	[16]
	25	0.09	2.10	8.6×10^{-9}	5.9×10^{-8}	0.63	RF	[16]
GeSi:H	300	2.2	0.94	2.5×10^{-4}	–	0.28	LF	[10]
	160	1.3	0.95	1.3×10^{-4}	7.5×10^{-6}	0.32	LF	[25]

Table 1. Optoelectronic characteristics comparison for silicon-based films deposited at different temperatures.

requires high substrate temperature and complex high vacuum process. The film-forming processes for organic materials can be classified in (1) coating process methods that include spin coating, blade coating, spray coating, and painting and (2) printing process methods thus include screen printing, offset printing, and inkjet printing [27]. Spin coating method has been one of the important techniques for the deposition of polymer materials. The final characteristics of the films depend on the specific material and its solvent at a given concentration, see, for example, **Figure 3**, it is shown that the thickness dependence as a function of the rotation velocity for PEDOT:PSS films deposited by spin coating at different IPA solvent concentrations. Spin coating deposition is a complex process that also depends among others properties of viscosity, molecular weight, diffusivity, and volatility of the material; however, it is a highly reproducible process [27]. Nevertheless, there are some aspects that limit the application of the technique for industrial production such as no possibility for deposition on large areas, serial production, and problems with patterning. A review of alternatives to spin coating method for the deposition of polymer materials is presented in Ref. [29], just to recognize that the "ideal" process for the deposition of organic materials is still unresolved and an urgent task for the future of this technology.

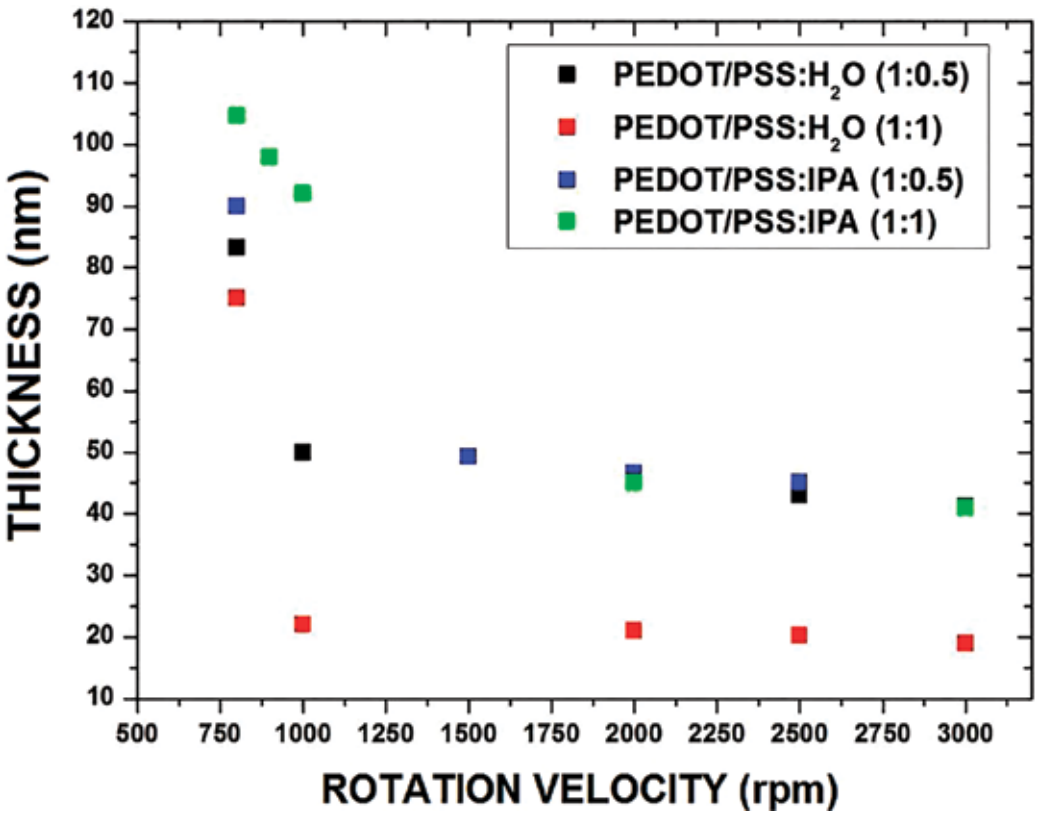

Figure 3. Deposited thickness of PEDOT:PSS films deposited by spin coating as function of frequency rotation for different dilution preparation.

http://dx.doi.org/10.5772/67565

Despite the large number of developed organic materials, there are a few materials that have been usefully applied in promising optoelectronic devices, i.e., PEDOT:PSS is a very attractive conductive polymer semiconductor for electronic and photovoltaic applications (not only for organic electronics) due to its optical transparency, high conductivity, and processing techniques. The use of PEDOT:PSS in hybrid organic-inorganic solar cells and devices has attracted the attention in recent years specially as a candidate for substitution of p-type a-SiC:H:B layer in silicon-based photovoltaic devices [28–30]. The Si/PEDOT interface has shown interesting properties such as effective formation of blocking barrier for electrons, acting similar to an "ideal" barrier [29]. Other advantage of PEDOT:PSS versus traditional inorganic p-type a-Si:H is the flexibility of processing; **Figure 4** shows the DC conductivity, $\sigma_{DC}(T)$, for the spin-coated PEDOT:PSS films deposited under different dilutions. A change in room temperature conductivity of one order of magnitude is obtained only with a change in concentration of dilution with isopropyl alcohol (IPA) [32]. This process seems to be simple in comparison to the required doping process for inorganic semiconductors. However, despite the application of PEDOT:PSS in structures and devices, only a few studies of the electrical properties has been performed. Organic materials are following similar history to amorphous semiconductors, where the practical applications were growing faster than the development of theoretical physics of the materials. In [31],

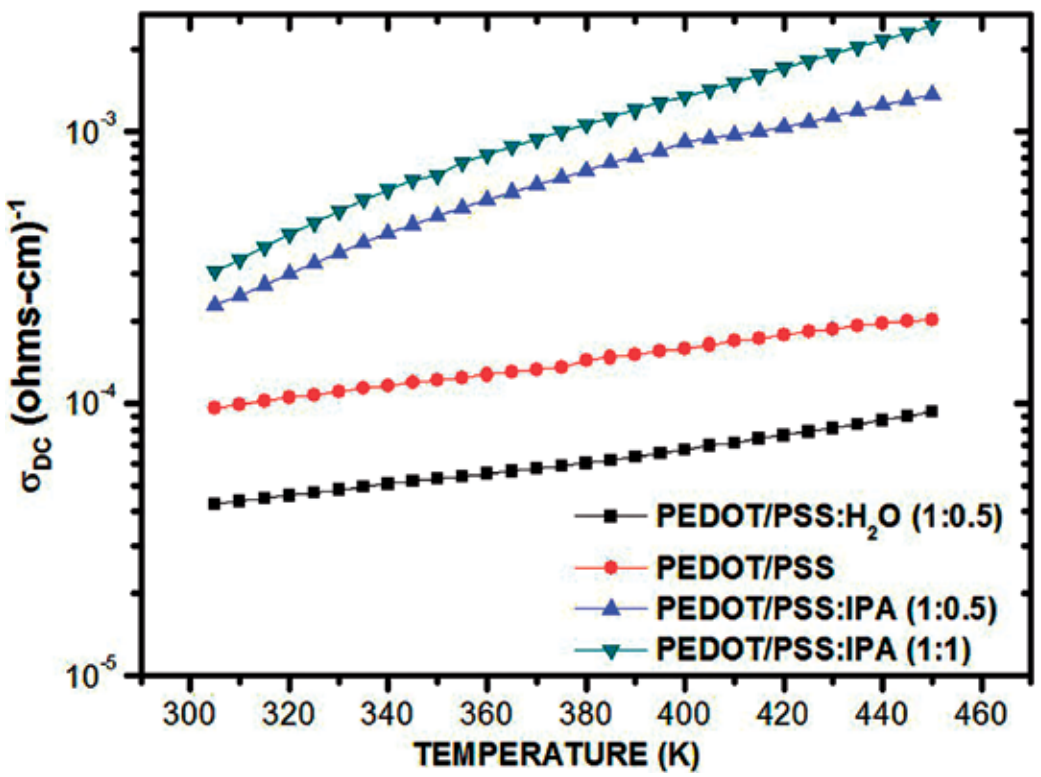

Figure 4. DC conductivity, $\sigma_{DC}(T)$, for the spin-coated films: PEDOT/PSS: H_2O (1:0.5), PEDOT:PSS (without dilution), PEDOT/PSS: isopropyl alcohol (IPA) (1:0.5), and PEDOT/PSS:IPA (1:1) from 300 to 440 K.

the temperature dependence of DC conductivity of spin-coated poly PEDOT:PSS films has been investigated, $\sigma_{DC}(T)$ was measured in films deposited from different mixtures of PEDOT:PSS (**Figure 4**). Experimental data was fitted with two different transport models: thermal activated conduction and variable range hopping (VRH) model. It was found that $\sigma_{DC}(T)$ of PEDOT:PSS/IPA (1:1) sample can be described by the one-dimensional (1D) VRH model; however, at least at below room temperature it is not possible to distinguish unambiguously a concrete model from these two. The versatility of organic materials allows different functions to realize with the same material. PEDOT:PSS has been studied also as replacement of transparent contact oxides (TCO) as it will be discussed in the next section.

2.3. Transparent contact issues

For several years, TCOs were a unique option used as transparent contacts in optoelectronic applications due to their transparency in visible range ($0.4 < \lambda < 0.7$ μ) and low resistivity ($R_{sq} < 100$ Ω/sq). TCOs can be deposited as thin films by techniques as chemical vapor deposition, pulsed laser deposition, spray pyrolysis, and sputtering. There are many studies with a wide background about the development of this technology and film properties [32]. However, to fabricate transparent contacts compatible with the new hybrid inorganic-organic technology and/or compatible with flexible substrates, it is necessary to achieve good optoelectronic properties at low process temperatures (<200°C). To reach this goal, the following approaches have been proposed: (1) to modify the standard deposition methods, (2) to propose new techniques of deposition, or most recently (3) to propose new materials with fabrication methods at room temperature, i.e., organic-based materials. Sputtering method has been modified to achieve TCOs with high optical transmittance and low resistivity at low temperature deposition. ITO (In_2O_3) films deposited by roll-to-roll sputtering at low substrate temperature <50°C show sheet resistance of 47.4 Ω/sq. and a transmittance of 83% [33]. On the other hand, AZO films have been extensively studied as alternative to ITO films due to their stability, high transmission, high conductivity, lower cost, and lower deposition temperature in comparison to ITO films (AZO films, R_{sq} ~ 8.5 Ω/sq and T_{avg} = 84.44% @ T_d = 200°C on glass) [34]. In [35], ZnO/Al (AZO) films were codeposited using pulsed-direct current (DC)-magnetron reactive sputtering processes at 188°C using "soft power." The obtained ZnO:Al films show a sheet resistance of about R_{sq} ~ 13 Ω/sq and a transmittance of ~85%.

Recently with the introduction of organic materials and new technologies, new options have been studied for substitution of traditional TCOs to overcome some disadvantages as low transmission in blue region, high cost, complex high vacuum process, mechanical characteristics, and scarcity. To achieve this, here are some proposals: thin film grids [36], high carbon-based materials [37], and organic polymers [38–40]. PEDOT:PSS has been one of the most investigated organic materials as alternative to TCOs, the polymer has shown higher transparency and conductivity than traditional ITO contacts. Additionally, PEDOT:PSS can be deposited by dispersion in water which is compatible with large area, flexible, and low-cost substrates [41]. The electrical conductivity of PEDOT:PSS can be increased by orders of magnitude using secondary "dopants" as solvents, polyols, surfactants, among others [42]. By solvent dilution and post-treatment method the conductivity of PEDOT:PSS films has reached values of 1418 Ω^{-1} cm^{-1}, low sheet resistance below 65 Ω/□, and transmission

in visible range >80%, which have been reported in [38]. In Ref. [43], silver nanostructures were used to enhance conductivity of PEDOT:PSS contacts using a codeposition of spray and inject printing techniques, and the lower sheet resistance achieved by this method was 26.2 Ω^{-1} cm^{-1} with an average transmission of 80.7%.

2.4. Flexible substrates issues

Hybrid inorganic-organic devices seem to be an attractive approach for large area, lightweight flexible solar cells. Flexible electronics also opens the landscape to new applications such as flexible displays, X-ray sensors, electronic textiles, and electronic skin [42]. Many materials have been investigated as flexible substrates: thin glass substrates [44], metal foils [45], and different polymeric films (PET, PEN, Polyimide – KAPTON®, etc.) [41]. The substrate-specific requirements depend strongly of the application, process fabrication, and technology: optical properties, surface roughness, thermal properties, chemical properties, mechanical properties, and electrical and magnetic properties [12]. In the case of applications in organic hybrid solar cells, special attention should be paid to thermal properties, optical properties, and surface roughness. **Table 2** presents a comparison of the main properties of flexible substrates. One of the most attractive materials for their flexibility, low cost, and transparency are the plastic substrates. **Figure 5** shows the spectral dependence of the optical transmittance in the visible range of plastic substrates. PEN and PET are most desirable materials for solar cells application due to the optical transmittance and relative low cost. Another interesting material is PTFE or TEFLON®; the comparison of transmittance spectra presented in **Figure 5** shows that TEFLON transparent thin film is an attractive candidate for application in solar cell application with transparency from 250 to 900 nm and high transmittance (~96%) of above 350 nm. However, TEFLON has a nonpolar surface or a relative low surface energy to the polymer and inorganic materials, which result in low adhesion [46]. Polymer substrates require relatively low processing temperature, below T = 250°C, in the case of both technologies, organic and PECVD Si-based materials, for fabrication of hybrid solar cells. In both technologies, several approaches have been developed for fabrication of flexible devices like PECVD roll-to-roll fabrication. Inorganic PECVD materials have a long history in this field [12]. However, flexible plastic substrates despite having a scope of challenges are very attractive for large-area scale, lightweight, and relatively low cost hybrid organic-inorganic devices.

Substrate	Temperature process (°C)	Transparency (%)	Flexibility	Planarization
Thin glass	600	Yes	Some	No
Metal foil	1000	No	Some	Yes
Polyamide	<300	Some	Yes	No
PEN	<180	Yes	Yes	No
PET	<120	Yes	Yes	Maybe
TEFLON	<240	Yes	Yes	Maybe

Table 2. Comparison of substrate properties for solar cell applications [12, 25].

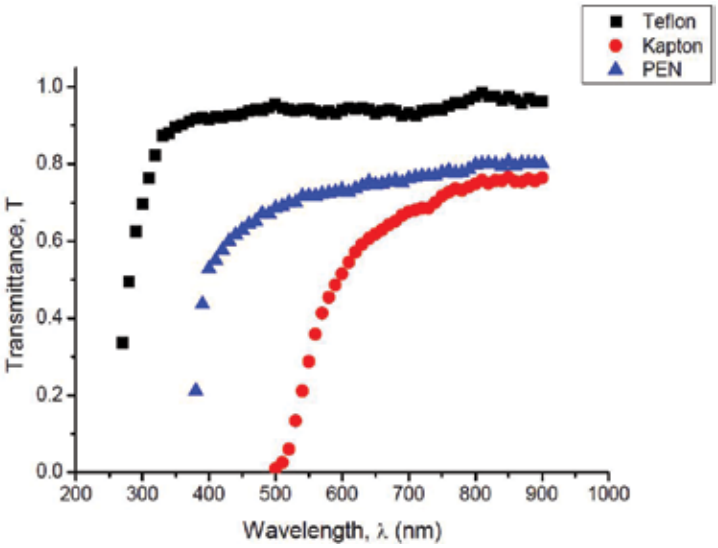

Figure 5. Spectral dependence of optical transmittance for TEFLON, KAPTON, and PEN.

3. Concept for inorganic-organic hybrid device structure

3.1. Concept

A concept for inorganic-organic device (CIOD) structures can be developed taking into account the following material aspects: (a) compatibility of deposition technologies for inorganic-organic semiconductors and electrode materials, (b) complementary of electronic properties of these materials resulting in improvement of device performance, and (c) some technological advantages in device fabrication, e.g., organic materials can be deposited by printable PC controlled technique resulting in simplification of patterning. Inorganic semiconductors can be presented by both crystalline materials and PECVD noncrystalline materials. The latter is applicable for large area flexible devices. In general, CIOD includes various combinations of crystalline and noncrystalline materials together with organic materials. In our further consideration, we shall be focused on PV applications based on PECVD films and organic materials because of their promise for large area flexible devices, although for achieving very high efficiency more complex (crystalline inorganic)-(noncrystalline inorganic)-(organic) material combinations would be of much interest.

3.2. Strategies for CIOD structures aimed at performance improvement

Performance of PV device is determined by: (a) generation of photo-induced carriers controlled by light absorption, (b) transportation of photo-induced carriers controlled by built-in electric field and diffusion, (c) life time of photocarriers that determine both concentration and transport of photocarriers, and (d) properties of interfaces, which control generation-recombination near interface and charge transport through the interface. We select p-i-n configuration as basic PV device structure, where p-layer is p-doped semiconductor, i-layer is intrinsic (nondoped)

http://dx.doi.org/10.5772/67565

semiconductor, and n-layer is n-type semiconductor. Internal built-in electric field in this structure is created because of difference in work functions for p- and n-layer. PECVD silicon is conventionally used as intrinsic semiconductor (nondoped), boron-doped as p-layer and phosphor-doped as n-layer. Optical gap for Si:H is typical E_{opt} = 1.7 eV. PECVD materials allow changes in optical gap and consequently spectral absorption in a wide range. To improve optical absorption in short wave range, PECVD silicon-carbon alloys SiC:H are used with optical gap E_{opt} up to 2.5 eV. For long wave range, PECVD silicon-germanium alloys are used with optical gap as low as E_{opt} = 1.2 eV. Interface properties in the structures even prepared in PECVD cluster tool systems depend strongly on process fabrication and deposition regimes used. Let us analyze the above-mentioned principal factors one by one and start with the increase of effective optical absorption in device structure. The latter can be obtained by means of bi-layer (inorganic-organic) absorber of nondoped materials. In this case, organic material typically with wider band gap than Si:H could improve absorption in short wave range. For improvement of absorption in long wave range, SiGe:H layer could be added. To improve transport of photocarrier in organic nondoped materials, built-in electric field can be formed by means of p- and n-doped PECVD films. It is well known, that device performance in shortwave range depends critically on frontal interface (usually it is p-i interface). Improved photocarrier collection for shortwave have been reported for interfaces with organic p-layer [28, 29]. On the other hand, organic semiconductor with narrow band gap have not sufficiently developed yet, therefore, long wave absorption can be improved by incorporation of SiGe:H films. Some of these ideas have been realized and their fabrication and characterization will be described further.

Most of mature solar cell technologies are being developed with silicon-based materials. The stability with sufficient efficiency of these solar cells has been demonstrated for several years. However, in comparison to new thin film organic materials, they have complex fabrication process, high relative cost, and do not suit well for large area flexible PV devices. New technologies such as organic polymer materials bring new approaches of fabrication techniques and materials that can be molecular designed and tailored with specific optoelectronic properties but efficiency and stability are relatively low in comparison to inorganic counterpart. Thus, the combination of both technologies is looking for devices that can take advantage of the strong optical absorption of organic polymer materials, high charge carrier mobility, and stability of inorganic materials while looking for simplification of process fabrication. Different approaches have been proposed to combine both technologies, the versatility of organic materials results in many possibilities for forming hybrid devices structures [47]. Silicon remains a good candidate for hybrid devices due to favorable and well-known electronic properties. Different ways have been reported to combine silicon with polymers in hybrid solar cell: hybrid crystalline silicon-PEDOT:PSS solar cell [29], nanowire-Si/polymer solar cells [48], and a-Si:H/PEDOT:PSS pin solar cell [28]. **Figure 6** shows examples of some ideas for application of organic and inorganic materials in hybrid solar cells. In the structure labeled H1 with configuration (ITO)(p) SiC:H/P3HT:PCBM/(n) Si:H), P3HT:PCBM bulk heterojunction film is used as active absorber film and conventional a-Si:H and a-SiC:H are used as n-type and p-type layers, respectively. The structure labeled H2 (ITO/PEDOT:PSS/(i) Si:H/(n) Si:H) is an a-Si:H p-i-n structure, where the p-type SiC:H layer was substituted by an organic conductive film (PEDOT:PSS). Finally, the structure labeled H3 is a double-absorber layer structure (ITO/PEDOT:PSS/P3HT:PCBM/(i) Si:H/(n) Si:H).

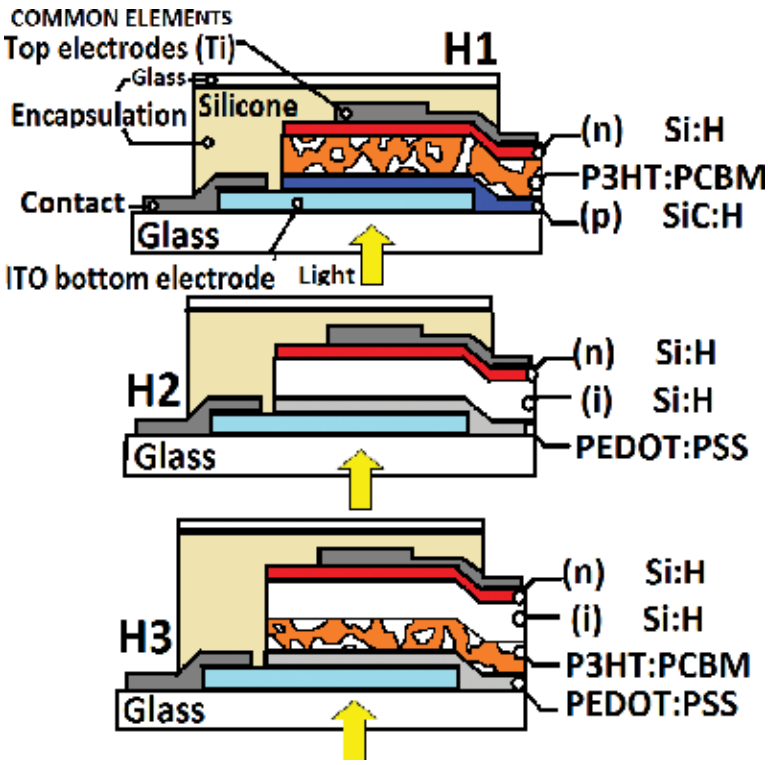

Figure 6. Hybrid photovoltaic structures based on Si:H and organic semiconductors (H1) ITO/(p) SiC:H/P3HT:PCBM/(n) Si:H, (H2) ITO/PEDOT:PSS/(i) Si:H/(n) Si:H, and (H3) ITO/PEDOT:PSS/P3HT:PCBM/(i) Si:H/(n) Si:H.

3.3. On electron energetical diagrams for hybrid device structures

Electron energetic diagram is a conventional and convenient instrument applied to the analysis of device structures and their performance. Such diagram can be created if electronic properties (optical gap, work function, electron affinity, etc.) are known (well measured) that does not exist even in crystalline semiconductors. Moreover, knowledge of bulk electronic characteristics is not sufficient because information on interfaces is required as well. As far as organic semiconductors are concerned, data reported on bulk electronic properties are very poor and those for interfaces have not been reported. In many publications, "energetic diagrams" look as a set of energetic sketches for different materials with different Fermi levels and some arrows denoted hypothetical electron transitions. This is misleading because in multilayered device structure without illumination a thermal equilibrium is suggested (i.e., exchange of particles and their energies between materials) meaning the same Fermi level in the system, rather than different ones in isolated materials. Under illumination, electronic diagram becomes significantly more complex and can only be created based on special experimental study of device structure. Nevertheless, design of energetic diagram based on available experimental data (even with some shortages and errors in details) is strongly motivated. In **Figure 7**, such hypothetical electron energetic diagrams in thermal equilibrium for H1,

http://dx.doi.org/10.5772/67565

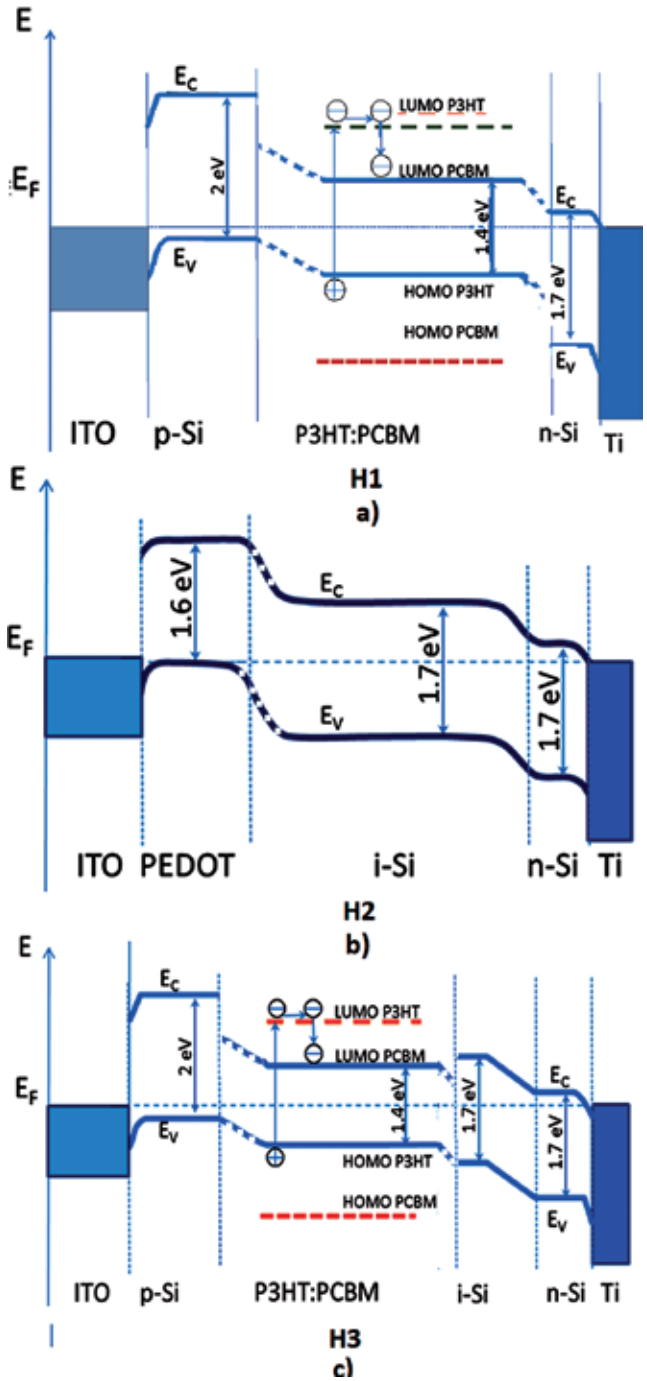

Figure 7. Electron energetic diagrams in thermal equilibrium for the studied structures: (a) ITO/(p) SiC:H/P3HT:PCBM/(n) Si:H (H1), (b) ITO/PEDOT:PSS/(i) Si:H/(n) Si:H (H2), and (c) ITO/PEDOT:PSS/P3HT:PCBM/(i) Si:H/(n) Si:H (H3). Dotted lines represent hypothetical interfaces and offsets in the energy levels due to lack of information on the values reported in literature.

H2, and H3 structures are represented, more details about them can be found in Ref. [28]. In H1, energetic diagram (**Figure 7a**) shows that the light absorption occurs in the organic bulk heterojunction formed by P3HT and PCBM. The creation of an exciton (bounded electron-hole pair) in P3HT is followed by separation of the charge at the internal interfaces of the heterojunction P3HT/PCBM. The inorganic p- and n-type silicon-based layers are used to create an internal electrical field to transport the "free" charge to electrodes. In H2 structure the PEDOT:PSS layer acts as a heavily doped p-type layer and its comparable optical gap (~1.6 eV) to amorphous silicon (~1.7 eV) forms an optimal internal build-in-field and prevents back diffusion of electrons at the frontal interface. In H3 structure improvement of light absorption is expected by using double active absorber layers (a-Si:H and P3HT:PCBM), the energetic diagram shows that one obstacle of this is that the alignment of energetic band between organic and inorganic materials is complex and may create barriers, which oppose to electron and hole transport.

4. Experimental results on fabrication and characterization of different configurations of silicon-organic p-i-n heterojunction structures

4.1. Fabrication

The fabrication flow chart for the H2 structure (ITO/PEDOT:PSS/(i) Si:H/(n) Si:H) is shown in **Figure 8**. The process begins with a coated ITO substrate. The bottom electrode was defined by etching using hydrochloric acid and then the substrate is cleaned by ultrasonic cleaning in acetone and then isopropyl alcohol. The PEDOT:PSS solution was prepared with a 1:6 weight ratio, filtered using a pore size filter of 0.45 μm and deposited by a spin-coating in N_2 ambient with a rotation speed of 2500 rpm that results in a thickness of the film of d = 45 nm. The inorganic layers were deposited by RF PECVD process in a multichamber system. The silicon films were grown by a 10% SiH_4 + 90% H_2 gas mixture for intrinsic film and 0.01% PH_3 + 9.9% SiH_4 + 90.09 % H_2 gas mixtures for n-type layers, at pressures of 550 mTorr and substrate temperature of 160°C. All the gases used were semiconductor purity from "Matheson Inc." The compatibility of PECVD process and organic materials for this flow process has been reported in [25].

4.2. Characterization

Figure 9 shows the DC current density—voltage characteristics J(U) under AM1.5 standard illumination for nonoptimized hybrid structures presented in **Figure 6**. As seen, the structure H1 with organic semiconductor as nondoped intrinsic material demonstrate low U_{OC} = 185 mV, while expected values based on difference of Fermi levels for p- and n-layers could be close to $\Delta E_F \approx 900$ mV. The reduced U_{OC} value may be related to low shunt resistance due to leakage transversal current resulting in low J_{SC} current. Mechanism of leakage current in such structures has not been studied yet and could be rather complex because of the complex structure of the organic material (e.g., see SEM image in **Figure 13**). The highest value of J_{SC} = 5.87 mA/cm^2 is observed in H2 structure with PEDOT/PSS as p-layer and i-Si:H as nondoped absorber and Si:H(P) as n-layer. U_{OC} = 400 mV in this structure is better than in H1 but still

http://dx.doi.org/10.5772/67565

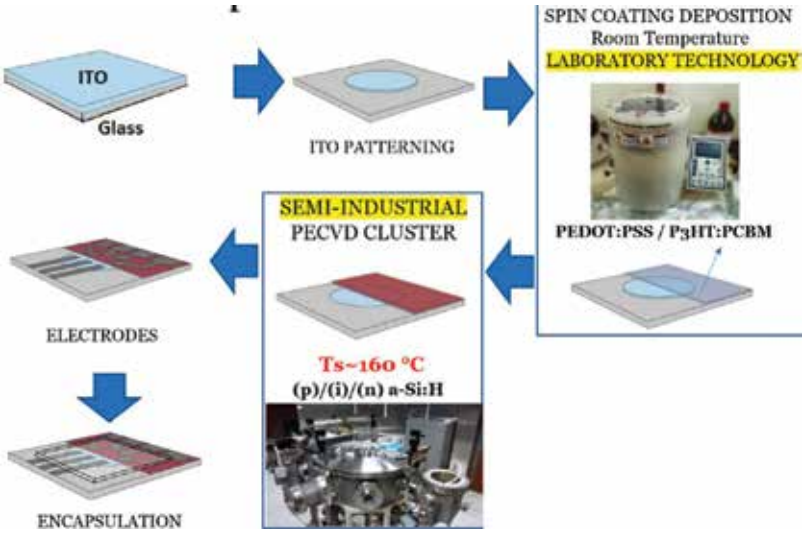

Figure 8. Flow fabrication for thin film silicon/organic p-i-n structure involving PECVD process and spin on coating deposition for inorganic and organic films, respectively.

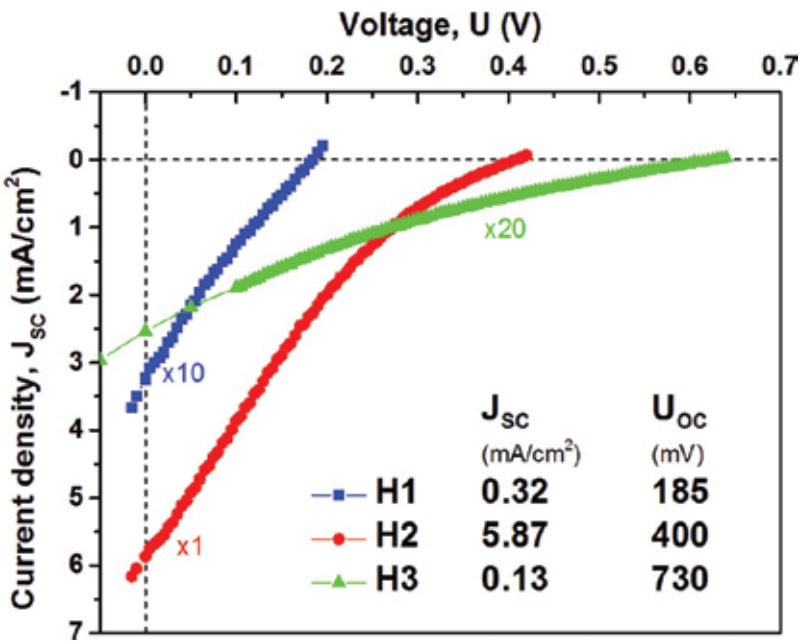

Figure 9. Current-voltage characteristics and extracted *U*oc, J_{SC}, *FF* values of hybrid photovoltaic structures based on Si:H and polymer organic semiconductors (H1) ITO/(p) SiC:H/P3HT:PCBM/(n) Si:H, (H2) ITO/PEDOT:PSS/(i) Si:H/(n) Si:H, and (H3) ITO/PEDOT:PSS/P3HT:PCBM/(i) Si:H/(n) Si:H.

less than that expected. The H2 structure clearly shows current suppression at low internal field, when the potential is close to U_{OC} suggesting still high value of transversal leakage current. The structure with double absorber layer H3 has the highest U_{OC} = 700 mV, but very low

current density J_{SC} = 0.13 mA/cm^2. It means that the structure has sufficient internal electric field but very low current. For speculative purpose, the following reasons of low current can be mentioned: (a) too high resistivity of nondoped organic and inorganic layers, (b) not optimal thicknesses for nondoped layers, and (c) blocking barrier between two nondoped layers. However, special study is necessary to determine unambiguously the mechanism of current reduction. In terms of device performance characteristics, the main results of comparison of three types of hybrid structures can be summarized as follows: the H2 structure shows the highest short circuit current density J_{SC} = 5.87 mA/cm^2, whereas the H3 structure has the highest open circuit voltage U_{OC} = 730 mV, while both J_{SC} and U_{OC} of the H1 structure are rather low. It is worth to note that this comparison provides only some guideline for further study.

Figure 10 presents the spectral dependence of short circuit current density *J*sc (λ) for the structures H1, H2, and H3 in comparison to the solar spectral irradiance. For *J*sc (λ) form comparison, the *J*sc (λ) curves were normalized to *J*sc (λ) response of an a-Si:H inorganic solar cell. An interesting relative higher photo current than that for inorganic reference sample is found in the region of short wavelength from λ = 410 to 354 nm associated to the frontal interface of the structures. It suggests better electronic properties of organic-inorganic frontal interfaces due to lower surface back diffusion coefficient of carriers generated close to this interface or/and lower surface recombination rate and probably more stable chemical interface [28]. Some confirmation on quality of undoped absorber material can be obtained from subgap for $h\nu < E_{opt}$ photocurrent. Slope of $J_{SC}(h\nu)$ characterized by E_0 in the vicinity of E_{opt} is approximately the same in the all structures meaning that the organic semiconductor has narrow band tail density of states. As far as deep states are concerned, the sample H1 shows the highest value, sample H2 higher value than that in the reference sample, but less than that in H1 sample. In the sample H3 was not able to measure signal for $h\nu$ < 1.6 eV. In other words, quality of nondoped absorber with organic semiconductor is still less than that for Si:H films that motivates further efforts in improvement of electronic properties of organic semiconductors.

Some sort of "optimization" (see details in [28]) has been performed for H2 type of structure. **Figure 11** shows the current voltage characteristics of an improved hybrid H2* structure in comparison to those for organic and inorganic solar cells. It is most interesting that J_{SC} = 17.7 mA/cm^2 value exceeds values for both reference samples (organic and inorganic Si:H p-i-n structure). This high value may result from: (a) higher electric field at the frontal interface PEDOT/PSS-i-Si:H, and consequently reducing back diffusion and increasing current, (b) reducing surface recombination rate at the interface, and (c) better electronic quality of Si:H film grown on PEDOT/PSS. Though the latter cannot be excluded, no experimental evidence on changes electronic properties of Si:H film in this structure. U_{OC} = 645 mV for this H2* structure is higher than that for organic and less than that for Si:H p-i-n structure. At low voltage in the vicinity of U_{OC}, photocurrent is suppressed indicating high transversal leakage current. Finally, the comparison of performance characteristics for H2* structure reported for PEDOT/(i) Si:H/(n) Si:H devices is performed (see **Table 3**). H2 structure demonstrates a large high value of short circuit current density J_{SC} = 17.7 mA/cm^2 in H2* structures, this makes promising further study of this kind of photovoltaic cell, especially if the transversal leakage current is significantly reduced.

http://dx.doi.org/10.5772/67565

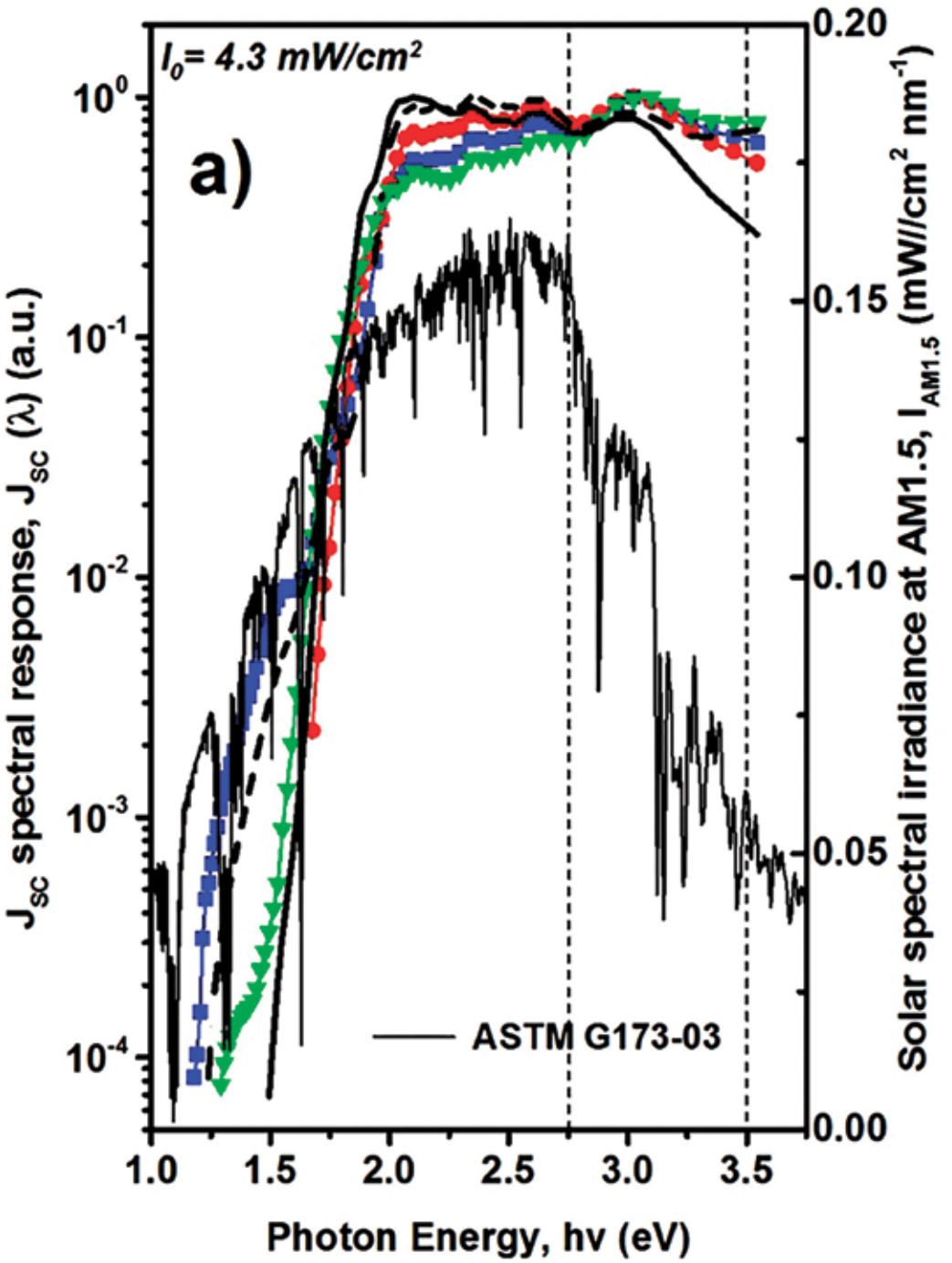

Figure 10. Spectral dependence of short circuit current density in the structures H1, H2, and H3 in comparison with solar spectral irradiance.

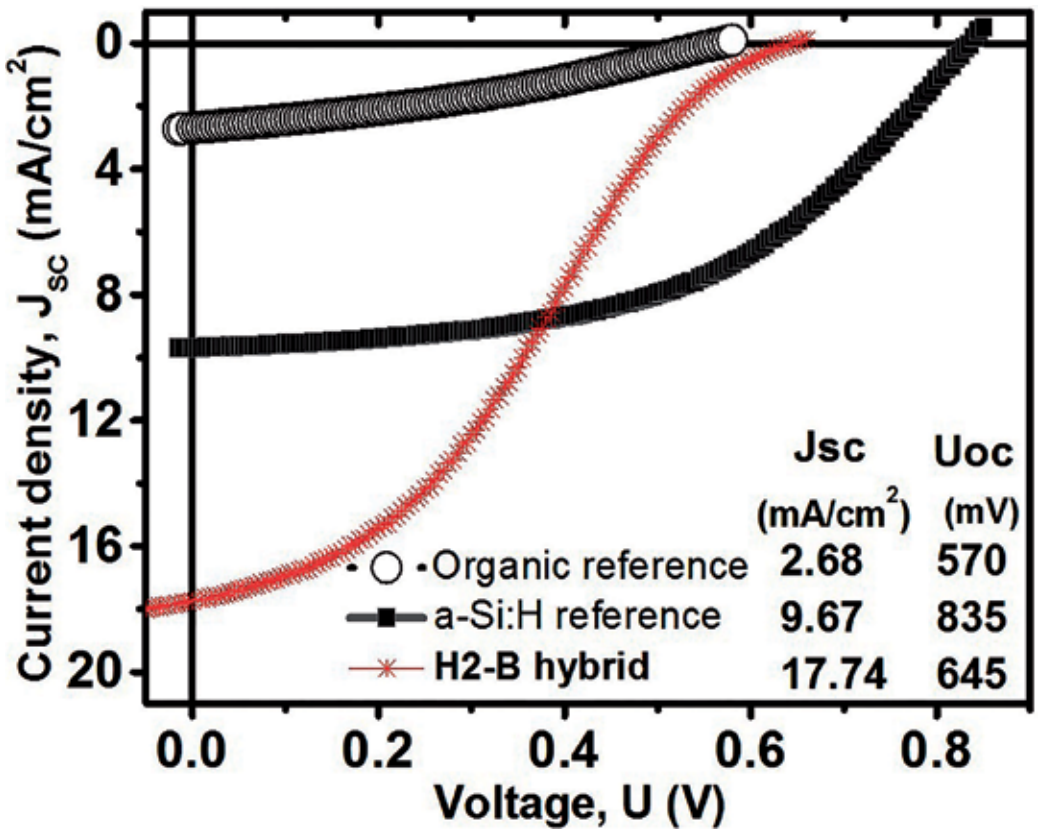

Figure 11. Current-voltage characteristics $J(U)$ and extracted U_{OC}, J_{SC}, FF and conversion efficiency values for hybrid photovoltaic structures in H2* configuration, organic, and inorganic reference solar cells.

Frontal interface	J_{SC} **(mA/cm²)**	U_{OC} **(V)**	FF	**PCE (%)**
PEDOT:PSS/(i)a-Si:H	4.55	0.88	51	2.1
	16.0	0.54	50	4.7
	17.74	0.64	32	3.75
a-SiC:H:B/(i) a-Si:H efficiency record	16.36	0.89	71	10.2

Table 3. Comparison of PV characteristics reported in literature with the best structure (H2) PEDOT:PSS/Si:H [28].

5. Hybrid structures on flexible substrates

Flexible solar cells on plastic substrates have several advantages such as lightweight and relative low cost. Inorganic and organic semiconductor technologies have demonstrated to be compatible with flexible substrates [12, 33–35]. However, the new concept of hybrid PECVD-polymer solar cell on flexible substrates has not been reported until now. A hybrid solar cell ((AZO/PEDOT:PSS/

http://dx.doi.org/10.5772/67565

(i) Si:H/(n) Si:H//Ag) on PEN and polyimide substrate shown in **Figure 12** have been fabricated and studied. A transparent electrode of AZO was deposited on the flexible substrate by sputtering method. The inorganic silicon layers were deposited by RF PECVD process at substrate temperature of T_d = 160°C and Ag top contact was deposited by sputtering at the same temperature and the PEDOT:PSS film was deposited by spin coating. A reference structure was fabricated on Corning glass substrate and demonstrated a *J*sc = 10.4 mA/cm² and *V*oc = 565 mV.

Similar structures on PEN with different AZO-film thickness were compared; it was found that the performance characteristics of the cell were strongly dependent on the thickness of the AZO film. The short circuit current density increased from *J*sc = 3.21 to 9.79 mA/cm² and the open circuit voltage from *V*oc = 405 to 565 mV for a AZO thickness change from *d* = 250 to 500 nm, respectively. Average roughness measured on AZO film deposited on plastic substrate as references shows a reduction from <*r*> = 1.11 nm for 250 nm thick AZO layer to <*r*> = 0.87 nm for 500 nm thick AZO layer, both on PEN substrate. Polyimide KAPTON® substrates from Du Pont™ are known for some applications such as circuits and space applications. The average roughness for 250 nm thick AZO films on polyimide show a small difference in value (1.11) in comparison to 250 nm thick AZO film on PEN substrate (1.4). The difference of average roughness between

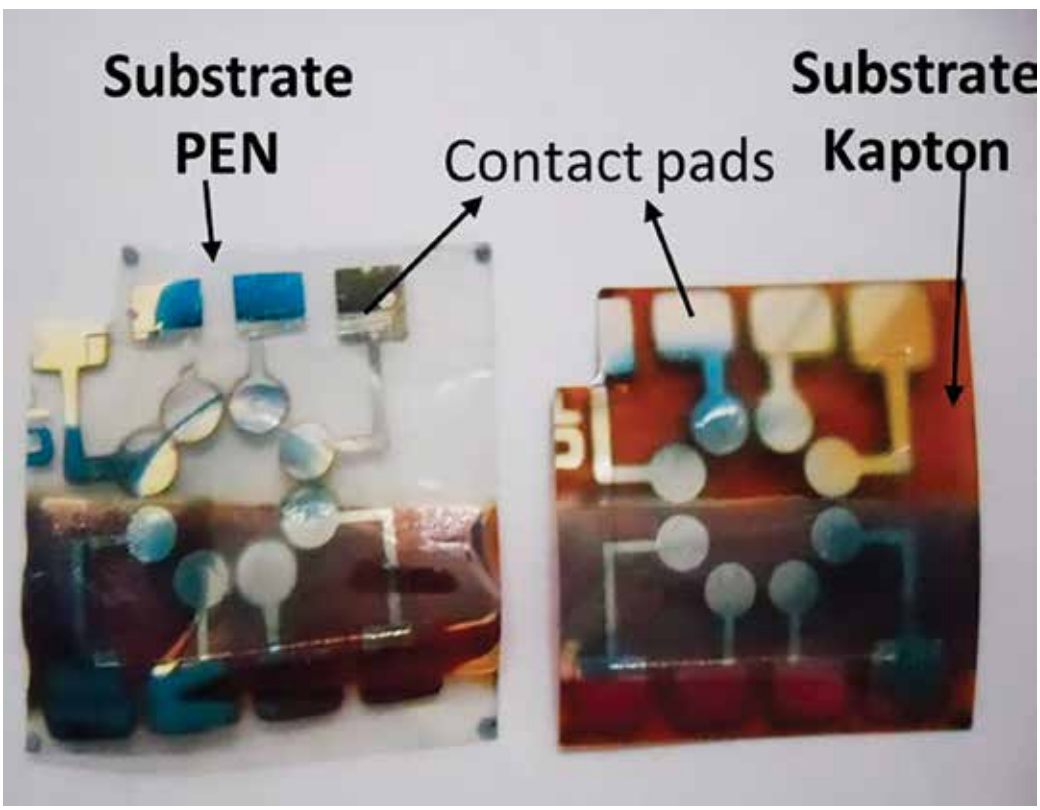

Figure 12. Hybrid photovoltaic structure on flexible substrate (PEN, left and right, KAPTON) based on Si:H and organic semiconductors PEDOT:PSS as p-type layer.

AZO on polyimide and PEN disappears for those with AZO film thickness of d = 500 nm. Polyimide has some advantages over other plastics such as high performance in electrical, chemical, and mechanical properties at relatively high temperature process of up to T = 450°C. However, its low transmission in visible range (**Figure 5**) limits implementation in solar cells. For similar solar cell structures and similar 500 nm thick AZO layer, the *J*sc reduces from 3.21 mA/cm^2 on PEN to 1.9 mA/cm^2 on polyimide because of the short wavelength limit (T < 50%) at 590 nm. The cross-sectional scanning electron microscopy (SEM) image of the solar cell on PEN is shown in **Figure 13**. The 500 nm thick AZO, 240 nm PEDOT:PSS, 300 nm thick (i) a-Si:H and 200 nm thick Ag layers and PEN substrate are well defined in the images. A large difference between the expected thickness (~45 nm) on glass substrate and PEN substrate (250 nm) was observed for PEDOT:PSS. This may be attributed to different surface properties for glass and PEN. As it can be seen, PEDOT layer looks as dispersive nonuniform material. Still it is not clear if this nonuniformity and its characteristics are intrinsic (inherent) material properties or they may depend on substrate (or previous layer) surface properties. Deviations of expected thickness and real thickness on plastic substrate were not observed for the PECVD films; however, the deformation (curvature, see **Figure 12**) of the substrates after device fabrication is an issue to be considered due to stress caused by deposition temperature and other factors in PECVD process. These curvatures are used to be the cause of misalignment effects on flexible devices. SEM images also illustrate how quality of substrate and defects of substrate are important. As we can see a defect in the substrate is transferred through all the thickness of AZO film and is

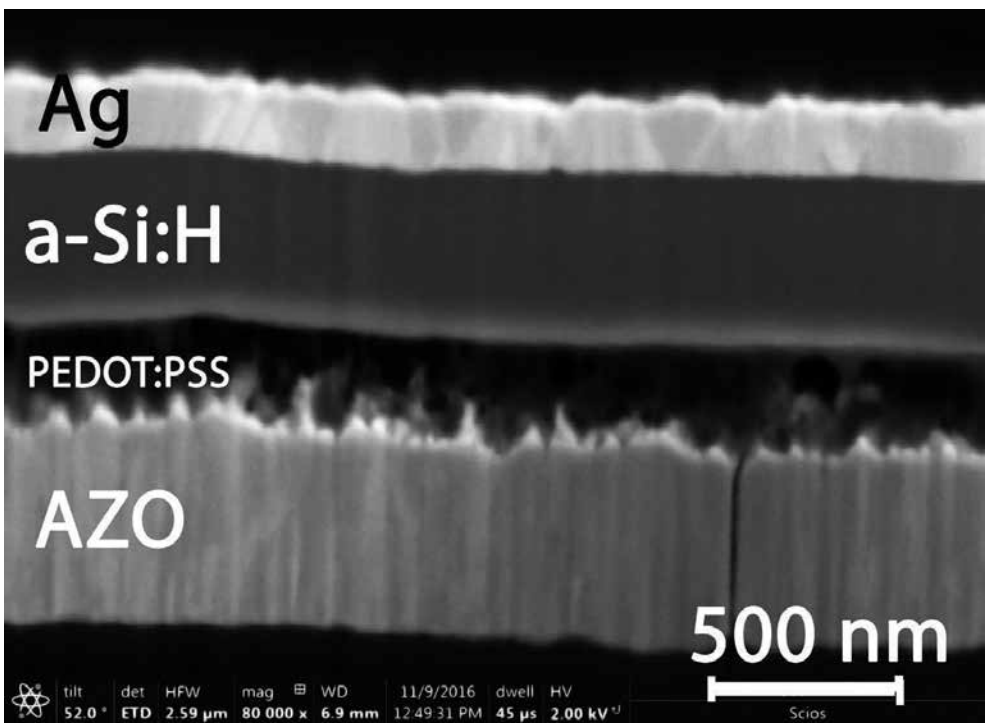

Figure 13. Hybrid solar cell cross-sectional SEM image on flexible substrate PEN/ITO/PEDOT:PSS/(i) Si:H/(n) Si:H (H2).

http://dx.doi.org/10.5772/67565

interrupted by the organic PEDOT:PSS layer. The surface quality is an important parameter that influences the final quality of the devices.

6. Summary and conclusion

In the beginning, a brief overview of polymer organic and PECVD inorganic material semiconductor technologies has been made to focus on optoelectronic characteristics and fabrication process at low substrate temperature for application on hybrid photovoltaic devices. Inorganic semiconductor materials deposited by PECVD have been reported in literature to be a mature technology compatible with large area flexible devices; while organic semiconductors and their technology are significantly less studied. On other hand, organic materials have shown potential as PV materials with several advantages in the fabrication process such as room temperature deposition and reduction of complex vacuum stages for deposition but the "ideal" process for the deposition of organic materials is still unresolved.

A concept of inorganic-organic photovoltaic devices mainly for PECVD inorganic materials has been considered. The concept is based on compatibility of both technologies and complementary electronic properties. Three types of hybrid structures have been fabricated and studied: (1) with OS as intrinsic absorber and p-, n-Si:H layers creating built-in electric field (H1 structures), (2) ITO/PEDOT:PSS/(i) Si:H/(n) Si:H structures (H2 type), and (3) structures with double intrinsic absorber such as ITO/PEDOT:PSS/P3HT:PCBM/(i) Si:H/(n) Si:H (H3). All the structures showed PV performance with different characteristics discussed and compared with those reported in the literature. Performance of the structures including those fabricated on flexible plastic substrates confirmed clear compatibility OS and PECVD technologies. The device diagnostics of the studied structures has been performed by measurements of photocurrent spectral dependencies. The measurements of subgap photocurrent revealed, that electronic quality of intrinsic OS materials, was sufficient, but worse comparing to that of Si:H films. The structures with OS frontal interfaces showed better short wavelength photocurrent response indicating better electronic properties of the interfaces comparing to reference samples. All the structures suffered from photocurrent suppression at voltages near U_{OC} values suggesting high transversal leakage current. Simple "optimization" of H2 structure resulted in substantial increase of photocurrent to the value J_{SC} = 17.7 mA/cm^2 that was higher than the values in the reference samples. Explanations of characterization data have speculative character and should be considered only as some guidelines and motivation for further study. Although some hybrid structures demonstrated substantial improvement of performance, while other hybrid structures showed poor performance, further R&D efforts seem to be promising and should be focused on deeper study of organic materials and related interface properties.

Acknowledgements

Ismael Cosme Bolaños acknowledges support from "CONACyT Cathedra" project No.2734. Hiram Enrique Martinez and Antonio Olivares acknowledge support from CONACyT through the scholarships number 362152 and 363344, respectively.

Nomenclatures

PECVD	Plasma enhanced chemical vapor deposition
CVD	Chemical vapor deposition
GD	Glow discharge
ESR	Electron-spin resonance
DOS	Density of states
LT	Low temperature
HIT	Heterojunction intrinsic thin configuration
P3HT:PCBM	Poly(3-hexythiophene):methano-fullerenephenyl-C61-butyric-acid-methyl-ester
PEDOT:PSS	Poly(3,4ethylenedioxythiophene):poly(4-styrenesulfonate)
IPA	Isopropyl alcohol
DC	Direct current
VRH	Variable range hopping
1D	One dimension
TCO	Transparent conductive oxide
PLD	Pulsed laser deposition
AZO	Aluminum zinc oxide
PET	Polyethylene terephthalate
PEN	Polyethylene naphthalate
PTFE	Polytetrafluoroethylene
CIOD	Concept for inorganic-organic device
PV	Photovoltaic
AM1.5	Air mass spectrum 1.5
SEM	Scanning electron microscopy

Author details

Andrey Kosarev[1]*, Ismael Cosme[2], Svetlana Mansurova[1], Antonio J. Olivares[1] and Hiram E. Martinez[1]

*Address all correspondence to: akosarev@inaoep.mx

1 National Institute for Astrophysics, Optics and Electronics, Optics and Electronics (INAOE), Puebla, Mexico

2 CONACyT-INAOE, Mexico

http://dx.doi.org/10.5772/67565

References

[1] J.M. Ziman, editor. Principles of the theory of solids. 2nd ed. Cambridge: Cambridge University Press; 1965. 452 p.

[2] H.F. Sterling, R.C.G. Swann. Chemical vapour deposition promoted by R.F. discharge. Solid-State Electronics. 1965;**8**:653-654.

[3] R.C. Chittick, J.H. Alexander, H.F. Sterling. The preparation and properties of amorphous silicon. Journals of Electrochemical Society. 1969;**166**:77-88.

[4] W.E. Spears, P.G. Le Comber. Substitutional doping of amorphous silicon. Solid State Communications. 1975;**17**:1193-1196.

[5] W.E. Spear, P.G. Le Comber, S. Kinmond, M.H. Brodsky. Amorphous silicon p-n junction. Applied Physics Letters. 1976;**28**:105.

[6] R. Martins, H. Aguas, V. Silva, I. Ferreira, A. Cabrita, E. Fortunato. Nanostructured silicon films produced by PECVD. Materials Research Society Symposium Proceedings. 2001;**664**:A9.6.1-A9.6.6.

[7] Y. Nasuno, M. Kondo, A. Matsuda. Passivation of oxygen-related donors in microcrystalline silicon by low temperature deposition. Applied Physics Letters. 2001;**78**:2330-2332.

[8] A. Matsuda. Formation kinetics and control of micro-crystallite in μc- Si:H from glow discharge plasma. Journal of Non-crystalline Solids. 1983;**59-60**:767-774.

[9] R. Cariou, M. Labrune, R.I. Cabarrocas. Thin crystalline silicon solar cells based on epitaxial films grown at 165°C by RF-PECVD. Solar Energy Materials and Solar Cells. 2011;**95**:2260-2263.

[10] A. Kosarev, A. Torres, C. Zuñiga, M. Adamo, L. Sanchez. Nano-structured GeySi1-y:H films deposited by low frequency plasma for photovoltaic application. Materials Research Society Symposium Proceedings. 2009;**1127**:1127-T04-03.

[11] J. Robertson. Deposition mechanism of hydrogenated amorphous silicon. Journal of Applied Physics. 2000;**87**:2608-2617.

[12] W.S. Wong, A. Salleo, editors. Flexible Electronics: Materials and Applications. 1st ed. USA: Springer Science + Business Media; 2009. 473 p.

[13] A. Terakawa. Review of thin-film silicon deposition techniques for high-efficiency solar cells developed at Panasonic/Sanyo. Solar Energy Materials & Solar Cells. 2013;**119**:204-208.

[14] Z. Mrázková, K. Postava, A. Torres-Rios, M. Foldyna, P. Roca i Cabarrocas, J. Pištora. Optical modeling of microcrystalline silicon deposited by plasma-enhanced chemical vapor deposition on low-cost iron-nickel substrates for photovoltaic applications. Procedia Materials Science. 2016;**12**:130-135.

[15] Y. Nasuno, M. Kondo, A. Matsuda. Microcrystalline silicon thin-film solar cells prepared at low temperature using PECVD. Solar Energy Materials & Solar Cells.2002;**74**:497-503.

[16] P. Alpuim, V. Chu, J.P. Conde. Amorphous and microcrystalline silicon films grown at low temperatures by radiofrequency and hot-wire chemical vapor deposition. Journal of Applied Physics. 1999;**86**(7):1.

[17] W.E. Spear, P.G. Le Comber. Electronic properties of substitutionally doped amorphous Si and Ge. Philosophical Magazine. 1976;**33**:935-949.

[18] D. Hauschildt, M. Stutzmann, J. Stuke, H. Dersch. Electronic properties of doped glow-discharge amorphous germanium. Solar Energy Materials. 1982;**8**(1-3):319-330.

[19] J. Xu, S. Miyazaki, M. Hirose. High-quality hydrogenated amorphous silicon-germanium alloys for narrow bandgap thin film solar cells. Journal of Non-Crystalline Solids. 1996;**208**(3):277-281.

[20] W.B. Jordan, B. Wagner. Effects of deposition temperature and film thickness on the structural, electrical, and optical properties of germanium thin films. MRS Proceedings. 2002;**715**:A18.2.

[21] F. Origo, P. Hammer, D. Comedi, I. Chambouleyron. The effect of ion-bombardment on the formation of voids during deposition of a-Ge:H. MRS Proceedings. 1998;**507**:477-482.

[22] A. Belfedal, Y. Bouizem, J.D. Sib, L. Chahed. Films thickness effect on structural and optoelectronic properties of hydrogenated amorphous germanium (a-Ge:H). Journal of Non-Crystalline Solids. 2012;**358**(11):1404-1409.

[23] C.-M. Wang, Y.-T. Huang, Y. Kuo-Hsi, H.-J. Hsu, C.-H. Hsu, H.-W. Zan, C.C. Tsai. Influence of hydrogen on the germanium incorporation in a-Si1-xGex:H for thin-film solar cell application. MRS Proceedings. 2010;**1245**:A04.02.1-04.02-6 .

[24] A. Kosarev, A. Torres, Y. Hernandez, R. Ambrosio, C. Zuniga, T.E. Felter, R. Asomoza, Y. Kudriavtsev, R. Silva-Gonzalez, E. Gomez-Barojas, A. Ilinski, A.S. Abramov. Silicon-germanium films deposited by low-frequency plasma-enhanced chemical vapor deposition: Effect of H2 and Ar dilution. Journal of Materials Research. 2006;**21**(1):88-104.

[25] I. Cosme. Study of GeSi:H materials deposited by PECVD at low temperatures (Td<200 °C) for device applications [thesis]. Puebla, MEX: INAOE; 2013. 157 p.

[26] C. Brabec, V. Dyakonov, U. Scherf, editors. Organic Photovoltaics. 2nd ed. Germany: Wiley-VCH Verlag GmbH & Co. KGaA; 2014. 642 p.

[27] F.C. Krebs. Fabrication and processing of polymer solar cells: A review of printing and coating techniques. Solar Energy Materials & Solar Cells. 2009;**93**:394-412.

[28] I. Cosme, A. Kosarev, S. Mansurova, A.J. Olivares, H.E. Martinez, A. Itzmoyotl. Hybrid photovoltaic structures based on amorphous silicon and P3HT:PCBM/PEDOT:PSS polymer semiconductors. Organic Electronics. 2016;**38**:271-277.

[29] K.A. Nagamatsu, S. Avasthi, J. Jhaveri, J.C. Sturm. A 12% efficient silicon/PEDOT:PSS heterojunction solar cell fabricated at <100°C. IEEE Journal of Photovoltaics. 2014;**4**(1):260-264.

[30] E.L. Williams, G.E. Jabbour, Q. Wang, S.E. Shaheen, D.S. Ginley, E.A. Schiff. Conducting polymer and hydrogenated amorphous silicon hybrid solar cells. Appl. Phys. Lett. 2005;**87**:223504-223506 .

[31] A. Olivares, I. Cosme, S. Mansurova, A. Kosarev, H.E. Martinez. Study of Electrical Conductivity of PEDOT:PSS at Temperatures >300 K for Hybrid Photovoltaic Applications. In: 12th International Conference on Electrical Engineering, Computing Science and Automatic Control (CCE); 2015; Mexico City. Mexico: CCE; 2015. p. 1-3.

[32] D. Ginley, H. Hosono, D.C. Paine, editors. Handbook of Transparent Conductors. 1st ed. Online: Springer US; 2011. 534 p.

[33] K.-H. Choi, J.-A. Jeong, J.-W. Kang, D.-G. Kim, J.K. Kim, S.-I. Na, D.-Y. Kim, S.-S. Kim, H.-K. Kim. Characteristics of flexible indium tin oxide electrode grown by continuous roll-to-roll sputtering process for flexible organic solar cells. Solar Energy Materials & Solar Cells Materials. 2009;**93**:1248-1255.

[34] H.J. Park, J.-W. Park, S.-Y. Jeong, C.-S. Ha. Transparent flexible substrates based on polyimides with aluminum doped zinc oxide (AZO) thin films. Proceedings of the IEEE. 2005;**93**(6): 1447-1450.

[35] S. Sanzaro, A.L. Magna, E. Smecca, G. Mannino, G. Pellegrino, E. Fazio, F. Neri, A. Alberti. Controlled Al3+ incorporation in the ZnO lattice at 188 °C by soft reactive co-sputtering for transparent conductive oxides. Energies. 2016;**9**:443.

[36] K. Tvingstedt, O. Inganäs. Electrode grids for ITO free organic photovoltaic devices. Advance Materials. 2007;**19**:2893-2897.

[37] J. Wu, H.A. Becerril, Z. Bao, Z. Liu, Y. Chen, P. Peumans. Organic solar cells with solution-processed graphene transparent electrodes. Applied Physics Letters. 2008;**92**:26.

[38] Y.H. Kim, C. Sachse, M.L. Machala, C. May, L. Müller-Meskamp, K. Leo. Highly conductive PEDOT:PSS electrode with optimized solvent and thermal post-treatment for ITO-free organic solar cells. Advanced Functional Materials. 2010;**94**(8):1076-1081.

[39] S.-I. Na, B.-K. Yu, S.-S. Kim, D. Vak, T.-S. Kim, J.-S. Yeo, D.-Y. Kim. Fully spray-coated ITO-free organic solar cells for low-cost power generation. Solar Energy Materials and Solar Cells. 2010;**94**(8):1333-1337.

[40] D. Alemu, H.-Y. Wei, K.-C. Ho, C.-W. Chu. Highly conductive PEDOT:PSS electrode by simple film treatment with methanol for ITO-free polymer solar cells. Energy & Environmental Sciences. 2012;**5**:9662-9671.

[41] X. Crispin, F.L.E. Jakobsson, A. Crispin, P.C.M. Grim, P. Andersson, A. Volodin, C. van Haesendonck, M. Van der Auweraer, W.R. Salaneck, M. Berggren. The origin of the high conductivity of poly(3,4-ethylenedioxythiophene) – poly (styrenesulfonate) (PEDOT–PSS) plastic electrodes. Chemistry of Materials. 2006;**18**(18):4354-4360.

[42] A. Elschner, S. Kirchmeyer, W. Lovenich, U. Merker, K. Reuter, editors. PEDOT: Principles and Applications of an Intrinsically Conductive Polymer. 1st ed. London: CRC Press; 2011. 355 p.

[43] Alshammari, A. S., Sam, F. L. M., Rozanski, L. J., Mills, C. A., Alenezi, M. R., Beliatis, M. J., Jayawardena, K. D. G. I., Underwood, J. M. and Silva, S. R. P., Controlled growth and spray deposition of silver nanowires for ITO-free, flexible, and high brightness OLEDs. Phys. Status Solidi A, 2016, DOI 10.1002/pssa.201600561

[44] A. Plichta, A. Habeck, S. Knoche, A. Kruse, A. Weber, N. Hildebrand. Flexible glass substrate. In: Crawford GP (ed), Flexible Flat Panel Displays. John Wiley & Sons Ltd, West Sussex, 2005; pp. 35-55.

[45] C.C. Wu, S.D. Theiuss, G. Gu, M.H. Lu, J.C. Sturm, S. Wagner, C.C. Wu, S.D. Theiuss, G. Gu, M.H. Lu, J.C. Sturm, S. Wagner, S.R. Forrest. Integration of organic LEDs and amorphous Si TFTs onto flexible and lightweight metal foil substrates. IEEE Electron Device Letters. 1997;**18**(12):609-612.

[46] H. Izadi, M. Golmakania, A. Penlidis. Enhanced adhesion and friction by electrostatic interactions of double-level Teflon nanopillars. Soft Matter. 2013;**9**:1985-1996.

[47] M. Wright, A. Uddin. Organic—inorganic hybrid solar cells: A comparative review. Solar Energy Materials & Solar Cells. 2012;**107**:87-111.

[48] X. Shen, B. Sun, D. Liu, S.-T. Lee. Hybrid heterojunction solar cell based on organic inorganic silicon nanowire array architecture. Journal of the American Chemical Society. 2011;**133**:19408-19415.

Chapter 9

Modeling of Silicon Photonic Devices for Optical Interconnect Transceiver Circuit Design

Binhao Wang

Additional information is available at the end of the chapter

http://dx.doi.org/10.5772/intechopen.68272

Abstract

Optical interconnect system efficiency is dependent on the ability to optimize the transceiver circuitry for low-power and high-bandwidth operation, motivating co-simulation environments with compact optical device simulation models. This chapter presents compact Verilog-A silicon carrier-injection and carrier-depletion ring modulator models which accurately capture both nonlinear electrical and optical dynamics. Experimental verification of the carrier-injection ring modulator model is performed both at 8 Gb/s with symmetric drive signals to study the impact of pre-emphasis pulse duration, pulse depth, and dc bias, and at 9 Gb/s with a 65-nm CMOS driver capable of asymmetric pre-emphasis pulse duration. Experimental verification of the carrier-depletion ring modulator model is performed at 25 Gb/s with a 65-nm CMOS driver capable of asymmetric equalization.

Keywords: microring modulator, carrier-injection, carrier-depletion, optical interconnects, silicon photonics, co-simulation, Verilog-A

1. Introduction

Due to low channel loss and the potential for wavelength division multiplexing (WDM), optical interconnects are well suited to address the dramatic requirements in high-speed interconnect capacity and transmission distance demanded by mega data centers and supercomputers [1, 2]. For these applications, silicon photonic platforms are attractive due to their large-scale photonic device integration capabilities and potential manufacturing advantages. As shown in **Figure 1**, compact and energy-efficient WDM interconnect architectures are possible with silicon photonic microring resonator modulators and drop filters [3], as these high-Q devices occupy smaller footprints than large-area Mach-Zehnder modulators [4] and offer inherent wavelength multiplexing without extra device structures, such as array waveguide gratings.

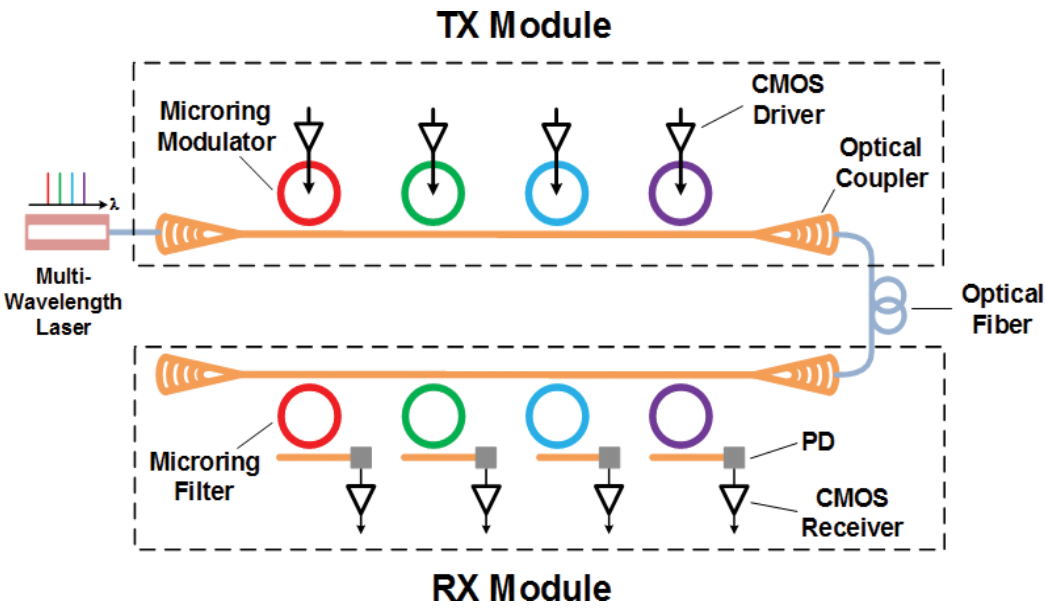

Figure 1. Silicon photonic ring resonator-based wavelength-division-multiplexing (WDM) interconnect system.

The most common high-speed silicon ring modulators operate based on the plasma dispersion effect, with devices based on carrier accumulation, depletion, and injection which display various trade-offs. Accumulation-mode modulators based on metal-oxide-semiconductor (MOS) capacitors can achieve high extinction ratios, but their modulation bandwidth is limited by the relatively high device capacitance [5]. At data rates near 10 Gb/s, injection-mode modulators based on forward-biased p-i-n junctions are an attractive device due to their high modulation depths and rapid bias-based resonance wavelength tuning capabilities [6, 7], but their speed with simple non-return-to-zero (NRZ) modulation is limited by both long minority carrier lifetimes and series resistance effects [8]. Depletion-mode modulators based on reverse-biased p-n junctions can achieve high speed (~40 Gb/s) [9], but require large drive voltages [10]. Injection-mode modulators provide higher energy efficiency and depletion-mode modulators offer higher bandwidth density. Sections 2 and 3 present two compact Verilog-A models for carrier-injection and carrier-depletion ring modulators including both nonlinear electrical and optical dynamics, respectively. Finally, Section 4 concludes the chapter.

2. Silicon carrier-injection ring modulator model

Pre-emphasis signaling, which improves optical transition times, is necessary in order to achieve data rates near 10 Gb/s with carrier-injection ring modulators [7, 8, 11, 12]. As the effective device time constant is different during a rising transition (limited by long minority carrier lifetimes) versus a falling transition (limited by series resistance), nonlinear pre-emphasis waveforms are often used [11, 12]. In addition, the device's optical dynamics must be considered in optimizing the pre-emphasis waveforms [13, 14]. The optical bandwidth is limited by the photon lifetime,

which is related to the ring resonator's Q factor, and the ring's phase delay during modulation should be considered to capture the nonlinear optical dynamics. In order to compensate these electrical and optical dynamics, the transmitter circuit must be carefully designed to supply a high-speed pre-emphasis signal with the proper pulse depth, pulse duration, and dc bias. This motivates co-simulation environments with compact optical device simulation models that accurately capture optical and electrical dynamics.

Although previous models have been developed for accumulation-mode [15] and depletion-mode [16] ring modulators, previous models for injection-mode ring devices [8, 17] have lacked accurate modeling of the large-signal p-i-n forward-bias behavior [18] and nonlinear optical dynamics in a format suitable for efficient co-simulation. This section presents a compact Verilog-A model for carrier-injection ring modulators which includes both nonlinear electrical and optical dynamics [19]. The model, which combines an accurate p-i-n electrical [18] and a dynamic ring resonator model [13], will be described and experimentally verified both at 8 Gb/s with symmetric drive signals to study the impact of pre-emphasis pulse duration, pulse depth, and dc bias, and at 9 Gb/s with a 65-nm CMOS driver capable of asymmetric pre-emphasis pulse duration.

2.1. Model description

As shown in **Figure 2**, the modeled carrier-injection ring modulator consists of a ring waveguide coupled to a straight waveguide, with p+ and n+ doping in the inner and outer ring regions, respectively. Accurate high-speed modeling requires inclusion of both electrical and optical dynamics, with **Figure 3** showing a flow chart of the model implementation. When a driving voltage is applied, the dynamic current response is determined by a p-i-n diode SPICE model based on a moment-matching approximation of the ambipolar diffusion equation [18]. After obtaining the current dynamics, the total carriers are calculated by integrating this diode current. However, as some of the carriers recombine and remain inside the waveguide during signal transients, only a portion act as free carriers and impact the effective ring index [20]. Utilizing a subsequent high-pass filter with a time constant equal to the carrier lifetime allows extraction of the free carriers used to calculate the ring index and loss changes due to the plasma dispersion effect [21]. Finally, the optical output power is related to the changes in refractive index and absorption coefficient by a dynamic ring resonator model which accurately considers the ring's cumulative phase shift [13].

The electrical SPICE model is described in **Figure 4**. Electrically, the carrier injection ring modulator is treated as a p-i-n diode (**Figure 4(a)**). As shown in **Figure 4(b)**, the total voltage across the device is distributed across the diode's intrinsic region, $V_{epi}(V(10, 12))$, two junctions, $V_j(V(12, 20))$, and the two terminal contact resistances, V_c. The charge, q_0, required for the total current response, is given by modeling the junction characteristics with the applied voltage, V_j, shown in **Figure 4(c)**. In order to accurately model both the dc and dynamic I-V characteristics, the total current I consists of the current injected into the intrinsic region, $I_{epi,}$ and the current due to the anode recombination effect, I_r. As shown in **Figure 4(d)**, I_r is calculated via q_0 and I_{epi} is modeled by a tenth-order network, modified from Ref. [18] for enhanced accuracy. The tenth-order network is designed according to an approximation of the transfer function (the

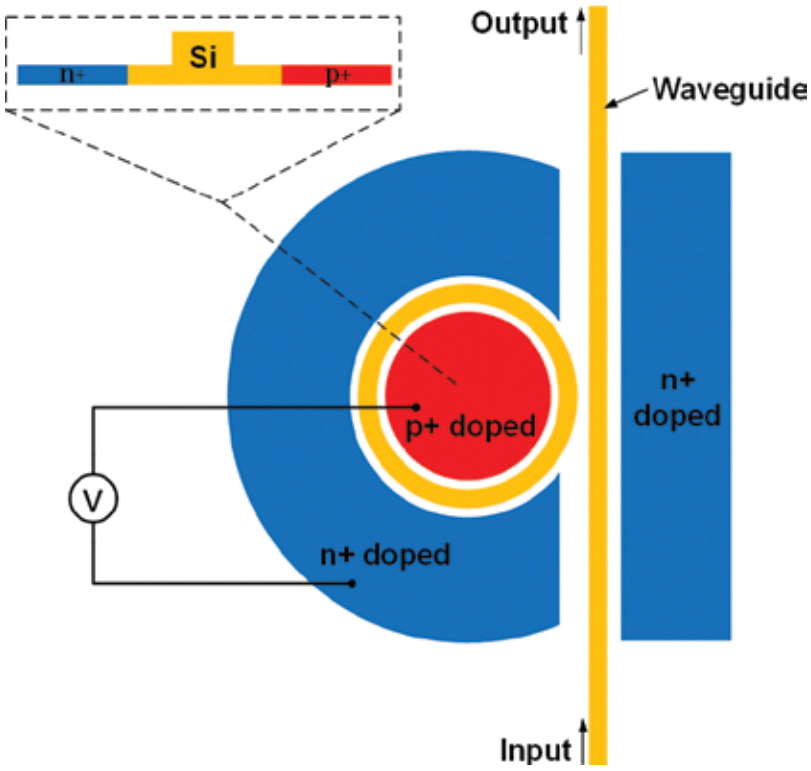

Figure 2. Top and cross-section views of a carrier-injection ring resonator modulator.

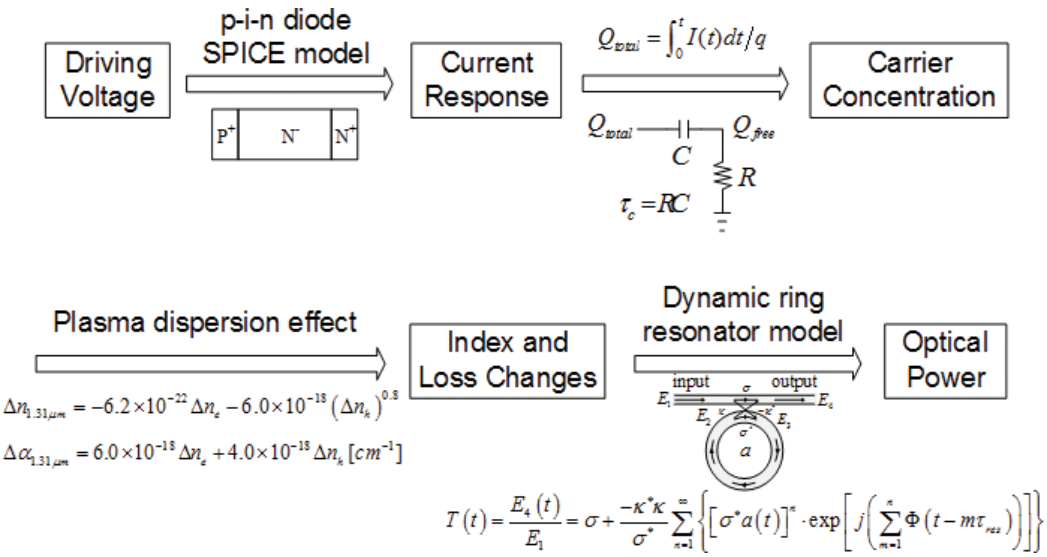

Figure 3. Model flow chart.

http://dx.doi.org/10.5772/intechopen.68272

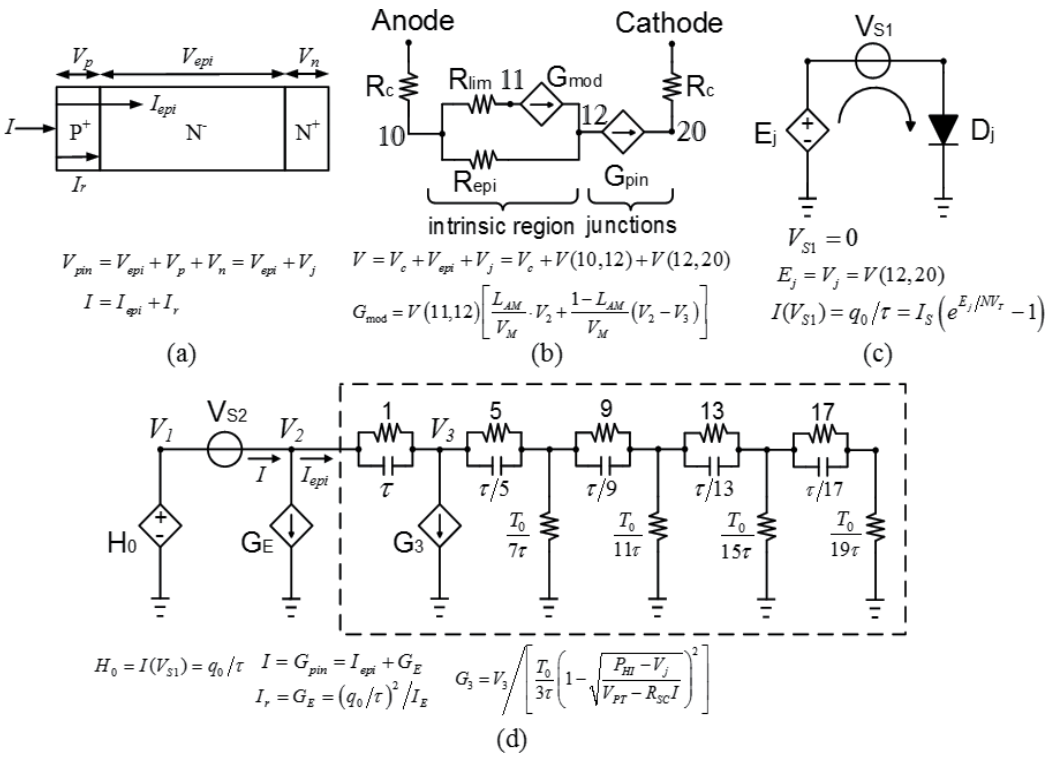

Figure 4. p-i-n Diode and SPICE model schematic: (a) p-i-n diode cross-section, (b) p-i-n voltage distribution model, (c) junction *I-V* characteristic model, and (d) p-i-n current distribution model. The above model is modified from Ref. [18] with the inclusion of contact resistors and by increasing the current distribution model to tenth-order for increased accuracy.

ratio of the intrinsic region current, I_{epi}, and charge, q_0) via asymptotic waveform evaluation (AWE), which is deducted from the ambipolar diffusion equation [22]. The current through the diode D_j, is equal to q_0/τ, is converted to a voltage via the current-controlled voltage source H_0 to drive a network which models the current dynamics in the intrinsic region. Three important nonlinear effects, described by current sources G_{mod}, G_E, and G_3, are included. G_{mod}, which is a function of $V(11,12)$, represents the conductivity modulation in the intrinsic region, G_E expresses the anode recombination effect, and G_3 implements the moving boundary effect during reverse recovery.

Table 1 summarizes the electrical model parameters and shows values for a 5 μm radius device. The extraction procedure for these parameters is described in **Figure 5**. After initializing the parameters with reasonable empirical values, their values are obtained via curve fitting to dc and high-frequency measurements. Eight of the parameters are extracted from the dc characteristic of **Figure 6(a)**. An iterative process is used to curve fit this data, with high sensitivity parameters R_C, I_S, and N first estimated, followed by the low-sensitivity parameters P_{HI}, I_E, V_M, R_{lim}, and R_{epi} related to the previously mentioned nonlinear effects. In the parameter extraction procedure, current levels above 100 μA are given higher weight in the curve fitting since the model is targeted for optical interconnect applications with NRZ modulation.

Parameter	Unit	Description	Empirical range	Value
R_C	Ω	Contact resistance	10–100	50
I_S	A	Saturation current	$1 \times 10^{-14} - 1 \times 10^{-12}$	5.78×10^{-14}
N	–	Emission coefficient	1–2	1.46
P_{HI}	V	Build-in voltage	0.5–1	0.7
T_0	s	Transit time	1×10^{-10}–1×10^{-9}	1.046×10^{-10}
I_E	A	Emitter recombination knee current	1.0×10^{-4}–1.0×10^{-2}	1.0×10^{-3}
V_M	V	High-injection voltage drop on the base	0–0.5	0.12
R_{lim}	Ω	Carrier-scattering series resistance	1×10^{-3}–3×10^{-3}	1.8×10^{-3}
L_{AM}	–	Forward-recovery coefficient	0–0.1	0.03
τ	s	Carrier lifetime in the base	1.0×10^{-10}–1.0×10^{-8}	1.0×10^{-9}
R_{epi}	Ω	Base region resistance	1.0×10^{2}–1.0×10^{3}	300
V_{PT}	V	Reverse-recovery coefficient	5–20	10
R_{SC}	Ω	Reverse-recovery coefficient	1–100	18

Table 1. Model parameters of the p-i-n diode, with values for a 5 μM device.

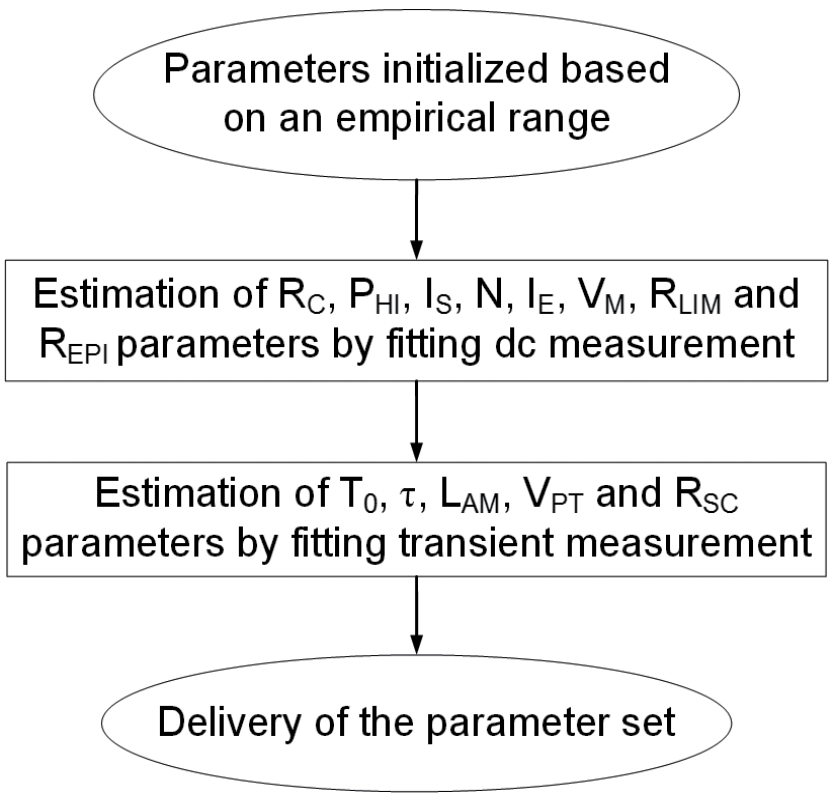

Figure 5. Electrical p-i-n diode parameter extraction procedure.

As shown in **Figure 6(a)**, excellent matching is achieved at these current levels at the cost of some minor error at low current conditions. The remaining five parameters are extracted from **Figure 6(b)** dynamic current response to a 10 Gb/s clock pattern with a voltage swing between −0.5 and 1.5 V. In a similar manner, high sensitivity parameters T_0 and τ are first estimated, followed by the low-sensitivity parameters L_{AM}, V_{PT}, and R_{SC}. Excellent amplitude matching is achieved between the transient simulation and measured results, implying that the current dynamics are captured well. While there is slightly more harmonic content in the measured results, this small error is not deemed critical for NRZ modulation applications. Overall, utilizing the measured dc *I-V* characteristic and transient response for parameter extraction allows for parameters R_C, I_S, N, P_{HI}, T_0, τ, R_{lim}, and R_{epi} to be well defined, while low-sensitivity parameters I_E, V_M, L_{AM}, V_{PT}, and R_{SC} are more softly defined.

After obtaining the dynamic current response, the total carriers are calculated by integrating the diode current with $Q = \int_0^t I(t)dt/q$. The total carriers consist of the following components [20]:

$$Q_{total}(t) = Q_{remain}(t) + Q_{recombine}(t) + Q_{free}(t), \tag{1}$$

which correspond to carriers remaining in the waveguide during signal transients, Q_{remain}, carriers recombining inside the p-i-n diode, $Q_{recombine}$, and the free carriers, Q_{free}, which impact the effective ring index and loss [21]. As shown in **Figure 7**, the remaining and recombining carriers increase with time, while the free carriers can be extracted utilizing a high-pass filter with a time constant equal to the carrier lifetime. These free carriers are then used to calculate the ring index and loss changes due to the plasma dispersion effect. At a wavelength of 1.31 μm, which is near the resonance wavelength of the devices characterized in this work,

$$\Delta n_{1.31\ \mu m} = -6.2\times10^{-22}\Delta n_e - 6.0\times10^{-18}(\Delta n_h)^{0.8} \tag{2}$$

$$\Delta \alpha_{1.31\ \mu m} = 6.0\times10^{-18}\Delta n_e + 4.0\times10^{-18}\Delta n_h\ [\mathrm{cm}^{-1}], \tag{3}$$

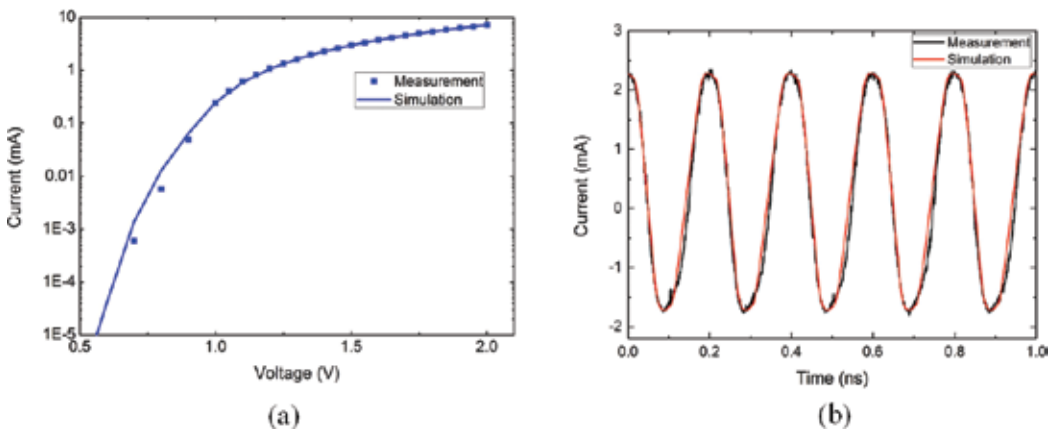

Figure 6. Measured and simulated (a) dc *I-V* characteristic and (b) transient response with a 10 Gb/s clock pattern with voltage swing between −0.5 and 1.5 V.

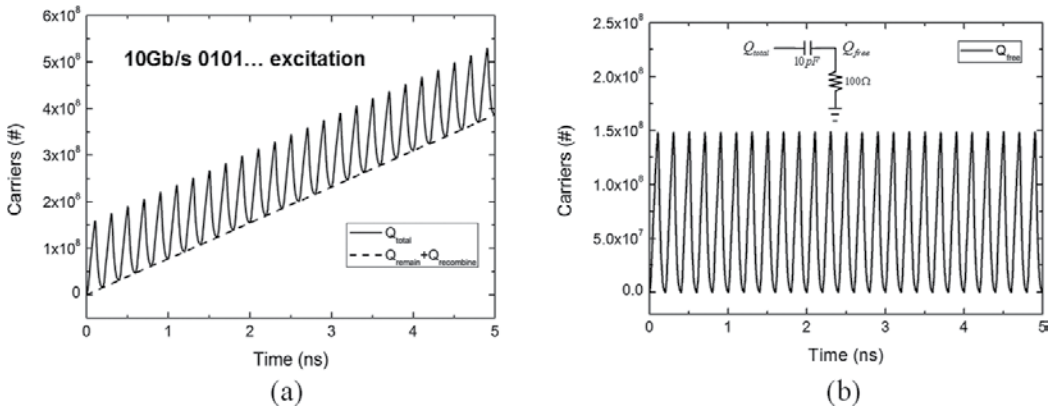

Figure 7. Carriers obtained from the electrical model with a 10 Gb/s clock pattern with voltage swing between −0.5 and 1.5 V: (a) total carriers and (b) free carriers extracted utilizing a high-pass filter with a time constant equal to the carrier lifetime.

where Δn_e and Δn_h are the electron and hole carrier densities [cm^{-3}], respectively. This model assumes $\Delta n_e = \Delta n_h$.

The optical output power is related to the change in refractive index and absorption coefficient by a dynamic ring resonator model which assumes lossless coupling and a single polarization (**Figure 8**). Considering the ring resonator's index dynamics, its time-dependent transmission is described by

$$T(t) = \frac{E_4(t)}{E_1} = \sigma + \frac{-\kappa^* \kappa}{\sigma^*} \sum_{n=1}^{\infty} \left\{ [\sigma^* a(t)]^n \cdot \exp\left[j\left(\sum_{m=1}^{n} \Phi(t - m\tau_{res}) \right) \right] \right\}, \tag{4}$$

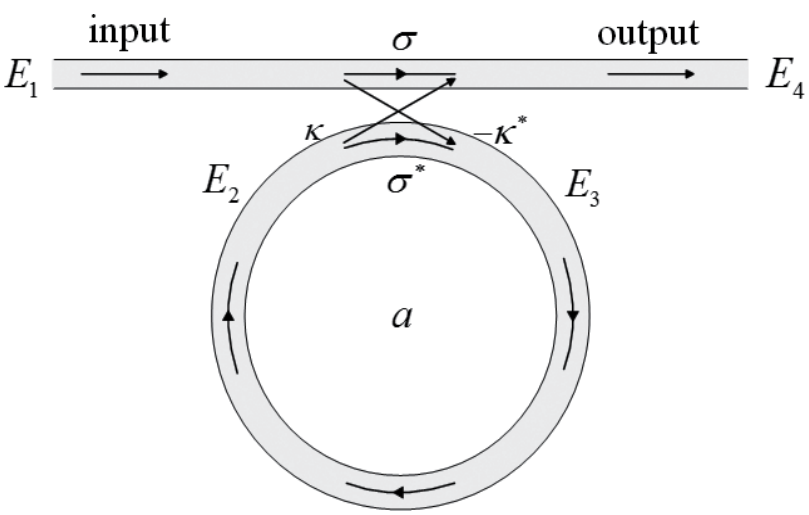

Figure 8. Microring resonator optical model.

where σ and κ are coupling coefficients, $|\kappa^2| + |\sigma^2| = 1$, a is the ring loss coefficient with zero loss corresponding to $a = 1$ and which relates to the absorption coefficient α as $a^2 = \exp(-\alpha L)$, L is the ring circumference, Φ is phase shift, τ_{res} is the resonator round-trip time, and $|T(t)|^2$ is the optical transmission power [13]. The three critical model parameters such as σ, a, and n_{eff} are extracted by curve fitting the steady-state transmission

$$T(t) = \sigma + \frac{-\kappa^* \kappa}{\sigma^*} \sum_{n=1}^{\infty} \left\{ [\sigma^* a(t)]^n \cdot \exp[jn\Phi(t)] \right\} = \frac{\sigma - a(t) \cdot \exp\left[j\left(\Phi(t)\right)\right]}{1 - \sigma^* a(t) \cdot \exp\left[j\left(\Phi(t)\right)\right]} \tag{5}$$

where

$$\Phi(t) = \frac{2\pi}{\lambda} n_{eff}(t) L, \tag{6}$$

λ is the optical wavelength and n_{eff} is the effective index. As shown in **Figure 9**, by fitting the measured through port optical spectrum from a 5-μm ring resonator with applied bias

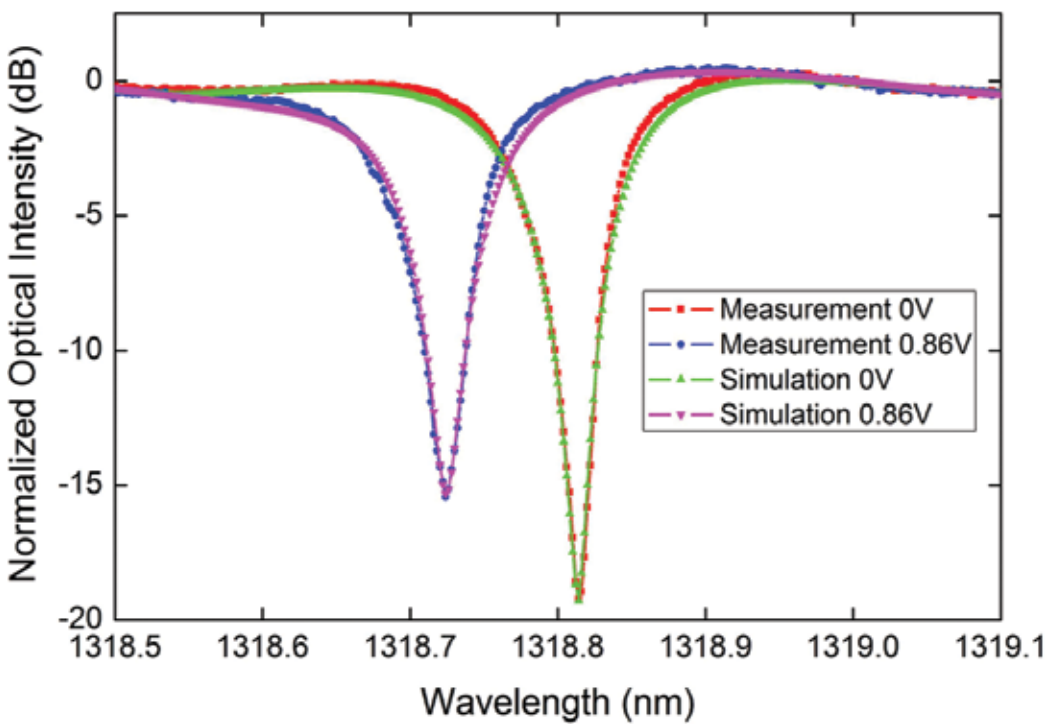

Figure 9. Measured and simulated ring resonator through port optical spectrums. These curves are normalized to the input laser power, accounting for ~10 dB of grating coupler loss.

voltages of 0 and 0.86 V, σ = 0.9944, a = 0.9931, and n_{eff} = 2.5188, are obtained. Utilizing these values in the model described by Eq. (4) allows for excellent matching with measured optical responses with large-signal high-speed modulation.

2.2. Comparison of simulated and measured results

This section presents a comparison of the presented model simulation results with high-speed large-signal measurements. Experimental verification of the model is performed both at 8 Gb/s with symmetric drive signals to study the impact of pre-emphasis pulse duration, pulse depth, and dc bias, and at 9 Gb/s with a 65-nm CMOS driver capable of asymmetric pre-emphasis pulse duration.

2.2.1. Symmetric pre-emphasis modulation with external driver

In order to demonstrate the ring modulator model accuracy, comparisons are made with the measured responses of a 5 μm radius carrier-injection ring modulator operating at 8 Gb/s with pre-emphasis modulation. As shown in the experimental setup of **Figure 10**, differential outputs of a high-speed pattern generator are combined to generate a pre-emphasis NRZ drive signal. The impact of pre-emphasis pulse duration, pulse depth, and dc bias is investigated, with a constant 2 Vpp swing maintained as these parameters are varied. Vertical couplers are used to provide light from a CW laser to the ring modulator input port and direct the modulated light out to a fiber connected to an optical oscilloscope for eye diagram generation.

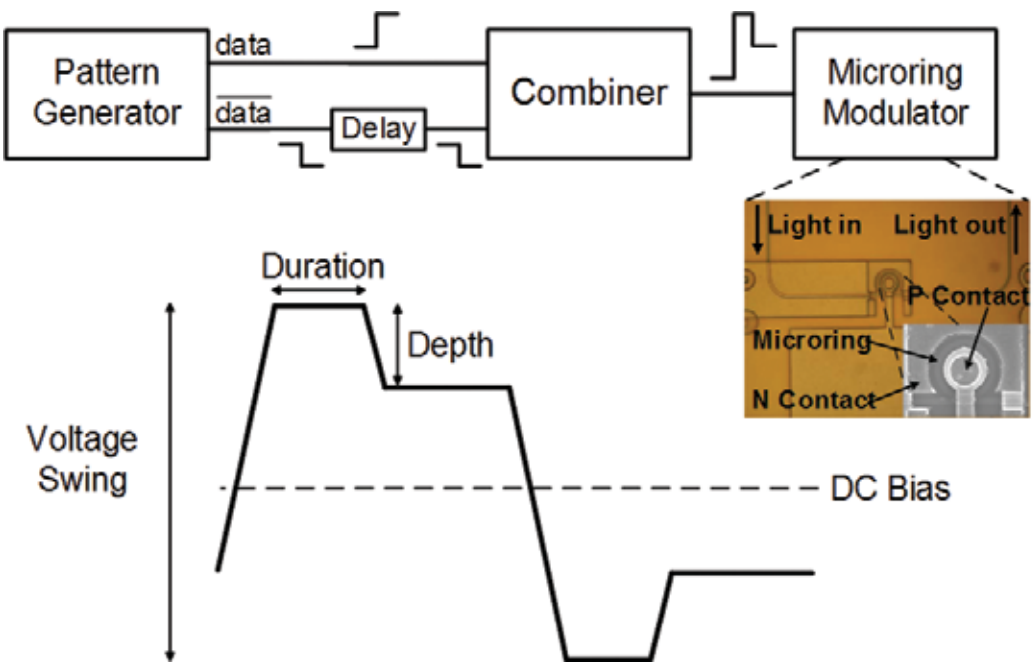

Figure 10. Pre-emphasis NRZ signal generation and waveform.

http://dx.doi.org/10.5772/intechopen.68272

In all the measured eye diagrams, the CW laser wavelength is tuned to align with the 0 V ring modulator resonance wavelength. Transition times of 40 ps are used in all the external modeling results, which match the equipment used in the measurements.

As predicted by the proposed ring model, utilizing a simple drive signal that is centered at a 0.7 V bias without pre-emphasis results in a very poor eye diagram with a 2^7–1 PRBS data pattern (**Figure 11**). Here the measured eye is completely closed by the system's random jitter, which is not included in the modeling results. Utilizing an optimal 0.8 V pre-emphasis pulse depth, the impact of pulse duration is shown in **Figure 12**. While a 40 ps duration allows the eye to partially open, the height and width are still degraded due to the long rise time caused by the minority carrier lifetime. Increasing the pulse duration to 80 ps provides optimal eye opening, with excellent matching between the simulated and measured eyes observed.

Relative to the optimal eye diagram of **Figure 12(b)**, **Figure 13** shows how the modeling results correlate with measurements as the pre-emphasis pulse depth is varied. An increase in pulse depth to 0.9 V results in excessive overshoot during a rising transition and slow settling to the steady-stage high level due to the relatively low amount of injected carriers after the pre-emphasis pulse. The model's transfer function does introduce some error in these low-carrier recombination dynamics, which results in some offset in the precise positioning of the falling-edge transitions, both **Figure 13** simulated and measured results show similar significant falling-edge deterministic jitter. A decrease in pulse depth to 0.7 V produces excessive charge for the steady-state high level, which results in slow fall times due to the modulator's series resistance limiting carrier extraction (**Figure 13(b)**).

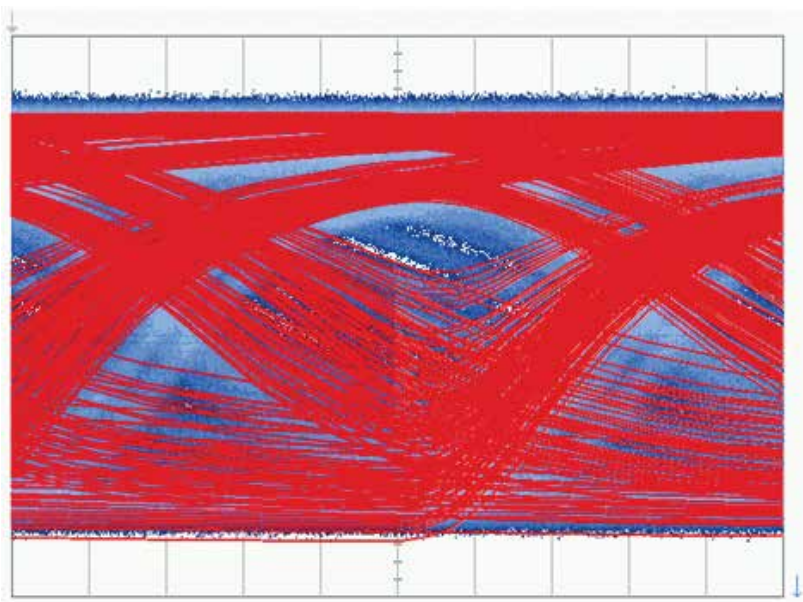

Figure 11. 8 Gb/s measured (blue) and simulated (red) optical eye diagrams with simple NRZ modulation without pre-emphasis [19].

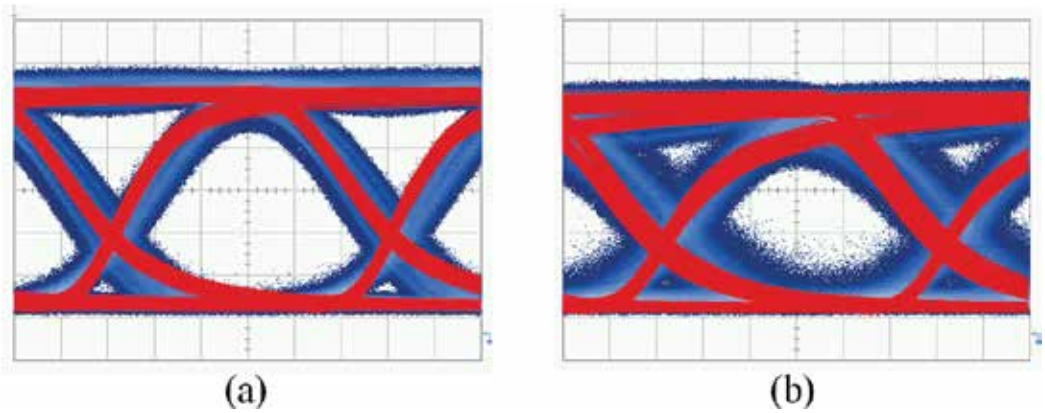

Figure 12. Impact of pre-emphasis pulse duration on 8 Gb/s measured and simulated optical eye diagrams with 0.8 V pulse depth, 0.7 V dc bias, and pulse duration of (a) 40 ps and (b) optimal 80 ps.

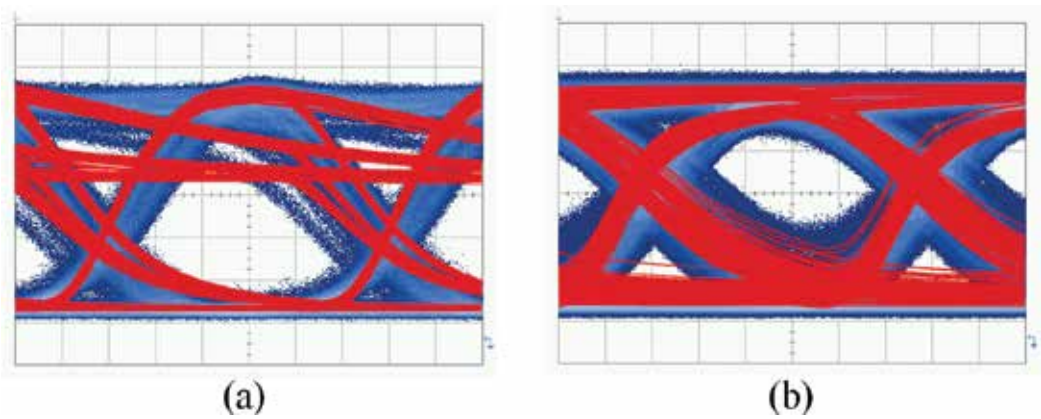

Figure 13. Impact of pre-emphasis pulse depth on 8 Gb/s measured and simulated optical eye diagrams with 80 ps pulse duration, 0.7 V dc bias, and pulse depth of (a) 0.9 V and (b) 0.7 V.

Figure 14 shows the impact of dc bias. As shown in **Figure 14(a)**, an increase in dc bias to 0.75 V produces excessive charge for the steady-state high level which is similar to a decrease in pulse depth to 0.7 V. A decrease in dc bias to 0.65 V results in slower carrier injection and degraded rising transitions (**Figure 14(b)**). Overall, results of **Figures 12–14** show excellent correlation between the proposed ring modulator model and measurements over varying pre-emphasis pulse duration, pulse depth, and dc bias.

2.2.2. Asymmetric pre-emphasis modulation with CMOS driver

A key objective of the model is to enable an opto-electronic co-simulation environment which allows for both the optimization of transceiver circuitry and the ability to study the impact of optical device parameters. The co-simulation capabilities are demonstrated by comparing simulated modeling results with the measured responses of the 5 μm radius carrier-injection

http://dx.doi.org/10.5772/intechopen.68272

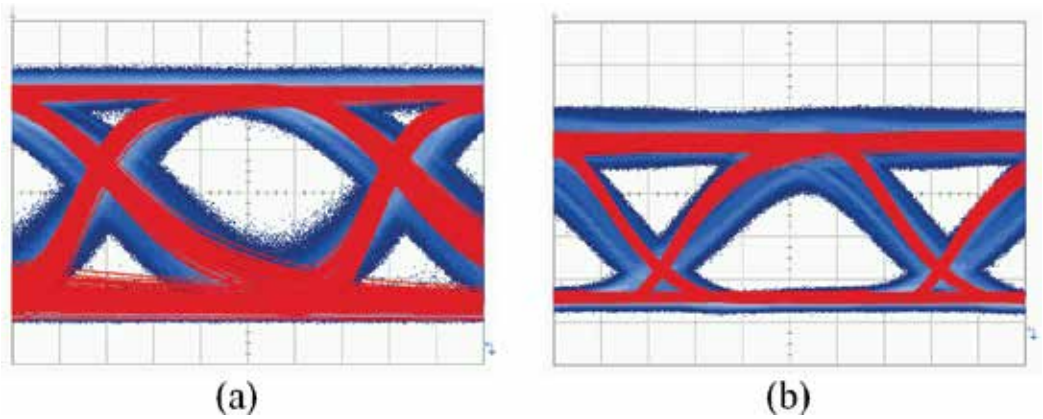

Figure 14. Impact of pre-emphasis dc bias on 8 Gb/s measured and simulated optical eye diagrams with 80 ps pulse duration, 0.8 V pulse depth, and dc bias of (a) 0.75 V and (b) 0.65 V.

ring modulator driven with a custom-designed CMOS driver. As shown in hybrid-integrated prototype in **Figure 15**, the pre-emphasis NRZ driver implemented in a 65-nm CMOS technology [12] is wire-bonded both to the PCB and the silicon ring modulator for testing. While the pre-emphasis pulse depth is fixed in this CMOS driver implementation, the prototype does have the ability to adjust the dc bias and the pre-emphasis pulse duration in an asymmetric manner for independent optimization of the rising and falling responses.

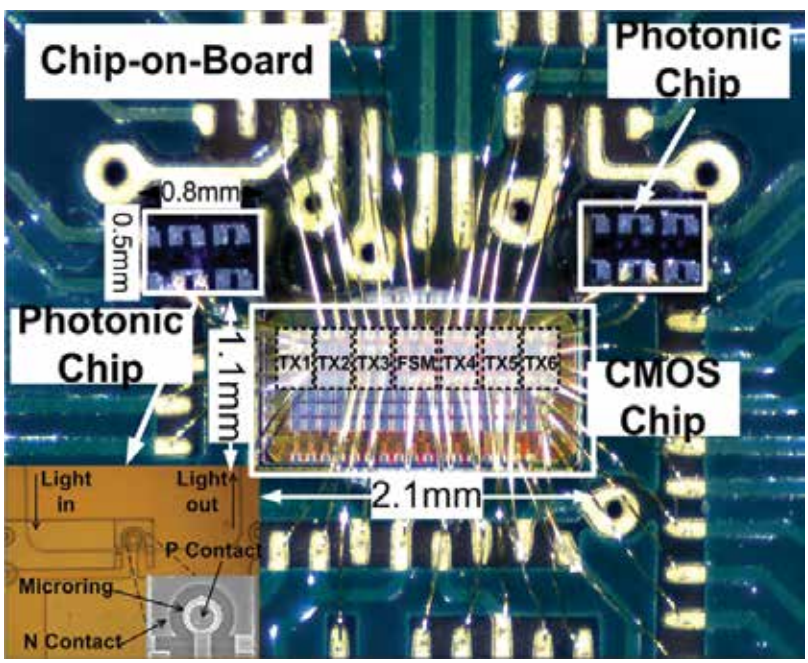

Figure 15. Hybrid-integrated optical transmitter prototype bonded for optical testing.

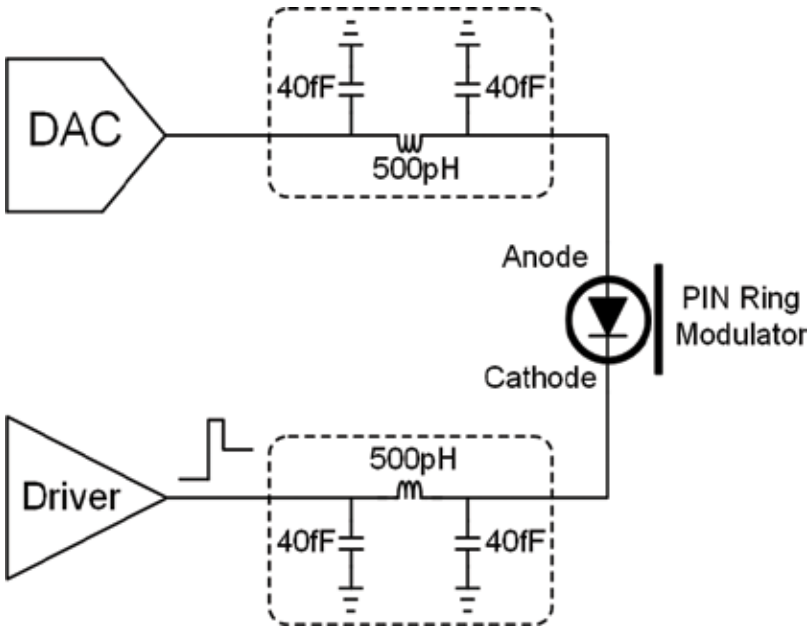

Figure 16. Co-simulation schematic with 65-nm CMOS high-speed CMOS driver, bias DAC, and Verilog-A carrier-injection ring resonator modulator model.

Figure 16 shows the co-simulation schematic in a CADENCE environment, with transistor-level schematics for the high-speed driver and bias digital-to-analog converter (DAC), lumped elements for the wirebond interconnect, and the Verilog-A carrier-injection ring resonator

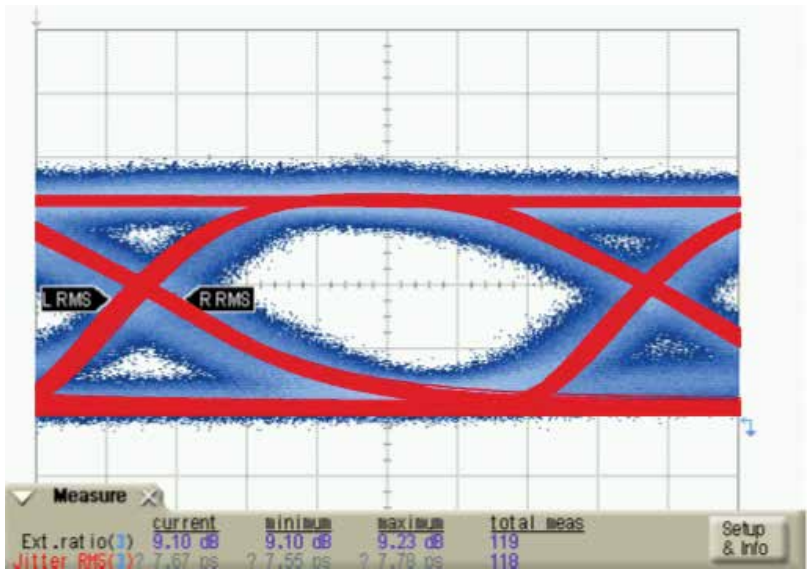

Figure 17. 9 Gb/s measured and co-simulated optical eye diagrams with the ring resonator modulator driven by the 65-nm CMOS driver.

modulator model. The single-ended driver provides a high-speed 2 Vpp output swing with independent dual-edge pre-emphasis duration tuning on the cathode of the ring modulator, while the 9-bit bias tuning DAC is connected to the anode for dc bias adjustment [12]. 500 pH inductors are used to model the ~0.5 mm bondwires that connect the high-speed driver and DAC to the modulator, while 40 fF capacitors model the chips' bondpads. **Figure 17** shows that the optimal 9 Gb/s measured and co-simulated eye diagrams, balancing extinction ratio and eye opening, are achieved when the anode bias is 1.45 V and asymmetric pulse durations for rising and falling transitions are 70 and 50 ps, respectively.

3. Silicon carrier-depletion ring modulator model

For carrier-injection ring modulators, large modulation depth and efficiency are achieved at the cost of relative low modulation bandwidth [12]. It limits application in ultra-high speed data communication. In contrast, carrier-depletion modulators have higher modulation speed ~40 Gb/s. A 320 Gb/s eight-channel WDM transmitter based on carrier-depletion ring modulators was demonstrated in Ref. [9]. The modulation speed of carrier-depletion ring modulators is limited by electrical bandwidth and optical bandwidth. The electrical bandwidth is determined by the RC bandwidth of the ring modulator where the voltage-controlled capacitance results in a nonlinear frequency response with a large voltage swing. The optical bandwidth is limited by photon lifetime related to the Q factor of ring resonators where the time rate of change in ring energy during modulation indicates nonlinear optical dynamics [23]. Therefore, an accurate carrier-depletion ring modulator model is essential to optimize transmitter circuitry while ring modulator models in Refs. [15, 16, 24, 25] did not demonstrate both nonlinear electrical dynamics and optical dynamics.

To design and optimize an optical interconnect transceiver circuitry, an accurate co-simulation environment is required for low-power and high-bandwidth operation. Photonic device models developed in Verilog-A provide the advantage of model compatibility with commercial SPICE circuit simulators. This section presents a Verilog-A carrier-depletion ring modulator model including nonlinear electrical and optical dynamics which provides a co-simulation environment for optical interconnect systems design. The model will be described and verified at 25 Gb/s with a 65-nm CMOS driver capable of asymmetric equalization.

3.1. Model description

The structure of the carrier-depletion ring modulator is shown in **Figure 18**. It consists of a rib waveguide of 500 nm width, 220 nm height, and 90 nm slab height coupled to a ring waveguide with radius of 7.5 μm, p-n junctions formed with outer p+ and inner n+-type doping with doping level near 2×10^{18} cm^{-3} on approximately 75% of the ring waveguide, p++ and n++-type doping utilized for ohmic contact formation, and an integrated heater with 550 Ω resistance formed by doping 15% of the ring with n+-type doping [26]. The ring modulator was fabricated at the IME A*STAR Singapore through OpSIS.

The proposed carrier-depletion ring modulator model is shown in **Figure 19**. The left side is the circuit model in which the electrical bandwidth is dominantly limited by resistances from

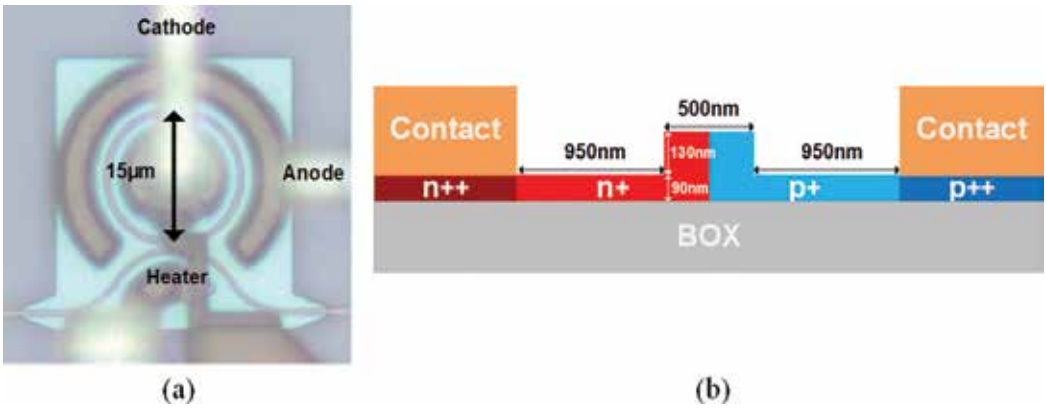

Figure 18. (a) Die photo and (b) cross-section view of carrier-depletion ring modulators.

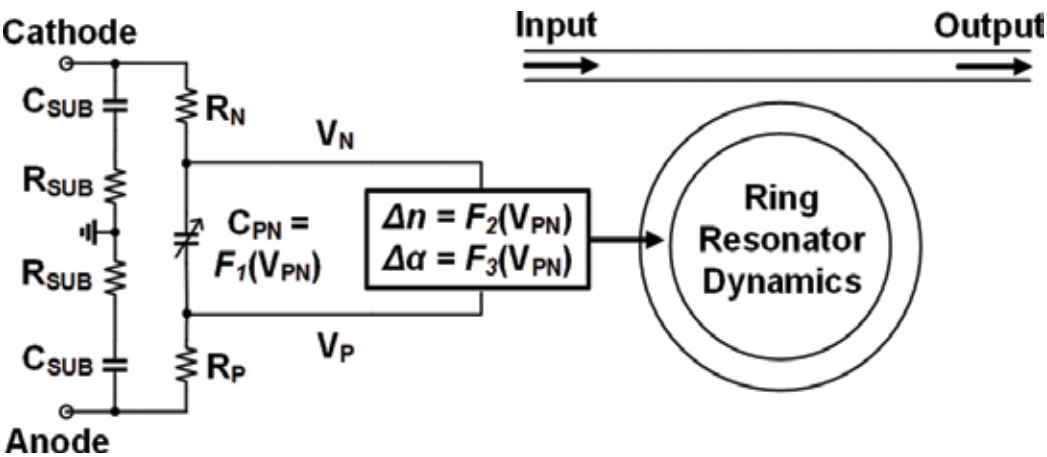

Figure 19. Carrier-depletion ring modulator model.

the electrodes to the junction and capacitance. The right side is the dynamic ring resonator model, and it is related to circuit model by functions of refractive index and absorption coefficient changes versus voltage drop on the junction. By fitting S11 parameter of the device, C_{sub} is 2.5 fF, R_{sub} is 750 Ω-cm, C_{pn} with no bias voltage is 25 fF, and R_p and R_n are 30 Ω [9]. Extracting the devices' carrier densities versus applied voltage with Lumerical allows calculation of the refractive index, n, and absorption coefficient, α, changes by the plasma dispersion effect [21], which for a $\lambda = 1.55$ μm input wavelength are formulated as

$$\Delta n_{1.55\ \mu m} = -8.8\times10^{-22}\Delta n_e - 8.5\times10^{-18}(\Delta n_h)^{0.8} \tag{7}$$

$$\Delta\alpha_{1.55\ \mu m} = 8.5\times10^{-18}\Delta n_e + 6.0\times10^{-18}\Delta n_h\ [\mathrm{cm}^{-1}], \tag{8}$$

Figure 20 shows how the single phase shifter ring modulator's effective index, absorption coefficient changes, and junction capacitance change versus applied reverse-bias voltage

where $C = \Delta Q/\Delta V$. By curve fitting **Figure 20**, the three parameters Δn, $\Delta\alpha$, and C are then extracted as a polynomial function of voltage.

$$f(V) = a_0 + a_1 V + a_2 V^2 + a_3 V^3 + a_4 V^4 \tag{9}$$

Table 2 gives the a_0-a_4 coefficients, where the valid voltage range is 0–5 V.

The dynamic optical output power is related to the changes in refractive index and absorption coefficient by a ring resonator modeling [23]:

$$\frac{\partial A}{\partial t} = \left(2\pi c j\left(\frac{1}{\lambda} - \frac{1}{\lambda_0}\right) - \frac{1}{\tau}\right)A + j\mu S_i \tag{10}$$

$$S_o = S_i + j\mu A, \tag{11}$$

where $1/\tau = 1/\tau_c + 1/\tau_l$ is an amplitude decay time constant associated with power coupling to bus waveguide τ_c and power lost due to absorption and scattering τ_l, c is light velocity, λ is laser wavelength, λ_0 is the ring resonant wavelength, A is the energy stored in the ring, μ is the mutual coupling between the ring and the bus waveguide, and S_i and S_o are incident and transmitted waves. The coupling factor μ satisfies $\mu^2 = \kappa^2 v_g/2\pi R = 2/\tau_c$, where κ is the coupling ratio, v_g is the ring group velocity, and R is the radius of the ring. The circuit model and ring resonator model are related by $2\pi(n_0 + \Delta n)R = m\lambda_0$ and $\tau_l = 1/\left(v_g exp\left((\alpha_0 + 0.75\Delta\alpha)2\pi R\right)\right)$, where ring effective index with no bias is ~2.57 and ring group index is ~3.89 extracted from Lumerical simulation, and the mode number m = 28 when R = 7.5 μm and λ = 1552.3 nm. By fitting the measured optical spectrum through port applied with reverse bias 0 and 4 V shown in **Figure 21**, three

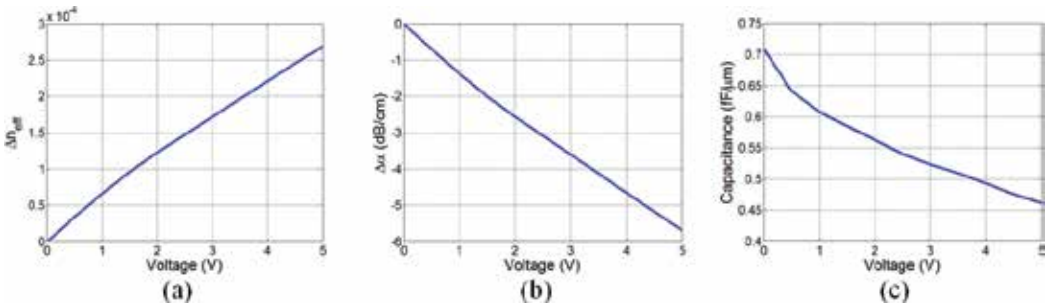

Figure 20. (a) The change of refractive index, (b) the change of absorption coefficient, and (c) the junction capacitance versus applied reverse-bias voltage.

Parameter	Unit	a_0	a_1	a_2	a_3	a_4
Δn_{eff}	–	-4.3×10^{-7}	7.3×10^{-5}	8.0×10^{-6}	1.1×10^{-6}	5.2×10^{-8}
$\Delta\alpha$	dB/cm	0.01	1.5	0.17	-2.3×10^{-2}	1.0×10^{-3}
C	fF/μm	0.71	−0.14	5.5×10^{-2}	-1.2×10^{-2}	1.0×10^{-3}

Table 2. Polynomial coefficients of Δn_{eff}, $\Delta\alpha$, and C.

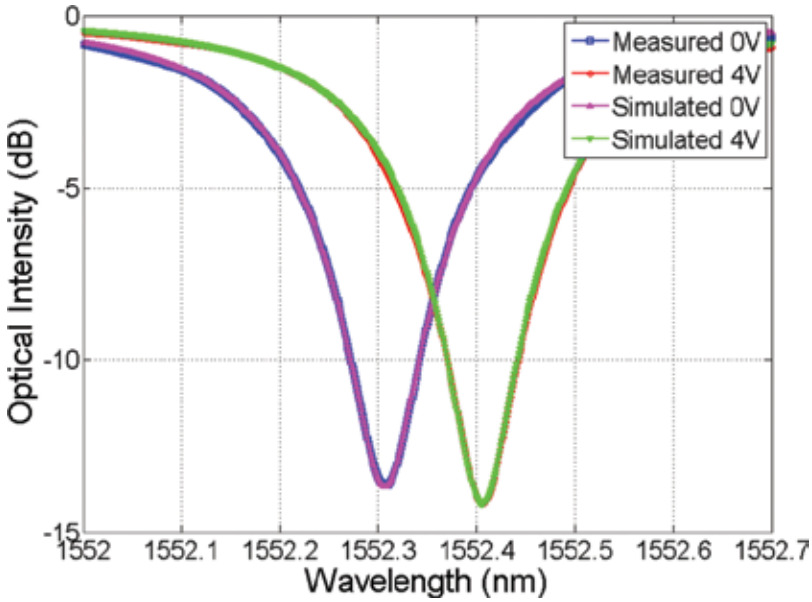

Figure 21. Measured and simulated optical spectrum at through port.

parameters of the model, τ = 9.07 ps, κ^2 = 0.0354, and n_0 = 2.5694, are obtained. The laser wavelength is set to be the resonant wavelength of the ring resonator at 1552.31 nm to maximize the extinction ratio (ER) for NRZ modulation.

3.2. Comparison of simulated and measured results

A key objective of the model is to enable an opto-electronic co-simulation environment which allows for both the optimization of transceiver circuitry and the ability to study the impact of optical device parameters. The co-simulation capabilities are demonstrated by comparing simulated modeling results with the measured responses of the 7.5 μm radius carrier-depletion ring modulator driven with a custom-designed CMOS driver. As shown in hybrid-integrated prototype in **Figure 22**, the AC-coupled differential driver implemented in a 65-nm CMOS technology [27] is wire-bonded both to the PCB and the silicon ring modulator for testing. The prototype has the ability to adjust the equalization to optimize high data rate performance.

Figure 23 shows the co-simulation schematic in a CADENCE environment, with transistor-level schematics for the high-speed differential driver, lumped elements for the wirebond interconnect, and the Verilog-A carrier-depletion ring resonator modulator model. The differential driver provides a high-speed 4.4 Vpp output swing with an asymmetrical feed-forward equalizer (FFE) to compensate the device nonlinearity [27]. 500 pH inductors are used to model the ~0.5 mm bondwires that connect the high-speed differential driver to the modulator, while 40 fF capacitors model the chips' bondpads.

http://dx.doi.org/10.5772/intechopen.68272

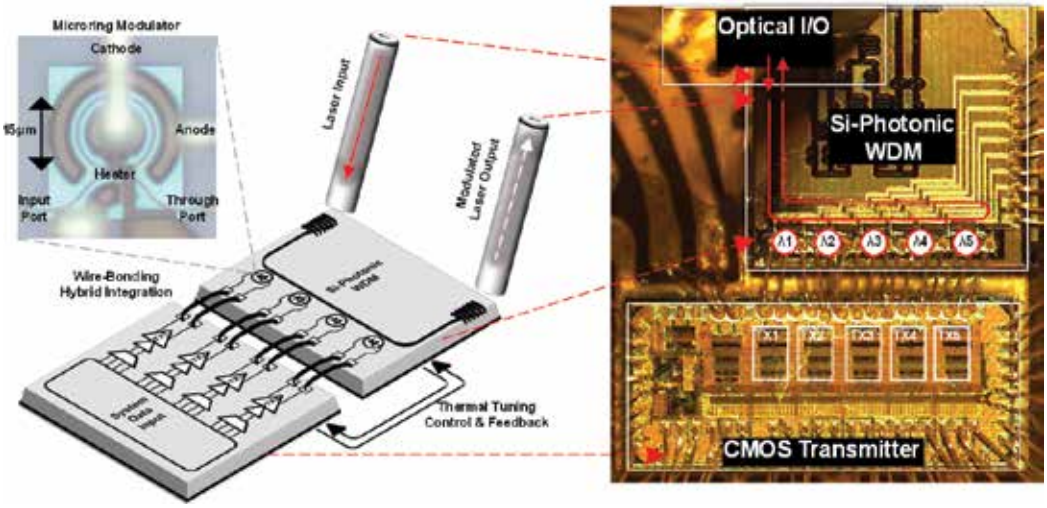

Figure 22. Optical transmitter prototype assembly.

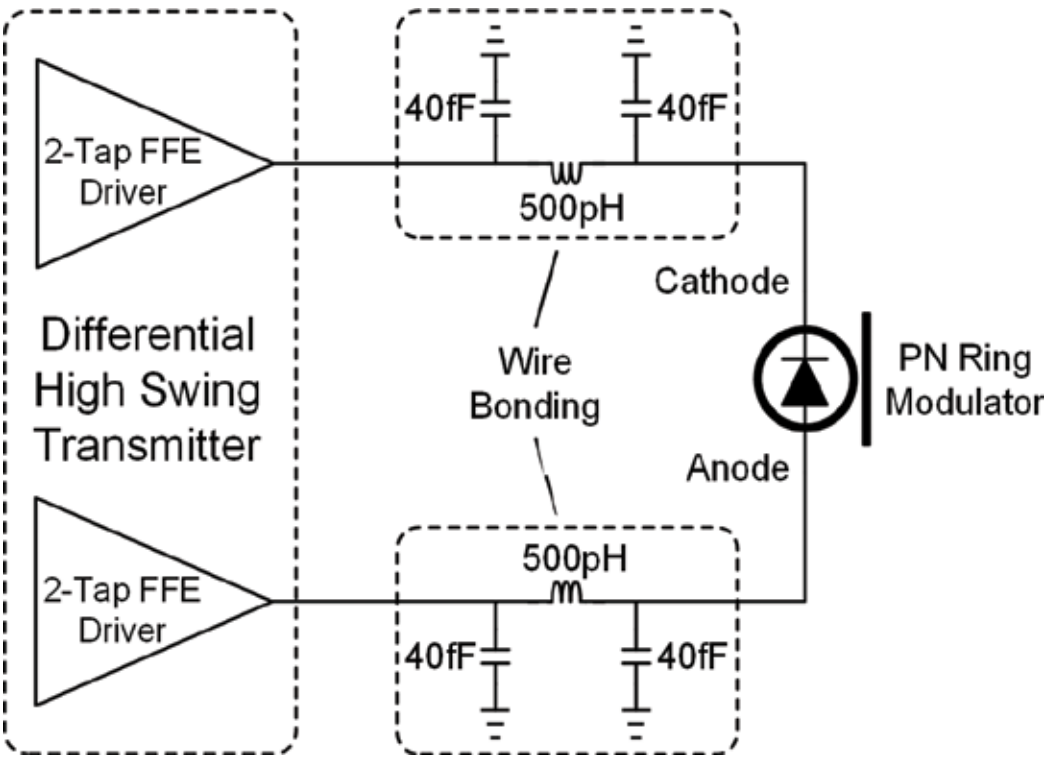

Figure 23. Co-simulation schematic with 65-nm high-speed differential CMOS driver and carrier-depletion ring resonator modulator model.

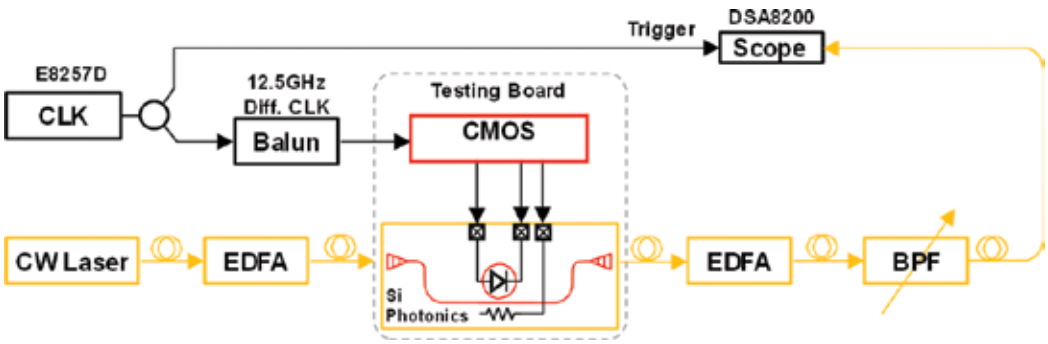

Figure 24. Experimental setup for optical testing.

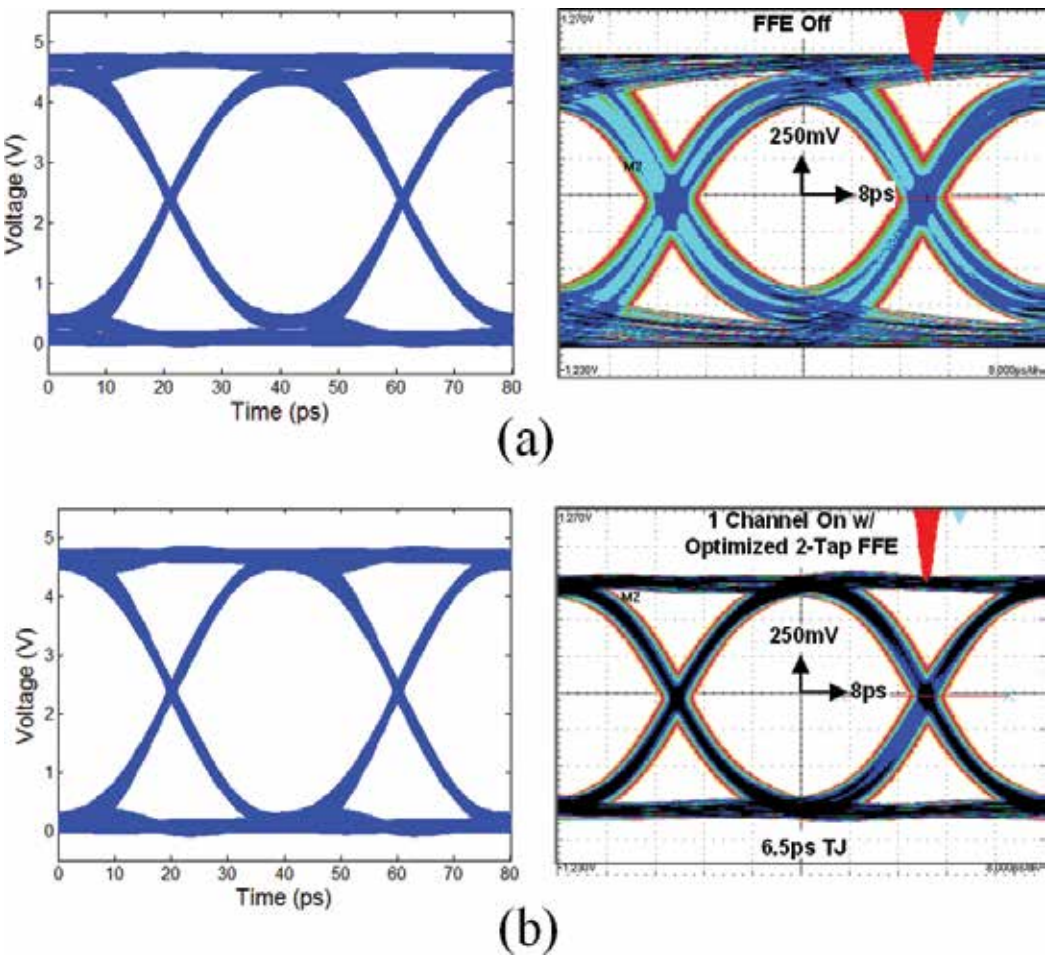

Figure 25. Measured and simulated 25 Gb/s electrical input eye diagrams (a) without equalization and (a) with optimized symmetric equalization.

http://dx.doi.org/10.5772/intechopen.68272

For model verification, 25 Gb/s measured and simulated eye diagrams are compared. The experimental setup is shown in **Figure 24**. The optical output from the CW laser is amplified by two erbium-doped fiber amplifiers (EDFAs) before and after the photonic chip to compensate input and output insertion losses due to the fiber-to-grating coupler coupling. A bandpass filter is utilized after EDFAs to suppress the amplified noise to increase the signal-to-noise ratio. A clock is utilized for a trigger of an oscilloscope and the input of the CMOS driver. The optical output is received by the oscilloscope.

Figure 25 shows the 25 Gb/s 2^7–1 PRBS CMOS driver signal for model simulation, which matches excellent with the measured eye diagrams including without equalization (**Figure 25(a)**) and with optimized symmetric equalization (**Figure 25(b)**). As shown in the 25 Gb/s eye diagrams of **Figure 26**, excellent matching is achieved between the measured and co-simulated results with and without equalizations. Due to the device bandwidth limitation and nonlinearity, the optical output power is distorted with an unequal amount of inter-symbol-interference (ISI) (**Figure 26 (a)**), which degrades the effective extinction ratio (ER). As shown in **Figure 26(b)**, this asymmetrical ISI is compensated by an optimized nonlinear equalizer.

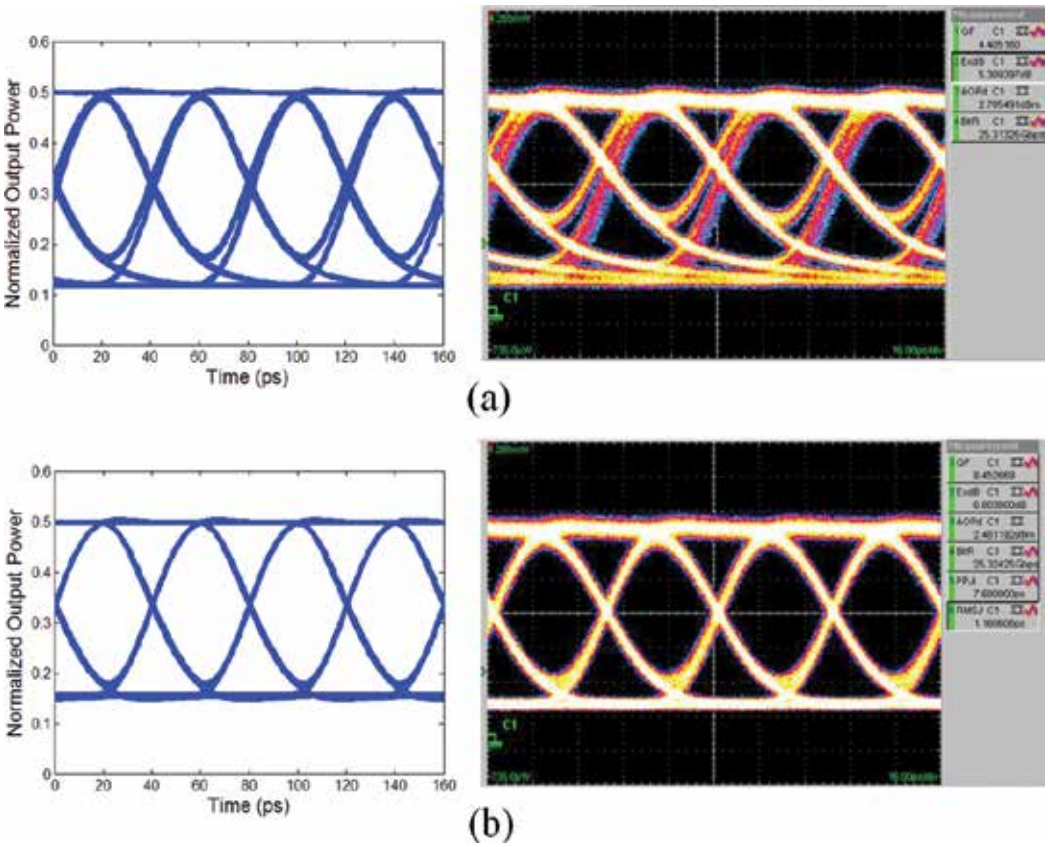

Figure 26. Measured and co-simulated 25 Gb/s optical output eye diagrams (a) without equalization and (b) with the same optimized asymmetric equalization.

4. Conclusions

Optical interconnect system efficiency is dependent on the ability to optimize the transceiver circuitry for low-power and high-bandwidth operation, motivating accurate co-simulation environments. The presented compact Verilog-A models for carrier-injection and carrier-depletion ring modulators include both nonlinear electrical and optical dynamics, allowing for efficient optimization of transmitter signal levels and equalization settings. For the model of carrier-injection microring modulators, excellent matching between simulated and measured optical eye diagrams is achieved both at 8 Gb/s with symmetric drive signals with varying amounts of pre-emphasis pulse duration, pulse depth, and dc bias, and at 9 Gb/s with a 65-nm CMOS driver capable of asymmetric pre-emphasis pulse duration. For the model of carrier-depletion ring modulators, excellent matching between simulated and measured optical eye diagrams is achieved at 25 Gb/s with a 65-nm CMOS driver capable of asymmetric equalization.

Acknowledgements

Parts of this chapter are reproduced from authors' recent journal publication, work, and so on [28].

Author details

Binhao Wang

Address all correspondence to: beehom927@gmail.com

Hewlett Packard Labs, Hewlett Packard Enterprise, USA

References

[1] Barwicz T, Byun H, Gan F, Holzwarth CW, Popovic MA, Rakich PT, Watts MR, Ippen EP, Kartner FX, Smith HI, Orcutt JS, Ram RJ, Stojanovic V, Olubuyide OO, Hoyt JL, Spector S, Geis M, Grein M, Lyszczarz T, Yoon JU. Silicon photonics for compact, energy-efficient interconnects [invited]. Journal of Optical Networking. 2007;**6**(1):63-73

[2] Miller DAB. Device requirements for optical interconnects to silicon chips. Proceedings of IEEE. 2009;**97**(7):1166-1185

[3] Xu QF, Schmidt B, Pradhan S, Lipson M. Micrometre-scale silicon electro-optic modulator. Nature. 2005;**435**(7040):325-327

[4] Liu AS, Jones R, Liao L, Samara-Rubio D, Rubin D, Cohen O, Nicolaescu R, Paniccia M. A high-speed silicon optical modulator based on a metal-oxide-semiconductor capacitor. Nature. 2004;**427**(6975):615-618

[5] Van Campenhout J, Pantouvaki M, Verheyen P, Selvaraja S, Lepage G, Yu H, Lee W, Wouters J, Goossens D, Moelants M, Bogaerts W, Absil P. Low-voltage, low-loss, multi-Gb/s silicon micro-ring modulator based on a MOS capacitor. In: Optical Fiber Communication Conference; 4-8 March; Los Angeles, CA; 2012. p. OM2E.4

[6] Titriku A, Li C, Shafik A, Palermo S. Efficiency modeling of tuning techniques for silicon carrier injection ring resonators. In: Optical Interconnects Conference; 4-7 May; San Diego, CA; 2014. pp. 13-14

[7] Chen CH, Li C, Shafik A, Fiorentino M, Chiang P, Palermo S, Beausoleil R. A WDM silicon photonic transmitter based on carrier-injection microring modulators. In: Optical Interconnects Conference; 4-7 May; San Diego, CA; 2014. pp. 121-122

[8] Xu Q, Manipatruni S, Schmidt B, Shakya J, Lipson M. 12.5 Gbit/s carrier-injection-based silicon micro-ring silicon modulators. Optics Express. 2007;**15**(2):430-436

[9] Liu Y, Ding R, Li Q, Zhe X, Li Y, Yang Y, Lim AE, Lo PGQ, Bergman K, Baehr-Jones T, Hochberg M. Ultra-compact 320 Gb/s and 160 Gb/s WDM transmitters based on silicon microrings. In: Optical Fiber Communication Conference; 9-13 March; San Francisco, CA; 2014. p. Th4G.6

[10] Li H, Li C, Xuan Z, Titriku A, Yu K, Wang B, Qi N, Shafik A, Fiorentino M, Hochberg M, Palermo S, Chiang P. A 5 × 25 Gb/s, 4.4 V swing, AC-coupled, Si-photonic microring transmitter with 2-tap asymmetric FFE and dynamic thermal tuning in 65 nm CMOS. In: IEEE International Solid-State Circuits Conference; 22-26 February; San Francisco, CA; 2015

[11] Moss B, Sun C, Georgas M, Shainline J, Orcutt J, Leu J, Wade M, Chen Y.-H, Nammari K, Wang X, Li H, Ram R, Popovic M, Stojanovic V. A 1.23 pJ/b 2.5 Gb/s monolithically integrated optical carrier-injection ring modulator and all-digital driver circuit in commercial 45 nm SOI. In: IEEE International Solid-State Circuits Conference; 22-26 February; San Francisco, CA; 2015

[12] Li C, Bai R, Shafik A, Tabasy EZ, Wang BH, Tang G, Ma C, Chen CH, Peng Z, Fiorentino M, Beausoleil RG, Chiang P, Palermo S. Silicon photonic transceiver circuits with microring resonator bias-based wavelength stabilization in 65 nm CMOS. IEEE Journal of Solid-State Circuits. 2014;**49**(6):1419-1436

[13] Ioannidis ZK, Radmore PM, Giles IP. Dynamic-response of an all-fiber ring resonator. Optics Letters. 1988;**13**(5):422-424

[14] Sacher WD, Poon JKS. Dynamics of microring resonator modulators. Optics Express. 2008;**16**(20):15741-15753

[15] Zhang L, Li Y, Yang JY, Song M, Beausoleil RG, Willner AE. Silicon-based microring resonator modulators for intensity modulation. IEEE Journal of Selected Topics in Quantum Electronics. 2010;**16**(1):149-158

[16] Buckwalter J, Zheng X, Li G, Raj K, Krishnamoorthy A. A monolithic 25-Gb/s transceiver with photonic ring modulators and Ge detectors in a 130-nm CMOS SOI process. IEEE Journal of Solid-State Circuits. 2012;**47**(6):1309-1322

[17] Wu R, Chen CH, Fedeli JM, Fournier M, Cheng KT, Beausoleil R. Compact models for carrier-injection silicon microring modulators. Optics Express. 2015;**23**(12):15545-15554

[18] Strollo AGM. A new SPICE model of power P-I-N diode based on asymptotic waveform evaluation. IEEE Transactions on Power Electronics. 1997;**12**(1):12-20

[19] Wang B, Li C, Chen CH, Yu K, Fiorentino M, Beausoleil R, Palermo S. Compact Verilog-A modeling of silicon carrier-injection ring modulators. In: Optical Interconnects Conference; 20-22 April; San Diego, CA; 2015. pp. 128-129

[20] Gan F. High-speed silicon electro-optic modulator for electronic photonic integrated circuits [dissertation]. Cambridge, MA: Electrical Engineering and Computer Science, MIT; 2007

[21] Soref RA, Bennett BR. Electrooptical effects in silicon. IEEE Journal of Quantum Electronics. 1987;**23**(1):123-129

[22] Pillage LT, Rohrer RA. Asymptotic waveform evaluation for timing analysis. IEEE Transactions on CAD. 1990;**9**:352-366

[23] Little BE, Chu ST, Haus HA, Foresi J, Laine JP. Microring resonator channel dropping filters. Journal of Lightwave Technology. 1997;**15**(6):998-1005

[24] Smy T, Gunupudi P, McGarry S, Ye WN. Circuit-level transient simulation of configurable ring resonators using physical models. Journal of the Optical Society of America B-Optical Physics. 2011;**28**(6):1534-1543

[25] Kononov E. Modeling photonic links in Verilog-A [thesis]. Cambridge, MA: Eletrical Engineering and Computer Science, MIT; 2012

[26] Ding R, Liu Y, Li Q, Xuan Z, Ma YJ, Yang YS, Lim AEJ, Lo GQ, Bergman K, Baehr-Jones T, Hochberg M. A compact low-power 320-gb/s wdm transmitter based on silicon microrings. IEEE Photonics Journal. 2014;**6**(3):6600608

[27] Li H, Xuan Z, Titriku A, Li C, Yu K, Wang B, Shafik A, Qi N, Liu Y, Ding R, Baehr-Jones T, Fiorentino M, Hochberg M, Palermo S, Chiang PY. A 25 Gb/s, 4.4 V-swing, AC-coupled ring modulator-based WDM transmitter with wavelength stabilization in 65 nm CMOS. IEEE Journal of Solid-State Circuits. 2015;**50**(12):3145-3159

[28] Wang B, Li C, Chen CH, Yu K, Fiorentino M, Beausoleil R, Palermo S. A compact Verilog-A model of silicon carrier-injection ring modulators for interconnect transceiver circuit design. Journal of Lightwave Technology. 2016;**34**(12):2996-3005

Chapter 10

Candidate Materials as Gain Media in Organic, Triplet-Based, Room-Temperature masers Targeting the ISM Bands

Erinn van Wynsberghe and Ayse Turak

Additional information is available at the end of the chapter

http://dx.doi.org/10.5772/intechopen.68232

Abstract

While lasers have enjoyed greater popularity, masers—which emit coherent radiation in the microwave spectrum—are also of critical importance to a variety of applications. Recently, an organic gain medium has been developed, which allows emission at room temperature without the traditional encumbrances of cryogenic cooling or an externally applied magnetic field, at vastly improved power efficiency. This discovery opens up new avenues for applications that were previously impractical. However, further investigation is still required for frequency tuning of the device, through the selection of alternate gain media beyond the original choice of pentacene-doped *p*-terphenyl and some linear acenes similar to the pentacene prototype. This chapter outlines some of the essential criteria necessary to achieve masing with an organic semiconductor gain medium, including zero-field splitting (ZFS), triplet sublevel division, and metastable population inversion. Three tables of possible candidate materials are presented based on this roster of criteria, particularly targeting emission in one of the industrial, scientific, and medical (ISM) bands. A selection of preferred guest molecules is recommended for in-situ testing as room-temperature masers gain media candidates.

Keywords: room-temperature maser, organic semiconductors, triplet sublevels, zero-field splitting, metastable population inversion, candidate

1. Introduction

The maser, the microwave analogue of the laser, has long been a device of considerable interest [1, 2]. With emission frequencies between 0.3 and 300 GHz, masers have had several significant applications, including precision frequency references for atomic clocks [3–5],

radio astronomy [6, 7], space and long-distance communication [8–11], radar [12, 13], remote sensing [14], ultrasensitive magnetic resonance spectroscopy [15], and medical imaging [14]. However, widespread use of such devices has been limited by low efficiency and complex technical requirements. Recent advances in room-temperature masers [16–19] have revitalized interest in its potential uses. Particularly, the work of Oxborrow [16, 20] using pentacene *p*-terphenyl as the masing material has opened up a whole new direction of experimental research, through spin manipulation in organic semiconductors materials. Without the traditional encumbrances of cryogenic cooling or an externally applied magnetic field, these new avenues pave the way for a new generation of miniaturized ultra-low-noise high-gain amplifiers, oscillators, and transceivers.

Of particular interest for a variety of applications are materials which have demonstrated emission in the range of 2.4–2.5 GHz, one of the industrial, scientific, and medical (ISM) bands. ISM frequencies are designated as unlicensed and reserved internationally for experimental and short-range applications such as microwave ovens, cordless phones, military radar, and industrial heaters. The ISM bands have seen a dramatic increase in usage over the past decade for wireless connectivity devices [21], including BlueTooth [22], Zigbee and WLAN [23], and Hiperlan, among others [24]. These bands represent an important frequency range for future internet-of-things applications. Although there have been significant advances in recent years, the only viable room temperature masing demonstrated thus far, from pentacene *p*-terphenyl, is limited to a single emission frequency well away from this desirable application range [16]. Additionally, the conversion efficiency (i.e. the energy output in microwaves compared to the energy input in visible light) at the laboratory scale is still only around 3% [20]. To move beyond this prototype material, a comprehensive examination of the necessary features for room temperature masing using organic semiconductors is required.

In this chapter, we examine a few of the essential criteria necessary to achieve masing with an organic semiconductor gain medium, including triplet zero-field splitting (ZFS), metastable population inversion, and triplet lifetime. We enumerate numerous organic components as alternatives candidates, based on advantageous conditions for these three criteria. Specifically, we target materials with ZFS values favorable to emission in the ISM band, as well as highlighting other interesting materials with desirable properties.

1.1. masers

MASER stands for microwave or molecular amplification by stimulated emission of radiation. Like its counterpart, the LASER (light amplification by stimulated emission of radiation), the maser converts an input of electrical or optical energy into a coherent, focused beam of photons. Both devices operate along similar lines and require the stimulation of atoms to elevate electrons to excited states. The electrons migrate to higher orbital levels if the atoms are "pumped," that is, receive energy from an external source. As those electrons lose their energy (after 10^{-8} seconds), they emit photons by emission and retreat to a lower energy level. If this process occurs naturally, it is referred to as spontaneous emission, whereas if it occurs by design, it is called stimulated emission. Stimulated emission occurs when a photon strikes an electron already suspended at an excited state level: the electron releases its energy and the

http://dx.doi.org/10.5772/intechopen.68232

exiting photon will be in phase with the striking photon. That is, the two photons will travel away coherently, with the same wavelength, frequency, and vector.

Key to coherent emission is the maintenance of stable population inversion. The pump must keep a greater percentage of electrons at the excited states, at a rate faster than the natural relaxation rate to the ground state. Excited state electrons must maintain their stimulated position long enough to allow incident photons to strike and cause coherent cascade emission. For masers, due to the small gap between the excited and ground states (1×10^{-6} to 1×10^{-3} eV), it is relatively easy to produce a high ratio of atoms in the excited state. Additionally, as the ratio of the Einstein coefficients (A, spontaneous emission and B, stimulated emission) varies with the cube of the frequency [25–27], spontaneous emission can generally be neglected for the microwave part of the spectrum.

Charles Townes and co-workers showed the first working maser using NH_3 gas as the gain medium [28]. In such a system, the two energy levels used are the two vibrational states of the ammonia molecule given by the oscillation of the nitrogen atom [1]. The difference between the wave function of the two configurations with N above and below the plane of hydrogen atoms yields an output radiation at 1.25 cm wavelengths [28]. By applying an electric field, the electric dipole moment in the ammonia molecules can be used to separate the two molecular configurations, maintaining a stable population inversion. This first maser proved very effective as a low-noise amplifier and was proposed as the first atomic clock standard by the National Institute of Standards and Technology (NIST) [29]. Further developments of gas [30], and then solid state masers [31, 32], focused on providing population inversion through the manipulation of spin states.

1.2. Disadvantages of traditional masers

Although it is relatively easy to produce population inversion with microwave emission, the major bottlenecks for its effective use in most applications are low power efficiency and complex operational requirements.

For the traditional gas or molecular masers, the modes that yield microwaves, either through conformational changes as in ammonia or spin states as in hydrogen [30], are inherently stable and require only physical separation to maintain stable population inversion. However, the population of molecules in the quantum state of interest is relatively low [33]. They also require high vacuum to prevent gas scattering collisions [28, 30, 33]. With a high vacuum, however, the gas molecules are spatially separated to such an extent that effective stimulation is limited, and the power output of gas-based masers is relatively low (pico to nanowatts) [33].

For solid state materials, the limitations are the opposite. If there are non-degenerate spin states, there can be a large population of atoms in the excited state, as thermal energy is generally sufficient to effectively pump the molecules across the small energy gaps. However, the lifetimes of such excited spin states are very short. Spin-lattice relaxation rates increase exponentially with rising temperature [34] to the degree that at room temperature, spin-relaxation times for many solid materials are in the nanosecond range due to rapid phonon scattering [35]. Additionally, the spin population inversion decreases at higher temperatures [16, 36].

Therefore, most solid state masing materials require cryogenic temperatures to maintain stable population inversion and sufficient lifetimes [10, 35, 37].

The requirement of non-degenerate spin states also limits the applicability of masers. If there is no naturally occurring split within the microwave frequency range, magnetic fields must be applied to induce Zeeman splitting of the degenerate energy states. Many gaseous and solid state materials require the application of large magnetic fields in order to emit at desirable frequencies [38–40].

1.3. Organic masers

One method of overcoming the major bottlenecks of room temperature masing is to use a material that has long excited state lifetimes and natural zero-field splitting, such as an organic semiconductor. Despite having low mobility and complex transport properties, organic semiconductors have significant advantages over inorganic semiconductors as a gain medium.

Lifetimes of spin excited states in organics are substantially longer than inorganic materials, microseconds instead of pico or nanoseconds [41]. In some aromatic molecules, lifetimes have been observed as high as milliseconds or even full seconds [42–45]. The long lifetime in organics is due to the weak spin-orbit coupling (SOC), as a result of the low molecular weight of the materials involved, such as carbon and hydrogen in small molecule arrangements (low Z value) or π-conjugated polymers [41]. The strength of spin-orbit interaction is proportional to Z^4 [46].

Oxborrow et al. demonstrated the only room-temperature solid state maser observed thus far based on a pentacene-doped *p*-terphenyl molecular crystal, where the spin lifetime can reach 135 μs at room temperature [16]. This result relies on the excitonic route to forming stable states with suitable separation for microwave emission. The organic maser functions by photoexciting a solid state gain medium composed of an organic guest molecule within a solid polymer crystal (which taken together comprise a Shpolskii matrix [47]) and then emitting photons by exciton decay within the triplet sublevels. Radiative emission is then guided and amplified by a resonance cavity to form a coherent pulsed or continuous maser beam [16].

The gain medium chosen by Oxborrow et al. [16, 20] was the well-studied molecule pentacene, a polycyclic aromatic hydrocarbon with five benzene rings, embedded in a *p*-terphenyl matrix [48–56]. Dispersing a small amount of this guest molecule within the polymer host matrix separates the guest molecules from one another to prevent quenching. Additionally, incorporating pentacene into a matrix frustrates the rotational degrees of freedom and splits the usually degenerate triplet states [48] allowing microwave emission at room temperature.

The key to the long lifetime is the formation of the triplet exciton state, which is quantum mechanically forbidden to decay to the ground state. As shown in **Figure 1**, emission from such a gain medium is based on optical excitation into the dipole-allowed singlet state, followed immediately by an intersystem crossing to the metastable triplet state, and then a return to the ground state (often through phosphorescence). Materials which additionally have non-degenerate triplet states can, as an intermediate step, have transitions between triplet states to produce the required microwaves.

http://dx.doi.org/10.5772/intechopen.68232

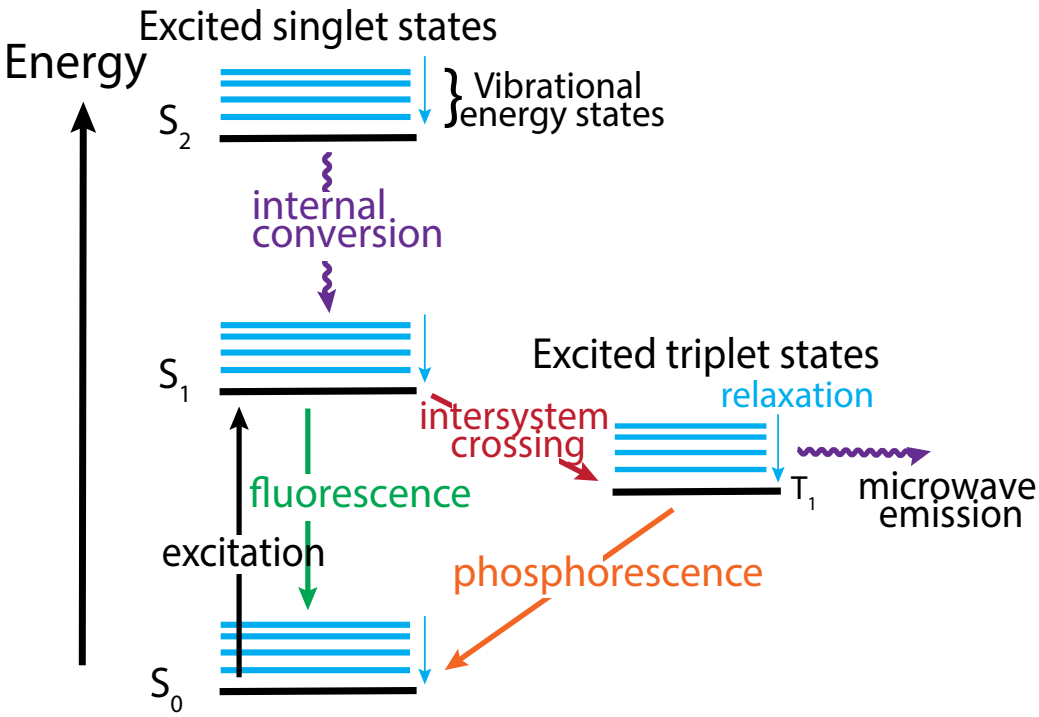

Figure 1. A Jablonski diagram showing the possible transitions that can occur for an organic-based maser.

The mechanism of electron transport in organic semiconductors also makes them advantageous as a gain medium. Semiconduction in organic molecules occurs in a π-conjugated system, where π orbitals are delocalized over some or all of the molecules. Transport of electrons through the π-orbital electrons also further suppresses both SOC and the hyperfine interaction ("HFI", the interaction between electron spin and the adjacent atomic nuclei) [57, 58]. As both singlet and triplet states in organic semiconductors result from room-temperature stable exciton spin pairs [59, 60], emission lifetimes can be substantially longer than those observed in inorganic systems.

Organics are generally cost-effective, easy to fabricate and test, versatile, flexible, plentiful, and lightweight [61–63]. Spin manipulation in organics—for improved optoelectronic devices, for spintronics, for spectroscopy—also has a long history [34, 41, 61, 64–70]. There are many candidate materials to investigate across the vast spectrum of organic molecules, providing numerous choices for applications.

2. Criteria for room-temperature, organic, triplet-based maser

As described above, organic semiconductors provide a new avenue for efficient solid state masers. Though pentacene *p*-terphenyl is the first successful room-temperature organic maser, it still suffers from some limitations. It is limited to a single output frequency of

1.45 GHz, its spin-relaxation lifetime is only 135 μs, its power conversion efficiency is only around 3% [20], it can only operate for pulses of about 300 μs [2], and the molecular crystal is unstable under high-power pumping and at high temperatures. Bogatko et al. [71], building on the success of pentacene, recently identified several possible new candidate materials based on a computational molecular design strategy. Focusing on the linear acenes and some of their derivatives, they were able to suggest new directions to overcome some of these limitations. However, a vast body of organic semiconductors beyond the linear acenes exists that can be explored and optimized as a gain medium, at a variety of emission frequencies, to expand the possibilities of room-temperature maser applications.

In the spirit of Oxborrow's original inspiration [2], we have examined the literature on organic semiconductors to present a list of additional potential gain medium candidates. First, we identify candidates that show solid state microwave emission over a variety of possible emission frequencies without an externally applied magnetic field. Then, we discuss the population inversions and triplet lifetimes that exist in such systems. Finally, we touch on some potential promising candidates that exhibit favorable conditions if a suitable host material can be found to operate effectively at room temperature.

2.1. Emission from triplet state

Fundamentally, to perform masing, photons must first be emitted by stimulation from a gain medium at a desired frequency (or wavelength). The designation of "microwave" applies to electromagnetic waves with wavelengths between 1 m and 1 mm, with frequencies between 300 MHz (100 cm) and 300 GHz (0.1 cm) [72].

In contrast to inorganic semiconductors, the excited states of organic molecules are highly localized. Rather than acting as free carriers, electrons or holes are bound to a molecule, forming a polaron. A polaron consists of the excited state molecule, its internal geometric distortion, and the distortion field with respect to its neighboring molecules, due to the addition or loss of charge. When positive and negative polarons (holes and electrons) interact, they form a room-temperature stable electron-hole pair (exciton) localized on one or a few molecules. This localization and the consequently large exchange splitting generate two distinct states, referred to as singlets (S_1 spin 0) and triplets (T_1 spin 1), depending on the spin interaction of the two carriers. In a singlet state, excitons have opposite spin orientations and the electronic energy levels do not split when the molecule is exposed to a magnetic field. In a triplet state, the electron has the same spin orientation (parallel) as the hole and energy-level splitting becomes possible.

As the name *triplet* implies, there are *three* distinct symmetric spin states, which arise from the interaction of charge carriers with parallel spins (see **Figure 2**). Usually, these levels are degenerate but can be split either through the application of a magnetic field (Zeeman effect) or through the molecular geometry (zero-field splitting).

As the α and β spin states respond oppositely to an applied magnetic field, the Zeeman effect (**Figure 2**) results in a tunable energy separation of the two spin states, which increases proportional to the applied magnetic field according to the expression [73]:

$$E = g\beta M_s H \tag{1}$$

http://dx.doi.org/10.5772/intechopen.68232

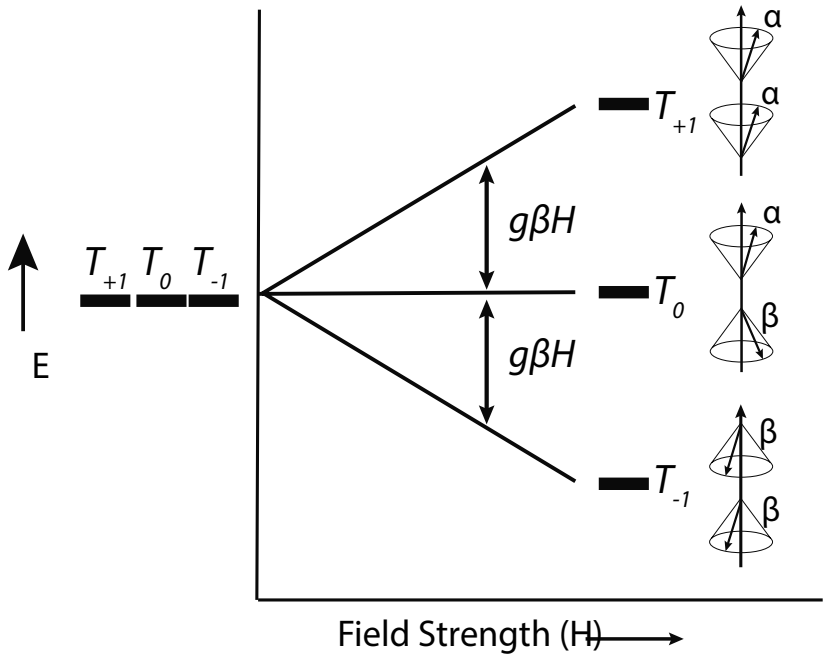

Figure 2. An energy diagram showing the splitting of the degenerate triplet sublevels under an applied magnetic field. Insets show the spin configuration for each of the triplet sublevels.

where g is the electronic g factor, β is the Bohr magneton, M_s is the spin quantum number, and H is the applied field.

However, some materials, particularly organic molecules, exhibit a splitting of the triplet states without an applied magnetic field due to the anisotropic electron distribution from the delocalized orbitals over the molecule [73], as shown in **Figure 3**.

Many organic semiconductors show this type of molecular splitting, with the energy gap described by the zero-field splitting parameters D and E. Generally, shortening along one spatial direction will lead to a decrease in the triplet energy, as seen in **Figure 3(b)** where T_z is lower for a planar symmetric molecule, such as coronene. Conversely, elongating the electrical field distribution along a spatial direction will increase the energy, as for pentacene, which has a long and short axis in the x-y plane. Along the backbone (oriented along X in our example), the triplet energy T_X will be slightly higher than along the transverse direction, T_Y. This arises because the orbitals are distributed over the entire molecule for many organic semiconductors, resulting in an asymmetric electron energy distribution. D is defined as the energy difference between T_Z and degenerate energy states as in (b) or between T_Z and the average of the two other energy states as in (c). It can be positive or negative, depending on whether there is confinement or elongation of the electron distribution over the molecule. The parameter E is half the energy difference of the T_X and T_Y energy states or the gap between X or Y and the degenerate energy level [73].

Of particular interest for a variety of applications are materials which have demonstrated emission in the range of 2.4–2.5 GHz, one of the ISM bands. These bands represent an impor-

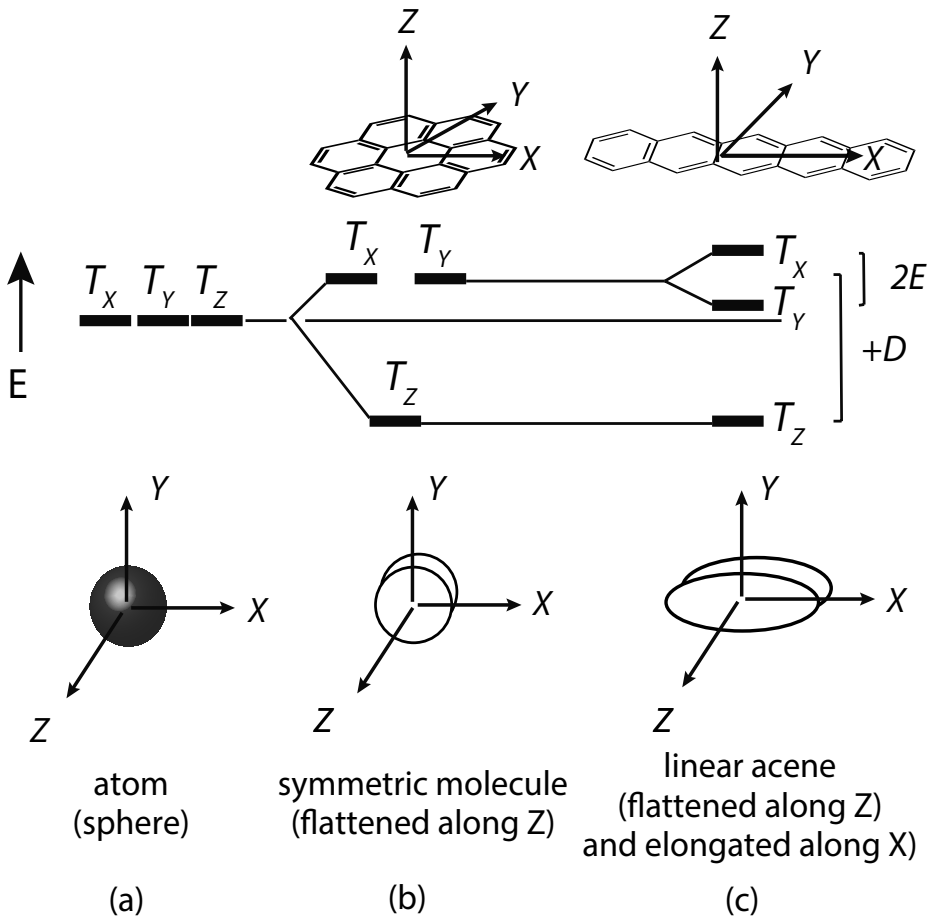

Figure 3. An energy diagram showing the splitting of the degenerate triplet sublevels with changes in molecular conformation. (a) A spherically symmetric electron distribution has degenerate triplet states in three dimensions. (b) A symmetric planar molecule, such as coronene, is symmetric in the *x*-*y* plane but has one non-degenerate level from shortening along the *Z*-axis. (c) An asymmetric planar molecule, such as pentacene, has three split states. As the molecule is elongated along the *X* axis, T_x has higher energy than T_y. The zero-field splitting parameters *D* and *E* describe the separation between the triplet states.

tant frequency range for future internet-of-things applications. Candidate guest materials with 2.4–2.5 GHz emission are presented in **Table 1**, along with other candidates with values slightly below that region. Due to the Zeeman effect, discussed above, these materials could also become viable candidates with application of a modest external magnetic field to open up the triplet energy gap.

The organic molecules presented in **Table 1** have calculated triplet emission frequency based on their reported zero-field splitting coefficients *D* and *E* (cm^{-1}). Many of the results are taken from data for randomly oriented molecules in a glassy solution, which only yield the absolute value of the ZFS coefficients [74]. As *D* and *E* can take on positive or negative values, we present two emission frequencies, by either adding to or subtracting *E* from *D*, before converting to frequency. In some of the literature, single emission frequencies were reported without

Guest	Host	ZFS (GHZ)		Ref.
		High	Low	
Azulene	Phenazine	2.191	1.778	[75]
3,4-benzopyrene	EPA or methanol[a]	2.272		[76]
3,4-benzopyrene	Glasses plastics	2.272		[42]
3,4-benzopyrene		2.278		[77]
Fluoroanthene	Glasses plastics	2.278		[42]
Fluoroanthene	Glasses plastics	2.449		[42]
Fluoroanthene	PMMA	2.449		[45]
Fluoroanthene	Ethanol glass	2.458	2.159	[78]
Phenazinium	Sulfuric acid-ethanol[a]	2.317	1.718	[79]
1,2-benzanthracene	Rigid glass	2.368		[77]
Triphenylamine	PMMA	2.401		[45]
Naptho[2,3-a]coronene	Decane[a]	2.413	1.856	[80]
Cata-hexabenzocoronene	PMMA	2.463	2.423	[81]
Aeridine-b9	Biphenyl	2.49	1.959	[80]
Dibenzo[a,g]coronene	Octane[a]	2.491	1.292	[80]
1,3-diazaazulene	Phenazine	2.494		[75]

The high and low ZFS correspond to the absolute difference between positive and negative values of D and E. For entries where either ZSF parameter values were not reported or the molecule was symmetric (hence $E = 0$), the single emission frequency is given under "high."

[a]An experiment performed at or near cryogenic or liquid N_2 temperatures to ensure host is a solid matrix.

Table 1. Candidate materials for organic semiconductor gain medium sorted by zero-field splitting emission frequency.

giving D and E values and are accordingly represented as one value here in the high column. If the molecule was symmetric about the x-y plane, yielding a 0 value for E, the single emission wavelength is listed also in the high column. Though the table is mostly sorted by "high" ZFS emission values, some variation was found in the reported values for a single material, due potentially to variation in temperature, host material, or experimental setup. For clarity, we have grouped molecules from different sources together rather than sorting them by their reported value. Note that we have made our calculations based on the values given in the referenced sources, even if the experiments were originally reported elsewhere.

2.2. Triplet relative population inversion

For masing action, a system must have a top-heavy population imbalance with more excitons in the upper states than lower states. Such a configuration will allow for stimulated emission of the heavily populated upper states, with plenty of openings within the lower states where excitons can decay down. For organic molecules, numerous examples exist of high ratio excitons in the

highest triplet sublevel, with a vastly smaller population in the lowest triplet state. For example, pentacene in *p*-terphenyl has a demonstrated a ratio of 0.76:0.16:0.08 relative population in the T_X: T_Y: T_Z sublevels. Other examples of notable population inversion are presented in **Table 2**.

Guest	Host	Relative Population			High/low ratio	Ref.
		High	Medium	Low		
Naphthalene	Naphthalene-d8	0.82	0.16	0.02	41	[82]
Naphthalene	*n*-pentane[a]	0.64	0.25	0.11	5.82	[83]
Naphthalene	Durene[a]	0.54	0.2	0.26	2.08	[84]
Pyrimidine-h4	Benzene[a]	0.92	0.05	0.03	34	[80]
Anthracene	*n*-heptane[a]	0.65	0.33	0.02	32.5	[82]
Anthracene	Biphenyl	0.39	0.55	0.06	6.5	[82]
Anthracene-d14	*p*-terphenyl-d14	0.38	0.43	0.19	2	[85]
Anthracene-h2d8	Biphenyl	0.34	0.35	0.31	1.09	[80]
Dibenzothiophene trap[b]	–	0.92	0.05	0.03	29.74	[80]
Benzophenone-b10[b]	–	0.57	0.38	0.05	10.74	[80]
Benzophenone-b10	Benzophenone-d10[a]	0.38	0.33	0.3	1.27	[80]
1,4-dibromonaphthalene		0.87	0.04	0.09	10	[80]
Pentacene	*p*-terphenyl	0.76	0.16	0.08	9.5	[16, 54]
p-dichlorobenzene	*p*-xylene[a]	0.5	0.4	0.1	4.87	[80]
Dimer	Biphenyl	0.64	0.22	0.14	4.6	[80]
Dimer	*p*-dichlorobenzene[a]	0.63	0.18	0.18	3.5	[80]
Benzene	Cyclohexane[a]	0.46	0.43	0.11	4.18	[86]
Benzene	Cyclohexane[a]	0.43	0.46	0.11	3.91	[82]

The convention of highest:middle:lowest energy Zeeman triplet line was used, and the entries are sorted in descending order of their respective ratios of high excitons, capable of emission, to low excitons, the receiving state of emitted excitons.

[a]The experiment is performed at or near-cryogenic or liquid N_2 temperatures to ensure host is a solid matrix.

[b]Neat film or crystal.

Table 2. Candidate materials for organic semiconductor gain medium with triplet sub-level relative populations.

In **Table 2**, relative populations are shown for the three triplet sublevels of each material, based on a variety of sources, and sorted in descending order of their respective ratio of high excitons (capable of emission) to low excitons (the receiving state of emitted excitons). The traditional model presents these three stages as *X*, *Y*, and *Z* descending, but here we use the more generic (and more representative) terms high, mid, and low as *X*, *Y*, and *Z* may be split to differing relative energies with respect to one another in any given material (negative *D* and *E* values will determine the placement of *X*, *Y*, and *Z* lines). Again, the entries are grouped by molecular name.

http://dx.doi.org/10.5772/intechopen.68232

2.3. Long triplet lifetime

An essential requirement for masing is that population inversion must be maintained consistently for a longer period of time than the ordinary excitation time scale. This is one of the most significant advantages of using an organic semiconductor as a gain medium for room temperature masing (see Section 1.3). In an organic maser, long lifetimes are achieved through the creation of the metastable triplet state, through intersystem crossing from the excited singlet. The advantage of operating within the triplet regime is that the excitons are dipole forbidden from decaying to the ground state due to the total spin moment $S = 1$. As Pauli exclusion forbids two electrons with parallel spins from occupying the same orbital, triplet excitons cannot decay to the ground state without spin flipping, phosphorescence, or nonradiative phonon perturbation. It can take significant time for those conditions to be met such that the exciton returns to the ground state (nanoseconds for pentacene and full seconds or tens of seconds for other organic molecules). This impediment to decay creates a natural metastable state, ideal for stimulated emission.

One of the most critical features for microwave emission is the spin-relaxation rate, which is substantially higher in organic materials compared to inorganic ones due to the low spin-orbit coupling in most organic molecules. For microwave emission, the most critical lifetime is the relaxation from the higher exciton sublevel (traditionally T_X and T_Y) down to the lowest triplet sublevel (i.e. T_Z). The triplet lifetime is also defined relative to the final decay from T_Z down to the ground state. This generally is an order of magnitude longer than the desired microwave frequency of emission. **Table 3** lists the reported triplet lifetimes for a variety of materials emitting in the microwave regime.

Guest	Host	Lifetime (s)	Ref.
Coronene	PMMA	56	[87]
Coronene-d12	Octane[a]	34.5	[87]
Coronene	Rigid glass	9.4	[69]
Coronene	Alphanol 79[a]	7.9	[88]
Coronene	PMMA	4.2	[45]
Benzophenone	Carbon tetrachloride crystal	52.1	[89]
Benzene[b]	–	26	[84]
Benzene	Cyclohexane[a]	16	[90]
Benzene	3-methylpentane sol.[a]	7	[91]
Benzene	Rigid glass	7	[69]
Phenanthrene (d)		25	[84]
Phenanthrene	Rigid glass	3.5	[77]
Phenanthrene	Rigid glass	3.3	[69]

Guest	Host	Lifetime (s)	Ref.
Triphenylene	PMMA	15.9	[69]
Triphenylene	Alphanol 79[a]	13.3	[88]
Triphenylene	PMMA	8	[45]
s-Triazine	3-methylpentane sol.[a]	13	[91]
Biphenyl	3-methylpentane sol.[a]	8	[91]
Tryptophan	Ethylene glycol-H_2O[a]	5.5	[92]
1,3,5-triphenylbenzene	Alphanol 79[a]	5.1	[88]
1,3,5-triphenylbenzene	3-methylpentane sol.[a]	4.5	[91]
Pentacene	*p*-Terphenyl	0.000135	[16]
Pentacene	PMMA	0.000045	[93]

[a]An experiment performed at or near cryogenic or liquid N_2 temperatures to ensure host is a solid matrix.
[b]Neat film or crystal.

Table 3. Candidate materials for organic semiconductor gain medium with long triplet lifetime.

2.4. Potential candidate materials

Table 4 summarizes the top candidate materials that should be studied further to exploit their long spin-relaxation lifetimes and high population inversion. Currently, complete information at room temperature is limited for these materials other than pentacene. However, as with pentacene [51], the low temperature behavior suggests that if a suitable Shpolskii matrix [47] can be found for these molecules which preserve the ZFS, then each would be an excellent candidate for a room-temperature maser gain medium.

Guest	Host	Emission (GHz)	Sublevels			High-low ratio	Temp (K)	Lifetime (s)	Refs.
			High	Medium	Low				
Naphthalene	Naphthalene-d8	2.968	0.82	0.16	0.02	41	1.3	3 [88]	[82]
Naphthalene	*n*-pentane[a]		0.64	0.25	0.11	5.8			[82]
Pyrimidine	Benzene[a]	2.187	0.92	0.05	0.03	34	1.2	0.14, 0.017, 0.012	[80]
Anthracene	*n*-heptane[a]	2.159	0.65	0.33	0.02	32.5	1.3	0.05 [77]	[82]
Anthracene	Biphenyl		0.39	0.55	0.06	6.5			[82]
Dibenzothiophene[b]	–	3.29, 1.76	0.92	0.05	0.03	30*	1.3	9, 0.36, 0.29	[80]
Pentacene	*p*-terphenyl	1.42	0.76	0.16	0.08	9.5	RT	0.000135	[16]
Phenazine	ETOH[a]	2.236		0.9	0.1	9*	77	0.011	[79]

Guest	Host	Emission (GHz)	Sublevels			High-low ratio	Temp (K)	Lifetime (s)	Refs.
			High	Medium	Low				
Phenazinium	ETOH[a]	2.018		0.9	0.1	9*	77	0.009	[79]
Phenanthrene	TBB[a]	2.384*	0.1	0.28	0.62	2.8*	1.6	0.26, 0.023	[80]
Triphenylene	Hexane[a]	1.443	0.4	0.43	0.17	2.34	1.2	8.3, 8.3, 27.8	[80]
Tryptophan	Glass	2.95	0.39	0.38	0.23	1.7		5.5	[94]
Tryptophan	Ethylene Glycol-H_2O[a]		0.282	0.347	0.371			4.17, 8.43, 26.5	[92]
Coronene	*n*-hexane	2.827	0.43	0.41	0.16	2.7**	1.6	4.24, 3.94, 59.9	[86]
Coronene	Octane		33.3	33.3	33.3	1.0**	1.35		[80]
Trans-stilbene[a]	–	3.79, 1.51	0.5	0.2	0.3	1.67	1.3	0.014, 0.014, 0.15	[82]

Three distinct triplet lifetimes of *X* (high), *Y* (mid), and *Z* (low) sublevels are reported.

[a]An experiment performed at or near cryogenic or liquid N_2 temperatures to ensure host is a solid matrix.

[b]Neat film or crystal.

*Emission occurs from *Y* down to *X*.

**Uniform shapes (such as coronene) have degenerate *X* and *Y*, so they both emit at the same wavelength, thereby increasing the population ratio.

Table 4. Top candidate materials for an organic semiconductor gain medium.

3. Summary

With significant improvements to power efficiency and operational parameters through the selection of alternative candidate materials, the maser could expand beyond its current niche applications for use in laser-to-radio frequency (RF) or light-to-RF conversion, for coherent emission in the millimeter or centimeter wavelengths, or for coherent transmission in radio frequencies. Possible areas of application include enhanced communication security (narrow casting as opposed to broadcasting), organic radio components such as low-noise or solar-powered amplifiers, direct optical powering of transceivers without an inefficient electrical conversion stage (suitable for sensors and emerging "internet-of-things" applications), radiative diagnoses and therapy, directed energy tools and weapons for military and defense applications, and wireless power transmission over vast distances including energy to and from planetary orbit (space-based solar power).

In this chapter, we have presented a list of possible candidate materials that have zero-field triplet emission over a variety of frequencies, including technologically interesting ISM bands. We have also shown promising materials that exhibit high population inversion and long triplet lifetimes, which are required to achieve room temperature masing.

Funding sources

This research was financially supported by Natural Science and Engineering Research Council, through the grant 436100-2013 RGPIN, and by the Canadian Foundation for Innovation, through the grant 31605 from the John R. Evans Leaders Fund.

Acknowledgements

Special thanks to Lindsay Vasilak, Kaijie Zhang, Fariha Husain, and Haley Glavina for their contributions to data collection.

Conflicts

The authors declare no conflicts of interest in the creation of this work.

Author details

Erinn van Wynsberghe and Ayse Turak*

*Address all correspondence to: turaka@mcmaster.ca

McMaster University, Hamilton, Ontario, Canada

References

[1] RP Feynman, RB Leighton, M Sands. Chapter 9: The ammonia maser. In: The Feynman lectures on physics (Vol. III: The new millennium edition: quantum mechanics). New York: Basic Books; 2011.

[2] G Brumfiel. Microwave laser fulfills 60 years of promise. Nature News. doi:10.1038/nature.2012.11199 http://www.nature.com/news/microwave-laser-fulfills-60-years-of-promise-1.11199 (2012).

[3] HTM Wang. Subcompact hydrogen maser atomic clocks. Proceedings of the IEEE 77 (7) (1989) 982-992. doi:10.1109/5.30750.

[4] J Vanier. Atomic clocks based on coherent population trapping: a review. Applied Physics B 81 (4) (2005) 421-442. doi:10.1007/s00340-005-1905-3.

[5] Y Haibo, W Zhengming, D Shaowu. Performance of hydrogen maser and its usage in local atomic time at NTSC. In 2007 IEEE International Frequency Control Symposium Joint with the 21st European Frequency and Time Forum, 2007, pp. 889-892. doi:10.1109/FREQ.2007.4319206.

[6] H Peters, B Owings, T Oakley, L Beno. Hydrogen masers for radio astronomy. In: 41st Annual Symposium on Frequency Control, 1987, pp. 75-81. doi:10.1109/FREQ. 1987. 201004.

[7] JA Giordmaine, LE Alsop, CH Mayer, CH Townes. A maser amplifier for radio astronomy at x-band. Proceedings of the IRE 47 (6) (1959) 1062-1069. doi:10.1109/JRPROC. 1959.287134.

[8] JG Smith. Ka-band (32-GHz) downlink capability for deep space communications. The Telecommunications and Data Acquisition Report Vol. 42- 88 (Oct-Dec) (1987) 96-103.

[9] MS Reid, RC Clauss, DA Bathker, CT Stelzried. Low-noise microwave receiving systems in a worldwide network of large antennas. Proceedings of the IEEE 61 (9) (1973) 1330-1335. doi:10.1109/PROC.1973.9271.

[10] RC Clauss, JS Shell. Ruby masers. In MS Reid (Ed), Low-noise systems in the deep space network (Deep space communication and navigation series). Jet Propulsion Laboratory; Pasadena, California 2008.

[11] JC Walling, FW Smith. Solid state masers and their use in satellite communication systems. Philips Technical Review 25 (11/12) (1963) 289-310.

[12] M Dillard. The amazing maser: the jewel that conquers space. Popular Electronics 12 (4) (1960) 41-45, 122-123.

[13] R Forward, F Goodwin, J Kiefer. Application of a solid-state ruby maser to an X-band radar system. In: WESCON/59 Conference Record, Vol. 3, 1959, pp. 119-125. doi:10.1109/WESCON.1959.1150334.

[14] IV Konoplev, L Fisher, K Ronald, AW Cross, ADR Phelps. Two-dimensional periodic lattice Cherenkov maser: scalability from 37.5GHz to 350GHz. In: 2010 Abstracts IEEE International Conference on Plasma Science, 2010, pp. 1-1. doi:10.1109/PLASMA. 2010.5533924.

[15] JC Mollier, J Hardin, J Uebersfeld. Theoretical and experimental sensitivities of ESR spectrometers using maser techniques. Review of Scientific Instruments 44 (12) (1973) 1763-1771. doi:10.1063/1.1686050.

[16] M Oxborrow, JD Breeze, NM Alford. Room-temperature solid-state maser. Nature 488 (7411) (2012) 353-356. doi:10.1038/nature11339.

[17] L Jin, M Pfender, N Aslam, P Neumann, S Yang, J Wrachtrup, R-B Liu. Proposal for a room-temperature diamond maser. Nature Communications 6 (2015) 8251. doi:10.1038/ncomms9251.

[18] H Kraus, VA Soltamov, D Riedel, S Väth, F Fuchs, A Sperlich, PG Baranov, V Dyakonov, GV Astakhov. Room-temperature quantum microwave emitters based on spin defects in silicon carbide. Nature Physics 10 (2) (2014) 157-162. doi:10.1038/nphys2826.

[19] SM Watts, BJ van Wees. A solid state paramagnetic maser device driven by electron spin injection. Physical Review Letters 97 (11) (2006) 116601. doi:10.1103/PhysRevLett.97. 116601.

[20] J Breeze, K-J Tan, B Richards, J Sathian, M Oxborrow, NM Alford. Enhanced magnetic Purcell effect in room-temperature masers. Nature Communications 6 (2015) 6215. doi:10.1038/ncomms7215.

[21] KR Foster. A world awash with wireless devices: radio-frequency exposure issues. IEEE Microwave Magazine 14 (2) (2013) 73-84. doi:10.1109/MMM.2012.2234641.

[22] JL Sevillano, D Cascado, F Díaz del Río, S Vicente, G Jimenez, A Civit-Balcells. Soft real-time communications over Bluetooth under interferences from ISM devices. International Journal of Communication Systems 19 (10) (2006) 1103-1116. doi:10.1002/dac.796.

[23] RG Garroppo, L Gazzarrini, S Giordano, L Tavanti. Experimental assessment of the coexistence of Wi-Fi, ZigBee, and Bluetooth devices. In: 2011 IEEE International Symposium on a World of Wireless, Mobile and Multimedia Networks, 2011, pp. 1-9. doi:10.1109/WoWMoM.2011.5986182.

[24] D Raychaudhuri, X Jing. A spectrum etiquette protocol for efficient coordination of radio devices in unlicensed bands. In: 14th IEEE Proceedings on Personal, Indoor and Mobile Radio Communications, 2003. PIMRC 2003, Vol. 1, 2003, pp. 172-176. doi:10.1109/PIMRC.2003.1264255.

[25] CC Davis. The relation between the Einstein A and B coefficients. In: Lasers and electro-optics: fundamentals and engineering. Cambridge University Press, Cambridge, UK 2014, pp. 25-30.

[26] RC Hilborn. Einstein coefficients, cross sections, f values, dipole moments, and all that. American Journal of Physics 50 (11) (1982) 982-986. doi:10.1119/1.12937.

[27] M Elitzur. Physical characteristics of astronomical masers. Reviews of Modern Physics 54 (4) (1982) 1225-1260. doi:10.1103/RevModPhys.54.1225.

[28] JP Gordon, HJ Zeiger, CH Townes. The maser-new type of microwave amplifier, frequency standard, and spectrometer. Physical Review 99 (4) (1955) 1264-1274. doi:10.1103/PhysRev.99.1264.

[29] SA Diddams, JC Bergquist, SR Jefferts, CW Oates. Standards of time and frequency at the outset of the 21st century. Science 306 (5700) (2004) 1318-1324. doi:10.1126/science.1102330.

[30] D Kleppner. Hydrogen-maser principles and techniques. Physical Review 138 (4A) (1965) A972–A983. doi:10.1103/PhysRev.138.A972.

[31] N Bloembergen. Proposal for a new type solid state maser. Physical Review 104 (2) (1956) 324-327. doi:10.1103/PhysRev.104.324.

[32] C Kikuchi, J Lambe, G Makhov, RW Terhune. Ruby as a maser material. Journal of Applied Physics 30 (7) (1959) 1061-1067. doi:10.1063/1.1776979.

[33] DC Lainé. Molecular beam masers. Reports on Progress in Physics 33 (3) (1970) 1001. doi:10.1088/0034-4885/33/3/304.

[34] S Reineke, MA Baldo. Room temperature triplet state spectroscopy of organic semiconductors. Scientific Reports 4 (2014) 3797. doi:10.1038/srep03797.

[35] AE Siegman. Microwave solid-state masers. New York: McGraw-Hill; 1964.

[36] A Blank, H Levanon. Toward maser action at room temperature by triplet-radical interaction and its application to microwave technology. RIKEN Review Vol. 44 (2002) 128-130.

[37] HJ Gerritsen. Recent developments in maser devices and materials. Applied Optics 1 (1) (1962) 37-44. doi:10.1364/AO.1.000037.

[38] HED Scovil, G Feher, H Seidel. Operation of a solid state maser. Physical Review 105 (2) (1957) 762-763. doi:10.1103/PhysRev.105.762.

[39] S. Antipov, W. Gai, O. Poluektov, J. G. Power, A. Kanareykin, P. Schoes- sow, L. Sch ächter, Microwave active media studies for paser, in: Proceedings of PAC09, Vol. FR5RFP, TRIUMF, Vancouver, BC, Canada, 2009, pp. 4535-4537.

[40] P. Schoessow, A. Kanareykin, L. Schachter, Y. Bogachev, A. Tyukhtin, E. Bagryanskaya, N. Yevlampieva, Studies of Particle Acceleration by an Active Microwave Medium, AIP Conference Proceedings 877 (1) (2006) 452-460. doi:10.1063/1.2409169.

[41] R Geng, TT Daugherty, K Do, HM Luong, TD Nguyen. A review on organic spintronic materials and devices: I. Magnetic field effect on organic light emitting diodes. Journal of Science: Advanced Materials and Devices 1 (2) (2016) 128-140. doi:10.1016/j.jsamd.2016.05.002.

[42] C Thomson. Electron spin resonance studies of the triplet state. Quarterly Reviews Chemical Society 22 (1) (1968) 45-74. doi:10.1039/QR9682200045.

[43] C Thomson. Zero-field splittings in aromatic triplet states: I. Naphthalene, pyrene and 1,12-benzperylene. Molecular Physics 10 (4) (1966) 309-315. doi:10.1080/00268976600100421.

[44] C Thomson. Zero-field splittings in aromatic hydrocarbons: II. Calculations with n-electron wave functions including overlap and extensive configuration interaction. Molecular Physics 11 (2) (1966) 197-203. doi:10.1080/00268976600101031.

[45] C Thomson. ESR studies of triplet states in plastics: effect of temperature on the spectra. The Journal of Chemical Physics 41 (1) (1964) 1-6. doi:10.1063/1.1725605.

[46] VA Dediu, LE Hueso, I Bergenti, C Taliani. Spin routes in organic semiconductors. Nature Materials 8 (9) (2009) 707-716. doi:10.1038/nmat2510.

[47] ÉV Shpol'skĭ. Line fluorescence spectra of organic compounds and their applications. Soviet Physics Uspekhi 3 (3) (1960) 372. doi:10.1070/PU1960v003n03ABEH003277.

[48] K Takeda, K Takegoshi, T Terao. Zero-field electron spin resonance and theoretical studies of light penetration into single crystal and polycrystalline material doped with molecules photoexcitable to the triplet state via intersystem crossing. The Journal of Chemical Physics 117 (10) (2002) 4940. doi:10.1063/1.1499124.

[49] J Köhler, ACJ Brouwer, EJJ Groenen, J Schmidt. On the intersystem crossing of pentacene in p-terphenyl. Chemical Physics Letters 250 (1) (1996) 137-144. doi:10.1016/0009-2614(95)01393-8.

[50] A Corval, C Kryschi, S Astilean, HP Trommsdorff. Resonant intersystem crossing in pentacene. The Journal of Physical Chemistry 98 (30) (1994) 7376-7381. doi:10.1021/j100081a024.

[51] JL Ong, DJ Sloop, TS Lin. Temperature dependence studies of the paramagnetic properties of the photoexcited triplet states of pentacene in p-terphenyl, benzoic acid, and naphthalene crystals. The Journal of Physical Chemistry 97 (30) (1993) 7833-7838.

[52] I Rebane. Difference values of spontaneous emission rate of a single-impurity molecule of pentacene in biaxial p-terphenyl crystal. Journal of Luminescence 122-123 (2007) 359-361. doi:10.1016/j.jlumin.2006.01.187.

[53] ACJ Brouwer, J Köhler, AM van Oijen, EJJ Groenen, J Schmidt. Single-molecule fluorescence autocorrelation experiments on pentacene: the dependence of intersystem crossing on isotopic composition. The Journal of Chemical Physics 110 (18) (1999) 9151. doi:10.1063/1.478837.

[54] T-C Yang, DJ Sloop, SI Weissman, T-S Lin. Zero-field magnetic resonance of the photoexcited triplet state of pentacene at room temperature. The Journal of Chemical Physics 113 (24) (2000) 11194. doi:10.1063/1.1326069.

[55] DJ Sloop. Electron spin echoes of a photoexcited triplet: pentacene in p-terphenyl crystals. The Journal of Chemical Physics 75 (8) (1981) 3746. doi:10.1063/1.442520.

[56] WP Ambrose, T Basché, WE Moerner. Detection and spectroscopy of single pentacene molecules in a p-terphenyl crystal by means of fluorescence excitation. The Journal of Chemical Physics 95 (10) (1991) 7150. doi:10.1063/1.461392.

[57] WJM. Naber, S Faez, WG van der Wiel. Organic spintronics. Journal of Physics D: Applied Physics 40 (12) (2007) R205. doi:10.1088/0022-3727/40/12/R01.

[58] S Sanvito. Molecular spintronics: the rise of sp interface science. Nature Physics 6 (8) (2010) 562-564. doi:10.1038/nphys1714.

[59] W Barford. Excitons in conjugated polymers. In: Electronic and optical properties of conjugated polymers, Clarendon Press; Oxford University Press, Oxford, UK, Vol. 66, 2002, pp. 90-111.

[60] S Brazovskii, N Kirova. Physical theory of excitons in conducting polymers. Chemical Society Reviews 39 (7) (2010) 2453. doi:10.1039/b917724h.

[61] F Pulizzi. A new face for organics. Nature Materials 8 (9) (2009) 696-697. doi:10.1038/nmat2519.

[62] A Facchetti. π-conjugated polymers for organic electronics and photovoltaic cell applications†. Chemistry of Materials 23 (3) (2011) 733-758. doi:10.1021/cm102419z.

[63] G Witte, C Wöll. Growth of aromatic molecules on solid substrates for applications in organic electronics. Journal of Materials Research 19 (7) (2004) 1889-1916. doi:10.1557/JMR.2004.0251.

[64] JS Wilson, AS Dhoot, AJAB Seeley, MS Khan, A Köhler, RH Friend. Spin-dependent exciton formation in π-conjugated compounds. Nature 413 (6858) (2001) 828-831. doi:10.1038/35101565.

[65] SR Forrest. Exciton formation statistics under electrical injection in organic semiconductor thin films. Journal of Luminescence 110 (4) (2004) 378-383. doi:10.1016/j.jlumin.2004.08.035.

[66] M-K Lee, M Segal, ZG Soos, J Shinar, MA Baldo. Yield of singlet excitons in organic light-emitting devices: a double modulation photoluminescence-detected magnetic resonance study. Physical Review Letters 94 (13) (2005) 137403. doi:10.1103/PhysRevLett.94.137403.

[67] M Reufer, MJ Walter, PG Lagoudakis, AB Hummel, JS Kolb, HG Roskos, U Scherf, JM Lupton. Spin-conserving carrier recombination in conjugated polymers. Nature Materials 4 (4) (2005) 340-346. doi:10.1038/nmat1354.

[68] J Wang, A Chepelianskii, F Gao, NC Greenham. Control of exciton spin statistics through spin polarization in organic optoelectronic devices. Nature Communications 3 (2012) 1191. doi:10.1038/ncomms2194.

[69] DS McClure. Triplet-singlet transitions in organic molecules. Lifetime measurements of the triplet state. The Journal of Chemical Physics 17 (10) (1949) 905-913. doi:10.1063/1.1747085.

[70] A Köhler, H Bässler. Triplet states in organic semiconductors. Materials Science and Engineering: R: Reports 66 (4-6) (2009) 71-109. doi:10.1016/j.mser.2009.09.001.

[71] S Bogatko, PD Haynes, J Sathian, J Wade, J-S Kim, K-J Tan, J Breeze, E Salvadori, A Horsfield, M Oxborrow. Molecular design of a room-temperature maser. The Journal of Physical Chemistry C 120 (15) (2016) 8251-8260. doi:10.1021/acs.jpcc.6b00150.

[72] DM Pozar. Microwave engineering (4th ed.). Hoboken, NJ: Wiley; 2011.

[73] KA Sandberg. Theoretical investigations of spin-spin interactions: semiempirical estimations of exchange parameters of diradical metalloporphyrin cations and zero field splitting parameters for conjugated diradicals, Ph.D. thesis, North Carolina State University, Raleigh, NC (1998).

[74] J de Jong, C MacLean. The zero-field splitting of cyano-substituted benzenes in their lowest excited triplet states. Journal of Magnetic Resonance 11 (3) (1973) 373-380. doi:10.1016/0022-2364(73)90063-2.

[75] SS Kim. The triplet state of azulene in phenazine crystals by electron paramagnetic resonance. The Journal of Chemical Physics 68 (1) (1978) 333. doi:10.1063/1.435464.

[76] B Smaller. Electron and nuclear magnetic interaction in triplet states of various organic phosphors. The Journal of Chemical Physics 37 (7) (1962) 1578-1579. doi:10.1063/1.1733340.

[77] JS Brinen, MK Orloff. Zero-field splitting in phosphorescent triplet states of aromatic hydrocarbons III. Correlation between D and the triplet state energy. Chemical Physics Letters 1 (7) (1967) 276-278. doi:10.1016/0009-2614(67)80018-6.

[78] J de Jong. Zero-field splitting of methyl-substituted phosphorescent aromatic molecules in their lowest triplet states. Journal of Magnetic Resonance 9 (1) (1973) 185-189. doi:10.1016/0022-2364(73)90174-1.

[79] M Deguchi, D Suzuki, R Ito, M Matsumoto, M Yagi. Time-resolved electron paramagnetic resonance of the lowest excited triplet state of phenazinium cation. Spectrochimica Acta Part A: Molecular and Biomolecular Spectroscopy 61 (6) (2005) 1147-1151. doi:10.1016/j.saa.2004.06.033.

[80] M Kinoshita, N Iwasaki, N Nishi. Molecular spectroscopy of the triplet state through optical detection of zero-field magnetic resonance. Applied Spectroscopy Reviews 17 (1) (1981) 1-94. doi:10.1080/05704928108060401.

[81] C Bräuchle. Symmetry distortions and pseudo-Jahn-Teller effect of peri- and catahexabenzocoronene in their triplet states as obsevered by ODMR techniques. Chemical Physics 67 (1) (1982) 97-109. doi:10.1016/0301-0104(82)88062-2.

[82] T Ikeyama, T Azumi. Triplet spin-sublevel selectivity of the S1-T1 intersystem crossing in trans-stilbene. Chemical Physics Letters 212 (6) (1993) 551-554.

[83] BR Henry, W Siebrand. Spin-orbit coupling in aromatic hydrocarbons. The radiative triplet lifetime of naphthalene. Chemical Physics Letters 3 (2) (1969) 90-92.

[84] AB Zahlan. The triplet state. Cambridge University Press, Cambridge, UK, 1967.

[85] J Köhler, ACJ Brouwer, EJJ Groenen, J Schmidt. Single molecule electron paramagnetic resonance spectroscopy: hyperfine splitting owing to a single nucleus. Science 268 (5216) (1995) 1457-1460. doi:10.1126/science.268.5216.1457.

[86] MA El-Sayed, WR Moomaw, JB Chodak. The mechanism of the S1 ⇝ Tx intersystem crossing process in aromatic hydrocarbons from PMDR. Chemical Physics Letters 20 (1) (1973) 11-16.

[87] WR Dawson, JL Kropp. Radiative and radiationless processes in aromatic molecules. Coronene and benzcoronene. The Journal of Physical Chemistry 73 (3) (1969) 693-699.

[88] M de Groot, JH Van der Waals. Paramagnetic resonance in phosphorescent aromatic hydrocarbons II: determination of zero-field splitting from solution spectra. Molecular Physics 3 (2) (1960) 190-200. doi:10.1080/00268976000100221.

[89] G-C Wang, MA Winnik, HJ Schäfer, W Schmidt. Phosphorescence and photochemical studies of some benzophenone dicarboxylic acid esters. Journal of Photochemistry 33 (3) (1986) 291-296. doi:10.1016/0047-2670(86)87091-5.

[90] MR Wright, RP Frosch, GW Robinson. Phosphorescence lifetime of benzene. An intermolecular heavy-atom effect, a deuterium effect, and a temperature effect. The Journal of Chemical Physics 33 (3) (1960) 934-935. doi:10.1063/1.1731296.

[91] JS Brinen, JG Koren, WG Hodgson. ESR and phosphorescence spectra of the triplet states of phenyl s-triazines and phenyl benzenes. The Journal of Chemical Physics 44 (8) (1966) 3095-3099. doi:10.1063/1.1727185.

[92] J Zuclich, J von Schütz, A Maki. Direct measurement of spin-lattice relaxation rates between triplet spin sublevels using optical detection of magnetic resonance. Molecular Physics 28 (1) (1974) 33-47. doi:10.1080/00268977400101501.

[93] M Orrit, J Bernard. Single pentacene molecules detected by fluorescence excitation in a p-terphenyl crystal. Physical Review Letters 65 (21) (1990) 2716.

[94] J Zuclich. Triplet-state electron spin resonance of the aromatic amino acids and proteins. The Journal of Chemical Physics 52 (7) (1970) 3586. doi:10.1063/1.1673527.

Chapter 11

Analysis of a Resonant AC-AC LED Driver

Teodosescu Petre Dorel, Szekely Norbert Csaba,

Sabau Madalina Sabina and Bojan Mircea

Additional information is available at the end of the chapter

http://dx.doi.org/10.5772/67472

Abstract

The study analyses the performance of different LED circuit configurations feed from a low power resonant driver under pulse quasi-triangular currents. The considered LED driver topology is based on a bridgeless single-stage AC-AC converter with bidirectional switches and a parallel LC resonant tank. The converter performances are simultaneously analyzed in correlation with the most important features, such as the electric efficiency, luminous efficacy, power factor correction capabilities, and flickering implications.

Keywords: light-emitting diodes, converters, resonant conversion, soft switching

1. Introduction

Nowadays, once with the improvements in process and technology, light-emitting diodes (LEDs) have become a very popular solution for lighting devices due to its superior efficacy performance. It is well known that many electronic converters are using an input rectifier and a high-electrolytic filtering capacitance [1, 2]. In high frequency commutations, this electrolytic capacitors have reliability issues, and this fact is limiting the lifetime of the overall LED system [3–7]. In addition, the use of high capacitance electrolytic capacitors remains a problem in achieving high power density and high power factor. Refs. [8–11] propose different topologies of AC-DC converters capable to increase the lifetime of LED driver, by using film capacitors instead of electrolytic capacitors. The basic idea of Ref. [8] is to increase the conduction time of the input current consuming more at the peak and less at the valley of the input power. A high power factor LED driver topology consisting of a derivate topology from a two-cascade flyback

converter is presented in Ref. [9]. Thus, the proposed single-stage, single-switch topology is able to provide high power factor without any unreliable electrolytic capacitors. Moreover, no feedback control circuit is required for minimizing the low-frequency ripple of the LED current. Ref. [10] proposes an AC/DC driver, which is able to provide constant current for LEDs and near-unity input power factor, as well. The idea of this chapter consists in modulating the input current, using pulsating current to drive LEDs and some energy storage elements to balance the power difference. Bearing in mind all these, it is unanimously accepted that in order to increase the lifespan of artificial LED lighting, the elimination of electrolytic capacitors is a must. Likewise, the need to increase the power factor of this electronic load together with constant output current is necessary measures for sustainable development of these technologies [12, 13].

For AC-DC LED drivers, light flicker introduced by the low-frequency pulsating current represents a real problem for the performance of the system and can also have negative influence on human vision [14]. Ref. [15] presents a series-resonant converter (SRC), which can be used as a power control stage able to reduce the low-frequency ripple of the LED current. Additionally, a good performance of the system is gained due to the low switching losses of the SRC and by using film capacitors instead of electrolytic capacitance at the output of power factor correction (PFC) stage. Ref. [16] offers another method capable to obtain a low current ripple by using an average current modulator in series with the LED load. In Ref. [17], a flicker-free electrolytic capacitor-less single-phase AC-DC LED driver is being introduced. By using a bidirectional buck-boost converter, the topology is capable to limit the AC component of the pulsating current and let only the DC component to drive the LEDs. The idea of obtaining an output low-current ripple for avoiding flicker problem is also found in Ref. [18]. This work offers a two-stage flyback/Buck converter topology for which a low output current ripple is obtained. Taking into account all the facts mentioned above, many research interests are related to the minimization of the low-frequency current ripples first because of optical behavior and lifespan of the LED and second because of the lower efficacy of LED in high current ripples [19]. Given that, a low ripple for the LED current can be considered a good practice in designing of high quality LED lighting systems.

In some situations, such as direct AC LED lighting devices [20–22], the high current ripples prove not to be a problem at frequencies of 100 Hz or higher. At these frequencies, the light flicker is considered invisible for most people as is presented in [23–25]. A negative impact for human vision is the stroboscopic effect from flicker, which can be permanently avoided at frequencies higher than 300 Hz.

The present work introduces a new AC-AC resonant converter topology, wherein the main novelty consists on directly feeding from mains a resonant LC tank by two bidirectional switches. In comparison with Ref. [26], the advantage is the elimination of the input diode rectifier, which mainly is translated into achieving higher efficiency. Also, the driver topology is characterized by inherent constant current and high power factor; thus, no close-loop control is considered. The results are presented in correlation with: the electric efficiency, luminous efficacy, power factor correction capabilities, and flicker parameters implications.

The study is organized with a nomenclature section followed by an introduction. Section 3 analytically analyzes the proposed topology and its working principles, while Section 4 deals in the practical measurements of the proposed topology. Section 5 is dedicated for the conclusion, and some hints on future work to be done for further improvements are provided.

http://dx.doi.org/10.5772/67472

2. Considered LED driver topology

In this section, the considered LED driver topology is introduced. The circuit is subject to a patent application [27] and is based on an AC-AC quasi-resonant LC parallel converter driving an output LED stage. The considered topology is presented in **Figure 1**.

It can be seen in **Figure 1** that the AC-AC converter is composed of two bidirectional switches, each having two MOSFETs connected with a common source. In this way, the transistors' control signals can be easily obtained from an IC (in this case, an IR21531 was used) or discrete self-oscillating driver. Using only two signals to control all four transistors is advantageous due to the simplicity and cost-related implications. In **Figure 2**, the presumptive waveforms of the main signals are displayed. From the upper part of the image, it can be seen that the transistors' command signals are represented by 50% duty-cycle signals.

In **Figures 3** and **4** for the input positive and negative half-cycles, the main circuit states depicting the current paths and the activated switches are highlighted. It can be noted that six different stages can be found on both the positive and negative input half-cycles, as presented in **Figure 2**.

Referring to **Figure 1**, the resulted simplified circuit is exemplified in **Figure 5**. The transistors T1 and T2 are represented by the bidirectional switch S1, while T3 and T4 by the bidirectional switch S2.

The analysis is made by considering the positive cycle of the input alternative voltage. Starting from the simplified converter model in **Figure 5**, from the presumptive waveforms in **Figure 2**, and the current paths in **Figure 3**, not considering the switching time frames, three main time intervals can be identified for a half-cycle:

(a) For the time interval defined in **Figure 2** between $t0$ and $t1$, corresponding to **Figure 3** state I, the switch S1 is conductive and S2 is in the OFF state, the converter equation is:

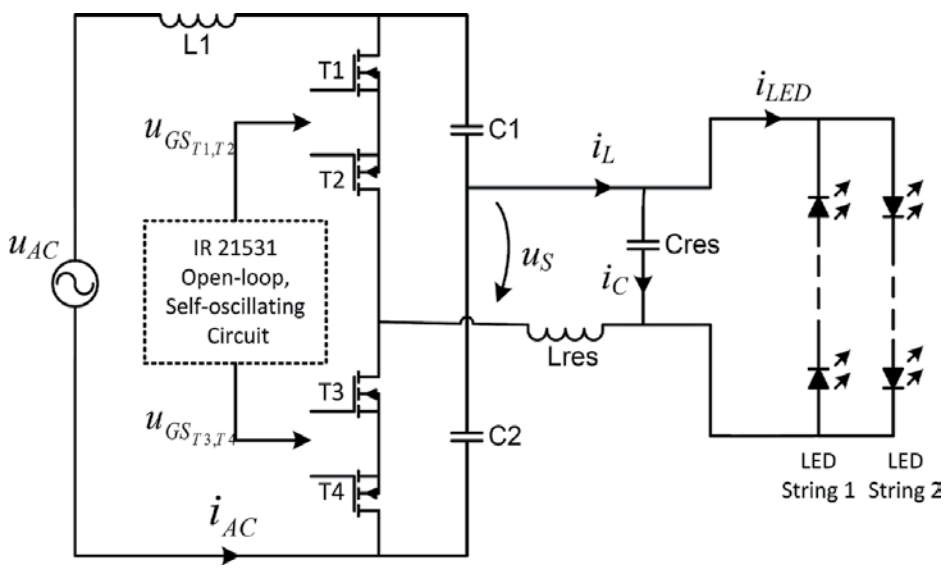

Figure 1. Considered LED driver.

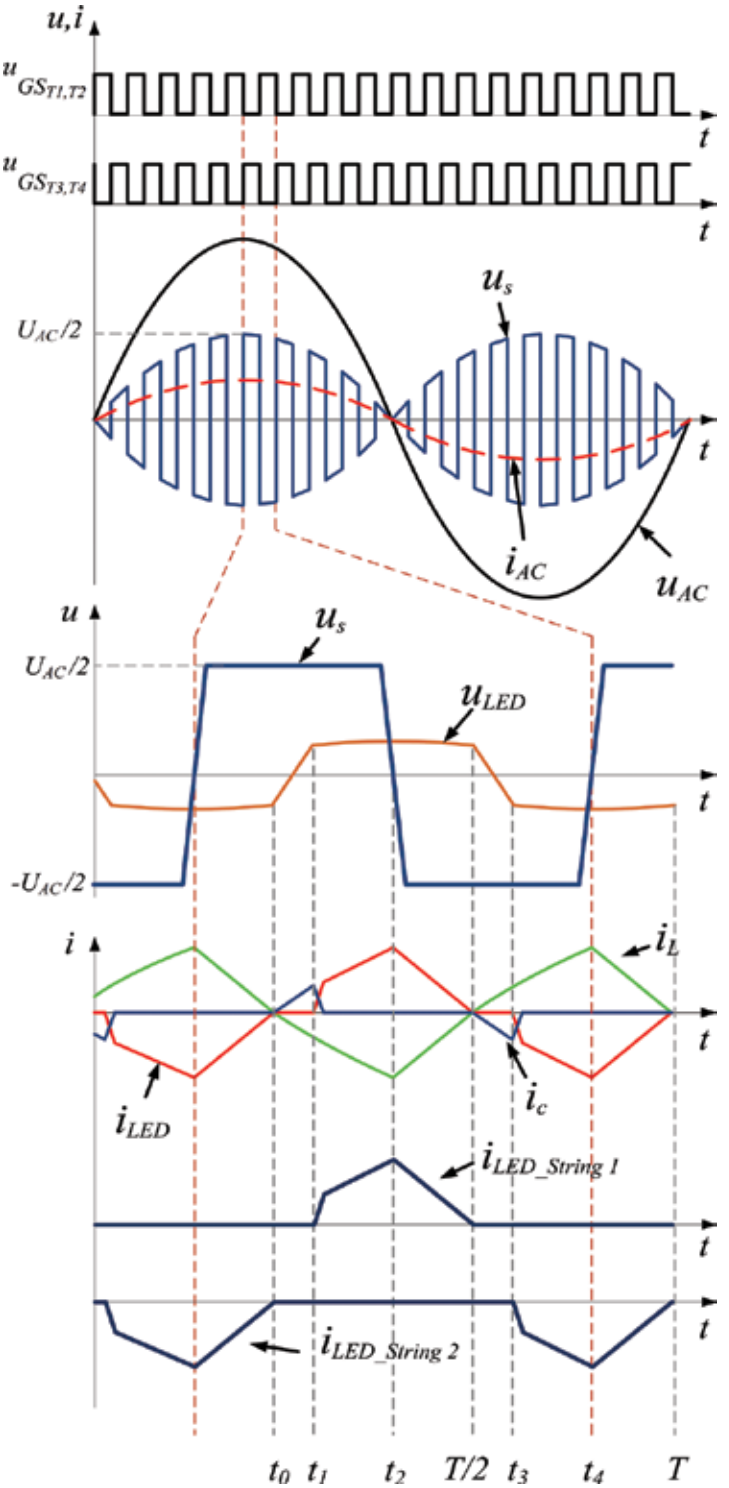

Figure 2. Presumptive waveforms of the AC-AC LED driver.

http://dx.doi.org/10.5772/67472

$$u_s(t) = L_{RES}\frac{di_L(t)}{d(t)} + u_{LED}(t) \tag{1}$$

Now, the circuit is in resonant mode, with no current in the LED ($i_{LED}(t) = 0$):

$$u_c(t) = \frac{1}{C_{RES}}\int i_c(t)dt \tag{2}$$

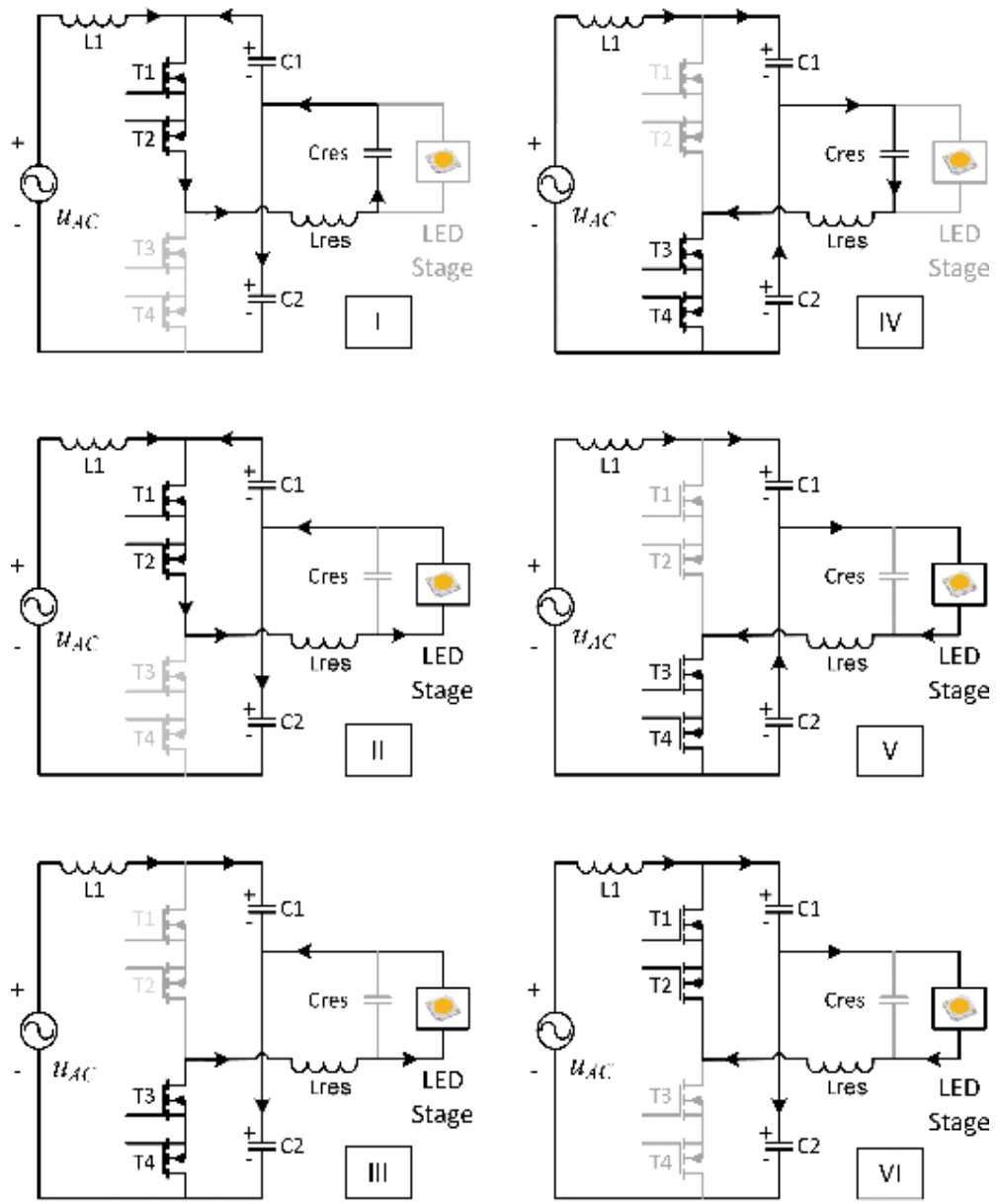

Figure 3. The six main time intervals for the input positive half-cycle.

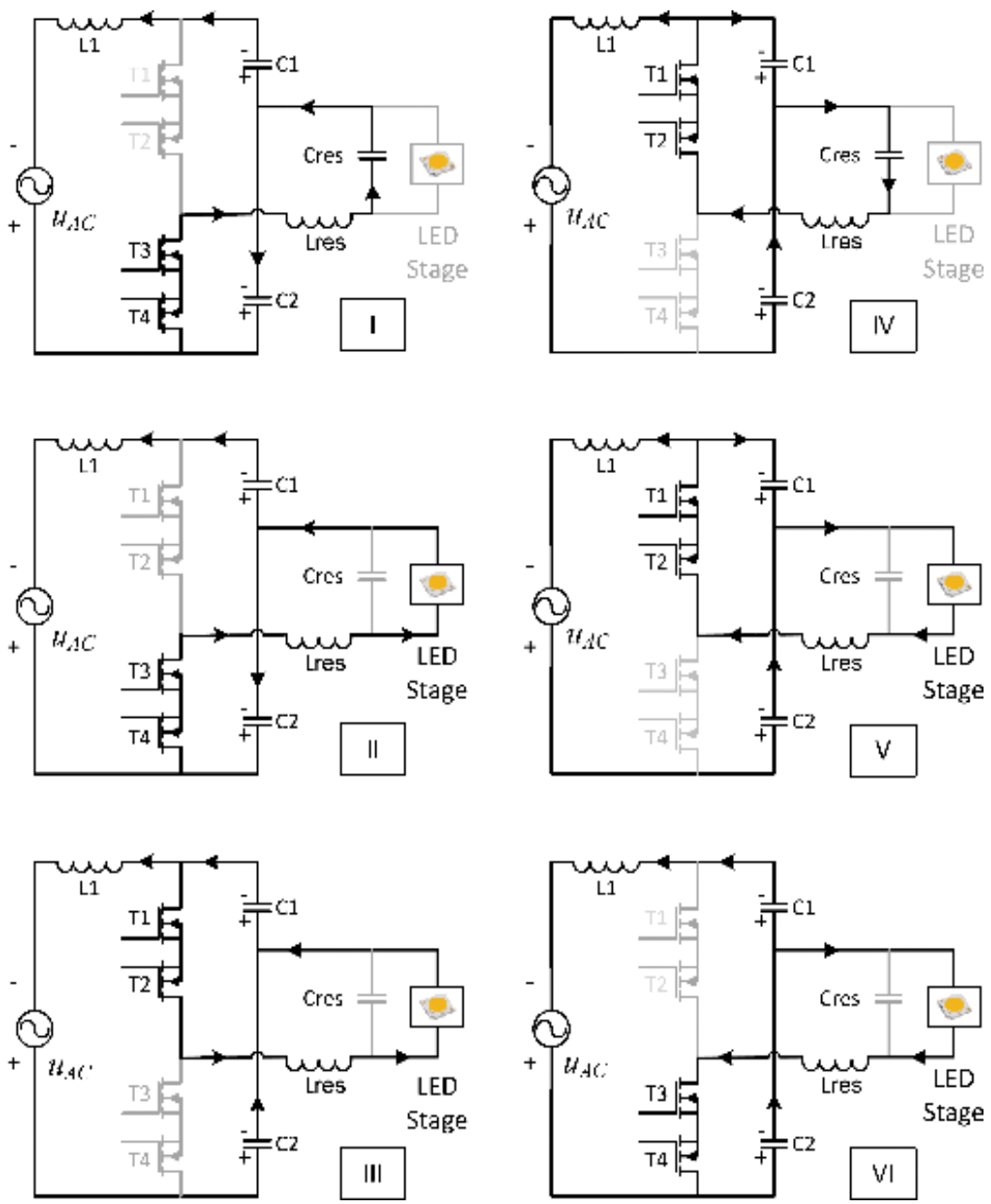

Figure 4. The six main time intervals for the input negative half-cycle.

For this time interval, the inductor current is equal to the capacitor current:

$$i_L(t) = i_C(t) \tag{3}$$

(b) For the time interval between t_1 and t_2, corresponding to **Figure 3**, state II, same as for previous interval, the switch S1 is in the ON state and the switch S2 in the OFF state:

http://dx.doi.org/10.5772/67472

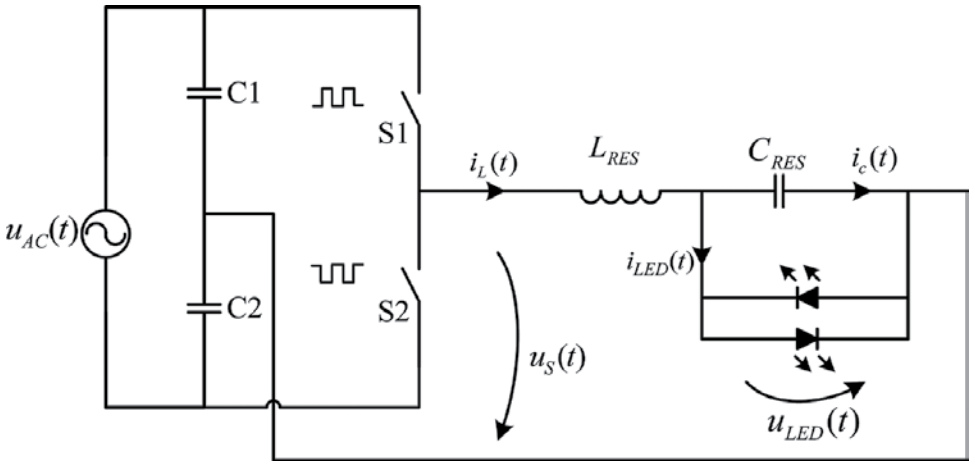

Figure 5. Simplified, model-based schematics of the consider LED driver.

$$u_s(t) = L_{\text{RES}} \frac{di_L(t)}{d(t)} + u_{\text{LED}}(t) \tag{4}$$

Now, $u_{\text{LED}}(t) > U_{\text{LED}}$ (the forward voltage of the direct biased LED), and for the considered time frame where $u_s(t) = \frac{U_{\text{AC}}}{2}$, the above equation becomes:

$$\frac{di_L(t)}{d(t)} = \frac{\frac{U_{\text{AC}}}{2} - U_{\text{LED}}}{L_{\text{RES}}} \approx \text{const.} \tag{5}$$

Because the direct biased LED is conductive, the capacitor current equals 0; thus, the coil current is equal to the LED current, as in:

$$i_L(t) = i_{\text{LED}}(t) \tag{6}$$

(c) For the time interval between t_2 and $T/2$, corresponding to **Figure 3**, state III, the switch S1 is in OFF state and the switch S2 is in ON state, the converter equation becomes:

$$-u_s(t) = L_{\text{RES}} \frac{di_L(t)}{d(t)} + u_{\text{LED}}(t) \tag{7}$$

In this time interval, $u_{\text{LED}}(t) > U_{\text{LED}}$, thus:

$$-\frac{di_L(t)}{d(t)} = \frac{\frac{U_{\text{AC}}}{2} - U_{\text{LED}}}{L_{\text{RES}}} \approx \text{const.} \tag{8}$$

Because the direct biased LED is still in conductive mode, the inductor current is equal to the LED current:

$$i_L(t) = i_{\text{LED}}(t) \tag{9}$$

At the time $t = T/2$, the direct biased LED current reaches the 0 value, and from this moment, the above presented behavior is being repeated for the remaining half cycle. As can be seen in **Figure 4**, the same behavior can be found during the negative cycle of the mains voltage.

It is known that the forward voltage of the LED changes with temperature, so in view of this:

$$-\frac{di_L(t)}{d(t)} = \frac{\frac{U_{AC}}{2} + U_{LED} \pm u_{LED}(^{\circ}C)}{L_{RES}} \tag{10}$$

One can admit that $u_{LED}(^{\circ}C) \ll \frac{U_{AC}}{2} + U_{LED}$, thus:

$$-i_{LED}(t) = \frac{\frac{U_{AC}}{2} + U_{LED} \pm u_{LED}(^{\circ}C)}{L_{RES}} \approx \text{const.} \tag{11}$$

Consequently, the proposed schematic has a current source behavior, with constant output current, regardless of the output LED load type/characteristics. From the input point of view, the circuit presents, to some extent, a natural corrective power factor function.

In **Figures 6** and **7**, the simulation results obtained with PSim 10 software point out the high power factor attained by the proposed circuit. The mains input current waveform for half a cycle is slightly liner/constant and, admittedly, the input current waveform shows, once more, the current source/constant current behavior of the converter.

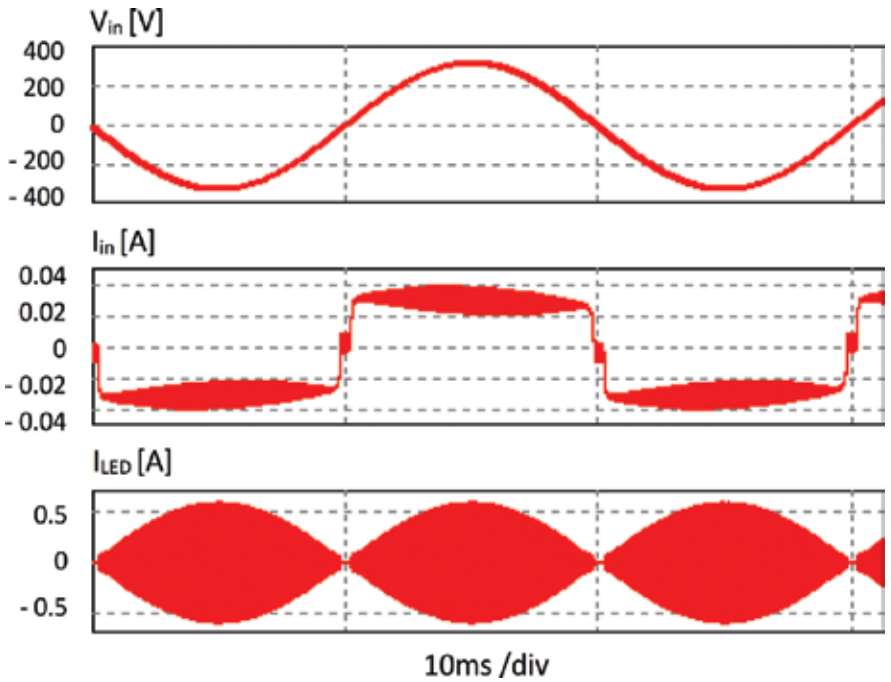

Figure 6. Simulated low frequency representation of the input voltage/current and output current i_{LED}.

http://dx.doi.org/10.5772/67472

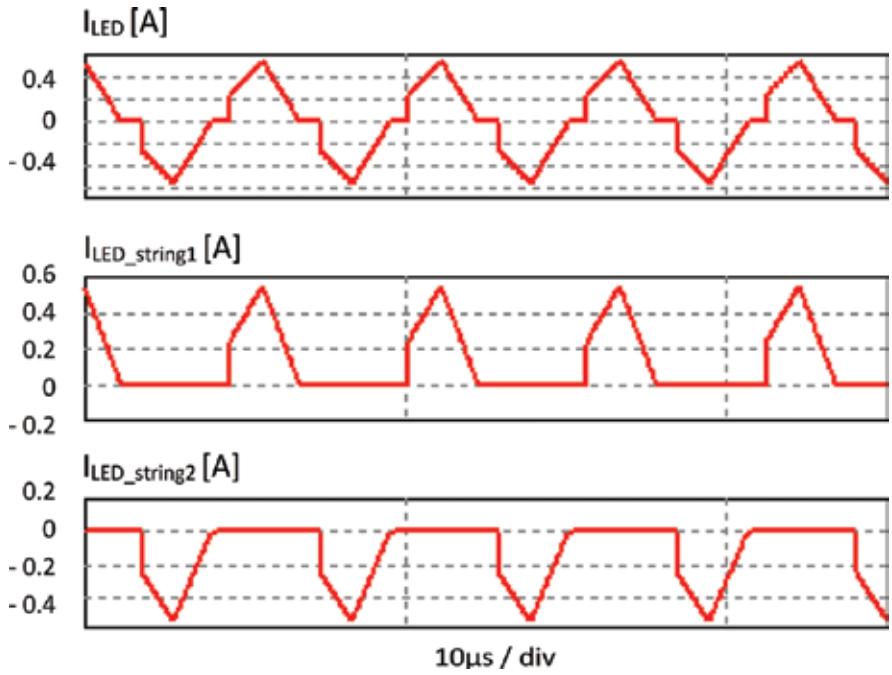

Figure 7. Simulated high frequency representation of the output current waveforms: output resonant tank current; LED string 1 current; LED string 2 current.

3. Practical implementation of the AC-AC LED driver

The practical measurements have been done on the converter topology from **Figure 1** (named the AC-AC type) using the following LED modules: CREE- XLamp CXA1304, CITIZEN-CLU028-1202C4-40AL7K3, and OPTOFLASH-OF-LM002-5B380. Because the Cree LED has an antiparallel diode, the circuit from **Figure 8**, named the AC-AC-1 type, is proposed where a fast diode, with low voltage drop, has been introduced in series with each LED strings.

General characteristics and converter components used are: IR21531 self-oscillating IC, IRF640 transistors, STPS2L40 high-frequency diode, L_{RES} – 2 mH resonant coil, C_{RES} – 2.2 nF resonant capacitor, C1-C2 100 nF voltage divider, L1 – 4 mH input filter, and 82 kHz switching frequency.

To reinforce the presumptive waveforms from **Figure 2**, the experimental results for the direct AC-AC driver considering the Citizen LED module are shown in **Figures 9–12**, wherein the signals are being presented both at low and high frequency ranges.

On the upper part of **Figure 9**, the input voltage $u_{AC}(t)$ and current $i_{AC}(t)$ are represented. On the lower part, the low frequency representation of the output resonant tank voltage, $u_s(t)$ and LED current, $i_{LED}(t)$ is highlighted. **Figure 10** presents the main output signals in relation with the transistor control signal $u_{GS,\ T1,\ T2}$. Therefore, the output voltage of the resonant tank, $u_s(t)$ is represented in conjunction with the LED voltage, $u_{LED}(t)$ and LED current, $i_{LED}(t)$.

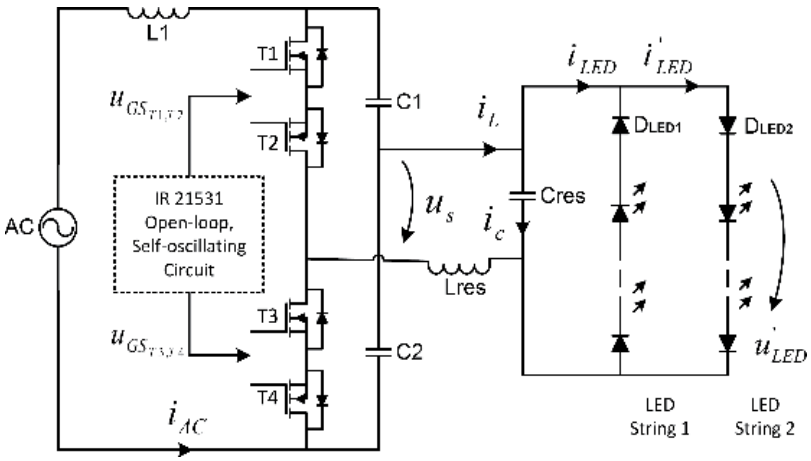

Figure 8. Proposed AC-AC-1 type converter.

Figure 11 highlights the voltage at the drains for the bidirectional switch composed of T1 and T2 transistors in conjunction with the gate control signals and the output LED current. One can notice that the gate signal used for the T1 and T2 transistors is applied after the voltage at the drains was lowered close to zero, thus ZVS (zero voltage switching) is attained. This represents one of the most important aspects in using resonant converters, where the switching losses are

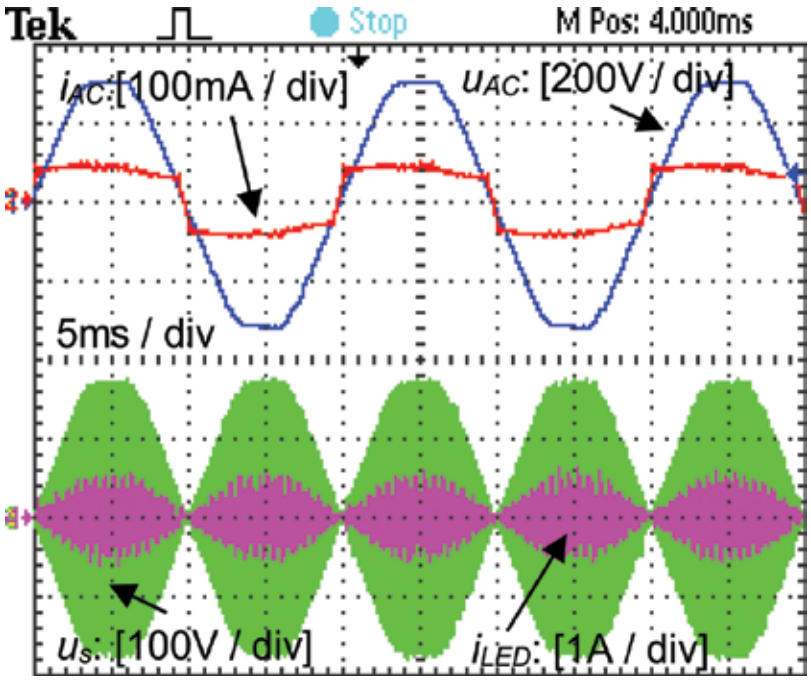

Figure 9. Low frequency signals representation: the input voltage $u_{AC}(t)$; the current $i_{AC}(t)$; the output resonant tank voltage, $u_s(t)$; the LED current, $i_{LED}(t)$.

http://dx.doi.org/10.5772/67472

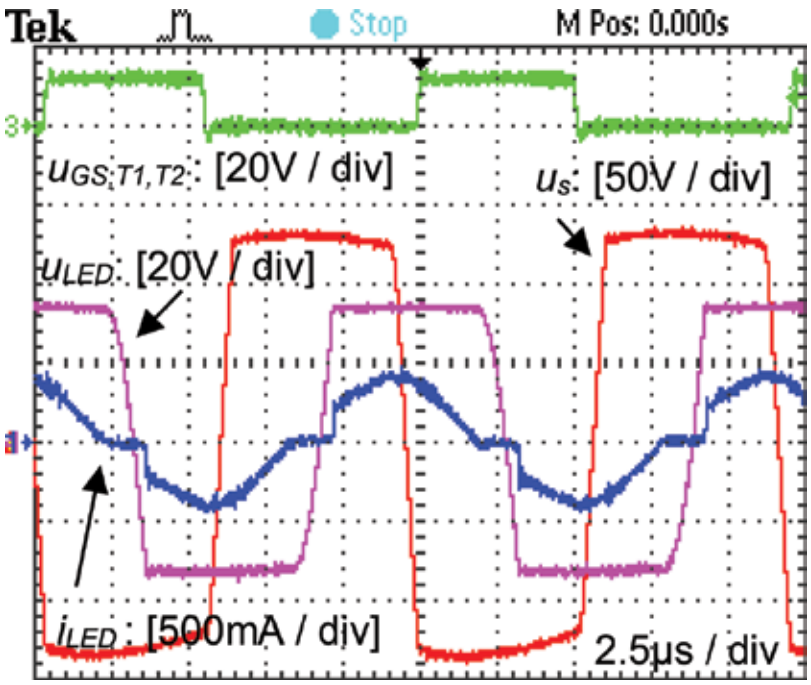

Figure 10. High frequency signals representation: transistor control signal $u_{GS,\ T1,\ T2}$;. The output voltage of the resonant tank, $u_s(t)$; LED voltage, $u_{LED}(t)$; LED current, $i_{LED}(t)$.

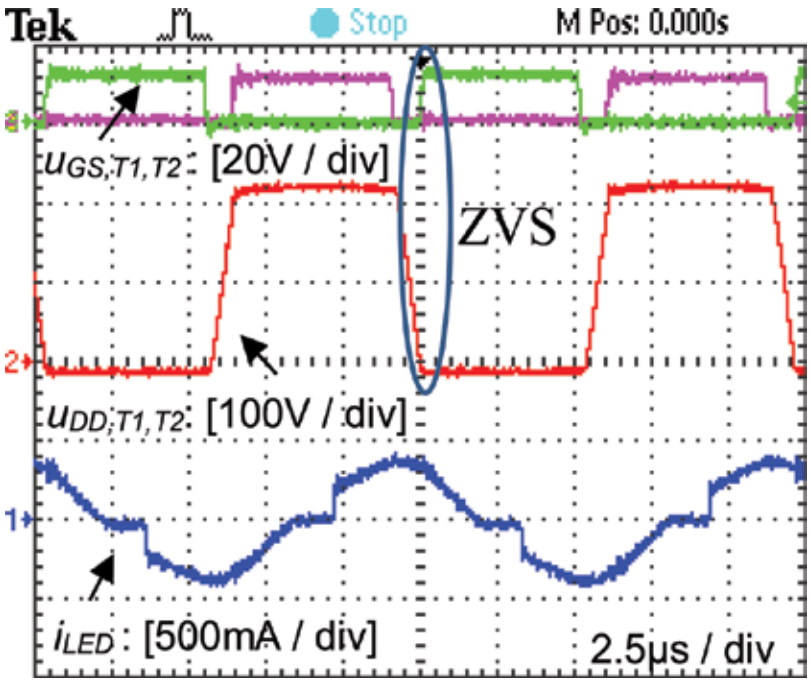

Figure 11. High frequency signals representation: the gate control signals (upper part); the voltage at the drains for the T1-T2 bidirectional switch; the output LED current (lower part).

narrowed to a minimum value. Moreover, the ZVS helps limiting the EMI levels caused by high-frequency switching converters.

Figure 12 shows, on the upper part, the output current of the resonant tank composed of the LED current, $i_{LED}(t)$, and the resonant capacitor current, $i_C(t)$. On the lower part of the picture, the LED String 1 current and the LED String 2 current are being represented.

The general performances of the converter with all the three LED modules are centralized in: **Table 1** for the Cree LED, **Table 2** for Citizen LED, and **Table 3** for the OptoFlash LED. The power measurements were completed by the use of the precision power analyzer KinetiQ PPA2530. The flicker measurements have been performed with the light sensor OPT101 from Texas Instruments. From these waveforms, the percent flicker and the flicker index were deducted.

For all the LED types, the converter components and the switching frequency were kept the same, and since the forward voltage of the modules was different, dissimilar input power values have been obtained. Analyzing the electric efficiency, it can be observed that higher efficiency is achieved at higher input power, regardless of the LED type used. Also, the power factor is negatively influenced by the lower input power level.

The implementation of control loops was not an objective of the present study. Thus, the study states that for low power, acceptable performances in terms of light quality, high efficacy, and long lifespan with no capacitive filtering, the single-stage AC-AC with two antiparallel LED

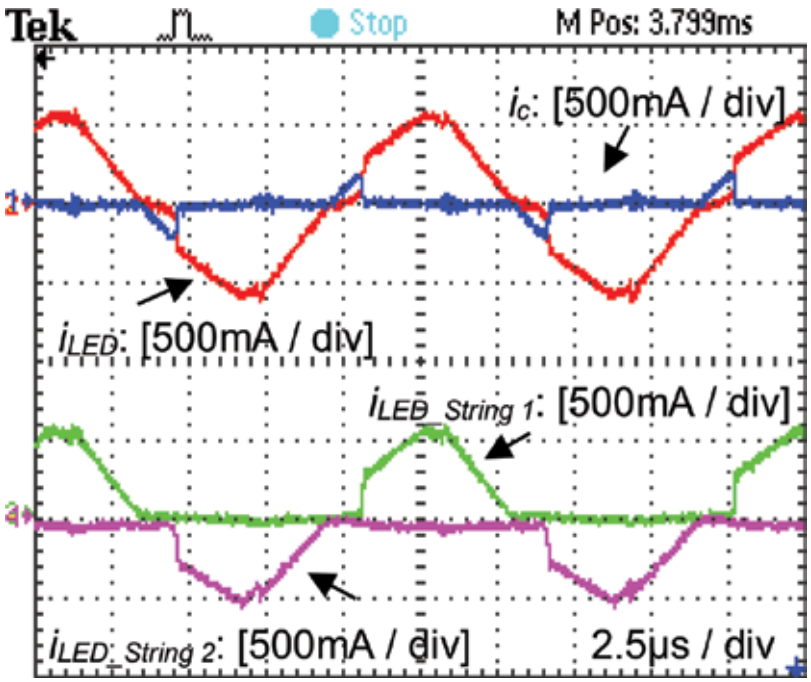

Figure 12. High frequency signals representation: the LED current, $i_{LED}(t)$ and the resonant capacitor current, $i_C(t)$ (upper part); LED String 1 current and the LED String 2 current (lower part).

	Input power [W]	Electric efficiency [%]	System efficacy [lm/W]	Power factor	THD [%]	Flicker index	Percent flicker [%]
AC-AC	–	–	–	–	–	–	–
AC-AC-1	5.03	79.6	102.39	0.916	28.0	0.35	100

Table 1. Practical measurements—LED-Cree.

	Input power [W]	Electric efficiency [%]	System efficacy [lm/W]	Power factor	THD [%]	Flicker index	Percent flicker [%]
AC-AC	7.9	91	134.36	0.95	29.8	0.3	100
AC-AC-1	7.97	90.3	128.68	0.952	29.1	0.30	100

Table 2. Practical measurements—LED-Citizen.

	Input power [W]	Electric efficiency [%]	System efficacy [lm/W]	Power factor	THD [%]	Flicker index	Percent flicker [%]
AC-AC	7.15	89.7	97.45	0.952	28.8	0.34	100
AC-AC-1	7.24	88.2	96.91	0.926	29	0.34	100

Table 3. Practical measurements—LED-Optoflash.

strings could be an interesting solution. For upgraded results, mainly related with light quality, output rectifying solutions with high capacitance filtering are solutions to be investigated. The inherent current source behavior of the converter and high power factor are naturally being accomplished. For further improvements, pure sinusoidal input current shape building and dimming functions can be implemented by means of variable frequency closed-loop control.

The proposed solution was closely analyzed, considering most of the known issues and good practices. The need for high power factor together with constant output current is the feature of an LED drive that is not the subject of discussion. Also, high efficacy, light quality, and lifespans in a cost-efficient technology are targets for high performance LED devices. The study attempts to address all aspects presented above, but as a well-known general rule, some of the above criteria are more important than others, which are defined by the target application.

4. Conclusion

The present research introduces a method of using the benefits of soft switching, by the implementation of a resonant converter in controlling the current for LED lighting devices. The topology is a single-stage AC-AC converter that is capable of obtaining high power factor in an inherent way, with no feedback control loop. What is more, the circuit has a strong current source behavior; thus, no imperative constant output current control is required. All the characteristics are inherently attained, with no control loops; thus, there is room left for further improvement.

Mainly related with the AC-AC stage, the feasibility of the suggested solution is increased if electronic components manufacturing companies are willing to introduce bidirectional controlled switches in a single-chip technology for all power/voltage range applications.

Future work can consider the output circuits with low or high capacitance filtering, closed loop constant current controls, discrete self-oscillating control circuit, and higher switching frequencies for lower inductance needed for the resonant coil.

Acknowledgements

This work was supported by a grant from the Romanian National Authority for Scientific Research, MEN-UEFISCDI, project PN-II-PT-PCCA-2013-4-0914, No. 60/2014 - in the frame of the project with the title"Innovative electric power grid protection device against low power factor electronic loads" (IEDPFC).

Nomenclature

C_{RES}	Resonant tank capacitor
D	Duty cycle; diode
i_{LED}	Input current for the LED arrangement circuit
i_{AC}	Alternative input current
i_C	Resonant tank capacitor current
i_L	Resonant tank inductor current
L_{RES}	Resonant tank inductor
S_n	Bidirectional switch n
t	Time
u_{AC}	Alternative input voltage
$u_{DD,T1,T2}$	Drains voltage for the T1-T2 bidirectional switch
u_{GS}	Gate-source control voltage
u_{LED}	LED voltage
U_{LED}	LED forward voltage
u_S	AC-AC converter output voltage

Author details

Teodosescu Petre Dorel*, Szekely Norbert Csaba, Sabau Madalina Sabina and Bojan Mircea

*Address all correspondence to: petre.teodosescu@emd.utcluj.ro

Technical University of Cluj-Napoca, Cluj-Napoca, Romania

References

[1] J. W. Yang and H. L. Do. High-efficiency ZVS AC-DC LED driver using a self-driven synchronous rectifier. IEEE Transactions on Circuits and Systems: Regular Papers. 2014;**61**(8):2505–2512. DOI: 10.1109/TCSI.2014.2309837

[2] C. Cheng, C. H. Chang, F. Yang and T. Chung. A novel single-stage high-power-factor LED driver for street-lighting applications. IEEE Power Electronics and Drive Systems. 2013;**IA-21**:330–333. DOI: 10.1109/PEDS.2013.6527039

[3] J. M. Alonso, D. Gacio, A. J. Calleja, F. Sichirollo, M. F. da Silva, M. A. Dalla Costa and R. N. do Prado. Reducing storage capacitance in off-line LED power supplies by using integrated converters. IEEE Industry Applications Society Annual Meeting (IAS); 7–11 October 2012; Las Vegas. New York: IEEE; 2012. p.1–8.

[4] D. Camponogara, D. Ribeiro Vargas, M. A. Dalla Costa, J. M. Alonso, J. Garcia and T. Marchesan. Capacitance reduction with an optimized converter connection applied to LED drivers. IEEE Transactions on Industrial Electronics. 2015;**62**:184–192. DOI: 10.1109/TIE.2014.2327591

[5] U.S. Department of Energy. Energy Efficiency Renew. Energy. Lifetime of white LEDs. Pacific Northwest Nat. Lab., Richland, WA, USA, Tech. Rep. 2009.

[6] L. Gu, X. Ruan, M. Xu and K. Yao. Means of eliminating electrolytic capacitor in AC/DC power supplies for LED lightings. IEEE Transactions on Power Electronics. 2009;**24**:1399–1408. DOI: 10.1109/TPEL.2009.2016662

[7] R. Wang, F. Wang, R. Lai, P. Ning, R. Burgos and D. Boroyevich. Study of energy storage capacitor reduction for single phase PWM rectifier. In: Applied Power Electr. Conf., APEC; 15–19 Feb. 2009; Singapore. IEEE; 2009. pp. 1177–1183. DOI: 10.1109/APEC.2009.4802812

[8] F. Zhang, J. Ni and Y. Yu. High power factor AC-DC LED driver with film capacitors. IEEE Transactions on Power Electronics. 2013;**48**(10):4831–4840. DOI: 10.1109/TPEL.2012.2233498

[9] J. C. W. Lam and P. K. Jain. A high power factor, electrolytic capacitor-less AC-input LED driver topology with high frequency pulsating output current. IEEE Transactions on Power Electronics. 2015;**30**(2):943–955. DOI: 10.1109/TPEL.2014.2309555

[10] W. Chen and S. Y. R. Hui. Elimination of an electrolytic capacitor in AC/DC light-emitting diode (LED) driver with high input power factor and constant output current. IEEE Transactions on Power Electronics. 2012;**27**(3):1598–1607. DOI: 10.1109/TPEL.2010.2103959

[11] Y. Wang, J. Huang, W. Wang and D. Xu. A single-stage single-switch LED driver based on Class-E converter. IEEE Transactions on Industry Applications. 2016;**PP**DOI: 10.1109/TIA.2016.2519324,

[12] A. Shrivastava, B. Singh and S. Pal. A novel wall-switched step-dimming concept in LED lighting systems using PFC zeta converter. IEEE Transactions on Industrial Electronics. 2015;**62**:6272–6283. DOI: 10.1109/TIE.2015.2416338

[13] Y. Wang, Y. Guan, K. Ren, W. Wang and D. Xu. A single-stage LED driver based on BCM boost circuit and LLC converter for street lighting system. IEEE Transactions on Industrial Electronics. 2015;**62**:5446–5457. DOI: 10.1109/TIE.2015.2416341

[14] A. Wilkins, J. Veitch and B. Lehman. LED lighting flicker and potential health concerns. In: IEEE Energy Convers. Congr. Expo.; 12 Sep–16 Sep 2010; Atlanta, GA, USA. IEEE; 2010. pp. 171–178.

[15] M. F. de Melo, W. D. Vizzotto, J. M. Alonso and M. A. Dalla Costa. Analysis of series-resonant LED driver applied to reduce the low-frequency current ripple transmission. IEEE 24th International Symposium on Industrial Electronics (ISIE). 2015; pp. 1166–1171.

[16] B. White, H. Wang, Y. Liu and X. Liu. An average current modulation method for single-stage LED drivers with high power factor and zero low-frequency current ripple. IEEE Journal of Emerging and Selected Topics in Power Electronics. 2015;**3**(3). DOI: 10.1109/JESTPE.2015.2424680

[17] S. Whang, X. Ruan, K. Yao, S. C. Tan, Y. Yang and Z. Ye. A flicker free electrolytic capacitor-less AC-DC LED driver. IEEE Transactions on Power Electronics. 2012;**27**(11). DOI: 10.1109/TPEL.2011.2180026

[18] H. Valipour, G. Rezazadeh and M. R. Zolghadri. Flicker-free electrolytic capacitor-less universal input off-line LED driver with PFC. IEEE Transactions on Power Electronics. 2015;**31**(9). DOI: 0.1109/TPEL.2015.2504378

[19] P. S. Almeida, V. C. Bender, H. A. C. Braga, M. A. Dalla Costa, T. B. Marchesan and J. M. Alonso. Static and dynamic photoelectrothermal modeling of LED lamps including low-frequency current ripple effects. IEEE Transactions on Power Electronics. 2015;**30**(7). DOI: 10.1109/TPEL.2014.2340352

[20] C. Park and C. T. Rim. Filter-free AC direct LED driver with unity power factor and low input current THD using binary segmented switched LED strings and linear current regulator. In: Applied Power Electronics Conference and Exposition (APEC); 17 Mar–21 Mar 2013; Long Beach, CA, USA. IEEE; pp. 870–874.

[21] H. Gao, K. Sun, J. Chen, X. Wu, Y. Leng, J. Xi and L. He. An electrolytic-capacitorless and inductorless AC direct LED driver with power compensation. In: Future Energy Electronics Conference; 03 Nov–06 Nov 2013; Department of Electrical Engineering, National Cheng Kung University, Taiwan. IEEE Power Electronics Society; pp. 1–5.

[22] Y. C. Chung, K. M. Lee, H. J. Choe, C. H. Sung and B. Kang. Low-cost drive circuit for AC-direct LED lamps. IEEE Transactions on Power Electronics. 2015;**30**(10). DOI: 10.1109/TPEL.2014.2374160

[23] Texas Instruments. The impact of low frequency ripple current on LEDs and LED drivers' by Texas Instruments at OSRAM Opto Semiconductors and LED drivers' by Texas Instruments at OSRAM Opto Semiconductors [Internet]. Oct. 2010. Available from: http://www.ledlight.osram-os.com/ [Accessed: April 2016].

[24] Lighting Research Center. SSIST: Alliance for solid-state illumination systems and technologies [Internet]. Available from: http://www.lrc.rpi.edu/programs/solidstate/assist/flicker.asp [Accessed: April 2016].

[25] E. Biery. Understand the lighting flicker frustration (magazine) [Internet]. Dec. 2015. Available from: http://www.ledsmagazine.com/ [Accessed: April 2016].

[26] P. D. Teodosescu, M. Bojan and R. Marschalko. Resonant LED driver with inherent constant current and power factor correction. Electronics Letters. 2014;**50**:1087–1088.

[27] P. D. Teodosescu, M. S. Sabau, N. C. Szekely, M. Bojan and R. Marschalko. Electronic device for LED lighting systems. Romanian State Office for Inventions and Trademarks (OSIM). 2015; request no. a 2015 00876.

Chapter 12

Ultraviolet Sensors Based on Two-Dimensional Zinc Oxide Structures

Naif H. Al-Hardan, Muhammad Azmi Abdul Hamid,
Roslinda Shamsudin and Norinsan Kamil Othman

Additional information is available at the end of the chapter

http://dx.doi.org/10.5772/67311

Abstract

In this chapter, we review the application of zinc oxide (ZnO) in ultraviolet (UV) sensing and emphasise on the two-dimensional (2D) ZnO structures. The synthesis of 2D ZnO structures, the morphologies, and the photoluminescence emission will be reviewed and highlighted. The performance of the UV sensors based on 2D ZnO structures is explored. The lack in the study of the 2D ZnO UV sensors might be due to the difficulties of controlling the growth of the 2D ZnO compared to the one-dimensional (1D) ZnO structures.

Keywords: two dimensional (2D), zinc oxide (ZnO), nanostructures, photoluminescence spectroscopy, ultraviolet (UV) sensors

1. Introduction

In the past few decades, zinc oxide (ZnO) has garnered attention due to its unique characterisations that been found to be useful in a variety of applications, such as rubber manufacturing, the ceramic industry, food additives, and pigments [1]. Furthermore, ZnO as a bio safe compound is found to be useful in applications linked to human life, such as in cosmetic, medical, and dental products [1, 2]. It has become one of the most promising compounds that can be employed in advance technology applications, and it demonstrates outstanding performance in various application fields, such as sensors for different analytics including those for hydrogen, oxygen, Volatile organic compounds (VOCs) [3–5], urea, cholesterol, and glucose [6–9].

In addition, ZnO also been employed as a photodetector in the ultraviolet (UV) region of the electromagnetic spectra [10–12] as well as in light emitting diodes (LEDs) [13], UV lasers [14], thin films transparent transistors (TFTs) [15], memory devices [16], and transparent conducting oxides for consumer devices [17]. The subject related to the applications of ZnO was boosted with the advantage of the easy synthesis process compared to the other competitive compounds, such as gallium nitride (GaN) and silicon carbide (SiC). Moreover, ZnO can be synthesised through different processes, and films were grown on different low-cost substrates, such as ordinary papers [18], polymers [19, 20], slide glasses [15], and silicon wafers [10]. Furthermore, high-quality ZnO can be prepared using simple methods with repeatable characteristics, including methods such as radio frequency (RF) magnetron sputtering [21], low temperature hydrothermal processes [22, 23], thermal evaporation [24, 25], sol-gel [26], electrodeposition [27], and chemical vapour deposition (CVD) [28]. Another advantage of ZnO is that it is easily synthesised into different structures in the nanoscale range (nanostructures). Those nanostructures have found potential applications in different areas, such as gas sensors, biosensors, UV sensors, UV lasers, and LEDs. The ZnO nanostructure forms are favourable over the thin film form, especially in nano-size device applications. Furthermore, it demonstrates a higher specific surface when compared with the thin film form [3, 7, 8, 10].

The ZnO nanostructures were classified dimensionally [29], such as one dimension (1D), which are typically nanowires, nanorods, and ribbons; two dimensions (2D), such as nanoplates, nanosheets, nanowalls, nanodisks; and three dimensions (3D), such as nanoballs, nanocoils, nanocones, nanopillars, and nanoflowers [30]. In the view of this chapter, we will focus on the 2D structures, as the remainder are out of the scope of this chapter.

The exceptional physical, optical, chemical and electronic properties of the 2D structures attracted the attention of many research groups globally. It was noted that these properties are due to the strong quantum confinement of electrons in 2D structures and the ultrahigh specific surface area [31].

Recently, 2D ZnO structures, such as nanosheets and nanoplates, have attracted attention due to their promising potential applications in different areas, ranging from catalysis to electronics [9, 31]. They also provide good opportunities to explore new physical and chemical applications of nanostructures with different dimensionalities [32].

In this chapter, we provide a comprehensive review of UV sensors based on the 2D ZnO structures. We focus on the synthetic process, crystallographic, morphology, optical characterisations, and the UV sensor device applications of these structures.

2. Synthesis methods of two-dimensional ZnO structures

Here, we summarised two of the most used methods in preparing 2D ZnO structures.

2.1. Solution-based chemical synthesis

In this process, the growth of ZnO is initiated with a thin film of ZnO seed layer coated on a substrate, typically a glass slide [33], silicon wafer [10], etc. This layer will control the

nucleation event. Several precursors were used to grow the ZnO nanostructure, such as zinc nitrate ($Zn(NO_3)_2$) with hexamethyltetramine ($C_6H_{12}N_4$–[HMT]) [34]. Alenezi et al. [35, 36] reported using zinc sulphate ($ZnSO_4$) with HMT to grow 2D ZnO nanostructures. In both cases, the precursors are dissolved in deionised water and the substrate with the seed layer is immersed in the solution. The vial containing the solution is kept inside an oven at temperature ranging from 50 to 95°C for several hours. Here, the Zn^{2+} species reacts with OH^- to form the $Zn(OH)_2$ intermediate complex, which decomposes to ZnO at high temperatures. This can be demonstrated in the following chemical reactions [37]:

$$\begin{aligned} &(CH_2)_6 N_4 + 6H_2O \leftrightarrow 6\mathrm{HCHO} + 4NH_3 \\ &NH_3 + H_2O \leftrightarrow NH_4^+ + OH^- \\ &2OH^- + Zn^{2+} \rightarrow ZnO(s) + H_2O \end{aligned} \tag{1}$$

In the case of using $ZnSO_4$, the nitride will change to sulphide [35].

The growth of 1D ZnO nanorods using $Zn(NO_3)_2$ with HMT was reported; however, it was demonstrated that adding of sodium citrate can produce plate-like ZnO crystals rather than rod-shaped particles [34]. The citrate is used, as it adsorbs strongly on mineral surfaces and significantly alters the mineral growth behaviour [38]. Using this method, Tian et al. [34] succeeded in growing 2D ZnO with plate (nanoplates) shapes. On the other hand, Alenezi et al. [35, 36] used $ZnSO_4$ to synthesise ZnO by employing a hydrothermal process. The ZnO structures were grown in 2D nanodisks. It was suggested that sulphate will behave as promoter agent that will hinder the nucleation on the (0001) direction and disrupt the growth processes in c-axis crystallographic directions. Interestingly, Ahmad et al. [9] succeed in growing 2D ZnO nanosheets using zinc nitrate with HMT; however, no clear explanations were introduced for the growth of the 2D ZnO nanosheets. However, this might be due to the silver seed layer that been coated over the silicon substrate prior to the growing process.

In conclusion, the ZnO nucleates and its growth takes place according to the inhabitant growth of ZnO crystals in the aqueous solution.

2.2. Electrodepositions

The electrochemical deposition method has been widely adapted for the growth of 2D ZnO structures. Several structures have been produced using this method, such as nanosheets [39], flake-like nanostructures [40], ZnO plate structures [27, 41], and ZnO nanowalls [42]. In this method, two or three electrodes are used; they are the working electrode, typically using conductive glass, such as indium tin oxide (ITO), and the second electrode is usually platinum (Pt), which serves as a counter electrode. The third electrode is the reference electrode, such as Ag/AgCl electrode. Zinc chloride ($ZnCl_2$) [27] or $Zn(NO_3)_2$ [42] is dissolved in deionised water, as the conductivity of the above solution is low; salts such as potassium chloride (KCl) [41] are to be added to increase the conductivity of the electrolyte. A potential is applied between the electrodes that depend on the cell configuration either for two-electrode or three-electrode cells. The cell is usually heated up to a temperature ranging between 70 and 85°C. The size of the 2D ZnO sheet-like structures was increased through adjusting the electrodeposition time [39]. The growth mechanism of the 2D ZnO nanostructures produced through the electrodeposition method might be summarised as follows. After the current is applied

to the cell, the free zinc ions (Zn^{2+}) in the solution move towards the cathode (substrate) and condense to Zn droplets on the substrate. These droplets agglomerate to the Zn spheres that form the core of the nanostructures. The Zn droplets react with the hydroxide to form ZnO on the substrate near the cathode. This can be summarised in the following reactions [40, 43]:

$$Zn^{2+} + 2OH^{-} \rightarrow Zn(OH)_2 \rightarrow ZnO + H_2O \quad (2)$$

Furthermore, it was noticed that electronegative ions affect the shape of the prepared ZnO structures through the electrodeposition method. Ions, such as Cl^{-} or CH_3COO^{-} [41], are adsorbed (capping) preferentially on the positive polar face of the (0001) plane. This will limit the crystal growth along the c-axis and redirect the growth in the $(10\bar{1}0)$ plane, and as a result, a platelet-like ZnO is produced [41, 42, 44]. It is worth noting that the substrate type has a significant effect on the morphology of the prepared ZnO structures. According to Kim et al. [45], the 2D ZnO structures can be obtained using conductive glass substrates, such as indium-doped ZnO and indium tin oxide (ITO). This was supported by several published works [27, 39, 42].

2.3. Miscellaneous methods for preparing 2D ZnO

In addition to the above methods, several methods were used for the preparation of 2D ZnO. However, these methods are less popular. Here, we summarised some of them. The 2D ZnO nanostructures were synthesised through the sol-gel method. In this method, glycerol as an organic poly solvent is added to zinc acetate to synthesise ZnO polycrystalline nanostructures in the form of flakes (2D) [46]. A metal-organic chemical vapour (MOCVD) process was also used to prepare 2D ZnO nanowalls on GaN/Al_2O_3 substrates [47]. Physical vapour deposition (PVD) was used to synthesise ZnO nanosheets for dye solar cell applications [48] High-pressure pulsed laser deposition (PLD) method was also used for growing 2D ZnO nanowalls. In addition, it was found that the lattice parameter of the substrate used for the growth of 2D ZnO plays a crucial rule in the growing process. Using GaN as substrate, ZnO can be easily grown in 2D structures. Whereby using alumina (Al_2O_3) and silicon will result in the growing of nanorods [49]. Vapour-liquid-solid (VLS) mechanism using a gold catalyst was used to grow 2D ZnO nanowalls in this process, a high deposition temperature is used (~900–1100°C) [50–52].

The above processes are not used frequently in the synthesis of 2D ZnO as the solution-based chemical process (such as chemical bath deposition, hydrothermal and electrodeposition).

3. Two-dimensional (2D) ZnO characterisations

3.1. The crystal structural and the morphology of the 2D ZnO

At ambient pressure and temperature, ZnO crystals are typically formed in the wurtzite structure, as shown in **Figure 1**. **Figure 1** shows the hexagonal lattice that belongs to the space Group P63 mc and is characterised by two interconnecting sublattices of Zn and O, such that

http://dx.doi.org/10.5772/67311

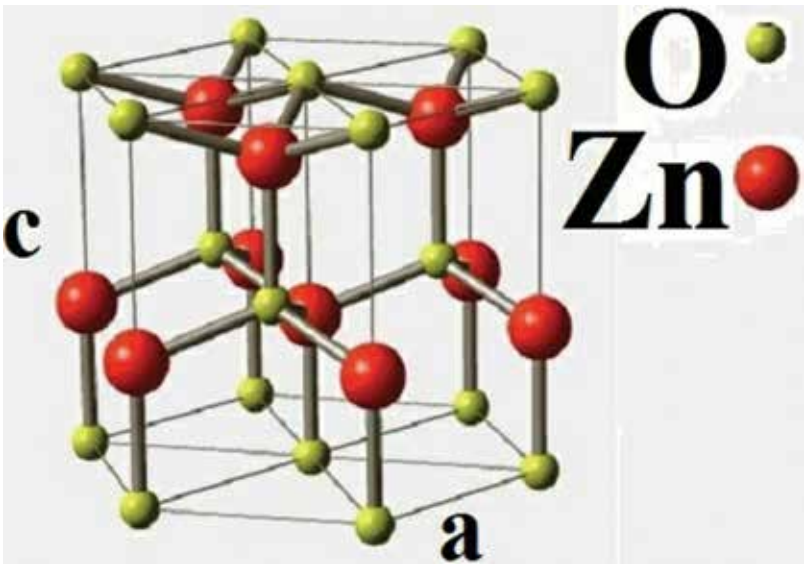

Figure 1. The hexagonal wurtzite structure of ZnO.

each Zn ion is surrounded by a tetrahedra of O ions and vice versa [53, 54]. The lattice parameters of the hexagonal unit cell are a = 3.2495 Å and c = 5.2069 Å, and the density is 5.605 gcm^{-3} [54].

The X-ray diffraction (XRD) pattern of the 2D ZnO films with different morphologies has been reported several times. The XRD patterns reveal the polycrystalline nature and can be indexed as hexagonal wurtzite structures of ZnO. Several published research studies showed the preferred orientation along the c-axis orientation of the (0001) plane [9, 27, 36, 39, 42, 55]. No significant difference in the XRD pattern was noticed for different morphologies of the prepared 2D ZnO. However, the morphology of 2D ZnO prepared through different methods reveals different shapes and diameters. It was found that controlling the experiment parameters results in significant changes in the morphology of the prepared 2D ZnO. Parameters such as substrate lattice mismatch between the substrate and the film will result in the modification of the ZnO structure [48]. The morphology of ZnO structures can be modified by adding salts, such as KCl and CH_3COONH, to the electrolyte in the electrodeposit method [41]. Furthermore, the variations in the electrochemical potential also gave rise to a variety of crystal morphologies [56]. **Figure 2** reveals different structures of 2D ZnO morphologies selected from published results and its corresponding X-ray diffraction patterns.

3.2. The optical properties of 2D ZnO

Photoluminescence (PL) analysis is the most widely applied technique to investigate optical properties of ZnO nanostructures [57, 58] because it can estimate the tightly bound excitons, the bandgap energy, and related defect transitions of ZnO. The photoluminescence measurements of ZnO structures have demonstrated highly efficient near-band-edge emission (NBE)

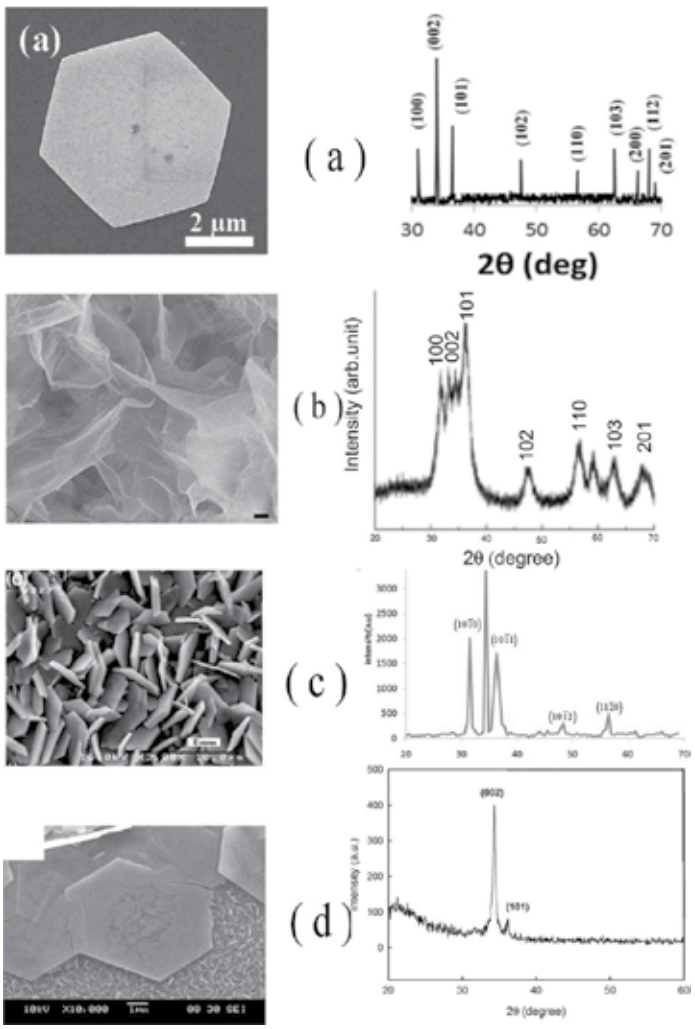

Figure 2. The electron scanning microscopy images of different 2D ZnO and their corresponding X-ray patterns. (a) Nanodisc ZnO prepared through hydrothermal (reprinted from [55] with permission from American Chemical Society (Copyright 2014)). (b) Nanowall ZnO prepared through high-pressure PLD (reprinted from [59] with permission from American Chemical Society Copyright 2009). (c) 2D ZnO nanosheets prepared through solvothermal process. (reprinted from [39] with Reprinted by permission from Macmillan Publishers Ltd: [Nature Communications] (39), copyright (2014), and (d) ZnO 2D plates prepared through electrodeposition using zinc chloride with potassium chloride (reprinted from [27]; with permission from Elsevier Copyright (2012)).

at the UV regions [58]. However, the hypothesis that strong UV emission means good crystalline quality is not correct because ZnO nanostructures commonly exhibit a large number of defects with ionisation energies ranging from 0.03 to 3.14 eV [58]. It is a difficult task to correlate the PL emissions with optical transitions. Thus, the PL emissions from the ZnO defect energy levels are extremely complex and still not fully understood [27]. Nevertheless, 2D ZnO structures show the typical PL emission at room temperature that reveals the near-band-edge

http://dx.doi.org/10.5772/67311

UV emission at the range of 3.30–3.19 eV. This UV emission had been attributed to different origins; it may be attributed to either excitonic or defect-related emission [59]. It was also attributed to the near band-edge emission of ZnO (3.37 eV) [35].

The other familiar band of PL emission of the ZnO compound is located near the visible region (2.75–1.45) eV. This band was related to the surface defects; the source of these defects may be attributed to the oxygen vacancies or zinc interstitials [57, 60]. Furthermore, the strong dependence of the PL peak locations and intensities of ZnO nanostructures on the size and shape of the nanostructures was noted [35, 61]. Several 2D ZnO structures, such as 2D plate [27], nanodisk [35], and nanosheet [59] ZnO structures, show low intensity of the near edge UV emission, which was attributed to the surface states being nonradioactive centres due to their large surface-to-volume ratio [60] and higher intensity in the visible broadband. This was attributed to the wide surface area of the 2D structures that make the density of surface defects higher compared to the other ZnO structures, such as nanorods and nanowires [57, 60].

4. UV Sensors based on 2D ZnO structures

At room temperature, ZnO is a semiconductor compound with a wide energy band gap (Eg) of 3.37 eV [62]. This makes ZnO, a potential candidate, as a UV sensor, and it is favourable over several materials for this application, such as gallium nitride [63] and silicon carbide [64]. ZnO has a large exciton binding energy (60 meV) compared with gallium nitride (26 meV), which makes it more suitable for optoelectronic applications, especially at temperatures near and above room temperature [27]. In addition, ZnO had advantages over them, as it can be easily grown with high quality on low coast substrates. Several published papers show the application of ZnO for UV sensors. The metal-semiconductor-metal (MSM) and the Schottky photodiode configuration prove to be feasible for such applications [10, 27, 65, 66]. Different ZnO structures were studied for the UV applications, such as nanowires [67, 68], nanorods [69, 70] and nanobelts [71]; however, few results were published on 2D ZnO structures, and they focused on one type of device structure. The MSM type photoconductive UV based on 2D ZnO structures was explored by several groups [27, 39, 55]. Here, we review the application of 2D ZnO for UV sensors application.

The main parameters that show the performance of UV photosensors can be summarised as follows:

1. The photosensitivity; the ratio of the photocurrent (I_{ph}) to the dark current (I_d) [40]:

$$\text{Photosensitivity} = \frac{I_{\text{ph}}}{I_d} \tag{3}$$

2. The responsivity (A/W) [10, 55] can be defined as the ratio of net current ($I_{ph} - I_d$) to the incident UV light power (I_{inc}):

$$\text{Responsivity} = \frac{I_{\text{ph}} - I_d}{I_{inc}} \tag{4}$$

It is noteworthy that this parameter has spectral dependence.

3. One of the most important features of a photodetector is the speed of its response. The rise and fall of time, T_R and T_f, of a photodetector is defined as the time for the signal to rise or fall from 10 to 90% or 90 to 10% of the final value, respectively [72].

There have been few published reports on the synthesis of 2D ZnO nanostructures and their application for UV sensing. In these published reports, ions such as chloride or sulphate were used to control the growth of the 2D ZnO. In both cases, the ions are adsorbed on the (0001) plane of ZnO, and as a result, the growth of ZnO will be altered to 2D ZnO as mentioned previously [27, 55, 73]. Different experimental parameters were used to control the morphology of the produced 2D ZnO structures. The effect of the electrodeposition time period on the sheet size of 2D ZnO was explored by Ardakani et al. [74]. Initially, it was noticed that the dark current values increased with the sheet size of the prepared 2D ZnO. The current values increased from 0.5 to 2500 nA as the size of the sheet increased from 600 to 6000 nm. It was also found that the photosensitivity of the smaller sheet size is higher than the larger sheet size (decreased from 20000 to 188). However, it was noted the significant effect of the sheet size on the responsivity of the prepared 2D ZnO and the increase of the sheet size from 600 to 6000 nm will result in the enhancement of the UV photo responsivity from 0.522 to 18.04 A/W. This was attributed to the higher photocurrent in samples with larger sheets. Alenezi et al. [35] prepared 2D ZnO nanodisks through a hydrothermal process. Two types of UV sensors based on the prepared ZnO nanodisk were prepared, a single nanodisk and multiple-nanodisk UV sensors. It was noticed that the dark current of the sensors are 12 and 0.5 nA for the single and multiple nanodisk UV sensors, respectively. The lower dark current value of the multi-nanodisk was attributed to the presence of nanodisk-nanodisk junctions and surface-area extensions. The photosensitivity of the multiple-nanodisk sensor is approximately 1.5 times higher than that of the single nanodisk. However, the responsivity of the single nanodisk was 3300 A/W. The responsivity value obtained for the single nanodisk was among the highest values compared with the other published values for the ZnO nanostructures [75].

The timing characteristics of different ZnO structure photodetectors were published, and the results revealed different response times ranging from nanoseconds to minutes. While a correlation between different forms of ZnO and the response time is difficult to comprehend, it is important to realise that the response time is not only determined by the quality of the ZnO films [66] but also dependent on the electrode spacing of the photodetector [76], which can be expressed as [77]:

$$T_R = \frac{L^2}{\mu V_b} \tag{5}$$

where T_R is the rise time, L^2 is the distance between the contacts, μ is electron mobility, and V_b is the bias voltage.

The results from different structures of ZnO-based UV sensors are depicted in **Table 1**.

Synthesis method	Structure	Dark current	Photosensitivity @ λ	Responsivity @ λ	Response time	Recovery time	Reference
Electrodeposition	2D plate	0.7 mA	260@330 nm/3 V	0.74 A/W@330 nm/3 V	26 s	11 s	[27]
Hydrothermal	2D disk	12 nA	1058@365 nm/3 V	3300 A/W@365 nm/3 V	7 s	–	[55]
Hydrothermal	Network of 2D nanosheet and 1D nanorods	61 pA	1500@300 nm	–	133 s	199 s	[73]
Electrodeposition	2D nanosheet	0.5 nA	20,000@5 V	0.522 A/W@365 nm/5 V	4 s	26.5 s	[39]
High-pressure PLD	2D nanowalls	570 μA	0.66@365 nm/3 V	–	–	–	[59]
MOCVD	Thin films	–	–	~24 A/W@325 nm/3 V	~1 s	~45 s	[77]
Hydrothermal	1D nanorods	–	–	0.61 A/W@8 V	20 s	1050 s	[80]
Hydrothermal	1D nanorods	7.35 μA	3.11@370 nm/5 V	2 A/W@370 nm 5 V	72 s	110 s	[81]
Thermal evaporation	1D Nanowires	0.04 nA	1500@365 nm/5 V	–	120 ms	110 ms	[82]
Burner flame transport synthesis	Nano needle network	–	4500@365 nm/2.4 V	–	67 ms	30 ms	[83]
Vapour phase transport	1D ZnO nanowires	–	250,000	–	~1 ms	~1 ms	[84]

Table 1. Comparison of UV photo sensors performance with different ZnO structures.

5. UV detection mechanisms in 2D ZnO structures

The mechanism of UV photodetection was proposed earlier, which is based on the adsorption and desorption process of the oxygen molecules on the surface of the metal oxide semiconductors [27, 78]. According to this mechanism, it has been found that the photoresponse of ZnO consists of two components [66]: a fast response and a slow response. The fast response results from the reversible solid state process, such as intrinsic interband or excitonic transition, the slow one is governed by the surface-related oxygen adsorption and photodesorption process or by the bulk defect-related recombination process. It was found that the slow photoresponse component is the dominant process in the ZnO films [66]. Furthermore, this process was fitted with either a first- or second-order exponential function, which can be expressed as [58]:

$$Y = A_1 \exp\left(\frac{x}{\tau_1}\right) + A_2 \exp\left(\frac{x}{\tau_2}\right) + Y_o \tag{6}$$

where the constant, Y_o, represents the steady-state photocurrent in the photoresponse or the ultimate dark current in the photorelaxation process. The values of A_1 and A_2 are weighting factors that quantify the relative contribution of each mechanism (where $A_1 + A_2 = 1$) [79], where τ_1 and τ_2 represent the photoresponse and photorelaxation process. The shorter carrier lifetime, which means a faster process, is assigned to τ_1, whereas the slower time constant τ_2 is considered a slower process (slow decay), which suggests persistent photoconductivity [77].

Initially, oxygen molecules are adsorbed at the surface of ZnO to create charged ions by capturing free electrons from the ZnO [27, 55, 66, 78]:

$$O_2(\text{gas}) + e^- \rightarrow O_2^-(\text{adsorbed}) \tag{7}$$

This leads to the formation of a depletion region near the surface, resulting in a decrease of film conductivity. As the ZnO is illuminated with photon energy above the energy gap ($h\nu > E_g$), pairs of electron holes are photogenerated:

$$h\nu \rightarrow e^- + h^+ \tag{8}$$

The holes migrate to the surface of the film along the potential gradient (as a result of band bending) and recombine with trapped electrons previously captured by the oxygen molecules:

$$h^+ + O_2^- \rightarrow O_2(\text{gas}) \tag{9}$$

Hence, carrier concentration enhancement (due to photo generated electrons) is established on the surface of the ZnO structures, resulting in narrower depletion layers and an increase of the film conductivity.

Although the UV sensing mechanism of the 2D ZnO structures is basically the same as that of the other form of ZnO structures, due to their high specific surface area, the 2D ZnO photodetector shows higher sensitivity as can be noticed from **Table 1** [9, 55, 59]. In comparison with 1D ZnO structures, the growth of 2D ZnO nanostructures is much more difficult partially due to its hexagonal polar structure. It is known that the plane of (0001) has the highest surface energy; as a result, there is a fast growth along the c-axis direction with a preferred 1D ZnO growth [31, 84]. This might result in the lack of information on the UV sensors based on 2D ZnO structures.

6. Conclusion

In summary, we have reviewed the performance of UV sensors based on 2D ZnO structures. The performances are competitive with those of the 1D ZnO structures. The lack of the published results of the performance of 2D ZnO-based UV photodetectors might be due to the process of producing 2D ZnO, which are more complicated compared to the ones used for the 1D ZnO structures.

Acknowledgements

This work was supported by the National University of Malaysia (UKM) through the short term grant number DIP 2016-029 (UKM).

Author details

Naif H. Al-Hardan*, Muhammad Azmi Abdul Hamid*, Roslinda Shamsudin and Norinsan Kamil Othman

*Address all correspondence to: azmi@ukm.edu.my and n.h.alhardan@gmail.com

School of Applied Physics, Faculty of Science and Technology, National University of Malaysia (UKM), Bangi, Selangor, Malaysia

References

[1] Moezzi, A., McDonagh, A.M., Cortie, M.B.: Zinc oxide particles: Synthesis, properties and applications. Chemical Engineering Journal **185**, 1-22 (2012). doi: 10.1016/j.cej.2012.01.076.

[2] Nohynek, G.J., Lademann, J., Ribaud, C., Roberts, M.S.: Grey goo on the skin? Nanotechnology, cosmetic and sunscreen safety. Critical Reviews in Toxicology **37**(3), 251-277 (2007). doi: 10.1080/10408440601177780.

[3] Ahn, M.W., Park, K.S., Heo, J.H., Kim, D.W., Choi, K.J., Park, J.G.: On-chip fabrication of ZnO-nanowire gas sensor with high gas sensitivity. Sensors and Actuators B Chemical **138**(1), 168-173 (2009). doi: 10.1016/j.snb.2009.02.008.

[4] Al-Hardan, N., Abdullah, M.J., Abdul Aziz, A., Ahmad, H.: Low operating temperature of oxygen gas sensor based on undoped and Cr-doped ZnO films. Applied Surface Science **256**(11), 3468-3471 (2010). doi: 10.1016/j.apsusc.2009.12.055.

[5] Al-Hardan, N.H., Abdullah, M.J., Aziz, A.A.: ZnO gas sensor – functionality and performance. In: Qiu, X. (ed.) Gas Sensors: Developments, Efficacy and Safety.. Nova Science Pub Incorporated, USA (2011).

[6] Israr, M.Q., Sadaf, J.R., Nur, O., Willander, M., Salman, S., Danielsson, B.: Chemically fashioned ZnO nanowalls and their potential application for potentiometric cholesterol biosensor. Applied Physics Letters **98**(25), 253705-253708 (2011). doi: 10.1063/1.3599583.

[7] Arya, S.K., Saha, S., Ramirez-Vick, J.E., Gupta, V., Bhansali, S., Singh, S.P.: Recent advances in ZnO nanostructures and thin films for biosensor applications: Review. Analytica Chimica Acta **737**, 1-21 (2012). doi: 10.1016/j.aca.2012.05.048.

[8] Ahmad, R., Tripathy, N., Hahn, Y.-B.: Highly stable urea sensor based on ZnO nanorods directly grown on Ag/glass electrodes. Sensors and Actuators B: Chemical **194**, 290-295 (2014). doi: 10.1016/j.snb.2013.12.098.

[9] Ahmad, R., Tripathy, N., Jang, N.K., Khang, G., Hahn, Y.-B.: Fabrication of highly sensitive uric acid biosensor based on directly grown ZnO nanosheets on electrode surface. Sensors and Actuators B: Chemical **206**, 146-151 (2015). doi: 10.1016/j.snb.2014.09.026.

[10] Al-Hardan, N.H., Jalar, A., Abdul Hamid, M.A., Keng, L.K., Ahmed, N.M., Shamsudin, R.: A wide-band UV photodiode based on n-ZnO/p-Si heterojunctions. Sensors and Actuators A: Physical **207**, 61-66 (2014). doi: 10.1016/j.sna.2013.12.024.

[11] Soci, C., Zhang A., Xiang, B., Dayeh, S.A., Aplin, D.P.R., Park, J., Bao, X.Y., Lo, Y.H. and Wang, D.: ZnO nanowire UV photodetectors with high internal gain. Nano Letters **7**(4), 1003-1009 (2007). doi: 10.1021/nl070111x.

[12] Guo, L., Zhang, H., Zhao, D., Li, B., Zhang, Z., Jiang, M., Shen, D.: High responsivity ZnO nanowires based UV detector fabricated by the dielectrophoresis method. Sensors and Actuators B: Chemical **166-167**, 12-16 (2012). doi: 10.1016/j.snb.2011.08.049.

[13] Bakin, A., El-Shaer, A., Mofor, A.C., Al-Suleiman, M., Schlenker, E., Waag, A.: ZnMgO-ZnO quantum wells embedded in ZnO nanopillars: Towards realisation of nano-LEDs. Physica Status Solidi (c) **4**(1), 158-161 (2007). doi: 10.1002/pssc.200673557.

[14] Dong, H., Liu, Y., Lu, J., Chen, Z., Wang, J., Zhang, L.: Single-crystalline tower-like ZnO microrod UV lasers. Journal of Materials Chemistry C **1**(2), 202-206 (2013). doi: 10.1039/C2TC00070A.

[15] Hoffman, R.L., Norris, B.J., Wager, J.F.: ZnO-based transparent thin-film transistors. Applied Physics Letters **82**(5), 733-735 (2003). doi: 10.1063/1.1542677.

[16] Xun, C., Xiaomin, L., Xiangdong, G., Xinjun, L., Chang, Y., Rui, Y., Ping, J.: All-ZnO-based transparent resistance random access memory device fully fabricated at room temperature. Journal of Physics D: Applied Physics **44**(25), 255104 (2011). doi: 10.1088/0022-3727/44/25/255104.

[17] Ellmer, K., Klein, A., Rech, B.: Transparent Conductive Zinc Oxide: Basics and Applications in Thin Film Solar Cells. Springer-Verlag: Berlin (2008).

[18] Gimenez, A.J., Yáñez-Limón, J.M., Seminario, J.M.: ZnO−paper based photoconductive UV sensor. The Journal of Physical Chemistry C **115**(1), 282-287 (2011). doi: 10.1021/jp107812w.

[19] Kriisa, M., Kärber, E., Krunks, M., Mikli, V., Unt, T., Kukk, M., Mere, A.: Growth and properties of ZnO films on polymeric substrate by spray pyrolysis method. Thin Solid Films **555**, 87-92 (2014). doi: 10.1016/j.tsf.2013.05.150.

[20] Yao, I.C., Tseng, T.-Y., Lin, P.: ZnO nanorods grown on polymer substrates as UV photodetectors. Sensors and Actuators A: Physical **178**, 26-31 (2012). doi: 10.1016/j.sna.2012.01.045.

[21] Al-Hardan, N.H., Abdullah, M.J., Aziz, A.A., Ahmad, H., Rashid, M.: The effect of oxygen ratio on the crystallography and optical emission properties of reactive RF sputtered ZnO films. Physica B **405**(4), 1081-1085 (2010). DOI: 10.1016/j.physb.2009.11.006.

[22] Djurisic, A.B., Chen, X.Y., Leung, Y.H.: Recent progress in hydrothermal synthesis of zinc oxide nanomaterials. Recent Patents on Nanotechnology **6**(2), 124-134 (2012). doi: 10.2174/187221012800270180.

[23] Sunandan, B., Joydeep, D.: Hydrothermal growth of ZnO nanostructures. Science and Technology of Advanced Materials **10**(1), 013001 (2009). doi: 10.1088/1468-6996/10/1/013001.

[24] Abdulgafour, H.I., Hassan, Z., Al-Hardan, N., Yam, F.K.: Growth of zinc oxide nanoflowers by thermal evaporation method. Physica B **405**(11), 2570-2572 (2010). doi: 10.1016/j.physb.2010.03.033.

[25] Karkeng, L., Abdul Hamid, M.A., Shamsudin, R., Al-Hardan, N.H., Mansor, I. and Chiu, W.: Temperature-driven structural and morphological evolution of zinc oxide nano-coalesced microstructures and its defect-related photoluminescence properties. Materials **9**, 300-315 (2016). doi: 10.3390/ma9040300.

[26] Kamalasanan, M.N., Chandra, S.: Sol-gel synthesis of ZnO thin films. Thin Solid Films **288**(1-2), 112-115 (1996). doi: 10.1016/s0040-6090(96)08864-5.

[27] Al-Hardan, N.H., Abdullah, M.J., Ahmed, N.M., Yam, F.K., Abdul Aziz, A.: UV photodetector behavior of 2D ZnO plates prepared by electrochemical deposition. Superlattices and Microstructures **51**(6), 765-771 (2012). doi: 10.1016/j.spmi.2012.03.030.

[28] Protasova, L.N., Rebrov, E.V., Choy, K.L., Pung, S.Y., Engels, V., Cabaj, M., Wheatley, A.E.H., Schouten, J.C.: ZnO based nanowires grown by chemical vapour deposition for selective hydrogenation of acetylene alcohols. Catalysis Science and Technology **1**(5), 768-777 (2011). doi: 10.1039/c1cy00074h.

[29] Pokropivny, V.V., Skorokhod, V.V.: Classification of nanostructures by dimensionality and concept of surface forms engineering in nanomaterial science. Materials Science and Engineering C-Bio S **27**(5-8), 990-993 (2007). doi: 10.1016/j.msec.2006.09.023.

[30] Tiwari, J.N., Tiwari, R.N., Kim, K.S.: Zero-dimensional, one-dimensional, two-dimensional and three-dimensional nanostructured materials for advanced electrochemical energy devices. Progress in Materials Science **57**(4), 724-803 (2012). doi: 10.1016/j.pmatsci.2011.08.003.

[31] Tan, C., Zhang, H.: Wet-chemical synthesis and applications of non-layer structured two-dimensional nanomaterials. Nature Communications **6**:7873-7886 (2015). doi: 10.1038/ncomms8873.

[32] Ju, D., Xu, H., Zhang, J., Guo, J., Cao, B.: Direct hydrothermal growth of ZnO nanosheets on electrode for ethanol sensing. Sensors and Actuators B: Chemical **201**, 444-451 (2014). doi: 10.1016/j.snb.2014.04.072.

[33] Tian, Z.R., Voigt, J.A., Liu, J., McKenzie, B., McDermott, M.J.: Biomimetic arrays of oriented helical ZnO nanorods and columns. Journal of the American Chemical Society **124**(44), 12954-12955 (2002). doi: 10.1021/ja0279545.

[34] Tian, Z.R., Voigt, J.A., Liu, J., McKenzie, B., McDermott, M.J., Rodriguez, M.A., Konishi, H., Xu, H.: Complex and oriented ZnO nanostructures. Nature Materials **2**(12), 821-826 (2003). doi: 10.1038/nmat1014.

[35] Alenezi, M.R., Alshammari, A.S., Jayawardena, K.D.G.I., Beliatis, M.J., Henley, S.J., Silva, S.R.P.: Role of the exposed polar facets in the performance of thermally and UV activated ZnO nanostructured gas sensors. The Journal of Physical Chemistry C **117**(34), 17850-17858 (2013). doi: 10.1021/jp4061895.

[36] Alenezi, M.R., Henley, S.J., Emerson, N.G., Silva, S.R.P.: From 1D and 2D ZnO nanostructures to 3D hierarchical structures with enhanced gas sensing properties. Nanoscale **6**(1), 235-247 (2014). doi: 10.1039/C3NR04519F.

[37] Schmidt-Mende, L., MacManus-Driscoll, J.L.: ZnO – nanostructures, defects, and devices. Materials Today **10**(5), 40-48 (2007). doi: 10.1016/s1369-7021(07)70078-0.

[38] Liu, C., Huang, P.M.: Atomic force microscopy and surface characteristics of iron oxides formed in citrate solutions. Soil Science Society of America Journal **63**(1), 65-72 (1999). doi: 10.2136/sssaj1999.03615995006300010011x.

[39] Sun, Z., Liao, T., Dou, Y., Hwang, S.M., Park, M.S., Jiang, L., Kim, J.H., Dou, S.X.: Generalized self-assembly of scalable two-dimensional transition metal oxide nanosheets. Nature Communications **5**:3813-3822 (2014). doi: 10.1038/ncomms4813.

[40] Hassan, N.K., Hashim, M.R.: Flake-like ZnO nanostructures density for improved absorption using electrochemical deposition in UV detection. Journal of Alloys and Compounds **577**, 491-497 (2013). doi: 10.1016/j.jallcom.2013.06.010.

[41] Xu, L., Guo, Y., Liao, Q., Zhang, J., Xu, D.: Morphological control of ZnO nanostructures by electrodeposition. The Journal of Physical Chemistry B **109**(28), 13519-13522 (2005). doi: 10.1021/jp051007b.

[42] Pradhan, D., Leung, K.T.: Vertical growth of two-dimensional zinc oxide nanostructures on ITO-coated glass: Effects of deposition temperature and deposition time. The Journal of Physical Chemistry C **112**(5), 1357-1364 (2008). doi: 10.1021/jp076890n.

[43] Chen, Z., Tang, Y., Zhang, L., Luo, L.: Electrodeposited nanoporous ZnO films exhibiting enhanced performance in dye-sensitized solar cells. Electrochimica Acta **51**(26), 5870-5875 (2006). doi: 10.1016/j.electacta.2006.03.026.

[44] Pradhan, D., Kumar, M., Ando, Y., Leung, K.T.: One-dimensional and two-dimensional ZnO nanostructured materials on a plastic substrate and their field emission properties. The Journal of Physical Chemistry C **112**(18), 7093-7096 (2008). doi: 10.1021/jp800799b.

[45] Kim, H., Moon, J.Y., Lee, H.S.: Growth of ZnO nanorods on various substrates by electrodeposition. Electronic Materials Letters **5**(3), 135-138 (2009). doi: 10.3365/eml.2009.09.135.

[46] Tseng, Y.-K., Chuang, M.-H., Chen, Y.-C., Wu, C.-H.: Synthesis of 1D, 2D, and 3D ZnO polycrystalline nanostructures using the sol-gel method. Journal of Nanotechnology **2012**, 8 (2012). doi: 10.1155/2012/712850.

[47] Shi, Z.-F., Zhang, Y.-T., Zhuang, S.-W., Yan, L., Wu, B., Cui, X.-J., Huang, Z., Dong, X., Zhang, B.-L., Du, G.-T.: Vertically aligned two-dimensional ZnO nanowall networks: Controllable catalyst-free growth and optical properties. Journal of Alloys and Compounds **620**, 299-307 (2015). doi: 10.1016/j.jallcom.2014.09.149.

[48] Jimenez-Cadena, G., Comini, E., Ferroni, M., Vomiero, A., Sberveglieri, G.: Synthesis of different ZnO nanostructures by modified PVD process and potential use for dye-sensitized solar cells. Materials Chemistry and Physics **124**(1), 694-698 (2010). doi: 10.1016/j.matchemphys.2010.07.035.

[49] Premkumar, T., Zhou, Y.S., Lu, Y.F., Baskar, K.: Optical and field-emission properties of ZnO nanostructures deposited using high-pressure pulsed laser deposition. ACS Applied Materials & Interfaces **2**(10), 2863-2869 (2010). doi: 10.1021/am100539q.

[50] Lao, J.Y., Huang, J.Y., Wang, D.Z., Ren, Z.F., Steeves, D., Kimball, B., Porter, W.: ZnO nanowalls. Applied Physics A **78**(4), 539-542 (2004). doi: 10.1007/s00339-003-2391-2.

[51] Grabowska, J., Meaney, A., Nanda, K.K., Mosnier, J.P., Henry, M.O., Duclère, J.R., McGlynn, E.: Surface excitonic emission and quenching effects in ZnO nanowire/nanowall systems: Limiting effects on device potential. Physical Review B **71**(11), 115439 (2005). doi: 10.1103/PhysRevB.71.115439.

[52] Kim, S.-W., Park, H.-K., Yi, M.-S., Park, N.-M., Park, J.-H., Kim, S.-H., Maeng, S.-L., Choi, C.-J., Moon, S.-E.: Epitaxial growth of ZnO nanowall networks on GaN/sapphire substrates. Applied Physics Letters **90**(3), 033107 (2007). doi: 10.1063/1.2430918.

[53] Ozgur, U., Alivov, Y.I., Liu, C., Teke, A., Reshchikov, M.A., Dogan, S., Avrutin, V., Cho, S.J., Morkoc, H.: A comprehensive review of ZnO materials and devices. Journal of Applied Physics **98**(4), 041301-041103 (2005). doi: 10.1063/1.1992666.

[54] Jagadish, C., Pearton, S.: Zinc Oxide Bulk, Thin Films and Nanostructures Processing, Properties and Applications. Elsevier: Amsterdam, The Netherlands (2006).

[55] Alenezi, M.R., Alshammari, A.S., Alzanki, T.H., Jarowski, P., Henley, S.J., Silva, S.R.P.: ZnO nanodisk based UV detectors with printed electrodes. Langmuir **30**(13), 3913-3921 (2014). doi: 10.1021/la500143w.

[56] Illy, B., Shollock, B.A., Macmanus-Driscoll, J.L., Ryan, M.P.: Electrochemical growth of ZnO nanoplates. Nanotechnology **16**(2), 320-324 (2005). doi: 10.1088/0957-4484/16/2/025.

[57] Djurisic, A.B., Leung, Y.H.: Optical properties of ZnO nanostructures. Small **2**(8-9), 944-961 (2006). doi: 10.1002/smll.200600134.

[58] Feng, Z.C.: Handbook of Zinc Oxide and Related Materials: Volume Two, Devices and Nano-Engineering. Taylor & Francis, (2012). Florida, USA.

[59] Cao, B.Q., Matsumoto, T., Matsumoto, M., Higashihata, M., Nakamura, D., Okada, T.: ZnO nanowalls grown with high-pressure PLD and their applications as field emitters and UV detectors. The Journal of Physical Chemistry C **113**(25), 10975-10980 (2009). doi: 10.1021/jp902603s.

[60] Cao, B., Teng, X., Heo, S.H., Li, Y., Cho, S.O., Li, G., Cai, W.: Different ZnO nanostructures fabricated by a seed-layer assisted electrochemical route and their photoluminescence and field emission properties. The Journal of Physical Chemistry C **111**(6), 2470-2476 (2007). doi: 10.1021/jp066661l.

[61] Gao, P., Chen, Y., Wang, Y., Zhang, Q., Li, X., Hu, M.: A simple recycling and reuse hydrothermal route to ZnO nanorod arrays, nanoribbon bundles, nanosheets, nanocubes and nanoparticles. Chemical Communications 19, 2762-2764 (2009). doi: 10.1039/B900391F.

[62] Lu, J.G., Ye, Z.Z., Huang, J.Y., Zhu, L.P., Zhao, B.H., Wang, Z.L., Fujita, S.: ZnO quantum dots synthesized by a vapor phase transport process. Applied Physics Letters **88**(6), 063110 (2006). doi: 10.1063/1.2172154.

[63] Wang, X., Zhang, Y., Chen, X., He, M., Liu, C., Yin, Y., Zou, X., Li, S.: Ultrafast, superhigh gain visible-blind UV detector and optical logic gates based on nonpolar a-axial GaN nanowire. Nanoscale **6**(20), 12009-12017 (2014). doi: 10.1039/C4NR03581J.

[64] Feng, Y., Xiaobin, X., Aslam, S., Yuegang, Z., Franz, D., Zhao, J.H., Weiner, M.: 4H-SiC UV photo detectors with large area and very high specific detectivity. IEEE Journal of Quantum Electronics **40**(9), 1315-1320 (2004). doi: 10.1109/JQE.2004.833196.

[65] Mridha, S., Basak, D.: Ultraviolet and visible photoresponse properties of n-ZnO/p-Si heterojunction. Journal of Applied Physics **101**(8), 083102-083105 (2007). doi: 10.1063/1.2724808.

[66] Zhong, J., Lu, Y.: ZnO-based ultraviolet detectors. In: Litton, C.W., Collins, T.C., Reynolds, D.C., Capper, P., Kasap, S., Willoughby, A. (eds.) Zinc Oxide Materials for Electronic and Optoelectronic Device Applications. John Wiley & Sons, (2011), United Kingdom.

[67] Chang, S.-P., Chien-Yuan, L., Shoou-Jinn, C., Chiou, Y., Ting-Jen, H., Cheng-Liang, H.: Electrical and optical characteristics of UV photodetector with interlaced ZnO nanowires. IEEE Journal of Selected Topics in Quantum Electronics **17**(4), 990-995 (2011). doi: 10.1109/JSTQE.2010.2046884.

[68] Chen, M.-W., Chen, C.-Y., Lien, D.-H., Ding, Y., He, J.-H.: Photoconductive enhancement of single ZnO nanowire through localized Schottky effects. Optics Express **18**(14), 14836-14841 (2010). doi: 10.1364/OE.18.014836.

[69] Mamat, M.H., Khusaimi, Z., Musa, M.Z., Malek, M.F., Rusop, M.: Fabrication of ultraviolet photoconductive sensor using a novel aluminium-doped zinc oxide nanorod–nanoflake network thin film prepared via ultrasonic-assisted sol–gel and immersion methods. Sensors and Actuators A: Physical **171**(2), 241-247 (2011). doi: 10.1016/j.sna.2011.07.002.

[70] Savu, R., Parra, R., Jancar, B., Zaghete, M.A., Joanni, E.: Influence of Hydrothermal synthesis conditions and device configuration on the photoresponse of UV sensors based on ZnO nanorods. IEEE Sensors Journal **11**(9), 1820-1825 (2011). doi: 10.1109/JSEN.2011.2105261.

[71] Cheng-Ying, C., Ming-Wei, C., Chia-Yang, H., Der-Hsien, L., Miin-Jang, C., Hau, H.: Enhanced recovery speed of nanostructured ZnO photodetectors using nanobelt networks. IEEE Journal of Selected Topics in Quantum Electronics **18**(6), 1807-1811 (2012). doi: 10.1109/JSTQE.2012.2200031.

[72] Keyes, R.J.: Optical and Infrared Detectors. Springer: Berlin Heidelberg, (2013).

[73] Maiti, U.N., Chattopadhyay, K.K., Karan, S., Mallik, B.: Synthesis of a zinc oxide nanosheet–nanowire network complex by a low-temperature chemical route: Efficient UV detection and field emission property. Scripta Materialia **62**(5), 305-308 (2010). doi: 10.1016/j.scriptamat.2009.11.026.

[74] Ardakani, G.A., Pazoki, M., Mahdavi, S.M., Bahrampour, A.R., Taghavinia, N.: Ultraviolet photodetectors based on ZnO sheets: The effect of sheet size on photoresponse properties. Applied Surface Science **258**(14):5405-5411 (2012). doi: 10.1016/j.apsusc.2012.02.024.

[75] Liu, K., Sakurai, M., Aono, M.: ZnO-based ultraviolet photodetectors. Sensors **10**(9), 8604-8634 (2010). doi: 10.3390/s100908604.

[76] Hullavarad, S.S., Hullavarad, N.V., Karulkar, P.C., Luykx, A., Valdivia, P.: Ultra violet sensors based on nanostructured ZnO spheres in network of nanowires: A novel approach. Nanoscale Research Letters **2**(3), 161-167 (2007). doi: 10.1007/s11671-007-9048-6.

[77] Liu, C.Y., Zhang, B.P., Lu, Z.W., Binh, N.T., Wakatsuki, K., Segawa, Y., Mu, R.: Fabrication and characterization of ZnO film based UV photodetector. Journal of Materials Science: Materials in Electronics **20**(3), 197-201 (2009). doi: 10.1007/s10854-008-9698-x.

[78] Li, Q.H., Gao, T., Wang, Y.G., Wang, T.H.: Adsorption and desorption of oxygen probed from ZnO nanowire films by photocurrent measurements. Applied Physics Letters **86**(12), 123117-123120 (2005). doi: 10.1063/1.1883711.

[79] Aga, R.S., Jowhar, D., Ueda, A., Pan, Z., Collins, W.E., Mu, R., Singer, K.D., Shen, J.: Enhanced photoresponse in ZnO nanowires decorated with CdTe quantum dot. Applied Physics Letters **91**(23), 232108-232111 (2007). doi: 10.1063/1.2822896.

[80] Azimirad, R., Khayatian, A., Safa, S., Almasi Kashi, M.: Enhancing photoresponsivity of ultra violet photodetectors based on Fe doped ZnO/ZnO shell/core nanorods. Journal of Alloys and Compounds **615**, 227-233 (2014). doi: 10.1016/j.jallcom.2014.06.157.

[81] Humayun, Q., Kashif, M., Hashim, U., Qurashi, A.: Selective growth of ZnO nanorods on microgap electrodes and their applications in UV sensors. Nanoscale Research Letters **9**(1), 29 (2014). doi: 10.1186/1556-276X-9-29.

[82] Ranwa, S., Kumar, M., Singh, J., Fanetti, M., Kumar, M.: Schottky-contacted vertically self-aligned ZnO nanorods for hydrogen gas nanosensor applications. Journal of Applied Physics **118**(3), 034509 (2015). doi: 10.1063/1.4926953.

[83] Gedamu, D., Paulowicz, I., Kaps, S., Lupan, O., Wille, S., Haidarschin, G., Mishra, Y.K., Adelung, R.: Rapid fabrication technique for interpenetrated ZnO nanotetrapod networks for fast UV sensors. Advanced Materials **26**(10), 1541-1550 (2014). doi: 10.1002/adma.201304363.

[84] Kind, H., Yan, H.Q., Messer, B., Law, M., Yang, P.D.: Nanowire ultraviolet photodetectors and optical switches. Advanced Materials **14**(2), 158 (2002). doi: 10.1002/1521-4095(20020116).

Chapter 13

The Optical Phenomena of Interplay between Nanobio Complexes: A Theoretical Insight into Their Biomedical Applications

Ruby Srivastava

Additional information is available at the end of the chapter

http://dx.doi.org/10.5772/67527

Abstract

The subnanometer-sized coinage metal nanoparticles (NPs) have attracted more attention due to their unique electronic structures and subsequent physical, chemical and excellent photoluminescent properties. The DNA-stabilized metal clusters had become a remarkably good choice for the selection of fluorescent color by the sequence of the stabilizing DNA oligomer. Similarly, the single-wall carbon nanotubes (SWCNTs) also have unique optical properties which make them useful in many applications. The interaction of DNA and SWCNT is also useful in molecular sensors and it is assumed that amplification of the DNA sensing element may be necessary in the presence of SWCNTs. As the application of NP-CNT system represents a great interest in nanobiotechnology, it can be used for the design of the electronic mobile diagnostic facilities for blood analysis and the chemical or drug delivery inside the living cell. The SWCNTs are used as a drug delivery vehicles used to target the specific cancer cells. Separately, along with DNA-NP, the DNA-CNT system also represents a great interest, nowadays, in biomedical applications due to diagnostics and treatment of oncology diseases. So combining the DNA-NP-SWCNT system can represent a potential target of modern research. The interplay of DNA, NP and SWCNTs has now become a current topic of research for further nanobiomedical applications.

Keywords: NP, SWCNT, DNA, optical properties, cancer

1. Introduction

Nanotechnology has become the latest emergent field which involves the production and use of nanostructures at a nanoscale. As the particles at atomic and molecular levels led to

new materials with less than 100 nm showing unique and unusual physical, chemical and biological properties which enabled their applications in diversified fields. The biological properties of nanoparticles are determined by the different characteristics of nanoparticles, which are their size, shape, surface charge, chemical properties and solubility, and degree of agglomeration [1–6]. In the exploding field of nanoscience and nanotechnology, coinage metal clusters and CNTs have attracted considerable attention owing to their unique optoelectronic properties for a wide range of potential applications [7–11]. These SWCNTs are used as components in the third generation of electronic and optical devices, including transistors, photodetectors [12–15], and biological sensors [16–18]. The subnanometer-sized coinage metal clusters have attracted more attention due to their excellent photoluminescent properties. These metal nanoparticles exhibit unique optical characteristics with an exponential decay of the absorption profile with Mie scattering [19–22]. Meanwhile, the UV-Vis absorption is more dominated by the plasmon resonance peaks in visible region for these metals. The UV absorption exhibits molecular-like optical transitions which are due to the quantum confinement and quasicontinuous electronic energy band structures [23–26].

CNTs are also used in construction of biochemical sensors especially in the field of supporting materials. The high surface area of CNTs made it possible to load nanoparticles to enhance their properties. The controlled synthesis of these carbon nanotubes (CNTs), which requires a nanoscale catalyst metal, is crucial for their application to nanotechnology. Chirality control is the most important issue for the electronic/photonic applications of CNTs [27]. For biomolecular nanotechnology, DNA is also a promising material due to the unique recognition capabilities, physicochemical stability, mechanical rigidity, and high precision process ability. The interplay of this CNT/coinage metal-DNA has broad applications as diagnostic sensors, biomarkers, and drug delivery nanorobotic design [17, 18, 28].

In this chapter, we will discuss the interplay between these nanobio complexes, their properties and applications separately by dividing these combination materials in three sections.

These sections are as follows.

1.1. DNA-SWCNTs hybrid systems

As the dispersion of hydrophobic CNTs in solution can be facilitated by noncovalent functionalization with helically wrapped single-stranded DNA, the DNA wrapped nanotube material is used for electronic and optical device applications [29]. DNA-associated CNTs have been used in molecular sensing and the potential use of DNA-wrapped CNT platforms shows promise in multiple applications. These nanotubes offer the potential of providing the scaffold on which the DNA molecules can be oriented, manipulated, and studied without the need for chemical functionalization which is given in **Figure 1**.

1.2. DNA-NP complexes

The unique optical properties of coinage metals in conjugation with the remarkable recognition capabilities of DNA molecules could lead to the development of miniaturization of

http://dx.doi.org/10.5772/67527

biological electronics and optical devices to include probes and sensors. The schematic representation of NP-DNA complexes are given in **Figure 2**.

1.3. DNA-SWCNT-NP complexes

The tertiary system of nucleotide chain-coinage metals-CNTs also represents a great interest in the modern research and applications of nanobiotechnologies, for example: electronic mobile diagnostic facility and nanorobotic design for a drug delivery inside living cell. The small nucleotide chain represents an important stage in the understanding of the interaction mechanism of a full DNA (**Figure 3**).

Now we will discuss the theory of these hybrid systems in more elaborative manner as follows.

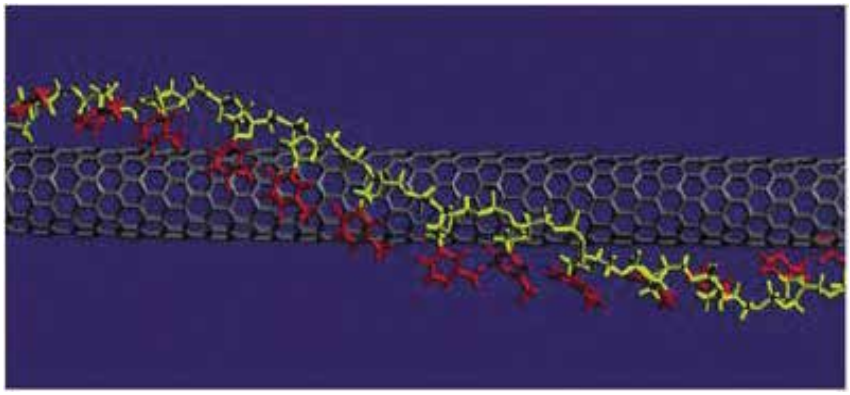

Figure 1. Theoretical model of structure of single stranded DNA (ss-DNA)-CNTs hybrids.

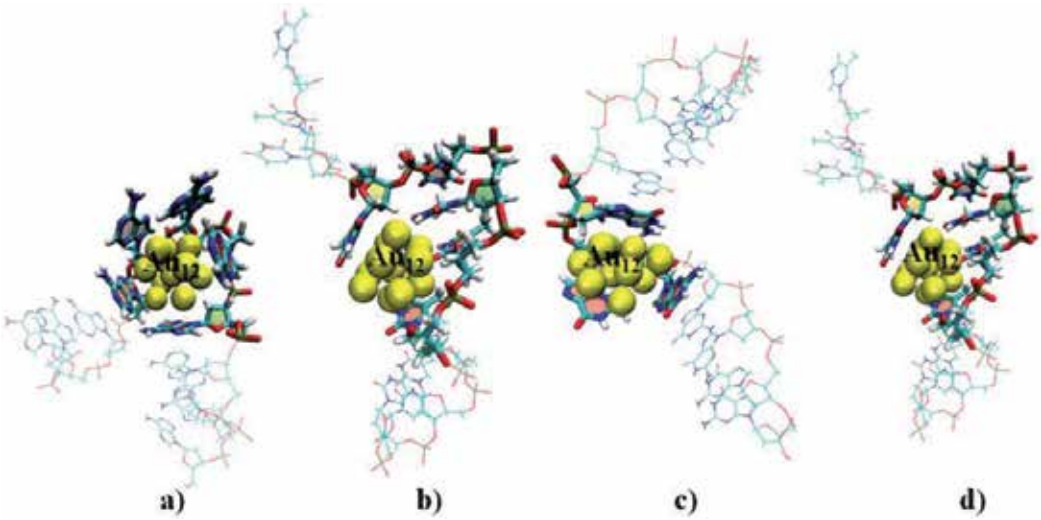

Figure 2. Schematic representation of (a) Au_{12}-ssdA_{12} (b) Au_{12}-ssdT_{12} (c) Au_{12}-ssdG_{12} (d) Au_{12}-ssdC_{12} gold metal-nucleobases.

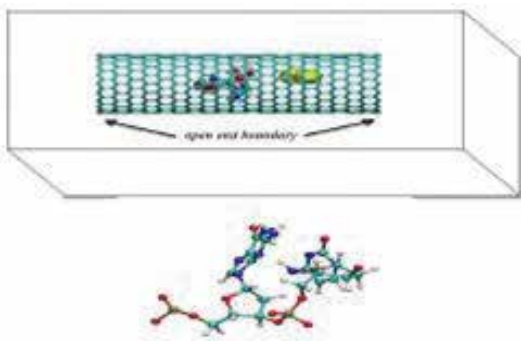

Figure 3. Schematic view of the simulation system of two nucleotide chain (NC)-gold nanoparticles (NPs)-carbon nanotube (CNT).

2. Theoretical section

2.1. DNA-SWCNTs hybrid systems

Carbon nanotubes (CNTs) belong to the family of synthetic carbon allotropes and are characterized by a network of sp^2 hybridized carbon atoms [30]. These nanotubes can be described as helical microtubules of graphitic carbon, which generate this material by an arc discharge evaporation process designed for the production of fullerenes (**Figure 4**).

Theoretically, we can construct the CNTs by rolling up a graphene sheet into cylinder with the hexagonal rings which can be joined seamlessly. The major parameters that play an important role are the chirality and (n, m) indices. By changing these parameters, diversified structures of single wall carbon nanotubes (SWCNTs) can be constructed, which defines the orientation of the hexagonal carbon rings in the honey comb lattice relative to the axis of the nanotube. Depending on the (n, m) indices, their metallic or semiconducting behavior is determined which is represented in **Figure 5**. The UV/Vis/NIR spectroscopy has proven to be the powerful tool on their characterization, making high information density related to the physicoelectronic properties through readily available and inexpensive techniques. SWCNTs represent one of the most direct realizations of the 1D electron system, attracting much theoretical interest. Due to the unifying electronic and photonic properties, they become the leading candidates to function in nanoscale circuits. The optoelectronic properties of SWCNTs were initiated by the discovery of bandgap photoluminescence (PL) from individually suspended SWCNTs in aqueous solution.

In absorption spectroscopy, the optical transitions of the SWCNTs are probed, which arises from the energy levels with significantly high density of states (van Hove singularities). These are caused by rolling-up the 2D graphene sheet into 1D carbon nanotube. Due to absorption of light, the electrons in the van Hove singularities of the valence band are elevated to the corresponding energy levels in the conduction band. The same process occurs in the case of metallic SWCNTs. However, the spacing between the van Hove singularities is larger so that only M_{11} transitions can probe in the UV/Vis region.

http://dx.doi.org/10.5772/67527

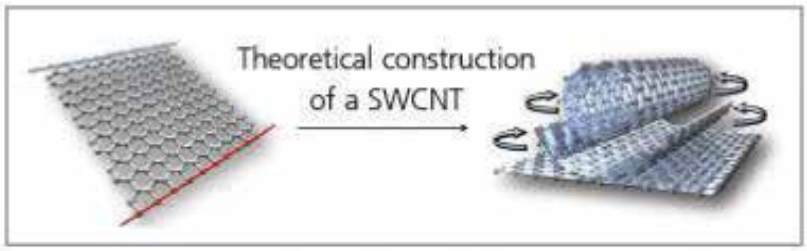

Figure 4. Schematic representation of SWCNT as a hollow cylinder of a rolled-up graphene sheet.

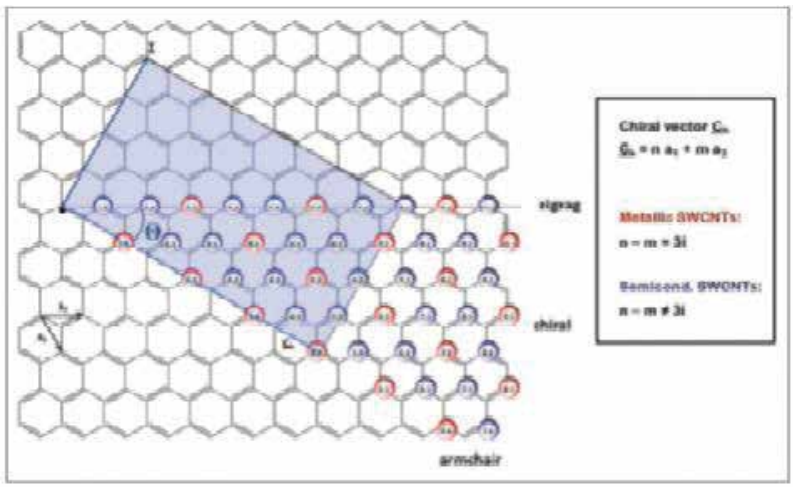

Figure 5. Schematic representation of unrolled graphene layer of carbon nanotube with the unit cell vector a_1 and a_2 which define the chiral vector C_k.

The most important thing is the symmetry breaking of the DNA wrap, which influence the electronic structure of SWCNTs, while for nonchiral tube, the helical perturbation causes natural optical activity. The structures of these SWCNTs are specified by integer pair (n, m) describing the chiral vector $C = na_1 + ma_2$. The general rule to represents these tubes are (i) (n, n) armchair tubes are metals, (ii) (n, m) with n – m = 3j (j nonzero integer) are semiconductors (gap = 1–100 meV), and (iii) others are semiconductors with (gap = 0.5–1 eV). The dispersion relations and corresponding density of states of armchair (n = m) and semiconducting nanotubes are shown in **Figure 6**. It is seen in the figure that metallic armchair nanotubes are gapless and nonarmchair nanotubes have small curvature-induced bandgaps [30–38].

The optical properties of SWCNTs are measured from dispersed/solubilized samples in the transmission mode. Impressive progress has been made in separating the SWCNTs by type, diameter, and chirality. The size-dependent colors of suspended colloidal particles have two distinctly different coloration mechanisms. On the front head is the quantum confinement, which plays the fundamental role, while the coloration mechanism depends on the metallic or semiconducting behavior of SWCNTs. Size-dependent fundamental bandgap

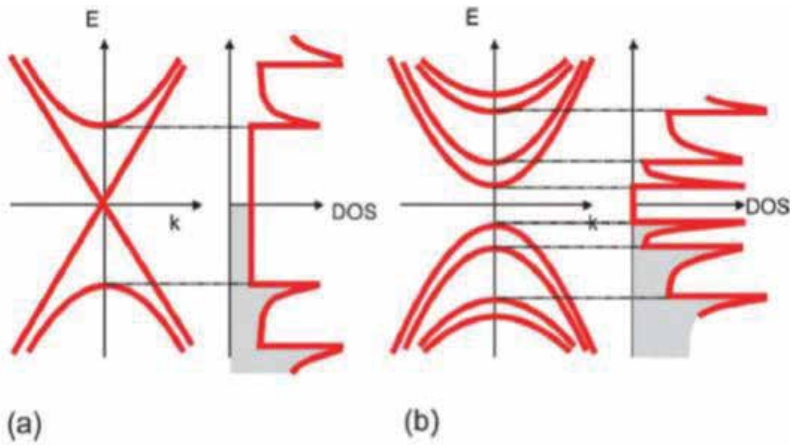

Figure 6. Schematic electronic energy dispersion relations and densities of states (DOS) of (a) metallic (b) semiconducting single wall carbon nanotubes (SWCNTs). Adapted with permission from Ref. [34].

(HOMO-LUMO gap) is the key parameter of the color determination for semiconducting nanoparticles, which changes with the quantum confinement [39–43].

For metallic nanoparticles, the colors are determined by the free carrier plasma resonance, whose frequency depends on the following factors: electron density, particle size, and particle shape. The potential applications of SWCNTs can be accomplished through covalent or noncovalent SWNT functionalization as the requirement is that they may be isolated from one another. The noncovalent approach preserves the intrinsic electrical, optical, and mechanical properties of SWNTs and can be achieved by dispersing SWNTs in aqueous solution using surfactants, polymers, or biomacromolecules such as DNA or polypeptides. The surfactants have the effect of lowering the energetic cost of hydrophilic/hydrophobic surfaces, which allows for water insoluble materials to be dispersed in the aqueous phase. These hydrophobic inorganic materials are also incorporated in modern biomedical materials [44–47]. Various surfactants are used to modify these hydrophobic surfaces to impart dispensability and biocompatibility. These functionalized materials can be conjugated with peptide or DNA for biological applications as biomarkers and biosensors. The absorption spectrum of different SWCNTs dispersed in aqueous solution of SDBS is given in **Figure 7**.

In one of the study, a separation method by various DNA sequence corresponding to chirality was reported [48]. Individual DNA-SWNTs dispersed in solution show photoluminescence [49, 50]. It occurs due to the recombination of the photoexcited electron and its hole, exciton [51]. As SWCNT is a monolayer material, so the exciton binding energy is highly affected by the environmental effect [52, 53]. However, it is not easy to define the environmental effect of DNA due to the various oligonucleotide sequences and the overlapping of buffer reagents and the effect of solution. It was observed that the PL peaks are red shifted compared to the SWCNTs suspended in air/vacuum [54–56]. The studies carried out by Homma et al [56] have experimentally shown the effect of DNA adsorption on the optical transitions of SWCNTs.

http://dx.doi.org/10.5772/67527

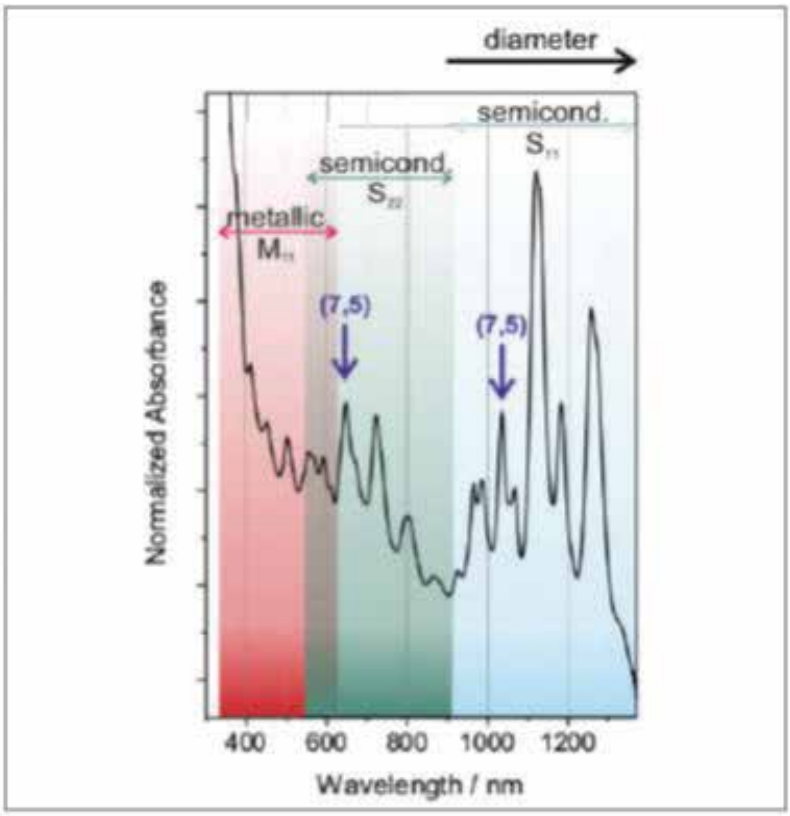

Figure 7. The absorption spectrum of different SWCNTs dispersed in aqueous solution of SDBS. The transitions of metallic and semiconducting SWCNTs are indicated by different colored shaded region. Adapted with permission from Ref. [55].

In the studies, the isolated DNA-SWCNTs were prepared under the dry condition and the intrinsic properties of single-stranded DNA-SWCNTs were studied. The homosequenced ssDNA was used to evaluate the effect of base type (A, T, G, C) and the absorption spectra are given in **Figure 8**.

Very interesting features of absorption spectra were investigated by molecular dynamics (MD) simulations [57, 58] and transition electron microscopy (TEM) [59]. Results indicated that the π-π interactions are responsible for the binding of ssDNA-SWCNTs. The significant red shift is caused by the strong π-π stacking of surfactant with SWCNTs [60–62]. The H-π interaction of DNA-SWCNT is not negligible [63]. Another interactions that play an important role are the n-π interactions of the –OH, –O–, and the $–NH_2$ group [64–65]. The contributions of each interaction have been taken by the MD simulation techniques. It is observed that the trend of absorption energies on the SWCNT surface is C < A < T < G [66–68] which is consistent with the experimental work on graphitic surfaces [69]. Though some other groups have reported the absorption energy trend as T < A < C < G [70, 71], which also justifies the experimental facts [72].

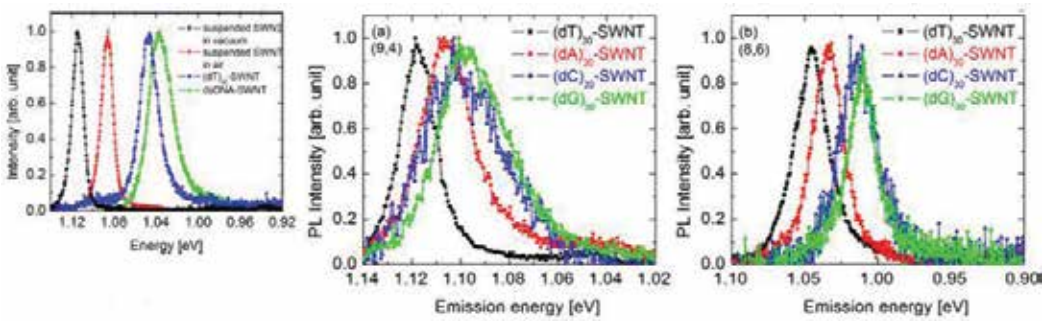

Figure 8. PL emission spectrum change depending on the DNA base type $(dT)_{30,}$ $(dA)_{30,}$ $(dC)_{30,}$ $(dG)_{30}$ for (9,4) SWCNT (a) and (b) (8,6) SWCNT. Adapted with permission from Ref. [55].

One more interesting feature was observed that the excitons in the ssDNA-SWNT are less sensitive to the environment compared with ssDNA-SWNT as no difference was observed between PL spectra from dsDNA-SWNT in solution and those in air.

2.2. Coinage metal-DNA interaction

Nanoscale particles have significantly different physical and chemical properties as compared to the corresponding bulk structure due to the quantum effect [73]. These size-specific physicochemical properties are widely used in molecular electronics and biosensor technology. The "bottom-up" approaches involve the self-assembly of small sized clusters into larger structures which utilizes the biohybrid complexes, where DNA, peptides, and biological molecules act as the templates [74–82]. The amine group of peptides assembles coinage metal cations and caps the growing nanoparticle surface, adsorption of single stranded DNA on gold surfaces, mercapto-group mediators and silver clusters as fluorescent probes for sensitive detections are few of the structural features of the biomolecular-metallic nanoparticle complexes [83]. DNA exhibits many capabilities as catalytic activities, specific binding affinities, and/or chemical stabilities [84]. Coinage metals also possess unique size and shape-dependent optical properties, biocompatibility, high stability, and large surface area [85]. These properties enable the extensive use of DNA with coinage metals in optical biosensors. DNA-conjugated coinage metal nanoparticles have been used as optical probes for various targets due to high sensitivity and selectivity as they are biocompatible, easy to prepare, and molecule-like optical properties. In the presence of ligand thiolates, polymers, proteins, phosgene, and DNA, these Au/Ag NCs possess fluorescence at different wavelengths with different quantum yields due to the high emission rates as of larger stokes shift for the coinage metal clusters [86–90]. DNAs are used as templates for coinage metal NCs preparation due to the stabilization of Ag^{+} ions by mismatched cytosine-cytosine pairs (duplex DNA) [91–93]. In some thiol complexes, fluorescence quenching is observed, as it is weakened by the interactions between the Ag NCs and DNA templates and cause partial oxidation of Ag NCs binding [94, 95]. The highly fluorescent and water soluble DNA-NC NCs have some characteristics as long lifetime, long stokes shift, and their sizes as compared to the biocompatibility and ease in bioconjugation.

http://dx.doi.org/10.5772/67527

For these reasons, they have become an attractive tool for ions detection, DNA, small organic molecules and proteins for cell staining [96–98]. They can be used for detection of proteins due to the specific interactions of the aptamers with their target proteins which produce the fluorescence due to the induced conformational changes in the aptamers [99]. They are also used for cytosol delivery [100–102] and as a potential candidate for analysis of biological and environmental samples, cell imaging, and diagnosis of diseases. These nanoparticles also have a negative impact on the environmental hazards. Prolonged exposure of nanoparticles causes allergies and diseases [103] yet gold nanorods in near infrared region is used for many biochemical applications. DNAs are used as templates to form stable complex with Ag^{+} for the preparation of stable and fluorescent DNA-Ag NCs [104]. Ag-NCs containing silver atoms (1–6) atoms exhibit the fluorescence excitation and emission spectra maxima in the visible region [102, 105, 106]. The emission spectra of C_{12}-Ag NCs (2–7 atoms) give the excitation and emission maxima for 650 and 750 nm, respectively. However, the understanding of the mechanism of the bonding between NC-DNA and factors, which control the efficiency, is rather limited and the bonding and optical properties of these complexes are still not known. Theoretical understanding of this cluster-DNA pair interaction stability of different isomers requires various structures which can be achieved by varying some important parameters as DNA sequences, the molar ratio of base/metal ions, reducing agents, ionic strength, and buffer pH [90, 107, 108]. Kryachko and Remacle [109] studied the gold-nucleobase interactions and explain the bonding of Au—N and Au—O anchor bond and the nonconventional N—H—Au hydrogen bonding. They further explained the Watson-Crick pair patterns with gold clusters on the proton affinities and deprotonation energies. The increase in cluster size to 6 results in short gold-gold bond and strengthened GC pairing. Kumar et al. [110] studied the neutral and anionic $Au_{4,8}$ clusters interaction with AT—GC pairs. Optimizing the singlet and triplet states for neutral and doublet and quartet states for anionic cluster they stated that singlet states are more stable than the triplet states. Furthermore, they model the eight gold atom clusters in two-four gold atom pairs. The schematic representation is given in **Figure 9**. It was found that in neural complexes, the significant charge is transferred from the base pairs to the cluster and in anionic clusters the excess charge is localized at the gold clusters.

Metiu and Soto-Verdugo [105] studied the silver-DNA pair interactions up to six cluster size. In the studies, they found that the cluster prefer binding to the doubly bonded nitrogen rings and the strength of this bonding is strong in cytosine (C), guanine (G), and adenine (A) and weak in thymine (T) while A, G, and C show mild charge transfer than the T. They analyze the absorption spectra and find that the low energy peak lower in energy and reduced in the strength when the position of two bases is perpendicular in middle panel. The binding sites of these cluster-base pairs are given in **Figure 10**.

The computational work has been carried out by using the generalized gradient approximation (GGA) approximations of density functional theory, and projector augmented-wave (PAW). The wave function is represented by a plane wave basis set with a cut-off energy of 400 eV. Large orthorhombic cells used as the clusters are bound to the single and two bases. The entire calculations were performed by Vienna Ab initio simulation package (VASP) [111ad]. The time-dependent DFT (TDDFT) absorption spectra were carried out in real space and real time as implemented in OCTOPUS [112] code. The studies carried out by them shows that

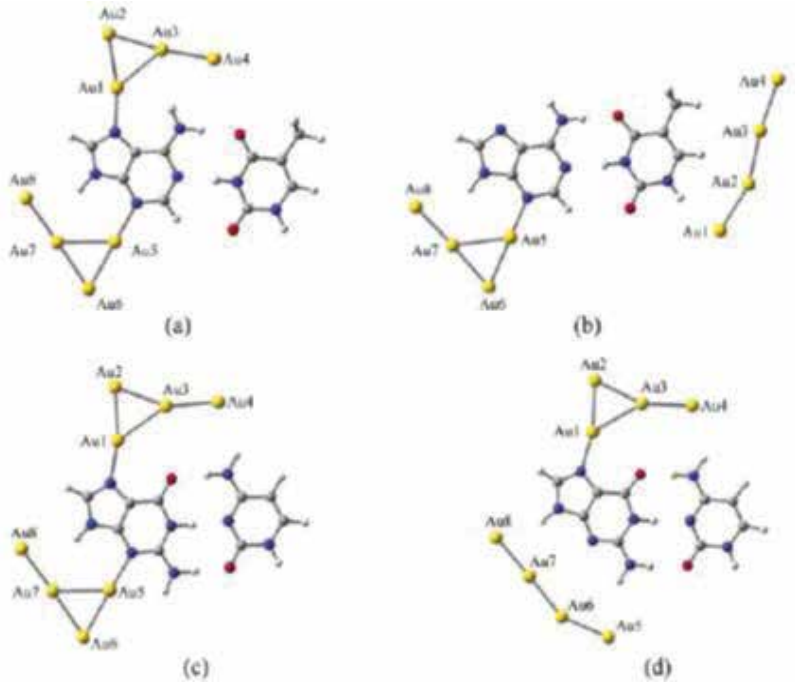

Figure 9. Schematic representations of A-Au_8 complexes in (a) singlet and (b) doublet states and GC-Au_8 complexes in (c) singlet and (d) doublet states.

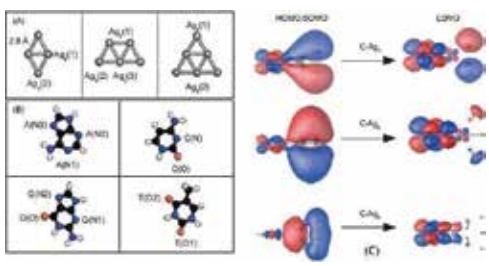

Figure 10. Schematic representation of the (a) binding sites of Ag clusters with the bases, (b) binding sites of bases where the Ag clusters can bind, and (c) orbitals involved in the lowest energy transitions. Adapted with permission from Ref. [105].

the clusters are planer structures. The absorption spectra produce new absorption peaks at low energies that strengthen and red shift the binding. The TDDFT calculations show that the absorption spectra of these isomers can have different spectra and the spectra of these planer cluster show sensitivity to the relative orientations of the base and cluster planes. The absorption spectra of these binding sites for silver-DNA bases are given in **Figure 11**.

In another study of propene-silver cluster [113] molecules, some geometry-energy configurations were used to select the preferred sites and bonding of cluster-base interaction. Studies by Shukla et al. [114] for Au_n even neutral (2—12) clusters on nucleic acid purine

http://dx.doi.org/10.5772/67527

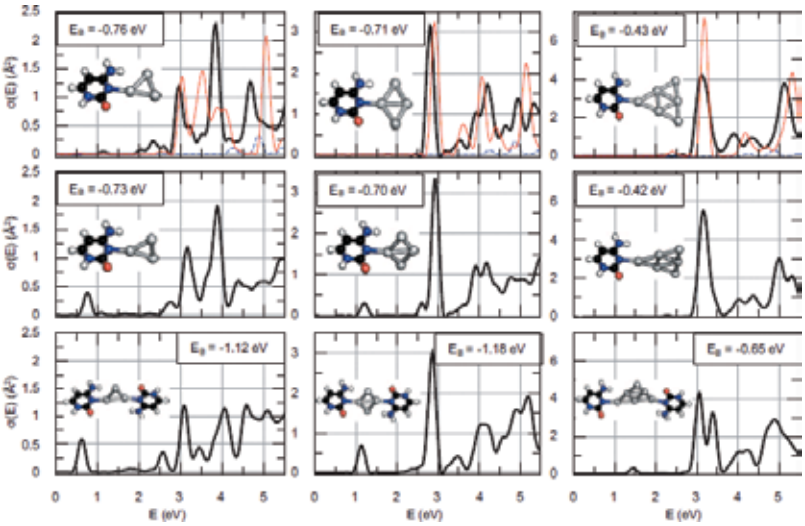

Figure 11. Absorption spectra of C-$Ag_{3,4}$ complexes. Top row consists of cluster bound to single base with both lies in the same plane. Second row consists of cluster and base perpendicular to each other. Bottom row consists of two bases in the same plane perpendicular to the cluster. Adapted with permission from Ref. [103].

base guanine (G) and the Watson-Crick GC pairs reveal that the gold clusters have strong interaction to the GC pair rather to the isolated guanine base. They focused the studies on the anchor bond Au—N7 major groove site and singlet states of gold clusters. By the natural population analysis they considered the NBO charges and find that electronic charge is transferred from G/GC pairs to the gold clusters. In the studies they predicted that gold clusters would form more stable complexes with GC base pairs rather than the guanine alone. Furthermore, it was predicted that the GC base pair slightly open the hydrogen bond to the major groove of the DNA. The schematic representation of the Au_n-G/GC bases is given in **Figure 12**. The substantial amount of charge transfer occurs between the G/GC base pairs to the clusters. The oxidation of gold clusters is more pronounced for WC pair rather than the isolated amino acid. As the electron attachment occurs at the gold cluster site, so these free electrons will protect the DNA. Further they concluded that the one-electron oxidation of these G/GC-Au_n complexes can trigger the oxidation through the π back donation of electronic charges to the gold clusters.

Motivated by the recent studies carried out by Verdugo et al. on Ag_n-DNA interactions n = (1–6), we have extended our studies for Ag_n-A, G/WC pair interactions and their absorption spectra studies for n = 8, 10, and 12 neutral clusters. We have shown the ability of DNA bases and Watson-Crick pairs to form directly stable anchoring sites with silver clusters. It is demonstrated that the DNA base clusters are stabilized not only by the anchoring Ag—N site but also by Ag—O bond site. The photophysical properties of Ag-DNA strands in solution are affected by the dipole interactions of water molecules. The spectral sensitivity of TDDFT results also help us to identify the base site bonding to the clusters, the size of the cluster, dipole interaction of silver-DNA pairs and the relative orientation of cluster-base planes. The schematic representation of these $Ag_{8\text{-}12}$-DNA/WC bases is given in **Figure 13**. We characterized in detail the properties of

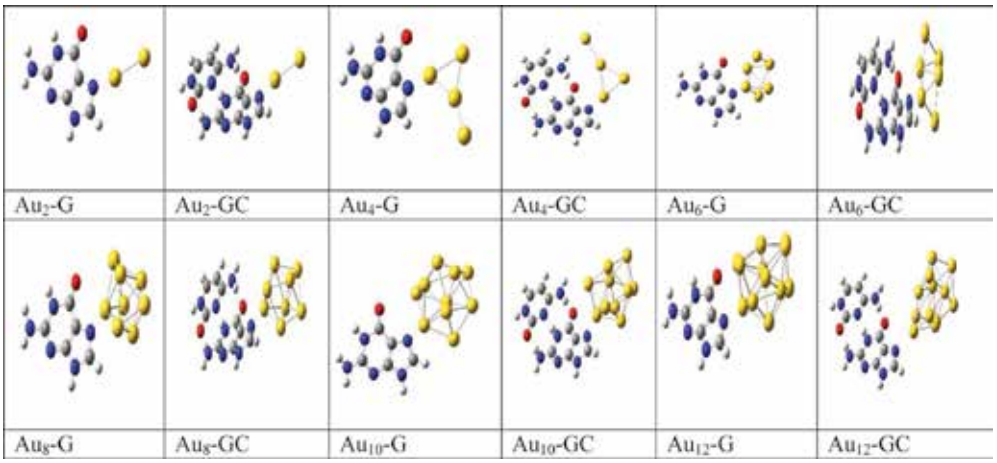

Figure 12. Schematic representation of G/GC-Au_n complexes for n = 2–12.

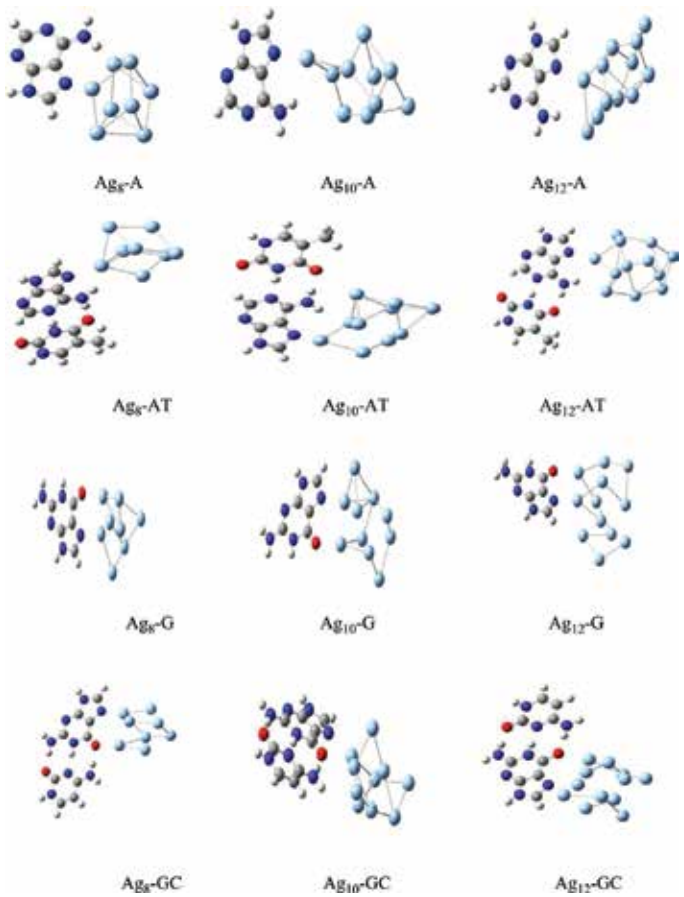

Figure 13. Optimized structures of DNA(A,G)/WC-Ag_n complexes for n = 8–12. [115].

http://dx.doi.org/10.5772/67527

these DNA base in order to identify the factors controlling their formation with special emphasis of the Ag cluster size and of the coordination of the Ag atom both on the anchor and of the nonconventional hydrogen bonding. Since we have not taken the solvent effects, the calculations present here are not able to decide the cluster-DNA binding in solution. Mulliken charge analysis was carried out to characterize the cluster-base charge transfer mechanism [115].

We have observed that the silver clusters form stable complexes with WC complexes rather than with the isolated A, G bases. It was also seen that the interaction of silver to the WC pair shorten the hydrogen bond distance to the major groove of the DNA site. Further, the amount of electronic charge transfer to the silver clusters is more for Ag_n-WC complexes. The absorption spectra for these base complexes lie in the visible region. As the UV (absorption-excitation) studies predict that the fluorescence proceeds via the nucleobases so we hope that the studies can provide new path for understanding the photophysics of these complexes and its utility in the discovery and purification of most stable Ag-DNA complexes [116, 117].

An interesting study was carried out by Schultz and Gwinn [118] in which it was predicted that the magic numbers in nucleotide-silver complexes lead to magic colors. The fluorescent products were formed from experimental testing of small sets of C-rich or G-rich cluster stabilized DNA oligomers, which applied to the specific application. Generally the randomly selected at least three out of four oligomers, with equal chances of placing A, C, G, or T bases at each site. Fluorescent Ag_n-DNA solutions are obtained by excluding the combination of less than a total of three C plus G bases (**Figure 14**).

Another study on combined molecular dynamics (MD) and density functional theoretical approach (DFT) was applied by Pati et al. [119] to investigate the $(Ag/Au)_{12}$-ssDNA complexes. It was observed that these individual ssDNA undergoes various conformational changes in MD simulations for 1.5 ns in aqueous media. Another interesting fact which comes in light is that ssdA12 shows greater binding affinity toward the Au_{12} cluster while ssdG12 interacts strongly with the Ag_{12} cluster. The optical absorption characteristics are less affected in the presence of DNA scaffold. It might be due to that the frontier orbital, which is localized mainly on the metal clusters or ssDNA. Further, the theoretical work was verified by the experimental results (**Figure 15**).

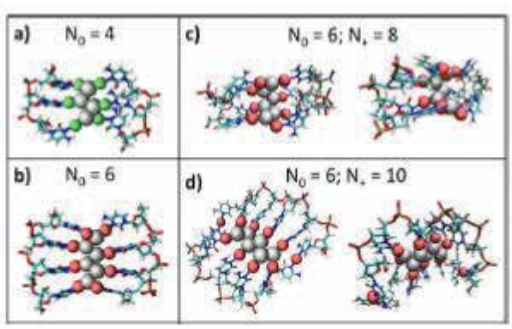

Figure 14. Schematic representations of Ag_n-DNA simulations for (a) $N_0 = 4$, (b) $N_0 = 6$, (c) $N_0 = 6, 8$, and (d) $N_0 = 6, 10$ simulations. Adapted with permission from Ref. [118].

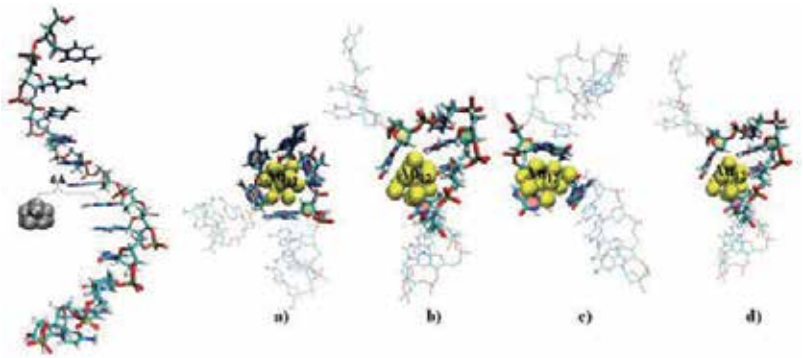

Figure 15. Schematic presentation of Au_{12}-DNA complexes. configurations of (a) Au12-ssdA12, (b) Au12-ssdT12, (c) Au12-ssdG12, and (d) Au12-ssdC12 nanocomposites after 1.5-ns simulation time. Adapted with permission from Ref. [119].

The computed absorption spectra of [1] (a) Ag12-ssdA12, (b) Ag12-ssdT12, (c) Ag12-ssdG12 and (d) Ag12-ssdC12 and [2] (a) Au12-ssdA12, (b) Au12- ssdT12, (c) Au12-ssdG12 and (d) Au12-ssdC12 are given in **Figure 16**.

The entire work was carried out on GROMACS [120] software and visualized by VMD [121] software. Further, the results showed that ssdG12 binds strongly with silver (Ag_{12}) cluster and ssdA12 with gold (Au_{12}) clusters and ssdT12 prefers to bind with Ag_{12} and Au_{12} cluster by O-site, while other DNAs bind by π stacking.

2.3. Nucleotide chain (NC)-gold nanoparticles (NPs)-carbon nanotube (CNT)

The tertiary system of NC-NPs-CNT system has now become an important tool in biotechnology. The development of electronic mobile diagnostic facilities, nanorobotic design for drug delivery inside living cell etc. are the latest development which is emerging in this field. These small Nucleotide chain plays an important role in the interaction mechanism of the full DNA complex with the nanoparticles and CNTs. These combinations have now become a

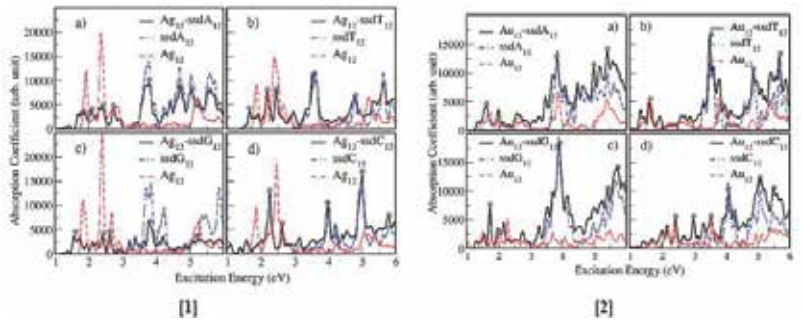

Figure 16. Computed absorption spectra of [1] (a) Ag12-ssdA12, (b) Ag12-ssdT12, (c) Ag12-ssdG12, and (d) Ag12-ssdC12; [2] (a) Au12-ssdA12, (b) Au12- ssdT12, (c) Au12-ssdG12, and (d) Au12-ssdC12. Adapted with permission from Ref. [119].

http://dx.doi.org/10.5772/67527

powerful tool for the diagnostic applications in the chemical or drug delivery. Though metal matrix nanocomposites with CNTs have good mechanical properties as high temperature and abrasion resistance, high shear resistance, their properties are mainly focused on the macro-mechanical properties rather than the microscopic properties. As the interface test are difficult to conduct, so md simulation techniques are used to study the interfacial behavior. The peculiarities of the NC-NP interactions and bond formation were investigated by Khusenov et al. [122] with the structural and dynamical behavior. MD simulations were carried out using the weak van der Waals interaction and intermolecular vibrations to enlighten for the molecular systems in which the quantum chemistry is used.

The entire interaction mechanism of whole ternary nucleic acid-gold particles-carbon nanotubes is very interesting and has found a broader interest in the field of nanobiotechnology, electronics, and biomedical field. There are so many applications where these systems are used. These systems have a great interest in the design and development of the electronic diagnostic units to express the blood analysis, the chemical and drug delivery inside a living cell. It was seen that the mechanical properties of the composites can be improved by modified coating of CNT with large volume fraction and large diameter. These properties determine the interfacial strength of the CNTs. It was seen in the studies that with fixed diameter of CNTs, the metal-coated CNT has yield, interfacial strength, and high elastic modulus than without metal matrix. This property can be used in design for high performance CNT/metal composites.

The CNTs has been used as drug delivery vehicles which have shown a potential interest because it targets to specific cancer cells with low dosage. They are used as a preferential candidate in the cell drug delivery as nucleic acid DNA aptamer. The conformational transition of aptamers around CNT may cause some modification in the charge distribution on the CNT surface. The charge conductivity is dependent on the conformational transitions of aptamers. So we can say that the nucleic acid-CNT interactions can change the charge distribution and consequent charge transfer through the CNT surface. Various suggested scheme can provide application in diagnostic purposes of DNA-CNT interaction process in target protein [123–132].

The simulations involve the DNA interactions with metallic NPs to targeted cancer therapy through the injections of metal, micro, or nanoparticles into the tumor tissue with laser or local microwave heating. The response of this DNA-NP, the DNA-CNT system presents a great interest due to diagnostic and treatment of oncology diseases. The stability predictions of DNA duplex and the accuracy vary largely from sequence length, base compositions and experimental conditions. Problem arises when the prediction occurs for the stability of DNA duplex from base sequences. The thermodynamic nearest-neighbor model (TNN) is a state of art approach to determine the stability of single or a pair of DNA (RNA) based on pairwise interactions and structural conformations.

These CNTs are based on the enhancing of sufficient solubility and efficient tumor targeting. Because of these aspects, CNTs are prevented from being toxic and alter the function of immune cells. The studies involve the DNA interaction with metal nanoparticles or highly localized proton beams. As the nanoparticles are having good electrical conductivities, so

they can destroy only the tumor cell and the normal cell remain undamaged. Inspite of that, such treatments are usually painful and kill normal cells apart from producing side-effects. In this work, the MD simulations were performed on a small nucleotide chain to investigate its interaction and binding process with gold particles and the carbon nanotube matrix.

The concept of these ternary systems is that the NC models interacting with the system have to possess a lot of similarities with a full nucleotide system interacting with NP/CNT environment. Carbon nanomaterials have been investigated not only for manufacturing new nanoscale devices as sensors, actuators, electromechanical switches, but also in the fabrication of biomechanical systems. These CNTs are ideal candidates for the encapsulation of drugs, nanofiltration membranes, atomic/molecular encapsulation, and hydrogen storage for powering green vehicles. Some metals as manganese ion (Mn^{2+}), gold atom (Au), platinum (Pt), sodium ion (Na^{1+}), and lithium ion (Li^{1+}) were investigated and it was found that Mn^{2+} and coinage metals candidate for drug delivery while Li^{1+} can be perfectly used for high-energy density rechargeable alkali batteries.

The 6–12 Lennard-Jones (L-J) potential in the MD simulation technique was employed assuming that carbon atoms are evenly distributed across the surface of carbon nanostructures. This assumption was taken so that the total potential energy between various nonbonded carbon nanomolecules can be determined analytically by performing a surface integral. These potential energies can be used to investigate the relative motions of the nanostructures, such as the oscillatory motion of a fullerene inside a single-walled carbon nanotube and to study the encapsulation of drug molecules inside single-walled nanotubes as the "magic bullet" [133, 134] and the encapsulation of hydrogen atoms inside metal-organic frameworks for hydrogen storage [135].

Though few physical properties such as electron charge exchanges, optical properties of the graphene sheet, and structural effects are explained, the local deficits of graphene are yet to be explained. The other properties as average physical quantities, the minimum intermolecular spacing, and the diffusion time for various atoms/ions are predicted by the group 126 using the simple formulae.

The CNT-DNA interactions are investigated by the Tersoff potential in combination to the classical trajectory calculations. These hybrid approaches are based on force fields and particle interactions. In this approach the molecules are described as a set of spheres and springs. In the MD simulations, it was observed that there is encapsulation-like behavior of DNA chain inside the CNT system. So we can say that this binary system can be the suitable candidate for the drug delivery and related systems. The quantum chemistry methods provide greater accuracy while for bonds formation/broken, the MD simulations techniques are used. Generally, Tersoff potential is used for MD simulations in carbon, silica, and germanium. Tersoff potential is pair wise potential, but coefficient in attractive term depends on local environment. Thus, Tersoff potential possesses a many body nature. The classical molecular dynamics was performed with the proper NVT ensemble and the time step with more than 100,000 with the temperature scaling interval with each 10 step. Two nucleotides were relaxed with gold particles and the nucleotide chain was located from gold atoms at distance of 5–10 A. The entire calculations were performed by DL_POLY_2.20 all-purpose general code [135]. The representation of these structures is given in **Figure 17**.

http://dx.doi.org/10.5772/67527

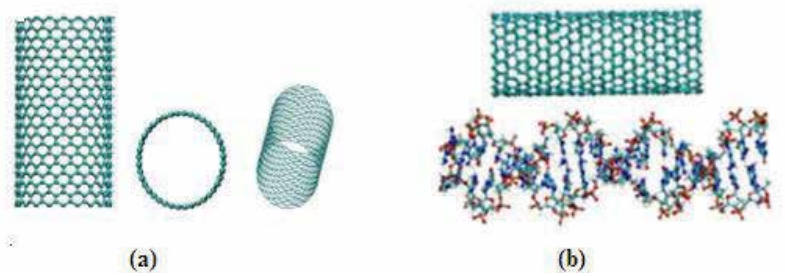

Figure 17. Structural representation of (a) CNT, and (b) CNT (top), and DNA (bottom).

Depending on their chemical structure, CNTs can be used as an alternative to organic, inorganic semiconductors as well as conductors. Nanotubes align themselves into "ropes" held together by van der Waals forces. The nature of the bonding of a nanotube can be explained by orbital hybridization [136, 137].

The simulation process was designed with three component system of two nucleotide chain (NC), gold nanoparticles, and a carbon nanotube (CNT) under different temperature conditions (T =100, 200, 300K). Three different models were taken with 1, 2, 3 gold particles with NC chains. Three different interactions as: weak, intermediated, and strong interactions were studied.

The entire ternary system was allowed to interact with each other via the vdW potential only. The quantum chemistry Tersoff potential (hybrid quantum chemistry and classical trajectory approach) has been used to investigate the NC interactions with CNT. The results were shown for three different temperatures for these ternary systems. The curve of **Figure 18** demonstrates the increase of the interaction potential energies with the temperature. It has been seen that the potential energy of the system is modified by adding one more gold atom to the system. So we can anticipate the potential energy will change for larger gold clusters.

The results predict that there is a probability of three (weak, intermediate, strong) bonds, within a CNT matrix. NC chain form close contact with the nearer gold atom. The NC-NPs interactions are modified at higher temperatures. Fluctuations occur for more NC intramolecular oscillations. Understanding this system at the micro level will help us to build a great understanding of full nucleotide-CNT-NP interactions. This mobile electronic device will definitely represent great interest for the purpose of nanorobotic design, delivery of drug

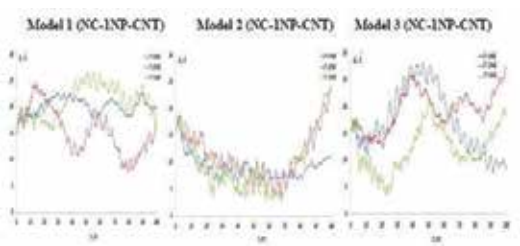

Figure 18. The graphical representation of NC-NP-CNT distances for different model configurations. Adapted with permission from Ref. [122].

delivery inside living organisms and diagnostic applications. In recent years the study of peptides and proteins adsorption onto metal surfaces has received wide attention. As the biomolecules play a significant role in determining biocompatibility of metal implants used in modern medicine, they can also be used in the preparation of new biosensors [138]. The main purpose of the implant material is to supply a surface to which biomolecules can be adsorbed and thus contribute to the healing processes. As it is the new emerging field, so many more researches should be needed to carry out in near future [139, 140].

3. Conclusions

In order to understand the dynamics of intracellular networks, signal transduction and cell-cell interactions, novel fluorescent sensors with versatility, high resolution, and sensitivity have made great progress in recent years. Carbon nanotubes are becoming a promising building block for biosensor technology. The first biosensors with integrated carbon nanotubes were electrical or FET sensors, several examples of optical carbon nanotube-based sensors were demonstrated in the past few years. Optical carbon nanotube-based sensors have shown their potential in several challenging biosensing applications. Some of the intrinsic carbon nanotube properties such as near-infrared fluorescence make them unique building blocks for biosensor devices and have advantages compared to other materials.

The two critical problems considered for the application of fluorescence microscopy in live cells is the cell autofluorescence in the visible spectrum and the requirement of long observation times. So, new fluorescent probes with near-infrared (NIR) emission and with more stable emission than current organic fluorophores are needed for the next generation of imaging techniques in biology. However, the good water-solubility, low toxicity, good photostability, and high biocompatibility of subnanometer-sized metal nanoclusters render them attractive alternatives as fluorescent probes for biological imaging. Moreover, large stokes shifts of metal nanoclusters can prevent spectral cross-talk and thus, enhance the detection signal. The change in optical property due to the self-assembly of DNA-linked nanoparticles demonstrates that the system has potential to be used as a novel technology for DNA detection. Similarly, the DNA-NP-CNT system represents a great interest in many aspects of modern biochemical and nanotechnological research. These devices can be used for the purpose of diagnostic applications, for the drug delivery inside the living cells and related nanorobotic design. Although several milestones have been achieved, ongoing efforts are necessary to engineer new biosensing devices for the medicinal applications.

Acknowledgements

The author acknowledges the financial assistance by the DST WOS A project (SR/WOS A/CS-1005/2015). The author is also grateful to her mentor Dr. G. Narahari Sastry, Head of Department, Center for Molecular Modeling for the support.

Author details

Ruby Srivastava

Address all correspondence to: amitruby1@gmail.com

CSIR-Indian Institute of Chemical Technology, Hyderabad, T.S. India

References

[1] Guo Z, et al. Immobilization and visualization of DNA and proteins on carbon nanotubes. Adv Mater. 1998;10:701-703. *DOI*: 10.1007/BF03185776.

[2] Watson JD, Crick FHC. Molecular structure of nucleic acids. Nature. 1953;171:737-738. *DOI*: 10.1038/171737a0.

[3] Mirkin CA, et al. A DNA-based method for rationally assembling nanoparticles into macroscopic materials. Nature. 1996;382:607-609. *DOI*: 10.1038/382607a0.

[4] Alivisatos AP, et al. Organization of nanocrystal molecules using DNA. Nature. 1996;382:609-611. *DOI*: 10.1038/382609a0.

[5] Mucic RC, et al. DNA-directed synthesis of binary nanoparticle network materials. J Am Chem Soc. 1998;120:12674-12675. *DOI*: 10.1021/ja982744.

[6] Maeda Y, et al. Two-dimensional assembly of gold nanoparticles with a DNA network template. Appl Phys Lett. 2001;79:1181-1183. *DOI*: 10.1002/anie.200501711.6668.

[7] Tsang SC, et al. Immobilization of platinated and iodinated oligonucleotides on carbon nanotubes. Angew Chem Int Ed. 1997;36:2197-2200. *DOI*: 10.1002/anie.201300130.

[8] Chen RJ, et al. Non covalent sidewall functionalization of single-walled carbon nanotubes for protein immobilization. J Am Chem Soc. 2001;123:3838-3839. *DOI*: 10.1021/ja010172bCCC.

[9] Shim M, et al. Functionalization of carbon nanotubes for biocompatibility and biomolecularrecognition. Nano Lett. 2002;2:285-288. *DOI*: 10.1021/nl015692j.

[10] Baker SE, et al. Covalently bonded adducts of deoxyribonucleic acid [DNA] oligonucleotides with single-wall carbon nanotubes: synthesis and hybridization. Nano Lett. 2002;2:1413-1417. *DOI*: 10.1021/nl025729f.

[11] Dwyer C, et al. DNA-functionalized single-walled carbon nanotubes. Nanotechnology. 2002;13:601-604. *DOI*: 10.1023/A:1020156316175.

[12] Lin Y, Taylor S, Li HP, Fernando KAS, Qu LW, Wang W, Gu LR, Zhou B, Sun YP. Advances toward bioapplications of carbon nanotubes. J Mater Chem. 2004;14:527-541. *DOI*: 10.1039/B314481J.

[13] Katz E, Willner I. Biomolecule-functionalized carbon nanotubes: applications in nanobioelectronics. Chem Phys Chem. 2004;5:1085-1104. *DOI*: 10.1016/j.carbon.2007.02.027.

[14] Lacerda L, Bianco A, Prato M, Kostarelos K. Carbon nanotubes as nanomedicines: from toxicology to pharmacology. Adv Drug Deli Very Rev. 2006;58:1460-1470. *DOI*: 10.1080/10934520903263603.

[15] Baughman RH, Cui CX, Zakhidov AA, Iqbal Z, Barisci JN, Spinks GM, Wallace GG, Mazzoldi A, De Rossi D, Rinzler AG, JaschinskiO, Roth S, Kertesz M. Carbon nanotube actuators. Science. 1999;284:1340-1344. *DOI*: 10.1126/*science*.284.5418.1340.

[16] So HM, Won K, Kim YH, Kim BK, Ryu BH, et al. Single-walled carbon nanotube biosensors using aptamers as molecular recognition elements. J Am Chem Soc. 2005;127:11906-11907. *DOI*: 10.1021/ja053094r.

[17] Jeng ES, Moll AE, Roy AC, Gastala JB, Strano MS. Detection of DNA hybridization using the near-infrared band-gap fluorescence of single-walled carbon nanotubes. Nano Lett. 2006;6:371-375. *DOI*: 10.1021/nl051829k.

[18] So HM, Park DW, Jeon EK, Kim YH, Kim BS, et al. Detection and titer estimation of escherichia coli using aptamer-functionalized single-walled carbonnanotube field-effect transistors. Small. 2008;4:197-201. *DOI*: 10.1002/smll.200700664.

[19] Creighton JA, Eadon DG. Ultraviolet–visible absorption spectra of the colloidal metallic elements. J Chem Soc., Faraday Trans. 1991;87:881-3891. *DOI*: 10.1039/FT99187FX09.

[20] Chen W, Chen SW. IrxPt100-x alloy nanoparticles *with* varied compositions [x = 100, 75, 67, 50, 34, and 0]. J Mater Chem. 2011;21:9169-9178. *DOI*: 10.1039/C1JM00077B.

[21] Chen W, Davies JR, Ghosh DR, Tong MC, Konopelskiand JP, Chen SW. Pyrene-functionalized ruthenium nanoparticles: novel fluorescence characteristics from intraparticle extended conjugation. Chem Mater. 2006;18:5253-5259. *DOI*: 10.1021/cm061595l.

[22] Lu YZ, Chen W. One-pot synthesis of heterostructured Pt–Ru nanocrystals for catalytic formic acid oxidation. Chem Commun. 2011;47:2541-2543. *DOI*: 10.1039/c0cc04047a.

[23] Wei WT, Lu YZ, Chen W, Chen SW. One-pot synthesis, photoluminescence, and electrocatalytic properties of subnanometer-sized copper clusters. J Am Chem Soc. 2011;133:2060-2063. *DOI*: 10.1039/c0cc04047a.

[24] Rao TUB, Pradeep T. Luminescent Ag7 and Ag8 Clusters by Interfacial Synthesis. Angew Chem Int Ed. 2010;49:3925-3929. *DOI*: 10.1002/anie.200907120.

[25] Jin RC, Jureller JE, Kim HY, Scherer NF. Plasmonics: theory and applications. J Am Chem Soc. 2005;127:12482-12483. *DOI*: 10.1021/ja0537169.

[26] Kelly KL, Coronado E, Zhao LL, Schatz GC. The optical properties of metal nanoparticles: the influence of size, shape, and dielectric environment. J Phys Chem B. 2003;107:668-677. *DOI*: 10.1021/jp02673y.

[27] Zhang Y, Zheng L. Towards chirality-pure carbon nanotubes. Nanoscale. 2010;2:1919-1929. *DOI*: 10.1039/c0nr00222d.

[28] So HM, Won K, Kim YH, Kim BK, Ryu BH, et al. Single-walled carbon nanotube biosensors using aptamers as molecular recognition elements. J Am Chem Soc. 2005;127:11906-11907. *DOI*: 10.1039/c0nr00222d.

[29] Saito R, Dresselhaus G, Dresselhaus MS, Physical Properties of Carbon Nanotubes. Imperial College Press, London. 1998. *DOI*: 10.1021/ma00107a006.

[30] Lizima S. Helical microtubules of graphitic carbon. Nature. 1991;354:56-58. *DOI*: http://dx.doi.org/10.1038/354056a0.

[31] Dresselhaus MS, Dresselhaus G, Avouris P. Carbon Nanotubes: Synthesis, Structure, Properties, and Applications. Applied Physics No. 18. Springer, Berlin. 2001. *DOI*: 10.1063/1.1762697.

[32] Reich S, Thomsen C, Maultzsch J. Carbon Nanotubes: Basic Concepts and Physical Properties, Wiley-VCH, Weinheim, Germany. 2004. *DOI*: 10.1002/9783527618040.ch1.

[33] O'Connell MJ. Carbon Nanotubes: Properties and Applications [Ed:], CRC Press, Taylor & Francis Group, Boca Raton, FL. 2006. *DOI*: 10.1039/c2py20161e.

[34] Jorio A, Dresselhaus G, Dresselhaus MS Carbon Nanotubes: Advanced Topics in the Synthesis, Structure, Properties and Applications. Springer, Berlin. 2008. *DOI*: 10.1007/3-540-39947-X

[35] Loudon R. One dimensional hydrogen atom. Am J Phys. 1959;27:649-655. *DOI*: http://dx.doi.org/10.1119/1.1934950.

[36] Elliot RJ, Loudon R. Theory of excitonic confinement in semiconductor quantum wires. J Phys Chem Solids. 1959;8:382-390. *DOI*: http://dx.doi.org/10.1143/JPSJ.66.1066.

[37] Elliot RJ, Loudon R. Theory of the absorption edge in semiconductors in a high magnetic field. J Phys Chem Solids. 1960;15:196-207. *DOI*: 10.1134/S1063776111160060.

[38] Hároz EH, Duque JG, Lu BY, Nikolaev P, Arepalli S, Hauge RH, Doorn SK, Kono J. Unique origin of colors of armchair carbon nanotubes. J Am Chem Soc 2012;134:4461-4464. *DOI*: 10.1021/ja209333m.

[39] Deslippe J, Spataru CD, Prendergast D, Louie SG. Bound excitons in metallic single-walled carbon nanotubes. Nano Lett. 2007;7:1626-1630. *DOI*: 10.1021/nl070577f.

[40] Dubay O, Kresse G, Kuzmany H. Phonon softening in metallic nanotubes by a Peierls-like mechanism. Phys Rev Lett. 2002;88:235506. *DOI*: https://doi.*org*/10.1103/*PhysRevLett*.88.235506.

[41] Lazzeri M, Piscanec S, Mauri F, Ferrari AC, Robertson J. Phonon linewidths and electron-phonon coupling in graphite and nanotubes. Phys Rev B: Condens Matter. 2006;73:155426. *DOI*: 10.1103/*PhysRevB*.73.155426.

[42] Ishikawa K. Ando T. Optical phonon interacting with electrons in carbon nanotubes. J Phys Soc Jpn. 2006;75:084713. *DOI*: http://dx.doi.org/10.1143/JPSJ.76.104711.

[43] Piscanec S, Lazzeri M, Robertson J, Ferrari AC, Mauri F. Optical phonons in carbon nanotubes: Kohn anomalies, Peierls distortions, and dynamic effects. Phys Rev B: Condens Matter. 2007;75:035427. *DOI*: https://doi.org/10.1103/*PhysRevB*.75.153401.

[44] Engel E, Michiardi A, Navarro M, Lacroix D, Planell JA. Nanotechnology in regenerative medicine: the materials side. Trends Biotechnol. 2008;26:39-47. *DOI*: 10.1016/j.tibtech.2007.10.005.

[45] Moghimi SM, Hunter AC, Murray JC. Nanomedicine: current status and future prospects. FASEB J. 2005;19:311-330. *DOI*: 10.1007/s10540-005-2887-4.

[46] Castner DG, Ratner BD. Biomedical surface science: foundations to frontiers. Surf Sci. 2002;500;28-60. *DOI*: 10.1016/s0039-6028[01]01587-4.

[47] Tirrell M, Kokkoli E, Biesalski M. The role of *surface science* in bioengineered materials. Surf Sci. 2002;500:61-83. *DOI*: 10.1016/S0039-6028[01]01548-5.

[48] Tu X, Manohar S, Jagota A, Zheng M. DNA sequence motifs for structure-specific recognition and separation of carbon nanotubes. Nature. 2009;460:250-253. *DOI*: 10.1038/nature08116.

[49] Ito M, Ito Y, Nii D, Kato H, Umemura K, and Yoshikazu Homma Y. The effect of DNA adsorption on optical transitions in single walled carbon nanotubes. J Phys Chem C. 2015;119:21141-2114. *DOI*: 10.1021/acs.jpcc.5b05087.

[50] Zheng M, Jagota A, Semke E D, Diner B A, Mclean RS, Lustig SR, Richardson RE, Tassi NG. DNA-Assisted dispersion and separation of carbon nanotubes. Nat Mater. 2003;2:338-342. *DOI* :10.1038/nmat877.

[51] Wang F, Dukovic G, Brus LE, Heinz T F. The optical resonances in carbon nanotubes arise from excitons. Science. 2005;308:838-841. *DOI*: 10.1038/nature02898.

[52] Ohno Y, Iwasaki S, Murakami Y, Kishimoto S, Maruyama S, Mizutani T. Excitonic transition energies in single-walled carbon nanotubes: dependence on environmental dielectric constant. Phys. Status Solidi B. 2007;244:4002-4005. *DOI*: 10.1039/c6nh00062b.

[53] Inoue T, Matsuda K, Murakami Y, Maruyama S, Kanemitsu Y. Diameter dependence of exciton-phonon interaction in individual single-walled carbon nanotubes studied by microphotoluminescence spectroscopy. Phys Rev. B. 2006;73:233401-1-233401-4. *DOI*: 10.1103/PhysRevB.73.233401.

[54] Lefebvre J, Fraser JM, Homma Y, Finnie P. Photoluminescence from single-walled carbon nanotubes: a comparison between suspended and micelle-encapsulated nanotubes. Appl Phys A: Mater Sci Process. 2004;78:1107-1110. *DOI*: http://dx.doi.org/10.1063/1.1789610.

[55] Yamazaki T, Fenniri H. Imaging carbon nanotube interaction with nucleobases in water using the statistical mechanical theory of molecular liquids. J Phys Chem C. 2012;116:15087-15092. *DOI*: 10.1021/jp3026804.

[56] Homma Y, Chiashi S, Yamamoto T, Kono K, Matsumoto D, Shitaba J, Sato S. Photoluminescence measurements and molecular dynamics simulations of water adsorption on the hydrophobic surface of a carbon nanotube in water vapor. Phys Rev Lett. 2013;110:157402. *DOI*: 10.1103/*PhysRevLett.*98.157402.

[57] Martin W, Zhu W, Krilov G. Simulation study of noncovalent hybridization of carbon nanotubes by single-stranded DNA in Water. J Phys Chem B. 2008;112:16076-16089. *DOI*: dx.doi.org/10.1021/jp305894c.

[58] Johnson RR, Kohlmeyer A, Johnson ATC, Klein ML. Free Energy landscape of a DNA-carbon nanotube hybrid using replica exchange molecular dynamics. Nano Lett. 2009;9:537-541. *DOI*: 10.1021/nl802645d.

[59] Malik S, Vogel S, Rösner H, Arnold K, Hennrich F, Köhler AK, Richert C, Kappes, MM. Physical chemical characterization of DNA-SWNT suspensions and associated composites. Compos Sci Technol. 2007;67:916-921. *DOI*: 10.1021/acs.jpcc.5b05087.

[60] Geometric and electronic structures of carbon nanotubes adsorbed with flavin adenine dinucleotide: a theoretical study. J Phys Chem C. 2007;111:4069-4073. *DOI*: 10.1021/jp068846y.

[61] Ju SY, Doll J, Sharma I, Papadimitrakopoulos F. Selection of carbon nanotubes with specific chiralities using helical assemblies of flavin mononucleotide. Nat Nanotechnol. 2008;3:356-362. *DOI*: 10.1038/ncomms1545.

[62] Sharifi R, Samaraweera M, Gascón J A, Papadimitrakopoulos F. Thermodynamics of the quasi-epitaxial flavin assembly around various-chirality carbon nanotubes. J Am Chem Soc. 2014;136:7452-7463. *DOI*: 10.1021/ja502714z.

[63] Wang H, Ceulemans A. Physisorption of Adenine DNA Nucleosides on zigzag and armchair single-walled carbon nanotubes: a first-principles study. Phys Rev B: Condens. Matter Mater. Phys. 2009;79:195419. *DOI*: 10.1103/*PhysRevB*.80.024201.

[64] Gowtham S, Scheicher RH, Pandey R, Karna SP, Ahuja R. First-principles study of physisorption of nucleic acid bases on small-diameter carbon nanotubes. Nanotechnology 2008;19:125701. *DOI*: http://dx.doi.org/10.1088/0957-4484/19/12/125701.

[65] Chiashi S, Watanabe S, Hanashima T, Homma Y. Influence of gas adsorption on optical transition energies of single-walled carbon nanotubes. Nano Lett. 2008;8:3097-3101. *DOI*: 10.1021/nl0716000.

[66] Amirani MC, Tang TA. QM:MM model for the interaction of DNA nucleotides with carbon nanotubes. Phys Chem Chem Phys. 2015;15:7564-7575. *DOI*: 10.1039/C4CP05222F.

[67] Johnson RR, Johnson ATC, Klein ML. The nature of DNA-base-carbon-nanotube interactions. Small 2010;6:31-34. *DOI*: 10.1021/acsami.6b05710.

[68] Lv W. The adsorption of DNA bases on neutral and charged [8, 8] carbon-nanotubes. Chem. Phys. Lett. 2011;514:311-316. *DOI*: 10.1016/j.cplett.2011.08.062.

[69] Antony J, Grimme S. Structures and interaction energies of stacked graphene-nucleobase complexes. Phys. Chem. Chem. Phys. 2008;10:2722-2729. *DOI*: 10.1039/B718788B

[70] Akdim B, Pachter R, Day PN, Kim SS, Naik RR. On modeling biomolecular-surface nonbonded interactions: application to nucleobase adsorption on single-wall carbon nanotube surfaces. Nanotechnology. 2012;23:165703. *DOI*: 10.1088/0957-4484/23/16/165703.

[71] Shukla MK, Dubey M, Zakar E, Namburu R, Czyznikowska Z, Leszczynski J. Interaction of nucleic acid bases with single-walled carbon nanotube. Chem Phys Lett. 2009;480:269-272. *DOI*: 10.1016/j.cplett.2009.09.031.

[72] Albertorio F, Hughes M E, Golovchenko JA, Branton D. Base dependent DNA-carbon nanotube interactions: activation enthalpies and assembly-disassembly control. Nanotechnology. 2009;20:395101. *DOI*: 10.1088/0957-4484/20/39/395101.

[73] Daniel MC, Astruc D. Gold nanoparticles: assembly, supramolecular chemistry quantum-size-related properties, and applications toward biology, catalysis, and nanotechnology. Chem Rev.2004;104:293-346. *DOI*: 10.1021/cr030698.

[74] Reynolds RA, Mirkin CA, Letsinger RL. A fluorescence-based method for determining the surface coverage and hybridization efficiency of thiol-capped oligonucleotides bound to gold thin films and nanoparticles. J Am Chem Soc. 2000;122:3795-3796. *DOI*: 10.1021/ja000133k.

[75] Park SJ, Taton TA, Mirkin CA. Array-based electrical detection of DNA with nanoparticle probes. Science.2002;295:1503-6. *DOI*: http://dx.doi.org/10.1088/0957-4484/14/12/006.

[76] Niemeyer, CM. Nanoparticles, proteins, and nucleic acids: biotechnology meets materials science. Angew Chem Int Ed. 2001;40:4129-4158. *DOI*: 10.1002/1521-3773[20010817]40:16<3001.

[77] Tarlov MJ, Steel AB. In Biomolecular Films: Design, Function, and Applications; Rusling JF., Ed, Marcel Dekker: New York.2003;111:545-608. *DOI*: 10.1021/ja035756n.

[78] Alivisatos AP, Johnsson KP, Peng X, Wislon TE, Loweth CJ, Bruchez MP., Jr, Schultz GC. Organization of 'nanocrystal molecules' using DNA. Nature [London]. 1996;382:609-611. *DOI*: 10.1038/382609a0

[79] Harnack O, Ford WE, Yasuda A,Wessels JM. Tris [hydroxymethyl] phosphine capped gold particles templated by DNA as nanowire precursors. Nano Lett. 2002;2:919-923. *DOI*: 10.1021/nl020259a.

[80] Seeman NC. DNA in a material world. Nature. 2003;421:427-431. *DOI*: 10.1021/nl020259a.

[81] Yan H, Park SH, Finkelstein G, Reif JH, LaBean TH. DNA-templated self-assembly of protein arrays and highly conductive nanowires. Science. 2003;301:1882-1884. *DOI*: 10.1126/*science*.1089389.

[82] Lazarides AA, Schatz GC. J Phys Chem B. DNA-Linked Metal Nanosphere Materials: Structural Basis for the Optical Properties. 2000;104:460-467. *DOI*: 10.1021/jp992179.

[83] Slocik JM, Moore JT, Wright DW. Monoclonal antibody recognition of histidine-rich peptide encapsulated nanoclusters. Nano Lett. 2002;2:169-173. *DOI*: 10.1021/nl015706l.

[84] Vedamalai M, Periasamy AP, Wang CW, Tseng YT, Ho LC, Shih CC, Carbon nanodots prepared from o-phenylenediamine for sensing of Cu^{2+} ions in cells. Nanoscale. 2014;6(21):13119-13125. *DOI*: 10.1039/C4NR03213F.

[85] Chandra AK, Nguyen MT, Uchimaru T, Zeegers-Huyskens T. Theoretical estimations of the 298K gas phase acidities of the pyrimidine-based nucleobases uracil, thymine and cytosine. J Phys Chem. A. 1999;103:8853-8862. *DOI*: 10.1021/jp0497312.

[86] Choi S, Dickson RM, Yu Y. Developing luminescent silver nanodots for biological applications. J Chem Soc Rev. 2012;41:1867-1891. *DOI*: 10.1039/C1CS15226B.

[87] Díez I, Ras RHA. Fluorescent silver nanoclusters. Nanoscale. 2011;3:1963-1970. *DOI*: 10.1039/C1NR00006C.

[88] Shang L, Dong S, Nienhaus GU. Photoinduced electron transfer of DNA/Ag biosens-bioelectron. Nano Today. 2011;6:401-418. *DOI*: 10.1016/j.nantod.2011.06.004.

[89] Shiang YC, Huang CC, Chen WY, Chen PC, Chang HT. Fluorescent gold and silver nanoclusters for the analysis of biopolymers and cell imaging. J Mater Chem. 2012;22:12972-12982. *DOI*: 10.1039/C2JM30563A.

[90] Ritchie CM, Johnsen KR, Kiser JR. Antoku Y, Dickson RM, Petty JT. Ag nanocluster formation using a cytosine oligonucleotide template. J Phys Chem C. 2007;111:175-181. *DOI*: 10.1021/jp0648487.

[91] Petty JT, ZhengJ, Hud, NV, Dickson RM. DNA-templated Ag nanocluster formation. J Am Chem Soc. 2004;126:5207-5212. *DOI*: 10.1021/ja031931o.

[92] O'Neill PR, Velazquez LR, Dunn DG, Gwinn EG, Fygenson DK. Hairpins with Poly-C loops stabilize four types of fluorescent Ag_n: DNA. J Phys Chem C. 2009;113:4229-4233. *DOI*: 10.1021/jp809274m.

[93] Gwinn EG, O'Neill PR, Guerrero AJ, Bouwmeester D, Fygenson DK. Sequence-dependent fluorescence of DNA-hosted silver nanoclusters. Adv Mater. 2008;20:279-283. *DOI*: 10.1002/adma.200702380.

[94] Han B, Wang E. Oligonucleotide-stabilized fluorescent silver nanoclusters for sensitive detection of biothiols in biological fluids. Biosens Bioelectron. 2011;26:2585-2589. *DOI*: 10.1039/c2jm35236b.

[95] Su YT, Lan GY, Chen WY, Chang HT. Detection of copper ions through recovery of the fluorescence of DNA-templated copper/silver nanoclusters in the presence of mercaptopropionic acid. Anal Chem. 2010;82:8566-8572. *DOI*: 10.1021/ac101659d.

[96] Latorre A, Somoza Á. DNA-mediated silver nanoclusters: synthesis, properties and applications. Chem BioChem. 2012;13:951-958. *DOI*: 10.1002/cbic.201200053.

[97] Han B, Wang E. DNA-templated fluorescent silver nanoclusters. Anal Bioanal Chem. 2012;402:129-138. *DOI*: 10.1007/s00216-011-5307-6.

[98] Shiang YC, Huang CC, Chen WY, Chen PC, Chang HT. Fluorescent gold and silver nanoclusters for the analysis of biopolymersand cell imaging. J Mater Chem. 2012;22:12972-12982. *DOI*: 10.1039/C2JM30563A.

[99] Choi S, Dickson RM, Yu Y. Developing luminescent silver nanodots for biological applications. J Chem Soc Rev. 2012;41:1867-1891. *DOI*: 10.1039/C1CS15226B.

[100] Zhoua Z, Du Y, Dong S. DNA-Ag nanoclusters as fluorescence probe for turn-on aptamer sensor of small molecules. Biosens Bioelectron. 2011;28:33-37. *DOI*: 10.1016/j.bios.2011.06.028.

[101] Choi S, Yu J, Patel SA, Tzeng YL, Dickson RM. Tailoring silver nanodots for intracellular staining. Photochem Photobiol Sci. 2011;10:109-115. *DOI*: 10.1039/C0PP90046J.

[102] Antoku Y, Hotta J-I, Mizuno H, Dickson RM, Hofkens J, Vosch, T. Transfection of living HeLa cells with fluorescent poly-cytosine encapsulated Ag nanoclusters. Photochem. Photobiol. Sci. 2010;9:716-721. *DOI*: 10.1039/B9PP00119K.

[103] Oberdorster G, Oberdorster E,Oberdorster. Nanotoxicology: an emerging discipline evolving from studies of ultrafine particles. J EnViron Health Perspect. 2005;113:823-839. *DOI*: 10.1126/*science*.1114397.

[104] Petty JT, Zheng J, Hud NV, Dickson RM. DNA-templated Ag nanocluster formation. J Am Chem Soc. 2004;126:5207-5212. *DOI*: 10.1021/ja031931o.

[105] Soto-VerdugoV, Metiu H, Gwinn E. The properties of small Ag clusters bound to DNA bases. J Chem Phys. 2010;132:195102-195112. *DOI*: 10.1021/jp404758j.

[106] Neidig ML, Sharma J, Yeh HC, Martinez JS, Conradson SD, Shreve AP. Ag K-Edge EXAFS Analysis of DNA-templated fluorescent silver nanoclusters: insight into the structural origins of emission tuning by DNA sequence variations. J Am Chem Soc. 2011;133:11837-11839. *DOI*: 10.1021/jacs.6b05040.

[107] Lan GY, Chen WY, Chang HT, Lan GY, Chen WY, Chang HT. Control of synthesis and optical properties of DNA templated silver nanoclusters by varying DNA length and sequence. RSC Adv. 2011;1:802-807. *DOI*: 10.1039/C1RA00181G.

[108] Pal S, Varghese R, Deng Z, Zhao Z, Kumar A, Yan H, Liu Y. Site-specific synthesis and in situ immobilization of fluorescent silver nanoclusters on DNA nanoscaffolds by use of the tollens reaction. AngewChem Int Ed. 2011;50:4176-4179. *DOI*: 10.1039/C1RA00181G.

[109] Kryachko ES, and Remacle F. Complexes of DNA Bases and watson-crick base pairs with small neutral gold clusters. J Phys Chem B. 2005;109:22746-22757. *DOI*: 10.1021/jp054708h.

[110] Kumar A, Mishra PC, and Suhai S. Binding of gold clusters with DNA base pairs: a density functional study of neutral and anionic GC-Au_n and AT-Au_n [n = 4, 8] complexes. J Phys Chem A. 2006;110:7719-771. *DOI*: 10.1021/jp060932a

[111] (a) Kresse G, Furthmüller J. Efficient iterative schemes for *ab initio* total-energy calculations using a plane-wave basis set. Phys Rev B. 1996;54:11169-11186. *DOI*: 10.1103/PhysRevB.54.11169 (b) Kresse G, Furthmüller J. Efficient iterative schemes for *ab initio* total-energy calculations using a plane-wave basis set. Comput Mater Sci. 1996;6:15-50. *DOI*: https://doi.org/10.1103. (c) Kresse G, and Hafner J, Ab initio molecular dynamics for liquid metals. Phys Rev B. 1993;47:558-561. *DOI*: https://doi.org/10.1103/*PhysRevB*.48.13115. (d) Kresse G, Hafner J, Phys. Rev. B 1994;49:14251-14269. *DOI*: https://doi.org/10.1103/*PhysRevB*.49.14251.

[112] Marques MAL, Castro A, Bertsch GF, Rubio A. Octopus: a first-principles tool for excited electron–ion dynamics. 2003;151:60-78. *DOI*: 10.1016/S0010-4655(02)00686-0.

[113] Chretien S, Gordon MS, Metiu H, Density functional study of the adsorption of propene on silver clusters, Ag_m^q [m = 1–5; q = 0, +1]. J Chem Phys. 2004;121:9925. *DOI*: 10.1063/1.1809600.

[114] Shukla MK, Dubey M, Zakar E, Leszczynski J. DFT Investigation of the interaction of gold nanoclusters with nucleic acid base guanine and the Watson-Crick guanine-cytosine base pair. J Phys Chem C. 2009;113(10):3960-3966. *DOI*: 10.1021/jp900055z.

[115] Srivastava R. Complexes of DNA Bases and Watson–Crick Base Pair Interaction with Neutral Silver Agn (n = 8, 10, 12) Clusters: A DFT and TDDFT Study, Journal of Biomolecular Structure and Dynamics. DOI: http://dx.doi.org/10.1080/07391102.2017.1310059

[116] Sengupta B, Ritchie CM, Buckman JG, Johnsen KR, Goodwin PM, Petty JT. Base-directed formation of fluorescent silver clusters. J Phys Chem C. 2008;18776-18782. *DOI*: 10.1021/jp804031v

[117] Yeh, HC, Sharma J, Han JJ, Martinez JS, Werner JH. A DNA-silver nanocluster probe that fluoresces upon hybridization. Nano Lett. 2010;10:3106-3110. *DOI*: 10.1021/nl101773c.

[118] Schultz D, Gwinn E. Stabilization of fluorescent silver clusters by RNA homopolymers and their DNA analogs: C,G versus A,T[U] dichotomy. Chem Commun. [Cambridge, U. K.] 2011;47:4715-4717. *DOI*: 10.1021/jz500146q.

[119] Samanta PK, Periyasamy G, Mannaand AK, Pati SK. Computational studies on structural and optical properties of single-stranded DNA encapsulated silver/gold clusters. J Mater Chem. 2012;22:6774-6782. *DOI*: 10.1039/c2jm16068d.

[120] Berendsen, et al. GROMACS: A message-passing parallel molecular dynamics implementation. Comp Phys Comm. 1995;91:43-56. *DOI*: 10.1016/0010-4655(95)00042-E.

[121] Humphrey W. Dalke A. and Schulten K. VMD – visual molecular dynamics. J Molec Graphics. 1996;14:33-38. *DOI*: http://dx.doi.org/10.1109/IPDPSW.2016.130.

[122] Khusenov MA, Dushanov EB, TKholmurodov KH, Zaki MM, Sweilam NH. On correlation effect of the Van-der-Waals and intramolecular forces for the nucleotide chain – metallic nanoparticles–carbon nanotube binding. Open Biochem J. 2016;10:17-26. *DOI*: 10.2174/1874091X01610010017.

[123] Dunford R, Salinaro A, Cai L, Serpone N, Horikoshi S, Hidaka H, Knowland J. Chemical oxidation and DNA damage catalyzed by inorganic sunscreen ingredients. FEBS Lett. 1997;418(1-2);87-90. *DOI*: http://dx.doi.org/10.1016/S0014-5793[97]01356-2.

[124] Monti S, Carravetta V, Zhang W, Yang J. Effects due to inter adsorbate interactions on the dipeptide/TiO_2 surface binding mechanism investigated by molecular dynamics simulations. J Phys Chem C. 2007;111:7765-7771. *DOI*: http://dx.doi.org/10.1021/jp071095v.

[125] Santa Lucia J Jr. A unified view of polymer, dumbbell, and oligonucleotide DNA nearest-neighbor thermodynamics. Proc Natl Acad Sci USA. 1998;95(4):1460-1465. *DOI*: http://dx.doi.org/10.1073/pnas.95.4.1460.

[126] Tulpan D, Andronescu M, Leger S. Free energy estimation of short DNA duplex hybridizations. BMC Bioinform. 2010;11:105. *DOI*: http://dx.doi.org/10.1186/1471-2105-11-105.

[127] Breslauer KJ, Frank R, Blöcker H, Marky LA. Predicting DNA duplex stability from the base sequence. Proc Natl Acad Sci USA. 1986;83(11):3746-3750. *DOI*: http://dx.doi.org/10.1073/pnas.83.11.3746.

[128] Freyre-Fonseca V, Delgado-Buenrostro NL, Gutiérrez-Cirlos EB, Calderón-Torres CM, Cabellos-Avelar T, Sánchez-Pérez Y, Pinzón E, Torres I, Molina-Jijón E, Zazueta C, Pedraza-Chaverri J, García-Cuéllar CM, Chirino YI. Titanium dioxide nanoparticles impair lung mitochondrial function. Toxicol. Lett. 2011;202(2):111-119. *DOI*: http://dx.doi.org/10.1016/j.toxlet.2011.01.025.

[129] Trouiller B, Reliene R, Westbrook A, Solaimani P, Schiestl RH. Titanium dioxide nanoparticles induce DNA damage and geneticin stability *in vivo* in mice. Cancer Res. 2009;69(22):8784-8789. *DOI*: http://dx.doi.org/10.1158/0008-5472.CAN-09-2496.

[130] Saquib Q, Al-Khedhairy AA, Siddiqui MA, Abou-Tarboush FM, Azam A, Musarrat J. Titanium dioxide nanoparticles induced cytotoxicity oxidative stress and DNA damage in human amnion epithelial (WISH) cells. Toxicol. In Vitro. 2012;26(2):351-361. *DOI*: http://dx.doi.org/10.1016/j.tiv.2011.12.011.

[131] Hilder TA, Hill JM. Carbon nanotubes as drug delivery nanocapsules. Curr. Appl. Phys. 2008;8(3-4):258-261. *DOI*: http://dx.doi.org/10.1016/j.cap.2007.10.011.

[132] Kholmurodov K. Molecular Dynamics of Nanobistructures; Nova Science Publishers Ltd.: New York, 2011. *DOI*: 10.4236/ojpc.2015.54012.

[133] Khusenov M, Dushanov E, Kholmurodov K. Molecular dynamics simulations of the DNA-CNT interaction process: Hybrid quantum chemistry potential and classical trajectory approach. J Mod Phys. 2014;5:137-144. *DOI*: http://dx.doi.org/10.4236/jmp.2014.54023.

[134] Smith W, Forester TR. DL_POLY_2.0: a general-purpose parallel molecular dynamics simulation package. J Mol Graph. 1996;14(3):136-141. *DOI*: http://dx.doi.org/10.1016/S0263-7855(96)00043-4.

[135] Yong CW. DL_FIELD – a force field and model development tool for DL_POLY. In: CSE Frontiers. STFC Computational Science and Engineering Department (CSED); Blake R. Ed Science and Technology Facilities Council: STFC Daresbury Laboratory 2010;38-40.

[136] Pu Q, Leng Y, Zhao X, Cummings PT. Molecular simulations of stretching gold nanowires in solvents. Nanotechnology. 2007;18(42):424007. *DOI*: http://dx.doi.org/10.1088/0957-4484/18/42/424007.

[137] Yang SH, Wei ZX. Mechanical properties of nickel-coated single-walled carbon nanotubes and their embedded gold matrix composites. Phys Lett A. 2010;374:1068-1072. *DOI*: http://dx.doi.org/10.1016/j.physleta.2009.12.035.

[138] Walther JH, Jaffe R, Halicioglu T, Koumoutsakos P. Molecular dynamics simulations of carbon nanotubes in water Proceedings of the Summer School Center for Turbulence Research. NASA Ames/Stanford University, California, USA. 2000;5-20.

[139] Kowalczyk P. Molecular insight into the high selectivity of double-walled carbon nanotubes. Electron. Suppl. Mater. (ESI) Physic Chem Chemic Phys. 2012;14:2784-2790.

[140] Ballone P, Jones RO. A reactive force field simulation of liquid-liquid phase transitions in phosphorus. J Chem Phys. 2004;121(16):8147-8157. *DOI*: http://dx.doi.org/10.1063/1.1801271.

Chapter 14

Sputtered Indium Tin Oxide Films for Optoelectronic Applications

Oleksandr Malik and
Francisco Javier de la Hidalga-Wade

Additional information is available at the end of the chapter

http://dx.doi.org/10.5772/67441

Abstract

High-quality indium tin oxide (ITO) films have been fabricated using a DC sputtering technique in a pure argon atmosphere with a postannealing in an oxygen environment at atmosphere pressure. Structural, morphological, and electro-optical parameters of the ITO films were studied at different annealing temperatures for the films fabricated on two types of glass substrates, soda lime and alkali-free substrates. A comparative analysis shows that low-cost soda lime substrates are suitable for the fabrication of high-quality nanocrystalline ITO films after annealing them at 300°C. This result is of great importance for reducing the cost of thin film solar cells, in which ITO films serve as transparent conducting electrodes. We present a comparison of the properties of sputtered ITO films with those fabricated using a spray pyrolysis deposition technique, which is useful for some optoelectronic applications.

Keywords: thin film, indium tin oxide, DC sputtering, postannealing, soda lime glass, alkali-free glass

1. Introduction

Thin films of transparent conducting oxides (TCOs) have been widely used as a transparent electrode due to their low electrical resistivity and high transparency. As a degenerated semiconductor, ITO can be used as an antireflection layer in n^+-p optical sensors and as a flat panel displays including liquid crystal displays, organic light emitting diodes, and plasma displays [1]. Among the various TCOs, indium oxide films doped with tin (ITO) are widely transparent conducting electrodes in optoelectronic devices [3–6].

ITO thin films can be prepared using a wide variety of techniques such as thermal evaporation, chemical vapor deposition, electron beam evaporation, sol-gel, pulsed laser deposition, magnetron sputtering, and spray pyrolysis [2].

DC and RF magnetron sputtering using ceramic ITO targets is the most widespread method for deposition of ITO films on different substrates. Usually, such sputtering is carried out in a mixed argon-oxygen atmosphere. Normally, sputtering in a pure argon atmosphere is a more simple, cheap and highly controllable technique. However, a practical realization of this process using commercial ITO targets presents some difficulties. Commercial ceramic sputtering targets of ITO usually are fabricated from a mixture of high-purity In_2O_3 and SnO_2 powders (90:10 wt%), according to the solubility limits of Sn in In_2O_3 (12.4–15 mol% SnO_2) [7–9], using hydrothermal processes in the temperature range of 1300–1500°C. A key condition for obtaining ITO films presenting the best parameters is achieved when specific sintering techniques are used, which are also effective to tailor distinct properties of the target materials. X-ray diffractometer (XRD) peaks and the coloration of the ceramic target are references of the complete transformation to indium tin oxide. A thermal treatment in air or oxygen leads to a light-green coloring of the target, whereas a thermal treatment in reducing atmospheres (such as H_2, for instance) results in a black coloring [10]. This specific color of the target can be due to the presence of foreign phases such as metallic tin and/or blue-black tin oxide SnO due to the dissociative decomposition of SnO_2 into SnO + 1/2 O_2. At the same time, the unstable phase SnO can turn into Sn_3O_4 and pure Sn, and Sn_3O_4 will decompose into SnO_2 + Sn.

If only argon is used as the working gas for the sputtering, the deviation in stoichiometry of the target will be duplicated onto the film leading to a poor transparency [11–15]. Therefore, a certain amount of oxygen needs to be added into the working gas, otherwise, the films must be annealed in an air/oxygen atmosphere for obtaining the expected stoichiometry and high transparency; thus, a quasi-reactive deposition in argon mixed with reactive gas O_2 takes the place in contrast to sputtering in pure argon gas. Sputtering target obtained from AJA Corporation and used in this work had a black color that is not usual for light or dark-green color of the ITO targets sintered in an oxygen atmosphere. According to Ref. [15], the use of a reduction atmosphere during the sintering process leads to a black coloring of the target. Thus, the knowledge of the thermal history of the mixed powders, which determines their characteristics, is fundamental in order to determine the target quality, which in turn has a profound impact on the characteristics of the sputtered thin layers [16]. According to Refs. [17, 18], the ITO targets fabricated under laboratory conditions with sintering only in an air atmosphere at 1300°C, during 6 hours, present a light coloring close to that of the initial powders. The stoichiometry of the ITO target confirmed by XRD analysis allows for the fabrication of highly transparent ITO films in a pure argon atmosphere without oxygen adding and a postannealing procedure. Since the chemical content of the as-deposited films, fabricated in a pure argon atmosphere by using the AJA target, was far from stoichiometry and had a very low transparency, for this study, we used a thermal annealing in an oxygen atmosphere at different temperatures. The crystalline structure, the work function, and the optical and electrical properties of the ITO films were investigated.

Another objective of our work was to analyze comparatively the films fabricated with a postannealing on two types of substrates, namely, low-cost soda lime and expensive alkali-free

http://dx.doi.org/10.5772/67441

glass (AFG) substrates. Currently, the cost of soda-lime glass substrates is 20–30 times lower than the cost of alkali-free borosilicate substrates. The applicability of such inexpensive glass substrates in a large-scale thin film solar cells production is a significant factor for reducing the cost of thin film solar cells, in which the ITO films are an integral part of the solar cell structure as the transparent conducting electrode. Nevertheless, some reported results [19, 20] show that the presence of a large amount of alkali ions (Na^+, K^+) in the soda-lime glass substrates is dangerous for the ITO film parameters if high deposition or annealing temperatures are used in the fabrication process. This is due to the out-diffusion of ions from the substrate into the ITO film, leading to the possible formation of secondary phases such as Na_2SnO_3 or $Na_2Sn_2O_5$ observed in SEM images [21]. These disadvantages from known published results were minimized by intercalating a barrier of TiO_2-SiO_2 composite films [19], or SiO_2 and Al_2O_3 films [20] between the ITO film and the soda-lime glass substrate.

2. Experimental

ITO films with a thickness of 200 ± 10 nm were deposited simultaneously on both, soda lime glass (SLG) (Corning 2947 Plain Microscope Slides) and alkali-free glass (AFG) (Corning 1737 near zero alkali aluminosilicate glass) substrates, using the AJA ATC Orion 5 UHV DC Magnetron Sputtering System with 2 inches heads. SLG and AFG substrates differ on their Na_2O content, which are 14% and less than 1%, respectively. The ITO target (90 wt% In_2O_3, 10 wt% SnO_2) was manufactured by AJA Corporation. Only pure argon was used as the working gas; the detailed deposition conditions can be found in our earlier reports [22, 23]. The substrate surface was not heated and maintained at a temperature below 50°C. The films removed from the sputtering system were thermally annealed during 60 min under a constant flow of a pure oxygen, at temperatures in the range of 200–500°C using a 50°C step, in an improved annealing equipment with a more uniform oxygen flux than the one used in an early published work [22].

The structural characterization of the ITO films was carried out using a Bruker D8 advanced X-ray diffractometer (XRD), with CuK_α radiation (λ = 0.15406 nm). Morphological features of the ITO films were examined using the Ambios USPM atomic force microscopy (AFM). The Keithley's Series 2400 source measurement unit and the Acopia HMS-5000 Hall Effect Measurement System were used for the electrical characterization. Optical measurements were carried out in the 400–1100 nm wavelength range using an F20 Filmetrics spectrometer.

3. Comparison of sputtered ITO films on SLG and AFG substrates

As-deposited, the ITO films grown at room temperature on both glass substrates were amorphous and black colored. The dark color of the films can be explained by nonstoichiometric film contents due to the inclusions of metals and indium, and tin sub-oxides present in the used sputtering target. Crystallization of the films in the (222) and (400) planes (**Figures 1** and **2**) with preferred grains (222) orientation was detected after a thermal annealing in oxygen at a temperature above 200°C.

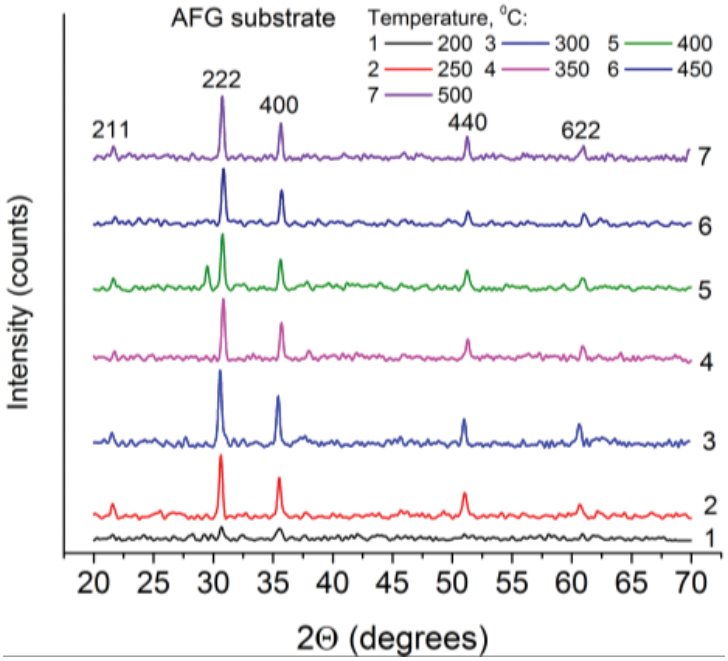

Figure 1. XRD diffraction patterns of the ITO films deposited on AFG substrates and annealed at different temperatures in an oxygen atmosphere.

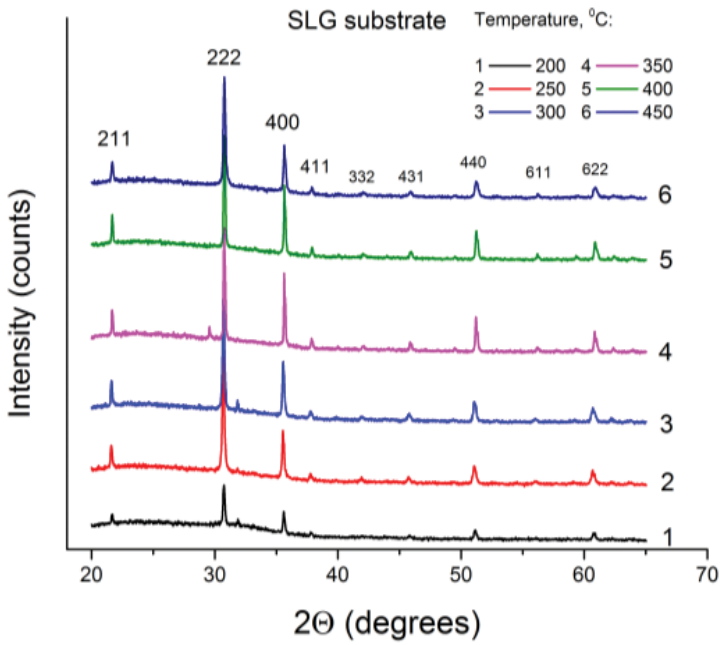

Figure 2. XRD diffraction patterns of the ITO films deposited on SLG substrates and annealed at different temperatures in an oxygen atmosphere.

http://dx.doi.org/10.5772/67441

The films deposited on both substrates and annealed at temperatures 200–450°C in the oxygen atmosphere are polycrystalline. Their XRD spectra (**Figures 1** and **2**) have a little difference in the height of peaks. The preferred grains orientation is (222). This result is consistent with the works presented by Raoufi and Alam [24] and Salehi [25], who obtained the same (222) predominant peak. The XRD peaks for the films deposited on SLG substrates are sharper than those from the films deposited on AFG substrates. The average crystallite size (s) was calculated from the (222) peak, as shown in **Figure 3**, using the well-known Scherrer formula [26].

The surface roughness of the films obtained from AFM analysis is shown in **Figures 4** and **5**. The substrate roughness serves as a reference.

From **Figures 4** and **5**, one can see that the roughness of the AFG substrates is significantly less than that for SLG substrates. However, the roughness of the ITO films deposited on the SLG substrates is less than that of the substrate roughness. We correlate this observed experimental fact with a planarization effect occurring during the film growing on the SLG substrate. A higher roughness of the SLG substrates serves as crystallization centers for the film growth that leads to a bigger crystallite size than that obtained for the ITO films deposited on ALG substrates. The reduction of the grains size of the ITO films deposited on the SLG substrates and annealed at temperatures above 350°C can be correlated with the beginning of the diffusion of Na^+ ions from the SLG substrate with the subsequent formation of secondary phases such as Na_2SnO_3 or $Na_2Sn_2O_5$ that inhibits the normal grain growth [20]. At the same time, the grains size of the ITO films on the AFG substrates is almost independent of the annealing temperature. **Figure 6** shows the dependence of the resistivity of the ITO films deposited on

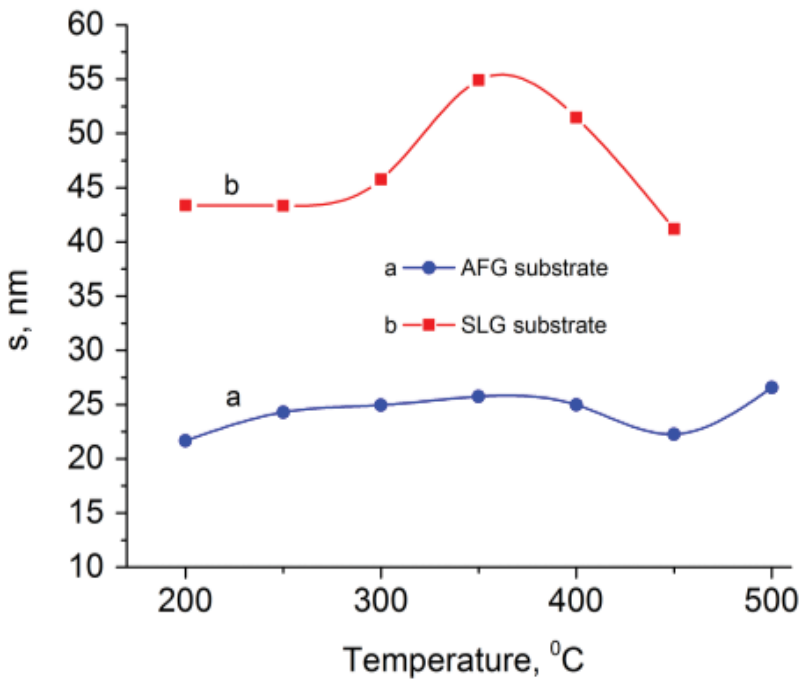

Figure 3. The average crystallite size calculated from the (222) peak.

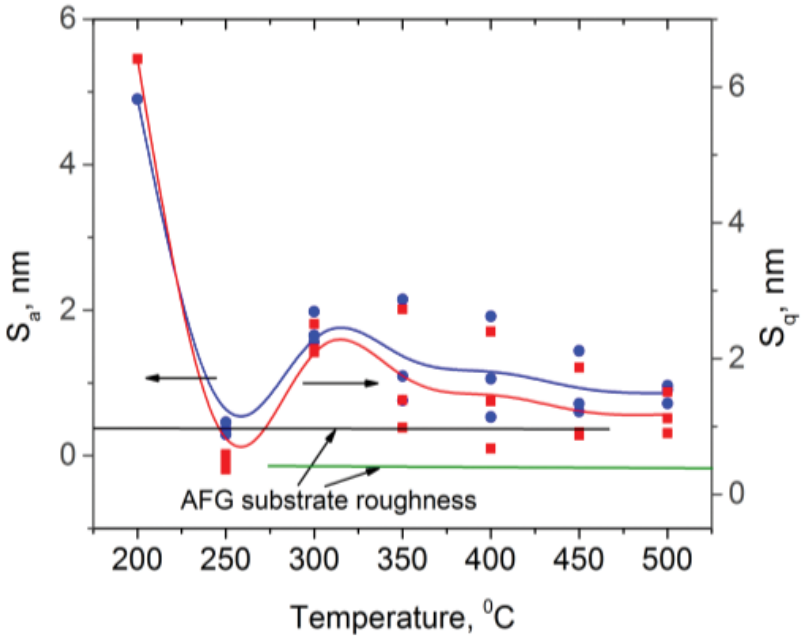

Figure 4. Average (S_a) and root mean square (S_q) roughness for the ITO film deposited on the AFG substrate and annealed in oxygen at different temperatures.

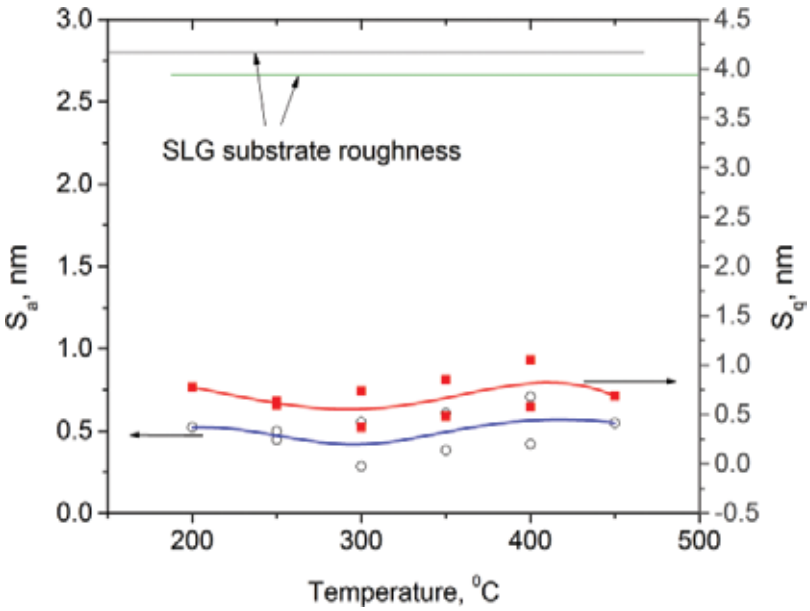

Figure 5. Average (S_a) and root mean square (S_q) roughness for the ITO film deposited on the SLG substrate and annealed in oxygen at different temperatures.

http://dx.doi.org/10.5772/67441

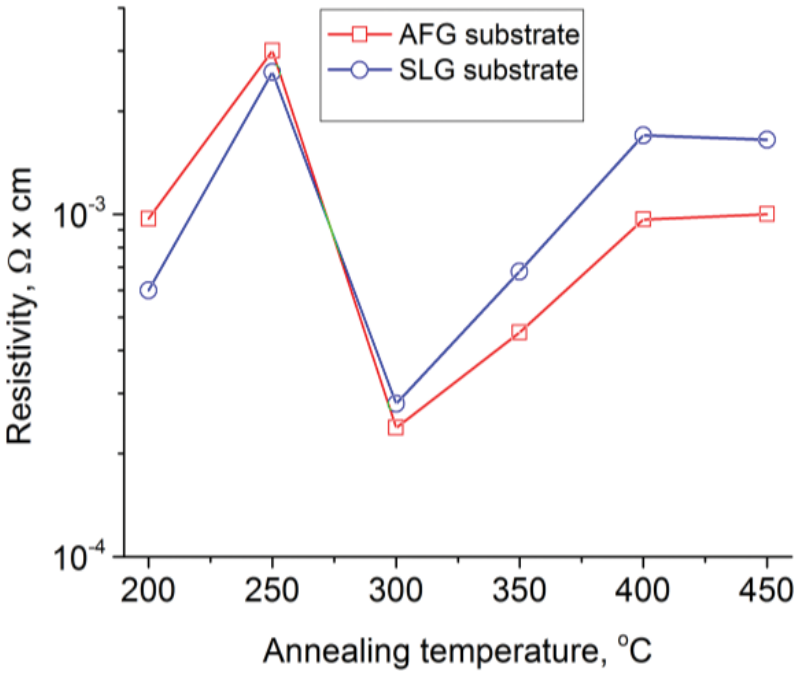

Figure 6. The resistivity dependence of the ITO films deposited on both types of substrates as a function of the annealing temperature in the oxygen atmosphere at different temperatures.

both types of substrates as a function of the annealing temperature in the oxygen atmosphere. The carrier concentration and carrier mobility obtained from Hall measurements are shown in **Figures 7** and **8**, respectively.

The as-deposited films are amorphous with a high concentration of nonstoichiometric contents such as metals and sub-oxides inclusions. This leads to a significant reduction of the resistivity in spite of the fact that the films were opaque and presented a black color. The film crystallization takes place at temperatures above 200°C. Higher annealing temperatures promote tin doping of the ITO films due to an effective replacement of the three-valence indium atoms by four-valence tin atoms in the crystal lattice of In_2O_3. A minimum value of the resistivity, (2–3) × 10^{-4} Ω×cm (**Figure 6**), is obtained at 300°C for both types of substrates. At higher annealing temperatures, an increasing resistivity is observed due to a reduction of oxygen vacancies that are doubly charged donor impurity in the ITO films; it is higher for the ITO films deposited on the SLG substrates, which can be due to the effect of alkali ions out-diffusion from the SLG substrate [19, 20]. The same explanation can be applied to the carrier concentration reduction (**Figure 7**) at annealing temperature above 300°C. The increment of the carrier mobility (**Figure 8**) with annealing temperatures for the ITO films deposited on both types substrates comes from an enhancement of the films structural morphology as well as a reduction of defects at the grain boundaries.

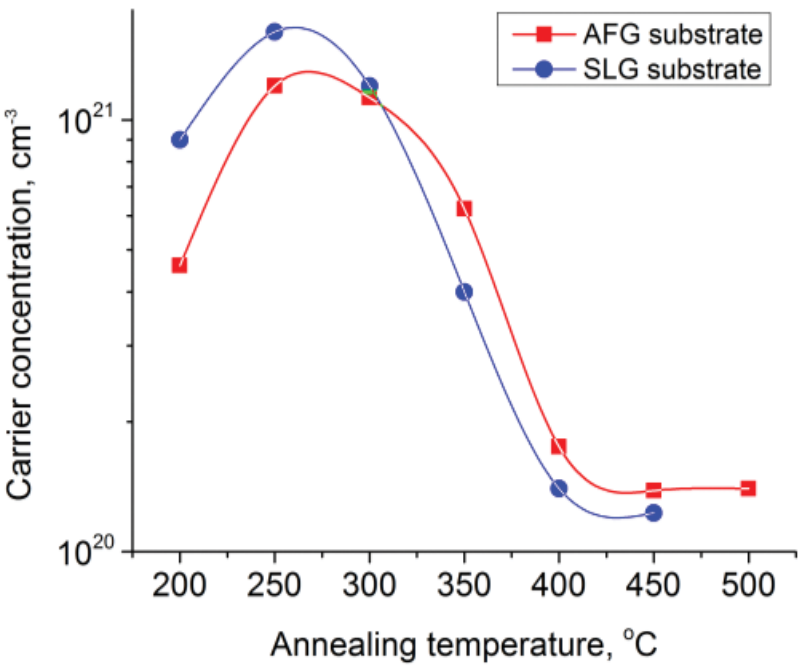

Figure 7. Dependence of carrier concentration on the annealing temperature for the ITO films deposited on AFG and SLG substrates.

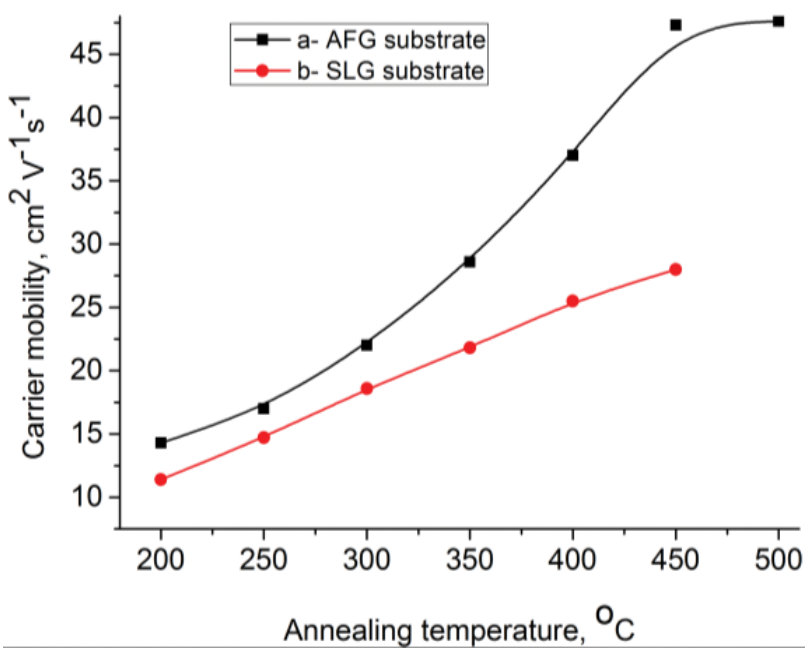

Figure 8. Dependence of carrier mobility on annealing temperature for the ITO films deposited on AFG and SLG substrates.

http://dx.doi.org/10.5772/67441

From the above-mentioned experimental results, we conclude that the highest structural and electrical parameters of the ITO films are obtained after a postannealing in the oxygen atmosphere at 300–350°C temperature range.

For practical applications of the ITO films as transparent conducting electrodes, the fabrication process needs to be optimized for obtaining a better balance between the transmittance (T) and the sheet resistance $R_s = \rho/d$, where ρ and d are the resistivity and the thickness of the film, respectively. However, a simultaneous obtaining of maximum transmission and conductivity is not possible to achieve in most cases. Haacke [27] proposed the figure-of-merit (FOM) $\phi_{TC} = T^{10}/R_s$ for comparison of films with different thickness and fabrication history. A higher FOM indicates a higher performance, this characterizes a film showing simultaneously a low sheet resistance (R_s) and a high transparency (T). However, the value of one of these parameters can compromise the value of the other. To avoid the influence of an interference effect in the thin films, the average integrated value of the films transmittance (T) at wavelengths in the range of 400–700 nm was used for the FOM value calculation. The dependence of integrated optical transmittance in visible spectral range (400–700 nm) of the ITO films deposited on AFG and SLG substrates is shown in **Figure 9** for different annealing temperatures.

Table 1 shows the structural, electrical parameters, the FOM for ITO films deposited on both glass substrates, AFG and SLG, after postannealing in the oxygen atmosphere at two different temperatures that are close to the optimal value.

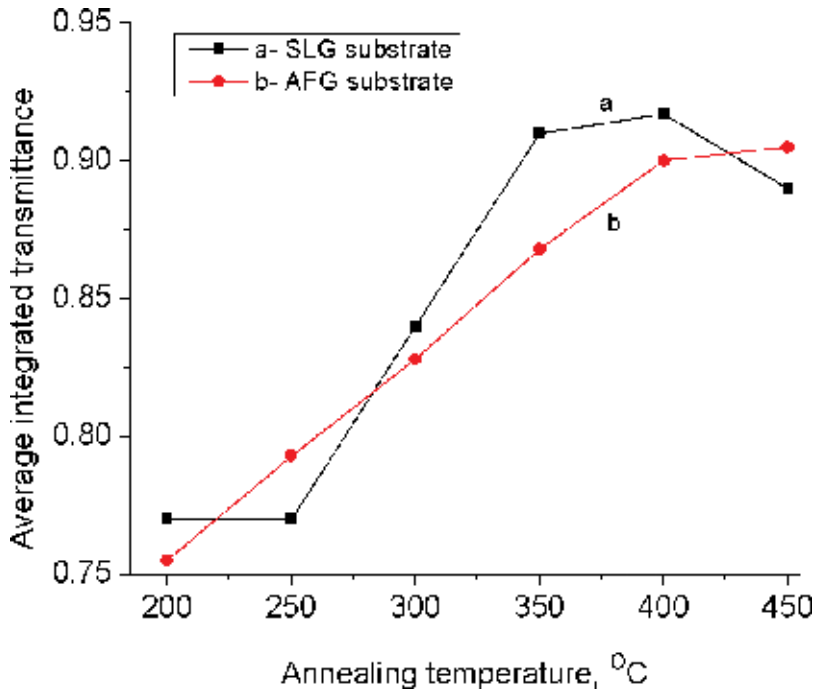

Figure 9. Dependence of the transmittance on annealing temperature for the ITO films deposited on SLG and AFG substrates.

Parameters/substrate	AFG	SLG	AFG	SLG
Annealing temperature (°C)	300	300	350	350
Substrate roughness (nm)	0.37	2.8	0.37	2.8
Ratio XRD peaks (222/400)	1.16	1.23	1.11	1.16
Grain size (nm)	25.0	45.0	25.0	55.0
ITO roughness (nm)	1.74	0.43	1.55	0.52
Specific resistance (10^{-4} Ω-cm)	2.2	2.8	4.2	6.8
Carrier concentration (10^{20} cm^{-3})	11.0	11.8	6.2	4.0
Mobility (cm^2 V^{-1} s^{-1})	25.0	17.5	28.0	23.0
Integral transparency	0.83	0.84	0.87	0.92
FOM (10^{-3} Ω^{-1})	14.1	12.5	11.8	12.8

Table 1. Comparison of properties of the ITO films deposited on AFG and SLG glass substrates after annealing in oxygen at 300 and 350°C.

From **Table 1**, the maximum $_{\phi TC}$ is observed for the films after postannealing in oxygen at 300– 350°C. At 300°C, where a minimum resistivity is observed, the films deposited on both substrates do not show a large difference in their FOM. Usually, ITO films present an FOM of the order of 10^{-3} Ω^{-1}. The highest known value of the FOM for commercially available sputtered ITO films is (14–17) × 10^{-3} Ω^{-1} [28, 29]. Also, we can compare the maximum value of the FOM obtained in this work (12 × 10^{-3} Ω^{-1}), with those reported for ITO films fabricated using other alternative methods: 6.6 × 10^{-3} Ω^{-1} by electron beam evaporation [30], 13 × 10^{-3} Ω^{-1} by sputtering [31], 13.6 × 10^{-3} Ω^{-1} by pulse laser deposition [32], 3.9 × 10^{-3} Ω^{-1} by spray pyrolysis [33], and 0.3 × 10^{-3} Ω^{-1} by sol-gel deposition [34].

We conclude that the ITO films sputtered in a pure argon atmosphere on low-cost SLG substrates, after annealing in oxygen at 300°C, are suitable for obtaining ITO films with high electro-optical parameters without the creation of a diffusion barrier between the substrate and the ITO film. The use of low-cost SLG substrates is an important factor for a significant reduction in the cost of thin film solar cells and modules for large-scale production. Moreover, a low annealing temperature allows for the fabrication of the ITO film on flexible plastic substrates. The ITO films, whose XRD spectra are shown in **Figure 10**, have been successfully fabricated on the Kapton substrate with annealing in oxygen at 300°C during 1 hour [23].

The incomprehensible preferred grains orientation (231) characteristics of a cubic film structure, or the (110) for hexagonal structure, need a further investigation. The electrical parameters of the 215-nm thick ITO films, deposited on Kapton plastic substrates at room temperature after annealing in an oxygen atmosphere during 1 hour at 300°C, are resistivity ρ = 3.2 × 10^{-4} Ω-cm, carrier concentration n = 1.4 × 10^{21} cm^{-3}, and mobility μ = 13.7 cm^2/V-s.

http://dx.doi.org/10.5772/67441

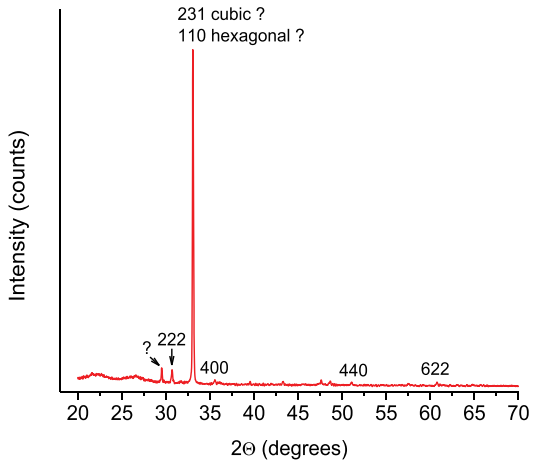

Figure 10. XRD spectra of the ITO film deposited on a Kapton substrate and annealed for 1 hour in oxygen at 300°C.

4. Comparison of sputtered and spray deposited ITO films

In this section, we present a comparison of the properties of the ITO films, fabricated using a two-step process for fabrication of films (sputtering an annealing), with those properties obtained using a one-step spray pyrolysis process [6, 23]; the second option is no expensive because it does not demand the use of sophisticated technological equipment. The spray pyrolysis is a stable and repetitive process very convenient for laboratory purposes and also for sufficiently large-scale production in the frame of small enterprises.

The spray pyrolysis technique was used for the deposition of 175–220 nm ITO films on an SLG substrate (Corning 1747). A glass atomizer was designed in order to produce small-size droplets. The SLG substrates were placed on a heater covered with a carbon disk in order to assure a uniform temperature, and the spraying was conducted using compressed air. The deposition rate was high at around 200 nm/min. For the ITO films deposition, 13.5 mg of $InCl_3 \times 4H_2O$ were dissolved in 170 ml of 1:1 water and ethylic alcohol mixture, with an addition of 5 ml of HCl to prevent hydrolysis. The different ratios of Sn/In achieved in the ITO films were controlled by adding in the solution a calculated amount of tin chloride ($SnCl_4 \times 5H_2O$). The substrate temperature was controlled using a thermocouple at 480 ± 5°C. The optimum distance from the atomizer to the substrate and the compressed air pressure were 25 cm and 1.4 kg/cm^2, respectively. We achieved a high deposition rate at around 200 nm/min. In order to prevent the deposition of the films under nonequilibrium thermal conditions, which can be due to a possible fast cooling of the substrate surface with the stream of the precursor and the compressed gas, periodical cycles of the deposition with durations of 1 s and intervals of 10 s were employed.

The X-ray diffraction patterns of the ITO films, prepared by spray pyrolysis at a substrate temperature of 480°C (**Figure 11**), show that these films are polycrystalline in nature for all the Sn/In ratios in the precursor and have a strong preferred columnar (400) grains orientation. Such

preferred grains orientation significantly differs from grains orientation for sputtered and annealed ITO films (**Figure 1**). The average grain size estimated from full width at half maximum (FWHM) of the (400) peak using the Scherrer formula [26] is 160 nm, this is bigger than the one obtained in sputtered and annealed films as well as the average roughness, S_a = 30 nm, determined from the analysis of AFM measurements.

Figure 12 shows the thickness and the sheet resistance (R_s) of the spray deposited ITO films prepared from the precursors with different values of the Sn/In ratio. The minimum R_s = 12 Ω/square or resistivity $\rho = 2 \times 10^{-4}$ Ω-cm was obtained for the films deposited using the solution with Sn/In = 5%. The dependencies of the carrier concentration and mobility on the Sn/In ratio are shown in **Figure 13**. Both parameters present their maximum for Sn/In = 5%. The posterior reduction of these parameters for a Sn/In ratio above 5% can be explained as due to the limit of solubility of tin in indium oxide and a possible formation of neutral complexes of tin inside the indium oxide lattice.

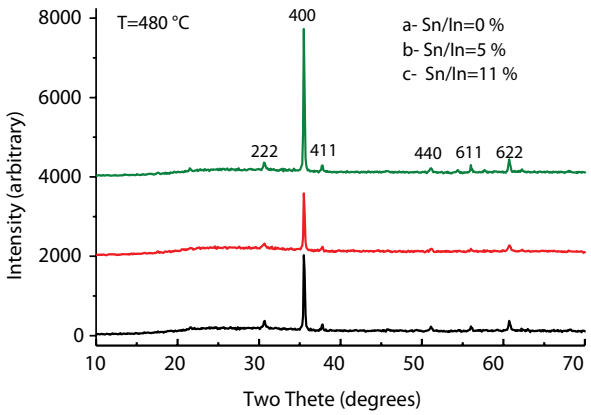

Figure 11. XRD diffraction patterns of the ITO films fabricated using solutions with different Sn/In ratios.

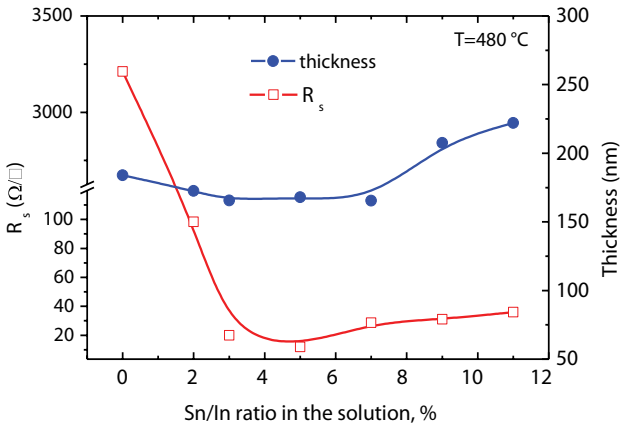

Figure 12. Sheet resistance and thickness of the sprayed ITO films fabricated using solutions with different Sn/In ratios.

http://dx.doi.org/10.5772/67441

The spray films deposited at 480°C, using the solution with a Sn/In = 5% ratio, showed the best electrical parameters, namely, a resistivity of 2 × 10^{-4} Ω-cm, a carrier concentration of 1.15 × 10^{21} cm^{-3}, and a mobility above 26 cm^2/V-s.

The optical transmittance (**Figure 14**) of the spray-deposited ITO films exceeded that of the sputtered/annealed films leading to a much higher FOM (**Figure 15**).

Comparison of properties of the ITO films deposited by sputtering and annealed in oxygen at 300°C with the properties of spray deposited films is shown in **Table 2**.

The practical optoelectronic applications (solar cell, hetero-photodiodes, and light emitting diode on silicon) of thin ITO films fabricated by spray pyrolysis are presented in our recently published articles [3–6].

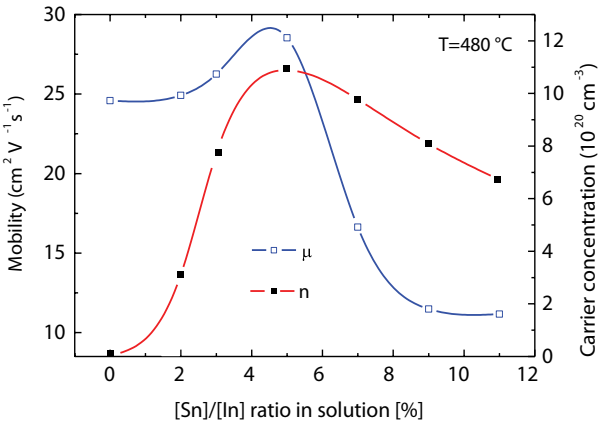

Figure 13. Hall mobility and carrier concentration of the sprayed ITO films fabricated using solutions with different Sn/In ratios.

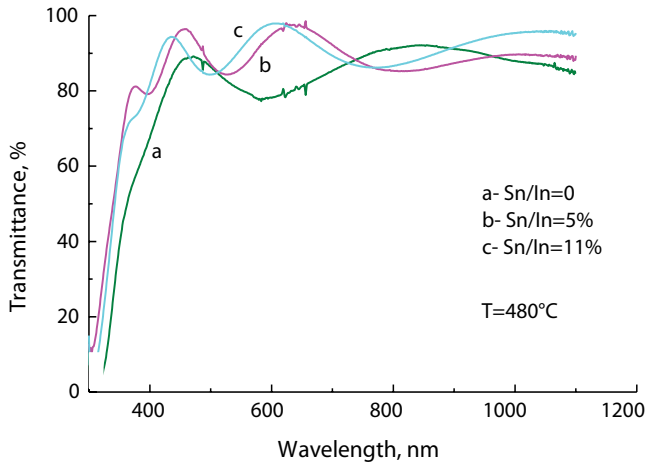

Figure 14. Optical transmittance spectra of the ITO films fabricated using solutions with different Sn/In ratios.

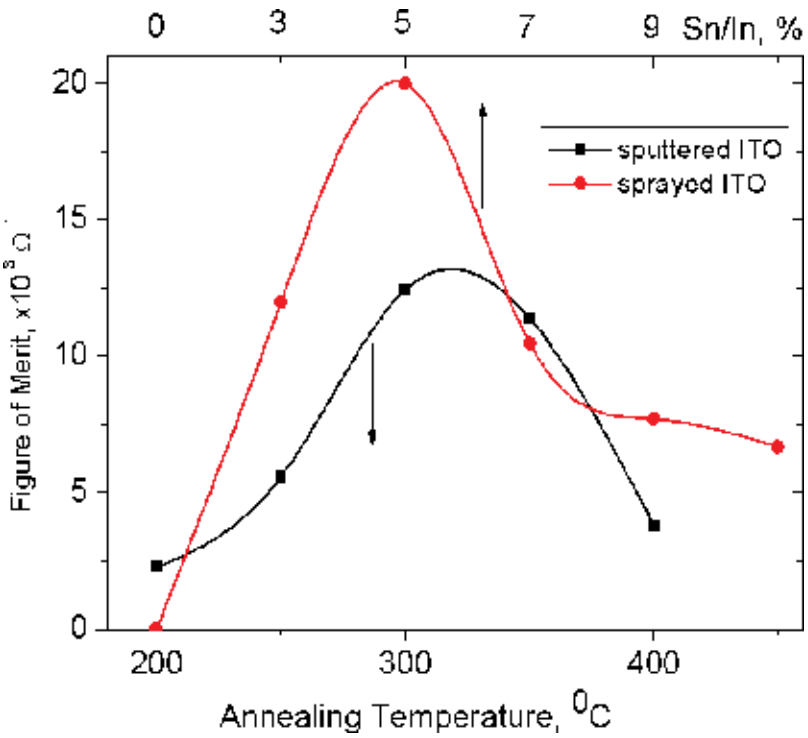

Figure 15. Comparison of the figure-of-merit (FOM) of the ITO films fabricated by sputtering with a subsequent annealing in oxygen at different temperatures, with the FOM of the films fabricated by spray pyrolysis using solutions with different Sn/In ratios.

Parameters	**Sputtered and annealed ITO film on SLG**	**Spray deposited ITO film**
Annealing temperature (°C)	300	-
Ratio Sn/In in solution (%)	-	5
Substrate roughness (nm)	2.7	2.7
Ratio XRD peaks (222/400)	1.23	0.032
Grain size (nm)	45.0	160
ITO roughness (nm)	0.43	30
Specific resistance (10^{-4} Ω-cm)	2.8	2
Carrier concentration (10^{20} cm^{-3})	11.8	11.5
Mobility (cm^2 V^{-1} s^{-1})	22.0	28
Integral transparency	0.83	0.85
FOM (10^{-3} Ω^{-1})	12.5	20

Table 2. Comparison of properties of the ITO films deposited by sputtering and annealed in oxygen at 300°C with the properties of spray deposited films.

5. Conclusions

The structural, electrical, and optical properties of sputtered and oxygen-annealed ITO films, deposited on alkali-free glass (AFG) and soda-lime glass (SLG) substrates, were studied. An important result of this work is the evidence that the sputtered ITO films in a pure argon atmosphere on low-cost SLG substrates, after annealing in oxygen at 300–350°C, show high optoelectronics parameters without the need of a diffusion barrier between the substrate and the ITO film. The electrical parameters of ITO films deposited on SLG substrates show a slight difference when compared to those obtained for the films deposited on AFG substrates at annealing temperatures no exceeding 350°C; the films deposited on SLG substrates exhibit better optical parameters (transmittance and value of FOM). Our conclusions are contrary to those reported in Ref. [20], where the ITO films on SLG substrates were annealed in a nitrogen atmosphere at 400°C. Our films were annealed in an oxygen atmosphere that leads to a binding of the diffused alkali ions with oxygen atoms diffused through the ITO films forming a stable oxide or peroxide at the film-substrate interface.

According to our results, we can conclude that SLG substrates are suitable for obtaining ITO films with high electro-optical parameters and small roughness due to a planarization effect. The use of such low-cost substrates is an important factor for a significant reduction in the cost of thin film solar cells and modules for large-scale production.

A comparative study shows that films deposited by spray pyrolysis present better electrical and optical properties than those obtained by sputtering. Hence, such a simple and low-cost deposition method is very promising for the fabrication of high-quality ITO films working as the ohmic contact in thin film optoelectronic devices as well as the active transparent conducting electrode inefficient solar cells and photodetectors with potential surface-barriers.

Author details

Oleksandr Malik* and Francisco Javier de la Hidalga-Wade

*Address all correspondence to: amalik@inaoeo.mx

Electronics Department, Óptica y Electrónica (INAOE), Instituto Nacional de Astrofísica, Puebla, Mexico

References

[1] A. L. Dawar, J.C. Joshi. Review semiconducting transparent thin films: their properties and applications. J. Materials Sci. 1984; 19:1-23.

[2] D. Ginley, H. Hosono, and D. C. Paine Eds. Handbook of Transparent Conductors, Springer, New York: 2011, 534 p.

[3] O. Malik, F.J. De la Hidalga-Wade, C. Zúñiga-Islas, and J. H. Abundis Patiño. UV-sensitive optical sensors based on ITO-GaP heterojunctions. Phys. Stat. Sol. (c). 2010; 7: 1176-1179.

[4] O. Malik, F. J. De la Hidalga-Wade, C. Zúñiga-Islas, and G. Ruíz-T. Efficient ITO-Si solar cells and power modules fabricated with a low temperature technology: results and perspectives. J. Non-Cryst. Solids. 2008; 354: 2472-2477.

[5] O. Malik, A. I. Martinez, and F. J. De la Hidalga-Wade. The physical reason of intense electroluminescence in ITO-Si heterostructures. Thin Solid Films. 2007; 515: 8615-8618.

[6] O. Malik, F.J. De la Hidalga-Wade. Spray deposited thin films of tin-doped indium oxide for optoelectronic applications. Adv. Mater. Res. 2013; 677: 173-178.

[7] H. Enoki, J. Echigoya, and H. Suto. The intermediate compound in the In_2O_3-SnO_2 system. J. Mater. Sci. 1991; 26: 4110.

[8] W. J. Heward, D. J. Swenson. Phase equilibrium in the pseudo-binary In_2O_3-SnO_2 system. J. Mater. Sci. 2007; 42: 7135-7140.

[9] G. B. González, T. O. Mason, J. S. Okasinski, T. Buslaps and V. Honkimäki.Determination of stability of tin in indium oxide in situ and ex situ x-ray diffraction. J. Am. Ceram. Soc. 2012; 95(2): 809-815.

[10] G. Falk. Sintering of transparent conductive oxides: from oxide ceramic powders to advanced optoelectronic materials. Sintering of Ceramics-New Emerging Techniques, A. Lakshmanan, Ed. InTech, Croatia: 2012, 587-610.

[11] T. Minami, H. Sonohara, T. Kakumu, and S. Takata. Physics of very thin ITO conducting films with high transparency prepared by DC magnetron sputtering. Thin Solid Films. 1995; 270(1-2): 37-42.

[12] M. Gheidari, H. H. Dabaghi, D. Kalhor, M. Iraj, M. Kazemzad, and F. Behafarid. Post annealing effects on the properties of sputtered nano-crystallite indium tin oxide thin films on flexible polyimide substrate. Phys. Stat. Sol. (c). 2008; 10: 3338-43.

[13] T. A. Gessert, Y. Yoshida, C. C. Fesenmaier, and T. J. Coutts. Sputtered In_2O_3 and ITO films containing zirconium. J. Appl. Phys. 2009; 105: 083547-53.

[14] M. Gulen, G. Yildirim, S. Bal, A. Varilci, I. Belenli, and M. Oz. Role of annealing temperature on microstructural and electro-optical properties of ITO films produced by sputtering. J. Mater. Sci.: Mater. Electron. 2013; 24: 467-474.

[15] T. A. Gessert, Y. Voshida, C. C. Fesenmaier, and T. J. Coutts. High-transparency sputtered In_2O_3 and ITO films containing zirconium. In: AVS 54th International Symposium & Exhibition, NREL/PR-520-42307, Seattle, Washington, USA: 2007, 14.

[16] C. P. Udawatte, K. Yanagisawa. Hydrothermal preparation of highly sinterable tin doped indium oxide powders: the effect of the processing parameters. In: Proceeding

of 7th International Conference on Ceramic Processing Science Proc., Inuyama City, Japan: 2000, 46.

[17] M. Nisha, S. Anusha, A. Antony, R. Manoj, and M. K. Jayaraj. Effect of substrate temperature on the growth of ITO films. Appl. Surf. Sci. 2005; 252: 1430-1436.

[18] N. Nisha. Growth and characterisation of radio frequency magnetron sputtered indium tin oxide thin films. PhD Thesis, Cochin University, Kerala, India: 2006, 116.

[19] R. Y. Tsai, F. C. Ho and M. Y. Hua. Annealing effects on the properties of indium tin oxide-films coated on soda lime glasses with a barrier layer of TiO_2-SiO_2 composite films. Opt. Eng. 1997; 3: 2335-2340.

[20] J. M. Lee, B. J. Choi, M. J. Ji, Y. T. An, and J. H. Park. Effect of barrier layers on the properties of indium tin oxide thin films on soda lime glass substrates. Thin Solid Films. 2009; 517: 4074-4077.

[21] R. Garkova, G. Volksch, and C. Russel. Precipitation of SnO_2 nano-crystallites from $Na_2O/B_2O_3/SnO_2/(Al_2O_3)$ glasses. J. Non-Cryst. Solids. 2005; 351: 2287-2293.

[22] O. Malik, F. J. De la Hidalga-Wade. Optoelectronics properties of tin-doped indium oxide films fabricated by DC magnetron sputtering in pure argon with post-annealing in oxygen atmosphere. J. Mater. Res. 2015; 30: 18941901.

[23] O. Malik, F. J. De la Hidalga-Wade. Comparison of tin-doped indium oxide films fabricated by spray pyrolysis and magnetron sputtering. Cryst. Res. Technol. 2015; 50: 516-520.

[24] D. Raoufi, J. Alam. Surface characterization and microstructure of ITO thin films at different annealing temperatures. Appl. Surf. Sci. 2007; 253(23): 9085-9090.

[25] A. Salehi. The effects of deposition rate and substrate temperature of ITO thin films on electrical and optical properties. Thin Solid Films. 1998; 324(1-2): 214-218.

[26] J. W. Kim, H. S. Kang, and S. Y. Lee. Effect of deposition rate on the property of ZnO thin films deposited by pulsed laser deposition. J. Electrical Eng. Tech. 2006; 1(1): 98-100.

[27] G. Haacke. New figure of merit for transparent conductors. J. Appl. Phys. 1976; 47(9): 4086-4089.

[28] GEOMATEC for ITO films, thin-films, and coating; www.geomatec-sputtering.com.

[29] Optics Balzers AG; www. opticsbalzers.com.

[30] H. R. Fallah, M. Ghasemi, A. Hassanzadeh, and H. Steki. The effect of annealing on structural, electrical and optical properties of nanostructured ITO films prepared by e-beam evaporation. MRS Bull. 2007; 42 (3): 487-496.

[31] C. Guillén, J. Herrero. Influence of oxygen in the deposition and annealing atmosphere on the characteristics of ITO thin films prepared by sputtering at room temperature. Vacuum. 2006; 80: 615-620.

[32] C. Viespe, I. Nicolae, C. Sima, C. Grigoriu, and R. Medianu. ITO thin films deposited by advanced pulsed laser deposition. Thin Solid Films. 2007; 515: 8771-8775.

[33] M. A. Aouaj, R. Diaz, A. Belayachi, F. Rueda, and M. Abd-Lefdil. Comparative study of ITO and FTO thin films grown by spray pyrolysis. MRS Bull. 2009; 44(7): 1458-1461.

[34] M. J. Alam, D. C. Cameron. Investigation of annealing effects on sol–gel deposited indium tin oxide thin films in different atmospheres. Thin Solid Films. 2002; 420-421: 76-82.

Chapter 15

Surface-Barrier Photodiodes with Transparent Electrodes for High-Performance Detection in the UV-NIR Spectrum

Oleksandr Malik and
Francisco Javier De la Hidalga-Wade

Additional information is available at the end of the chapter

http://dx.doi.org/10.5772/67469

Abstract

The aim of this chapter is to present a short review in the field of design, fabrication technology, and testing of high-efficiency surface-barrier photodiodes with electrodes based on thin-film transparent conducting oxides (TCO) such as tin-doped indium oxide (ITO) and fluorine-doped tin oxide (FTO). Most of this review is based on our own results obtained and reported during the last 30 years. Besides a brief description of the low-cost spray pyrolysis deposition technique, mainly used in our work for deposition of the TCO films on a semiconductor surface, structural, morphological, and optoelectronic properties of these TCO films are discussed. As an example, a successful application of these TCO films is shown and used in high-efficiency surface-barrier photodiodes for a wide spectral range, from near ultraviolet (UV) to near infrared (NIR), and fabricated on different semiconductor substrates such as traditional Si, wide energy band ZnS, and GaP compound semiconductor substrates. The possible use of the Si surface-barrier structures as radiation-resistant detectors and gamma radiation detectors is discussed. The properties of high-efficiency surface-barrier photodiodes based on a perspective ternary semiconductor compound, $Hg_3In_2Te_6$ mercury indium telluride (MIT), for detection of 1.3 μm and 1.55 μm radiation for applications in fiber optics, are also reported.

Keywords: surface-barrier photodetectors, thin film, tin-doped indium oxide, fluorine-doped tin oxide, spray pyrolysis

1. Introduction

Physics of surface-barrier (SB) devices is based on the well-known Schottky barrier, named after Walter H. Schottky, which is a potential energy barrier for carriers formed at a metal-semiconductor

(M-S) junction [1]. In the design of SB photodetectors, the main function of the barrier is to separate carriers photogenerated inside the semiconductor substrate. Such photodiodes are very simple device structures; because a p-n junction is not necessary, it does not present optical losses in the highly doped p-layer and also present a very high speed of response on modulated optical signal. The SB structure is very useful for fabrication of optoelectronic devices on semiconductors, in which a p-n junction cannot be created due to doping troubles. At the same time, in order to use M-S structures as radiation detectors, the metal electrode needs to be extremely thin (<15 nm) to avoid the radiation absorption losses and also must be chemically resistant to prevent device degradation in time. A thinner metallization leads to devices susceptible to degradation. Among all the metals, only some of them such as Au, Pt, and Ni are suitable for this application. Moreover, the high reflectivity of these metallic layers demands the use of antireflection coatings. The electrical properties of SB photodetectors based on M-S structures in many cases can be enhanced by the introduction of a very thin (<3 nm) insulating layer between the metallic film and the semiconductor (M-I-S structures). The presence of this insulator layer reduces the number of localized states at the semiconductor interface and hence serves to reduce interface carrier recombination. Its presence can also reduce significantly thermionic emission current because of an increase in the potential barrier for majority carriers [2]. At that, the thickness of the insulating layer must not reduce the transport of minority carriers from the semiconductor to the metal.

For best photoelectrical properties of SB radiation detectors based on M-S and M-I-S structures, the metallic opaque layer can be changed by a thin film based on some transparent conducting oxide (TCO), such as tin-doped indium oxide (ITO) or fluorine-doped tin oxide (FTO), which are widely used for optoelectronic applications. Such films can be deposited on a semiconductor surface by different technological methods as thermal vacuum deposition, e-beam deposition, sputtering, chemical vapor deposition, sol-gel deposition, and spray pyrolysis [3]. Spray pyrolysis is a low-cost and simple technological method used successfully since 1976 for the fabrication of efficient solar cells based on metal oxide (ITO, FTO)-silicon structures [4–11]. In such structures, the TCO films work as an active metal-like transparent conducting electrode. Thickness tuning of the TCO films allows for its use as an effective antireflection coating for reducing radiation losses.

In this chapter we pay attention to application of spray-deposited ITO and FTO films for fabrication of high-efficiency SB photodetectors for applications in a wide spectral region. The material presented in this chapter is based on original results reported in this field during the last 35 years; hence, this review will be very useful for a large number of readers.

2. Spray pyrolysis processing

Spray pyrolysis [12] is a process in which a thin film is deposited by spraying a solution on a heated surface, where the constituents react to form a chemical compound. The chemical reactants are selected such that the products other than the desired compound are volatile at the temperature of deposition. Usually, two types of processing are used: the process in which the droplet resides on the surface as the solvent evaporates, leaving behind a solid that may further react in the dry state and the process where the solvent evaporates before the droplet reaches the surface and the dry solid impinges on the surface, where decomposition occurs.

http://dx.doi.org/10.5772/67469

Three sprayed solution were used for photodetectors fabrication. The ITO films were deposited from solution contents 13.5 mg of $InCl_3 \times 4H_2O$ dissolved in 170 ml of water and ethylic alcohol (1:1) mixture, with an addition of 5 ml of HCl to prevent hydrolysis. The different ratios of Sn/In in the solution were controlled by adding in the solution a calculated amount of tin chloride ($SnCl_4 \times 5H_2O$) [13]. As alternative, the ITO layers can be deposited by spraying a solution of Indium (III) acetate, $In(OOCCH_3)_3$ dissolved in ethanol at 25°C by adding Tin(IV) chloride, $SnCl_4 \times 5H_2O$, and HCl. Ratio Sn/In in the solution varied by calculated amount of tin chloride. A glass atomizer was designed in order to produce small-size droplets. The spraying was conducted using compressed air. Substrates were placed on heater having fixed temperature of 460 ± 2°C. The heater was covered with polished carbon disk having a high thermal conductivity and chemical resistance in order to assure a uniform temperature of the substrates. The substrate temperature was controlled with a thermocouple. The optimum distance from the atomizer to the substrate and the compressed air pressure were 25 cm and 1.4 kg/cm^2, respectively. In order to prevent the deposition of the films under nonequilibrium thermal conditions, due to a possible fast cooling of the substrate surface with the stream of the precursor and the compressed gas, periodical cycles of the deposition, with durations of 1 sec and intervals of 10 sec, were employed.

Fluorine-doped tin oxide (FTO) films [14] were deposited from solution contents a 0.2 M solution of tin chloride ($SnCl_4 \times 5H_2O$) dissolved in methanol. A small amount of NH_4F dissolved in water was added in the starting solution for the preparation of the precursor with 0–1 F/Sn molar concentrations. A few drops of HCl were added to the precursor solution in order to prevent the hydrolysis of the tin chloride due to the presence of water. The flow rate of the precursor during the deposition process was 10 ml/min. Other deposition parameters were the same as for the ITO films.

For fabrication of the M-S or M-I-S structures, the ITO and FTO films were deposited on chemically prepared surface of semiconductor substrates. A Corning glass or sapphire substrates placed on the heater together with the semiconductor substrates were used as referents for the measurement of the films' properties. The structural characterization of the ITO films was conducted using a Bruker D8 Advanced X-ray diffractometer (XRD), with Cu K_α radiation (λ = 0.15406 nm). The morphological features of the ITO films were examined using the Ambios USPM atomic force microscope (AFM). Keithley's Series 2400 Source Measurement Unit and the Ecopia HMS-5000 Hall Effect Measurement System were used for electrical characterization. The optical measurements were carried out using the F20 Filmetrics and the Agilent 8453 spectrometers.

3. Properties of the metal oxide films

Both, the ITO and FTO films deposited with conditions described above were microcrystalline. X-ray diffraction (XRD) spectra for films with optimal doping concentration are shown in **Figure 1**.

The optimal doping concentration for the ITO and FTO films means the value of doping at which is obtained the lowest sheet resistance $R_s = \rho/d$, where ρ and d are the film resistivity and thickness,

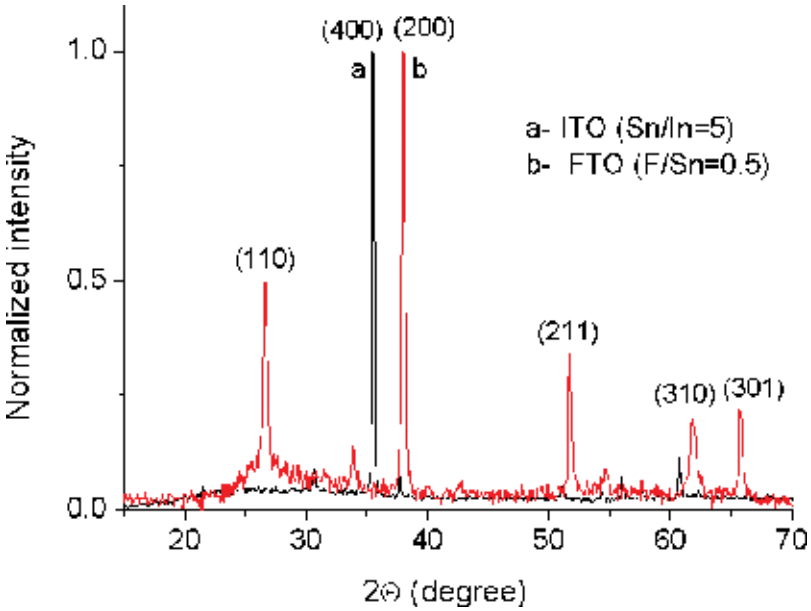

Figure 1. XRD patterns for sprayed ITO and FTO films.

respectively. At the same time, the value of transmittance (T) is important. For practical applications of the TCO films as transparent conducting electrodes, the fabrication process needs to be optimized for obtaining a better balance between R_s and T. However, a simultaneous obtaining of maximum transmission and conductivity is not possible to achieve in most cases. Haacke [15] proposed the figure of merit (FOM) $\phi_{TC} = T^{10}/R_s$ for comparison of films with different thickness and fabrication histories. A higher FOM value indicates a higher performance; this characterizes a film showing simultaneously a low sheet resistance (R_s) and a high transparency (T). However, the value of one of these parameters can compromise the value of the other. To avoid influence of an interference effect in the thin films, the average integrated value of the films transmittance (T_{int}) at wavelengths in the 400–700 nm spectral range is better to be used for the FOM value calculation. **Table 1** presents structural, electrical, and optical parameters of the ITO and FTO films deposited at 460°C from the solutions containing the optimal doping concentration.

The parameters obtained allow to conclude that high-quality FTO and ITO films can be fabricated by a simple and inexpensive spray deposition method. Our recently published works [13, 14] give more detailed information about the dependence of the film properties on the doping concentration as well as a comparison of our results with the ones published in literature.

FTO and ITO are degenerated wide band gap semiconductors. Films of these materials can be used as transparent conducting electrodes in ultraviolet (UV) SB photodetectors. In nominally doped semiconductors, the Fermi level lies between the conduction and valence bands. As the doping concentration is increased, electrons populate states within the conduction band which pushes the Fermi level higher in energy, and in the case of degenerate level of doping, the Fermi level lies inside the conduction band. At that, using transmission/reflection spectroscopy, the

http://dx.doi.org/10.5772/67469

Parameters	Spray deposited FTO film	Spray deposited ITO film
Ratio F/Sn in solution	0.5	–
Ratio Sn/In in solution	–	5
Preferred grain orientation	200	400
Grain size (nm)	120	110
Specific resistance (10^{-4} Ω cm)	1.8	2
Carrier concentration (10^{20} cm^{-3})	16.0	11.5
Mobility ($cm^2V^{-1}s^{-1}$)	21.0	28
Integrated transmittance (T_{int})	0.84	0.85
FOM (10^{-3} Ω^{-1})	38	20

Table 1. Comparison properties of the FTO and ITO films deposited by spray pyrolysis from the solutions with optimal doping concentration (ratio of F/Sn and Sn/In).

optical energy gap (E_{opt}) can be measured. This value is not coinciding with value E_g that is a distance between the valence and conduction bands as is shown in **Figure 2**. The difference ΔE is named as Burstein-Moss shift [16]. In the case of a degenerate semiconductor, an electron from the top of the valence band can only be excited into conduction band above the Fermi level (which now lies in conduction band) since all the states below the Fermi level are occupied states. Pauli's exclusion principle forbids excitation into these occupied states. The value of ΔE is proportional to the carrier concentration. Burstein-Moss shift for FTO and ITO films, characteristics of which are shown in **Table 1**, is 0.5–0.8 eV. At that, the value of optical energy gap determined from analysis of transmittance (**Figure 3**) for the FTO and ITO films is 4.3 eV and 4.8 eV, respectively. From **Figure 3** we made an important conclusion that FTO films are more suitable for UV SB photodetectors.

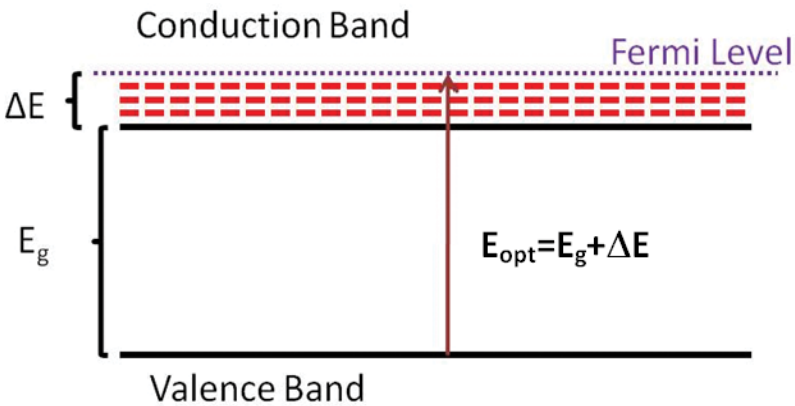

Figure 2. Illustration of the Burstein-Moss shift in degenerated semiconductors.

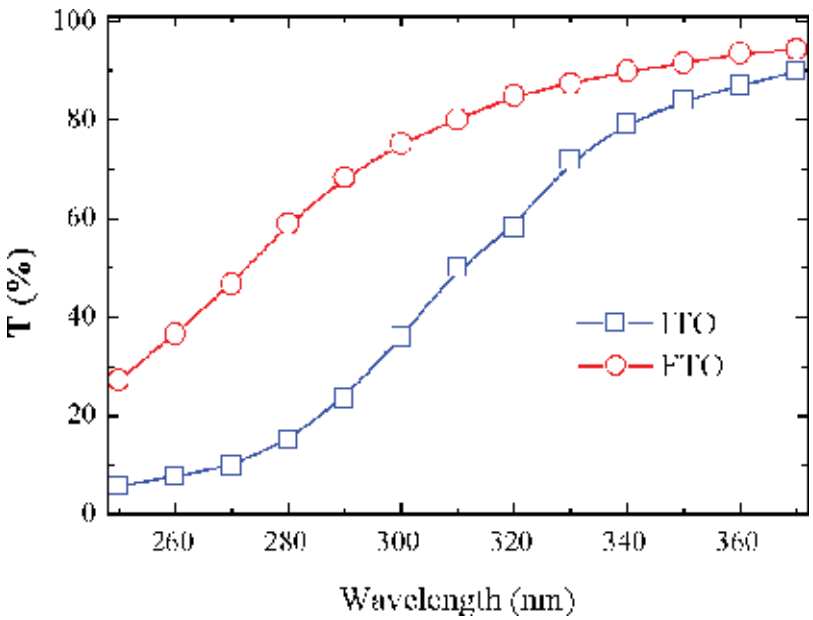

Figure 3. Transmittance of FTO and ITO films in the UV spectral range.

4. Surface-barrier photodetectors for the UV spectral range

There are many applications (biomedical, astronomy, flame safeguard systems, and others) that require the measurement of blue or UV radiation in the presence of visible light. The spectral selectivity of photodiodes depends on a band gap of semiconductor which is shown in **Figure 4**.

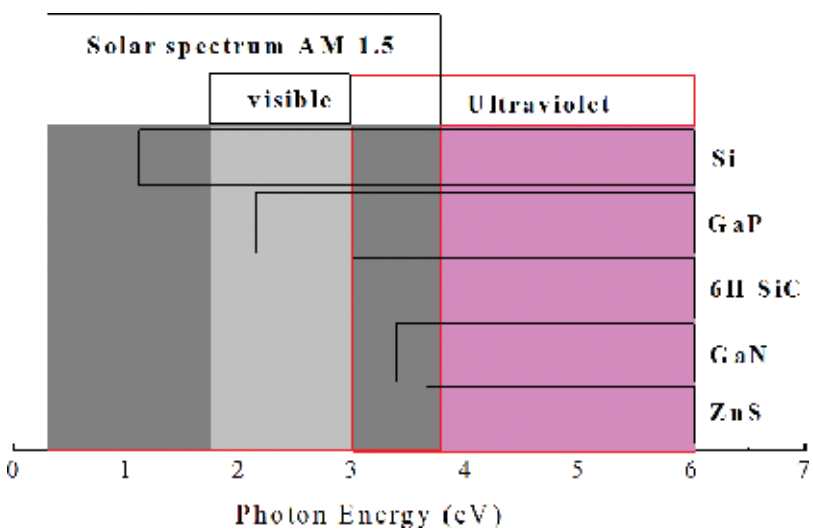

Figure 4. Semiconductors of interest for visible, UV, and solar-blind photodetectors.

http://dx.doi.org/10.5772/67469

In this direction, researchers are paying attention to large-band-gap semiconductor compounds such as GaP, SiC, and GaN in contrast to Si-based photodiodes in which the selectivity can be provided with additional blocking filters or dielectric coating to fit them with the spectral region of interest.

4.1. Solar-blind UV photodetectors based on monocrystalline ZnS

The large-band-gap (3.6 eV) zinc sulfide (ZnS) greatly reduces the sensitivity to photons in the terrestrial solar radiation, and it is an attractive material for developing solar-blind photodetectors.

N-type ZnS monocrystalline wafers were used for the fabrication of ITO-ZnS and FTO-ZnS [17, 18] UV SB photodetectors, with active areas ranging from 5 to 100 mm^2. FTO and ITO films have been deposited at the top surface of the monocrystals by spray technique at conditions described in Section 2. The backside ohmic contact to the ZnS was made as described in [17]. The current-voltage characteristic of FTO-ZnS photodetector with an area of 1 cm^2 is shown in **Figure 5**.

Figure 6 shows the spectral response of the FTO-ZnS photodetector [18] in comparison with characteristic of ITO/ZnS [17] and SiC [19] UV photodetectors.

In contrast to ITO-ZnS detectors, the maximum spectral sensitivity peak of the FTO/ZnS photodetectors shifted from 330 to 290 nm, due to the higher transparency of the FTO layer in UV, when compared to the transparency of the ITO layer (**Figure 3**). The combination of a low dark current and a high sensitivity originates a low value for the noise-equivalent power (NEP), ranging from 10^{-14} to 10^{-12} $W/Hz^{1/2}$, that is a function of the area of the sensors. In **Figure 7**, the

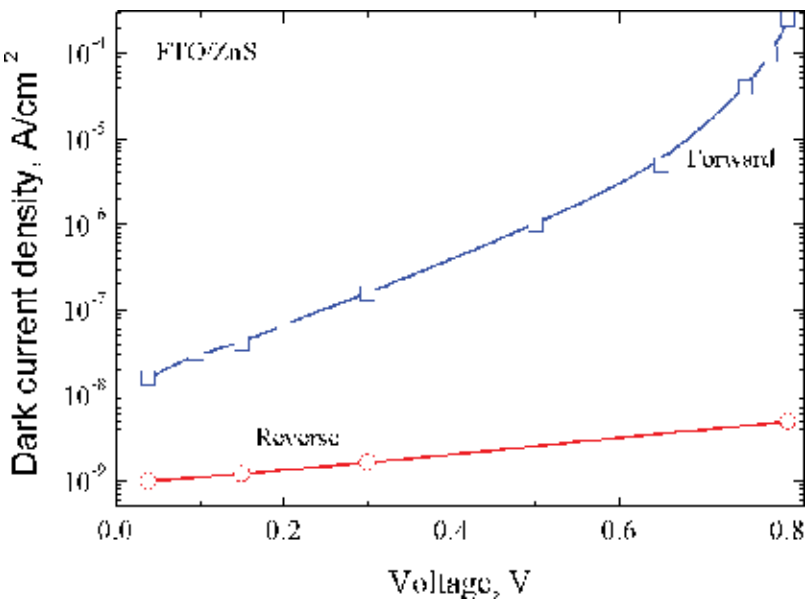

Figure 5. Current-voltage characteristic of FTO-ZnS photodetector with an area of 1 cm^2.

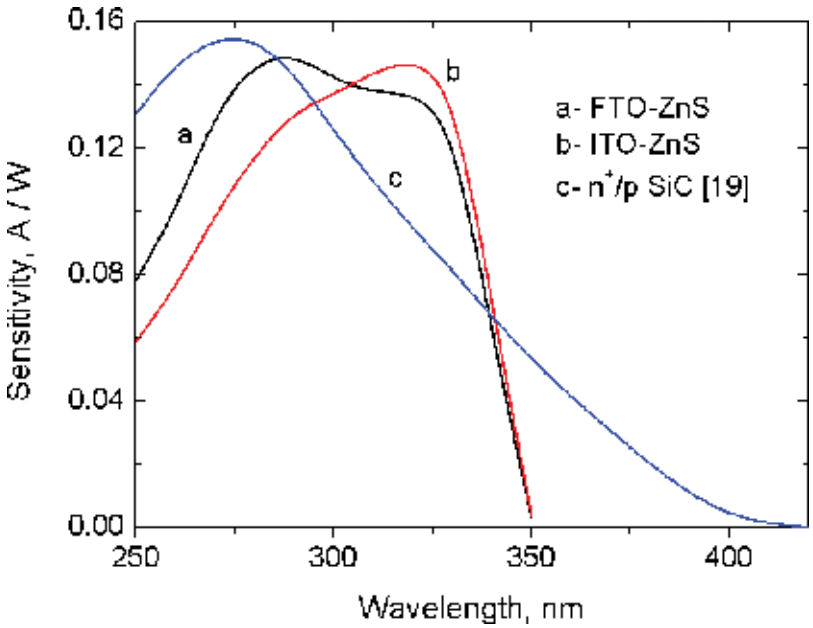

Figure 6. Spectral sensitivity of FTO-ZnS and ITO-ZnS photodetectors in comparison with a SiC UV photodetector [19].

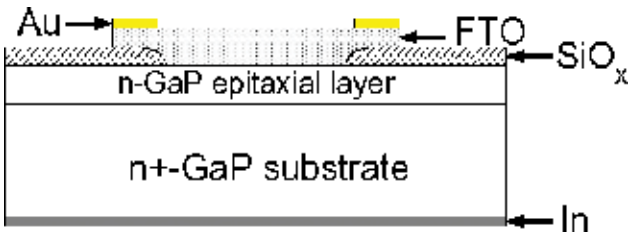

Figure 7. Schematic cross section of the FTO/n-n+ GaP SB photodetector.

dependence of the photocurrent on incident light power is shown. A linear dependence of photocurrent on incident light power ranging from 10^{-8} to 10^{-3} W was found.

Thus, SB UV FTO-ZnS photodetectors show excellent characteristics as solar-blind UV detectors with high, 66%, external quantum efficiency, and can be used for different technical applications without losing their photoelectrical parameters under direct solar irradiation.

4.2. UV photodetectors based on epitaxial GaP

Our research results about SB photodetectors with transparent TCO electrode deposited by spray pyrolysis technique on gallium phosphide (GaP) with a band gap 2.27 eV were reported during the last 20 years [20–24]. Here, a brief resume of these works in comparison with reported by other authors is done.

http://dx.doi.org/10.5772/67469

A simple and low-cost pyrolysis technique has been used to form the high transparent conducting FTO or ITO electrode on prepared surface of GaP n-n^+ epitaxial structures with 10–12 μm thick epitaxial layers. The estimated electron density in the epitaxial layer is around 10^{16} cm^{-3}. The back ohmic contact was formed by indium diffusion. **Figure 7** shows the schematic cross section of a photodiode based on the FTO-GaP heterostructure.

The typical dark current-voltage (I-V) characteristic of the FTO-GaP photodiode with an active area of 3 mm^2 measured at room temperature is shown in **Figure 8**.

The results show excellent junction properties of FTO-GaP photodiodes. The equivalent shunt resistance R_{sh}≈100 GΩ was evaluated at a bias ±50 mV, and this resistance is a main source of the

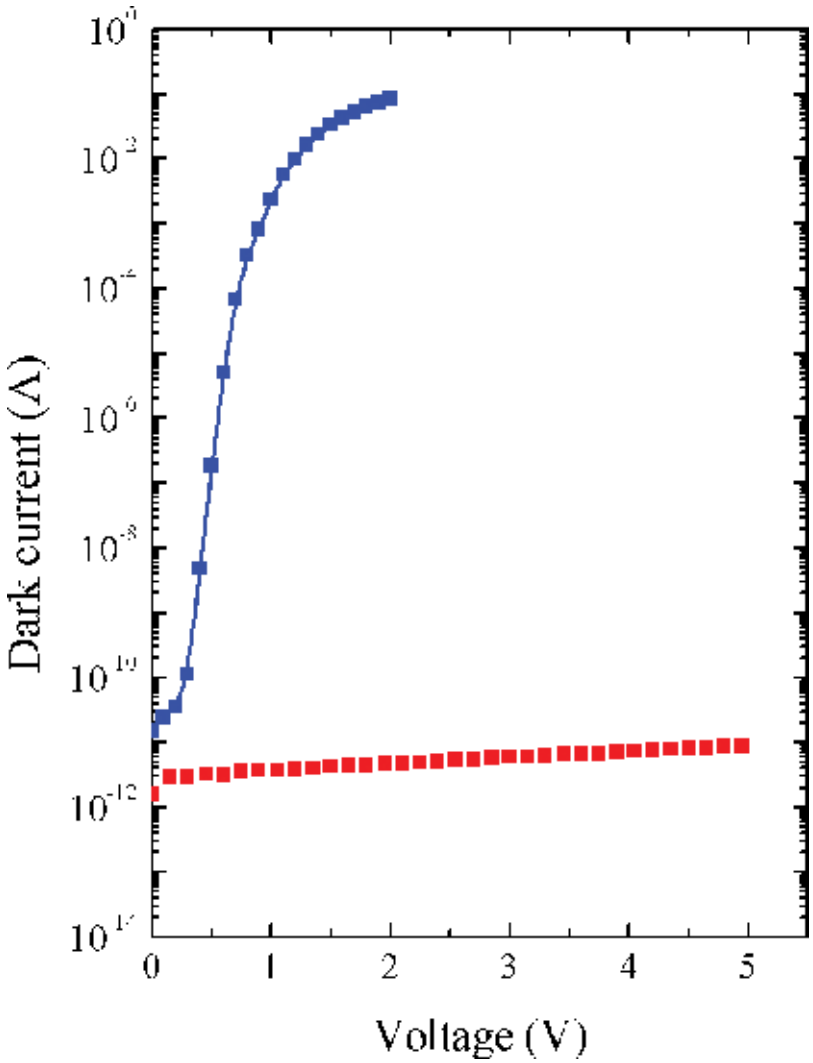

Figure 8. The typical I-V characteristics of FTO-GaP photodetector.

device noise, which limits the detectivity in short-circuit current mode. The FTO film resistance causes the non-exponential current increasing at forward bias higher than 0.6 V. A saturation current of $I_o \approx 10^{-15}$ A and an ideality factor $n = 1.1$ were determined from the exponential region of the forward I-V characteristic. The donor concentration $N_D = 3.8 \cdot 10^{16}$ cm^{-3} and the built-in potential $V_{bi} = 1.33$ V in the GaP epitaxial layer were determined from the C-V characteristics at 10^3 Hz. The thickness of FTO film is an important factor for spectral sensitivity of the developed photodetectors due to the possibility using this film as an effective antireflection coating. The spectral sensitivity of FTO-GaP SB photodetectors having different thicknesses of the FTO electrode as well as ITO-GaP photodetector with 65 nm thick ITO film is shown in **Figure 9**.

The typical performance parameters of the photodiodes with TCO layer are summarized in **Table 2**. The maximal spectral sensitivity depends on the thickness of the TCO film.

Maximal sensitivity of commercial GaP photodetectors based on Au-GaP Schottky barriers (G1962, EDP-365-0-2.5, JEP 5-365) fabricated by well-known companies Hamamatsu, Roithner LaserTechnik, and electro optical components (EOC) lies in the range of 0.07–0.12 A/W with electric parameters that do not exceed as reported here. More close parameters were rep orted for Ag-GaP photodetectors [25]; maximal spectral sensitivity of which was reported as 0.12 A/W.

High-efficient FTO-GaP photodetectors [23] have been used in the design of the radiometric heads of the UVR-21 UV radiant power meter [26]. The UVR-21 UV (**Figure 10**) is an easy-to-use, handheld power meter with unique future intended to make the calibrated measurements of UV-A, UV-B, and UV-C radiation. At the heart of the URV-21 is spectral-filtered

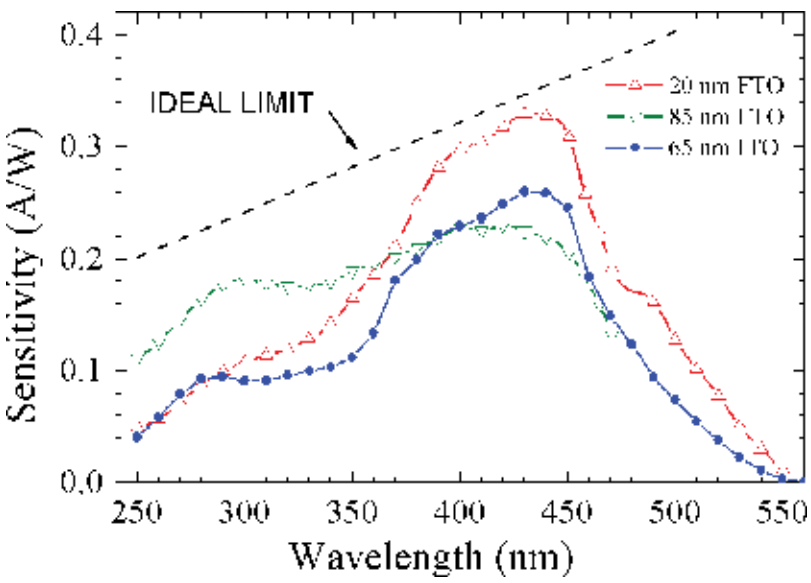

Figure 9. The spectral sensitivity of FTO-GaP and ITO-GaP SB photodetectors for different thicknesses of the transparent conducting electrode.

http://dx.doi.org/10.5772/67469

Electrode material	FTO	ITO
Active area (mm^2)	3	3
Terminal capacitance (nF)	2	1.5
Dark current at V = 1V (pA)	2	20
Shunt resistance (GΩ)	100	30
Peak sensitivity wavelength (nm)	439	435
Peak sensitivity (A/W)	0.2–0.26	0.2–0.26
Peak quantum efficiency (%)	57–74	57–74
Noise-equivalent power ($W/Hz^{1/2}$)	1.7×10^{-15}	3×10^{-15}

Table 2. Comparison of the properties of photodetectors with FTO and ITO electrodes deposited by spray pyrolysis.

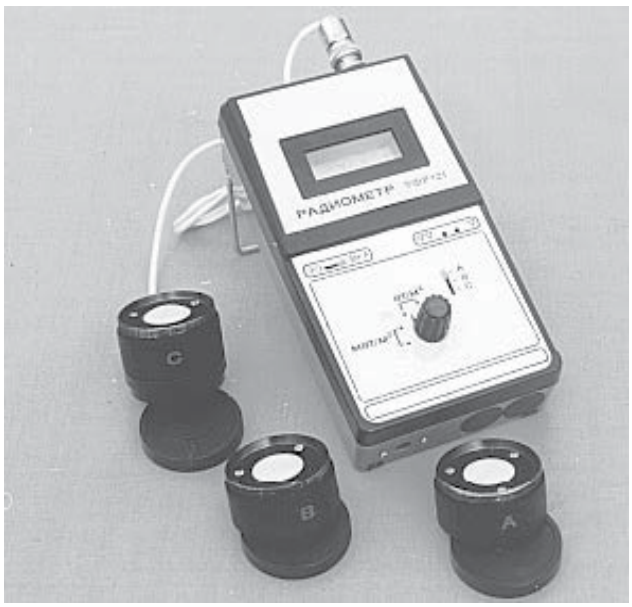

Figure 10. A handheld UV radiant power meter UVR-21 with FTO-GaP–based radiometric heads.

FTO-GaP-based radiometric heads. The interference filters to select requirement spectral band were fabricated on quartz substrates by vacuum deposition. The interchangeable UV radiometric heads allow measuring UV-A, UV-B, and UV-C radiation in the range from 10^{-3} to 10^{3} Wm^{-2}. A rechargeable NiCd battery life is 6–8 hours. Specification limit of measurement relative error is less than 5%.

The performance data of UV radiometric heads are shown below.

Spectral range (nm)		
UV-C radiometric head	220	280
UV-B radiometric head	280	315
UV-A radiometric head	135	400
Irradiance range (Wm^{-2})	10^{-3}	10^{3}
Linearity error (%)		<1
Response uniformity (%)		<1
Measurement error (%)		<5
Cosine error (%) at zenith angle		
30°		3
60°		7
80°		15

5. Silicon surface-barrier photodetectors for visible and near-infrared spectral range

The first results about silicon photodiodes were published more than 60 years ago, and the first detailed investigations of the silicon surface-barrier diodes with thin gold electrode have been published in 1962 [27, 28] by researches from the USA. The first superior electric and photoelectric characteristics of SnO_2-Si heterojunction diodes fabricated by a simple process of spraying a solution containing a tin compound were published in 1975 [29] by authors from Japan.

In this chapter, a brief review of our original results [30, 31] in the field of different types of SB silicon photodetectors with transparent conducting FTO and ITO electrodes is shown.

5.1. Fabrication, properties, and applications of FTO-Si surface-barrier photodetectors

The main technological fabrication steps of FTO-Si photodetectors are shown in **Figure 11**.

Photodetectors were fabricated on the base of high resistivity (1–2 kΩ cm) n-type oxidized silicon wafers with phosphorous-doped backside. Because the photolithographic patterning of the FTO film is difficult due to a high resistance of FTO film to acids, lift-off method was chosen for patterning. On the silicon dioxide layer previously by spray pyrolysis was deposited ITO or ZnO film that sufficiently easy can be etched in HCl solution. The active area of photodetectors after lift-off technological step was 50 mm^2. Current-voltage characteristic of photodetectors with 50 mm^2 area is shown in **Figure 12**.

5.1.1. Γ-Radiation detectors

The Γ-radiation detectors were designed on the base of the FTO-Si photodetectors with single crystal $Bi_4Ge_3O_{12}$ scintillator optically matched on the FTO electrode by silicon-based metal-organic lubricant. The optical matching of the photodetector with the scintillator is illustrated in **Figure 13**.

http://dx.doi.org/10.5772/67469

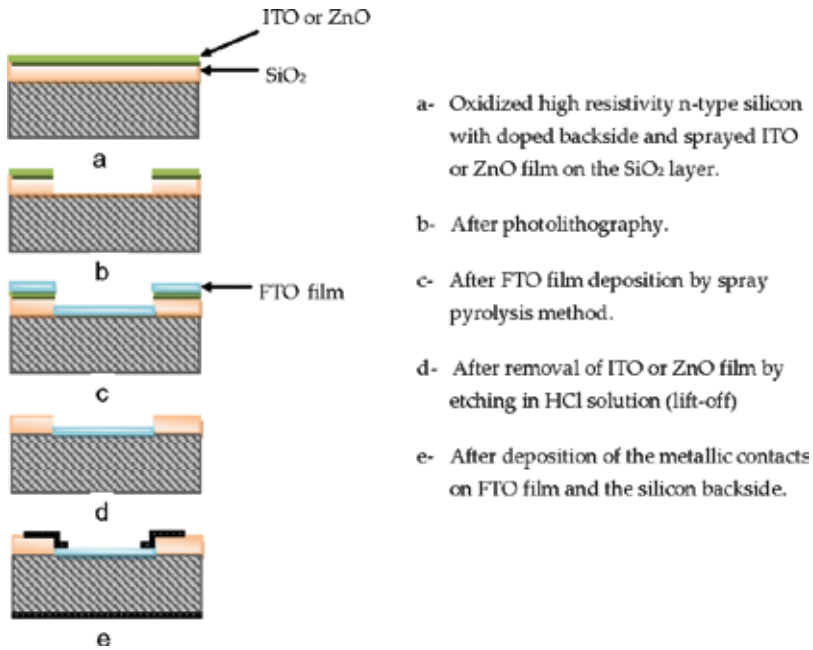

Figure 11. Technological fabrication steps of the FTO-Si photodetectors. (a) Oxidized high-resistivity n-type 350 μm thick silicon with doped backside and sprayed ITO or ZnO film on SiO_2 layer. (b) After photolithography. (c) After FTO film deposition by spray pyrolysis method. (d) After removal of ITO or ZnO film by etching in HCl solution (lift-off). (e) After deposition of the metallic contacts on FTO film and the silicon backside.

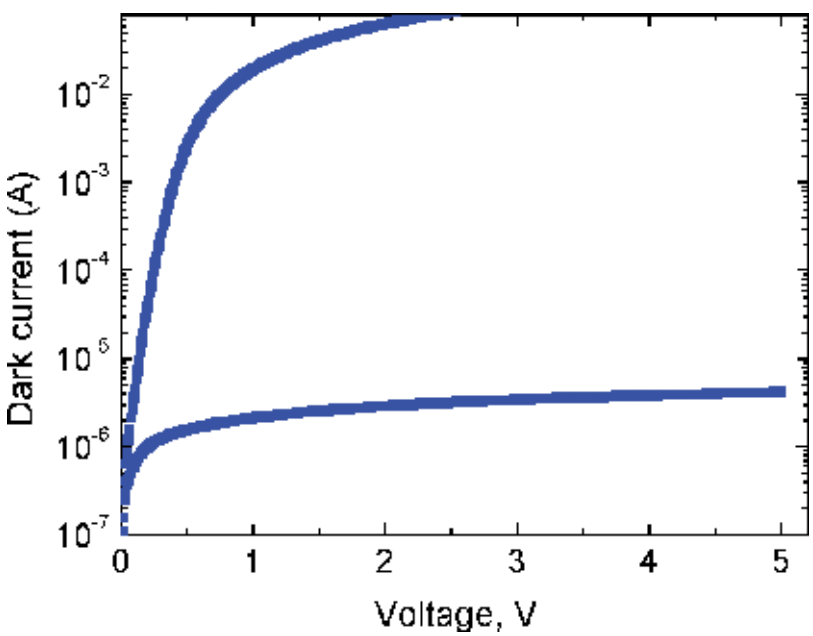

Figure 12. Current-voltage characteristic of FTO-Si photodetectors with 50 mm^2 area.

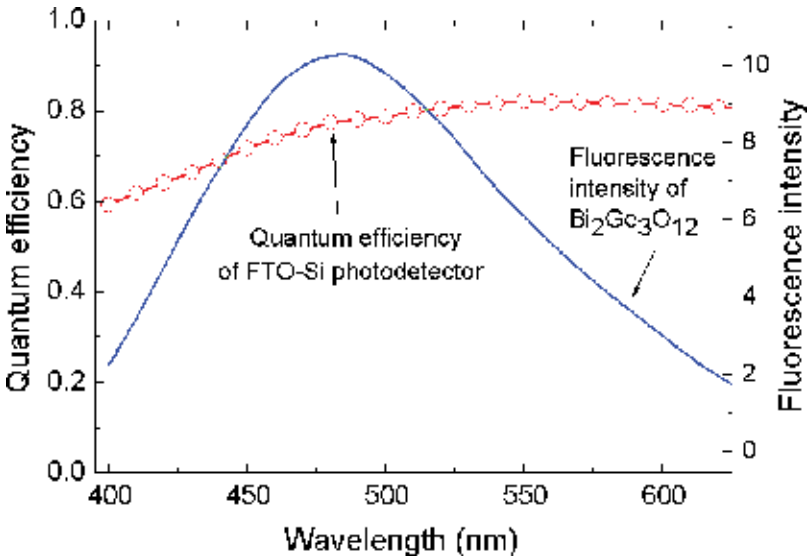

Figure 13. Illustration of optical matching of the photodetector with the scintillator.

Cooling of photodetectors up to 176 K reduces the dark current to a value around 10^{-10} A, while fluorescence lifetime of the scintillator (~ 3 ms) increases 10 times. Registration of low-level photocurrent produced by the photodetector under irradiation by γ-particles from ^{137}Cs was made by using a cooled preamplifier with noise of 250 e^- RMS.

Figure 14 shows recorded pulse height spectra when the photodetector with $Bi_4Ge_3O_{12}$ scintillator is irradiated from a137 Cs (Cs-137) source of γ-rays having energy of 661.5 keV. The registered signal is related to the main photon peak radiation from metastable nuclear isomer ^{137m}Ba (Ba-137). The energy resolution (FWHM/peak) is 16.5%. The FTO-Si photodetector with low noise amplifier was cooled to 176 K and operated at 5 V reverse voltage bias.

Figure 15 shows recorded pulse height spectra when the photodetector with $Bi_4Ge_3O_{12}$ scintillator is irradiated from 22Na (Na-22) source of γ-rays. The registered signals are related to two emission peaks, due to electron-positron annihilation (E_γ = 511 keV) and due to nuclear energy transition (E_γ = 1.27). The FTO-Si photodetector with low noise amplifier was cooled to 250 K and operated at 40 V reverse voltage bias.

Our silicon SB detectors of γ-rays fabricated by a simple and low-cost spray pyrolysis technique operate at low-voltage bias, and this is an advantage in comparison with much more expensive solid-state detectors based on cadmium telluride or mercuric iodide operating at reverse biases of order 100 V. Not cooled silicon detectors of γ-rays based on commercial Hamamatsu photodiodes (S1790-01) show low energy resolution of about 4% with 122 keV γ-rays from ^{97}Co radiation spectra [32].

http://dx.doi.org/10.5772/67469

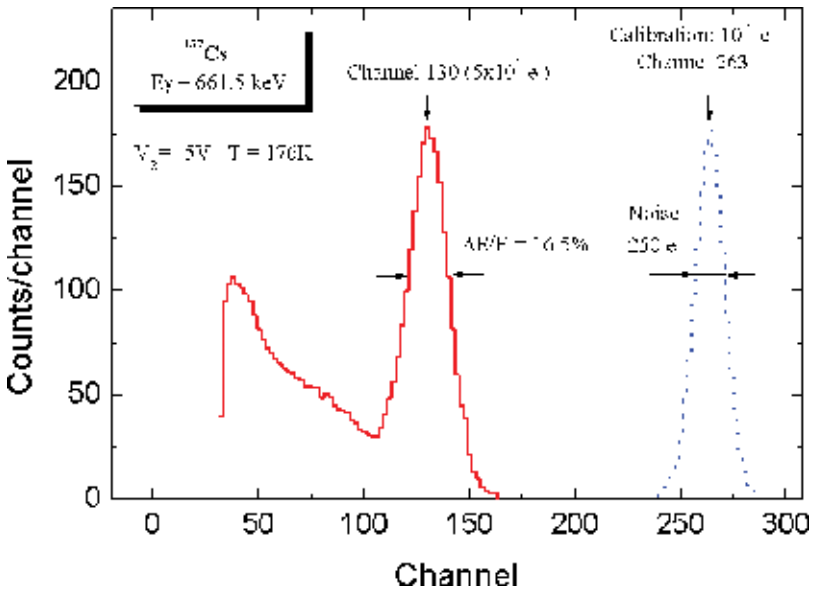

Figure 14. The pulse height spectra when $Bi_4Ge_3O_{12}$ scintillator is irradiated from 137Cs source of γ-rays having energy of 661.5 keV.

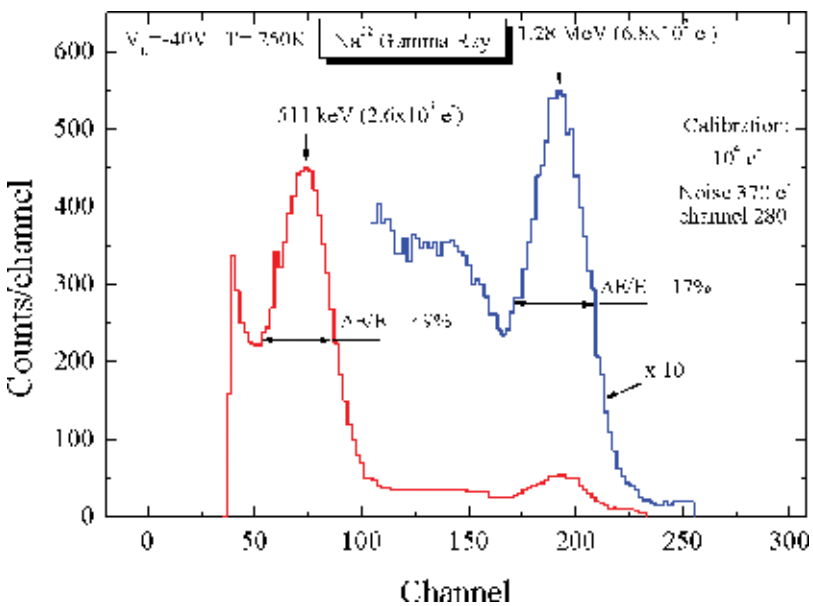

Figure 15. The pulse height spectra when $Bi_4Ge_3O_{12}$ scintillator are irradiated from 22Na source of γ-rays.

5.1.2. Radiation-resistant surface-barrier silicon photodetectors

Many technical applications require radiation-tolerant photodetectors that operate under high-energy particle irradiation, in particular under irradiation by reactor neutron at high flux of fast neutrons [33]. Commercial photodiodes such as the Hamamatsu Photonics photodiode S1723 was tested with respect to fast neutron radiation [34]. Significant changes of the leakage current and of the noise at a fluency of neutrons as low as 2.5×10^{10} n cm^{-2} were found. Damage also reduces the spectral sensitivity of the silicon photodiodes at long wavelengths due to a dramatic reduction of the minority lifetime.

Fast and radiation-resistant surface-barrier ITO-Si photodetectors have been fabricated using silicon epitaxial n-n$^+$ structures with 8 or 25 μm thick undoped epitaxial layer. The epitaxial layers with donor concentration 10^{13} cm^{-3} were grown by chemical vapor deposition on high-doped (10^{19} cm^{-3}) 300 μm n$^+$-silicon substrate. The silicon dioxide layer was grown on the surface of the epitaxial layer. An active device area (3–5 mm^2) was defined by chemically etching SiO_2 film. The ITO film as transparent conducting electrode with thickness of about 85 nm was deposited by spray pyrolysis method. A Cr/Ni metallic contact was deposited on the backside of n$^+$ substrate. The front metallic contact to ITO layer was created by the lift-off photolithography technique. After probing, the wafer with numerous fabricated devices was diced, and the chips were mounted on T0-8 body using silver epoxy.

The idea of the radiation-resistant photodiodes is based on existence of built-in electric field inside of the epitaxial silicon layer due to its nonuniform auto-doping as a result of the solid-state diffusion of antimony from the heavy-doped substrate during the growing process [35]. If built-in electric field is overlapped with the electric field inside the depletion layer, photogenerated minority carrier will be separated by a drift mechanism, and its recombination in defects formed by radiation will be negligible. Such photodetector will be high resistant to neutron flux even at zero bias.

An inhomogeneous impurity distribution of donors (N_D) inside the epitaxial layer estimated with capacitance-voltage (C-V) measurements [36] is shown in **Figure 16**, where the experimental points were approximated by two exponential curves (dotted lines). The doping variation in the epitaxial layer causes appearance of the built-in electric field $E = (kT/q)(1/N_D)(dN_D/dx)$.

The current-voltage characteristics of the ITO-Si photodetectors fabricated using 25 μm epitaxial silicon structures is shown in **Figure 17**.

In photodetectors with 25 μm epitaxial layer operating without voltage bias, a strong built-in electric field due to auto-doping effect does not overlapped with the electric field in depletion region. At that, part of photogenerated minority carriers needs to cross a distance without electric field by diffusion inside the epitaxial layer. However, after exposition under a neutron flux of about 10^{14} cm^{-3}, lifetime of the minority carriers is reduced from 36 μs to 12 ns, and photogenerated carriers recombine in this neutral area. For radiation resistance, thinner epitaxial layer needs to be used. **Figure 18** shows the spectral sensitivity of ITO-Si photodetectors at zero bias voltage fabricated on 8 μm epitaxial layers under irradiation by fast neutrons with flux of 3×10^{14} cm^{-2}.

http://dx.doi.org/10.5772/67469

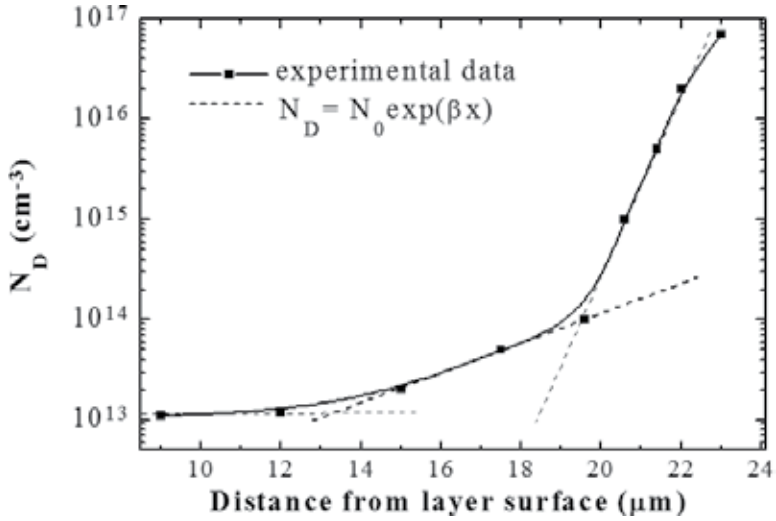

Figure 16. The donor concentration distribution inside the 25 μm epitaxial layer. Distance is shown from the epitaxial layer surface.

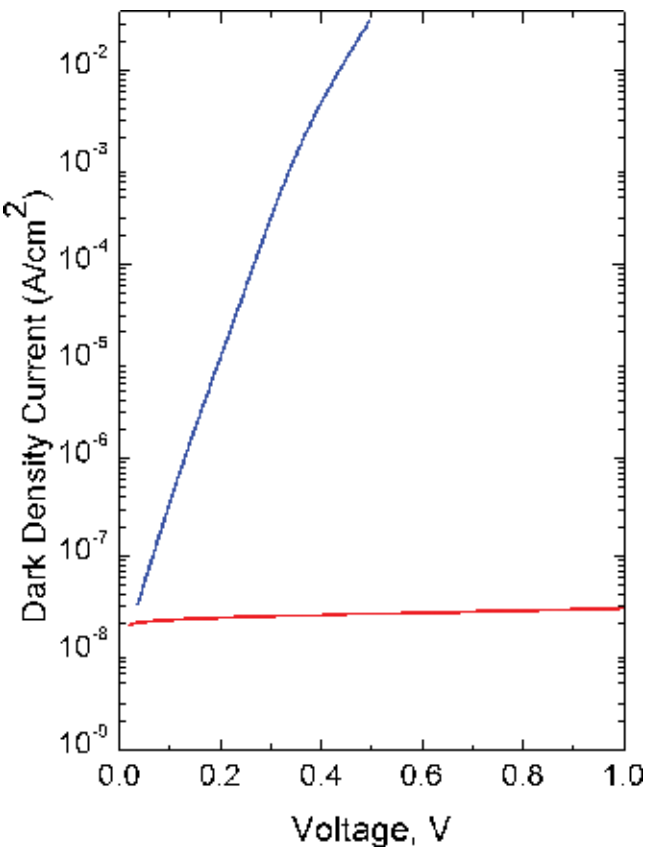

Figure 17. Current-voltage characteristics of ITO-Si photodetectors with an area of 3 mm².

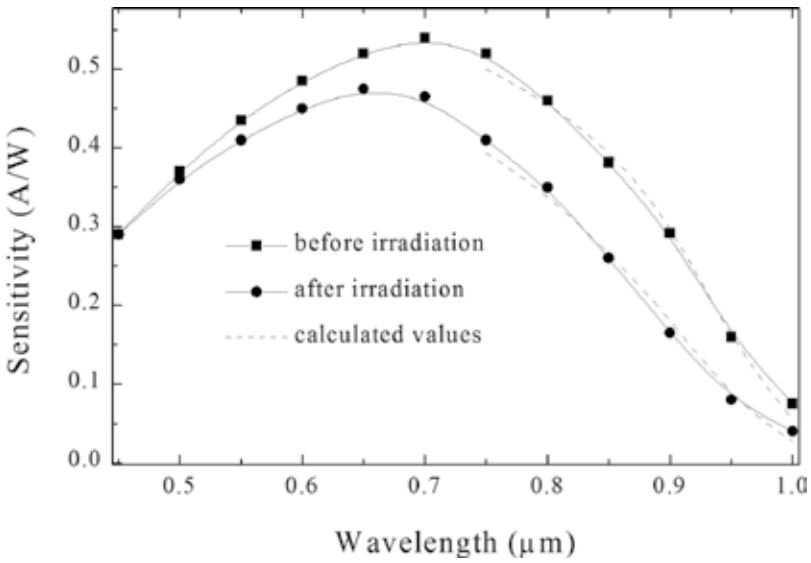

Figure 18. Spectral sensitivity of ITO-Si photodetectors at zero bias voltage fabricated on 8 μm epitaxial layers under irradiation by fast neutrons with a flux of 3×10^{14} cm^{-2}.

We suppose that ~20% reducing sensitivity of irradiated photodiodes in near-infrared spectral range is caused by lack of a contribution in photocurrent from carriers' photogenerated inside of heavy-doped silicon substrate. After neutron irradiation, such contribution is not significant in this spectral region due to a considerable shortage of the minority carrier lifetime. Thus, ITO-Si photodetectors with 8 μm epitaxial layers operating at zero voltage bias are extremely resistant to very big neutron flux. Photodetectors fabricated on the epitaxial layers with bigger thickness need to operate with the voltage bias. However, radiation damage produces an unacceptable level of the dark current because of dramatically reduction of the minority carrier lifetime. Devices with reported design can be used in optoelectronic equipment operating at hard radiation conditions without loss of their principal parameters.

6. Surface-barrier photodetectors for 1.3–1.55 μm

In this section, a new SB photodetector based on HgInTe-semiconductor compound. The development and improvement of fiber-optic communication system imply the use of high-speed and high-efficiency photodetectors. The transmission signal with a wavelength of 1.55 μm is especially important for long-distance communications. For this purpose, epitaxial layers of quaternary $In_xGa_{1-x}As_yP_{1-y}$ alloy with x = 0.57 and y = 0.95 are practically used for effective detector fabrication. Twenty-five years ago, the perspective of SB photodiodes based on $Hg_3In_2Te_6$ or mercury indium telluride (MIT) semiconductor has been shown [37–39]. The next years increasing interest in photodetectors based on this semiconductor [40–42]. The

http://dx.doi.org/10.5772/67469

$Hg_3In_2Te_6$ is a direct energy gap semiconductor with E_g = 0.72 eV at 300 K, close to germanium, and crystallizes in the zinc blend structure in which case 1/3 of all sites in the cationic sub-lattice are vacant. These stoichiometric vacancies with a concentration of about 10^{12} cm^{-3} determine unique properties of this semiconductor. It is inactive to dopants up to the doping concentration of 10^{20} cm^{-3} for fabrication p-n junctions, electrical properties of the MIT are indifferent to active defects [43], and material is high resistant to ionizing radiation [44]. The properties of the SB Au-MIT [40], Ni-MIT [41], and ITO-MIT [43] photodetectors were studied. In this section, electrical and optical properties of SB photodetectors on the base of the MIT single crystals with the ITO film as transparent conducting electrode deposited on chemically treated MIT surface are reported. Almost the same detectors in which the chemical treatment was changed on treatment in oxidizing RF plasma were patented recently in China [45], but their characteristics are not published.

The starting material for the photodetector fabrication was an *n*-type MIT mechanically and chemically polished wafer with carrier concentration of about 1×10^{13} cm^{-3}. The wafers were etched in 5% solution of Br_2 in N,N-dimethylformamide at the etching speed approximately of 0.3 μms^{-1}. The density of surface defects visible with a microscope was found as 30 cm^{-2}. After etching, wafers were boiled in azeotropic acetonitrile-based mixture and dried in N_2 atmosphere. The roughness of surface after the abovementioned polishing was determined as 0.03 μm.

The attempts to form a Schottky potential barrier on the MIT surface directly by the deposition of the ITO film lead to a weak rectifying nature of the ITO-MIT contact. The best rectifying characteristic has been observed if the ITO deposition was performed on a thin (0.02–0.03 μm) oxide layer chemically grown on the MIT surface. For chemical growth of oxide layer on the MIT surface, wafer was dipped on a few minutes in (1:1:1) solution prepared H_2O_2, N,N-dimethylformamide, and NH_4OH, previously heated to beginning of intensive foaming. The oxide thickness was measured using an ellipsometer. The chemically grown oxide composition was studied by X-ray photoelectron spectroscopy (XPS) [39]. Results of measurements are shown in **Figure 19**.

Analysis of XPS peaks corresponding the binding energies of the In $3d_{5/2}$, Te $3d_{5/2}$, and Hg 4f at 444.8 eV, 576.4 eV, and 100.7 eV, respectively, allows estimating the oxide composition: 40 at. % In_2O_3, 50 at. % TeO_2, and 10 at. % HgO. Almost the same oxide content was reported in Ref. [45], where the oxide layer was fabricated by RF plasma oxidation. The ITO film can be deposited on the oxide surface by spray pyrolysis technique or by sputtering.

In this work, we focused our attention on two SB photodetector types, fabricated on the thick (700 μm) and the thin (70 μm) MIT substrates. Typical current-voltage characteristic of ITO-oxide-MIT photodetectors with 3 mm^2 active area is shown in **Figure 20**.

Density of the dark current is almost the same as reported in [40, 41], but the spectral external quantum efficiency of the ITO-oxide-MIT photodetectors is more than 90% (**Figure 21**) and very differs from one reported for the Au-MIT [40] and Ni-MIT [41] Schottky-based photodetectors with 20–50% quantum efficiency.

Note that the quantum efficiency of ITO-MIT photodetectors with the ITO film deposited by sputtering on the MIT surface without specially created oxide layer is only about 60% [46].

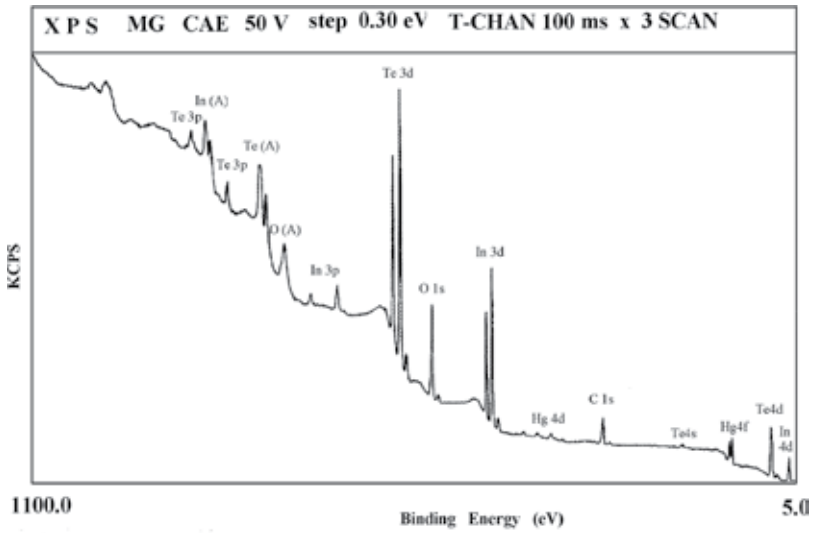

Figure 19. XPS spectrum of chemically grown oxide on the MIT surface.

The time response characteristic of the photodetectors fabricated using 70 μm thick MIT wafers measured at the reverse voltage bias of 120 V irradiated by laser pulse with 1.3 μm wavelength is shown in **Figure 22**.

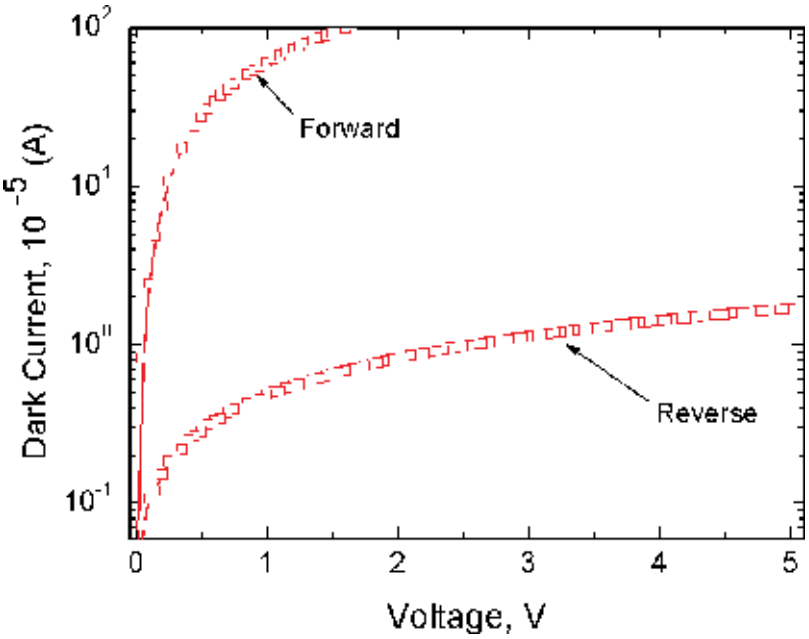

Figure 20. The current-voltage characteristic of ITO-oxide-MIT photodetectors with 3 mm^2 active area.

http://dx.doi.org/10.5772/67469

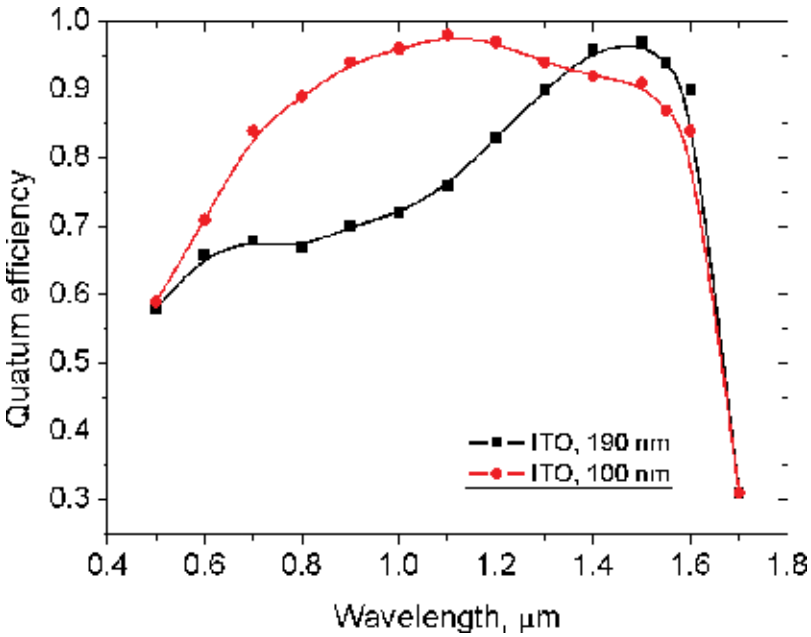

Figure 21. The spectral external quantum efficiency of the ITO-oxide-MIT photodetectors for two thicknesses of the ITO film.

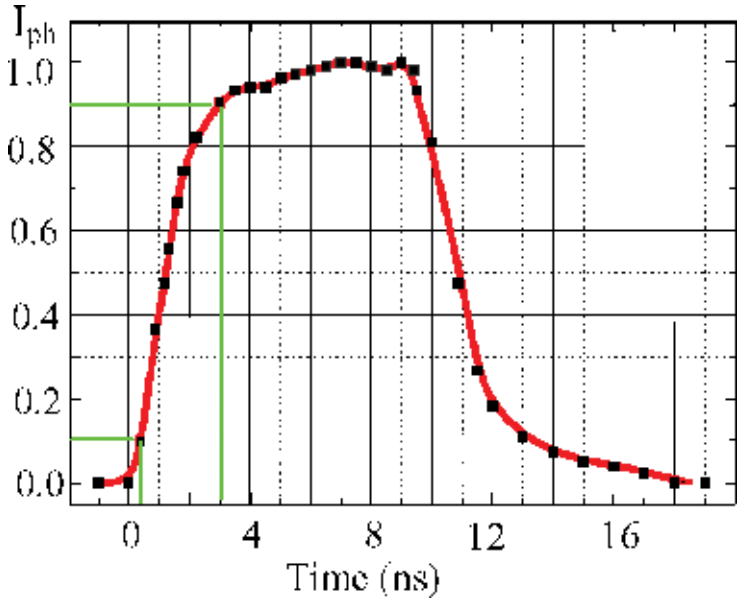

Figure 22. The time response characteristic of the 70 μm thick MIT photodetectors with 3 mm² area at a reverse voltage bias of 120 V irradiated by a laser pulse with 1.3 μm wavelength.

7. Conclusions

We presented the properties of surface-barrier photodiodes suitable for a wide spectral range and fabricated using a simple and low-cost spray deposition method that does not require expensive technological equipment. Of course, in this short report, it was not possible to describe in detail some technological aspects, such as the chemical treatment of the semiconductors used for the photodetectors. Readers can found further information in the works referenced in this chapter. The aim of this work was to review illustratively a simple technological method for the fabrication of high-efficiency surface-barrier photodiodes for applications in a wide spectral range, from UV to near infrared, using different semiconductor materials. This method has been successfully used for the fabrication of high-efficiency silicon solar cells whose characteristics have already been reported [47].

Author details

Oleksandr Malik* and Francisco Javier De la Hidalga-Wade

*Address all correspondence to: amalik@inaoep.mx

Electronics Department, Instituto Nacional de Astrofísica, Óptica y Electrónica (INAOE), Puebla, Mexico

References

[1] R. T. Tung. The physics and chemistry of the Schottky barrier height. Appl. Phys. Rev. 2014; 1: 1-55.

[2] S. J. Fonash. Solar cell device physics. Academic Press. NY 1981: 331 p. ISBN 0-12-261980-3.

[3] A. L. Dawar, J. C. Joshi. Review semiconducting transparent thin films: their properties and applications. J. Mater. Sci. 1984; 19: 1-23.

[4] J. DuBow, D. Burk, and J. Sites. Efficient photovoltaic heterojunctions of indium tin oxides on silicon. Appl. Phys. Lett. 1976; 29(8): 494-496.

[5] J. Manifacier, L. Szepessy. Efficient sprayed In_2O_3 n-type silicon heterojunction solar cell. Appl. Phys. Lett. 1977; 31; 459-462.

[6] T. Feng, A. K. Ghosh, and C. Fishman. Spray deposited high efficiency SnO_2-silicon solar cells. Appl. Phys. Lett. 1979; 35(3): 266-268.

[7] A. Malik, V. Baranyuk, and V. Manasson. Solar cells based on the SnO_2-SiO_2-Si heterojunction. Appl. Sol. Energy. 1979; 2: 83-84. ISSN: 0003-701x.

[8] A. Malik, V. Baranyuk, and V. Manasson. Improved model of solar cells based on In_2O_3/SnO_2-SiO_x-nSi structures. Appl. Solar Energy. 1980; 1:1-2.

[9] S. Ashok, P. Sharma, and S. Fonash. Spray-deposited ITO-silicon SIS heterojunction solar cells. IEEE Trans. Electron. Dev. 1980; ED-27(4): 725-730.

[10] O. Malik, F. J. De la Hidalga-W, C. Zúñiga-I, and G. Ruíz-T. Efficient ITO-Si solar cells and power modules fabricated with a low temperature technology: results and perspectives. J. Non Cryst. Solids. 2008; 354: 2472-2477.

[11] O. Malik, F. J. De la Hidalga-W, C. Zúñiga-I, and G. Ruíz-T. Efficient ITO-Si solar cells and power modules fabricated with a low temperature technology: results and perspectives. J. Non Cryst. Solids. Elsevier. 2008; 354: 2472-2477.

[12] J. B. Mooney, S. B. Radding. Spray pyrolysis processing. Ann. Rev. Mater. Sci. 1982; 12: 81-101.

[13] O. Malik, F. J. De la Hidalga-Wade. Comparison of tin-doped indium oxide films fabricated by spray pyrolysis and magnetron sputtering. Cryst. Res. Technol. 2015; 50(7): 516-521.

[14] O. Malik, F. J. De la Hidalga-Wade, and R. Ramírez Amador. Fluorine-doped tin oxide films with a high figure of merit fabricated by spray pyrolysis. J. Mater. Res. 2015; 30(13): 2040-2045.

[15] G. Haacke. New figure of merit for transparent conductors. J. Appl. Phys. 1976; 47: 4086-4089.

[16] E. Burstein. Anomalous optical absorption limit in InSb. Phys. Rev. 1954; 93: 632-633.

[17] A. Malik, A. Seco, E. Fortunata, and R. Martins. New UV-enhanced solar blind optical sensors based on monocrystalline zinc sulphide. Sens. Actuators A. 1998; 67: 68-71.

[18] V. Machnii, A. I. Malik, and N. Melnik. Solar blind photodiode based on ITO/ZnS heterostructures. Sov. Phys. Tech. Phys. 1990; 60: 146-147.

[19] D. Caputo, G. de Cesare, F. Irrera, and F. Palma. Solar-blind UV photodetectors for large area applications. IEEE Trans. Electron. Devices. 1966; 43: 1351-1356.

[20] A. I. Malik, G. G. Grushka. Optoelectronic properties of metal oxide-gallium phosphide heterojunctions. Sov. Phys. Semicond.. 1991; 25(10): 1017-1020. ISSN 0038-5700.

[21] A. Malik, A. Seco, E. Fortunato, R. Martins, B. Shabashkevich, and S. Piroszenko. A new high ultraviolet sensitivity FTO-GaP Schottky photodiode fabricated by spray pyrolysis. Semicond. Sci. Technol. 1998; 13: 102-107.

[22] Yu. Vygranenko, A. Malik, M. Fernandes, R. Schwarz, and M. Vieira. UV-Visible ITO/GaP photodiodes: characterization and modeling. Phys. Status. Sol. A. 2001; 185(1): 137-144.

[23] A. I. Malik, B. Shabashkevich, and S. Piroszenko. Photodiode for the ultraviolet spectral range. Patent of Ukraine N. 71544.

[24] O. Malik, F. J. De la Hidalga-Wade, C. Zuniga-Islas, and J. Abundus Patiño. UV-sensitive optical sensors based on ITO-gallium phosphide heterojunctions. Phys. Status Sol. C. 2010; 7(3-4): 1176-1179.

[25] A. N. Pikhtin, S. A. Tarasov, and B. Kloth. Ag-GaP Schottky photodiodes for UV sensors. IEEE Trans. Electron. Dev. 2003; 50(1); 215-217.

[26] V. C. Boutenko, Y. G. Dobrovolskiy, S. I. Piroszenko, B. Shabashkevich, V. G. Yoriev. Radiometer of power luminosity in the ultraviolet spectral range. Patent of Ukraine N. 82843.

[27] E. Ahlstrom. W. W. Gartner. Silicon surface barrier photocells. J. Appl. Phys. 1962; 33(8): 2602-2606.

[28] A. J. Tuzzolino, E. L. Hubbard, M. A. Perkins, and C. Y. Fan. Photoeffects in silicon surface-barrier diodes. J. Appl. Phys. 1962; 33(1): 148-155.

[29] H. Kato, J. Fujimoto, T. Kanda, A. Yoshida, and T. Arizumi. SnO_2-Si photosensitive diodes. Phys. Status Sol. A. 1975; 32: 255-261.

[30] A. Malik, R. Martins. Metal oxide/silicon heterostructures: new solution for different optoelectronic applications. MRS Proc. 1997; 487: 375-380.

[31] A. Malik, M. Vieira, and M. Fernandes. Surface-barrier Si-based photodetectors fabricated by spray pyrolysis technique. Philosophical Mag. B. 2000; 80(4); 781-790.

[32] C. Bilton, S. Hedges, P. R. Hobson, and D. C. Imrle. Low-cost silicon photodiodes for X-ray detection. J. Phys. E Sci. Instrum. 1988; 21: 809-811.

[33] M. Hasegawa, S. Mori, T. Ohsugi, H. Kojima, A. Taketani, T. Kondo, and M. Noguchi. Radiation damage of silicon junction detectors by neutron irradiation. Nucl. Instrum. Methods. 1989; A277: 395-400.

[34] W. Dabrowski, K. Korbel, and A. Skoczeń. Fast neutron damage of silicon PIN photodiodes. Nucl. Instrum. Methods Phys. Res. A. 1991; 301(2): 288-294.

[35] B. A. Joyce, J. C. Weaver, and D. J. Maule. Impurity redistribution processes in epitaxial silicon layers. J. Electrochem. Soc. 1965; 112(11): 1100-1106.

[36] P. J Baxandall, D. J Colliver, and A. F Fray. An instrument for the rapid determination of semiconductor impurity profiles. J. Phys. E Sci. Instrum. 1971; 4: 213-221.

[37] A. I. Malik, G. G. Grushka, and N. R. Tevs. High-efficiency measuring photodiodes based on mercury indium telluride. Sov. Tech. Phys. 1990; 35: 723-726.

[38] A. I. Malik, G. G. Grushka. Self-calibrated radiometric IR photodiode based on the defect semiconductor $Hg_3In_2Te_6$ for the spectral range 0.85-1.5 μm. Sov. Tech. Phys. 1990; 35: 1227-1231.

[39] A. I. Malik, M. Vieira, M. Fernandes, F. Macarico, and Z. Grushka. Near-infrared photodetectors based on HgInTe-semiconductor compound. Proc. SPIE. Photodetectors: Materials and Devices IV. 1999; 3629: 433-442.

[40] L. A. Kosyachenko, Yu. S. Paranchich, V. N. Makagonenko, V. M. Sklyarchuk. E. F. Sklyarchuk, and I. I. German. Electrical performance of HgInTe surface-barrier photodiodes. Tech. Phys.. 2003; 48(5): 647-650.

[41] L. A. Kosyachenko, I. S. Kabanova, V. M. Sklyarchuk, O. F. Sklyarchuk, and I. M. Rarenko. $Hg_3In_2Te_6$-based photodiodes for fiber optic communication. Phys. Status Solidi A. 2009; 206(2): 351-355.

[42] L. Zhang, X. L. Zhang, W. G. Sun, and Z. X. Lu. Proc. SPIE. 2011; 8193: 1-6.

[43] O. L. Maslyanchuk, L. A. Kosyachenko, I. I. German, I. M. Rarenko, V. A. Gnatyuk, and T. Aoki. Electrical and optical properties of $Hg_3In_2Te_6$ single crystals. Phys. Status Solidi C. 2009; 6(5): 1154-1157.

[44] O. G. Grushka, V. T. Maslyuk, S. M. Chupyra, O. M. Mysliuk, S. V. Bilichuk, and I. I. Zabolotskiy. The effect of irradiation with electrons on the electrical parameters of $Hg_3In_2Te_6$. Semiconductors. 2012; 46(3): 312-314. ISSN 10637826.

[45] Te-In-Hg photoelectronic detector chip manufactured method. Patent of China N. CN101060144A 2014.

[46] L. A. Kosyachenko, I. M. Rarenko, E. F. Sklyarchuk, I. I. German, and Sun Weiguo. Electrical characteristics of the ITO/HgInTe photodiodes. Semiconductors. 2006; 40(5): 554-557.

[47] O. Malik, F. J. De la Hidalga-W. Physical and technological aspects of solar cells based on metal oxide-silicon contacts with induced surface inversion layer. In: Application of solar energy, R. Rugescu Editor. 2013. Intech, Croatia. ISBN 978-953-51-0969-3.

Chapter 16

Spectral Responses in Quantum Efficiency of Emerging Kesterite Thin-Film Solar Cells

Sanghyun Lee and Kent J. Price

Additional information is available at the end of the chapter

http://dx.doi.org/10.5772/68058

Abstract

The spectral responses in quantum efficiency provide essential information about current generation, recombination, and diffusion mechanisms in a photodetector, photodiode, and photovoltaic devices as the quantum efficiency is a function of the voltage and light biases and the spectral content of the bias light and/or location of the devices. Recently, P-type Kesterite thin-film solar cells are emerging as they have a high absorption coefficient ($>10^4$ cm^{-1}) and ideal direct bandgap (1.4–1.5 eV), which make them a perfect candidate for photovoltaic application. However, a champion device from Zincblende (CdTe) or Chalcopyrite (CIGS) solar cells shows ~21% efficiency (<21.5%, First Solar and <21.7%, ZSW, respectively) while Kesterite devices suffer from severe losses with <12.6% efficiency. Furthermore, the maximum theoretical efficiency based on Shockley-Queisser limit is about 32.2%, which indicates there is much room for the improvement. Consequently, the implication from the current situation highlights the need for a systematic analysis of the loss mechanism in Kesterite devices. In this work, we carried out a systematic study of the efficiency limiting factors based on quantum efficiency to model the quantum efficiency response of current CZTSSe thin-film solar cells. This will provide the guidance for proper interpretation of device behaviors when it is measured by quantum efficiency.

Keywords: solar cells, thin film, spectral response, quantum efficiency, photovoltaics

1. Introduction

Recently, polycrystalline thin-film CdTe and $Cu(In,Ga)Se_2$ (CIGS) solar cells are commercially successful with dramatic conversion efficiency improvements and cost reduction in module mass production as well as the balance of system (BoS), which is the cost except the module production cost. A champion device from CdTe (Zincblende) and CIGS (Chalcopyrite) solar cells shows >21%

efficiency (<21.5%, First Solar and < 21.7%, ZSW, respectively). However, some of these materials used in thin-film solar cells technology are not benign to the environment, which cause toxicity issues and possible scarce in the earth's crust, whereas competing Si solar cell technology uses the second most abundant element, Silicon, in the earth's crust. To fully facilitate the advantage of low manufacturing cost in the polycrystalline thin-film solar cells technology, a research on Kesterite solar cells using earth's abundant materials has gained momentum to pursue low-cost, environment-friendly, and highly efficient Kesterite photovoltaic devices [1–4]. P-type Kesterite solar cells have high absorption coefficient, 10^4 cm^{-1} and ideal direct bandgap (1.0–1.5 eV), which make them a perfect candidate for photovoltaic application [1–6]. Kesterite solar cells are also called CZTSSe (Copper Zinc Tin Sulphur Selenium) solar cells following the crystal structure. However, the record power conversion efficiency is 12.6% with laboratory-level samples [1, 6], which are processed with non-vacuum-based techniques. Since the development is in an early stage, the development of Kesterite solar modules is not considered yet due to incompetence in the market. However, the maximum theoretical efficiency based on Shockley-Queisser limit is about 32.2%, which indicates there is much room for improvement and hence many opportunities [7, 8].

To reduce the discrepancy between actual and maximum possible efficiency, there are major issues that need to be addressed such as absorber quality (electronic band structure, secondary phases, defect concentration, grain boundaries, optical property), CdS or (CdS-less) buffer quality, Molybdenum (Mo) back contact quality, and the quality of interfaces. One of the main challenges is different types of recombination processes at different interfaces such as buffer/window, heterojunction, and absorber/back contact. At these interfaces, recombination active defects are present due to intrinsic lower symmetry effects [9], lattice mismatch, band tails (still open discussion) [10–13], and segregation of impurities aggravated by grain boundaries, which are inevitable for polycrystalline solar cells. The recombination current enhances forward diode current that deteriorates the conversion efficiency, which is inevitable for polycrystalline Kesterite solar cells. The recombination current enhances forward diode current which worsens the conversion efficiency, which is one of the reasons to have lower open circuit voltage (*Voc*). Open circuit voltage results from the forward bias owing to the bias of the solar cell junction with the light-generated current. This is a point where diode current is equivalent to light-generated current (J_L), affected by the saturation current (J_0) of the solar cell. Since *Voc* is expressed through the saturation current as $Voc = (kT/q)\ \ln[(J_L/J_0) + 1]$, *Voc* depends on the recombination in the device, which is strongly dependent on the saturation current. Another factor that influences the diode saturation current is a function of the bandgap, which increases with bandgap.

Despite a recent significant improvement in Kesterite solar cells, one of the most fundamental problems that remain is lower *Voc* [14–17]. Moving *Voc* beyond 750 mV in Kesterite solar cells requires improvements in both built-in voltage and recombination. At the heterojunction of thin-film solar cells, the recombination that contributes to the diode current can occur on different recombination paths. Recombination may occur at the heterojunction interface, in the space charge region (SCR), in the quasi-neutral region (QNR), and at the back contact. In particular, the interface and near-interface recombination (SCR) mainly contribute to the recombination current, which is influenced by a number of recombination active defects and grain boundaries, the number of minority carriers at the junction edge, and diffusion length. One way to characterize the dominant recombination path is the quantum efficiency analysis.

http://dx.doi.org/10.5772/68058

In this chapter, we present the study of photocurrent loss mechanism based on analytical and numerical models of quantum efficiency, which provide insights into the generation and transport of carriers in the CZTSSe solar cell. Numerical models are computational results of solving continuity equation and Poisson equation, whereas analytical models are based on key parameters such as the lifetime of carriers, depletion width, diffusion length and drift length, surface recombination velocity, and thickness of the absorber layer. Key parameters of CZTSSe solar cells are focused to quantitatively describe the spectral responses of quantum efficiency by considering the recombination losses near or at the CdS/CZTSSe interface as well as the CZTSSe absorber layer. The dependency of charge collection efficiencies in the space charge region and CZTSSe absorber is discussed with respect to uncompensated impurity concentration, defect energy state, drift and diffusion components of short circuit current, and recombination velocities.

2. Analytical description of spectral responses in quantum efficiency

For this analytical study, we developed the collection efficiency model for thin-film solar cells and put in the mathematical expression. The external quantum efficiency, $EQE(\lambda, V)$ is the ratio of the number of charge carriers collected by the photovoltaic device to the number of photons of a given wavelength or energy onto the device. When the various wavelengths of light in the spectrum are applied, quantum efficiency corresponds to the spectral responses (amperes per watt) of solar cells per unit area, unit second, unit wavelength (Remember the units in solar spectra radiation).

$$EQE(\lambda, V) = \frac{I_{ph}}{q\Phi_p} = \frac{I_{ph}}{q}\left(\frac{h\upsilon}{P_{opt}}\right) \tag{1}$$

where I_{ph} is the photocurrent, Φ_p is the photon flux which is equivalent to $P_{opt}/h\nu$, and P_{opt} is the optical power.

The external quantum efficiency is related to transmission, $T(\lambda)$ of all the materials prior to CZTSSe absorber film, which consists of anti-reflection coating (ARC), transparent conducting front contact oxide (TCO), a buffer layer, and an n-type CdS layer. The internal quantum efficiency, $IQE(\lambda, V)$ is associated with the external quantum efficiency as follows.

$$EQE(\lambda, V) = \left(1 - R_{AFC}(\lambda)\right) \cdot T_{TCO}(\lambda) \cdot T_{buffer}(\lambda) \cdot T_{CdS}(\lambda) \cdot IQE(\lambda, V) \tag{2}$$

where T_{TCO} is the transmission of transparent conduction oxide (TCO), T_{buffer} is the transmission of buffer (ZnO), and T_{CdS} is the transmission of CdS.

2.1. Experimental details

In **Figure 1**, the quantum efficiency spectra of the CZTSSe solar cell are measured from 300 to 1400 nm. The cell design is based on the common substrate structure, which consists of soda-lime glass (SLG)/Molybdenum (Mo) layer followed by depositing CZTSSe film (1.8–2.0 um).

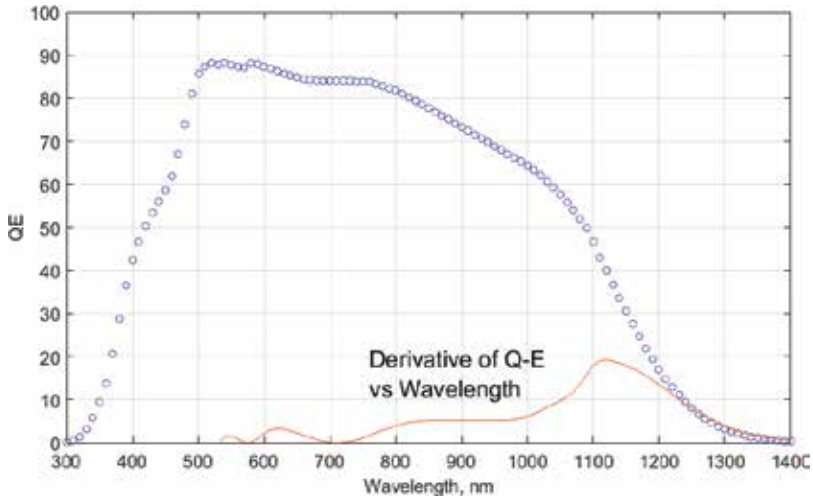

Figure 1. Spectral responses of the external quantum efficiency of a CdS/CZTSSe device measured from 300 to 1400 nm.

The buffer CdS was developed by 0.05 μm and intrinsic ZnO (0.05–0.1 μm) is deposited to prevent damage during ITO deposition at the post-ZnO deposition. Indium tin oxide (ITO) is deposited (350–400 nm) as a transparent conductive window layer; the device is completed with Ni/Al front metal fingers and MgF_2 ARC.

The spectral responses of this sample were characterized in the range of 300–1400 nm with Xenon arc lamp and the spectral distribution of the photon flux at the outlet slit was calibrated with NIST calibrated photodiode G425.

In the wavelength region 300–500 nm, measured spectral responses from the devices demonstrate typical CdS layer response, which agrees with the literature [1–5]. Above 500 nm, the measured spectral response is limited by the band gap of CZTSSe, λ_{Eg} (= hv/Eg). The bandgap calculated from the derivative of Q-E is 1.11 eV for this device and the total quantum efficiency-calculated short circuit current is 33.59 mA/cm^2. Across wavelength regions, the overall reduction in the quantum efficiency in **Figure 1** is due to the grid shading and front surface reflection as described in the literature [18]. Between 300 and 500 nm, the widely accepted loss mechanisms in quantum efficiency are TCO/ZnO absorption and CdS buffer absorption. Higher the transmission of light through TCO, ZnO, and CdS, lower the quantum efficiency losses. Hence the transmission in Eq. (2) needs to be minimized to maximize the spectral response from the device.

2.2. Energy band diagram

Under the steady-state illuminated condition, we derive the total current density under the applied biased conditions. One of the important parameter sets that determines the spectral responses in photovoltaic devices is the space charge region width, *W*. Although it is widely accepted that CdS does not fundamentally contribute photogenerated current, any changes in effective donor impurity concentration or uncompensated impurity (N_d-N_a) and photoconductivity of CdS buffer layer

http://dx.doi.org/10.5772/68058

greatly impact the space charger region due to an asymmetrical p-n heterojunction nature. In fact, there are a number of defects in CdS, which contribute to the increase of effective uncompensated donor concentration. In this case, the depletion layer of n-CdS/p-CZTSSe is located in almost all the p-CZTSSe absorber layer, which is fundamentally similar to an abrupt n+/p junction diode or a Schottky diode. Following the band structure [19], the depletion width (**Figure 2**) in the n-CdS/p-CZTSSe is derived as follows [20].

$$W = \sqrt{\frac{2\epsilon\epsilon_r(\phi_0 - qV)}{q^2(N_a - N_d)}} \tag{3}$$

where ϵ_r is the relative permittivity, ϵ is the permittivity of free space, $\phi_0 = qV_{bi}$ is the barrier height at the absorber side (V_{bi} is the built-in potential), V is the applied voltage, and $N_a - N_d$ is the uncompensated acceptor concentration in the CZTSSe absorber layer.

2.3. Analytical description of bias-dependent quantum efficiency

Under the steady-state illuminated condition, we derive the total current density under widely accepted assumptions, which are no thermal generation current and no photocurrent contribution by n-type CdS layer. Hence, the electron-hole generation rate by absorption is described by the below.

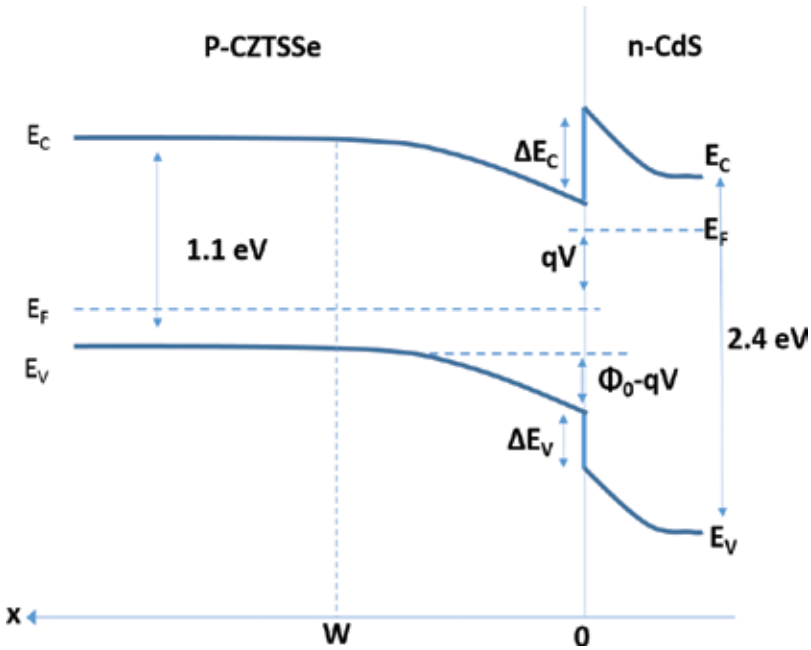

Figure 2. Energy band diagram of n-CdS/p-CZTSSe heterojunction at biased condition (V).

$$G_e(x) = \Phi_p \alpha \exp(-\alpha x) \tag{4}$$

where Φ_p is the incident photon flux per unit area and α is the absorption coefficient of CZTSSe.

To isolate non-transmission terms in the quantum efficiency Eq. (2), we distinguish $EQE(\lambda, V)$ and $IQE(\lambda, V)$ so that we will be able to focus on developing a model for carrier collection function with $IQE(\lambda, V)$. As mathematically derived by Gartner [21] and Sze [20] with boundary conditions, quantum efficiency is the sum of a drift component in the space charge region and a diffusion component in the quasi-neutral region. After simplifying the exact solution of Lavagna's model [22], Kosyachenko derived IQE [23].

$$IQE = \frac{1 + \frac{S}{D_n}\left(\alpha + \frac{2}{W} \cdot \frac{qV_{bi} - qV}{kT}\right)^{-1}}{\frac{S}{D_n}\left(\frac{2}{W} \cdot \frac{qV_{bi} - qV}{kT}\right)^{-1}} - \frac{\exp(-\alpha W)}{1 + \alpha L_n} \tag{5}$$

With the assumption of an abrupt p-n junction, the internal quantum efficiency is described based on the widely accepted Gartner formula [21, 22] as no significant contribution of electron collection by CdS is expected [23, 24].

$$IQE = 1 - \frac{\exp(-\alpha W)}{1 + \alpha L_n} \tag{6}$$

where W is the space charge region width and L_n is the diffusion length of the electron ($\sqrt{D_n \tau_n}$). Photogenerated carriers in the space charge region are assumed to be completely collected as a drift component after integrating the drift current (J_{drift}) [20].

$$J_{drift} = -q\int_0^W \phi_0 \alpha \exp(-\alpha x) dx = q\phi_0\{1 - \exp(-\alpha W)\} \tag{7}$$

$$IQE_{drift} = 1 - \exp(-\alpha W) \tag{8}$$

Photogenerated carriers outside of space charge region are collected by the diffusion process with no electric field [22] as follows.

$$IQE_{diff} = IQE - IQE_{drift} = 1 - \frac{\exp(-\alpha W)}{1 + \alpha L_n} - \{1 - \exp(-\alpha W)\} = \frac{\exp(-\alpha W)}{1 + 1/\alpha L_n} \tag{9}$$

Consequently, the total internal quantum efficiency is the sum of Eqs. (8) and (9). With complete collection of the carrier in the space charge region, EQE is revised after introducing the interface recombination term.

$$EQE(\lambda, V) = \left(1 - R_{ARC}(\lambda)\right) \cdot T_{TCO}(\lambda) \cdot T_{buffer}(\lambda) \cdot T_{CdS}(\lambda) \cdot IQE(\lambda, V) \cdot h(v) \tag{10}$$

$$h(v) = \left(1 + \frac{S_{junction}}{\mu_e E_{junction}}\right)^{-1} \tag{11}$$

where *h(V)* is the interface recombination function due to the lattice mismatch between CdS and CZTSSe absorber, $IQE_{absorber}$ is the internal quantum efficiency of CZTSSe absorber [25], and $S_{junction}$ is the surface recombination velocity, μ_e is electron mobility, and $E_{junction}$ is the electric field at the junction.

However, a complete collection model in the space charge neglects including the space charge region recombination, and a couple of researchers identified that significant uncompensated acceptors and defects cause the recombination in the space charge region [23]. Hardrich revised a collection function (CF_{SCR}) [24] for space charge region with the hypothesis of constant field.

$$CF_{SCR\_CEF} = \exp\left(-\frac{t}{\tau_e}\right) = \exp\left(-\frac{2x}{\mu_e \tau_e E_{max}}\right) = \exp\left(-\frac{x}{L_{drift}}\right) \tag{12}$$

where τ_e is the lifetime of the electron minority carrier in the p-doped CZTSSe absorber, t is the time, constant electric field (CEF) is assumed as half of maximum ($E_{max}/2$), and L_{drift} is defined as $\mu_e \tau_e E_{max}/2 = \mu_e \tau_e (V_{bi} - V)/W$. Hence, $IQE_{absorber}$ in the space charge region under constant field yields,

$$IQE_{drift\_CEF} = \int_0^W \alpha exp(-\alpha x) \cdot \exp\left(-\frac{x}{L_{drift}}\right) dx \tag{13}$$

$$IQE_{drift\_CEF} = \frac{L_{drift}}{L_{drift} + (1/\alpha)} \cdot \left\{1 - \exp\left(-W.\left(\alpha + \frac{1}{L_{dirft}}\right)\right)\right\} \tag{14}$$

However, the electric field in the space charge region is not constant. Assuming constant doping at the junction, it linearly decreases along the depth of the CZTSSe absorber. Constant doping does not reflect the exact real situation of the doping profile due to doping concentration fluctuation with grain boundaries, fixed charges, impurities, and so on. We mathematically simplify the case with the linear electric field (LEF) at the junction. Hence, we are able to develop an alternative expression for the linearly decreasing electric field in the space charge region. An alternative expression for the collection in the space charge region begins with the definition of the drift velocity, assuming the one-dimensional charge movement, which limits the lateral movement caused by non-uniformity. To simplify the mathematical processes, we define new x-coordinate, $x' = 0$ at the interface between the space charge region and the quasi-neutral region (x' = W-x). Therefore, the drift time for the electron is as below.

$$t_{drift} = \int_0^{t_{drift}} dt = \int_x^W \frac{1}{v_{x'}} dx' = \int_{x'}^W \frac{1}{\mu_e E(x')} dx' \tag{15}$$

where an electron generated at point x′ is swept to the edge of the space charge region. The electric field inside the space charge region decreases linearly toward the quasi-neutral region of the p-type absorber layer and *E(x′)* can be revised to be *Emax·(x′/W)*.

$$t_{drift} = \int_{x'}^{W} \frac{dx'}{(E_{max}\mu_e/W)\cdot x'}\, dx' = \frac{1}{E_{max}\mu_e/W} ln\left(\frac{W}{x'}\right) \tag{16}$$

$$CF_{SCR\_LEF} = exp\left(-\frac{t_{drift}}{\tau_e}\right) = exp\left(-\frac{W}{\mu_e\tau_e E_{max}} ln\left(\frac{W}{x'}\right)\right) = \left(\frac{x'}{W}\right)^{\frac{W}{\mu_e\tau_e E_{max}}} \tag{17}$$

By defining κ ($= \mu_e\tau_e E_{max}$), the collection function under the linear electric field is

$$CF_{SCR\_LEF} = \left(\frac{x'}{W}\right)^{\frac{W}{\kappa}} \tag{18}$$

And if you integrate throughout x (replacing x' into W-x) and use gamma function (Γ),

$$IQE_{drift\_LEF} = -\int_{W}^{0} \alpha e^{-\alpha(W-x')} \cdot \left(\frac{W-x'}{W}\right)^{\frac{W}{\kappa}} dx' = -\frac{\Gamma(1+\frac{W}{\kappa},\ -\alpha(x-W))}{\alpha^{\frac{W}{\kappa}} W^{\frac{W}{\kappa}}}\Bigg|_0^W \tag{19}$$

$$IQE_{drift\_LEF} = (\alpha W)^{-\frac{W}{\kappa}} \cdot \Gamma(1+\frac{W}{\kappa},\ \alpha W) \tag{20}$$

For a diffusion component of the photoelectric quantum response, the exact solutions for electron and hole are described [20] for the case of p-layer in a p-n junction, including surface recombination at the back surface CZTSSe absorber. We assume only electron contribution of the absorber layer, considering the hole collection is negligible due to strong compensation with a large number of high p-type compensating defects in CdS [23].

$$IQE_{diff} = \frac{\alpha L_n}{\alpha^2 L_n^2 - 1}\exp(-\alpha W)\cdot \left\{\alpha L_n - \frac{\frac{S_b L_n}{D_n}\left[\cosh\left(\frac{d-W}{L_n}\right) - \exp(-\alpha(d-W))\right] + sinh\left(\frac{d-W}{L_n}\right) + \alpha L_n \exp(\alpha(d-W))}{\frac{S_b L_n}{D_n}\sinh\left(\frac{d-W}{L_n}\right) + \cosh\left(\frac{d-W}{L_n}\right)}\right\} \tag{21}$$

where d is the thickness of the CZTSSe absorber layer and S_b is the recombination velocity at the back surface of the absorber. The sum of drift and diffusion components is the total internal quantum efficiency. The total internal quantum efficiency of the absorber for the constant electric field is the sum of Eqs. (14) and (21), and the IQE for the linear electric field is the sum of Eqs. (20) and (21).

$$IQE_{CEF} = \frac{L_{drift}}{L_{drift} + (1/\alpha)} \cdot \left\{1 - \exp\left(-W \cdot \left(\alpha + \frac{1}{L_{dirft}}\right)\right)\right\} + \frac{\alpha L_n}{\alpha^2 L_n^2 - 1}\exp(-\alpha W)$$
$$\cdot \left\{\alpha L_n - \frac{\frac{S_b L_n}{D_n}\left[\cosh\left(\frac{d-W}{L_n}\right) - \exp(-\alpha(d-W))\right] + sinh\left(\frac{d-W}{L_n}\right) + \alpha L_n \exp(\alpha(d-W))}{\frac{S_b L_n}{D_n}\sinh\left(\frac{d-W}{L_n}\right) + \cosh\left(\frac{d-W}{L_n}\right)}\right\} \tag{22}$$

http://dx.doi.org/10.5772/68058

$$IQE_{LEF} = (\alpha W)^{-\frac{W}{\kappa}} \cdot \Gamma(1+\frac{W}{\kappa},\ \alpha W) + \frac{\alpha L_n}{\alpha^2 L_n^2 - 1}\exp(-\alpha W)\cdot$$
$$\left\{ \alpha L_n - \frac{\frac{S_b L_n}{D_n}\left[\cosh\left(\frac{d-W}{L_n}\right) - \exp(-\alpha(d-W))\right] + sinh\left(\frac{d-W}{L_n}\right) + \alpha L_n \exp(\alpha(d-W))}{\frac{S_b L_n}{D_n}\sinh\left(\frac{d-W}{L_n}\right) + \cosh\left(\frac{d-W}{L_n}\right)} \right\} \tag{23}$$

Consequently, external quantum efficiency is the product of the total internal quantum efficiency, which includes recombination in the space charge region (Eqs. (22) and (23)), recombination at the interface (Eq. (1)), and the optical losses prior to CZTSSe absorption.

$$EQE_{CEF} = (1-R_{ARC})T_{TCO}T_{Buffer}T_{CdS}\cdot$$
$$\left\{\frac{L_{drift}}{L_{drift}+\left(\frac{1}{\alpha}\right)}\cdot\left[1-exp\left(-W\cdot\left(\alpha+\frac{1}{L_{dirft}}\right)\right)\right] + \frac{\alpha L_n}{\alpha^2 L_n^2-1}exp(-\alpha W)\cdot\right.$$
$$\left.\left\{\alpha L_n - \frac{\frac{S_b L_n}{D_n}\left[\cosh\left(\frac{d-W}{L_n}\right) - \exp(-\alpha(d-W))\right] + sinh\left(\frac{d-W}{L_n}\right) + \alpha L_n\exp(\alpha(d-W))}{\frac{S_b L_n}{D_n}\sinh\left(\frac{d-W}{L_n}\right) + \cosh\left(\frac{d-W}{L_n}\right)}\right\}\right\}$$
$$\cdot\left(1+\frac{S_{junction}}{\mu_e E_{junction}}\right)^{-1} \tag{24}$$

$$EQE_{LEF} = (1-R_{ARC})T_{TCO}T_{Buffer}T_{CdS}\cdot\left\{(\alpha W)^{-\frac{W}{\kappa}}\cdot\Gamma(1+\frac{W}{\kappa},\ \alpha W) + \frac{\alpha L_n}{\alpha^2 L_n^2-1}\exp(-\alpha W)\cdot\right.$$
$$\left.\left\{\alpha L_n - \frac{\frac{S_b L_n}{D_n}\left[\cosh\left(\frac{d-W}{L_n}\right) - \exp(-\alpha(d-W))\right] + sinh\left(\frac{d-W}{L_n}\right) + \alpha L_n\exp(\alpha(d-W))}{\frac{S_b L_n}{D_n}\sinh\left(\frac{d-W}{L_n}\right) + \cosh\left(\frac{d-W}{L_n}\right)}\right\}\right\}$$
$$\cdot\left(1+\frac{S_{junction}}{\mu_e E_{junction}}\right)^{-1} \tag{25}$$

For the non-uniform field, mathematical expressions are developed with an exponential electric field [26] or two different electric field regions [27, 28]. However, it is argued that including the non-uniform electric field with additional parameter sets only adds confusion with no additional insights [29]. Hence, we will explore the quantum efficiency response with a constant electric field model for our analysis for simplification.

2.4. Impurity concentration and electron lifetime by analytical models

Figure 3 shows the computed spectral responses of the external quantum efficiency, $EQE(\lambda)$ with the impact of the uncompensated acceptor impurity at the n-CdS/p-CZTSSe interface. The absorption coefficient, $\alpha(\lambda)$ was taken from Ref. [28] and the front surface recombination velocity (S_f), the default depletion width is 0.3 μm, and the electron lifetime (τ_n) were 10^3 cm/s and 10^{-9} s [29, 30]. In **Figure 3**, the Q-E shape changes disproportionally with significant red light response reduction >600 nm as the uncompensated impurity concentration changes

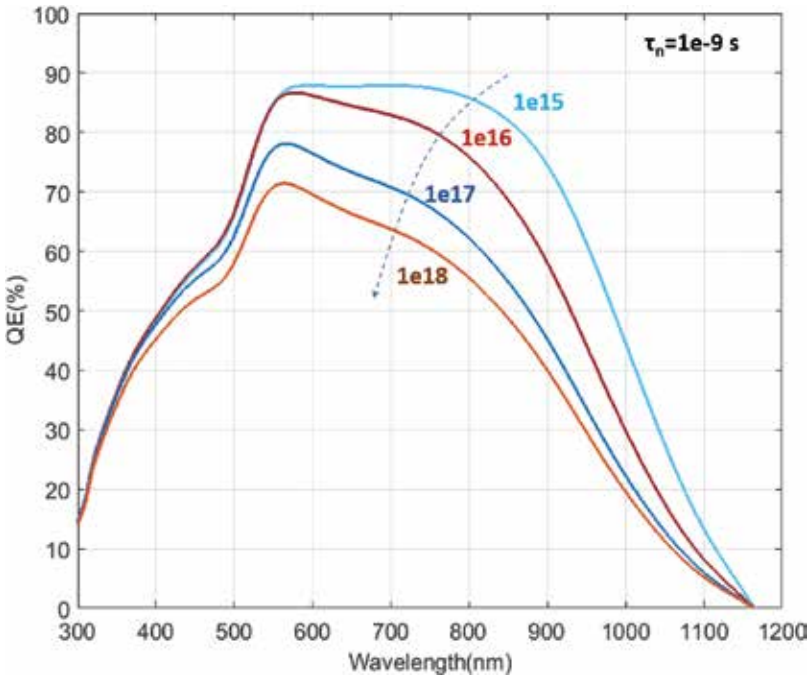

Figure 3. EQE for uncompensated acceptor concentration (N_a–N_d), 10^{15}, 10^{16}, 10^{17}, and 10^{18} cm^{-3}.

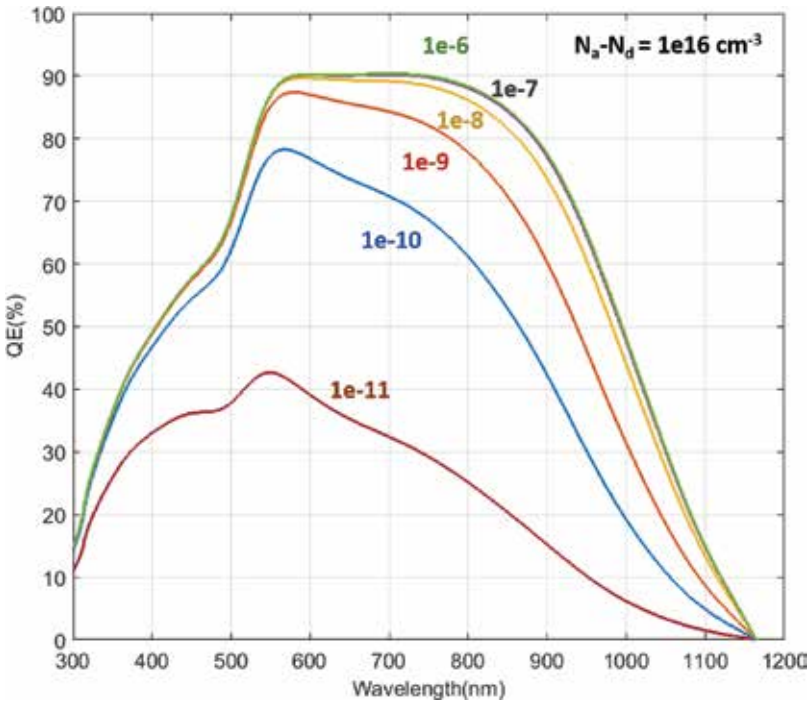

Figure 4. EQE spectra with minority carrier lifetime (τ_n), 10^{-6}, 10^{-7}, 10^{-8}, 10^{-9}, 10^{-10}, and 10^{-11} s.

(N_a–N_d). When the concentration of (N_a–N_d) increases from 10^{15} cm^{-3} to 10^{18} cm^{-3}, the external quantum efficiency decreases. The decrease in EQE(λ) is due to the expansion of the depletion layer, which induces efficient photogenerated minority carrier from the absorber bulk. However, the decrease in photosensitivity between 300 and 500 nm is relatively small, which is mainly influenced by the absorption and recombination of ZnO and CdS. This is also well demonstrated in the Q-E responses with a set of electron lifetime (τ_n) in **Figure 4**, which shows less changes in Q-E between 300 and 500 nm except the extreme case of 10 ps. With the same depletion width by the same uncompensated impurity concentration, electron lifetime that can facilitate an electron to travel throughout the quasi-neutral region to the space charge region can show higher carrier collection and fewer carrier losses in the range from 600 to 900 nm as electron lifetime decreases from 10^{-6} to 10^{-10} s.

2.5. Impact of deletion width by analytical model

In order to provide the losses caused by recombination at the CdS/CZTSSe interface, we now check the spectral response broken into drift and diffusion components in Q-E spectra. **Figure 5** demonstrates the drift component in dashed line and the diffusion component in dash-dotted line as the depletion width increases from 0.1 to 0.9 μm. At the depletion width, 0.9 μm, the photogenerated carrier in the absorber near 600–1000 nm can be efficiently collected mainly via the space charge region by showing the sufficient drift component compared to the weak diffusion component of photogenerated current. However, once the depletion width decreases

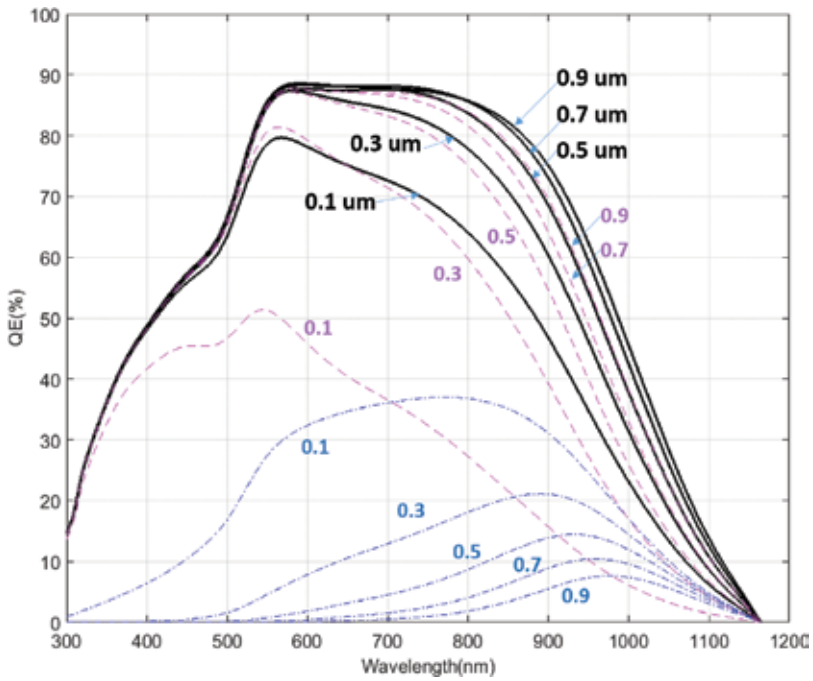

Figure 5. EQE spectra with the depletion width, 0.1, 0.3, 0.5, 0.7, and 0.9 μm broken into the diffusion and drift components. The total EQE (black) is a sum of the diffusion component (blue) and the drift component (magenta).

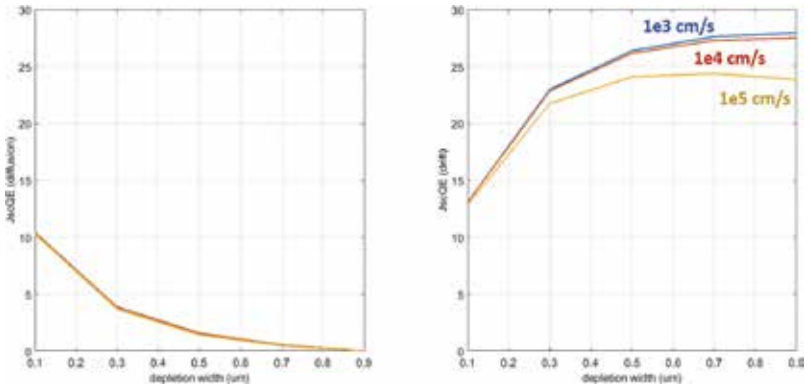

Figure 6. JscQE (drift) and JscQE (diffusion) under the standard AM 1.5 solar radiation (1 sun, 100 mW/cm^2) under different front surface recombination velocities (10^3, 10^4, and 10^5 cm/s).

from 0.9 μm, the drift component begins to weaken in the CZTSSe absorber in 600–1000 nm and the diffusion component increases. At the depletion width, 0.1 μm, the contribution to the carrier collection by drift component is almost equivalent to that of the diffusion component. Based on the calculation of Q-E spectra about each drift and diffusion component, **Figure 6** shows the drift current short circuit current component, JscQE (drift) and the diffusion short circuit current component, JscQE (diffusion) under the standard AM 1.5 solar radiation (1 sun, 100 mW/cm^2) under different front surface recombination velocities (10^3, 10^4, 10^5 cm/s). As *Sf* increases, there are no noticeable changes in the diffusion component whereas the drift component decreases faster.

3. Comparison with modeling and simulation of CZTSSe devices

In this section, we investigate quantum efficiency by utilizing SCAPS simulator (Solar Cell Capacitance Simulator) version 3.2.01 to computationally model the quantum efficiency response of current CZTSSe thin-film solar cells. This will also provide the proper interpretation of device behaviors when it is measured by quantum efficiency. In particular, we focus on the influence of near-interface defect states on quantum efficiency at particular bias conditions with the intention of evaluating peculiar quantum efficiency responses by defect distributions with adjusting 1D numerical parameters in this work.

Each material parameter as an input includes thickness, relative permittivity, electron mobility, hole mobility, acceptor concentration, donor concentration, band gap, and effective density of states. The simulated device structure of CZTSSe thin-film solar cell is with ZnO window layer, CdS buffer, CZTSSe absorber, and Molybdenum (Mo) back contact. In intrinsic defects in the CZTSSe bulk, we updated the parameter sets from the analytical description to reflect the real situation to understand the general trend by interface defect states. Parameters used for this device structures are listed in **Table 1**. Considering the complexity of interface defects at absorber/back contact, absorber/buffer, and buffer/window, we adopted the basic input parameters from the literature, theories, or reasonable estimates [12, 28, 31]. In reality, there is a significant amount of intrinsic bulk defects with different charge states in the CZTSSe

Parameters	Symbol (unit)	ZnO	CdS	CZTSSe
Thickness	d (nm)	200	50	2500
Band gap	Eg (eV)	3.3	2.4	1.2–1.3
Electron affinity	χ (eV)	4.4	4.2	4.1
Relative permittivity	ϵ/ϵ_r	9	10	10
Effective density of state (CB)	N_C (10^{18} cm^{-3})	2.2	2.2	2.2
Effective density of state (VB)	N_V (10^{19} cm^{-3})	1.8	1.8	1.8
Electron thermal velocity	v_n (10^7 cm/s)	1.0	1.0	1.0
Hole thermal velocity	v_p (10^7 cm/s)	1.0	1.0	1.0
Electron mobility	μ_n (cm^2/V-s)	100	100	100
Hole mobility	μ_p (cm^2/V-s)	25	25	25
Donor concentration	N_D (10^{17} cm^{-3})	10.0	1.0	0
Acceptor concentration	N_A (10^{14} cm^{-3})	0	0	2.0
Bulk defect type	a, d, n	d	a	d/a/n
Bulk defect concentration	N_t (10^{14} cm^{-3})	10,000	100	1/1/5

Types of defect are: a, acceptor; d, donor; n, neutral.

Table 1. Parameters set used in this work.

absorber layer as well as ZnO, CdS layers. To introduce different amounts of intrinsic defects in the CZTSSe bulk, we updated the parameter sets from the analytical description to reflect the real situation to understand the general trend by interface defect states. Parameters used for this device structure are listed in **Table 1**. Considering the complexity of interface defects at absorber/back contact, absorber/buffer, and buffer/window, we adopted the basic input parameters from the literature, theories, or reasonable estimates [31–36].

3.1. Interface trap-free case

In the first step, the numerical simulations of both current-voltage (I-V) and quantum efficiency (Q-E) characteristics have been carried out without traps near the heterojunction interface. The default illumination spectrum and operation temperature are set to the standard AM 1.5 condition and 300 K, respectively. A typical result of the I-V curve simulated for a CZTSSe solar cell without heterojunction defects is demonstrated in **Figure 7(a)**. As expected, we observed an ideal steep I-V curve with conversion efficiency, 15.3% with emphasis on higher *Voc* (661 mV) and FF (72.5%) than any reported experimental *Voc* and FF justifying the assumption of an intrinsic defect-free interface.

The simulated I-V curve in **Figure 7** shows the dramatic improvement of *Voc* with nearly zero conductance (<2.6 mS/cm^2) at short circuit condition (in other words, a slope of I-V curve at zero bias) which can be explained by the alleviated recombination and the improved carrier collection with the associated depletion width change. In particular, the reduced recombination can lower the total forward diode current by showing the ideal slope at the short circuit current

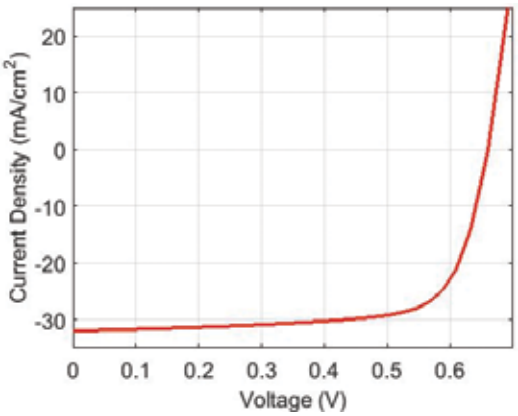

Figure 7. I-V of ideal CZTSSe solar cells without interface defects with efficiency (15.3%), Voc (661 mV), FF (72.5%), and Jsc (32.0 mA/cm^2).

condition [25]. With an ideal device having no near-interface defects in the simulation, an ideal uniform absorber setting keeps the shape and the ratio of the quantum efficiency curves, (H(V)/H(−1 V)) under biases since the shape of the curves in quantum efficiency depends on wavelength and is almost independent of bias voltage [20]. One way to confirm the uniformity of reduced carrier collection at each wavelength region is to compare carrier collection at each bias with full collection by applying negative bias, for example, −1 V [20]. In **Figures 8** and **9**, each quantum efficiency at different biases is normalized by dividing with the quantum efficiency at −1 V. The normalized Q-E (QE(V)/QE(−1 V)) shows two features by comparing each bias-dependent quantum efficiency. First, wavelength-dependent quantum efficiency drop is observed regardless of bias level. Secondly, the shape of each normalized quantum efficiency curve is kept almost the same. In other words, a nearly uniform collapse of quantum efficiency over a wide range of wavelength is demonstrated with the trend of increasing absorber collection loss due to reduced depletion width by applied biases at region 2 (500–800 nm) and region 3 (800–1033 nm).

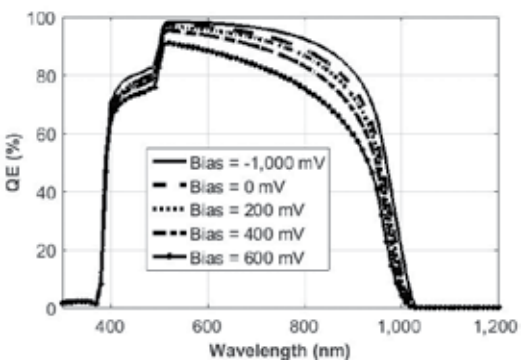

Figure 8. Q-E of ideal CZTSSe solar cells without interface defects at bias conditions (−1.0, 0.0, 0.2, 0.4, and 0.6 V).

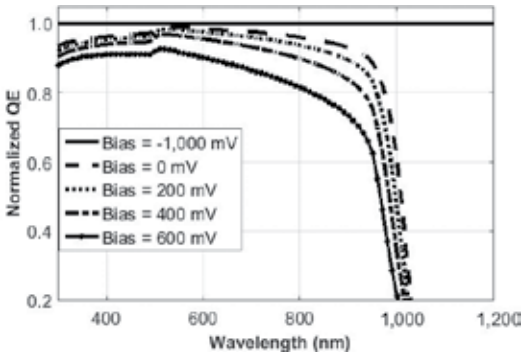

Figure 9. Normalized Q-E of ideal CZTSSe solar cells (QE(V)/QE(−1 V)) at bias conditions (−1.0, 0.0, 0.2, 0.4, and 0.6 V).

3.2. Interface and near-interface defect states case

Before discussing the simulated results, it is worth describing the systematic trends affected by varying the interface defect parameters for the different types of defects. First, we consider acceptor- and donor-type defects near both conduction and valence bands as well as mid-gap. In SCAPS simulation, we can introduce three different parameter sets of interface defects for both acceptor and donor types that significantly affect the performance of the device (capture cross sections, defect energy level: E_t, defect density). However, real CZTSSe cells consist of complex multilayers, which form defects and/or defect compounds at the surface of CZTSSe layer, next to the CdS buffer layer. Furthermore, the direct measurement of this layer's electronic properties is difficult to be separated from other layers' electronic properties which are exacerbated by complicated window structures with CdS, ZnO, and TCO layer interdiffusion. To avoid the complexity of modeling, we focus on numerical modeling of electronic properties, in particular, quantum efficiency by introducing a thin defective interface layer between CdS and absorber.

3.2.1. Trend by defect distribution and concentration

In the first step, numerical simulations have been carried out with a set of defect concentrations within a defective interface layer. To be consistent with the reported literature, theories, or reasonable estimates, capture cross sections are fixed at 1.0×10^{-12} cm^2 for electrons and 1.0×10^{-15} cm^2 for holes at donor-type defect and at 1.0×10^{-15} cm^2 for electrons and 1.0×10^{-12} cm^2 for acceptor-type defect [12, 28–31, 33–37]. For a comparative study of the ideal device in the previous section, the device structure is updated with very thin (5 nm) defective interface layer between CdS and CZTSSe. Input parameters are set to the same as those of CdS buffer except thickness and doping densities which are set to the same values of 1.0×10^{14} cm^{-3} for donor and acceptor assuming the intermixing of n-type dopant (CdS) and p-type dopant (CZTSSe).

Figure 10 shows the simulated quantum efficiency with an inserted defective interface layer between CZTSSe and CdS buffer layers as a function of defect concentration. As we begin with defect density 1.0×10^{15} cm^{-3} in this thin layer as deep acceptor-type bulk defect which is different from donor-like interface trap (as in the conventional Si model), we located this type of defect between 0.9 and 1.5 eV above the top of the valence band around the mid-gap (1.2 eV).

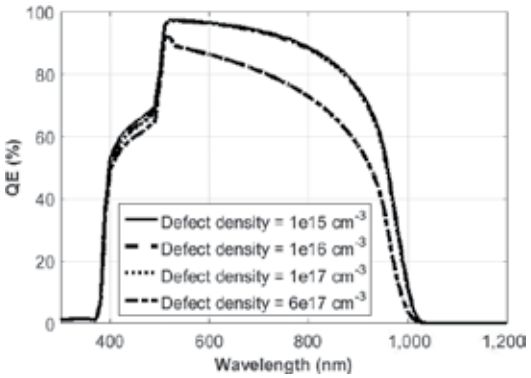

Figure 10. Q-E of CZTSSe device with the inserted interface defective layer between CdS and CZTSSe, varying acceptor-type defect density from 1.0×10^{15} to 6.0×10^{17} cm^{-3}.

As defect concentration increases until 1.0×10^{17} cm^{-3} no specific collection loss at particular regions is observed. However, once defect concentration increases more than 6.0×10^{17} cm^{-3}, serious collection loss at the absorber is demonstrated in regions 2 (500–800 nm) and 3 (800–1033 nm). In region 1 (300–500 nm), there is not much collection loss while slight inflection of collection occurs near 500 nm.

3.2.2. Impact by deep acceptor-type defect distribution

Based on the findings above, defect concentration is set at 6.0×10^{17} cm^{-3} as deep acceptor-type defects, 0.9 eV below and above from the bottom of the conduction band and top of the valence band, respectively. Consequently, the results of the simulated biased quantum efficiency are demonstrated in **Figure 11**. Beginning at −1 V (not shown), quantum efficiency over all wavelength regions shows similar spectral response compared to that of the device without defects in **Figure 8**. Once bias increases up to 0 V, absorber loss slightly increases as mentioned in **Figure 8**. As expected, this reduction in quantum efficiency is caused by the decrease of the depletion layer. However, as bias increases up to 0.2 V, the stronger drop of Q-E spectrum happens at both < 500 nm and > 550 nm disproportionately. Conversely, the reduction of quantum efficiency between 500–550 nm is less severe that the other regions. This peculiar Q-E response occurs with a peak near 520–530 nm (in other words, near blue light region), reported at their measurements in Refs. [12, 37].

Apparently, the reduction in $\lambda < 400$ nm, which is relatively non-sensitive, is due to absorption by the CdS layer and the transparent conducting oxide/substrate. In the spectral region, < 500 nm, the absorption by CdS at 0.2 V is slightly decreased due to the smaller photocurrent contribution and adjustment of space charge region of window layer under the presence of strongest electric field at the heterojunction. On the other hand, the intensified quantum efficiency drop in <500 nm and distinctively >550 nm looks interesting. When it comes to describing the bias-dependent quantum efficiency, the Gartner model describes the photogenerated carrier collection with the bias-dependent depletion width (Eq. (6)) and diffusion length, which describes the exact expression (Eq. (21)) as we discussed in the previous section [20, 36].

http://dx.doi.org/10.5772/68058

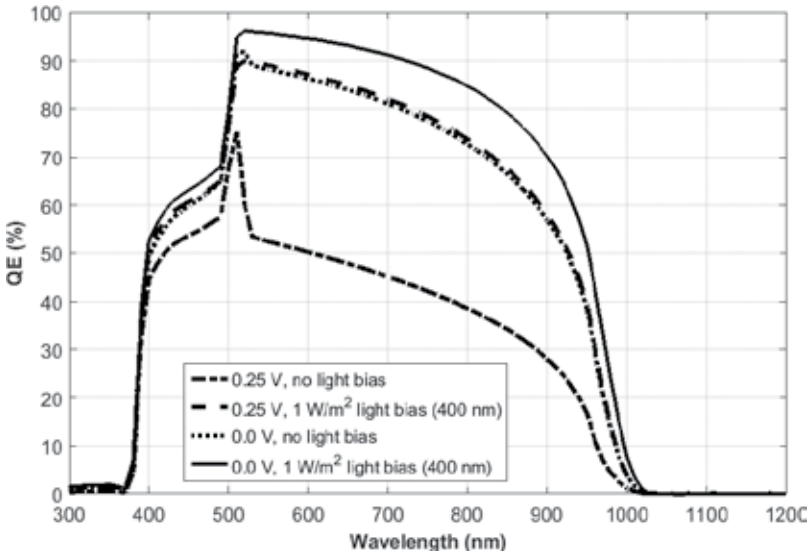

Figure 11. Light-biased (1 mW/cm^2, 0.01 sun at 400 nm) Q-E of CZTSSe solar cell with the defective interface layer at 0 and 0.25 V.

With the given depletion width (W_d), diffusion length (L_n), absorber thickness (d), and surface recombination velocity (S_n), the exact expression predicts the trend of spectral response in thin-film solar cells under the presence of voltage and, in particular, quantum efficiency response for an ideal device. However, the exact model or the Hecht-like equation in Ref. [29] is solely dependent on the depletion width (or applied bias) and diffusion length. Under applied voltage biases compared to the full collection, the analytical quantum efficiency analysis is unable to demonstrate the intensified reduction at both <500 nm and >550 nm but it rather provides partial interpretation of the quantum efficiency with the above equations by keeping a similar shape of curves. Hence, analytical expressions do not represent the peculiar Q-E response near 520–530 nm over other wavelength regions from our simulation.

However, the intensified drop in both <500 nm and distinctively >550 nm can be explained by assuming deep acceptor-type defects near the heterojunction interface layer. In this interface layer, a higher concentration of deep ionized-acceptor (negative charge) type defects 0.3 eV above and below the mid-gap impacts the electric field and hence the space charge region of absorber toward the back contact. These deep acceptor-type defects induce electronic doping at room temperature by trapping holes from the valence band, which eventually lower the band bending of the CdS/CZTSSe interface layer upon additional blue light. In other words, higher electric field near the heterojunction interface increases absorption by a part of the absorber toward CdS and near-CdS layer, whereas it reduces absorption by the majority of CZTSSe absorber toward the back contact. This reduced depletion width by higher interface defects can be deteriorated by increased biases such as 0.2 and 0.25 V, which furthers the depletion width decrease. One way to confirm depletion width reduction induced by CdS/absorber interface defects is to apply weak blue light bias (400 nm) and observe spectral

response at >550 nm in quantum efficiency. Using this model, weak light bias (1 mW/cm^2, 0.01 sun) is applied to the same device at 0 and 0.25 V in **Figure 11**. Weak blue light bias onto window and buffer layers almost fully recovers CZTSSe absorber carrier collection even at 0.25 V. After filtering out noises in the regions of <400 and >1000 nm, light-biased Q-E is normalized by dividing with the standard no-light-biased Q-E in **Figure 12**. This clearly indicates that weak blue light bias intensifies the carrier collection of absorber in regions 2 and 3 (>550 nm) at both 0 and 0.25 V, whereas minimal increases are shown in region 1 (<500 nm). At 0.25 V, the depletion width of CZTSSe absorber without light bias is narrower than that with weak blue light bias. Hence, weak light bias activates hole trapping through deep acceptor-type defects and near-interface defects between 0.9 and 1.5 eV and recovers the depletion width.

The presence of ionized deep acceptor-type bulk defects (0.9–1.5 eV) in the defective interface layer can effectively decrease the depletion width near the heterojunction interface by increasing negative charge density (**Figure 13**), which could only be activated by weak bias light via hole charge trapping. The band diagram and carrier density of holes and electrons indicate

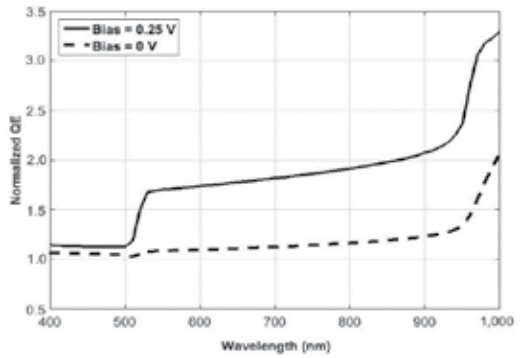

Figure 12. Light bias-dependent normalization of Q-E (Q-E at blue light bias divided by Q-E at no light bias) illustrating weak blue light bias (400 nm).

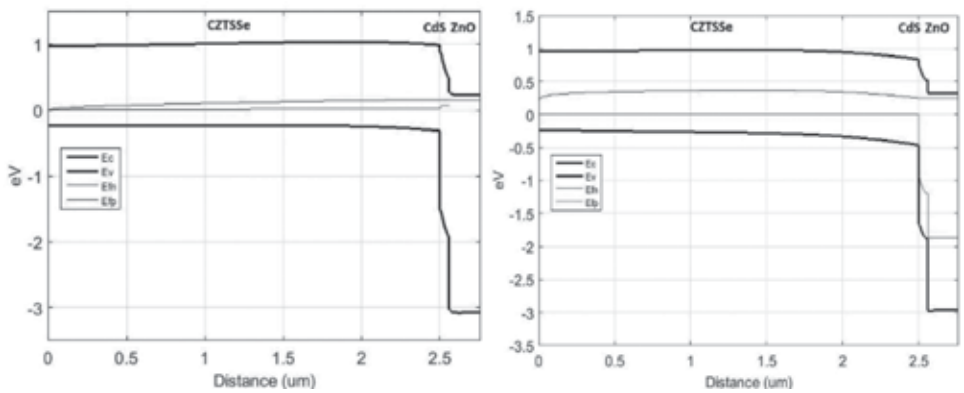

Figure 13. Band diagram without light bias at 0.25 V (left) and with light bias at 0.25 V (right), showing larger depletion width.

higher electric field with less hole concentration at the interface, resulting in smaller depletion width in the presence of the defective interface layer in **Figure 13**.

4. Summary

The spectral response of CZTSSe thin-film solar cells has been modeled analytically and numerically with simulation study under a set of different parameters and biased conditions about efficiency-limiting factors through quantum efficiency. The analytical model describes the drift and diffusion photocurrent components to reflect the recombination losses in the space charge region and near the CdS/CZTSSe heterojunction interface. The trend that we found about the uncompensated impurity concentration, minority carrier lifetime, surface recombination velocity, and the depletion width shows qualitatively good agreement with the reported data in the literature. Furthermore, the simulations address the role of interface and near-interface defects for the spectral response of thin-film solar cells. For this simulation study, it is assumed that deep acceptor-type near-heterojunction interface defects from 0.9 to 1.5 eV above the top of the valence band are difficult to increase the depletion width, which provide additional electronic doping in space charge region. These ionized acceptor-type defects at room temperature can trap holes from the valence band only activated by additional bias light and reduce the effective doping concentration at the heterojunction interface. Consequently, these deep acceptor-type defects cramp the depletion width and hence, weaker spectral responses near red and IR regions. This trend is intensified with biased quantum efficiency conditions. The findings of this work give further insight into the issues and provide some requirements on the parameter sets of the CZTSSe absorber layer as well as the CdS/CZTSSe heterojunction interface layer, which shows fairly good agreement with numerical calculation and reported experimental results.

Author details

Sanghyun Lee[1]* and Kent J. Price[2]

*Address all correspondence to: sanghyun.lee0304@gmail.com

1 School of Engineering and Information Systems, Morehead State University, Morehead, KY, USA

2 Department of Physics, Morehead State University, Morehead, KY, USA

References

[1] W. Wang, M.T. Winkler, O. Gunawan, T. Gokmen, T.K. Todorov, Y. Zhu, D.B. Mitzi. Device characteristics of CZTSSe thin-film solar cells with 12.6 % efficiency. Adv. Energy Mater. 2014;**4**:1301465.

[2] D. Mitzi, T. Todorov, K. Wang, S. Gunha. The path towards a high-performance solution-processed kesterite solar cell. Sol. Energy Mater. Sol. Cells. 2011;**95**:1421–1436.

[3] Y. Kumar, G. Babu, P. Bhaskar, V. Raja. Preparation and characterization of spray-deposited Cu_2ZnSnS_4 thin films. Sol. Energy Mater. Sol. Cells. 2009;**93**:1230–1237.

[4] C.P. Chan, H. Lam, C. Surya. Preparation of Cu_2ZnSnS_2 films by electrodeposition using ionic liquids. Sol. Energy Mater. Sol. Cells. 2010;**94**:207–211.

[5] H. Katagiri, K. Jimbo, S. Yamada, T. Kamimura, W.S. Maw, T. Fukano, T. Ito, T. Motohiro. Detailed balance limit of efficiency of p-n junction solar cells. Appl. Phys. Express. 2008;**1**:41201.

[6] M. Paranthaman, W. Wong-Ng, R. Bhattacharya, editors. Semiconductor materials for solar photovoltaic cells (1st ed.). Springer International Publishing, Switzerland; 2016. doi:10.1007/978-3-319-20331-7_2.

[7] P. Jackson, D. Hariskos, R. Wuerz, W. Wischmann, M. Powalla. Compositional investigation of potassium doped $CuInGaSe_2$ solar cells with efficiencies up to 20.8 %. Phys. Stat. Sol. RRL. 2014;**8**:219–222.

[8] W. Shockley, H.K. Queisser. Detailed balance limit of efficiency of p-n junction solar cells. Jpn. J. Appl. Phys. 1961;**32**:510–519.

[9] G. Lucovsky, S. Lee, J.P. Long, H. Seo, J. Luning. Interfacial transition regions at germanium/Hf oxide based dielectric interfaces: qualitative differences between non-crystalline Hf Si oxynitride and nanocrystalline HfO2 gate stacks. Microelectron. Eng. 2009;**86**(3):224–234.

[10] J. Moore, C. Hages, R. Agrawal, M. Lundstrom. The importance of band tail recombination on current collection and open-circuit voltage in CZTSSe solar cells. Appl. Phys. Lett. 2016;**109**:021102.

[11] T. Gokmen, O. Gunawan, T. Todorov, D. Mitzi. Band tailing and efficiency limitation in kesterite solar cells. Appl. Phys. Lett. 2013;**103**:103506.

[12] T. Gokmen, O. Gunawan, D.B. Mitzi. Semi-empirical device model for $Cu_2ZnSn(S,Se)_4$. Appl. Phys. Lett. 2014;**105**:033903.

[13] J. Moore, C. Hages, N. Carter, R. Agrawal, J. Gray, M. Lundstrom. Current–voltage analysis of band tail effects in CZTSSe through numerical simulation. 2015 IEEE 42nd Photovoltaic Specialist Conference (PVSC). 2015.

[14] D. Mitzi, O. Gunawan, T. Todorov, D. Barkhouse. Preparation of Cu_2ZnSnS_4 films by electrodeposition using ionic liquids. Phil. Trans. R. Soc. A. 2013;**371**(20110432):1–22.

[15] O. Simya, A. Mahaboobbatcha, K. Balachander. A comparative study on the performance of Kesterite based thin film solar cells using SCAPS simulation program. Superlatt. Microstruct. 2015;**82**:248–261.

[16] T. Jager, Y. Romanyuk, B. Bissig, F. Pianezzi, S. Nishiwaki, P. Reinhard, J. Steinhauser, J. Schwenk, A. Tiwari. Improved open-circuit voltage in $Cu(In,Ga)Se_2$ solar cells with high work function transparent electrodes. J. Appl. Phys. 2015;**117**:225303.

[17] F.-J. Haug, R. Biron, G. Kratzer, F. Leresche, J. Besuchet, C. Ballif, M. Dissel, S. Kretschmer, W. Soppe, P. Lippens, K. Leitner. Improvement of the open circuit voltage by modifying the transparent indium-tin oxide front electrode in amorphous n-i-p solar cells. Prog. Photo. 2012;**20**(6):727–734.

[18] S. Hegedus, W. Shafarman. Thin-film solar cells: device measurements. Prog. Photovolt. Res. Appl. 2004;**12**(2–3):155–176. doi:10.1002/pip.518.

[19] C. Hages, N. Carter, R. Agrawal, T. Unold. Generalized current–voltage analysis and efficiency limitations in non-ideal solar cells: case of $Cu_2ZnSn(S_xSe_{1-x})_4$ and $Cu_2Zn(Sn_yGe_{1-y})(S_xSe_{1-x})_4$. J. Appl. Phys. 2014;**115**:234504.

[20] S. Sze, K. Ng. Physics of semiconductor devices (3rd.). New York: John Wiley & Sons; 2007.

[21] W. Gartner. Depletion-layer photoeffects in semiconductors. Phys. Rev. 1959;**116**:84–87.

[22] M. Lavagna, J.P. Pique, Y. Marfaing. Theoretical analysis of the quantum photoelectric yield in Schottky diode. Solid State Electron. 1977;**20**:235–240.

[23] L.A. Kosyachenko. Problems of efficiency of photoelectric conversion in thin-film CdS/CdTe solar cells. Semiconductors. 2006;**40**(6):710–727.

[24] M. Hadrich, H. Metzner, U. Reislohner, C. Kraft. Modelling the quantum efficiency of cadmium telluride solar cells. Sol. Energy Mater. Sol. Cells. 2011;**95**:887–893.

[25] A.L. Fahrenbruch, R.H. Bube. Fundamentals of solar cells: photovoltaic solar energy conversion (1st ed.). Academic Press, New York; 1983.

[26] A. Nakane, H. Tampo, M. Tamakoshi, S. Fujimoto, K.M. Kim, S. Kim, H. Shibata, S. Niki, H. Fukiwara. Quantitative determination of optical and recombination losses in thin-film photovoltaic devices based on external quantum efficiency analysis. J. Appl. Phys. 2016;**120**(6):064505. doi:10.1063/1.4960698.

[27] K. Misiakos, F. Lindholm. Analytical and numerical modelling of amorphous silicon p-i-n solar cells. J. Appl. Phys. 1988;**64**:383.

[28] V. Chu, J. Conde, D. Shen, S. Wagner. Photocurrent collection in a Schottky barrier on an amorphous silicon-germanium alloy structure with 1.23 eV optical gap. Appl. Phys. Lett. 1989;**55**:262.

[29] S. Hegedus, D. Desai, C. Thompson. Voltage dependent photocurrent collection in CdTe/CdS solar cells. Prog. Photovolt. Res. Appl. 2007;**15**:587–602.

[30] A. Pu, F. Ma, C. Yan, J. Huang, K. Sun, M. Green, X. Hao. Sentaurus modelling of 6.9% Cu_2ZnSnS_4 device based on comprehensive electrical & optical characterization. Sol. Energy Mater. Sol. Cells. 2017;**160**:372–381. doi:10.1016/j.solmat.2016.10.053.

[31] O. Gunawan, T.K. Todorov, D.B. Mitzi. Loss mechanisms in hydrazine-processed $Cu_2ZnSn(Se,S)_4$ solar cells. Appl. Phys. Lett. 2010;**97**:233506.

[32] P. Viktorovich, G. Moddel, J. Blake, W. Paul. Carrier-collection efficiencies in amorphous hydrogenated silicon Schottky-barrier solar cells. J. Appl. Phys. 1981;**52**:6203.

[33] W. Zhao, W. Zhou, X. Miao. Numerical simulation of CZTS thin film solar cell. In 7th IEEE International Conference on Nano/Micro Engineered and Molecular Systems, 2012, pp. 502–505.

[34] T. Gokmen, O. Gunawan, D.B. Mitzi. Modelling polycrystalline semiconductor solar cells. Thin Solid Films. 2000;**361–362**(033903):527–532.

[35] A. Polizzott, I.L. Repins, R. Noufi, S-Hi We, D.B. Mitzi. The state and future prospects of kesterite photovoltaics. Energy Environ. Sci. 2013;**6**:3171–3182.

[36] R.D. Rugescu, L. Kosyachenko. Solar energy (1st ed.). InTech, Croatia; 2010, pp. 105–130.

[37] G. Brammertz, S. Oueslati, M. Buffiere, J. Bekaert, H.E. Anzeery, K.B. Messaoud, S. Sahayarj, T. Nuytten, C. Koble, M. Meuris, J. Poortmans. Investigation of properties limiting efficiency in $Cu_2ZnSn(S,Se)_4$-based solar cells. IEEE J. Photovolt. 2015;**527–532** (5):649–655.

Edited by Sergei L. Pyshkin and John Ballato

Optoelectronics - Advanced Device Structures (Book IV) is following the Optoelectronics (Books I, II, and III) published in 2011, 2013, and 2015, as part of the InTech collection of international works on optoelectronics. Accordingly, as with the first three books of the collection, this book covers recent achievements by specialists around the world. The growing number of countries participating in this endeavor as well as joint participation of the US and Moldova scientists in edition of this book testifies to the unifying effect of science. An interested reader will find in the book the description of properties and applications employing organic and inorganic materials, as well as the methods of fabrication and analysis of operation and regions of application of modern optoelectronic devices.

ISBN 978-953-51-4744-2

Photo by Milanares / iStock

IntechOpen